JOURNAL OF THE ELECTROCHEMICAL SOCIETY

LECTROCHEMICAL
CIENCE AND TECHNOLOGY

OLID-STATE
CIENCE AND TECHNOLOGY

EVIEWS AND NEWS

VOL. 122, NO. 7 JULY 1975

JESOAN 122 (7) 845-1004, 193C-220C

FUTURE MEETINGS
Of The Electrochemical Society

DALLAS, TEXAS—OCTOBER 5, 6, 7, 8, 9 & 10, 1975

Headquarters at the Sheraton Dallas Hotel

Planned symposia for the Dallas Meeting include the following Divisions and subjects:

Battery—Leclanché Cells, Nonaqueous Cells, General Session; **Corrosion**—Repassivation Kinetics, General Session; **Corrosion and Electrodeposition**—Electrodeposition of Organic Coatings; **Corrosion, Electronics, Electrothermics and Metallurgy, and Dielectrics and Insulation**—Techniques for Surface and Thin-Film Analysis and Depth Profiling; **Dielectrics and Insulation**—Dielectric Materials for Hybrid and Thin-Film Circuits, Thermal and Photostimulated Current in Insulators, General Session; **Dielectrics and Insulation and Electronics**—Recent Developments in MOS Technology; **Electrodeposition**—General Session; **Electronics**—Electrochemical Techniques for Electronic Device Fabrication, Semiconductor General Session, Materials and Processes General Session; **Electrothermics and Metallurgy**—High Temperature Processes Induced in Materials by the Absorption of Radiation, General Session; **Electrothermics and Metallurgy and Electronics**—Liquid Phase and Molecular Beam Epitaxy: Electronic and Magnetic Materials; **New Technology Subcommittee and Electrothermics and Metallurgy**—Energy Storage.

WASHINGTON, D.C.—MAY 2, 3, 4, 5, 6 & 7, 1976

Headquarters at the Sheraton Park Hotel

Planned symposia for the Washington Meeting include the following Divisions and subjects:

Battery and Electronics—Materials for Batteries and Fuel Cells; **Corrosion**—Magnetohydrodynamics, General Session; **Dielectrics and Insulation**—Dielectrics for Image and Hologram Storage and Display Devices, Refractory Materials for Display Devices, General Session; **Dielectrics and Insulation and Electronics**—Etching of Dielectrics and Insulators; **Dielectrics and Insulation, Electronics, and Electrothermics and Metallurgy**—Control and Utilization of Defects in Solids; **Electronics**—Semiconductor General Session, Surface Properties of Phosphors and Photoconductors, Luminescence General Session, Materials and Processes General Session; **Electronics and Electrothermics and Metallurgy**—International Symposium on Solar Energy, Seventh International Conference on Electron and Ion Beam Science and Technology; **Electrothermics and Metallurgy and Industrial Electrolytic**—Electrochemical Extraction Processes; **Industrial Electrolytic**—Engineering Analysis and Scale-Up of Electrochemical Systems; **Industrial Electrolytic and Organic and Biological Electrochemistry**—Industrial Electro-Organic Processes; **Physical Electrochemistry**—Spectroscopic Methods in Electrochemical Studies, General Session; **New Technology Subcommittee and Corrosion**—Corrosion in Molten Salts.

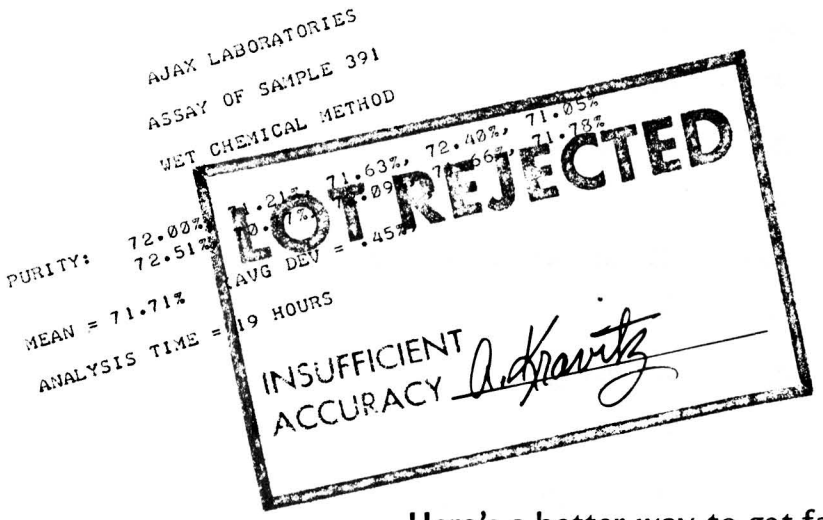
LAS VEGAS, NEVADA—OCTOBER 17, 18, 19, 20, 21 & 22, 1976

Headquarters at the Caesar's Palace Hotel

Planned symposia for the Las Vegas Meeting include the following Divisions and subjects:

Battery—Low Maintenance and Maintenance-Free Lead-Acid Batteries, Porous Electrodes, Theory and Practice, General Session; **Corrosion**—Corrosion in Scrubber Systems, Corrosion Problems in Geothermal Energy Systems, General Session; **Corrosion and Electrothermics and Metallurgy**—Properties of High Temperature Alloys; **Dielectrics and Insulation and Electronics**—Dielectrics and Semiconductors on Insulating Electronic Materials and Devices for Storage and Display; **Dielectrics and Insulation, Electronics, and Electrothermics and Metallurgy**—The Chemistry and Crystallography of Chemical Vapor Deposition of Electronic Materials; **Electrodeposition**—General Session; **Electrodeposition and Industrial Electrolytic**—High Current Density Electrode Processes; **Electronics**—LED's Mechanisms and Injection Lasers: Process Technology and Degradation, Semiconductor General Session, Materials and Structures for Integrated Optical Networks, Materials and Processes General Session; **Electrothermics and Metallurgy**—High Temperature Processes of Geological Interest; **New Technology Subcommittee**—Power Conditioning and Power Transport.

are you getting the accuracy you need for the time you're putting in?



Here's a better way to get fast, accurate, precise assays of copper, silver, gold, rhodium, uranium and other precious metals.

When it's accuracy that counts, and you don't have all day (and night) to do the work, controlled potential coulometry can help. Often a complete assay can be completed in less than 10 minutes to an accuracy better than 0.1% and a precision of 0.05%.

The Princeton Applied Research Model 380 Controlled Potential Coulometry System provides all the hardware and glassware required for this valuable technique. All you provide is the sample to be analyzed. You can forget about time-consuming tasks like calibration curves, preparation of standards, end-point detectors and the like. The digital readout of the coulometer provides an absolute measure of the sample content.

AJAX LABORATORIES

ASSAY OF SAMPLE 391

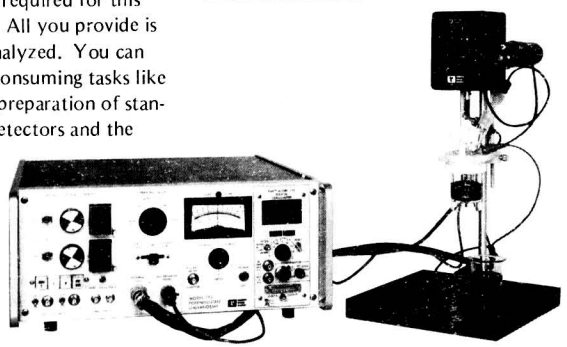
CONTROLLED POTENTIAL COULOMETRY

PURITY: 71.92%, 71.82%, 71.76%, 71.72%, 71.93%
71.72%, 71.66%, 71.88%, 71.84%, 71.86%

MEAN = 71.81% (AVG DEV = .08%)

ANALYSIS TIME = 54 MINUTES

OK.



Now that there is an accurate, viable alternative to the complex procedures used for precious metal assays, you owe it to yourself to investigate the advantages of the Model 380 System.

To help your investigation we'd be delighted to send you our Application Notes on how a 380 System can do copper, silver and gold assays. Write Princeton Applied Research Corporation, P. O. Box 2565, Princeton, New Jersey 08540, or telephone 609/452-2111 and we'll provide you with the solutions to your problems. In Europe, contact Princeton Applied Research GmbH, D8034 Unterpfaffenhofen, Waldstrasse 2, West Germany.

PRINCETON APPLIED RESEARCH

274

THE ELECTROCHEMICAL SOCIETY BOOKS IN PRINT

Monograph Series

The following hardbound volumes are sponsored by The Electrochemical Society, Inc. and published by John Wiley & Sons, Inc., 605 Third Avenue, New York, N.Y. 10016. Members of the Society can receive a 33% discount by ordering from Society Headquarters. Books and invoice are mailed by publisher. Nonmembers (including subscribers) must order direct from the publisher. All prices subject to change without notice.

Corrosion Handbook, edited by Herbert H. Uhlig (1948). 1188 pages, **$30.25.**

Electrochemistry in Biology and Medicine, edited by Theodore Shedlovsky (1955). 369 pages, **$15.25.**

Arcs in Inert Atmospheres and Vacuum, edited by W. E. Kuhn. A 1956 Spring Symposium (1956). 188 pages, **$10.75.**

Ultrafine Particles, William E. Kuhn, Editor-in-Chief (1963). 561 pages, **$20.50.**

First International Conference on Electron and Ion Beam Science and Technology, edited by R. Bakish (1965). 945 pages, **$27.95.**

Chemical Physics of Ionic Solutions, edited by B. E. Conway and R. G. Barradas. A 1964 Spring Symposium (1966). 622 pages, **$31.00.**

The Electron Microprobe, edited by T. D. McKinley, K. F. J. Heinrich, and D. B. Wittry. A 1964 Fall Symposium (1966). 1035 pages, **$36.25.**

Vapor Deposition, edited by C. F. Powell, J. H. Oxley, and J. M. Blocher, Jr. (1966). 725 pages, **$27.75.**

The Stress Corrosion of Metals, by Hugh I. Logan (1966). 306 pages, **$19.75.**

The Corrosion of Light Metals, by H. P. Godard, W. B. Jepson, M. R. Bothwell, and R. L. Kane (1967). 360 pages, **$17.75.**

High-Temperature Materials and Technology, edited by I. E. Campbell and E. M. Sherwood (1967). 1022 pages, **$36.75.**

Alkaline Storage Batteries, by S. Uno Falk and Alvin J. Salkind (1969). 656 pages, **$36.75.**

The Primary Battery, Volume I, edited by George W. Heise and N. Corey Cahoon (1971). 500 pages, **$30.25.**

Zinc-Silver Oxide Batteries, edited by Arthur Fleischer and John J. Lander (1971). 544 pages, **$31.50.**

The Corrosion of Copper, Tin, and Their Alloys, by Henry Leidheiser, Jr. (1971). 411 pages, **$38.50.**

Corrosion in Nuclear Applications, by W. E. Berry (1971). 572 pages, **$28.00.**

Handbook on Corrosion Testing and Evaluation, edited by W. H. Ailor (1971). 873 pages, **$44.00.**

Modern Electroplating, edited by Frederick A. Lowenheim. Third Edition (1974). 801 pages, **$29.95.**

Society Symposium Series

The following softbound symposium volumes are sponsored and published by The Electrochemical Society, Inc., P.O. Box 2071, Princeton, N.J. 08540. Orders filled at the list price given, subject to availability. Enclose payment with order.

Vacuum Metallurgy. J. M. Blocher, Jr., Editor. A 1954 symposium. 216 pages, **$5.00.**

High-Temperature Metallic Corrosion of Sulfur and Its Compounds. Z. A. Foroulis, Editor. A 1969 symposium. 276 pages, **$4.50.**

Electron and Ion Beam Science and Technology, Fourth International Conference. R. Bakish, Editor. A 1970 symposium. 680 pages, **$7.50.**

Fundamentals of Electrochemical Machining. C. L Faust, Editor. A 1970 symposium. 365 pages, **$4.50.**

Electron and Ion Beam Science and Technology, Fifth International Conference. R. Bakish, Editor. A 1972 symposium. 420 pages, **$5.50.**

Electrochemical Contributions to Environmental Protection. T. R. Beck, O. B. Cecil, C. G. Enke, J. McCallum, and S. T. Wlodek, Editors. A 1972 symposium. 173 pages, **$4.00.**

Oxide-Electrolyte Interfaces. R. S. Alwitt, Editor. A 1972 symposium. 312 pages, **$9.00.**

Electrets. Charge Storage and Transport in Dielectrics. M. M. Perlman, Editor. A 1972 symposium. 700 pages, **$18.00.**

Marine Electrochemistry. J. B. Berkowitz, M. Banus, M. J. Pryor, R. Horne, P. L. Howard, G. C. Whitnack, and H. V. Weiss, Editors A 1972 symposium. 416 pages, **$15.00.**

Semiconductor Silicon 1973. H. R. Huff and R. R. Burgess, Editors. A 1973 symposium. 936 pages, **$15.00.**

Electrochemical Bioscience and Bioengineering. H. T. Silverman, I. F. Miller, and A. J. Salkind, Editors. A 1973 symposium. 268 pages, **$8.00.**

Chemical Vapor Deposition, Fourth International Conference. G. F. Wakefield and J. M. Blocher, Jr., Editors. A 1973 symposium. 608 pages, **$16.00.**

Fine Particles. W. E. Kuhn and J. Ehretsmann, Editors. A 1973 symposium. Approx. 700 pages, **$15.00.**

Chlorine Bicentennial Symposium. T. C. Jeffery, P. A. Danna, and H. S. Holden, Editors. A 1974 symposium. 404 pages, **$11.00.**

Electrocatalysis. M. W. Breiter, Editor. A 1974 symposium. 378 pages, **$12.00.**

Corrosion Problems in Energy Conversion and Generation. C. S. Tedmon, Jr., Editor. A 1974 symposium. 474 pages, **$12.00.**

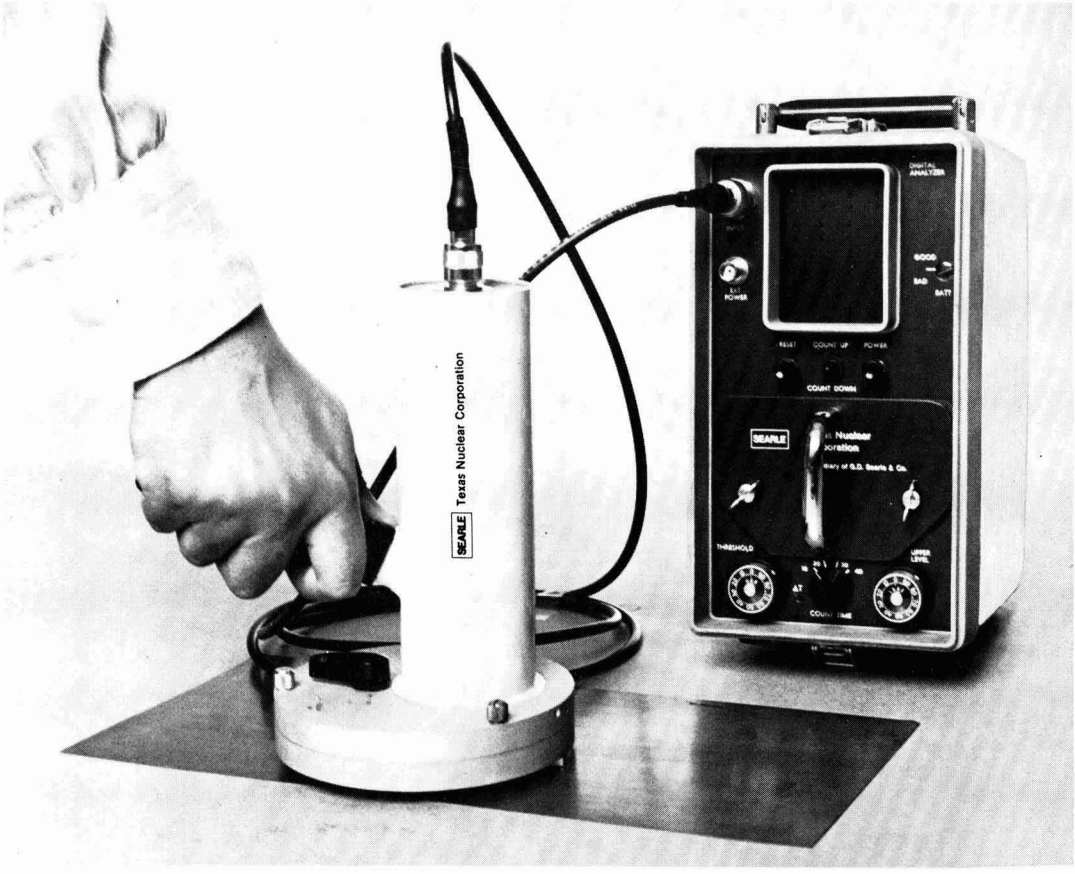
Electron and Ion Beam Science and Technology. Sixth International Conference. R. Bakish, Editor. A 1974 symposium. 596 pages, **$16.00.**

Properties of Electrodeposits—Their Measurement and Significance. R. Sard, H. Leidheiser, Jr., and F. Ogburn, Editors. A 1974 symposium. 430 pages, **$13.00.**

Chemistry and Physics of Aqueous Gas Solutions. W. A. Adams, G. Greer, J. E. Desnoyers, G. Atkinson, G. S. Kell, K. B. Oldham, and J. Walkley, Editors. A 1975 symposium. 522 pages, **$11.00.**

Metal-Slag-Gas Reactions and Processes. Z. A. Foroulis and W. W. Smeltzer, Editors. A 1975 symposium. 1032 pages, **$20.00.**

Non-destructive anode testing for noble metal coating in less than 30 seconds



- Provides precision quantitative measurement of anode performance.
- Ease of testing — measurement of either mass per unit area or actual thickness in micron units.
- Simple to use.
- Factory pre-calibration and guaranteed performance.
- Portable Analyzer, battery powered.

Write for complete application and instrument details.

SEARLE **Texas Nuclear Corporation**

Subsidiary of G.D. Searle & Co.
Box 9267 Austin, Texas 78766 USA
Telephone: (512) 836-0801 Telex: 77-6413

JOURNAL OF THE

JULY 1975

EDITOR
Norman Hackerman

DIVISIONAL EDITORS

BATTERY
R. J. Brodd — G. F. Nordblom
Elton J. Cairns — Boone B. Owens
F. P. Malaspina — J. L. Weininger

CORROSION
Theodore R. Beck — Ken Nobe
J. W. Faust, Jr. — Earl S. Snavely, Jr.
Z. A. Foroulis — J. Bruce Wagner
Jerome Kruger

DIELECTRICS AND INSULATION
Robert S. Alwitt — John Szedon
Newton Schwartz — Lawrence Young
Donald M. Smyth

ELECTRODEPOSITION
Ugo Bertocci — Seymour Senderoff
Nathan Feldstein

ELECTRONICS
Ephraim Banks — Jerome Prener
George R. Cronin — Bertram Schwartz
Murray Gershenzon — Alan J. Strauss
Simon Larach — P. Wang
I. Arnold Lesk — J. M. Woodall
Ernest Paskell

ELECTROTHERMICS AND METALLURGY
Joan B. Berkowitz — W. W. Smeltzer
Daniel Cubicciotti — *Jack H. Westbrook*
W. E. Kuhn

INDUSTRIAL ELECTROLYTIC
Richard C. Alkire — Scott Lynn

ORGANIC AND BIOLOGICAL ELECTROCHEMISTRY
Manuel M. Baizer — Stanley Wawzonek
Arthur A. Pilla

PHYSICAL ELECTROCHEMISTRY
Allen J. Bard — Barry Miller
A. J. de Bethune — David K. Roe
Larry R. Faulkner — C. W. Tobias
R. M. Hurd — F. G. Will
George J. Janz

EDITORIAL STAFF
Nancy S. Walters, **Assistant to the Editor**
Jack H. Westbrook, **News Editor**
Julius Kleror, **Book Review Editor**

PUBLICATION STAFF
Sarah A. Kilfoyle, **Publication Editor**
Rachel B. Cochran, **Publication Assistant**

PUBLICATION COMMITTEE
Newton Schwartz, **Chairman**
Bruce E. Deal
Robert T. Foley
Norman Hackerman
Jerome Kruger
Paul C. Milner
Jerome S. Prener
Jack H. Westbrook

ADVERTISING OFFICE
P.O. Box 2071
Princeton, N.J. 08540

ELECTROCHEMICAL SCIENCE AND TECHNOLOGY

TECHNICAL PAPERS

T. F. Sharpe ... 845 — Low-Rate Cathodic Linear Sweep Voltammetry (LSV) Studies on Anodized Lead

E. J. Casey, C. L. Gardner ... 851 — Anodic Passivation by "CdO" Studied by ESR

K. Niki, F. M. Delnick, N. Hackerman ... 855 — Behavior of Salicylaldoxime and 8-Hydroxyquinoline at a Copper Electrode

Ph. Aubrun, P. Rocquet ... 861 — The Mechanism of Metallic Chromium Electrodeposition in the Cathodic Dichromate Treatment of Tinplate

N. Hedgecock, P. Tung, M. Schlesinger ... 866 — On the Structure and Electrical Properties of Electroless Ni-B Films

S. Pancharatnam, R. A. Huggins, D. M. Mason ... 869 — Catalytic Decomposition of Nitric Oxide on Zirconia by Electrolytic Removal of Oxygen

J. F. Ambrose, L. L. Carpenter, R. F. Nelson ... 876 — Electrochemical and Spectroscopic Properties of Cation Radicals
III. Reaction Pathways of Carbazolium Radical Ions

I. Vartires, W. H. Smith, A. J. Bard ... 894 — Electrohydrodimerization Reactions
V. Liquid Ammonia as a Solvent for Reductive Coupling of Diethyl Fumarate, Cinnamonitrile, and Acrylonitrile

S. N. Frank, A. J. Bard ... 898 — Electrochemical Oxidation of Iminobibenzyl and Related Compounds

D. N-K. Wang, G. R. B. Elliott, C. H. Pitt ... 905 — Emf's across CdI_2-Cd_2I_2 Electrolytes Using Electrodes of Bare W, Molten Cd, and Molten Au-Cd: Bare Electrode Effects, Use of n = 2, Premonitory Phenomena and Liquid Structure in Au-Cd, and the Cd-CdX_2 Phase Diagrams

A. J. Panson, G. Economy, C. Liu, T. S. Bulischeck, W. T. Lindsay, Jr. ... 915 — Sodium Phosphate Solubility and Phase Relations Basis for Invariant Point Chemistry Control

ELECTROCHEMICAL SOCIETY

Vol. 122 • No. 7

R. Barrue
J. F. Rialland
. . . 918
Chemisorption on Powdery Indium Amalgams: Catalysis of the Oxygen Reduction

S. D. James
. . . 921
Undervoltage Deposition of Alkali Metal at Carbon Electrodes in the LiCl-KCl Eutectic Melt

C. M. Mohr, Jr.
J. Newman
. . . 928
Mass Transfer to an Eccentric Rotating Disk Electrode

J. J. Kelly
C. H. de Minjer
. . . 931
An Electrochemical Study of Undercutting during Etching of Duplex Metal Films

TECHNICAL NOTE

L. J. Weirick
. . . 937
Electrochemical Determination of Porosity in Nickel Electroplates on a Uranium Alloy

SOLID-STATE SCIENCE AND TECHNOLOGY

TECHNICAL PAPERS

D. Chatterji
D. W. McKee
G. Romeo
H. S. Spacil
. . . 941
The Effects of Lead on the Hot Corrosion of Nickel-Base Alloys

J. L. Sommerdijk
A. Bril
. . . 952
Efficiency of Dy^{3+}-Activated Phosphors

I. F. Chang
B. L. Gilbert
T. I. Sun
. . . 955
Electrochemichromic Systems for Display Applications

P. J. Severin
F. C. Eversteyn
. . . 962
On the Correction to be Applied to the Thickness of an Epitaxial Layer Measured with Infrared Multiple Interference

W. Mielke
. . . 965
Penetration of Gold and Platinum Through Phosphorus-Doped N^+ Layers in Silicon

J. S. Greeneich
. . . 970
Developer Characteristics of Poly-(Methyl Methacrylate) Electron Resist

DIVISION OFFICERS

Battery Division
Bernard Agruss, Chairman
Howard R. Karas, Vice-Chairman
John P. Wondowski, Secretary-Treasurer
General Battery Corp.
P.O. Box 1262
Reading, Pa. 19603

Corrosion Division
Roger Staehle, Chairman
Jerome Kruger, Vice-Chairman
Ken Nobe, Secretary-Treasurer
University of California
Dept. of Engineering
Los Angeles, Ca. 90024

Dielectrics and Insulation Division
Benjamin H. Vromen, Chairman
Laurence D. Locker, Vice-Chairman
Kim Ritchie, Treasurer
Rudolf G. Frieser, Secretary
IBM Corp.
Computer Division
Bldg. 330-145, Dept. 365
East Fishkill Facility
Hopewell Junction, N.Y. 12533

Electrodeposition Division
John L. Griffin, Chairman
Vladimir Hospadaruk, Vice-Chairman
Nathan Feldstein, Secretary-Treasurer
Surface Technology, Inc.
P.O. Box 2027
Princeton, N.J. 08540

Electronics Division
Bertram Schwartz, Chairman
Glenn Cullen, Vice-Chairman (Semiconductors)
Melvin Tectozky, Vice-Chairman (Luminescence)
Mort Panish, Vice-Chairman (General)
Michael Kestigian, Treasurer
Thomas Sedgwick, Secretary
IBM Corp.
Thomas J. Watson Research Center
P.O. Box 218
Yorktown Heights, N.Y. 10598

Electrothermics and Metallurgy Division
Robert Bakish, Chairman
John M. Blocher, Jr., Vice-Chairman
Stephen H. Spacil, Junior Vice-Chairman
J. Bruce Wagner, Jr., Secretary-Treasurer
Northwestern University
Dept. of Materials Science
Evanston, Ill. 60201

Industrial Electrolytic Division
D. N. Goens, Chairman
Thomas C. Jeffery, Vice-Chairman
Richard C. Alkire, Secretary-Treasurer
University of Illinois at Urbana-Champaign
School of Chemical Sciences
Dept. of Chemical Engineering
297 Roger Adams Laboratory
Urbana, Ill. 61801

Organic and Biological Electrochemistry Division
Manuel M. Baizer, Chairman
Arthur A. Pilla, Vice-Chairman
Larry Miller, Secretary-Treasurer
Colorado State University
Dept. of Chemistry
Fort Collins, Colo. 80521

Physical Electrochemistry Division
James D. E. McIntyre, Chairman
Stanley Bruckenstein, Vice-Chairman
Fritz G. Will, Secretary-Treasurer
General Electric Co.
Research and Development Center
Schenectady, N.Y. 12301

SOCIETY OFFICERS AND STAFF

Theodore R. Beck, President
Electrochemical Technology Corp.
10035 31st Ave. NE
Seattle, Wash. 98125

Michael J. Pryor, Vice-President
Metals Research Laboratories
Olin Corporation
91 Shelton Ave.
New Haven, Conn. 06504

Douglas N. Bennion, Vice-President
5532 Boelter Hall
University of California
School of Engineering and Applied Science
Los Angeles, Calif. 90024

Dennis R. Turner, Vice-President
Bell Laboratories
Room 7F-506
Murray Hill, N.J. 07974

Paul C. Milner, Secretary
Bell Laboratories
Room 1D-259
Murray Hill, N.J. 07974

Frederick J. Strieter, Treasurer
78-14 Fallmeadow Lane
Dallas, Tex. 75240

Ernest G. Enck, Executive Secretary
The Electrochemical Society, Inc.
P.O. Box 2071
Princeton, N.J. 08540

V. H. Branneky, Assistant Executive Secretary
The Electrochemical Society, Inc.
P.O. Box 2071
Princeton, N.J. 08540

Marie Falloon, Financial Secretary
The Electrochemical Society, Inc.
P.O. Box 2071
Princeton, N.J. 08540

Manuscripts submitted to the Journal should be sent, in triplicate, to the Editorial Office at P.O. Box 2071, Princeton, N.J. 08540. They should conform to the revised "Instructions to Authors" available from Society Headquarters. Manuscripts so submitted, as well as papers presented before a Society technical meeting, become the property of the Society and may not be published elsewhere in whole or in part without written permission of the Society. Address such requests to the Editor.

The Electrochemical Society does not maintain a supply of reprints of papers appearing in its Journal. A photoprint copy of any particular paper may be obtained from University Microfilms, Inc., 300 N. Zeeb St., Ann Arbor, Mich. 48106.

Inquiries regarding positive microfilm copies of volumes should be addressed to University Microfilms, Inc., 300 N. Zeeb St., Ann Arbor, Mich. 48106.

Walter J. Johnson, Inc., 355 Chestnut St., Norwood, N.J. 07648, have reprint rights to out-of-print volumes of the Journal, and also have available for sale back volumes and single issues, with the exception of the current calendar year. Anyone interested in securing back copies should correspond directly with them.

Published monthly by The Electrochemical Society, Inc., at 215 Canal St., Manchester, N.H.; **Executive Offices, Editorial Office and Circulation Dept.,** and **Advertising Office** at P.O. Box 2071, Princeton, N.J. 08540, combining the JOURNAL and TRANSACTIONS OF THE ELECTROCHEMICAL SOCIETY. Statements and Opinions given in articles and papers in the JOURNAL OF THE ELECTROCHEMICAL SOCIETY are those of the contributors, and The Electrochemical Society assumes no responsibility for them.

Claims for missing numbers will not be allowed if received more than 60 days from date of mailing plus time normally required for postal delivery of JOURNAL and claim. No claims allowed because of failure to notify the Circulation Dept., The Electrochemical Society, P.O. Box 2071, Princeton, N.J. 08540, of a change of address, or because copy is "missing from files." Subscription to members as part of membership service; subscription to nonmembers $50.00 plus $5.00 for postage outside U.S. and Canada. Single copies $3.25 to members, $5.00 to nonmembers.

© Copyright 1975 by The Electrochemical Society, Inc.

Second Class Postage Paid at Princeton, New Jersey, and at additional mailing offices. Printed in U.S.A.

SOLID-STATE SCIENCE (Cont.)

J. Matsui ... 977 — Cross-Slip Dislocations and Their Multiplication in (001)-Oriented Silicon Wafers

H. G. Tompkins ... 983 — Diffusion of Cobalt Out of Cobalt-Hardened Gold Measured with Auger Electron Spectroscopy

H. Mutoh, Y. Mizokami, H. Matsui, S. Hagiwara, M. Ino ... 987 — Multilayer Metallization with Planar Interconnect Structure Utilizing CVD Al_2O_3 Film

K. I. Hagemark, P. E. Toren ... 992 — Determination of Excess Zn in ZnO. The Phase Boundary Zn-$Zn_{1+x}O$

T. L. Chu, R. W. Kelm, Jr. ... 995 — The Preparation and Properties of Aluminum Nitride Films

TECHNICAL NOTES

K. H. Bachem, H. Bruch ... 1000 — Vapor Deposition of Sulfur-Doped GaAs Layers

W. Primak ... 1002 — Postirradiation Alkali Migration

REVIEWS AND NEWS

S. Ruben ... 199C — Alkaline Primary Cells

NEWS

... 202C

JOURNAL OF THE ELECTROCHEMICAL SOCIETY

ELECTROCHEMICAL SCIENCE AND TECHNOLOGY

JULY 1975

Low-Rate Cathodic Linear Sweep Voltammetry (LSV) Studies on Anodized Lead

Thomas F. Sharpe*

Electrochemistry Department, Research Laboratories, General Motors Corporation, Warren, Michigan 48090

ABSTRACT

Low-rate (~ 0.5 mV/sec) cathodic linear sweep voltammetry (LSV) experiments were conducted on preanodized antimonial and nonantimonial lead. The sweeps were supplemented by current-time traces obtained during the short term (≤ 1 hr) anodic treatment above the $PbO_2/PbSO_4$ reversible potential in H_2SO_4 electrolytes. Despite complications from additional substrate corrosion during the sweeps, semiquantitative observations were possible and the cathodic discharge could be resolved into α- and β-PbO_2 components. A major finding was that antimony in the lead retards the formation of β-PbO_2 in the preliminary anodic treatment. Implications from the results with regard to the behavior of the Pb-acid battery positive plate are briefly discussed.

In view of the fundamental information gained in recent years on the behavior of PbO_2 through the use of linear sweep voltammetry (LSV) (1-3), it would appear that such a technique might be useful for studying the differences in behavior of specific lead alloys used as grids for lead-acid battery positive plates. Although Panesar (4) has reported anodic and cathodic LSV studies on both antimonial and nonantimonial lead, many details concerning the PbO_2 reduction step were not considered. In his studies, anodization was effected by a low-rate (0.5 mV/sec) sweep extending from the potential for hydrogen evolution up to that for oxygen evolution. Under these conditions, the time above the $PbO_2/PbSO_4$ reversible potential was very short and the value of the potential was continuously changing, thereby making it impossible to relate the PbO_2 discharge phenomena to the potential of anodic treatment.

For Panesar's anodic treatment, only one cathodic current peak was resolved that could be ascribed to PbO_2 reduction in the subsequent cathodic scan. It is known, however, that two polymorphs of PbO_2 (α and β) exist, and that each may exhibit a different discharge overpotential (5-7). Depending upon the time and potential of anodic treatment, both polymorphs may be present in the corrosion film (8, 9). From x-ray diffraction, it has been established that β-PbO_2 resides primarily in the outer portion of the film and that α-PbO_2 exists, along with tetragonal PbO (PbO_t) in the inner portion of the film closer to the metal. The latter species are thermodynamically unstable in acid medium, but it is believed that they are formed in a localized high pH environment that is protected from the bulk acid by a $PbSO_4$ layer highly impermeable to H_2SO_4 (10).

In the present work, attempts are made to resolve in greater detail the PbO_2 discharge products using low-rate cathodic LSV following specified conditions of anodization. The sweeps were supplemented by current-time transients that were obtained during the anodization at constant potentials above the $PbO_2/PbSO_4$ reversible potential. It was of particular interest to compare antimonial and nonantimonial lead because of the well-known fact that antimonial grids prolong positive plate cycle life.

Experimental

The alloys chosen for this study were Pb/4.5% Sb and Pb/0.05% Ca. Both alloys contained the same level of concentration of Sn (0.6%) and were essentially free of other alloying constituents; therefore, the difference in behavior between the alloys in this study is ascribed to the effect of antimony. Test electrodes were current collector tabs cut from battery grids and the portion exposed to the electrolyte had a geometric area of 5 cm^2. The test electrodes were wiped with cotton wet with acetone, air-dried, and then given a 1 mA/cm^2 cathodic treatment for 5 min in the test cell prior to anodic treatment. The counterelectrode was sheet lead of 99.99+% purity and the reference electrode was Hg/Hg_2SO_4. The electrolyte was either 1.16 (2.7M) or 1.26 sp gr (4.5M) H_2SO_4 prepared from reagent grade chemical and distilled water. All experiments were conducted at ambient temperature (~25°C).

The $PbO_2/PbSO_4$ reversible potential values in each acid were determined by measuring (with a high-impedance electometer) the steady-state rest potentials of anodic films formed on Pb/Ca alloy for 2 hr at oxygen evolution potentials. These were 1142 ± 5 mV in 1.26 sp gr H_2SO_4 and 1067 ± 5 mV in 1.16 sp gr H_2SO_4.

For the potential sweeps, the 10 turn potentiometer of a commercial potentiostat was driven by an electric motor whose speed could be changed to give the desired linear sweep rate. All currents and potentials were continuously monitored with a strip chart recorder. Following preliminary work, greater sensitivity on the potential scale was achieved by synchronizing the speed of the recorder to the chosen sweep rate so that each major division (2.54 cm) of the strip chart corresponded to 12 mV.

* Electrochemical Society Active Member.

Key words: lead electrode, lead dioxide electrode, lead corrosion, lead-acid battery.

Results and Discussion

Lead preanodized at constant current.—In preliminary work, cathodic potential sweeps were obtained on test electrodes after they were anodized at constant current, and typical results are shown in Fig. 1. The sweeps were started immediately after switching off the current and covered a potential range of about 200 mV on each side of the $PbO_2/PbSO_4$ reversible potential. The cathodic current peaks, just below that potential, correspond to the reduction of PbO_2 to $PbSO_4$. Two peaks were observed; a major peak b and a minor peak b'. For the Pb/Sb alloy the minor peak became well defined after anodization at the higher current.

Just following the reduction of PbO_2, Panesar (4) reported an anodic current peak which he correlated to a cathodic current peak appearing at more negative potentials. From thermodynamic considerations these must be assigned[1] respectively, to the formation and reduction of PbO_t in the interior of the corrosion film. In the present work, a number of anodic current constituents were present in the scans, and it is shown subsequently that these are portions of an anodic current peak that extends throughout much of the PbO_2 discharge potential range. It has been demonstrated (6, 10) that in the vicinity of the $PbO_2/PbSO_4$ reversible potential, oxidation and reduction processes can occur at nearly the same potential. As a result, if the oxidation process gives rise to sufficient anodic current, the net current will exhibit anodic values, even though a reduction (cathodic) reaction (*e.g.*, $PbO_2 \rightarrow PbSO_4$) is occurring. This is believed to account for the rather peculiar voltammetric behavior observed in Fig. 1 and subsequent figures.

[1] See the discussion of Panesar's paper in Ref. (10).

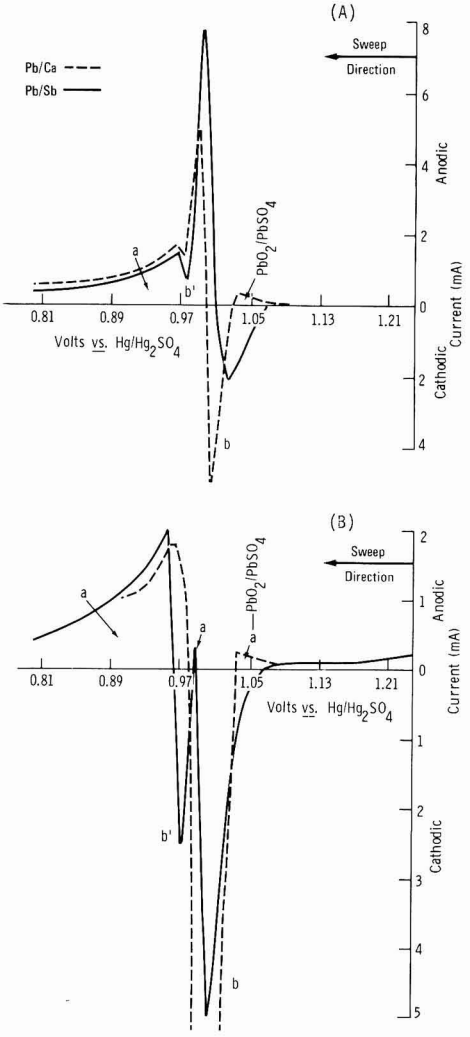


Fig. 1. Cathodic sweeps on Pb electrodes that were preanodized at (A) 5 mA and (B) 25 mA for 3 hr. Electrode area = 5 cm^2; H_2SO_4 = 1.16 sp gr; sweep rate = 0.28 mV/sec.

Lead preanodized at constant potential.—To gain greater insight, the shape of the sweeps was followed as a function of preanodization potential in increments at least as small as 50 mV above the $PbO_2/PbSO_4$ reversible value. During potentiostatic control, a continuous current-time (i-t) trace was obtained. The i-t traces for Pb/Ca alloy are similar to those previously reported by Ruetschi and Angstadt (11). Current-time traces at constant potential for Pb/Sb alloys have not been reported previously.

Results for Pb/Ca alloy.—Current-time traces obtained from 1150 to 1400 mV and corresponding selected cathodic sweeps in 1.26 sp gr H_2SO_4 are given in Fig. 2. After the 1 hr potentiostatic treatment, the potentials of the test electrodes were immediately de-

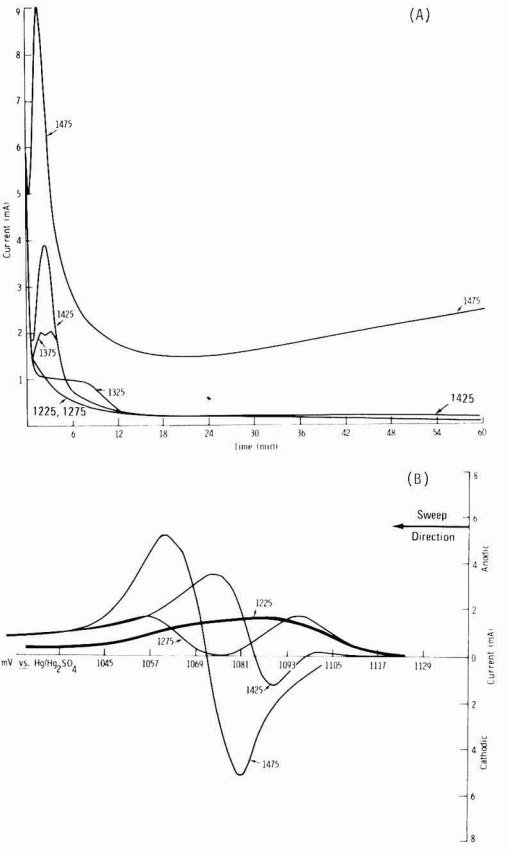


Fig. 2. Current-time curves (A) and subsequent cathodic sweeps (B) for Pb/Ca electrodes in 1.26 sp gr H_2SO_4. Numbers on curves indicate potential of anodic treatment. Electrode area = 5 cm^2; sweep rate = 0.42 mV/sec.

creased to the $PbO_2/PbSO_4$ reversible potential, and then the sweeps were started.

Following control at 1225 mV (about 75 mV above $PbO_2/PbSO_4$) the current in the scans was entirely anodic, as emphasized by the heavy line in Fig. 2B. At 1275 mV a current peak in the cathodic direction emerged, indicating the reduction of some tetravalent Pb compound. Up to that potential, the i-t traces indicated only the formation of $PbSO_4$ (11). It is assumed that the tetravalent compound corresponds to α-PbO_2 that formed by the oxidation of PbO_t beneath the partially passivating $PbSO_4$ layer.

After control at successively higher potentials, the onset of the cathodic current peak shifted to higher potentials along the anodic current profile and increased substantially in capacity. This trend is illustrated in greater detail in Fig. 3 after control at 50 mV increments and at a slower sweep rate. The shift and buildup in capacity can be correlated to the buildup of a pronounced peak in the i-t transients (Fig. 2A) that has been ascribed (11) to the oxidation of $PbSO_4$ to β-PbO_2 in the outer part of the corrosion layer. It appears, therefore, that the 1325-1375 mV interval marks the transition at which the cathodic peak in the scans becomes affected primarily by the discharge of β-PbO_2.

At or above 1475 mV, the current increase in the i-t transient, after the first few minutes (Fig. 2A and Fig. 4A) signifies the onset of oxygen evolution and pronounced base metal corrosion. The corresponding sweeps (Fig. 4B) indicate a shoulder emerging on the negative-potential side of the growing β-PbO_2 discharge peak. This is ascribed to the buildup of additional dischargeable α-PbO_2 that is expected to form by the direct oxidation of base metal at these high potentials.

A complicating issue in the cathodic scans is a background anodic current that extends throughout much of the $PbO_2/PbSO_4$ reversible potential region. As a result, net currents are involved and as mentioned above, despite the presence of dischargeable PbO_2, the net current may show an anodic value. This is especially exemplified in Fig. 5 where the effect of increasing time at high potential (1575 mV) is considered. At first, the current is slightly anodic which may be due to the further formation of $PbSO_4$. As the alkalinity beneath the $PbSO_4$ film becomes established (and as the electrode becomes progressively roughened by further anodic treatment), the anodic current would be expected to increase through the further anodic generation of Pb^{2+} to form PbO_t. At the same time, the buildup of PbO_2 also occurs (as confirmed on replicate electrodes by increasing time arrests at the $PbO_2/PbSO_4$ reversible potential after 30 sec anodic treatment) but not in sufficient quantity

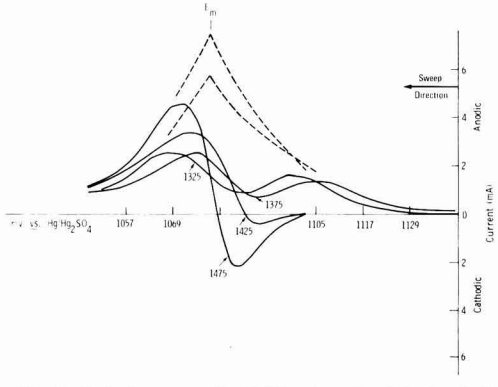


Fig. 3. Cathodic sweeps for Pb/Ca electrodes following 1 hr control at potential values indicated on sweeps. H_2SO_4 = 1.26 sp gr; electrode area = 5 cm^2; sweep rate = 0.21 mV/sec.

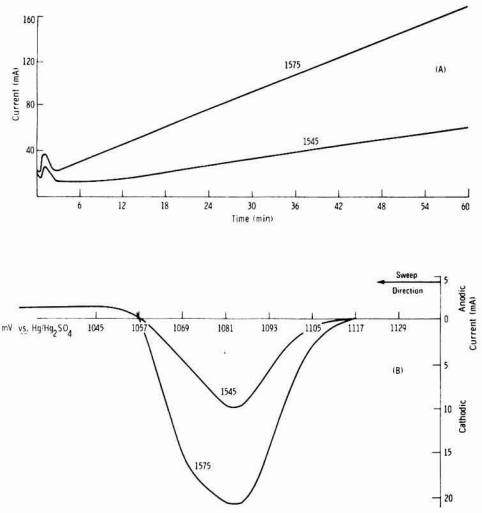


Fig. 4. Current-time curves at 1545 and 1575 mV (A) and subsequent cathodic sweeps (B) for Pb/Ca electrodes in 1.26 sp gr H_2SO_4. Electrode area 5 cm^2; sweep rate 0.42 mV/sec.

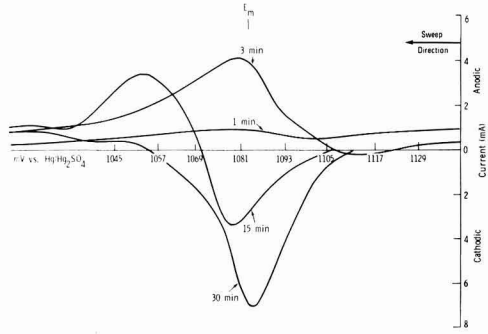


Fig. 5. Cathodic sweeps for Pb/Ca electrodes after control at 1575 mV for various times in 1.26 sp gr H_2SO_4. Electrode area = 5 cm^2; sweep rate = 0.42 mV/sec.

to compensate for that effect so the net current increases in the anodic direction. However, as the amount (and therefore the discharge capacity) of the PbO_2 increases, the net current builds in the cathodic direction.

Although the exact anodic current profile is always obscured by dischargeable PbO_2, there is seen in Fig. 5 a tendency toward a peak value at about 1.08V. This is in agreement with results obtained after control at lower potentials, where ascending and descending portions of the anodic current profile are well defined and can be extrapolated (cf., broken lines, Fig. 3). Similar maxima (E_m) have been observed based on steady-state corrosion current (11) and weight loss (12, 13) measurements. Lander (12) established that the E_m (on the Hg/Hg_2SO_4 scale) is a function of acid concentration, and the value interpolated from his data is in good agreement with the present observations.

It is also observed from Fig. 5 that the peak ascribed to β-PbO_2 reduction continues to grow beyond the time observed for $PbSO_4$ oxidation in the i-t curve. X-ray diffraction has indicated (9) that the amount of β-PbO_2 in the corrosion film is substantially larger than that provided by the oxidized $PbSO_4$. This has been ascribed (9) to an ionic current of Pb^{4+} passing through the corrosion film at high potentials to give

additional β-PbO_2 at the solution/corrosion film interface.

Selected i-t transients and subsequent cathodic sweeps obtained in 1.16 sp gr H_2SO_4 are shown in Fig. 6, and the buildup of dischargeable PbO_2 as a function of time at high potentials (1515 mV) are shown in Fig. 7. The discharge occurs ~75 mV below that observed in 1.26 sp gr which is, of course, expected from the difference in $PbO_2/PbSO_4$ rest potential values. The shape of the sweeps, however, is somewhat different, which can be explained primarily on the basis of increased substrate corrosion during the sweeps. A comparison between the sweeps in Fig. 7 and Fig. 5, obtained after the earliest stages of anodization under conditions where the i-t curves can be superimposed, indicates a greater tendency in the more dilute acid toward net currents in the anodic direction. Although this could be the result of a kinetic limitation on the PbO_2 discharge brought about by decreasing the acid strength, such an effect is not expected to be significant at these slow sweep rates. However, by decreasing the bulk concentration of acid, the *p*H in the interior of the film would be further increased, thereby favoring a greater anodic current flow. This is in agreement with Lander's observation (12) that weight loss at the potential of maximum anodic current increases with decrease in acid concentration.

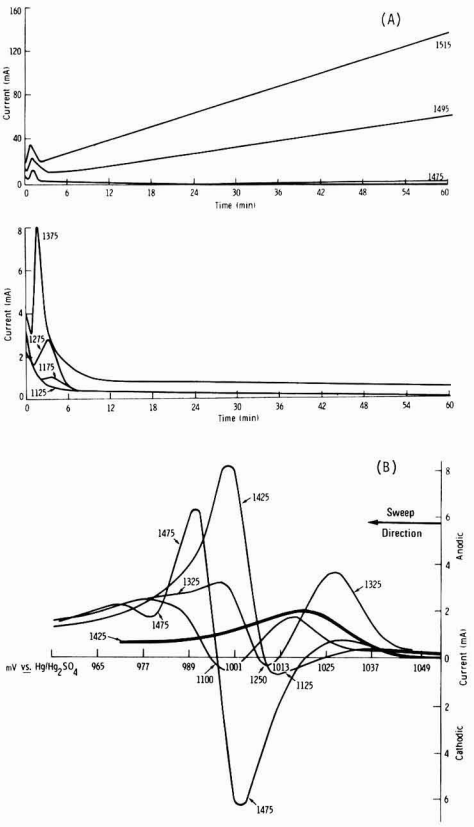


Fig. 6. Current-time curves (A) and subsequent cathodic sweeps (B) for Pb/Ca electrodes in 1.16 sp gr H_2SO_4. Numbers on curves indicate potential of anodic treatment. Electrode area = 5 cm²; sweep rate = 0.42 mV/sec.

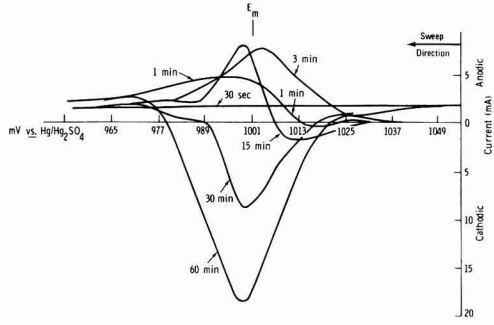


Fig. 7. Cathodic sweeps for Pb/Ca electrodes after control at 1515 mV for various times in 1.16 sp gr H_2SO_4. Electrode area = 5 cm²; sweep rate = 0.42 mV/sec.

Results for Pb/Sb alloy.—Current-time traces and corresponding cathodic sweeps in 1.26 sp gr H_2SO_4 are shown in Fig. 8. A notable feature is that the current peak for $PbSO_4$ oxidation to β-PbO_2 does not occur below 1375 mV, a significantly higher overvoltage than required to effect that reaction on Pb/Ca alloy. After control at or below that potential, the current is only slightly anodic in the sweeps. Above that potential an anodic current profile develops which gradually becomes masked after control at successively higher potentials by the buildup of two cathodic current peaks. The buildup of the cathodic peaks along the ascending and descending branches of the anodic current profile is also shown in Fig. 9, which gives the effect of anodization time at high potential (1575 mV).

The same experiments were repeated in 1.16 sp gr H_2SO_4, but for brevity only that series showing the effect of time at a high potential (1515 mV) is shown (Fig. 10). As in the case for the Pb/Ca alloy, the difference in sweep profiles as the acid strength is decreased appears to be the result of increased substrate corrosion during the sweeps. From the results in Fig. 9 and 10, a reasonable estimation of the peak

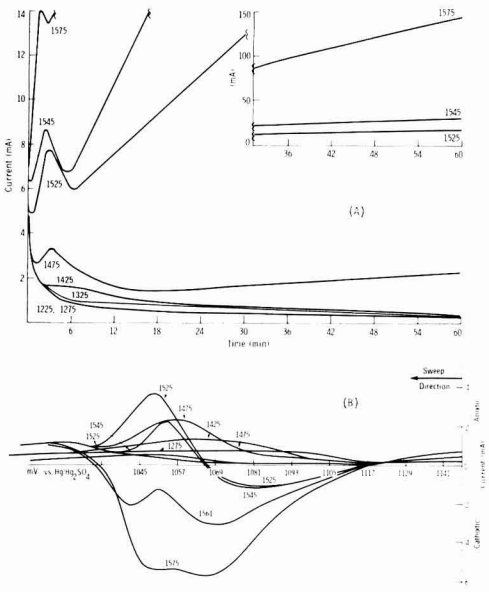


Fig. 8. Current-time curves (A) and subsequent cathodic sweeps (B) for Pb/Sb electrodes in 1.26 sp gr H_2SO_4. Numbers indicate potential of anodic treatment. Electrode area = 5 cm²; sweep rate = 0.42 mV/sec.

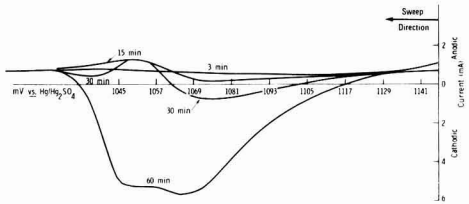


Fig. 9. Cathodic sweeps for Pb/Sb electrodes after control at 1575 mV for various times in 1.26 sp gr H_2SO_4. Electrode area = 5 cm^2; sweep rate = 0.42 mV/sec.

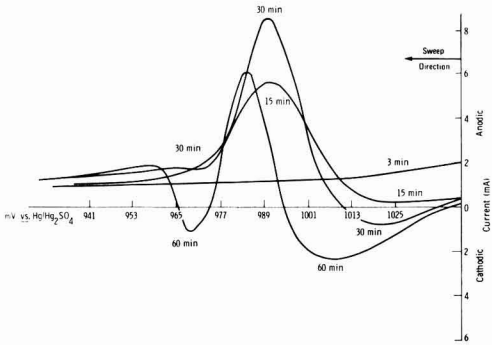


Fig. 10. Cathodic sweeps for Pb/Sb electrodes after control at 1515 mV for various times in 1.16 sp gr H_2SO_4. Electrode area = 5 cm^2; sweep rate = 0.42 mV/sec.

anodic current potentials (E_m's) are 1050 and 990 mV, respectively. These are slightly lower than the corresponding indications on Pb/Ca alloy (1075 and 1003 mV).

The two cathodic discharge peaks emerging after control at high potentials, as well as the peaks observed after constant current anodic treatment (Fig. 1) appear to correspond to the two plateaus observed by Ruetschi (6) during the constant current discharge of Pb/Sb alloy that had been anodized at constant current. In that work, however, an unambiguous assignment of each plateau to a specific PbO_2 polymorph could not be made. By analogy to the results for Pb/Ca alloy in the present work, the peak discharging at the higher potential would be assigned to β-PbO_2. A further indication that this is the correct choice is shown in Fig. 11, where an electrode that was discharged in the course of anodic treatment exhibited a growth of the peak at the higher potential. Such an intermittent discharge would provide additional $PbSO_4$ for oxidation, thereby enhancing the β-PbO_2 discharge peak.

Summary and Conclusions

Cathodic potential sweeps were obtained on an antimonial (Pb/4.5% Sb) and a nonantimonial (Pb/0.05% Ca) alloy after specific conditions of short-term anodization above the PbO_2-$PbSO_4$ reversible potential. The situation is complicated by additional substrate corrosion during the sweeps which gives rise to a substantial background anodic current that extends throughout much of the PbO_2 discharge potential range. As a result, net currents are always obtained, and the sweep profiles may exhibit the extremes shown schematically by the solid lines in Fig. 12. After control near the $PbO_2/PbSO_4$ reversible potential, or at higher potentials for very short periods of time, the current may be entirely anodic (a). It is believed that at the low-sweep rates employed the maximum anodic current in the scans (observed

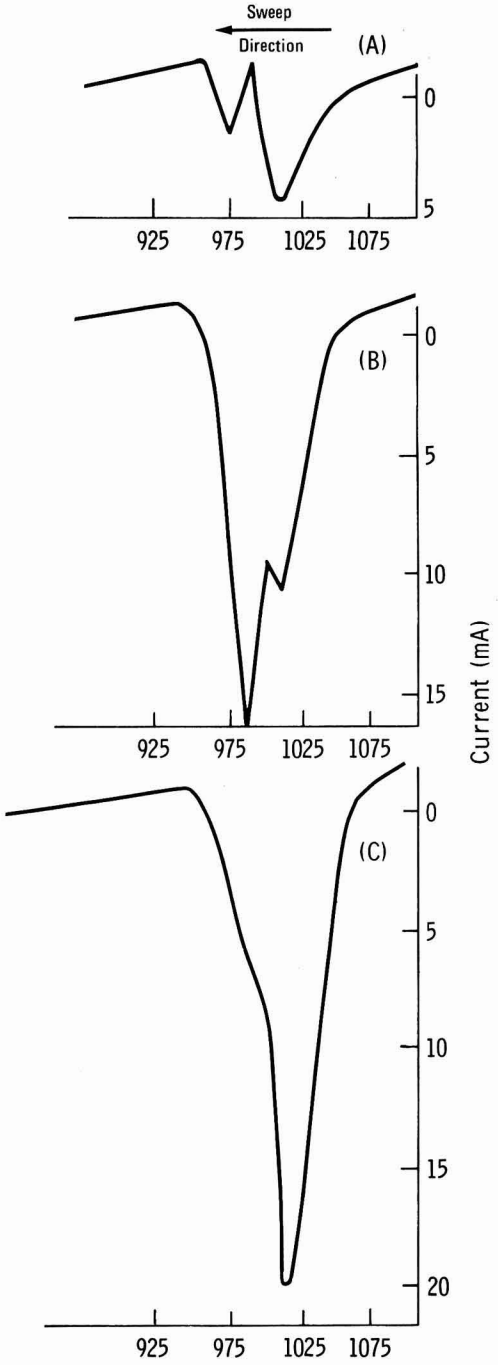


Fig. 11. Cathodic sweeps for Pb/Sb electrodes in 1.16 sp gr H_2SO_4 after control at 1525 mV for (A) 1.5 hr, (B) and (C) 3 hr. In (C), electrode was given intermittent discharge to 925 mV after 1.5 hr. Electrode area = 5 cm^2; sweep rate = 0.28 mV/sec.

prior to the buildup of appreciable discharge product) can be related reasonably well to the potential at which maximum corrosion would occur (E_m) under steady-state conditions near the $PbO_2/PbSO_4$ reversible potential.

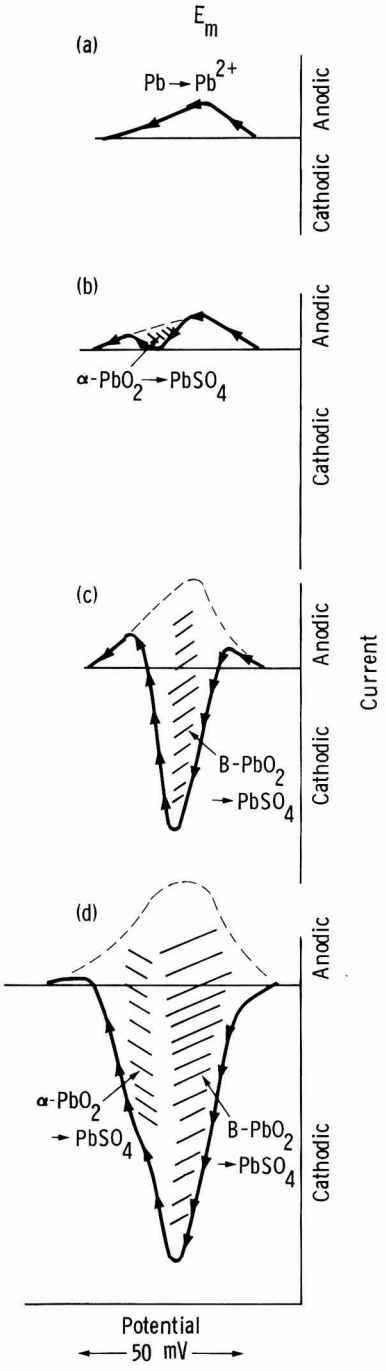


Fig. 12. Schematic showing possible cathodic sweeps for preanodized lead (see text).

As dischargeable PbO_2 is built up, the anodic current (broken lines, Fig. 12) may become partially or totally obscured. The sweep profile may then be influenced primarily by the discharge of α-PbO_2 (Fig. 12b), β-PbO_2 (Fig. 12c) or a composite of the two (Fig. 12d). The cathodic current peak intensities depend upon potential and time of anodic treatment and are strongly influenced by antimony in the lead.

Comparisons between nonantimonial and antimonial lead.—For nonantimonial (Pb/Ca) lead, the cathodic sweeps essentially follow the series of profiles in Fig. 12 after anodic control at progressively higher overvoltages. From the i-t curves obtained during the anodic treatment, the conversion of $PbSO_4$ to β-PbO_2 became evident at overvoltages of no more than 175 mV (*vs.* $PbO_2/PbSO_4$).

A striking feature of the Pb/Sb alloy was that substantially higher overvoltages (η = 375 mV) were required before effects due to oxidation of $PbSO_4$ to β-PbO_2 were observed in the i-t curves. A low rate of buildup of β-PbO_2 on antimonial alloy has also been observed by x-ray diffraction following anodic treatment at constant current (14). This may stem from parasitic oxidation of the antimony, occurring preferentially to the oxidation of $PbSO_4$ in the corrosion film. The difficulty in forming PbO_2 on antimonial lead has also been recognized in cathodic protection applications (15).

After control at high potentials (η = 425 mV) the concommitant growth of α- and β-PbO_2 discharge peaks was observed, but the β-PbO_2 discharge peak was substantially lower in capacity than that observed on the nonantimonial lead after comparable anodic treatment.

Antimony in positive plate grids.—Proposals as to why antimony prolongs positive plate cycle life have been based primarily on the observed effects of antimony on morphology and other properties of the PbO_2 active material (16). Antimony has also been shown to affect grid growth (17). An estimation of the importance of the numerous factors involved would indeed be a formidable task. However, it has been generally observed that corrosion films on nonantimonial lead, which, in view of the present work, contain substantial quantities of β-PbO_2, are more powdery and loosely adherent than those found on antimonial lead. The desirable effect from antimony, therefore, may be to inhibit the buildup of excess β-PbO_2 during the formation step, thereby providing a thinner, and presumably more tenacious film on which the active material of the plate can be formed. If this mechanism is operable, then it would appear that other effects that have been observed after formation and cycling would be of a secondary nature.

At the rather modest level of antimony concentration considered here (4.5%), there was also an indication that Sb shifts the E_m to more negative values. Although the trend was marginal, it was in a direction that would extend positive plate cycle life. It may be of interest to examine that trend, as well as the other findings of this study, as a function of antimony concentration in the alloy.

Manuscript submitted Nov. 6, 1974; revised manuscript received March 6, 1975.

Any discussion of this paper will appear in a Discussion Section to be published in the June 1976 JOURNAL. All discussions for the June 1976 Discussion Section should be submitted by Feb. 1, 1976.

Publication costs of this article were partially assisted by General Motors Corporation.

REFERENCES

1. J. P. Carr and N. A. Hampson, *This Journal*, **118,** 1262 (1971).
2. J. P. Carr, N. A. Hampson, and R. Taylor, *J. Electroanal. Chem.*, **33,** 109 (1971).
3. For a comprehensive summary, see J. P. Carr and N. A. Hampson, *Chem. Rev.*, **72,** 679 (1972).
4. H. S. Panesar, in "Power Sources 3," D. H. Collins, Editor, p. 79, Oriel Press, Newcastle-Upon-Tyne (1971).
5. H. B. Mark, *This Journal*, **109,** 634 (1962).
6. P. Reutschi and B. D. Cahan, *ibid.*, **105,** 369 (1958).
7. E. Voss and J. Freundlich, in "Batteries," D. H.

Collins, Editor, p. 73, Pergamon Press, New York (1963).
8. D. Pavlov, C. N. Poulieff, E. Klaja, and N. Iordanov, *This Journal*, **116**, 316 (1969).
9. D. Pavlov and N. Iordanov, *ibid.*, **117**, 1103 (1970).
10. P. Ruetschi, *ibid.*, **120**, 331 (1973).
11. P. Ruetschi and R. Angstadt, *ibid.*, **111**, 1323 (1964)
12. J. J. Lander, *ibid.*, **103**, 1 (1956).
13. E. Voss, "Trans. Second Int. Symp. Batteries, Interdepartmental Committee on Batteries, Bournemouth, Oct. 1960," Sydenham and Co., Ltd., Oxford Road, Bournemouth, England.
14. T. F. Sharpe, Abstract No. 347, p. 828 Electrochemical Society Extended Abstracts Spring Meeting, San Francisco, California, May 12-17, 1974.
15. J. H. Morgan, *Corrosion Technol.*, **5**, 347 (1948).
16. E. J. Ritchie and J. Burbank, *This Journal*, **117**, 299 (1970).
17. A. C. Cannone, D. O. Feder, and R. V. Biagetti, *Bell System Tech. J.*, **49**, 1279 (1970).

Anodic Passivation by "CdO" Studied by ESR

E. J. Casey* and C. L. Gardner

Defence Research Establishment Ottawa, Ottawa, Ontario, Canada K1A 0Z4

ABSTRACT

The appearance of superoxide O_2^- and ozonide O_3^- ions in strong KOH electrolyte at temperatures 25° to −40°C during the anodic oxidation of cadmium and oxygen evolution has been investigated using the electron spin resonance technique. The fact that O_2^- forms at the higher temperatures and O_3^- predominates at −40°C correlates with the appearance of β-$Cd(OH)_2$ at higher and γ-$Cd(OH)_2$ at lower temperatures, but it is argued that this correlation is coincidental and that it is the character of the surface states of the elusive and dynamic "CdO" underlayer beneath the $Cd(OH)_2$ that determines which paramagnetic species is produced. These new facts and the interpretation are discussed within the framework of the solid state/solution-precipitation mechanism.

In this paper the evidence for a form of cadmium oxide as the instrument of anodic passivation of cadmium in aqueous KOH from 33° to −40°C is reviewed, and some new evidence obtained via ESR is added and interpreted. The mechanism by which the metal ceases to be anodically oxidizable after a period of active oxidation is one important element of the information needed if more efficient utilization of the metal in negative plates of alkaline batteries is to be achieved. Other important elements, such as those related to surface exposed and to pore structure (1), are not reviewed here.

Review of Evidence for CdO as an Intermediate Product

Since 1950, Epelboin (2) has written extensively about the probability of the existence of monovalent intermediates such as Cd^+ resulting from anodic, one-electron charge-transfer steps, especially during electropolishing of metals. The evidence is still equivocal, direct proof still lacking in the case of cadmium. By 1950 Huber (3) and Ershler *et al.* (4) had found CdO by x-ray diffraction of samples taken from the surface of Cd anodized at high potentials. Lake and Casey (5) studied the electrical behavior of cadmium before, during, and after passivation, and inferred that a solid-film intermediate, "CdO," must be a substantial intermediate in the reactions which eventually lead to $Cd(OH)_2$ in KOH and to $CdCO_3$ in K_2CO_3 solutions, and which ultimately causes the passivation.

Many workers have sought CdO, without finding it, in the passivating layer. Falk (6a) found none at room temperature in Sweden (20°C). Sanghi *et al.* (6b) found none at room temperature in India (33°C!). Nor did Croft (6c), nor Thirsk *et al.* (6d). Nor did others (7). The hexagonal platelets of β-$Cd(OH)_2$ are usually identified as the product, either by x-ray diffraction of moist or dry particulate samples, or by electron diffraction of dried, anodically formed, very thin films. However, Breiter and Vedder (8), and later Okinaka and Whitehurst (9a), found the more recently identified (10) needlelike monoclinic γ-$Cd(OH)_2$ as the major product: the former authors during experiments at room temperature and the latter group during experiments at low temperatures. The γ-$Cd(OH)_2$ seems to be more readily reducible to metallic cadmium than is the β-form, especially at low temperatures, during the electrochemical charging reaction (9a). More recently (9b), the needles have been shown by the scanning electron microscope technique at 25° and possibly [note the authors' uncertainty, Ref. (9b)] up to 40°C in porous electrodes.

No attempts were made by the authors of any of the quoted work to freeze-dry, or otherwise to stop any hydrolysis, hydration, or protonation of CdO which could occur after anodic treatment ceases and during manipulation of the wet sample.

Yoshizawa and Takehara (11a), however, did find CdO by x-ray diffraction of samples buried within thick plates. Ohse found it also (11b), and concluded that it formed underneath the $Cd(OH)_2$. The results found by Devanathan *et al.* (11c) suggested to those workers that the CdO and $Cd(OH)_2$ form at the same time. Okinaka (12) also found CdO, following a period of vigorous oxygen evolution in solutions of low KOH concentration [conditions much like Huber's (3)]. Galushko *et al.* (13) recently reported further experimental conditions (low concentration of KOH, mild anodic treatment) under which CdO could accumulate, be identified, and its electrochemical reduction studied.

Indirect evidence also exists that CdO forms as an intermediate. Thus Breiter and Weininger (8b), using triangular voltage sweeps for anodic oxidation and cathodic reduction, found a reduction peak just about where one would expect the polarized Cd/CdO potential on an electrode which had not been heavily passivated anodically; they concluded that CdO was indeed formed and then remained stable long enough to be electrochemically reduced. Okinaka (12) showed that the CdO reduction peak occurs also following anodic oxidation during ring-disk experiments.

On Mechanisms

Throughout the past fifteen years there have been several papers containing discussion of the relative merits of and the role of two proposed mechanisms of the anodic oxidation: (*i*) the "solid-state mechanism"

* Electrochemical Society Active Member.
Key words: CdO, cadmium, anodic passivation, ozonide O_3^-.

(Cd^{++} penetrating an underlayer [CdO? $Cd(OH)_2$?] to the solid/solution interface and reacting with electrolyte there); (*ii*) the "solution-precipitation mechanism" (Cd^{++} ions dissolving directly from Cd metal, as $Cd(OH)_3^-$, perhaps, to precipitate as $Cd(OH)_2$.

Either one offers a good first approximation (6a, 6b) over a narrow range of experimental conditions. Neither, however, can describe polarization data taken on cadmium over a wide range of current density, temperature, and electrolyte composition, both before and after passivation, but especially during passivation. As far as we are aware, only the combined solid-phase/solution-precipitation mechanism (see Fig. 1) has the flexibility needed. Thus an underlayer which is difficult to detect is pictured as being covered by the x-ray-detectable final reaction product: cadmium ions penetrate the nonstoichiometric "CdO," the outer surface of which is continually dissolving (*i.e.*, complexing) and precipitating out again as the final product, $Cd(OH)_2$. At passivation this dynamically self-refurbishing glassy underlayer seals over, dissolves only slowly, and is continuously being replaced.

A mechanism for the escape of the soluble complexes from the "CdO" surface has been proposed (15). It has already been shown that when this part of the process is significantly slowed down by conducting the experiments at −40°, the total anodic film need be only about 6 CdO-layers thick to effect passivation (15). It was early argued [see Fig. 5, Ref. (5b)] that the underlayer must be nonstoichiometric everywhere except at one interior plane: rich in $O^=$ near the CdO/electrolyte interface, rich in Cd^{++} near the Cd/CdO interface; thin and glassy, nonstoichiometric, continuous; of the variable composition so elegantly demonstrated directly by Hoar quite recently on iron-tin using Auger techniques (16).

No direct physical identification of CdO as an intermediate during active oxidation of cadmium or even after passivation of cadmium at low oxygen overpotentials, has been acquired, presumably because it is (*a*) buried beneath the final hydrolysis product, and (*b*) rapidly converted to final product under all but exceptional conditions. The final reaction products may be formed through soluble intermediates such as $Cd(OH)_3^-$ or $Cd(OH)_4^=$ in KOH, $Cd_3(CO_3)_4^=$ in K_2CO_3, or through poorly characterized hydroxy-carbonates in mixed electrolytes (14a and b). The question of what soluble complexes exist in high concentrations of KOH has not been conclusively answered, some evidence favoring $Cd(OH)_3^-$ and other favoring $Cd(OH)_4^=$. Gilman and Sangermano (17a) recently wrestled with this difficulty, as had others earlier (17b, 17c).

Such investigations have elaborated the complexity of the anodic oxidation of cadmium. The search continues for new evidence.

Detection of Anodically formed O_3^- and O_2^-

By the late 1960s, we were applying ESR techniques to the anodic oxidation of cadmium and silver, and to other similar basic problems. It was found (18) that O_3^- and other paramagnetic species such as O_2^-, and $CuO_2^=$, produced anodically on some metals in aqueous KOH, at temperatures well below 0°C, were stable enough to be identified, and that their concentrations could be measured. Concerning cadmium we have reported (18a) that O_2^- is the detectable product of anodic oxidation in aqueous KOH at the higher temperatures (−10° to −20°C), while O_3^- is the observable product at the really low temperatures (down to −40°). Temperature inversion from one species to the other was sought but not observed (18b). The technique has been improved, and O_2^- has been detected in the anolyte during oxygen evolution off Cd even at room temperature, both in this work and elsewhere (18c).

Figure 2 shows the distinctly different spectra of O_2^- and O_3^-. The O_2^- was produced chemically by the decomposition of H_2O_2 in KOH solutions. The O_3^- was produced electrochemically during O_2 evolution on oxidized silver, as before (19). In each case electrolyte samples were quick-frozen in liquid nitrogen and spectra recorded on the frozen samples at 77°K, as described in Ref. (19). Characteristic *g*-values are given for each. The g_z for O_2^- shifts much more with the electrostatic environment to which it is bound than do g_x and g_y. [See Lunsford's Table 2 (20).]

Measurements taken with an electrochemical cell placed directly in the microwave cavity were insensitive, as the cavity was detuned by gas bubbles. After anodic oxidation for ~5 min at ~100 mA/cm² at the temperature shown, samples of electrolyte from near the cadmium anode were withdrawn into thin quartz tubes and quick-frozen in liquid nitrogen. Spectra of

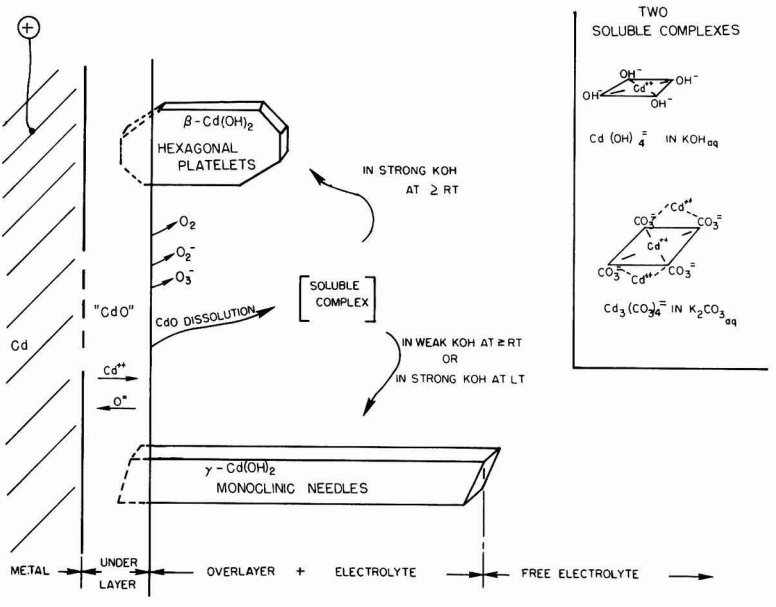


Fig. 1. Schematic indicating solid-state/solution-precipitation mechanism for anodic oxidation of cadmium. After passivation by the underlayer and the onset of oxygen evolution, the radicals O_2^- and O_3^- can be detected in the electrolyte at low temperatures. The underlayer continues to dissolve and be reformed during oxygen evolution. This seems to correlate with radical formation.

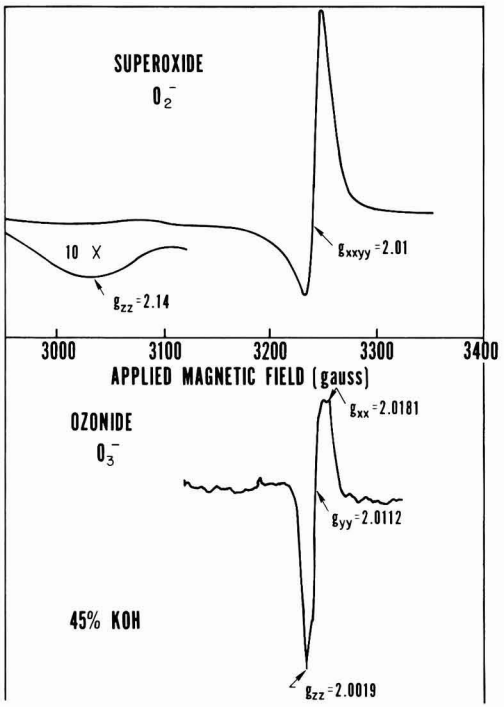


Fig. 2. ESR spectra taken at 77°K of O_2^- and O_3^-. Note distinctly different line shapes as expressed by the g-values. The g_{zz} peak of O_2^- is shown amplified 10× for clarity.

these samples were then taken at 77°K. From Fig. 3 it can be seen that the superoxide ion O_2^- is the main paramagnetic product detected from +25° to −25°C, while at −35° the O_3^- predominates. At −40° in 45% KOH the spectrum is that of O_3^- only, there being no evidence at all for O_2^-. Careful inspection reveals that the absorption by species "X," at $g = 2.00$, which will be discussed below, appears from under that of O_2^- as the spectrum of O_2^- fades out at lower temperatures.

So far no evidence has been obtained with the ESR technique for the anodic formation of free-radical intermediates from Cd except during oxygen evolution, *i.e.*, after passivation. The question of whether any free-radical intermediates which might be formed before and/or during passivation can somehow be detected by this method is still an open one: it will be necessary to find conditions under which the intermediates can desorb into the electrolyte, accumulate there, and then be stable while a sample of the anolyte is being quick-frozen and examined in the ESR cavity. The following discussion, therefore, refers only to the situation after passivation, after completion of the "CdO" underlayer.

Discussion

Of the several metals studied so far cadmium is the only one from which both O_2^- and O_3^- have been detected having been produced during anodic oxygen evolution. From the fact that O_2^- is formed at the higher temperatures investigated and O_3^- at the lower, one can infer that the passivating glassy underlayer is different at different temperatures. Perhaps it is more highly protonated at −10° than at −40°, and the primary product of the discharge of OH_{ads}^-, namely O_{ads}^-, is more weakly bound at −10° than at −40°. The mechanism could change as follows. Since the second discharge event produces O_{ads} in both cases, the O_{ads}^- can rapidly combine with one O_{ads} to evolve O_2^- from the surface of the underlayer at −10°, while at

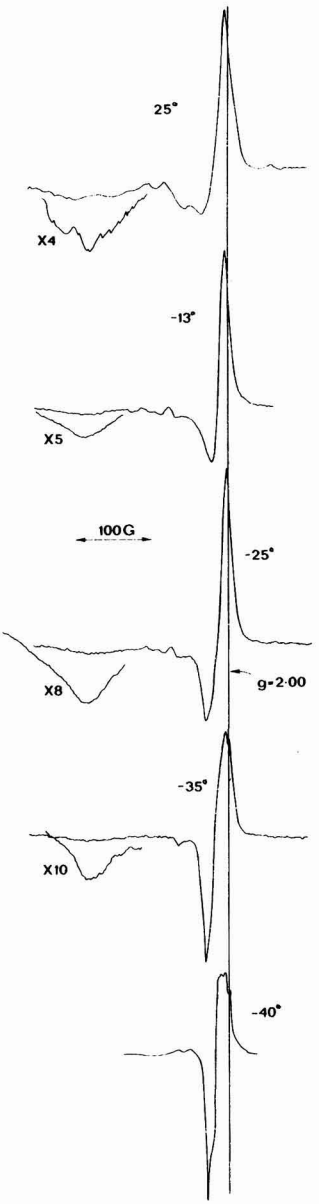


Fig. 3. Spectra of strong KOH anolyte samples extracted in a capillary and quick-frozen to 77°K, following anodic oxygen evolution off cadmium at temperatures shown. Clear spectra of O_2^- for 25° and O_3^- for −40°C. "X" is just perceptible near $g = 2$ at −35° and −40°.

−40° it gets away more slowly and then only by combining with two O_{ads} to evolve O_3^-. In summary, the discharge reactions

$$OH_{ads}^- \rightarrow O_{ads}^- + e + H^+ \quad \text{and} \quad O_{ads}^- \rightarrow O_{ads} + e$$

followed by

$$O_{ads}^- + O_{ads} \rightarrow O_2^- \qquad \text{at } -10°$$

and

$$O_{ads}^- + 2\,O_{ads} \rightarrow O_3^- \qquad \text{at } -40°$$

produce the paramagnetic species detected.

These mechanisms seem simpler than those proposed in our earlier work (18, 19), namely

$$2\,OH_{ads} \rightarrow H_2O_2 \rightarrow \tfrac{1}{2}\,O_2 + H_2O$$

$$H_2O_2 + OH^- \rightarrow HO_2^- + H_2O$$

$$HO_2^- + OH \rightarrow O_2^- + H_2O$$

and

$$O_{ads}^- + O_2 \rightarrow O_3^-$$

although there is no experimental reason to favor one over the other at this juncture.

A cautionary note is introduced by the possibility that O_3^- is not observed at the higher temperatures from Cd simply because it decays too fast (in the cadmium-saturated electrolyte) and not that it never was formed in the first place, as we have implied above. This will be a hard point to prove experimentally.

In addition to the oxygen species the elusive species "X," which gives a sharp ESR absorption peak at $g = 2.0023$, is produced as a second anodic reaction product of cadmium [and several other metals (18)] in strong KOH at low temperatures. The nature of species X is still uncertain. Its decay rate varies markedly (minutes to less than seconds) (19). In the case of cadmium oxidation this sharp absorption line (Fig. 2, $-35°$ and $-40°$) could be due to conduction electrons in colloidal metal which has been undermined during anodic dissolution, a manifestation of the classical "chunk effect" (21). Or, it might be due to complexed electrons arising from oxidation of Cd^+ by electrolyte. Although it is unlikely to be due to Cd^+ itself [whose magnetic parameters (22) are $g = 1.992$ to 2.001, and a large hyperfine splitting for the isotope 114, none for the more abundant isotope 112], it could be due to the electron which has just been ejected from anodically formed Cd^+ and which is temporarily resting in the metal-ion/hydroxyl-ion/water complex, $M(OH)_n^{2-n} \cdot xH_2O$. The analogy with Epelboin's recent work (23) on Be^+ produced anodically in an aprotic solvent elicits further thought along these lines. However, since the absorption peak at 2.0023 is devoid of fine structure, ESR work to date cannot distinguish unambiguously between colloidal metal or complexed electron.

The elements of the solid-phase/solution-precipitation mechanism given in this paper seem able to accommodate the new facts obtained by ESR as well as many seemingly incompatible observations earlier reported. New techniques which can permit *in situ* examination of composition, structure, and electrical properties are still needed, however, as is a quantitative theory which can describe the discontinuities of the passivation process. To delay the onset of passivation during anodic oxidation of the metal remains the primary practical objective of work of this kind.

The ESR results reported in this paper can be considered as relevant to the mechanisms operating at the cadmium electrode of a cadmium-alkali cell which has been driven into cell reversal (*i.e.*, forced discharge) at low temperatures. Attack of cell components by anodically produced free radicals, which are mobile in the electrolyte, can be anticipated.

Acknowledgment

This was issued as DREO Report No. 721.

Manuscript submitted Sept. 3, 1974; revised manuscript received Feb. 13, 1975.

Any discussion of this paper will appear in a Discussion Section to be published in the June 1976 JOURNAL. All discussions for the June 1976 Discussion Section should be submitted by Feb. 1, 1976.

Publication costs of this article were partially assisted by Defense Research Establishment Ottawa.

REFERENCES

1. E. S. Carr, "Proceedings of 25th Power Sources Symposium," p. 57, PSC, Red Bank, N. J. (1972); E. J. Casey and B. E. Vergette, *Electrochim. Acta*, **14**, 897 (1970), and reference there in.
2. I. Epelboin, *Métaux*, **32**, 55 (1975); *Z. Electrochem.*, **59**, 689 (1955), *e.g.*
3. K. Huber, *This Journal*, **100**, 376 (1953); *Z. Physikal.*, **62**, 675 (1958); K. Huber and S. Stucki, *Helv. Chim. Acta*, **51**, 1343 (1968).
4. S. A. Rozentsveig, B. V. Ershler, E. L. Shtrum, and M. M. Ostanina, *Tr. Soveshch. Elecktrokhim. Akad. Nauk SSSR, 1950*, p. 571 (1953).

5a. P. E. Lake and E. J. Casey, *This Journal*, **105**, 52 (1958); b. P. E. Lake and E. J. Casey, *ibid.*, **106**, 913 (1959).

6a. S. U. Falk, *ibid.*, **107**, 661 (1960); b. I. Sanghi, S. Visvanathan, and S. Ananthanarayanan, *Elektrochim. Acta*, **3**, 65 (1960); c. G. T. Croft, *This Journal*, **106**, 278 (1959); G. T. Croft and D. Tuomi, *ibid.*, **108**, 915 (1961); d. R. D. Armstrong, E. H. Boult, D. F. Porter, and H. R. Thirsk, *Electrochim. Acta*, **12**, 1245 (1967).

7a. J. P. G. Farr and N. A. Hampson, *Electrochem. Technol.*, **6**, 10 (1969); b. H. Y. Kang, *This Journal*, **118**, 462 (1970).

8a. M. Breiter and W. Vedder, *Trans. Faraday Soc.*, **63**, 1042 (1967); b. M. Breiter and J. L. Weininger, *This Journal*, **113**, 651 (1966); M. Breiter and J. L. Weininger, in "Power Sources 1966," D. H. Collins, Editor, p. 269, Pergamon Press, London (1967).

9a. Y. Okinaka and C. M. Whitehurst, *This Journal*, **117**, 583 (1970); b. D. Chua and R. J. Diefendorf, "Proceedings 25th Power Sources Conf. 1972," p. 52.

10a. P. M. de Wolff, *Acta Cryst.*, **21**, 432 (1966); b. O. Glemser, U. Hauschild, and H. Reichert, *Z. Anorg. Allgem. Chem.*, **290**, 58 (1957). See however Feitknecht *et al.*, *Helv. Chim. Acta*, **34**, 2266 (1951) and *Chimia*, **11**, 166 (1957) concerning stabilization by Cl^-.

11a. S. Yoshizawa and Z. Takehara, *Electrochim. Acta*, **5**, 240 (1961); b. R. W. Ohse, *Z. Elecktrochim.*, **64**, 1171 (1960); c. M. A. V. Devanathan and S. Lakshmann, *Electrochim. Acta*, **13**, 667 (1968).

12. Y. Okinaka, *This Journal*, **117**, 289 (1970).
13. V. P. Galushko, E. F. Zavgorodnyaya. R. V. Podolskaya, and Yu. P. Rodak, *Elecktrokhim.*, **8**, 1216 (1972).

14a. E. J. Casey, A. R. Dubois, P. E. Lake, and W. J. Moroz, *This Journal*, **112**, 371 (1965); b. W. Feitknecht, *Fortschr. Chem. Forsch.*, **2**, 670 (1953), AERE Harwell Translation, p. 622.

15. E. J. Casey, *Chem. Can.*, **12**, 49 (1960).
16. T. P. Hoar, M. Talerman, and E. Trad, *Nature*, **244**, 41 (1973).

17a. S. Gilman and L. D. Sangermano, *This Journal*, **118**, 1953 (1971); b. P. C. Milner and U. B. Thomas, *Advan. Electrochem. Electrochem. Eng.*, **5**, 1 (1967); c. W. Feitknecht and P. Schindler, *Pure Appl. Chem.*, **6**, 130 (1963).

18a. C. L. Gardner and E. J. Casey, *Can. J. Chem.*, **49**, 1782 (1971); b. C. L. Gardner and E. J. Casey, *Faraday Discussions No. 56*, Sept. 1973; c. R. L. Deming, Private communication, 1974.

19. C. L. Gardner and E. J. Casey, *Can. J. Chem.*, **52**, 930 (1974).
20. J. H. Lunsford, *Catalysis Rev.*, **8**, 135 (1973).
21. W. J. James and M. E. Straumanis, *This Journal*, **118**, 1960 (1971), *e.g.*
22. R. S. Eachus, M. C. R. Symons, and J. K. Yandell, *Chem. Comm. 1969*, p. 979.
23. H. Aida, I. Epelboin, and M. Garreau, *This Journal*, **118**, 1961 (1973).

Behavior of Salicylaldoxime and 8-Hydroxyquinoline at a Copper Electrode

Katsumi Niki,*,[1] Frank M. Delnick, and Norman Hackerman†**

Department of Chemistry, Rice University, Houston, Texas 77001

ABSTRACT

Effects of salicylaldoxime (SAO) and of 8-hydroxyquinoline (HQ) on the anodic dissolution of copper were studied by using a potentiokinetic polarization method and phase-selective a-c polarography at a rotating copper disk electrode at various *p*H values. At *p*H 1.5, where cupric ions do not precipitate as the chelates of SAO and HQ, the anodic dissolution of copper was retarded slightly by these additives. At *p*H 2.8 and 5.0, where SAO precipitates cupric ions quantitatively, the anodic dissolution of copper was markedly retarded by SAO, especially from the rotating disk electrode. The anodic polarization curves of copper in the SAO solutions were similar to those obtained in the passivation of iron. A thin protective chelate film was formed on the copper electrode. At very positive potentials, the chelate film ruptured and the anodic dissolution of copper started. On the other hand, HQ chemisorbed strongly on the copper electrode from *p*H 2.8-5.0, where HQ also precipitates cupric ions, and the copper dissolution was retarded markedly. The Cu-HQ chelate did not act as a barrier for the copper dissolution in this *p*H range.

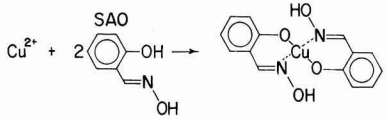
Numerous studies have been made to elucidate the mechanism of corrosion inhibition by organic substances. Inhibitors of the first class are physically adsorbed on the metal surfaces. This adsorption is nonspecific and reversible. On the other hand, for inhibitors of the second class the adsorption is chemical in nature and is specific to the metal. For instance, as a general rule, organic inhibitors are more effective with ferrous metals than with nonferrous metals. It can be predicted that for a given inhibitor the order of increasing effectiveness is likely to be: Zn < Cu < Ni <Fe. It is interesting, also, that the series cited above is a familiar one in terms of the stability of chelate complexes.

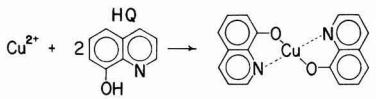
Hayakawa and Ida (1) estimated the stability constants for a series of hydroxyazo compounds of aluminum and they suggested that inhibition of aluminum corrosion in alkaline solutions by these compounds should be increasingly effective with increasing stability of the complex. These chelating agents were considered to form protective films of aluminum chelates on the aluminum surface.

Benzotriazole forms a water-insoluble precipitate with both cuprous and cupric ions and has been used as an efficient corrosion inhibitor for copper in a wide variety of environments (2-7). Cotton (2-4) concluded that benzotriazole inhibits the corrosion of copper by forming a Cu(I)-benzotriazole compound on the copper surface. Poling (8) showed from infrared reflectance spectra that the protective film was highly inert Cu(I)-benzotriazole complex polymer.[2] Wall and Davis (9) suggested that benzotriazole reacts to form an invisible insoluble chelate on the copper surface. On the other hand, Mansfeld *et al.* (7) suggested, on the basis of ellipsometric studies, that benzotriazole is chemisorbed on the copper surface.

Ushenina and Klyuchnikov (10) studied the influence of various chelating agents on the corrosion rates of iron, cobalt, zinc, and copper. Both benzotriazole and 8-hydroxyquinoline retarded the corrosion of copper considerably in ammoniacal buffer. Inhibitor efficiencies of these chelating agents were 90.2 and 44.3%, respectively. On the other hand, the inhibitor efficiency of salicyladoxime in ammoniacal buffer was only 6.2%. They stated that when the chelate is formed directly on the surface as a compact film having good adhesion to the metal (discharge and nucleation mechanism), it retards corrosion. When the chelate is formed in the bulk of the solution and is then deposited (dissolution-precipitation mechanism), the film has only a slight retarding effect on corrosion.

In the present work we have investigated the anodic dissolution of copper in the presence of salicylaldoxime (SAO) and 8-hydroxyquinoline (HQ). Cu^{2+} is precipitated quantitatively by SAO at *p*H values higher than 2.6 (12), and by HQ at *p*H values between 5.3 and 14.5 (incomplete precipitation begins at *p*H 3.5) (11), according to the following reactions:





Solutions of *p*H 1.5, 2.8, and 5.0 were chosen so that the relation between the stability and/or solubility of the chelates and the inhibition efficiency could be studied.

Experimental

All chemicals except SAO (Eastman) were analytical grade and were used without further purification. All solutions were prepared using doubly distilled water (deionized and then distilled). The composition of the buffer solutions was as follows: *p*H 1.5, 0.05M H_2SO_4; *p*H 2.8, 0.2M monochloroacetic acid, 0.1M NaOH; and, *p*H 5.0, 0.1M sodium acetate, 0.033M acetic acid.

The ionic strength of these solutions was adjusted to 0.5 by the addition of sodium sulfate. All solutions were deaerated using purified nitrogen. A single-crystal copper rod (6.0 mm in diameter) with the

* Electrochemical Society Active Member.
** Electrochemical Society Student Member.
† Electrochemical Society Honorary Member.
[1] Present address: Department of Electrochemistry, Yokohama National University, Yokohama, Japan.
Key words: chemisorption, chelate, inhibition.

[2] Benzotriazole (BTA) forms a water-insoluble stoichiometric compound Cu(I) (BTA) with cuprous ions, whereas it precipitates a nonstoichiometric Cu(II) $(BTA)_x$ (x = 1.4-2.0) with cupric ions.

(100) plane as the electrode surface was sheathed in a Teflon cylinder. The electrode surface was polished mechanically with No. 600 emery paper and then electropolished in concentrated phosphoric acid. After washing with distilled water, the electrode was attached to a Beckman rotating electrode assembly with variable drive. A potentiostat with a linear-sweep voltage source (constructed locally with Teledyne-Philbrick operational amplifiers) was used. The phase-selective a-c polarograph was built according to the circuit given by Matsuda *et al.* (13). Unless otherwise stated, all polarization curves were obtained potentiokinetically with a sweep rate of 50 mV/min, after polarizing the rotating copper electrode to a predetermined potential in the region of hydrogen evolution. All measurements were carried out at 25° ± 1°C, and potentials were measured against a saturated calomel electrode.

Results

pH 1.5.—The polarization curves for the rotating copper disk electrode in the solutions of *p*H 1.5 containing the chelating agents are shown in Fig. 1a and 1b. Both SAO and HQ retarded the dissolution rate of copper. The Tafel slope for the copper dissolution was not altered by the addition of either SAO or HQ. The polarization curve shifted to more cathodic potentials with an increase in the rate of rotation. At high anodic polarizations the current tends to be diffusion controlled, as reported by Leckie (14). The effect of additives on the polarization of copper at high anodic polarization was significantly decreased but did not disappear. However, the effect of rotation disappeared.

Salicylaldoxime.—The polarization curves in the presence of SAO at *p*H 2.8 are shown in Fig. 2a and

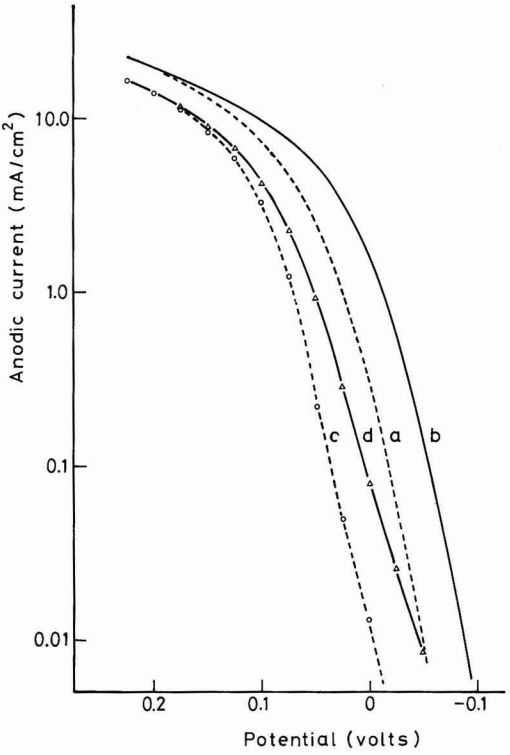


Fig. 1a. Tafel plots in SAO solution at *p*H 1.5. In the base solution with stationary disk electrode (SDE) (curve a), and with rotating disk electrode (6000 rpm) (RDE) (curve b). In 5.0 mM SAO solution with SDE (curve c), and with RDE (6000 rpm) (curve d).

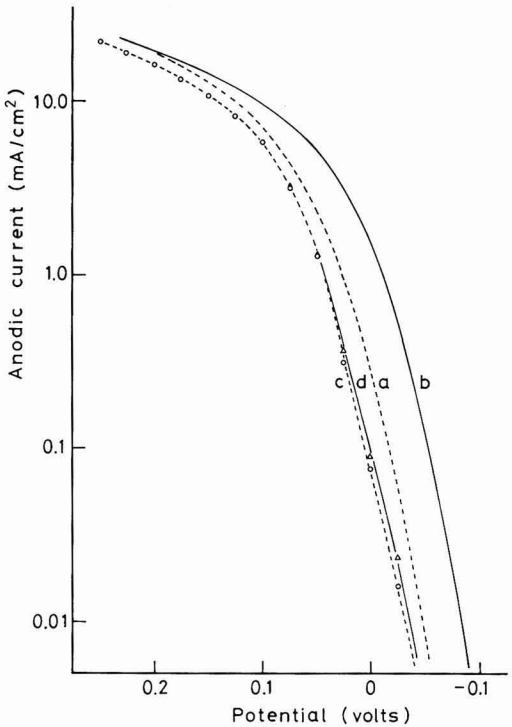


Fig. 1b. Tafel plots in HQ solution at *p*H 1.5. In the base solution with SDE (curve a), and with RDE (6000 rpm) (curve b). In 5.0 mM HQ solution with SDE (curve c), and with RDE (6000 rpm) (curve d).

2b: A current maximum and minimum were observed, followed by a current increase at more anodic potentials. The polarization curves shifted slightly toward cathodic potentials as the rate of rotation was increased at lower current densities (in the potential region of the current peak). The peak current was higher and the peak potential more anodic at the lower concentration of SAO and lower rotation rate. The current in the passive region which followed the current peak decreased with increasing concentration of SAO. At higher anodic polarizations (trans-passive potential, region), a white precipitate of $Cu(SAO)_2$ was seen to fall from the stationary disk electrode. The curves corresponding to increasing and decreasing polarization did not coincide. The current at decreasing polarization was higher than that observed during increasing polarization in the passive region and the current peak was not observed, as shown in Fig. 2a.

In the steady-state potentiostatic polarization curves from cathodic to anodic direction, the current peak was not observed.

In the acetate buffer solution at *p*H 5.0 (Fig. 3a and b), the effect of SAO on the copper dissolution was qualitatively similar to that at lower *p*H values, but was more pronounced. The current peak occurred at about −0.05V, which is more cathodic than at *p*H 2.8. The current peak was also observed with the stationary electrode when the concentration of SAO was more than 10 mM at *p*H 5.0 and 20 mM at *p*H 2.8, respectively. The polarization curves in the trans-passive region were not influenced significantly by the rotation rate (600-6000 rpm) (Fig. 3a), and depended slightly on the concentration of SAO (Fig. 3b); the electrode surface showed local corrosion on a shiny background after polarization in this region. However, it remained shiny when the anodic

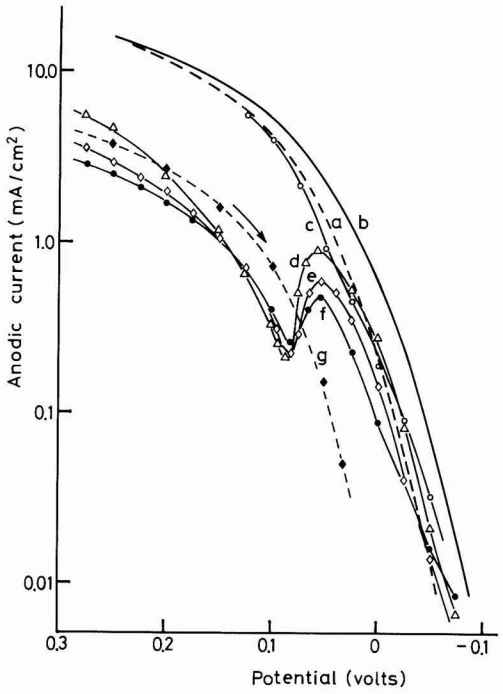


Fig. 2a. Tafel plots in 5 mM SAO solution at pH 2.8 with various rotation rates. In the base solution with SDE (curve a), and RDE (6000 rpm) (curve b). In 5 mM SAO solution with SDE (curve c), 600 rpm (curve d), 1200 rpm (curve e), 3000 rpm (curve f), and with RDE (1200 rpm) polarized from anodic to cathodic direction (curve g).

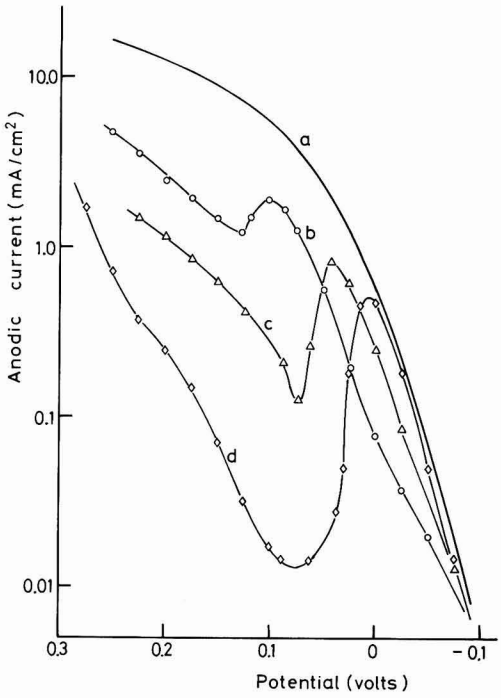


Fig. 2b. Tafel plots in SAO solutions at pH 2.8 with RDE (3000 rpm). In the base solution (curve a), 2.5 mM SAO (curve b), 5.0 mM SAO (curve c), and 10 mM SAO (curve d).

polarization was stopped at potentials more cathodic than the second increase in current rise.

Cyclic voltammetry at the copper electrode in the SAO solution (Fig. 4) showed that the surface film formation was irreversible. The chelate film was partially reduced at potentials more cathodic than about −0.6V. Successive anodic sweeps started from potentials more cathodic than −0.6V gave a larger anodic current peak at −0.1V; the chelate film formed during the anodic process was almost completely reduced at −1.0V.

The total amount of electrical charge involved in the Cu-SAO chelate film formation in the potential region of the current peak depended on the pH of the solution, the concentration of SAO, and the rate of rotation of the electrode (Table I). With increase in the rotation rate, the amount of electrical charge involved in the chelate film formation decreased slightly.

The impedance of the copper electrode in the presence of SAO at pH 5.0 was measured by using the phase-selective a-c polarograph and was represented

Table I. Effect of concentration

The amount of charge (mcoulomb/cm²) required to form the protective film by salicylaldoxime

Concentration, mM	pH 2.8	pH 5.0
2.5	—	18.1
5.0	30.8	11.4
10.0	28.5	7.3
20.0	17.2	1

Rotation speed 3000 rpm.

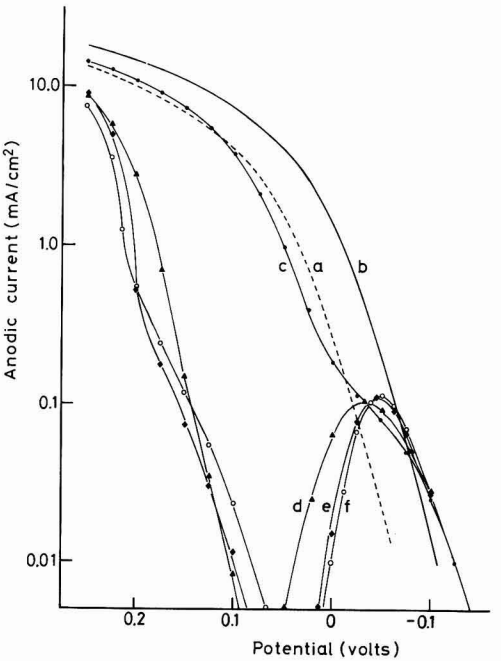


Fig. 3a. Tafel plots in 5 mM SAO solution at pH 5.0 with various rotation rates. In the base solution with SDE (curve a), and with RDE (6000 rpm) (curve b). In 5 mM SAO solution with SDE (curve c), 600 rpm (curve d), 1200 rpm (curve e), and 3000 rpm (curve f).

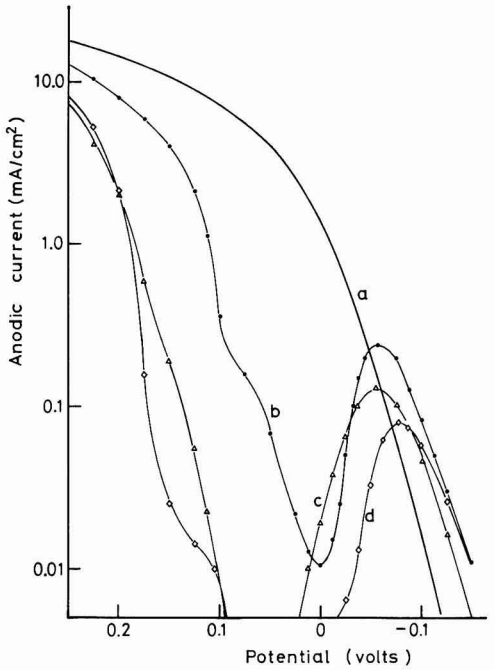


Fig. 3b. Tafel plots in SAO solution at pH 5.0 with RDE (3000 rpm). In the base solution (curve a), 2.5 mM SAO (curve b), 5.0 mM SAO (curve c), and 10 mM SAO (curve d).

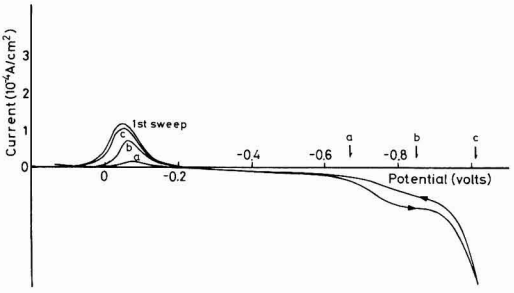


Fig. 4. Cyclic voltammograms of RDE (3000 rpm) in 5.0 mM SAO solution at pH 5.0. The first sweep started at −0.4V toward anodic. Arrows indicate the points where the direction of potential scan was reversed. The peaks are labeled with respect to the corresponding reversal of potential. Scan rate is 0.5 V/min.

as a series combined of a capacitance, C_s, and a resistance, R_s (Fig. 5). In the double layer region, C_s decreased markedly on addition of SAO. On the other hand, R_s remained constant regardless of the concentration of SAO. In the region of the d-c peak, C_s increased slightly, and then decreased to a very small value in the passive region, whereas R_s increased steeply to a very large value.

8-Hydroxyquinoline.—In a solution of 5.0 mM HQ at pH 2.8 (Fig. 6), the dissolution rate increased monotonically as the potential became more anodic, and no current peak was observed. With the rotating disk electrode, a shoulder was observed in the anodic polarization curves at about 2×10^{-4} A/cm². At current densities smaller than 2×10^{-4} A/cm², the polarization curve shifted slightly to the more cathodic region and above this current density it shifted toward the anodic side on rotating the electrode. The

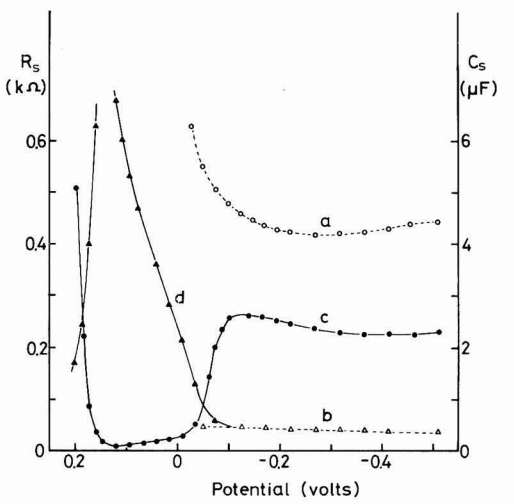


Fig. 5. The resistive and capacitive components (R_s and C_s are in series) of the copper electrode in 5.0 mM SAO solution at pH 5.0. In the base solution (curve a) C_s and (curve b) R_s. In the SAO solution (curve c) C_s and (curve d) R_s.

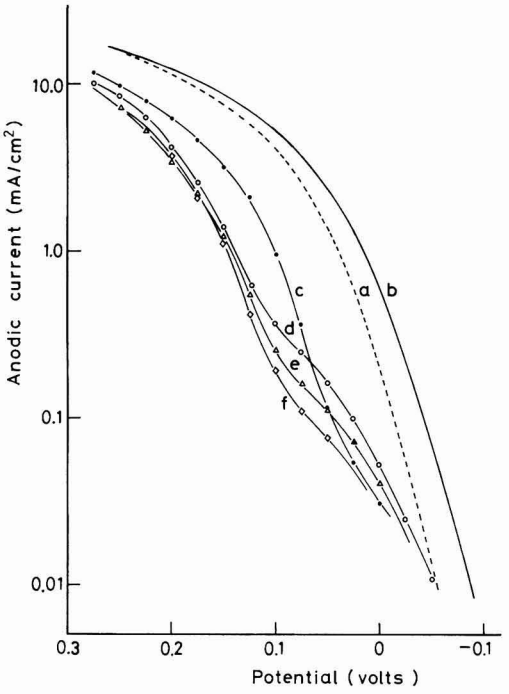


Fig. 6. Tafel plots in 5 mM HQ solution at pH 2.8 with various rotation rates. In the base solution with SDE (curve a) and with RDE (6000 rpm) (curve b). In 5.0 mM HQ solution with SDE (curve c), 600 rpm (curve d), 1200 rpm (curve e) and 3000 rpm (curve f).

effect of rotation rate on the polarization curve was small in a 5 mM HQ solution at pH 5.0 (Fig. 7). With an increase in the rotation rate the polarization curve shifted slightly to more anodic potentials.

Figure 8 shows C_s and R_s for the copper electrode in a 5 mM HQ solution (pH 5). HQ depressed C_s markedly in the double layer region as in the case of the SAO solution and C_s showed a considerable increase

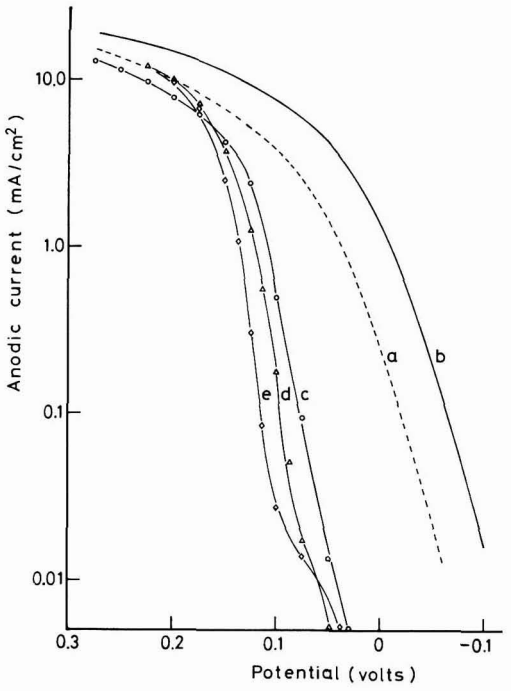


Fig. 7. Tafel plots at *p*H 5.0 in the presence of HQ. In the base solution with SDE (curve a) and with RDE (6000 rpm) (curve b). In 5.0 mM HQ solution with SDE (curve c), 3000 rpm (curve d), and 6000 rpm (curve e).

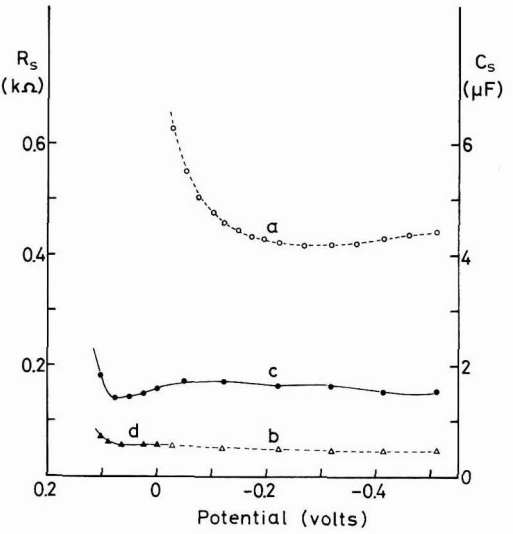


Fig. 8. The resistive and capacitive components (R_s and C_s are in series) of the copper electrode in the 5.0 mM HQ solution at *p*H 5.0. In the base solution (curve a) C_s and (curve b) R_s. In the HQ solution (curve c) C_s and (curve d) R_s.

in the potential region where the d.c. started to increase.

Discussion

At pH 1.5.—About one-half of SAO and most of HQ molecules are protonated in the solution at *p*H 1.5 (15, 16). According to earlier work (17, 18), SAO would therefore be expected to be a better corrosion inhibitor. If we assume that the deceleration of the copper dissolution is only due to a blocking effect and that the surface coverage is independent of the electrode potential, the Tafel slope should not be affected by organic additives because the mass transport to or from the electrode is not disturbed by the additives (19). The shift of the Tafel plots with rotation in the absence of SAO was comparable with that in the presence of SAO; this suggests that the adsorption of SAO did not disturb the diffusion of products from the electrode. Capacity measurements indicated that the potential dependence of the SAO adsorption was very small in this potential region. Although the solubility of HQ is smaller than that of SAO at *p*H 1.5, the inhibitor efficiency of SAO was slightly better than that of HQ. The adsorption of SAO on the copper electrode is probably chemical in nature.

Salicylaldoxime.—In the *p*H range where Cu^{++} precipitates as a chelate with SAO, the polarization curves are similar in shape to those observed for the passivation of iron. In this case, however, the current peak corresponds to the faradaic process for the formation of an insoluble Cu-SAO chelate film at the electrode surface. After the copper electrode surface was covered by the insoluble film the dissolution of copper was completely inhibited. The protective film of Cu-SAO chelate may be very similar to that formed by benzotriazole which reacts at the copper surface to form benzotriazole complexes. Poling (8) identified these complexes as a near stoichiometric Cu(I)-benzotriazole polymer. With increasing anodic polarization beyond the potential of the current peak, the anodic current reached a minimum (which corresponds to the passivation region of iron) and then started to increase again. The current increase in the transpassive potential region was caused by a rupture of the protective chelate film. This is evidenced by a visible localized corrosion of the copper surface.

Hysteresis of the polarization curve also suggests chelate film formation and rupture of the film at very anodic potentials, as in the case of passivation of iron.

In the *pH range where SAO precipitates* Cu^{2+} as Cu-SAO chelate, the formation of Cu-SAO chelate at the copper electrode is thermodynamically more favorable than the dissolution of copper as Cu^{2+}. At *p*H 2.8, however, the rate of chelate film formation at the copper electrode is slow, and the SAO film chemisorbed on the copper electrode, suggested by the data of Fig. 5, inhibited the dissolution of copper. With increase in the electrode potential, the faradaic process took place for the formation of Cu-SAO chelate as a first step. The chelate film formation is probably due to the reaction between the chemisorbed SAO and copper at the copper electrode surface. This mechanism was supported by the fact that the effect of rotation of the electrode on the polarization curves was insignificant at lower current densities. The mass transport of SAO to the electrode surface was so slow with the stationary electrode that the dissolution of copper as Cu^{2+} became predominant at higher current densities and the effect of SAO disappeared at very positive potentials.

With the rotating disk electrode the mass transport of SAO to the electrode was sufficient to form the chelate film on the electrode and the chelate film formation was a predominant reaction at the copper electrode in the current peak region. With increase in the rotation rate of the electrode the mass transport of SAO to the electrode was enhanced and the height of the current peak became smaller because the dissolution of copper was completely inhibited and the peak potential shifted cathodically. This behavior was very similar to the dependency of the polarization curves on the concentration of SAO as shown in Fig. 2b.

At pH 5.0, SAO also accelerates the faradaic process for formation of the chelate film on the electrode in the potential region of the current peak. The polarization curves shifted toward the cathodic region with increase in pH values of the solution. This is due to the formation of a more stable chelate film at pH 5.0 than that at pH 2.8.

The anodic process for the chelate film formation on the copper electrode in the presence of SAO can be considered to be due to: (*i*) the chelate film formation taking place at the electrode covered by the chemisorbed SAO, θ_{ad} $(1 - \theta_{film})$, where θ_{ad} is the fraction of the electrode surface covered by the chemisorbed SAO and θ_{film} is the fraction of the electrode surface covered by the chelate film; $Cu + 2(SAO)_{ad} \rightarrow Cu(SAO)_2$, and (*ii*) copper dissolution taking place at the uncovered electrode surface and Cu^{2+} formed by the anodic process reacting with SAO in the diffusion layer at the electrode interface and this Cu-chelate diffusing away from the electrode.

The mathematical solution of this process was very complicated and hence impractical for the analysis of the experimental data.

We made the further simplification that the electrode surface covered by the chemisorbed SAO was considered to be appreciably high on the basis of the differential capacity measurements so that the dissolution of copper as Cu^{2+} from the uncovered surface was ignored. The fraction of the electrode surface covered by SAO, θ_{ad}, was assumed to be a constant because the peak currents shown in Fig. 3a were far less than the flux of the limiting diffusion of SAO to the electrode surface under the present condition. The current-potential relation in the potentiokinetic measurement can be easily calculated by using Eq. [1] and [2]

$$i = 2\mathbf{F}k\,\theta_{ad}^2(1 - \theta_{film})\exp(2\beta\mathbf{F}E/RT) \quad [1]$$

$$i = S\mathrm{d}\theta_{film}/dt \quad [2]$$

$$E = E_i + vt \quad [3]$$

where i (A/cm^2) is the faradaic current for the chelate film formation; k the rate constant for the chelate formation at $E = 0$, β the anodic transfer coefficient; θ_{film} and θ_{ad} (%) the fraction of the electrode surface covered by the chelate film and chemisorbed SAO, respectively; S (coulombs/cm^2) the amount charge required to cover the electrode surface by the chelate film; v (V/sec) the scan rate, and t (sec) time. A solution of Eq. [1] is easily obtained as follows: (*i*) Substitute i and E into Eq. [1], and then integrate Eq. [1] to get θ_{film} as a function of time. (*ii*) Substitute $\theta_{film}(t)$ into Eq. [1] and then set its time derivative equal to zero to get t_{max}, the time required to reach the current peak potential from $E = E_i$.

One can obtain

$$t_{max} = \underline{\overline{K}}_1 - \underline{\overline{K}}_2 \ln \theta_{ad} \quad [4]$$

where

$$\underline{\overline{K}}_1 = \frac{RT}{2\beta\mathbf{F}v}\ln\left(\frac{S\beta v}{RTk}\right) - \frac{Ei}{v}$$

and

$$\underline{\overline{K}}_2 = \mathrm{RT}/\beta\mathbf{F}v$$

Then one can easily obtain the peak current

$$i_{max} = \ln(2\beta\mathbf{F}v/RT) - 1 + (RTk\theta_{ad}^2/S\beta v)$$

$$\times \exp(2\beta\mathbf{F}E_i/RT) = \underline{\overline{K}}_3 + \underline{\overline{K}}_4\,\theta_{ad}^2 \quad [5]$$

The peak potential shifts linearly toward cathodic values with log θ_{ad} and the peak height increases linearly with θ_{ad}^2.

The shift of the peak potential with respect to the SAO concentration is shown in Fig. 9. Since θ_{ad} is a function of concentration of SAO, the steeper the slope of plots, the stronger is the adsorption of SAO on the copper electrode. Qualitatively, the adsorption of SAO onto the copper electrode becomes stronger with increasing pH of the solution. Similar behavior was observed with EDTA, adsorbed on a mercury electrode (20).

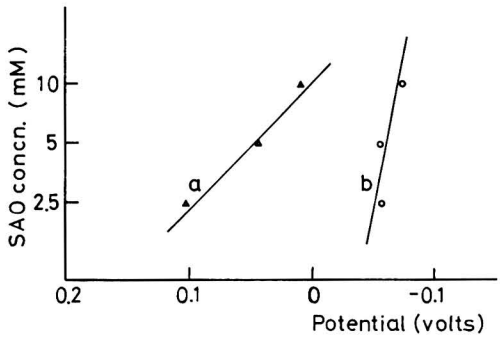


Fig. 9. Shift of peak potential with the concentration of SAO at pH 2.8 (curve a) and pH 5.0 (curve b).

The marked decrease in the capacitive component, C_s, of the copper electrode in the presence of SAO (Fig. 5) suggested that SAO adsorbed strongly on the electrode in the pH range where the Cu-SAO chelate is stable. In the current peak region of the above condition, the capacitive component became very small and the resistive component reached several thousands ohms. These changes strongly suggested the chelate film formation on the electrode surface. With the stationary disk electrode in the 5 mM SAO solution at pH 5.0, both C_s and R_s started to increase from the values in the double layer region at about +0.05V which is 75 mV more anodic than those in the base solution. This is probably due to the dissolution of copper as Cu^{2+} because of the insufficient supply of SAO onto the electrode to form a compact chelate film.

If we assume that the chelate film is formed through the dissolution-precipitation mechanism (21) the peak current in the cyclic voltammogram with a rotating disk electrode should increase with increasing rotation rate such as in the passive film formation on copper (22). In the present case, however, the peak current decreased with an increase in the rotation rate. This behavior indicates a discharge-nucleation mechanism for the formation of the Cu-SAO chelate on the copper electrode (21).

Assuming the density to be 2 g/cm^3, the thickness of the surface film calculated from the amount of charge required for its formation ranged from 100Å, in 20 mM SAO solution at pH 5.0, to 1000Å, in 5.0 mM SAO solution at pH 5.0. These thicknesses are comparable with those reported by Poling (8) for the Cu-benzotriazole film on copper electrode.

8-Hydroxyquinoline.—In the HQ solution at pH 2.8, a shoulder was observed in the polarization curves with the rotating disk electrode (Fig. 6). The cathodic shift of the polarization curve at lower current densities (2×10^{-4} A/cm^2) would be explained from the analogy of the copper electrode in the HQ solution to that in the SAO solution. The effect of HQ in the pH 5.0 solution is more pronounced than that in the pH 2.8 solution and the polarization curves were not influenced by the rotation rate (Fig. 7).

A strong adsorption of HQ on the copper electrode in the pH range where HQ precipitates cupric ions was evidenced by the capacitance curve in the double layer region (Fig. 8). Both capacitive and resistive components of the copper electrode in the pH 5.0 solution remained at almost the same value up to about +0.1V which corresponded to the potential at which the anodic dissolution of copper started. No decrease of the capacitive component was observed in the HQ solution. This result suggests that the inhibition of copper dissolution by HQ is not due to the chelate film on the

electrode but mainly to the chemisorbed film. This mechanism is also supported by the evidence that the rotation rate did not show any significant influence on the anodic polarization curves. The formation of a Cu-HQ chelate film on the electrode was evidenced by the result that the decreasing polarization curve (from anodic to cathodic) was higher than that of the increasing ones. However, the adhesion of the film on the electrode was not so strong as to decrease the capacitive component of the electrode, in contrast to the case of the SAO solution.

Conclusion

It was shown that the adsorption of both SAO and HQ on the copper electrode became stronger with increase in pH of the solution. This tendency is parallel to the stability of the copper chelates of SAO and HQ. In the pH range where SAO and HQ precipitate cupric ions as a chelate, the adsorbability of these chelating agents increased markedly and the anodic dissolution rate of copper was retarded to a considerable extent. In the SAO solutions the anodic polarization curves of copper were similar in shape to those for the passivation of iron. The Cu-SAO chelate film was formed in the active-to-passive transition region and the copper electrode became passive after the surface was covered by the chelate film. In the HQ solutions, on the other hand, the chemisorbed film retarded the dissolution of copper. The Cu-HQ chelate did not adhere to the copper electrode.

Acknowledgment

The authors express their appreciation to the Robert A. Welch Foundation, Houston, Texas, for its support of this research. One of the authors (K.N.) also expresses his appreciation to Dr. Reita Tamamushi and Mr. Kiyoshi Matsuda, Institute of Physical and Chemical Laboratory, Japan, for the phase-selective polarographic work, and to Dr. H. H. Bauer, University of Kentucky, for his helpful discussions and suggestions in the course of preparing this manuscript.

Manuscript submitted Feb. 5, 1973; revised manuscript received Feb. 20, 1975. This was Paper 79 presented at the Miami Beach, Florida, Meeting of the Society, Oct. 8-13, 1972.

Any discussion of this paper will appear in a Discussion Section to be published in the June 1976 JOURNAL. All discussions for the June 1976 Discussion Section should be submitted by Feb. 1, 1976.

Publication costs of this article were partially assisted by Rice University.

REFERENCES

1. Y. Hayakawa and I. Ida, *Denki Kagaku (J. Electrochem. Soc. Japan)*, **26,** 643 (1958).
2. J. B. Cotton, *Trans. Inst. Marine Eng.*, **77,** 165 (1965).
3. J. B. Cotton, "Proceedings 2nd International Congress on Metallic Corrosion," p. 590, NACE, New York (1963).
4. I. Dugdale and J. B. Cotton, *Corrosion Sci.*, **3,** 69 (1963).
5. J. B. Cotton and I. R. Scholes, *Brit. Corrosion, J.*, **2,** 1 (1967).
6. P. L. Bonora, G. P. Bolognesi, P. A. Borea, G. L. Zucchini, and G. Brunoro, "3rd European Symposium on Corrosion Inhibitors," p. 685, Ferrara (1971).
7. F. Mansfeld, T. Smith, and E. P. Parry, *Corrosion*, **27,** 289 (1971).
8. G. W. Poling, *Corrosion Sci.*, **10,** 359 (1970).
9. K. H. Wall and I. Davies, *J. Appl. Chem.*, **15,** 389 (1965).
10. U. F. Ushenina and N. G. Klyuchnikov, *Zhur. Prikl. Khim.*, **44,** 191 (1971).
11. H. R. Fleck and A. M. Ward, *Analyst*, **58,** 388 (1933).
12. N. Furman and F. J. Flagg, *Ind. Eng. Chem., Anal. Ed.*, **12,** 738 (1940).
13. K. Matsuda, K. Takahashi, and R. Tamamushi, *Sci. Papers Inst. Phys. Chem. Res.*, **64,** 62 (1970).
14. H. P. Leckie, *This Journal*, **117,** 1478 (1970).
15. K. E. Jabalpurwala, K. A. Venkamachalam, and M. B. Kabadi, *J. Inorg. Nucl. Chem.*, **26,** 1011, 1027 (1964).
16. R. Nasanen, P. Lumme, and A. L. Mukula, *Acta Chem. Scand.*, **5,** 1199 (1951).
17. N. Hackerman, R. M. Hurd, and R. R. Annand, *Corrosion*, **18,** 371 (1962).
18. N. Hackerman and A. C. Makrides, *Ind. Eng. Chem.*, **46,** 523 (1954).
19. K. K. Niki and N. Hackerman, *J. Phys. Chem.*, **73,** 1023 (1969).
20. K. Niki, K. Suzuki, G. P. Sato, and N. Mori, *J. Electroanal. Chem.*, **49,** 27 (1974).
21. A. K. N. Reddy, *ibid.*, **28,** 217 (1970).
22. T. Yoshimura, Y. Imanaka, and M. Yamashita, *Sci. Eng. Rev.*, Doshisha Univ., **14,** 43 (1974).

The Mechanism of Metallic Chromium Electrodeposition in the Cathodic Dichromate Treatment of Tinplate

Ph. Aubrun and P. Rocquet

Centre de Recherches du Fer Blanc, B. P. 135, 57100 Thionville, France

ABSTRACT

The passivation film deposited on tinplate by a cathodic treatment in a dichromate solution partly consists of metallic chromium. In order to clarify this rather surprising electrodeposition of metallic chromium, the successive reactions taking place were characterized. As a consequence, it is explained why the metallic chromium electrodeposition is made possible, and for what reason the deposit is of limited amount. The role played by the high hydrogen overvoltage on tin is emphasized.

At the end of its manufacturing process, electrolyte tinplate is subjected to a passivation treatment which improves its properties. Generally, this treatment consists of making the strip cathodic in a low-acid, sodium dichromate solution (CDC treatment). Tinplate is thus coated with a thin film containing metallic chromium (1, 2). This has been established by means of anodic dissolutions of the film, part of which involves six electrons per atom-gram of chromium. One cannot fail to be surprised by the following two items: First, how

Key words: tinplate passivation films, mechanism of chromium electrodeposition.

Table I. Conditions of metallic chromium deposition

	CDC treatment	Conventional chromium plating
Electrolyte: concentration	0.09M $Na_2Cr_2O_7 \cdot 2H_2O$	0.5M CrO_3
Acidity	pH 3-8	pH 1
Catalyzer	None	Yes
Current density	1 A/dm²	20 A/dm²

can metallic chromium be deposited under conditions so different from those under which this metal is generally deposited (Table I)? Second, why does the amount of metallic chromium obtained through tinplate CDC treatment rapidly reach a limit, dependent on the experimental factors, whereas it increases proportionally to the time with conventional chromium plating of iron (Fig. 1)?

A good understanding of the mechanism of metallic chromium electrodeposition during CDC treatment is required to explain these two facts. This is the subject of the first part of the present paper; then the two characteristics of this electrodeposition are explained in the last parts.

Successive Steps Leading to the Metallic Chromium Electrodeposition during CDC Treatment

In the case of conventional chromium plating of iron, the potentiokinetic cathodic polarization curve indicates the reaching of successive reactions (3). Prior to metallic chromium deposition, the building up of two films of chromium oxides and hydrogen evolution are noted (Fig. 2). It is noteworthy that if one substitutes the conventional chromium electrolyte with a dilute sodium dichromate solution, the successive waves of Fig. 2 disappear; at the same time, there is no metallic chromium electrodeposition.

Now, if we plot a curve of the same type, but relating to a tin electrode and a dilute sodium dichromate solution, we note (Fig. 3) the same features as those shown in Fig. 2, but only if we have used rolled tin or hot-dipped tinplate, cathodically cleaned in a Na_2CO_3

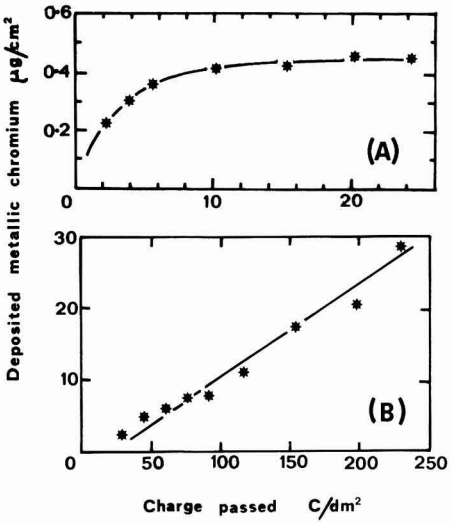


Fig. 1. Comparison between the rates of metallic chromium electrodeposition in the CDC treatment (A) and the conventional chromium plating of iron (B). (A) Cathode of electrolytic tinplate flow-melted and alkaline-cleaned. $Na_2Cr_2O_7 \cdot 2H_2O$ 25 g/liter (0.083M); pH 5.1; temperature 47°-49°C; 2 A/dm². (B) Cathode of mild steel cold-rolled, annealed, and alkaline-cleaned. CrO_3 50 g/liter (0.5M); H_2SO_4 0.5 g/liter; 20 A/dm².

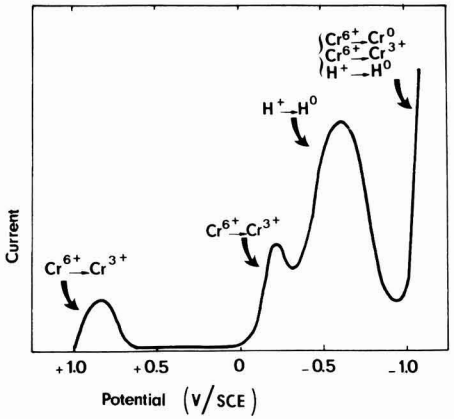


Fig. 2. Cathodic polarization curve of iron in a chromium plating bath (CrO_3-H_2SO_4) plotted potentiokinetically. Published by A. T. Vagramyan and D. N. Usachev, *Zhur. Fiz. Khim.*, **32**, 1900 (1958); after (3).

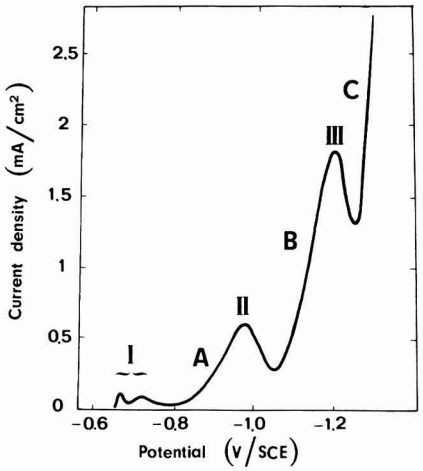


Fig. 3. Cathodic polarization curve plotted potentiokinetically with pure tin in an aqueous solution of $Na_2Cr_2O_7 \cdot 2H_2O$, 0.085M; pH 5.2; temperature 55°C; sweep rate 6 V/hr. Curve shape remains unchanged in the range of: $Na_2Cr_2O_7 \cdot 2H_2O$, 0.02-0.25M; temperature 25°-70°C; sweep rate 0.166-60 V/hr.

aqueous solution (5 g/liter). Under the same conditions, peak II does not appear with electrolytic tinplate as flow-melted, although we still notice the final deposition of metallic chromium. This particular behavior of electrolytic tinplate is probably due to an absorption of phenolsulfonic acid in the tin coating, as revealed by experiments which are not reported in this paper.

Comparison between Fig. 2 and 3 provides information on the studied mechanism. Thus, peak I (or the group of peaks I) would correspond to the building up of a primary chromium oxide film after the reduction of the tin oxides, peak II to the building up of a secondary chromium oxide film which changes at peak III. The final slope C results from a visible hydrogen evolution and from a chromium deposit under the metallic and oxide forms as indicated by chemical analysis.

The above propositions were investigated by repetitive potentiokinetic oxidation and reduction to specific potentials.

Electrochemical oxidations and reductions which do not reach the A slope (Fig. 3) show how the shape of

the group of peaks I depends on the potential of the oxidation taking place prior to the reduction. When this oxidation potential is increased, the group first consists of a single peak I, to which a second peak with a more cathodic potential is added, then again a single peak but with an even more cathodic potential (Fig. 4). Additional experiments (4) allow us to assign the *reductions of* Sn(II), Sn(IV), and SnOx (1) to these successive peaks. Prior to peak I, the electrode was already coated with chromium due to immersion in the electrolyte, as a subsequent oxidation (around + 0.8 V/SCE) reveals the peak where oxidation of metallic chromium and chromium oxide generally takes place (4-6). Chemical analysis (1) allows us to specify that only chromium oxide is present. However, it is to be noted that tin oxide reduction at peak I increases this deposit of chromium oxide (which will be qualified as primary) as it raises the height of the oxidation peak which is located at + 0.8 V/SCE.

Peak II very likely corresponds to a film of chromium oxide as, after the dissolution of the primary chromium oxide through electrochemical oxidation at + 0.8 V/SCE, a tin polarization up to the A slope is sufficient to recover subsequently an oxidation peak at + 0.8 V/SCE (Fig. 5). Therefore, this new film will be called "secondary." The reaction which originates it is apparently reversible as indicated in Fig. 6. It is thought that chromium oxide may have valency III in the secondary film.

As long as the cathodic scanning end remains in the B slope, the secondary film of chromium oxide retains its solubility and the originating reaction retains its *reversibility* (Fig. 7). *As soon as the maximum of peak* III has been passed, peak II disappears whatever the scanning direction may be. This disappearance is progressive as long as the cathodic end remains between

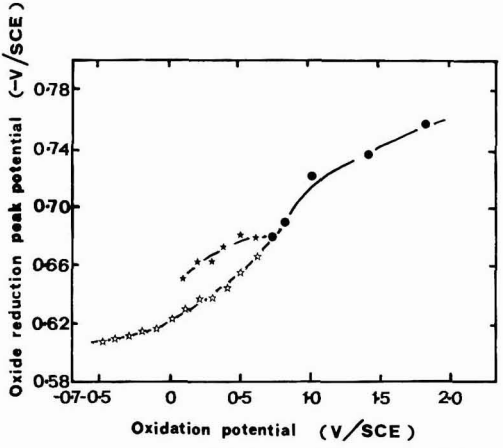


Fig. 4. Reduction potential(s) of tin oxide(s) *vs.* potential of oxidation done before. ☆☆☆ SnO; ★★★ SnO_2; ●●● what we have called SnO_x (1). Solution of $Na_2Cr_2O_7 \cdot 2H_2O$, 0.085M deaerated by nitrogen bubbling; pH 5.2; temperature 55°C; sweep rate 6 V/hr.

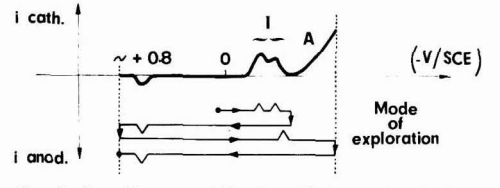


Fig. 5. Repetitive potentiokinetic oxidation and reduction to specific potentials. See text.

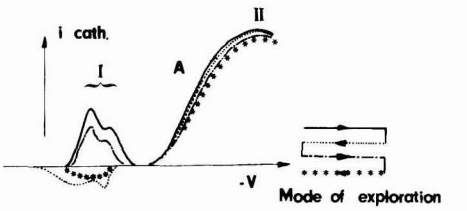


Fig. 6. Repetitive potentiokinetic oxidation and reduction to specific potentials. See text.

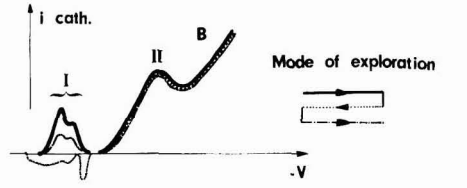


Fig. 7. Repetitive potentiokinetic oxidation and reduction to specific potentials. See text.

peak III and the valley which separates it from the C slope (Fig. 8); it occurs suddenly when the cathodic end is in the C slope (Fig. 9). Peak III corresponds to a change in chromium oxide film, but not to its destruction: in fact, oxidation of the sample at + 0.8 V/SCE is sufficient to obtain the peak of chromium oxidation (Fig. 9) and to regenerate the electrode as a subsequent reduction will reveal the peak II again. (In order to avoid any possible interference of the primary chromium oxide film, the sample was oxidized at + 0.8 V/SCE prior to the first scanning in the cathodic direction of Fig. 8.)

As previously indicated, deposits of metallic chromium and of trivalent chromium oxide build up and a hydrogen evolution occurs in the C slope. It is noteworthy that we regenerate the electrode which reaches the C slope through a simple oxidation at + 0.8 V/SCE: *a subsequent cathodic polarization restores peaks* I, II, and III (Fig. 10).

The reaction sequence of tin CDC treatment is reminiscent of the one of conventional chromium plating of iron. Using tin, we have pointed out the successive

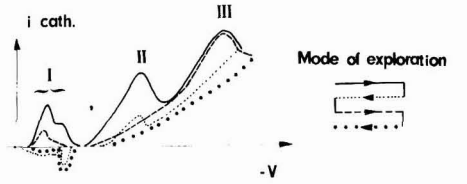


Fig. 8. Repetitive potentiokinetic oxidation and reduction to specific potentials. See text.

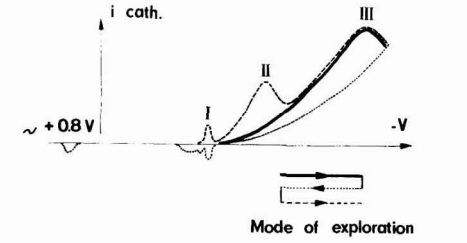


Fig. 9. Repetitive potentiokinetic oxidation and reduction. See text. The first sweep begins after the last one drawn in Fig. 8.

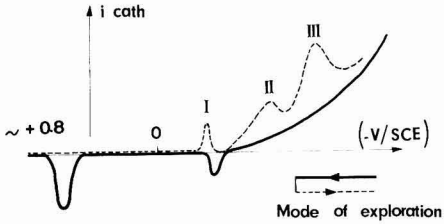


Fig. 10. Repetitive potentiokinetic oxidation and reduction. See text. The start point is in the slope C.

steps: (*i*) building up of a chromium oxide primary film; (*ii*) reduction of tin oxides and strengthening of the primary film; (*iii*) building up of a secondary film of chromium oxide; (*iv*) alteration of this film at the time of a hydrogen evolution; and (*v*) hydrogen evolution, deposition of metallic chromium and chromium oxide.

Limited Amount of Metallic Chromium Deposition

As stated above, the amount of metallic chromium deposited through CDC treatment reaches a limit (4, 8) (see first diagram of Fig. 1).

It has been shown that this limited amount can be deposited at several times as long as the surface film is not damaged by water rinsing. This is clearly reflected in a galvanokinetic cathodic polarization experiment (Fig. 11, in which the various features of Fig. 3 are easily traced), the results of which are shown in Table II.

This limited amount of metallic chromium which may be deposited depends on experimental factors (8) (temperature, acidity, foreign ion content of the electrolyte) which also alter the magnitude of peaks II and III on the potentiokinetic curve of the cathodic polarization. Comparison of the effects of these factors on the limited metallic chromium deposition and on the polarization curve (Table III) shows that an intensification of peaks II and III increases the limited amount of metallic chromium. We can say that the limited amount of metallic chromium is directly dependent on the amount of chromium oxide of the secondary film (and possibly the primary film) which is modified by the reaction of peak III.

Consequently, the maximum amount of metallic chromium to be deposited is determined when the electrode reaches the C slope.

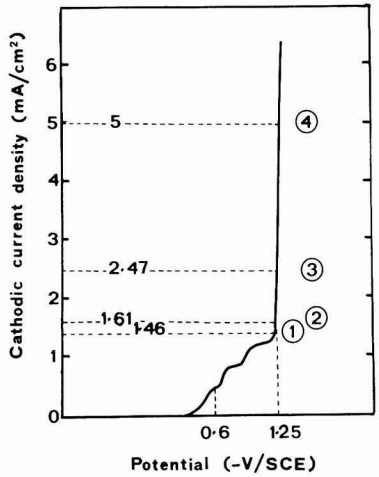


Fig. 11. Cathodic polarization curve plotted galvanokinetically. Pure tin. $Na_2Cr_2O_7 \cdot 2H_2O$, 0.085M; pH 5.2; temperature 55°C; sweep rate 0.25 A/cm²/mn. Encircled numbers refer to the text and to Table II.

Let us now consider the shape of the C slope when increasing amounts of metallic chromium are deposited through CDC treatment on a tin electrode. Figure 12 shows that it rises progressively, moves toward less cathodic potentials, and finally stabilizes. This matches the cathodic polarization curve of a chromium electrode dipped in this dichromate electrolyte.

To conclude, metallic chromium which is deposited on tin during CDC treatment originates from the film or films of chromium oxides built up during the previous steps and its amount is limited. After deposition, the electrode changes and becomes a chromium electrode.

Reason for Metallic Chromium Deposition during CDC Treatment

We have shown in the previous part that dichromate solution is unable to continue the metallic chromium deposition once the electrode becomes a chromium electrode. We can therefore assume that this deposition is due to the nature of the tin electrode.

Table II. Possibility for a two-step deposition of the limited amount of metallic chromium

Cathode reduction up to[a] →	Metallic chromium level[b]	Cathodic reduction up to [a]	+ Water rinsing +	Cathodic reduction up to[a] →	Metallic chromium level[b]
1	0.23	1	No	4	2.7
1	0.23	1	Yes	4	1.6
2	0.29	2	No	4	2.4
3	1.31	3	No	4	2.6
4	2.5	4	No	4	2.5

[a] Numbers in this column refer to circled numbers in Fig. 11.
[b] Metallic chromium levels are given for guidance and are expressed in μg/cm².

Table III.

Factor	Influence on the peaks of the polarization curve	Influence on the maximum amount of metallic chromium deposited during full-scale or laboratory passivation trials
Dichromate concentration	None between 13 and 74 g/liter $Na_2Cr_2O_7 \cdot 2H_2O$	None
pH increase	Reduces peaks II and III	Decrease
Rise in temperature	Intensifies peaks II and III	Increase
Additions of Cl^- or SO_4^{2-}	At high content levels, lightly reduce peaks II and III	Not obvious at low industrial contents
Phosphate addition	Little effect on peak II, but lessens peak III	Delays the deposition
Increase of the amount of tin oxide	Little influence on peaks II and III from which peak I element has been subtracted	Negligible if any

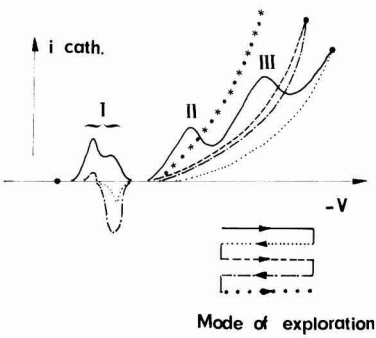


Fig. 12. Repetitive potentiokinetic oxidation and reduction. See text. *** refers to the cathodic polarization curve plotted in the same conditions but with a metallic chromium electrode.

As one of the properties of tin is a very high hydrogen overvoltage, which is not true for metallic chromium, we may ask ourselves if this is actually the determinative factor.

In order to answer this question, we have studied the potentiokinetic curve of cathodic polarization of some other common metals. Lead is the only metal to present the same peaks as those of tin (Fig. 13). The other metals (platinum, iron, copper, nickel, cadmium, chromium, silver, and zinc) present normal curve sections. Among the metals investigated, tin and lead are the only two to possess the higher hydrogen overvoltage in their final curve sections.

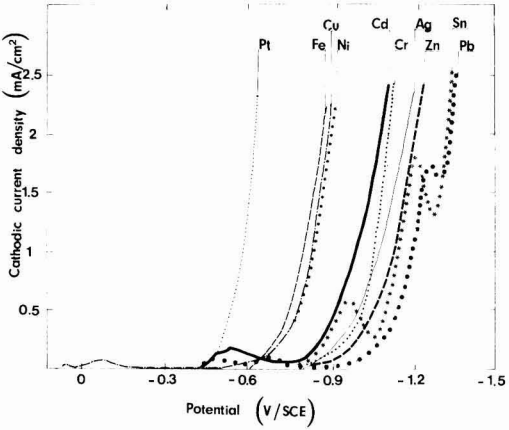


Fig. 13. Cathodic polarization curves plotted potentiokinetically with many metals; $Na_2Cr_2O_7 \cdot 2H_2O$, 0.085M; pH 5.2; temperature 55°C; sweep rate 6 V/hr.

As a result, CDC treatment deposits metallic chromium due to the high hydrogen overvoltage on tin. We are thus in compliance with the result given in the last part: Deposition is only possible when tin is not coated with a metallic chromium film, the thickness of which has therefore to be very uniform.

Conclusions

The points developed in this report allow us to state that:

1. CDC treatment includes the following successive reactions: (*i*) building up of a chromium oxide primary film; (*ii*) reduction of tin oxides and strengthening of the primary film; (*iii*) building up of a chromium oxide secondary film; (*iv*) alteration of this film (or films) at the time of hydrogen evolution; and (*v*) hydrogen evolution, deposition of metallic chromium and chromium oxide.

2. Metallic chromium deposition, under conditions very different compared with those of conventional chromium plating of iron, is made possible by the high overvoltage of hydrogen on tin.

3. Metallic chromium deposition stops when the electrode changes to become a metallic chromium electrode. The amount which can be deposited is limited by the amount of chromium oxide which has built up during the previous steps: It is therefore dependent on the experimental conditions.

Manuscript submitted Dec. 28, 1973; revised manuscript received Feb. 12, 1975. This was Paper 76 presented at the Boston, Massachusetts, Meeting of the Society, Oct. 7-11, 1973.

Any discussion of this paper will appear in a Discussion Section to be published in the June 1976 JOURNAL. All discussions for the June 1976 Discussion Section should be submitted by Feb. 1, 1976.

Publication costs of this article were partially assisted by Centre de Recherches du Fer Blanc.

REFERENCES

1. P. Rocquet and Ph. Aubrun, *Corrosion* (Fr.), **5**, 229 (1968).
2. S. E. Rauch, Jr. and R. N. Steinbicker, *This Journal*, **120**, 735 (1973).
3. H. Okada and K. Yamamoto, *Electrochem. Technol.*, **6**, 389 (1968).
4. P. Rocquet and Ph. Aubrun, Unpublished results.
5. S. C. Britton, *Brit. Corrosion J.*, **1**, 91 (1966).
6. D. Salm, *BHP Tech. Bull.*, **16**, 2 (1972).
7. H. Okada, Thesis, University of Hokkaido, p. 139 (1962).
8. P. R. Carter, *This Journal*, **108**, 782 (1961).
9. P. Rocquet and Ph. Aubrun, *Brit. Corrosion J.*, **5** 113 (1970).

On the Structure and Electrical Properties of Electroless Ni-B Films

N. Hedgecock, P. Tung, and M. Schlesinger*

Department of Physics, University of Windsor, Windsor, Ontario, Canada N9B 3P4

ABSTRACT

An electron microscope study and measurements of electrical resistivity have been performed on electrolessly deposited Ni-B thin films. In contrast to Ni-P films, the islands of Ni-B films show a marked internal structure. Ni-B films have higher electrical resistivity than equally thick Ni-P films.

Electroless deposition of the nickel-boron system is possible using either alkali borohydrides or amine boranes as reducing agents. A survey of early work has been given by Goldie (1). More recent studies have been made by Fléchon *et al.* (2-4), Petrov *et al.* (5), and Gorbunova *et al.* (6, 7).

The as-deposited state of both Ni-P and Ni-B is highly disordered, and metastable in that heat-treatment irreversibly induces a state of higher crystallinity. In both systems, the initial state is a solid solution of phosphorus (8) or boron (4, 6) in nickel. For the deposits studied in this work the phosphorus and boron contents were about 20 and 25 per cent atomic, respectively.

Heat-treatment of Ni-P above 325°C produces two components, fcc nickel and tetragonal Ni_3P. The latter in bulk form has an electrical conductivity close to that of nickel, and indeed has an electronic band structure remarkably similar to that of nickel (9).

X-ray and thermal studies of Ni-B (3-7) have revealed analogous formation of nickel borides after annealing in vacuum. The formation of Ni_3B occurs around 300°C, accompanied by an abrupt change in electrical properties (3, 4). Above 400°C, Ni_2B and possibly other borides are formed.

The present work describes further studies of electroless Ni-B films, involving electron microscopy and measurements of electrical resistivity. Results are presented for both freshly deposited and heat-treated films prepared under different conditions. Some results are also compared with those obtained from our earlier work on the nickel-phosphorus system (8).

* Electrochemical Society Active Member.
Key words: electroless, thin film, nickel-boron.

Experimental

Electron microscopy.—A Hitachi HU-12 electron microscope operated at 100 kV was employed for obtaining transmission micrographs and selected area diffraction patterns. An aluminum foil standard was used to calibrate measurements of diffraction patterns. In many cases, the diffraction rings obtained were broad, indicating small crystallite size, and limiting the accuracy of measurement to about 1%.

The Ni-B films were grown on glass microscope slides coated with Formvar (4g polyvinyl formal in 1 liter ethylene dichloride). The Formvar layer was subsequently floated off in distilled water, and samples were deposited on copper grids for insertion into the microscope.

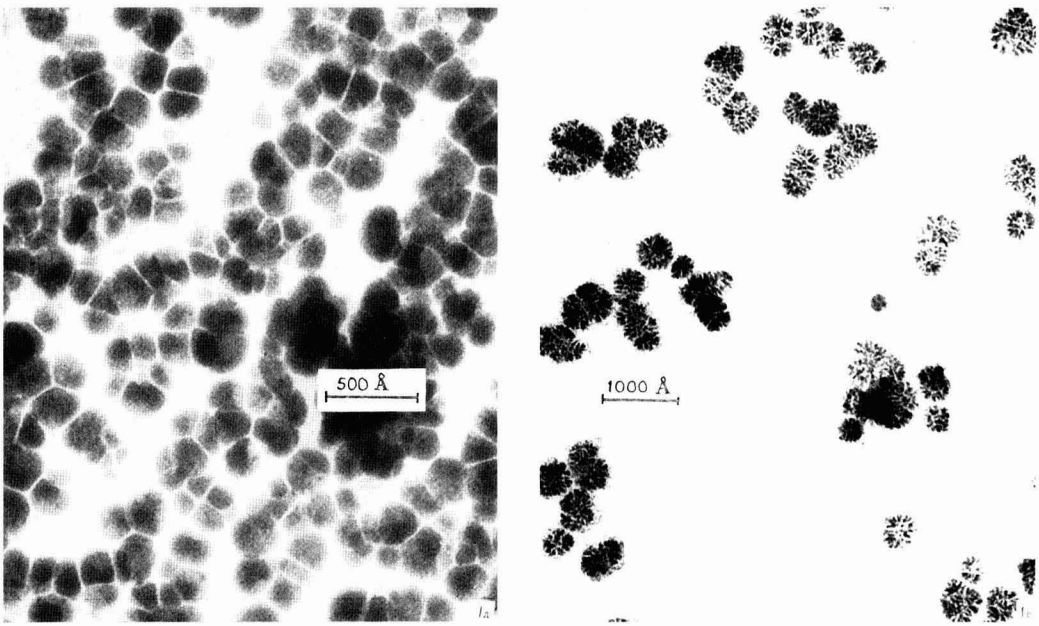


Fig 1. Transmission electron micrographs of thin films of (a, left) Ni-P deposited at room temperature from acidic (pH = 5.3) solution, (b, right) Ni-B deposited at 60°C using conventional $SnCl_2$/HCl sensitizer.

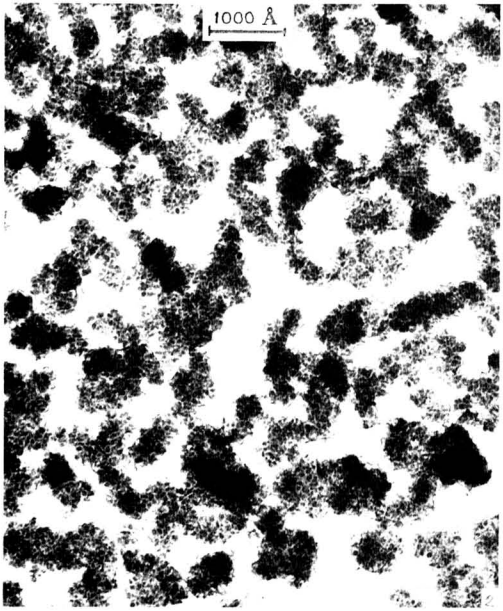


Fig. 2. Transmission electron micrograph of a thin film of Ni-B deposited at 60°C using improved ($SnCl_2$/HCl with additional aged $SnCl_4$) sensitizer.

Three different sensitizers were employed in preparing the substrates for deposition: fresh $SnCl_2$/HCl with and without additional aged $SnCl_4$, and aged (4-6 days) $SnCl_2$/HCl. All were used in conjunction with the usual $PdCl_2$/HCl activator. The properties of these solutions have been investigated previously (10) and (11). The metallizing bath was that given as "B" by Gorbunova *et al.* (7). It employs borohydride as the reducing agent, has a pH of 14, and contains no stabilizer. This solution was maintained at 60°C; deposition times ranged from 40 sec for the thin samples prepared for electron microscopy to 100 sec for the thickest samples used in the electrical measurements.

Samples were examined in the electron microscope before and after heat-treatment at 400°C. The heating was carried out in an evacuated glass tube which was flushed with dry nitrogen prior to evacuation. The pressure in the tube during heating was about 10^{-5} Torr. The heating sequence was as follows: 45 min heating from room temperature to 400°C; 45 min at 400°C; 45 min cooling back to room temperature.

Electrical resistivity.—The four-probe method of van de Pauw (12) was used to determine the resistivity of films of various thicknesses. For these measurements, deposition was made directly onto microscope slide glasses. Circular samples of 1 in. diameter were subsequently made by placing the deposited glasses in a Teflon mask, and etching away the unwanted Ni-B with a solution of HCl and HNO_3. Spring-loaded stainless steel contacts were located symmetrically on the periphery of the circular samples for the measurements. The resistivity was determined both before and after the same heat-treatment as described above. The current in the samples was restricted to 100 μA during the measurements. For comparison, similar samples of Ni-P films of various thicknesses were made and their resistivity measured before and after the heat-treatment. For both Ni-B and Ni-P samples, the improved sensitizer was used. Film thicknesses were determined using the Tolansky interferometric method.

Results and Discussion

Electron microscopy.—Electron micrographs reveal both similarities and differences between Ni-P and Ni-B deposits. Figure 1 shows (a) Ni-P deposited at room temperature from acidic (pH = 5.3) solution and (b) Ni-B deposited at 60°C using conventional sensitizer. In both cases the deposit is composed of islands, typical of the initial stage of thin film growth in general. Moreover the islands are circular in shape and of rather uniform size. For Ni-P, these islands resemble liquid drops and have no discernible internal features. In contrast, the Ni-B islands usually show a characteristic "flowerlike" internal structure. The diffraction

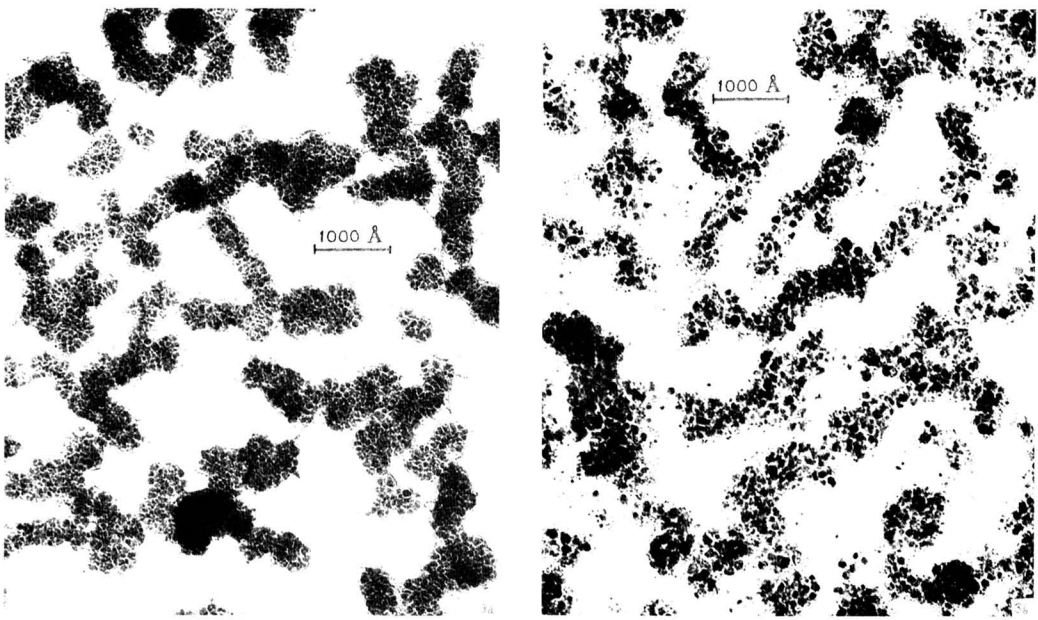


Fig. 3. Transmission electron micrographs of a thin film of Ni-B (a, left) freshly deposited (b, right) after heat-treatment at 400°C

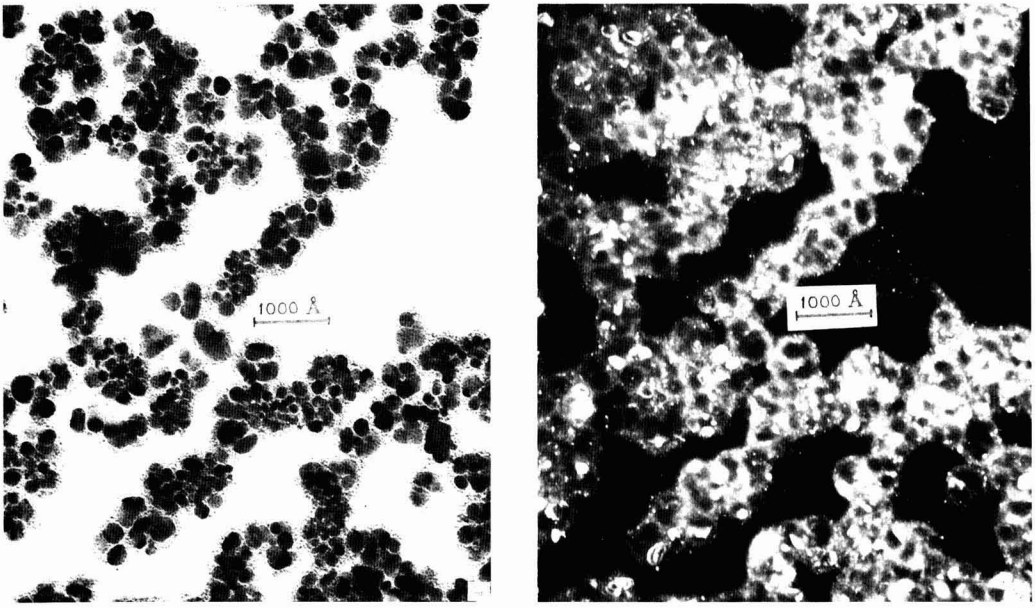


Fig. 4. Transmission electron micrograph of a thin film of Ni-B after heat-treatment at 400°C in (a, left) bright field mode (b, right) dark field (111) mode.

patterns obtained in the two cases are indistinguishable; they consist of a few very broad rings, characteristic of liquidlike or fine polycrystalline structures having essentially no long-range order.

A typical result obtained with improved sensitizer is shown in Fig. 2. The higher island density and uniformity of the deposit is evident, as is the tendency of the islands to join in clusters (10). The diffraction pattern obtained in this case shows sharper rings, some of which can be identified with a face-centered cubic structure.

The result of heat-treatment of Ni-B is a deposit consisting of small crystals. Diffraction patterns reveal clearly fcc structure with a lattice constant matching that of bulk nickel within our experimental error. No conclusive evidence for the presence of Ni_3B was found. This is presumably due to the fact that the diffraction intensity of the fcc nickel component is much greater than that of the small amount of boride formed in our annealing procedure. Electron diffraction studies of heat-treated Ni-P only revealed Ni_3P after annealing above 500°C (13), although the phosphide starts to form at 325°C. Figure 3 shows (a) freshly deposited Ni-B and (b) the same sample after heat-treatment. It appears that the cells within the islands have been replaced by crystallites of approximately the same size (typically 50Å) as the original cells. This trend has been seen in many other samples. Dark field microscopy shows even more clearly the presence of crystals ranging in size from 30 to 300Å. This can be readily seen by comparison of the bright and dark field micrographs shown in Fig. 4.

Electrical resistivity.—The results of measurements of the electrical resistivity of Ni-B and Ni-P films of various thicknesses are shown in Fig. 5. They are in general agreement with previous work on Ni-B (4) and Ni-P (14). The following observations can be made: (*i*) Within each system, the effect of heat-treatment appears to be a shift in resistivity which roughly preserves the shape of a curve drawn through the experimental points. This shift amounts to about 2 orders of magnitude for Ni-B over the thickness range studied, and 3-4 orders of magnitude for Ni-P. For thicknesses greater than 600Å, the resistivity of a Ni-B film is about one order of magnitude greater than that of an equally thick Ni-P film. (*ii*) The transition from continuous films, indicated by the sharp rise in resistivity with decreasing thickness, occurs at about 500Å for Ni-B compared with about 250Å for Ni-P (14). The island size is comparable in the two systems under the same sensitization conditions, and it seems therefore likely that this effect is attributable to the internal structure of the Ni-B islands. If the islands are fragmented into cells, then a larger number of contacts between cells would be required to produce a drop in resistivity.

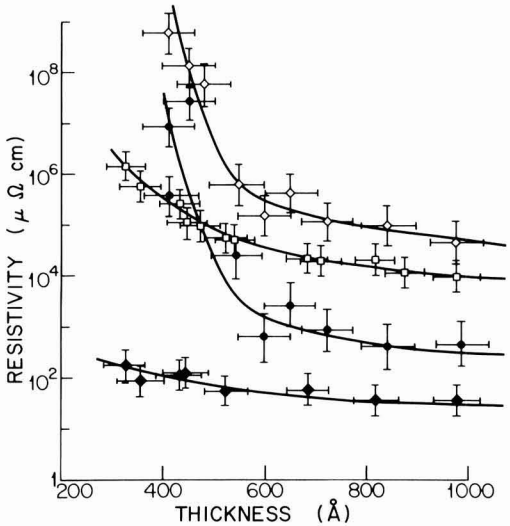


Fig. 5. Resistivity of films as a function of thickness: NiB ◇ freshly deposited; ● heat-treated at 400°C; Ni-P □ freshly deposited; ◆ heat-treated at 400°C.

Acknowledgment

This work has been supported by the National Research Council of Canada. The research constitutes part of a M.Sc. thesis submitted by one of us (P.T.) to the University of Windsor.

Manuscript submitted June 24, 1974; revised manuscript received Jan. 29, 1975.

Any discussion of this paper will appear in a Discussion Section to be published in the June 1976 JOURNAL. All discussions for the June 1976 Discussion Section should be submitted by Feb. 1, 1976.

Publication costs of this article were partially assisted by the University of Windsor.

REFERENCES

1. W. Goldie, "Metallic Coating of Plastics," Vol. 1, Electrochemical Publications Ltd., London (1968).
2. J. Fléchon and F. Voiriot, *Bull. Soc. Chim. France*, **3**, 509 (1963).
3. J. Fléchon and F. Voiriot, *J. Phys.*, **24**, 767 (1963).
4. J. Fléchon and F. A. Kuhnast, *J. Chim. Phys.*, **69**, 1136 (1972).
5. Yu. N. Petrov, V. V. Kovalev, and M. M. Marcus, *Dokl. Akad. Nauk SSSR* (Chem.), **198**, 389 (1971).
6. M. V. Ivanov, V. P. Moiseev, and K. M. Gorbunova, *Dokl. Akad. Nauk SSSR* (Physical Chem.), **194**, 719 (1970).
7. K. M. Gorbunova, M. V. Ivanov, and V. P. Moiseev, *This Journal*, **20**, 613 (1973).
8. J. P. Marton and M. Schlesinger, *ibid.*, **115**, 16 (1968), and references therein.
9. J. Drake and M. Schlesinger, *Solid State Comm.*, **11**, 1597 (1972).
10. N. Feldstein, S. L. Chow, and M. Schlesinger, *This Journal*, **120**, 875 (1973).
11. N. Feldstein, M. Schlesinger, N. E. Hedgecock, and S. L. Chow, *ibid.*, **121**, 738 (1974).
12. L. J. van der Pauw, *Philips Res. Rept.*, **13**, 1 (1958); *Philips Tech. Rev.*, **20**, 220 (1968).
13. S. T. Pai, J. P. Marton, and J. Brown, *J. Appl. Phys.*, **43**, 282 (1972).
14. M. Schlesinger and J. P. Marton, *ibid.*, **40**, 507 (1969).

Catalytic Decomposition of Nitric Oxide on Zirconia by Electrolytic Removal of Oxygen

S. Pancharatnam, R. A. Huggins,* and D. M. Mason

Department of Chemical Engineering and Department of Material Sciences, Stanford University, Stanford, California 94305

ABSTRACT

Zirconia stabilized with 8 mole per cent of scandia has a very high oxygen ion conductivity and can "pump" oxygen from oxygen-bearing gases thus decomposing them. In this study the rate of decomposition of the air-pollutant species, nitric oxide, to harmless species (via the reaction: $2NO \rightarrow N_2 + O_2$) was found to be markedly catalyzed when a potential above 1V was applied across a zirconia disk coated with either a porous platinum or porous gold electrode. It is known that platinum can both form oxides and catalyze the decomposition of NO; whereas, gold does neither. The catalytic decomposition of NO on platinum metal is inhibited by O_2, such behavior being attributed to preferential chemisorption of O_2 over NO as well as the possible formation of an inhibiting platinum oxide surface. The original rationale for this investigation was the possibility that the decomposition of NO might be enhanced if O_2 were electrolytically "pumped" away from a platinum electrode deposited on zirconia, keeping the platinum oxygen-free. However it was not anticipated that at high potentials dissociation rates a thousandfold that on nonporous platinum electrodes occur in the presence of either a platinum or gold porous electrode. No reactivity at all was observed on a nonporous gold electrode. These results suggest that catalysis occurs mainly on a surface other than the platinum or gold, namely, on the zirconia surface itself. It is proposed that F-centers on the zirconia surface formed by the applied potential are primarily responsible for the observed enhanced catalysis.

A number of studies (1-4) have shown that the catalytic decomposition of nitric oxide (NO) on platinum is markedly inhibited by oxygen. This behavior has been attributed to preferential chemisorption of O_2 over NO as well as possible formation of a surface oxide (3, 4). Recent development of solid oxide electrolytes possessing high oxygen ion mobility and relatively low electronic conductivity has made it possible to "pump" oxygen at very low concentrations ($<10^{-20}$ atm) by the application of an electrical potential. Therefore it was suggested and tested in a preliminary measurement (5), that by using platinum as the electrode material deposited on stabilized zirconia, O_2 might be removed electrochemically from the Pt surface leading to substantial enhancement of the rate of NO decomposition. The purpose of this paper is to present the results of more extensive experiments (6, 7) confirming the pumping of oxygen from NO along with some postulated reaction mechanisms. The wealth of information concerning the preparation, properties, and applications of solid electrolytes has been reviewed in numerous places (8, 9). Although the zirconia pump has been previously employed for the decomposition of oxygen-bearing gaseous compounds such as CO, CO_2, and H_2O (11-13) it is believed that the present application relating to the enhancement of the catalytic activity of the zirconia itself by imposing an electrical potential and forming F-centers as active sites has not been reported.

Experimental Procedures

The apparatus used consisted of a high vacuum source (10^{-6} Torr) for purification of NO by distil-

* Electrochemical Society Active Member.

Key words: nitric oxide, solid electrolyte zirconia, air pollution, catalytic muffler.

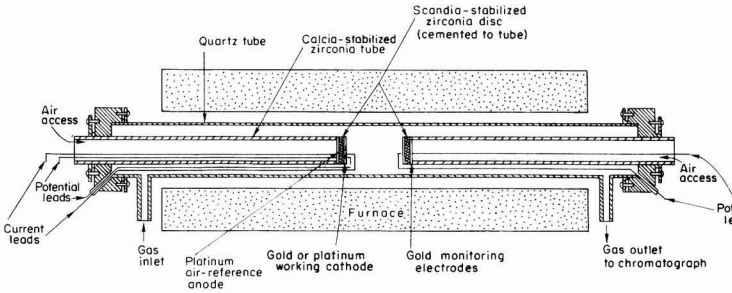


Fig. 1. Zirconia reactor assembly.

lation with subsequent condensation and storage. The reactor-gas distribution system contained a gas-phase chromatograph for analyzing the product nitrogen formed by the decomposition of NO and details of design of this system are given elsewhere (7). The chromatograph used was a single column Varian Model A90-P3 with a thermal conductivity detector. The column was made of 1/4 in. OD × 8 ft long stainless steel tubing hand-packed with 60-80 mesh Linde molecular sieve 13×. The column was preactivated at 250°C for 5 min with a rapid purge of helium at a flow rate of 120 ml/min and the optimal operating conditions were found to be as follows: the carrier gas helium was introduced at a flow rate of 30 ml/min while the reference flow rate was 6 ml/min; the filament current was maintained at 180 mA; the volume of samples was 0.75 ml; the temperatures of the distillation column, injector, and detector were 75°, 55°, and 100°C, respectively. A resolution of 50 ppm N_2 in 100% NO was possible, which set the lower acceptable limit on the conversion of NO, *viz.*, 0.01% for pure NO and 1% for a mixture of 1% NO in helium.

The experimental observations consisted of measuring current-voltage characteristics at 600°-800°C for various concentrations of NO in the feed and for various gas flow rates. All electrical measurements were made on a Fluke 8200A digital voltmeter with an input impedance of 10^{14} ohm.

The reactor assembly is shown in Fig. 1. The working electrode consisted of a zirconia disk electrolyte with either platinum or gold deposited as electrode material. The monitor electrode system consisted of another zirconia disk with gold electrodes for measuring oxygen formed at the working electrode. The disks consisted of 8 mole per cent (m/o) scandia-stabilized zirconia of dimensions: 1 mm thick × 12 mm diameter with a superficial area of 0.713 cm^2. The disk was cemented to one end of a calcia-stabilized zirconia supporting tube of dimensions 12.5 mm OD × 300 mm long. This disk construction permitted easy application of electrode materials and facilitated inspection and characterization of the surface morphology by photomicrography prior to and after the experimental runs. Also by approaching the conditions of a continuous-flow differential reactor with uniform accessibility of reactants to the surface with negligible resistance to gas-phase mass transport, this disk-configuration allowed unambiguous chemical rate data to be obtained directly. In a practical system however such a configuration consisting of a series of ring-shaped electrode-electrolyte cells deposited on the outside of a porous zirconia tube with electrical interconnectors might more appropriately be employed. This design has been used for solid-state fuel cells for "burning" coal gases (14). Simplified kinetics and diffusion models for such tubular reactor systems under both laminar and turbulent flow regimes are available (7).

The extent of decomposition of NO on the cathode surface was determined coulometrically as well as by measuring the concentration of N_2 in the exit gas by chromatographic techniques. The polarization studies were restricted to currents less than 50 mA/cm^2 and overpotentials less than 2V to avoid irreversible electrolysis of the zirconia. The influence on the over-all current-voltage characteristics of rate processes at the anode, with air being used as the reference oxygen-bearing gas, was negligible under the conditions of these experiments (7, 11).

Results

Nonporous platinum film cathode.—The cathodic polarization behavior for a 0.4 μm thick nonporous sputtered platinum film electrode is shown in Fig. 2 for 700°C where current *vs.* overpotential, $(E\text{-}E^\circ)$, is plotted. (E° is the open-circuit voltage, E the closed-circuit voltage.) The behavior at 600° and 800°C was qualitatively similar and complete experimental data are presented elsewhere (7). The straight thin line through the origin represents the measured ohmic cell resistance of 11 ohms at an alternating current frequency of 1000 Hz.

The current is simply related to the reaction rate by the relationship

$$I = 2A\rho\mathbf{F}r \qquad [1]$$

where A = superficial electrode area, ρ = roughness

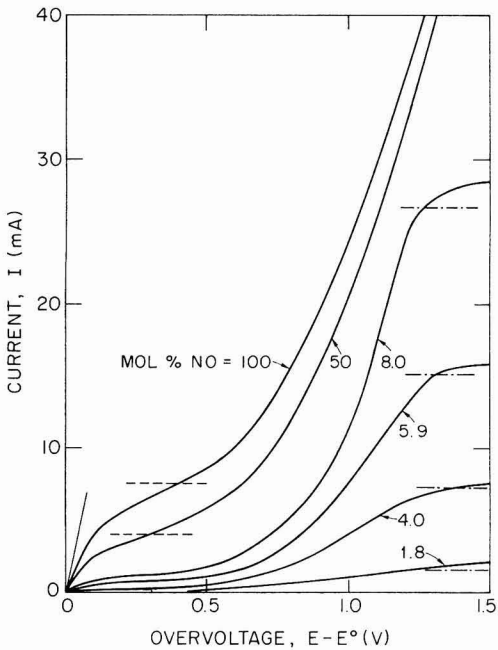


Fig. 2. NO decomposition on zirconia with a nonporous platinum cathode at 700°C. ———— 100 Hz (a.c.), - - - - current equivalent based on nitrogen produced at open circuit, —·—·— current equivalent based on maximum constant nitrogen produced at overvoltages greater than 1.5V.

factor, and **F** = Faraday's constant. The number two is the equivalence for oxygen ion formation. The reaction rate (r) is given in mols NO/sec-cm^2.

Two sets of horizontal lines intersecting the curves have been included in Fig. 2. The left-hand set of lines intersecting the curves near the point of inflection represents the current calculated from Eq. [1] from the chromatographically measured rate of nitrogen produced by NO decomposition at open circuit. The right-hand set of horizontal lines represents the current equivalent to the observed rate of N_2 generated for overpotentials around 1.5V. It should be noted that these latter lines are below the plateaus of current observed in Fig. 2. It is evident that there are two reaction-rate limiting processes represented by the two sets of lines. The limiting current at the lower overpotentials and high NO concentration was generally ill-defined resulting in a point of inflection, though definite plateaus occurred at lower NO concentrations. Plateaus at the higher overpotentials are evident for all concentrations. The fractional conversion of NO was generally less than 1% and the influence of gas flow rate (50-100 ml/min) on the I *vs.* E-E° behavior was inappreciable, demonstrating that the process is not affected by gas phase mass-transfer rates. The O_2 concentration measured by the downstream gold electrodes varied between 10^{-3}-10^{-4} atm at zero current and 10^{-5}-10^{-6} atm at potentials greater than 1V.

The relationship between the measured N_2 production rate and the measured electrical current (or its equivalent in terms of O_2 pumped) calculated from Eq. [1] for the data in Fig. 2 is shown in Fig. 3, which is typical of all runs. The line of unit slope represents the equivalence, in accordance with Eq. [1] between coulombs passing through the electrolyte and O_2 (or N_2) produced at the surface. The deviations to the left of this line which can be seen at low currents (and potentials) and high NO concentrations indicate a condition where not all of the O_2 formed by the decomposition of NO is electrochemically removed. The rate of production of O_2 (or N_2) rises slightly in approaching the equivalence line. This behavior is depicted in a different fashion by the left-hand set of horizontal lines in Fig. 2.

The deviations to the right of the equivalence line in Fig. 3 occur at the lower NO concentrations with high currents (and potentials). This behavior is probably due to the contribution of a measurable amount of electronic current added to the O_2-pumping current. In Fig. 2 this behavior is seen in the deviation of the right-hand set of horizontal lines from the plateaus. These lines represent a process limited by the maximum inherent rate of reaction of NO decomposition on oxygen-free platinum. These two current limiting phenomena will now be further analyzed.

Behavior at low overpotentials.—Since the low voltage saturation current shows a good correlation with the rate of NO decomposition at zero potential (and current), the rate has been plotted in Fig. 4 *vs.* the concentration of NO in the feed. Owing to the insensitivity of the chromatographic analysis of N_2, the rate of decomposition could be precisely determined only for NO concentrations of the order of 10 m/o or greater. The straight lines drawn through the origin in Fig. 4 represent the reaction rate calculated from the rate expression given in (3) with $P_{O_2} \to 0$

$$r_1 = \frac{k[\mathrm{NO}]}{1 + KP_{O_2}} \qquad [2]$$

where

$$k = 8.1 \exp\left(\frac{-17{,}100}{RT}\right) \mathrm{cm\ sec^{-1}} \qquad [2a]$$

and

$$K = 13.9 \exp\left(\frac{6600}{RT}\right) \mathrm{atm^{-1}} \qquad [2b]$$

The points represent the open-circuit decomposition rates determined by the chromatographic measured rate of formation of N_2.

Because of the small superficial area of the disk electrodes it was impossible to determine the surface area by any conventional means such as BET adsorption measurements. Thus the NO rate data from (3) with known surface areas were used for the oxygen saturated electrodes in this study. The surface roughness factor (ρ) for the present data was used as an adjustable parameter to give agreement with (3) and a value of $\rho \cong 3$ fits the data well.

Behavior at high overvoltages.—The high overvoltage limiting current plateaus displayed in Fig. 2 are represented on a log-log scale in Fig. 5 where limiting current, I_1 is plotted *vs.* NO concentration in the exit gas which was approximately equal to that in feed gas owing to the low conversions that occurred. The data are well approximated by straight lines of slope 2 which indicates that the rate-determining step has a second order dependence on NO. Except for the deviations from this behavior at high concentrations of NO, a rate expression of the form

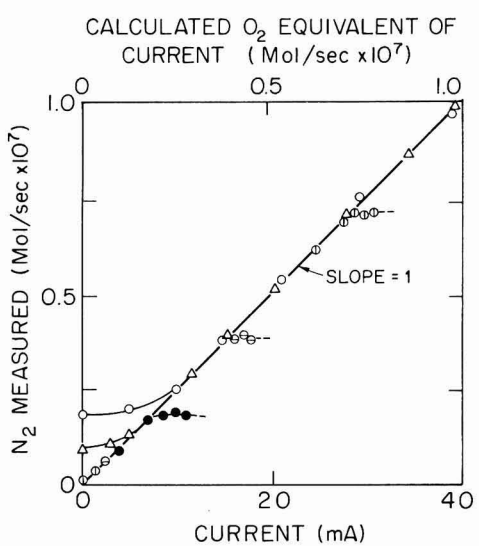


Fig. 3. Test of the equivalence of N_2 produced on nonporous platinum on zirconia *vs.* current at 700°C. Mole per cent NO in feed: ○, 100; △, 51; ◐, 8; ⊖, 6; and ●, 4.

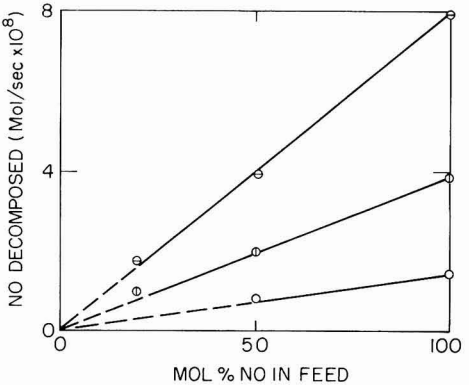


Fig. 4. Rate of decomposition of NO on nonporous platinum-coated zirconia for open circuit, ○ 600°C; ◐ 700°C; ⊖ 800°C (roughness factor of 3 assumed). - - Data from Ref. (3).

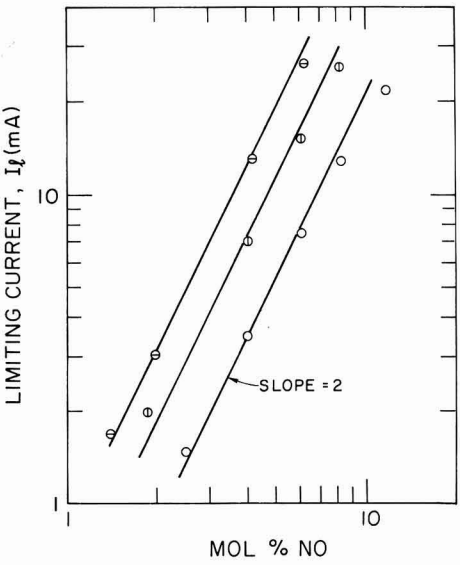


Fig. 5. Limiting current equivalent to maximum N_2 produced on zirconia with nonporous platinum electrode at overpotential > 1.5V. ○ 600°C; ◐ 700°C; ⊖ 800°C.

$$r_{II} = k_2[NO]^2 \quad [3]$$

may be used. An Arrhenius plot of log k_2 *vs.* $1/T$ shown in Fig. 6 yields the following expression for k_2

$$k_2\left(\frac{cm^4}{mol/sec}\right) = 5.05 \times 10^8 \exp\left(\frac{-17{,}000}{RT}\right) \quad [4]$$

Since diffusion of oxygen through platinum has been shown to have an activation energy of 35-60 kcal/mol (14), the low activation energy for k_2 rules out a diffusion-controlling mechanism. It will be shown subsequently that the high voltage behavior corresponds to the dissociation of NO on oxygen-free platinum.

Porous platinum electrodes.—The cathodic current overvoltage characteristics shown in Fig. 7 were typical for temperatures of 700°C and greater. The limiting current shown as the left-hand set of horizontal dashed lines are equivalent to the open current N_2 production rate. As was the case of the nonporous film electrode data (Fig. 2), the low-potential current saturation is again noticeable either as points of inflection at high NO concentrations or as plateaus at low NO concentrations. However (as seen by comparing Fig. 2 and 7) in contrast with the case of the nonporous platinum electrode, the current at high overvoltages increases continuously with increasing overvoltage and merges with the electronic transport curve I_e without exhibiting a plateau. From the measured rate of N_2 generation, the current equivalents for high overpotentials are shown in the right-hand set of horizontal lines in Fig. 7. The striking feature of the porous electrode is the extremely low concentration of NO in the feed gas at which extremely high decomposition rates have been observed. The effect of gas flow rate (80-100 ml/min) evidenced in Fig. 7 is predominantly due to the high rates of decomposition and high conversions of NO ranging from 40-70%. It is believed that under these conditions the cathode no longer behaves as a differential reactor and also mass transfer in the gas phase may be influencing the process, resulting in the observed increase in current with increasing flow rate.

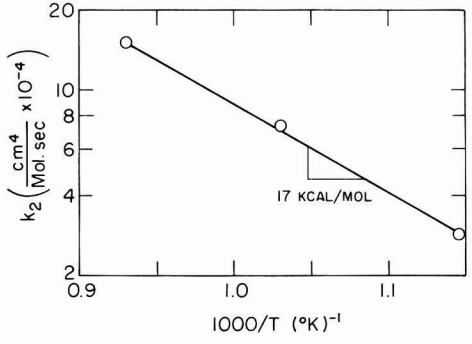


Fig. 6. Second order NO decomposition rate coefficient on zirconia with nonporous Pt electrode *vs.* $1/T$. (Roughness factor ≅ 3.)

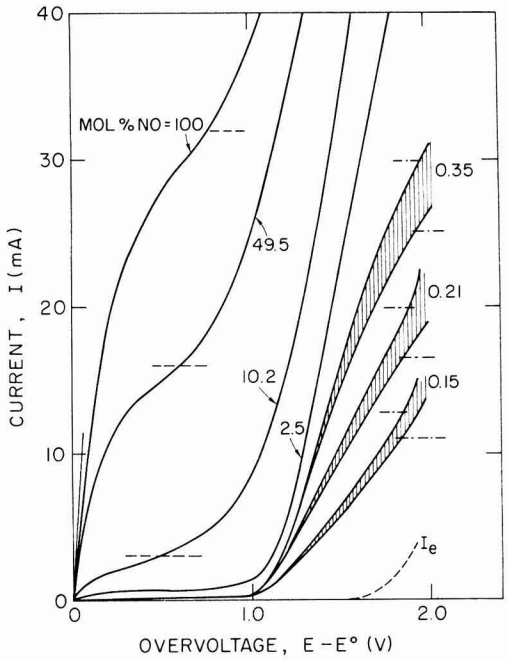


Fig. 7. NO decomposition on zirconia coated with porous platinum at 800°C. (Shaded area represents influence of flow rate, 80-100 ml/min.) ——— (1000 Hz a.c.), - - - - - - current equivalent based on nitrogen produced at open circuit, —·—·— current equivalent based on nitrogen produced at high overvoltages.

Porous Pt electrode at low overpotentials.—The low potential limiting behavior was analyzed by comparing the zero-current rate of decomposition of NO with the rate expression given in Eq. [2]. As in the case of nonporous Pt, the agreement was found to be satisfactory when a roughness factor of about 6 was employed.

Porous Pt electrode at high potentials.—A plot of the equivalent high potential limiting current *vs.* concentration of NO in exit gas is shown in Fig. 8. Despite the scatter in the data, a first order dependence of I_l on [NO] is indicated over the experimental range of NO concentrations. The corresponding value of the first order rate constant k, has been shown in Fig. 9 as a function of $1/T$ which gives an approximate expression for k_1

$$k_1(cm\ sec^{-1}) \simeq 4.7 \times 10^5 \exp\left(\frac{-25{,}500}{RT}\right) \quad [5]$$

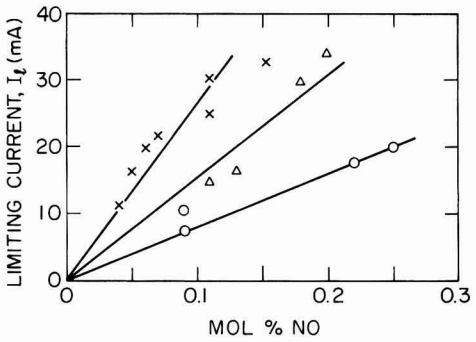


Fig. 8. Limiting current equivalent to maximum N_2 produced on zirconia with porous platinum electrode at high overvoltages (> 1.5V). ○, 700°C; △, 750°C; ×, 800°C.

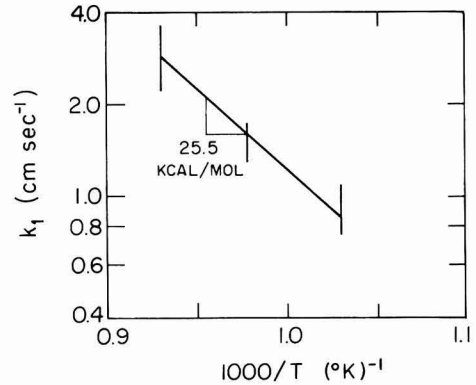


Fig. 9. k_1, first order NO decomposition rate coefficient on zirconia with porous platinum electrode vs. $1/T$ (roughness factor ≅ 6).

The experimental difficulties associated with the relatively high rates of reaction and poor sensitivity of chromatographic analysis for low concentrations of NO and N_2 have resulted in a rather small operating range of temperatures and NO concentration.

Nonporous and porous gold electrodes.—The cathodic behavior of porous gold at 800°C is shown in Fig. 10. No limiting current or limiting decomposition rates were observed in the whole range of overpotentials investigated. The current was found to be essentially ionic over the range shown and decomposition of NO at open circuit was negligible, indicating neither the gold nor zirconia is catalytic. No ionic current or NO decomposition was observed at any potential for a nonporous gold electrode, confirming the noncatalytic nature of gold with respect to NO decomposition. Appreciable ionic current was, however, obtained when the originally nonporous electrode surface was scored to expose the zirconia, thus strongly supporting the hypothesis that an enhanced catalytic decomposition of NO occurs on the zirconia surface itself.

Discussion of Results

NO decomposition on nonporous Pt.—It is speculated that the high potential limiting process represents the decomposition of NO on a clean platinum surface, uncontaminated with oxygen, obeying the following Rideal-Eiley mechanism found to apply to nonelectrochemical catalysis (4)

$$NO + (*) \rightleftarrows (NO - *) \qquad [6a]$$

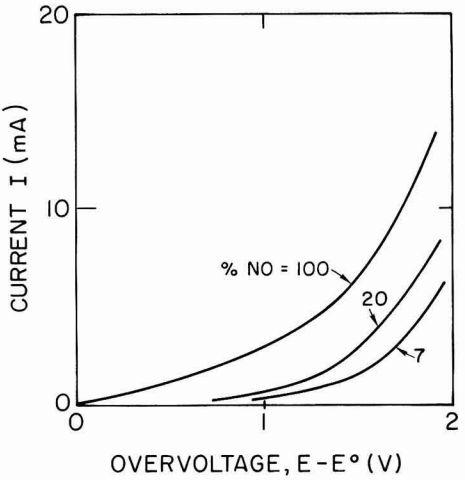


Fig. 10. NO decomposition on zirconia with a porous gold electrode. (Flow rates varied between 40 and 80 ml/min.)

$$NO + (NO - *) \rightarrow \text{- - -} N_2 + O_2 \qquad [6b]$$

$$O_2 + 2(*) \rightleftarrows 2(O - *) \qquad [6c]$$

where (*) denotes an adsorption site on the Pt surface and (NO − *) and (O − *) represent respective species adsorbed on a site. Steps [6a] and [6c] are assumed to be at equilibrium and step [6b] is rate determining. The exact nature of all the processes involved in step [6b] cannot be determined from these experiments, but some speculation will be subsequently made. The rate expression for the above reaction scheme with a constant number of total sites [* + (NO − *) + (O − *)] is

$$r_{II} = \frac{k_2[NO]^2}{1 + K_1[NO] + K_2[O_2]^{1/2}} \qquad [7]$$

Equation [7] reduces to Eq. [3] for low fractional coverage of active sites by NO, *i.e.*, ($K_1[NO] << 1$) and for $[O_2] \rightarrow 0$.

The rates of decomposition of NO on Pt observed by various techniques are compared in Fig. 11 in terms of "turnover number," (molecules of NO reacting per surface site per second) based on a nominal value of 10^{15} sites/cm^2. For comparison with Ref. (3) the data of various batch studies have been extrapolated to 48 Torr using first order kinetics. This assumption is reasonable because at the high concentrations of NO actually used in the batch studies (400-2000 Torr) first order kinetics were closely obeyed (*e.g.*, $1 << K_1[NO]$ in Eq. [7]). Two sets of results were reported in Ref. (3); the lower rates (curve 6 with rate expression Eq. [2]) were observed when O_2 was fed along with NO, and the higher rates (curve 7) correspond to O_2-free gas feeds, but with 0.1-0.3% O_2 generated by the decomposition of NO. Both of these rates had been extrapolated to zero O_2 concentration. The following mechanism was proposed in Ref. (3) for the case of O_2-free gas feeds

$$NO + (*) \rightleftarrows (NO - *) \qquad [8a]$$

$$NO + (NO - *) \rightarrow N_2O + (O - *) \qquad [8b]$$

$$N_2O + (*) \rightarrow N_2 + (O - *) \qquad [8c]$$

$$2(O - *) \rightleftarrows O_2 + 2(*) \qquad [8d]$$

Steps [8a] and [8d] were assumed to be in equilibrium; step [8b] was assumed to be rate determining. For total sites equal to [* + (NO − *) + (O − *)] this mechanism leads to a rate expression identical to

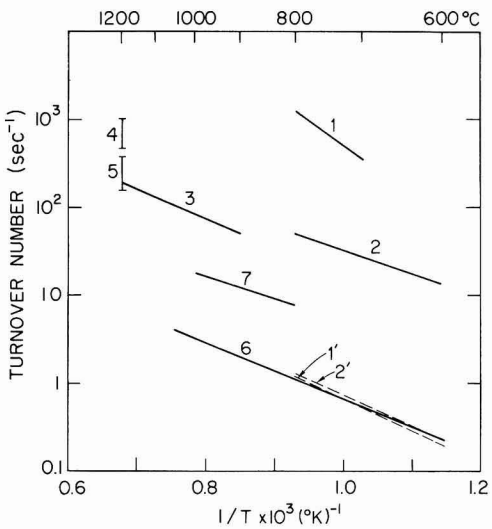


Fig. 11. Summary of data on turnover for NO decomposition on platinum at 48 Torr. 1', porous Pt, open circuit; 2', nonporous Pt, open circuit. Curve 1, porous Pt maximum rate of N_2 formation corresponding to clean platinum and F-center catalysis. Curve 2, nonporous Pt maximum rate N_2 formation corresponding to clean platinum surface. Curve 3, heated Pt wire [Ref. (4)]. Curve 4, heated Pt wire [Ref. (2)]. Curve 5, Heated Pt wire [Ref. (1)]. Curve 6, [Ref. (3)] Pt foil with O_2 in feed extrapolated to zero (O_2). Curve 7, [Ref. (3)] Pt foil without O_2 in feed extrapolated to zero (O_2).

Eq. [7]. If the assumption is made that (NO — *), (O — *) >> (*) or the total sites are equal to (NO — *) + (O — *), the resulting rate expression is

$$r_{II} = \frac{k[NO]}{1 + K[O_2]^{1/2}/[NO]} \qquad [9]$$

For $(O_2) \rightarrow 0$ this rate expression leads to first order kinetics with respect to NO. The agreement between the results of electrochemical studies with Pt and the various batch studies is quite good. The lower rates observed in the study of Ref. (3) even for O_2-free gas feeds may be attributed to appreciable coverage of the active sites by oxygen owing to the relatively large conversion of NO to O_2 in the region of the catalyst. This hypothesis is supported by the reported nature of chemisorption of O_2 on Pt (16-18).

NO decomposition with porous Pt.—The high rate of decomposition of NO observed at high overpotential which characterizes porous Pt leads one to believe that an entirely different mechanism of NO decomposition occurs than in the case of nonporous Pt.

The decomposition of NO on metal oxides has been studied extensively (3) and a catalytic sequence of five steps with similarity to Eq. [8a]-[8d] for oxygen free feed can be speculated

$$NO + (*) \rightleftarrows (NO - *) \qquad [10a]$$

$$NO + (NO - *) \rightarrow N_2O + (O - *) \qquad [10b]$$

$$N_2O \rightarrow N_2 + O_a \qquad [10c]$$

$$(O - *) + O_a \rightleftarrows O_2 + (*) \qquad [10d]$$

$$2\,O_a \rightarrow O_2 \qquad [10e]$$

where O_a represents a mobile surface-O atom. The rate expression found experimentally was unimolecular in NO, identical to Eq. [2], which may be obtained from the above reaction sequence along with the assumptions that: step [10a] is irreversible; step [10d] is in quasi-equilibrium; the concentration of mobile oxygen O_a is constant; and [*], [O — *] >> [NO — *], or the total site concentration equals [*] + [O — *]. The activation energy for k (Eq. [2]) ranged from 20 to 30 kcal/mol with a value of 28 kcal/mol being reported for pure zirconia, which was also reported by Fraser and Daniels (18). From the dissociation energies of NO (151 kcal/mol) and NO^- (112 kcal/mol) it was argued (3) that the active site (*) is probably an oxygen ion vacancy with at least one trapped electron, *i.e.*, an "F-center."

Taking into consideration the injection of electrons from the cathode and transport of vacancies from the anode, the following modified electrocatalytic sequence is proposed

$$V_O{}^{\cdot\cdot}(s) + 2e'(\text{cathode}) \rightleftarrows V_O x \text{ (F-center)} \qquad [11a]$$

$$NO + V_O x \rightarrow N + O_O x \qquad [11b]$$

$$NO + N - O_O x \rightarrow N_2O + O_O x^{(s)} \qquad [11c]$$

$$N_2O + V_O x \rightarrow N_2 + O_O x^{(s)} \qquad [11d]$$

$$O_O x^{(s)} + V_O{}^{\cdot\cdot(b)} \underset{\text{anode}}{\overset{\text{from}}{\rightleftarrows}} V_O{}^{\cdot\cdot(s)} + O_O x^{(b)} \qquad [11e]$$

where $V_O{}^{\cdot\cdot}$ = a vacant oxygen ion; e' = an electron; $V_O x$ = an oxygen ion vacancy with two trapped electrons; $O_O x$ = a normal oxygen ion; and the superscripts (s) and (b) denote lattice positions in the surface and in the bulk of the electrolyte, respectively. Under the influence of an impressed potential, the exchange step [11e] would be driven toward the right, thus leading to an acceleration of the steps [11c] and [11d]. Hence as in the case of a nonelectrochemical reaction, step [11b] would be the rate-determining step for the over-all decomposition. Assuming a high concentration of F-centers sustained by an applied potential, the surface average concentration of (NO) and (O) may be neglected with total sites equal to $V_O x$ and the following rate expression resulting

$$r_{III} = k'[V_O x][NO] = k''[NO] \qquad [12]$$

The rate is proportional to the surface concentration of F-centers which would increase with increasing cathodic applied overpotential. From Eq. [1] and [12] one would expect a continuous increase of current with overpotential until all of the NO in the feed has been decomposed. In reality migration of electrons and F-centers to the anode can occur before this limit is reached and thus set an apparent upper limit on the value of k''. The activation energy for k'' observed in the current experiments (25.5 ± 5 kcal/mol) shows a fair agreement with that found in (3) supporting the belief that the nature of active sites and the rate-controlling step are probably the same in both the studies.

An interesting study of the nonstationary state behavior of metal oxides was made in (3). In the absence of oxygen presaturation, initial decomposition rates 6-10 times greater than the steady-state values were reported. This behavior was explained by postulating higher concentration of F-centers generated on the surface when the catalyst was flushed with pure helium. In other words a partially reduced surface seems to result at very low concentration of O_2 in the gas. The turnover numbers (Fig. 12) reported in (3) for zirconia at 400-1000°C seem to be lower than the values in the current study by 6-8 orders of magnitude. The reaction rates observed in the electrochemical experiments can be satisfactorily explained by assuming that only 1% of the surface sites have been converted to F-centers and the sticking probability for the adsorption of NO on an F-center is about 0.01. Association of catalytic activity with surface defects has been confirmed in recent studies on ZnO (20) and d-band perovskites (21). The hypothesis that the surface of zirconia can be made active to NO decomposition by applying an electrical potential is also confirmed quali-

tatively by the studies on a gold cathode. The results of the gold experiments, however, could not directly be compared quantitatively with those on porous Pt because of the lack of identical electrode morphology and due to the catalytic action of Pt which dominates the current-potential behavior at high NO concentrations and low potentials.

Conclusion

Decomposition of NO on nonporous Pt with electrolytic removal of O_2 reinforces the previous observation that the presence of O_2 not only inhibits the decomposition of NO but also alters the kinetic behavior. A second order rate mechanism observed in the present study is in agreement with the previous findings from batch as well as continuous flow experiments.

The feasibility of altering the catalytic activity by controlling the oxygen concentration has been established in another way. The tremendous enhancement of the rate of NO decomposition in the case of either porous platinum or gold demonstrates a convenient and powerful technique of reducing oxygen bearing species, *viz.*, the injection of F-centers on the surface of the electrolyte at sufficiently high overpotentials. This mechanism is supported by the following facts: (*i*) catalytic enhancement for zirconia covered with a nonporous layer of platinum is that typical for pure platinum in a nonelectrolytic system and (*ii*) with nonporous gold electrodes no decomposition occurs at all, typical of gold in a nonelectrolytic system. From these observations it may be concluded that any noble metal porous electrode could be chosen for dissociating NO on zirconia in the presence of F-centers.

A summary of the general behavior of the zirconia electrochemical system is as follows:

1. For low potentials (0-0.5V) the rate of decomposition of NO with both porous and nonporous platinum electrodes is found to be first order with respect to NO consistent with the reported rate data for "O_2-saturated" platinum metal catalysts.
2. For nonporous Pt films the limiting current at higher potentials (1.3-1.6V) corresponds to the second order rate of decomposition of NO mixtures containing 5-10 m/o NO reported for O_2-free platinum. These rates are about fiftyfold higher than on oxygen saturated platinum surfaces.
3. On either porous platinum or porous gold surfaces, at potentials around 1.5V, first order rates of the order of a thousandfold that in case 1. are obtained, owing to the presence of highly catalytic F-centers on the zirconia surface.

Remaining to be studied systematically is the porous electrode configuration with carefully controlled electrode morphology and surface areas. Also to permit unambiguous kinetics data the disk electrode system should be redesigned so that reactant gases strike the electrode surface head-on, thus increasing mass-transfer rates and insuring at high reaction rates that the reactor behaves differentially with uniform accessibility to reactant species.

Acknowledgment

The authors are grateful for the support of the Environmental Protection Agency (Grant No. 5R01 801337) which made this investigation financially feasible.

Manuscript submitted July 30, 1974; revised manuscript received Feb. 26, 1975. This was Paper 334 presented at the San Francisco, California, Meeting of the Society, May 12-17, 1974.

Any discussion of this paper will appear in a Discussion Section to be published in the June 1976 JOURNAL. All discussions for the June 1976 Discussion Section should be submitted by Feb. 1, 1976.

Publication costs of this article were partially assisted by Stanford University.

REFERENCES

1. T. E. Green and C. N. Hinshelwood, *J. Chem. Soc.*, **129**, 1709 (1926).
2. P. W. Bachman and G. B. Taylor, *J. Phys. Chem.*, **33**, 447 (1929).
3. A. Amirnazmi, Ph.D. Thesis, Stanford University (1973). Also A. Amirnazmi, J. E. Benson, and M. Boudart, *J. Catal.*, **30**, 55 (1973).
4. S. Pancharatnam, K. Lim, and D. M. Mason, *Chem. Eng. Sci.*, Accepted for publication (1975).
5. S. Wittingham and R. A. Huggins, Private communication.
6. S. Pancharatnam and D. M. Mason, Paper presented at the 39th Annual Chemical Engineering Symp. of Am. Chem. Soc., Chicago, Illinois (Jan. 1973).
7. S. Pancharatnam, Ph.D. Thesis, Stanford University (1974).
8. T. H. Etsell, and S. M. Flengas, *Chem. Rev.*, **70**, 339 (1970).
9. Per Kofstad, "Non-Stoichiometry, Diffusion and Electrical Conductivity in Binary Metal Oxides," Wiley-Interscience, New York (1972).
10. S. Wittingham and R. A. Huggins, Paper presented at the 5th Materials Research Symp., N.B.S., Gaithersburg, Md. (Oct. 1971).
11. T. H. Etsell and S. M. Flengas, *This Journal*, **118**, 1890 (1971).
12. J. Weissbart, W. H. Smart, and T. Wydeven, *Aerospace Med.*, **40**, 136 (1969).
13. J. Weissbart and W. H. Smart, Abstract 37, p. 92, The Electrochemical Society Extended Abstracts, Fall Meeting, Atlantic City, N. J., Oct. 4-8, 1970; W. H. Smart and J. Weissbart, Abstract 38, p. 99, *ibid.*
14. E. F. Sverdrup, C. J. Warde, and R. L. Eback, *Energy Conversion*, **13**, 129 (1973).
15. J. E. Bauerle, *J. Phys. Chem. Solids*, **30**, 2657 (1969).
16. H. L. Grüber, *J. Chem. Phys.*, **66**, 48 (1972).
17. V. S. Boronin, V. S. Nikulina, and O. M. Poltorak, *Russ. J. Phys. Chem.*, **41**, 1443 (1967).
18. G. R. Wilson and W. K. Hall, *J. Catal.*, **24**, 306 (1972).
19. J. M. Fraser and F. Daniels, *J. Phys. Chem.*, **62**, 215 (1958).
20. J. D. Levine, A. Willis, W. R. Bottoms, and P. Mark, *Surface Sci.*, **29**, 144 (1972).
21. F. J. Morin and T. Wolfram, *Phys. Rev. Letters*, **30**, 1214 (1973).

Electrochemical and Spectroscopic Properties of Cation Radicals

III. Reaction Pathways of Carbazolium Radical Ions

James F. Ambrose,*[1] Lawrence L. Carpenter,[2] and Robert F. Nelson
Department of Chemistry, University of Georgia, Athens, Georgia 30602

ABSTRACT

Previous work had elucidated the anodic oxidation pathways of carbazole and several N-substituted derivatives. These studies have now been extended to seventy-six ring-substituted carbazoles using electrochemical and spectroscopic techniques to study the reactivity of the various substituted carbazole cation radicals. Generally, it was found that 3, 6, and 9 (N) positions are extremely reactive; if these sites are not blocked by inert substituents the cation radicals generated by electrolytic oxidation react rapidly via coupling-deprotonation. In some cases, substituents are eliminated from the 3 and 6 positions in the cation radicals followed by coupling to form substituted bicarbazyls. In other cases, relatively stable cation radicals were obtained and their EPR and visible absorption spectra were recorded. It was found that the reactivities of substituted carbazole cation radicals are considerably greater than those of analogous di- and triphenylaminium ions due to the planarity of the carbazole aromatic rings.

Carbazole, a relatively unimportant molecule in the past, is of considerable interest at present due to the uses of substituted carbazoles in polymerization studies and as inhibitors of zoxazolamine-induced paralysis (1). In addition, polycyclic carbazoles have been established as carcinogenic agents by a number of workers (2-4) and methyl-substituted carbazoles have been isolated from cigarette smoke (5, 6). Since the carcinogenic activity of these molecules may be associated with their redox properties, and considering that present and future studies may verify the presence of other substituted carbazoles in our environment, it was deemed desirable to carry out a broad survey of the anodic oxidation pathways of a number of variously substituted carbazoles. Due to solubility problems, these studies were limited to nonaqueous media, namely acetonitrile. This work is also designed to serve as a basis for investigating the oxidation behavior of simple and biologically important indoles. Preliminary work has shown that indole and its derivatives are extremely reactive upon anodic oxidation, so it was hoped that a good deal of background knowledge could be obtained from studies of the less reactive carbazoles. Due to the large number of compounds involved, substitution patterns as well as substituent effects upon the reaction pathways of the carbazole cation radicals were generally elucidated; however, several compounds have been incompletely characterized and so full disclosure must await further, more detailed investigations. Because of this survey nature, considerable license has been taken with regard to speculation on the mechanisms and products involved; on-going studies will hopefully refute or verify these speculations but in any case it is felt that the ideas forwarded are at least plausible and often likely.

Previous work had established that carbazole, upon anodic oxidation, forms a very unstable cation radical that reacts via coupling-deprotonation to 9,9′- and 3,3′-bicarbazyls;[3] higher polymers were thought to form upon prolonged electrolysis (8). When alkyl or phenyl groups were placed on the carbazole nitrogen only the corresponding 3,3′-bicarbazyls formed, in quantitative yields, and they appeared to be quite stable under electrolytic conditions. These findings were in agreement with previous work on the chemical oxidations of carbazole and its derivatives (8-13).

There is a paucity of data available in the literature on the chemical oxidation pathways of ring-substituted carbazoles; however, chemical substitution reactions indicate that the active ring sites are the two positions *para* to the nitrogen (3 and 6) and, to a lesser extent, those *ortho* to it (1 and 8). It was anticipated that by blocking the 3, 6, and 9 positions relatively stable cation radicals would be formed; these could then be studied using EPR as a probe to elucidate the electron distribution in the cation radicals. It was found that the carbazole nucleus is so reactive, in fact, that upon oxidation normally inert substituents undergo unusual decomposition reactions in several cases. Some success was achieved in the EPR and visible absorption spectral studies of the primary cation radicals, however, and the preliminary results are reported herein, along with the electrochemical data on these interesting and sometimes piquant molecules.

Experimental

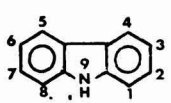
All of the electrochemical studies were carried out in acetonitrile (MeCN) using tetraethylammonium perchlorate (TEAP) as supporting electrolyte. Purifications of these materials, as well as the general instrumentation employed, have been previously described (7).

Throughout this paper radical stabilities are cited as half-lives; these are estimates from cyclic voltammograms taking into account voltage sweep rates and cathodic to anodic peak current ratios. The uncertainty in the values is estimated at ± 10-20%.

Rotating disk studies were performed with a 10,000 rpm Motomatic E-550 motor and E-550M master control unit using the rotoamperometric technique for rapid data collection (14). Evaluation of coupling rate constants were carried out at low concentrations (10^{-4} to 10^{-5} F), so all rotoamperograms were corrected for background currents. A previously published working curve was employed for the determination of numerical values for the coupling rate constants (15).

Electrochemical n values were obtained using a Wenking 61RH potentiostat and a digital coulometry assembly employing two counters, one for gating, and one for totalizing (16). The gating counter was found

* Electrochemical Society Student Member.
[1] Present address: Department of Chemistry, University of Kansas, Lawrence, Kansas 66044.
[2] Undergraduate Research Fellow, Sacramento State College, Sacramento, California 95819.
Key words: carbazole, anodic oxidation, electrosynthesis, cation radicals.
[3] We are employing the traditional carbazole nomenclature where the nitrogen is numbered "9" as opposed to the standard heterocyclic numbering where N is "1". The ring carbons are numbered clockwise, with the bridge-head carbons omitted.



to be very useful for following the course of the decaying electrolysis current; chemical complications in the electrochemical processes were immediately apparent using this sensitive technique. Most of the n-value determinations were carried out at parent concentrations of 10^{-3} to 10^{-5} F. At these levels the electrolyses were found to be extremely sensitive to impurities in the MeCN and TEAP. Therefore, both solvent and supporting electrolyte were freshly prepared before coulometry experiments. If these precautions were not taken, n values that were found to be about 2.0 under proper conditions varied up to values as high as 5 to 7 and even then low steady-state currents were often obtained.

Preparative electrolyses.—Preparative electrolyses were effected using a home-built potentiostat designed to deliver ± 70V, ± 3A. Typically, 100 mg of the carbazole derivative was dissolved in 150 ml MeCN/0.1F TEAP and exhaustively electrolyzed at a large platinum gauze at a potential 200 mV past the anodic peak current voltage. The reference electrode was a SCE and the auxiliary was a carbon rod contained within a porous ceramic cup. The solution was then rereduced at −0.7V to convert any products to the neutral form and reduce off protons liberated in the coupling reactions. Electrolysis solutions were then taken to dryness by evaporation of the solvent (ambient conditions) and the residue was partitioned with benzene/hot water mixtures. The benzene layer was concentrated by evaporation and chromatographed on Woelm neutral alumina. The products were then recrystallized from the appropriate solvent mixture.

Electrolyses were carried out on compounds from each major group where radical reaction pathways were detected. For the 3- and 3,6-disubstituted carbazoles intractable mixtures were obtained following electrolysis in unbuffered MeCN, but in the presence of the organic base 2,4,6-trimethylpyridine good yields of the corresponding N,N′-coupled products could be isolated. Pertinent data are given below for the various classes of compounds.

3-Methylcarbazole.—100 mg was oxidized in the presence of 2,4,6-trimethylpyridine (threefold molar excess) at 1.3V to 3,3′-dimethyl-9,9′-bicarbazyl (87% yield), recrystallized from benzene/EtOH as off-white crystals, mp 176°-178°. Calculated for $C_{26}H_{20}N_2$: C, 86.7; H, 5.55; N, 7.78. Found: C, 86.5; H, 5.62; N, 7.74.

3-Fluoro-N-Ethylcarbazole.—100 mg was oxidized in MeCN/0.1F TEAP at 1.4V to 3,3′-difluoro-N,N′-diethyl-6,6′-bicarbazyl (86% yield), recrystallized from benzene/EtOH as pale yellow flakes, mp 201°-203°. Calculated for $C_{28}H_{22}N_2F$: C, 79.2; H, 5.24; N, 6.60. Found: C, 79.2; H, 5.26; N, 6.63.

3,6-Dibromocarbazole.—100 mg was oxidized in the presence of a threefold molar excess of 2,4,6-trimethylpyridine in MeCN/TEAP at 1.5V to 3,3′,6,6′-tetrabromo-N,N′-bicarbazyl (93% yield), recrystallized from benzene/EtOH as small white cubes, mp 248°-250° [Ref. (9) 248°-250°].

N-(p-Methoxyphenyl)carbazole.—100 mg was oxidized in MeCN/TEAP at 1.4V to N,N′-bis (*p*-methoxyphenyl)-3,3′-bicarbazyl (88% yield), recrystallized from benzene/hexane as a cream colored amorphous solid, mp > 275°. Calculated for $C_{38}H_{28}N_2O_2$: C, 83.7; H, 5.17; N, 5.14. Found: C, 83.5; H, 5.15; N, 5.09.

N-(p-nitrophenyl)carbazole.—100 mg was oxidized in MeCN/TEAP at 1.6V to N,N′-bis (*p*-nitrophenyl)-3,3′-bicarbazyl (72% yield), recrystallized from benzene/hexane as a yellow amorphous solid, mp 240°-245° (decomp.). Calculated for $C_{36}H_{22}N_4O_4$: C, 75.2; H, 3.86; N, 9.74. Found: C, 75.3; H, 3.82; N, 9.77.

Preparation and characterization of carbazole derivatives.—Many of the compounds studied have been previously reported in the literature. These synthetic routes were followed with some modifications in workups; structures were verified by comparison of melting points with literature values, where possible, and by spectroscopic data in all cases. New compounds were verified by their CHN analyses.

Infrared spectra, obtained on a Perkin-Elmer 621 spectrometer, proved very useful in structure and purity determinations. Carbazoles substituted at the nitrogen atom do not show the strong N-H stretching peak at about 3400 cm^{-1} present in carbazole and its ring-substituted derivatives. The disappearance of this peak was used to chart the progress of Ullmann reactions when a carbazole was reacted with a *para*-substituted iodobenzene to produce substituted N-phenylcarbazoles. Carbazoles with either one or both rings unsubstituted show two strong out-of-plane bending (*ortho*-disubstituted ring) peaks at about 725 and 750 cm^{-1}; these peaks were used to ascertain the completeness of 3,6-disubstitution reactions. N-phenylcarbazole, N-*p*-biphenylcarbazole, and ring-substituted N-phenylcarbazoles show a weak out-of-plane bending (monosubstituted ring) peak at 760 cm^{-1}. If the compound has an unsubstituted carbazole ring the 760 cm^{-1} peak will appear as a shoulder on the 750 cm^{-1} peak. The *para*-substituted N-phenylcarbazoles show a strong out-of-plane bending (*para*-disubstituted ring) peak between 825 and 850 cm^{-1}, the position depending upon the electron-donating ability of the *para*-substituent. A rough Hammett-type correlation was obtained whereby the peak frequency was found to shift to lower values with increasing electron-donating ability. Carbazoles substituted at the 3-position show a strong out-of-plane bending peak around 810 cm^{-1} and a medium intensity peak between 840 and 905 cm^{-1}, both indicative of a 1,2,4-trisubstituted aryl ring.

The position of this latter peak was found to depend upon the electron-donating effect of the substituent in much the same way as does the 725-750 cm^{-1} peak found in *para*-substituted N-phenylcarbazoles.

Carbazoles disubstituted at the 3 and 6 positions also show both the 1,2,4-trisubstitution peaks but the medium intensity peak is usually 5-15 cm^{-1} lower than in the corresponding 3-substituted carbazoles. The fact that this lowering occurs for substituents such as NH_2 and NMe_2 is reasonable but why it also is observed with electron-withdrawing groups is not understood at present. This latter peak was found to be well suited for determining the extent of synthetic reactions such as halogenations and acylations where both 3- and 3,6-substituted products could be formed. For mixtures, two peaks are readily discernable.

The purity and structure of some of the 3,6-disubstituted N-ethyl- and N-phenylcarbazoles were confirmed by nmr spectroscopy using a Perkin-Elmer R20 spectrometer; an ABX splitting pattern in the aromatic region is readily observed. Many others could not be analyzed via nmr due to either limited solubility or spectral complexity.

Column chromatography using benzene, hexane, or heptane as the solvent and either basic or neutral alumina (Woelm) as the support was invaluable in purification of all but the carboxyl-substituted carbazoles. Also, the 3,6-dinitro-substituted carbazoles were chromatographed with acetone or nitrobenzene on neutral alumina.

The carbazole-3-carboxylic acids were purified by sublimation and the carbazole-3,6-dicarboxylic acids by repeated formation of the salt in aqueous base and reprecipitation of the free acid with strongly acidic solutions.

In halogenation and acylation reactions, separation of the mono- and di-substituted products was often a problem. In these cases, recrystallization from refrigerated methanol solutions was used to separate the mixtures. In the cold solutions the disubstituted carbazoles precipitated first and were collected before crystallization of the monosubstituted derivatives began.

Brief descriptions of the compound preparations are given below. Although some of it is repetitive of litera-

ture methods, modifications in work-up were effected in every case.

3-Substituted carbazoles.—3-Aminocarbazole was obtained from Aldrich Chemical Company and was purified by recrystallization three times from ethanol, mp 255°-258° [Ref. (17) 254°]. Methylation with trimethylphosphate gave 3-dimethylaminocarbazole, which was recrystallized twice from heptane, mp 114°-115° [Ref. (18) 114°-116°]. Diazotization of the hydrochloride salt of 3-aminocarbazole, followed by treatment with sodium tetrafluoborate, heating in xylene and extraction with benzene gave 3-fluorocarbazole. The crude material was chromatographed on neutral alumina and recrystallized twice from benzene/hexane, mp 208°-209° [Ref. (19) 202°-203°]. 3-Chlorocarbazole was prepared by treating carbazole with an equimolar amount of sulfuryl chloride in chloroform, followed by chromatography with benzene on basic alumina. Two recrystallizations from cold methanol and one from ethanol (charcoal) yielded the product, mp 197°-198° [Ref. (20) 196°-197°]. 3-Bromocarbazole was prepared by reacting carbazole with an equimolar amount of N-bromosuccinimide in carbon tetrachloride containing a small amount of benzoyl peroxide. Chromatography with benzene on basic alumina, followed by two recrystallizations from cold methanol and one from ethanol (charcoal) yielded white flakes, mp 195°-197° [Ref. (21) 194°-196°]. Heating of 3-bromocarbazole with cuprous cyanide in pyridine at 215°-225° for 24 hr produced a solid reaction mass which was chromatographed twice with benzene on basic alumina; recrystallization from ethanol/heptane yielded 3-cyanocarbazole, mp 183°-184° [Ref. (22) 184°-185°]. Treatment of carbazole with an equimolar iodide-iodate solution (23) yielded 3-iodocarbazole, which was purified by chromatography on basic alumina with benzene and two recrystallizations from cold methanol and one from ethanol (charcoal) to yield the product, mp 195°-196° [Ref. (23) 192°-194°]. 3-Nitrocarbazole was prepared by nitration of N-nitrosocarbazole and subsequent removal of the nitroso group (24). Chromatography with benzene on neutral alumina and recrystallization from benzene yielded a yellow powder, mp 213°-214° [Ref. (21) 212°-213°]. 3-Methylcarbazole was synthesized by formylation of carbazole followed by a Wolff-Kishner reduction (25); the product was chromatographed twice on neutral alumina with benzene and recrystallized from methanol, mp 205°-207° [Ref. (26) 206°-207°]. N-Benzoylcarbazole was obtained commercially and converted to 3-benzoylcarbazole by a Fries rearrangement, mp 206° [Ref. (27) 206°].

3-Substituted-N-ethylcarbazoles.—3-Nitro-N-ethylcarbazole and 3-amino-N-ethylcarbazole were donated by Southern Dyestuffs Company and were purified by chromatography with benzene on basic alumina. Recrystallizations from benzene/ethanol yielded the products, mp 128°-129° [Ref. (28) 128°] and 111°-112° [Ref. (28) 113°-114°], respectively. Methylation analogous to that for 3-aminocarbazole yielded 3-dimethylamino-N-ethylcarbazole, which was recrystallized once from heptane, mp 62°. Calculated for $C_{16}H_{18}N_2$: C, 80.7; H, 7.60; N, 11.7. Found: C, 80.8; H, 7.67; N, 11.7. Acetylation of the amino derivative yielded, after recrystallization from ethanol, 3-acetamido-N-ethylcarbazole, mp 194°-196° [Ref. (29) 203°-204°]. Diazotization of the 3-amino-N-ethylcarbazole hydrochloride salt and work-up similar to that for 3-fluorocarbazole yielded 3-fluoro-N-ethylcarbazole, which was chromatographed on basic alumina to yield a colorless oil which solidified after several months' standing, mp 44°-48°. Calculated for $C_{14}H_{12}NF$: C, 78.9; H, 5.67; N, 6.57. Found: C, 79.2; H, 5.63; N, 6.52. 3-Formyl-N-ethylcarbazole was obtained from Aldrich Chemical Company and purified by benzene chromatography on basic alumina followed by recrystallization from benzene/hexane, mp 88°-89° [Ref. (30) 92°-93°]. Wolff-Kishner reduction (25) and two recrystallizations from methanol yielded 3-methyl-N-ethylcarbazole, mp 43°-44° [Ref. (25) 45°]. Methods similar to those described for the 3-substituted carbazoles were employed to obtain 3-chloro-N-ethylcarbazole, mp 66°-67° from cold methanol [Ref. (31) 81°-82°]; 3-bromo-N-ethylcarbazole, mp 78°-80° from ethanol [Ref. (30) 81°-82°]; 3-iodo-N-ethylcarbazole, mp 78°-80° from methanol [Ref. (30) 82°-83°]. Treatment of the bromo derivative with cuprous cyanide in pyridine produced 3-cyano-N-ethylcarbazole which was purified in the same fashion as the 3-cyanocarbazole to yield the product mp 113°-115° from benzene/hexane. Calculated for $C_{15}H_{12}N_2$: C, 81.8; H, 5.49; N, 12.7. Found: C, 81.8; H, 5.55; N, 12.7. 3-Acetyl-N-ethylcarbazole was prepared by Friedel-Crafts acylation of N-ethylcarbazole; the product was recrystallized twice from ethanol, mp 112°-114° [Ref. (31) 115°]. Similarly, 3-benzoyl-N-ethylcarbazole was synthesized from N-ethylcarbazole and benzoyl chloride and chromatographed with benzene on basic alumina, followed by recrystallization twice from ethanol to yield mp 90°-92°. Calculated for $C_{21}H_{17}NO$: C, 84.3; H, 5.72; N, 4.68. Found: C, 84.2; H, 5.72; N, 4.59. The N-ethylcarbazole-3-carboxylic acid was prepared by lithiation of the 3-bromo derivative followed by addition of CO_2 to yield the product, mp 232°-234° [Ref. (32) 224°-226°]. Esterification of the latter product with ethanol gave ethyl-N-ethylcarbazole-3-carboxylate, which was purified by benzene chromatography on basic alumina to yield a colorless, viscous oil. Calculated for $C_{17}H_{17}NO_2$: C, 76.4; H, 6.40; N, 5.24. Found: C, 76.3; H, 6.38; N, 5.25.

3,6-Disubstituted carbazoles.—3,6-Dinitrocarbazole was donated by Southern Dyestuffs Company mixed with the 1,6 isomer. They were separated by selective solubilities of the potassium salts (33) followed by chromatography with acetone on neutral alumina and recrystallization from acetone, mp > 350° [Ref. (33) 386°-387°]. 3,6-Dichlorocarbazole, mp 204°-205° from methanol [Ref. (31) 201°-203°], 3,6-dibromocarbazole, mp 211°-212° from methanol [Ref. (9) 211°-213°], and 3,6-diiodocarbazole, mp 205°-206° from methanol [Ref. (9) 204°-206°] were synthesized in manners similar to the monohalogenated derivatives except that two moles of halogenating reagent was used per mole of carbazole. Purification methods were identical. 3,6-Diacetylcarbazole was prepared by Friedel-Crafts acylation and recrystallization twice from ethanol, mp 236°-238° [Ref. (32) 233°]. The 3,6-dicyanocarbazole was synthesized by heating 3,6-dibromocarbazole with an excess of cuprous cyanide in pyridine at 220°-230° for 48 hr. The product was extracted from the hot reaction mass with benzene and chromatographed on neutral alumina; recrystallization was effected from benzene, mp > 300° [Ref. (22) > 360°]. Photolysis of bis (*p*-anisylamine) in cyclohexane at 300 nm for 24 hr yielded 3,6-dimethoxycarbazole. The crude product was purified by benzene chromatography twice on basic alumina followed by recrystallization from benzene/ethanol, mp 175°-177°. Due to the presence of large amounts of unreacted parent, great care must be taken in the chromatographic separation; the carbazole comes off the column after the parent diphenylamine. Calculated for $C_{14}H_{13}NO_2$: C, 74.0; H, 5.94; N, 6.16. Found: C, 74.2, H, 5.89; N, 6.13.

Several *t*-butylated carbazoles were kindly donated by F. A. Neugebauer of the Max-Planck Institute, Heidelberg, Germany, namely the 3,6-di-*t*-butylcarbazole, 1,8-di-*t*-butylcarbazole, 1,3,6-tri-*t*-butylcarbazole, 1,3,8-tri-*t*-butylcarbazole, and 1,3,6,8-tetra-*t*-butylcarbazole.

3,6-Disubstituted-N-ethylcarbazoles.—Treatment of 3-nitro-N-ethylcarbazole with 1.2 equivalents of nitric acid in refluxing acetic acid produced 3,6-dinitro-N-ethylcarbazole as a precipitate. The crude material was chromatographed on neutral alumina with acetone and recrystallized twice from nitrobenzene, mp > 300°. Calculated for $C_{14}H_{11}N_3O_4$: C, 59.0; H, 3.90; N, 14.7. Found: C, 58.8; H, 3.86; N, 14.7. Reduction of this compound with tin/HCl in ethanol, followed by neutralization gave 3,6-diamino-N-ethylcarbazole which was

purified by repeated acid-base recrystallization, mp 188°-189°. This compound air oxidizes very readily and darkens rapidly upon standing. Calculated for $C_{14}H_{15}N_3$: C, 74.6; H, 6.71; N, 18.7. Found: C, 74.5; H, 6.75; N, 18.6. Methylation of the diamino derivative with trimethylphosphate, followed by benzene/basic alumina chromatography (twice) and recrystallization from benzene/heptane yielded 3,6-bis(dimethylamino)-N-ethylcarbazole, mp 120°-122°. Calculated for $C_{18}H_{23}N_3$: C, 76.8; H, 8.23; N, 14.9. Found: C, 76.5; H, 8.27; N, 15.0. Photolysis of N-ethylbis-(*p*-anisyl)amine in cyclohexane at 300 nm for 24 hr, followed by chromatography with benzene on basic alumina and recrystallization from ethanol produced 3,6-dimethoxy-N-ethylcarbazole, mp 178°-180°. Calculated for $C_{16}H_{17}NO_2$: C, 75.3; H, 6.71; N, 5.49. Found: C, 75.1; H, 6.58; N, 5.62. 3,6-Dichloro-N-ethylcarbazole, mp 117°-118° from methanol [Ref. (31) 113°], 3,6-dibromo-N-ethylcarbazole, mp 137°-138° from ethanol [Ref. (31) 136°], 3,6-diiodo-N-ethylcarbazole, mp 152°-153° from ethanol [Ref. (32) 154°], 3,6-dimethyl-N-ethylcarbazole, mp 62°-63° from benzene/heptane [Ref. (25) 67°] and 3,6-diacetyl-N-ethylcarbazole, mp 182°-183° from benzene [Ref. (31) 182°] were all prepared in manners similar to those for the monosubstituted analogs with the exception that the substituting reagents were doubled in concentration (or, in the case of the methyl derivative the substitution reaction was carried out twice). 3,6-Dipropionyl-N-ethylcarbazole was prepared similarly to the diacetyl compound to yield mp 133° [Ref. (31) 132°]. Wolff-Kishner reduction of the diacetyl derivative followed by chromatography with benzene twice on basic alumina generated the 3,6,N-triethylcarbazole. Recrystallization twice from cold methanol yielded the pure product, mp 81°-85° [Ref. (29) oil]. 3,6-Di-*t*-butyl-N-ethylcarbazole was prepared by a Friedel-Crafts alkylation of N-ethylcarbazole with *t*-butylchloride. Chromatography with benzene on basic alumina and recrystallization from benzene/heptane yielded the product, mp 151°-153°. Calculated for $C_{22}H_{29}N$: C, 85.9; H, 9.53; N, 4.55. Found: C, 85.5; H, 9.47; N, 4.56. N-Ethylcarbazole-3,6-dicarboxylic acid was prepared by a hypobromite oxidation of 3,6-diacetyl-N-ethylcarbazole according to the method of Buu-Hoi (29), mp > 300° [Ref. (29) > 300°]. Dimethyl-N-ethylcarbazole-3,6-dicarboxylate was synthesized by esterification of the diacid with methanol and was purified by recrystallization twice from methanol/benzene/pet. ether, mp 187°-188° [Ref. (36) 187°]. Treatment of 3,6-dibromo-N-ethylcarbazole with excess cuprous cyanide according to the previously mentioned procedure for cyanations, followed by benzene extraction, chromatography on neutral alumina and recrystallization from benzene gave 3,6-dicyano-N-ethylcarbazole, mp 230°-231°. Calculated for $C_{16}H_{11}N_3$: C, 78.3; H, 4.54; N, 17.1. Found: C, 78.1; H, 4.52; N, 17.1. 3-Acetyl-6-methyl-N-ethylcarbazole and 3-acetyl-6,N-diethylcarbazole were obtained from N. P. Buu-Hoi and were used without further purification.

Substituted N-phenylcarbazoles.—The purification of N-phenylcarbazole has been previously described (7). N-(*p*-nitrophenyl)carbazole was prepared from carbazole and nitrobenzene by the method of de Montmollin (37) and was recrystallized once from toluene and then once from benzene, mp 211°-213° [Ref. (37) 212°]. Reduction of this compound with tin/HCl in ethanol produced N-(*p*-aminophenyl)carbazole, which precipitated out after several hours' refluxing as the hydrochloride salt. The free base can be obtained from the salt by neutralization but it is difficult to purify, apparently forming a matrix with many solvents. Chromatography using benzene on a basic alumina column followed by evaporation of the solvent from the eluent gave an oil [Ref. (38) resin]. After several hours' heating *in vacuo* a brown, glass-like solid was obtained which possessed a large variable melting point range. Methylation of the amino derivative with trimethylphosphate (careful heating required!), followed by chromatography with benzene on basic alumina and recrystallization from benzene/hexane yielded N-(*p*-dimethylaminophenyl)carbazole, mp 213°-215° [Ref. (39) 210°-212°]. Acetylation of the amino derivative gave N-(*p*-acetamidophenyl)carbazole; recrystallization twice from ethanol yielded the desired compound, mp 258°-260° [Ref. (38) 260°]. Several of these N-*para* substituted phenylcarbazoles were obtained using a modified Ullmann reaction in which an appropriately *para*-substituted iodobenzene is allowed to react mole-per-mole with carbazole in the presence of copper powder and potassium carbonate. The mixture is heated for 12-24 hr at about 200° without solvent (the iodobenzenes melt and serve as the solvent; in some cases a few ml of xylene was added to keep the mixture fluid). The hot reaction mixture is extracted with benzene (in which unreacted carbazole is almost totally insoluble), and the benzene solution is chromatographed on basic alumina. The first fraction contains the substituted phenylcarbazole; all were then recrystallized from benzene/hexane or benzene/ethanol. Pertinent data on these compounds, many of which are believed to be new, are given below:

N-(*p*-anisyl)carbazole, from benzene/ethanol, mp 154°-155° [Ref. (40) 149°-150°].

N-(*p*-methylthiophenyl)carbazole, from benzene/ethanol, mp 153°-155°. Calculated for $C_{19}H_{15}NS$: C, 78.9; H, 5.22; N, 4.84. Found: C, 78.7; H, 5.18; N, 4.76.

N-(*p*-biphenyl)carbazole, from benzene/ethanol, mp 225°-227° [Ref. (42) 224°-226°].

N-(*p*-tolyl)carbazole, from benzene/ethanol, mp 106°-108° [Ref. (42) 105°-107°].

N-(*p*-*t*-butylphenyl)carbazole, from benzene/ethanol, mp 191°-192°. Calculated for $C_{22}H_{21}N$: C, 88.2; H, 7.06; N, 4.68. Found: C, 88.2; H, 7.12; N, 4.62.

N-(*p*-fluorophenyl)carbazole, from benzene/ethanol, mp 120°-122°. Calculated for $C_{18}H_{12}NF$: C, 82.7; H, 4.63; N, 5.36. Found: C, 82.6; H, 4.69; N, 5.29.

N-(*p*-chlorophenyl)carbazole, from benzene/ethanol (charcoal), mp 141°-143° [Ref. (37) 146°].

N-(*p*-bromophenyl)carbazole, from benzene/ethanol, mp 142°-143° [Ref. (43) 146°-147°].

N-(*p*-iodophenyl)carbazole, from benzene/ethanol then benzene/hexane, mp 139°-140°. Calculated for $C_{18}H_{12}NI$: C, 58.6; H, 3.28; N, 3.80. Found: C, 59.0; H, 3.30; N, 3.74.

N-(*p*-carbomethoxyphenyl)carbazole, from benzene/ethanol, mp 116°-118°. Calculated for $C_{20}H_{15}NO_2$: C, 79.7; H, 5.01; N, 4.65. Found: C, 79.5; H, 5.03; N, 4.57.

N-(*p*-cyanophenyl)carbazole, from benzene/ethanol, mp 180°-183° [Ref. (37) 165°].

Several other 3,6-disubstituted N-phenylcarbazoles were synthesized by methods similar to the N-ethyl analogs; below the crystallization media and physical data are given for these compounds:

3,6-Di-*t*-butyl-N-phenylcarbazole, from benzene/heptane (twice), mp 144°-146°. Calculated for $C_{26}H_{29}N$: C, 87.8; H, 8.21; N, 3.94. Found: C, 87.7; H, 8.24; N, 3.95.

3,6-Diiodo-N-phenylcarbazole, from heptane (twice), mp 179°-182°. Calculated for $C_{18}H_{11}NI_2$: C, 43.7; H, 2.24; N, 2.83. Found: C, 43.9; H, 2.30; N, 2.79.

3,6-Dibromo-N-phenylcarbazole, from benzene, mp 159°-160°. Calculated for $C_{18}H_{11}NBr_2$: C, 53.9; H, 2.76; N, 3.49. Found: C, 53.9; H, 2.75; N, 3.53.

3,6-Dichloro-N-phenylcarbazole, from benzene/heptane, mp 140°-141°. Calculated for $C_{18}H_{11}Cl_2$: C, 69.2; H, 3.55; N, 4.49. Found: 69.4; H, 3.59; N, 4.43.

3,6-Dichloro-N-(*p*-chlorophenyl)carbazole was prepared via an Ullmann reaction involving 3,6-dichlorocarbazole and *p*-chloroiodobenzene. It was twice chromatographed with benzene on basic alumina and recrystallized from benzene/ethanol, mp 174°-175°. Calculated for $C_{18}H_{10}NCl_3$: C, 62.4; H, 2.91; N, 4.04. Found: C, 62.8; H, 3.02; N, 3.93. Photolysis of tris(*p*-tolyl)amine at 300 nm in cyclohexane for 24 hr, followed by chromatography with benzene on neutral alumina and recrystallization from benzene/heptane yielded 3,6-dimethyl-N-(*p*-tolyl)carbazole, mp 105°-107°. Calculated

for $C_{21}H_{19}N$: C, 88.4; H, 6.71; N, 4.91. Found: C, 88.2; H, 6.72; N, 4.90.

Spectroscopic studies.—Visible absorption spectra were obtained on a Cary 14 spectrometer by external electrolysis of the carbazole solution and immediate transfer to a standard cuvette. Only those carbazoles whose cation radicals were known from electrochemical data to be quite stable were studied in this manner.

The EPR spectra were recorded on a Varian E-3 spectrometer using either external electrolytic generation or by chemical oxidation with iodine/propylene carbonate. Although interpretations are incomplete at present, we are confident that the spectra obtained are those of the primary carbazole cation radicals, based on the stabilities of the compounds as determined by electrochemical methods.

HMO calculations.—HMO calculations were carried out using a simple Hückel program modified for cation radical systems; the heteroatom parameters were those shown below:

carbazole nitrogen: $h_N = 1.0$ $k_{C-N} = 0.8$

(same for N—H or N—Et)

C—NR_2 R = H, Me	$h_N = 1.0$	$k_{C-N} = 0.8$
C—OMe	$h_C = 2.0$	$k_{C-C} = 0.8$ (methyl carbon neglected)
C—Me	$h_C = -0.3$	(inductive model, neglecting methyl carbon)
C—F	$h_F = 3.0$	$k_{C-F} = 0.7$
C—Cl	$h_{Cl} = 2.0$	$k_{C-Cl} = 0.4$
C—Br	$h_{Br} = 1.5$	$k_{C-Br} = 0.3$
C—C≡N	$h_{C\ (cyano)} = 0.0$, $h_N = 1.0$,	$k_{C-C} = 0.9$, $k_{C\equiv N} = 2.0$
C—NO_2	$h_N = 2,2$, $k_{N-O} = 1.67$	$k_{C-N} = 1.2$, $h_O = 1.4$,

The "frontier orbital" approach was employed, in which one assumes that the reactivity of the cation radical is best described by the c^2 coefficients in the highest filled orbital (HFMO).

Results and Discussion

Due to the large number of compounds studied, the electrochemical data are broken down into compound classes according to the mode of substitution. It was found that there are characteristic reaction pathways for the cation radicals in each group but there are also variations and so each substitution group is discussed in some detail.

Since spectral data have only been obtained on those molecules possessing stable radicals all compound classes are considered together in these sections.

Electrochemical Data

Carbazoles and N-substituted derivatives.—Although the electrochemistry of these molecules has been presented in detail previously (7), a brief review at this point will serve as a useful basis for discussing the ring-substituted derivatives.

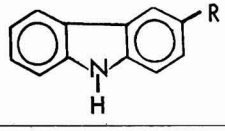
When carbazole is oxidized in MeCN/TEAP at platinum, the initial step is a (proposed) removal of one electron to form a very unstable cation radical. This cation radical reacts by deprotonation-coupling (the sequence is not known) to form the 9,9′- and 3,3′-bicarbazyls. Both bicarbazyls were chemically synthesized and were thus available for comparison. The 3,3′-bicarbazyl is more easily oxidized than carbazole itself and so the former loses two electrons in two reversible one-electron steps to yield a moderately stable dication with extensive conjugation. The 9,9′-bicarbazyl is only formed initially under cyclic voltammetric conditions and could not be isolated from controlled-potential electrolyses in unbuffered MeCN; the 3,3′-bicarbazyl was isolated in moderate yields. The 9,9′-bicarbazyl was found to form quantitatively, however, when electrolyses were carried out in the presence of an organic base such as pyridine. This fact led to the conclusion that the carbazole cation radical forms the 9,9′-bicarbazyl by diffusing out into solution, followed by deprotonation of the central nitrogen and subsequent coupling of the resultant free radicals in solution before they can diffuse back to the electrode to be further oxidized.

Interestingly, the 9,9′-bicarbazyl was found to oxidize considerably more anodic than carbazole (E_p's of 1.85 and 1.20V, respectively) in a multielectron, irreversible process accompanied by severe filming to form unknown products.

In accordance with this scheme, N-alkyl- and N-phenylcarbazoles were found to form only the corresponding 9,9′-disubstituted-3,3′-bicarbazyls cleanly in quantitative yields. Due to the steric hindrance afforded by the alkyl and phenyl groups no 1,1′- or 3,1′-coupling products were detected.

3-Substituted carbazoles.—The electrochemical data for these compounds are presented in Table I. In general, the electrochemistry of this class is similar to that

Table I. Electrochemical data for 3-substituted carbazoles

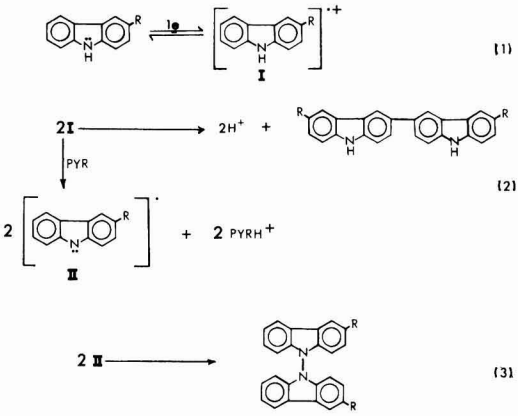


No.	R =	$E_{p/2}$[a]	$it^{1/2}/C$	n value	Product(s) (% yield), comments
I	NH_2	0.47	44	0.99	Irreversible one-electron oxidation, coupled product appears to form
II	NMe_2	0.38	46	0.98	Stable cation radical, second reversible process at $E_{p/2}$ = 1.00V, moderately stable dication, no bicarbazyls appear to form
III	Me	1.12	133	2.6[b]	Bicarbazyl[c] forms in poor yield
IV	F	1.23	132	3.4[b]	Bicarbazyl[c] forms in poor yield
V	Cl	1.27	115-121[d]	3.4[b]	Bicarbazyl[c] forms in poor yield
VI	Br	1.26	107-115[d]	3.2[b]	Bicarbazyl[c] forms in poor yield
VII	I	1.25	102	3.0[b]	Bicarbazyl[c] forms in poor yield
VIII	COPh	1.36	100	2.8[b]	Bicarbazyl[c] forms in poor yield
IX	CN	1.43	106-123[d]	4.0	Bicarbazyl[c] forms in poor yield
X	NO_2	1.51	113-122[d]	4.0	Product(s) unknown

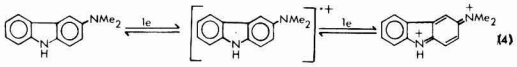
[a] In volts *vs.* SCE, taken from linear scan voltammograms; values shift anodic with increasing scan rate.
[b] Low steady-state currents are observed at these n values; the cut-off point is not uniform for all compounds and so only the trend in the n values is meaningful.
[c] From controlled-potential electrolyses in MeCN/TEAP; in all cases the bicarbazyl is the 3,3′-disubstituted-6,6′-bicarbazyl in yields of 20-40%.
[d] Chronoamperometric value increases with increasing electrolysis time (1-8 sec).

of carbazole itself. Since both the N(9) and 6 sites are open in these molecules one has the possibility for N-N, N-ring, and ring-ring couplings. Cyclic voltammograms show the presence of 6,6'- and N,N'-disubstituted bicarbazyls as in the case of carbazole with the exception of the fluoro derivative, which shows only 6,6'-bicarbazyl formed. However, controlled-potential electrolyses in MeCN/TEAP yield only the 3,3'-disubstituted-6,6'-bicarbazyls in poor yields; this has also been reported for carbazole (7). In addition, when the electrolyses are conducted with 2,4,6-trimethylpyridine added to the solution one obtains only N-N coupling; this is observed on both cyclic voltammograms and in controlled-potential electrolyses. This was also reported for carbazole and seems to point to a general rule that N-N coupling can only occur if the cation radical is deprotonated (7). This is shown graphically in Fig. 1 for 3-methylcarbazole; the curves are not well defined, but it is apparent that addition of the pyridine derivative wipes out formation of the ring-ring coupled product and gives essentially a quantitative yield of the 9,9'-bicarbazyl. In accordance with this, the peak current of the initial oxidation wave on curve B is about half that in curve A and the 3,3'-disubstituted-6,6'-bicarbazyl couple seen on curve A is absent in the presence of the relatively strong pyridine base on curve B. The oxidation process for the substituted 9,9'-bicarbazyl is a multielectron process (7) and so the bicarbazyl wave height on curve B is quite large relative to the primary oxidation wave. Formation of the 9,9'-bicarbazyl was verified by carrying out a preparative-scale electrolysis after which it was isolated in high yield (see Experimental section).

This reactivity pattern was found to be general for all of the 3-substituted carbazoles except for the amino and dimethylamino derivatives and is identical to the scheme presented previously for carbazole itself (7); the R group denotes all the substituents shown in Table I except amino and dimethylamino



The rather high n values observed as one goes to more electron-withdrawing substituents is indicative of significant secondary chemical reactions in these systems. The dimethylamino derivative is completely different in that it has a stable cation radical, as verified by a complicated but well-resolved EPR spectrum (*vide infra*). Further one-electron oxidation to the dication quinonediimine occurs and this couple is also reversible. This is to be anticipated due to the highly conjugated species that can be generated by loss of two electrons



The dication does react slowly, and the cation radical more slowly still (half-lives of about 30-40 sec and 20-30 min, respectively), but neither appears to form a bicarbazyl in either the 6 or 9(N) positions. This is not surprising, since the charge density at the open 6-ring position is very low in this molecule. Simple HMO calculations show that the 6-position will not be a center of reactivity and thus the 6,6'-bicarbazyl is not likely to form. The reactive site is instead predicted by HMO calculations to be the dimethylamino group and its *ortho* ring carbons and so the reaction pathway may be similar to that for N,N-dimethylaniline, where coupling has been shown to take place through the N-methyl groups and, possibly, the ring positions *ortho* to it (44).

3-Aminocarbazole undergoes a different oxidation pathway in that the first step, also a one-electron process, is irreversible. The cyclic voltammograms and n value of unity suggest formation of a product generated by intermolecular coupling and subsequent oxidation with concomitant protonation of parent material (thus rendering it electroinactive at the parent oxidation potential) according to the general mechanism

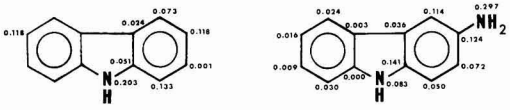
$$2C \overset{2e}{\rightleftharpoons} 2C^{\cdot+} \xrightarrow[\text{fast}]{\text{coupling}} C_2 + 2H^+ \qquad [5]$$

$$C_2 \overset{2e}{\rightleftharpoons} C_2^{++} \qquad [6]$$

$$2C + 2H^+ \rightleftharpoons 2CH^+ \text{ (electroinactive)} \qquad [7]$$

Thus, a total of four electrons is taken up and four parent molecules are removed from the system either by electrolysis or protonation. From known reactivities of aniline derivatives and the observed instability of the 3-aminocarbazole cation radical compared to that of the dimethylamino derivative, one would anticipate that the NH_2 group is directly involved in the coupling reaction; however, it is not certain at this time whether N-N or N-ring compounds are being generated.

Considering all the potential active sites, a large number of coupled products are possible. Although the 6-position is open, simple HMO calculations again predict a reactivity pattern characteristic of a substituted aniline, analogous to the dimethylamino derivative; thus, 6,6' coupling is not likely. The numbers shown below are c^2 values[4] for the highest filled orbitals occupied by a single electron for carbazole and 3-aminocarbazole (the picture for the dimethylamino compound would be very close to the latter); one sees that these crude calculations predict a drastic change in reactivity, a change that is qualitatively confirmed by the experimental data



In the 3-amino compound, the charge density is very low in the unsubstituted ring and is largely restricted to the amino group and the ring positions *ortho* and *para* to it. Of all the possible coupled products, the two shown below seem most likely based on these calculations



Studies are now under way to determine the structure(s) of the coupled product(s) derived from both 3-amino- and 3-amino-N-ethylcarbazole.

3-Substituted-N-ethylcarbazoles.—It was anticipated that blocking of the carbazole nitrogen with an ethyl

[4] The c^2 values (squares of atomic orbital coefficients) are roughly proportional to the unpaired electron densities, and it has been empirically observed that the values for each atom taken only from the highest filled orbital, rather than summing the values for all the occupied orbitals, give reliable reactivity patterns for aromatic cation radicals.

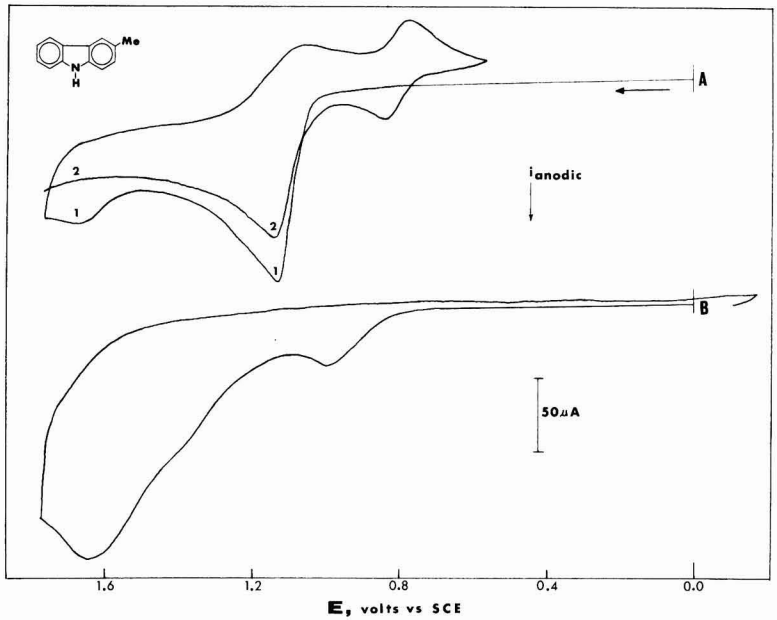
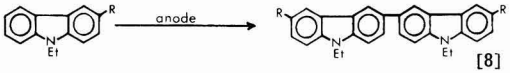


Fig. 1. Curve A: Cyclic voltammogram of 1.2 × $10^{-3}F$ 3-methylcarbazole in MeCN/TEAP, sweep rate = 150 mV/sec. Curve B: Cyclic voltammogram of the same solution with excess 2,4,6-trimethylpyridine added, sweep rate = 50 mV/sec.

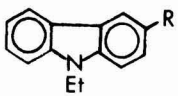
group would render the previous systems somewhat less complicated, in a similar fashion to the previous studies on carbazole and N-ethylcarbazole (7). With the nitrogen blocked, N-N and N-ring coupling cannot occur and one should obtain only the 3,3'-disubstituted-N,N'-diethyl-6,6'-bicarbazyls by bond formation through the only available active site (excluding the amino and dimethylamino derivatives)



[8]

This is observed for most of these compounds, as shown in Table II and Fig. 2. By and large, the bicarbazyls are the major products in these systems, but most of the coupled products are somewhat unstable and react further, particularly in the presence of impurities in the solvent or supporting electrolyte. As for the 3-substituted carbazoles, the n values cited in Table II were taken at parent concentrations of 10^{-3} to $10^{-4}F$ and the amounts of bicarbazyl cited were estimated from peak currents on cyclic voltammograms of exhaustively electrolyzed $10^{-3}F$ solutions. Very good product yields were only obtained at low concentrations and in very pure solvent, so the numbers cited in Table II are probably near the optimum values to be expected. At higher concentrations further reactions ensue in many cases and telomers or other unidentified products are obtained. As with the 3-substituted carbazoles, low steady-state currents were encountered in exhaustive electrolyses, but they were generally quite a bit lower, indicating that the 3-substituted-N-ethylcarbazoles are considerably "cleaner." Cyclic voltammograms of exhaustively electrolyzed solutions suggest that prepara-

Table II. Electrochemical data for 3-substituted-N-ethylcarbazoles



No.		$E_{p/2}$	$it^{1/2}/C$	n value	Product(s) (% yield), comments
XI	R = NH_2	0.48	45	0.75	Unstable cation radical, coupled product appears to form
XII	NMe_2	0.36	47	0.96	Stable cation radical, second reversible process at $E_{p/2}$ = 0.98V, stable dication, no dicarbazyls appear to form
XIII	NHCOMe	0.96	48-52[a]	2.12[b]	6,6'-bicarbazyl,[c] other products
XIV	Me	1.09	103-110[a]	2.08[b]	6,6'-bicarbazyl (40), other products
XV	F	1.20	95	2.03	6,6'-bicarbazyl (100)
XVI	Cl	1.28	93	1.93[b,c]	6,6'-bicarbazyl (60)[d]
XVII	Br	1.25	91	2.13[b,c]	6,6'-bicarbazyl (50)[d]
XVIII	I	1.24	88	2.20[b,c]	6,6'-bicarbazyl (60)
XIX	CHO	1.34	103-89[e]	2.09[b,c]	6,6'-bicarbazyl; films badly and is largely insoluble
XX	COMe	1.30	87	2.12[b]	6,6'-bicarbazyl (90)
XXI	COPh	1.30	91	2.12[b]	6,6'-bicarbazyl (85)
XXII	COOH	1.32	74-81[e]	2.11[b]	6,6'-bicarbazyl (90) totally insoluble
XXIII	COOEt	1.35	93	2.22[b]	6,6'-bicarbazyl (70)[d]
XXIV	CN	1.44	94-118[a]	2.24[b,c]	6,6'-bicarbazyl (60)
XXV	NO_2	1.46	102-110[a]	2.26[b,c]	6,6'-bicarbazyl (50)

[a] Chronoamperometric value increases with increasing electrolysis time (1-8 sec).
[b] Low steady-state currents are observed at these n values; however, they are considerably lower than in the case of the 3-substituted carbazoles (see text).
[c] n value is very sensitive to solvent/supporting electrolyte impurities.
[d] Yields are lower at higher carbazole concentrations.
[e] Current-time curves are distorted due to severe filming.

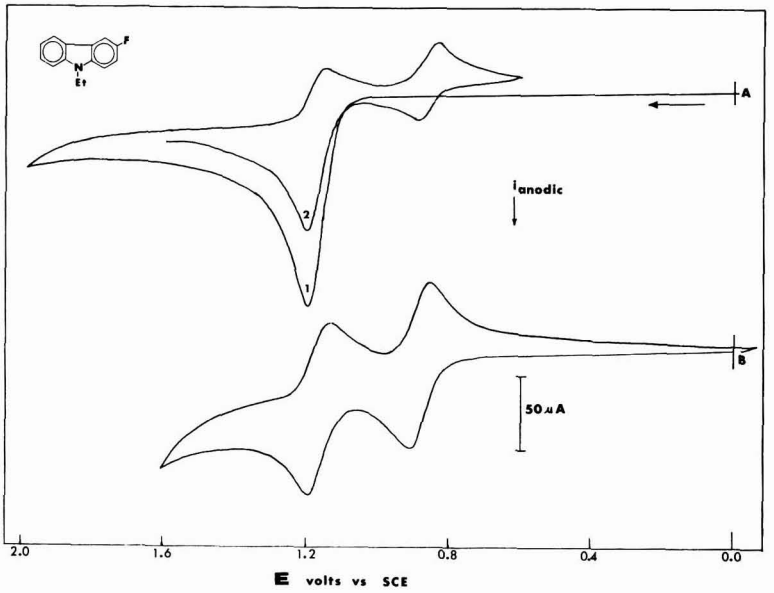


Fig. 2. Curve A: Cyclic voltammogram of 9.6×10^{-4}F 3-fluoro-N-ethylcarbazole in MeCN/TEAP, sweep rate = 100 mV/sec. Curve B: Cyclic voltammogram of the same solution following exhaustive electrolysis at 1.4V, sweep rate = 67 mV/sec.

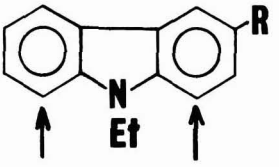
tive studies on these systems would be difficult at best. However, several derivatives can be electrolyzed on a preparative scale (~0.5g) to give moderate yields of bicarbazyls, among them the fluoro, iodo, acetyl, benzoyl, ethylcarboxylate, cyano, and nitro compounds (see Experimental section).

At short electrolysis times, these systems are model two-electron over-all ECE processes and so several attempts were made to measure the coupling rate constants for bicarbazyl formation using rotating disk voltammetry and digital simulation methods (14). In all cases, the coupling rates were too fast to measure, which indicates that a lower limit for the second-order k's would be a value of about 10^8 mole^{-1} sec^{-1}. This is not surprising since the carbazole ring system is planar and thus the charge densities at the 6-positions are quite high for the molecules in this series compared to, say, 4-substituted triphenylamines, which have second-order coupling rate constants ranging from 0.6 to 10^4 mole^{-1} sec^{-1} (45). Thus, the primary reaction pathway of these cation radicals is intermolecular coupling to form the corresponding bicarbazyls; these latter species then further decompose in a variety of secondary follow-up reactions.

In some cases, these secondary reactions following bicarbazyl formation can be speculated upon. The acetamido derivative yielded an appreciable amount of bicarbazyl but also a second product that appears to be a hydrazine-type derivative formed by deacetylation of the acetamido group and coupling through the 3-amino substituents. The methyl derivative also exhibited secondary reactions and cyclic voltammograms of exhaustively electrolyzed solutions indicated that further coupling through the methyl groups might be taking place in a similar fashion to the behavior previously reported for N,N-dimethyl-p-toluidine (46).

In several instances, the bicarbazyls formed were found to be only sparingly soluble and tended to film the electrode severely. In these cases, the product was collected by filtration of the electrolysis solution; the IR spectra indicated that these were perchlorate salts, probably of the bicarbazyl dication. This phenomenon was very marked for the aldehyde and carboxylic acid derivatives, although the ethyl ester was relatively uncomplicated and exhibited no filming.

In other cases, the nature of the secondary reactions could not be ascertained but previous chemical oxidation studies have shown that the 1 and 8 ring positions, denoted by arrows below, are active and can be readily substituted in the absence of steric inhibition. These



ring sites could also be susceptible to attack in the bicarbazyls and so further couplings past the latter cannot be ruled out. This is also consistent with the observed fact that the stabilities of the bicarbazyls increase markedly as the carbazole nitrogen is substituted with first ethyl and then phenyl groups (*vide infra*). However, whereas further couplings past the bicarbazyl may be occurring, it should be pointed out that these reactions would never yield an n value greater than two, since the formation of successive telomers introduces increasingly greater possibilities for more conjugated systems generated by removal of electrons, but at the same time involves the consumption of more parent molecules. Thus, the secondary reactions leading to higher n values are more likely degradation of the bicarbazyl skeleton or the attached substituents. If further coupling reactions were involved, they would have to be intramolecular in nature.

Again, different behavior is observed for the amino and dimethylamino derivatives, these being quite similar to the 3-substituted analogs in not undergoing the standard bicarbazyl couplings. The major exception is that the N-ethyl compounds have more stable cation radical and diimine forms; in fact, 3-dimethylamino-N-ethylcarbazole exhibits two nicely reversible redox steps, as shown in Fig. 3. Comparison of the current-voltage curves for compounds I, II, XI, and XII confirms a general characteristic of p-phenylenediamine-type molecules in that protection of the nitrogen with alkyl or phenyl groups lends considerable stability to both the cation radical and diimine species. As with compound II, however, both the cation radical and diimine of compound XII slowly react to form unknown products.

When the 3-amino group is not methylated (No. XI) the cation radical is much less stable, although reversi-

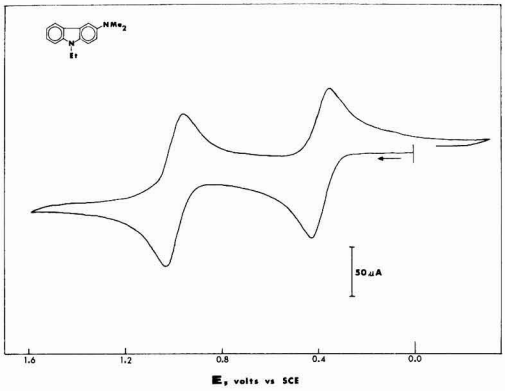


Fig. 3. Cyclic voltammogram of 1.0 × $10^{-3}F$ 3-dimethylamino-N-ethylcarbazole in MeCN/TEAP, sweep rate = 150 mV/sec.

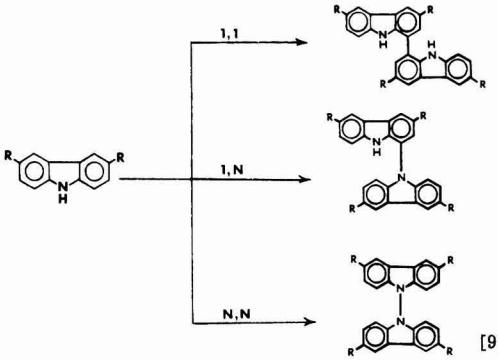
bility can still be observed on both the first and second anodic waves even at sweep rates as low as 200 mV/sec. At sweep rates of about 2 V/sec and above the first process is completely reversible, and a half-life of about 0.5 sec for the primary cation radical can be estimated. As with compound I, however, little is known about the process taking place and the n value of 0.7-0.8 (average value = 0.75), which was obtained repeatedly and appears to be genuine, is quite perplexing. This is, of course, different than for 3-aminocarbazole, which had an n value of unity. It is difficult to propose a mechanism involving 0.75 electrons per molecule with simple coupling as the only pathway. If the oxidized form of the bicarbazyl were to lose one or two protons this would generate n values of 0.80 or 0.67, respectively; it is conceivable that a mixture of these two processes is taking place, but it seems more likely that a completely different mechanistic pathway yet to be considered is operative here.

It is interesting to note that the primary radical of the acetamido derivative, No. XIII, is moderately stable, having a half-life of about 30 sec. As mentioned above, the reaction pathways of this radical are complex but again they are different than for No. XI and XII and are more characteristic of the other derivatives in this series in that an appreciable amount of the 6,6'-bicarbazyl is formed. It appears that the acetamido group is withdrawing electron density from the unsubstituted ring, but not to the extent that the —NH_2 and —NMe_2 groups do; these latter substituents stabilize the primary radicals by markedly decreasing electron density at the reactive 6-position. The result is that for these two compounds the electrochemistry is more characteristic of p-phenylenediamine-type molecules. There is probably also a steric factor for the acetamido derivative in that any coupling reactions involving the 3-substituent will be hindered by the acetyl group.

In all of the other compounds, No. XIV-XXV, simple HMO calculations indicate that the 3-substituents either have little effect on the 6-position electron density or actually increase it (relative to N-ethylcarbazole) making coupling more likely. The result is that in all cases the primary cation radicals are extremely short lived.

Thus, radical stabilities in this series can be interpreted in terms of the electron density at the reactive 6-position. Substituents such as —NH_2,—NMe_2, and —NHCOMe (and presumably —OR and —SR) can accommodate the unpaired electron density in the cation radicals and thus remove electron (and charge) density from the open ring. The others from —Me through —NO_2 do not and in fact enhance coupling at the 6-position.

3,6-Disubstituted carbazoles.—For this series, it is apparent that barring substituent elimination, the only likely coupling sites would be the 1, 8, and 9 (N) positions. Thus, only the 1,1- 1-N, and N-N coupled products should, in principle, be possible



[9]

As with the other systems previously mentioned, the feasibility of these products forming depends upon the status of the carbazole nitrogen (protonated or unprotonated) and the electron densities at the remaining reactive coupling sites. In addition, since all of the above reactions would be expected to be rapid and the carbazole nitrogen and 1 and 8 ring positions are unprotected cation radicals in this series would be predicted to be quite unstable.

Cyclic voltammetric data for these compounds are varied, as is seen in Fig. 4, and the electroanalytical data in Table III further indicate the diverse and generally poorly defined behavior in MeCN/TEAP. Current-voltage and current-time curves for a number of the derivatives in this series were markedly affected by adsorption of either parent material or electrolysis products and cyclic voltammograms run after exhaustive electrolyses were very poorly defined and showed little in the way of discernable products.

Only the methoxy derivative, No. XXVI, shows reversibility at low sweep rates and in fact the cation radical is quite stable, having a half-life ($t_{1/2}$) of several minutes. The primary radicals for the other compounds in this group are quite unstable, having $t_{1/2}$'s of 0.1-1.0 sec, but all of these radicals are much more stable than those of previously mentioned compounds with open 3 or 6 positions, with the exception of the aminocarbazoles. This marked stabilizing effect of methoxy groups has been noted previously (45, 47, 48) and is due to delocalization of charge and electron density out onto the methoxy's, with a resultant decrease at reactive sites in the carbazole nucleus. This is shown below, where electron densities are again represented by c^2 values for the HFMO; with the 3 and 6 positions blocked activity would be expected to shift to the 1, 8, and 9 sites, but as can be seen the latter are considerably deactivated



Of the other functional groups, only the t-butyl is predicted to have a similar effect, but to a much lesser extent. The others actually increase the electron density at the active sites and so further destabilize the primary cation radicals in a regular fashion, the stability decreasing from chloro to nitro.

It is interesting to note that the HMO calculations show an appreciable enhancement in electron density at the 4 and 5 ring carbons *ortho* to the methoxy groups (similar to the 3-aminocarbazole systems) to a point where these positions must be considered as possible coupling sites. Since methoxy is classically an *ortho-para* director this is not totally unexpected, but it will

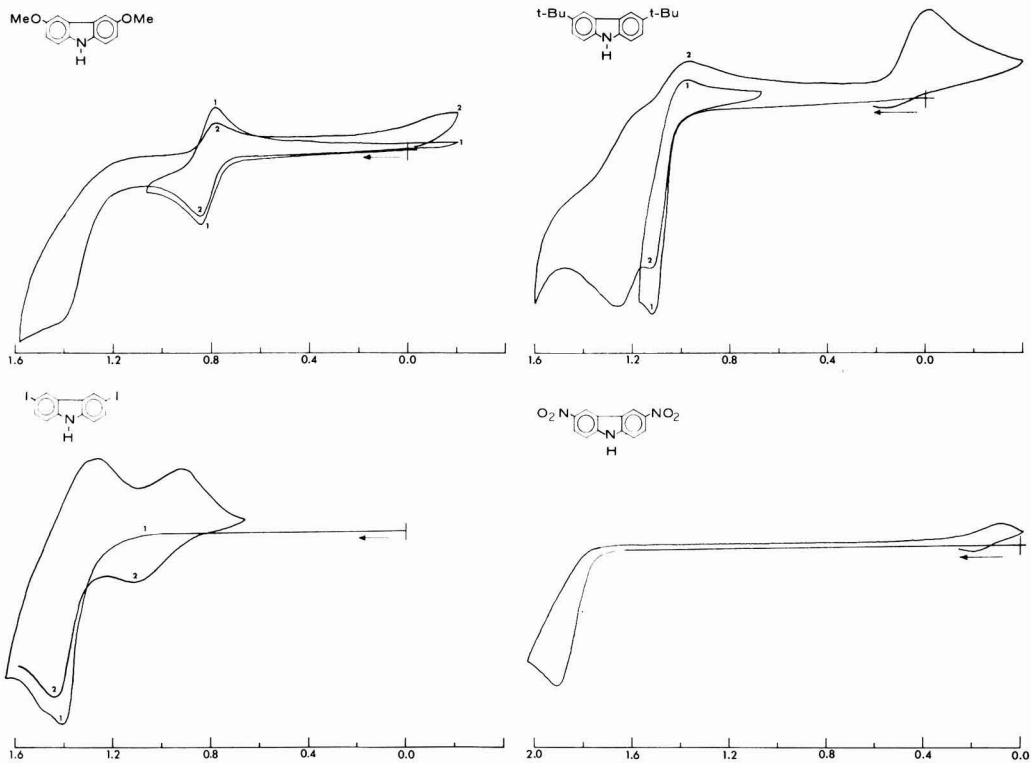


Fig. 4. Cyclic voltammograms of 3,6-disubstituted carbazoles in MeCN/TEAP. Abscissa is in volts vs. SCE and for all curves the solutions were 1.0 × 10^{-3}F in the carbazoles and the sweep rate was 150 mV/sec. In some cases, scans are numbered sequentially.

be indeed interesting if further work on the reaction pathways of these molecules verifies the HMO prediction. It is particularly germane, since EPR studies have indicated that the spin density at the 4 and 5 positions is quite low in some substituted carbazoles (*vide infra*) (49).

Little has actually been determined concerning the reactivity routes of No. XXVII-XXXIII in MeCN/TEAP. Some substituent elimination does occur for the halogen derivatives, leading to 6,6′-disubstituted-3,3′-bicarbazyls; this can readily be seen in Fig. 4 for 3,6-diiodocarbazole. The follow-up peaks in the region between 1.0 and 1.4V match perfectly with those for the 6,6′-bicarbazyl formed from 3-iodocarbazole. Of the other derivatives, it has only been determined that the primary cation radicals are very unstable ($t_{1/2} \simeq 1$ sec) and the decay pathways do not appear to involve substituent elimination.

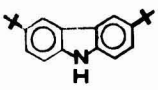
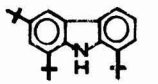
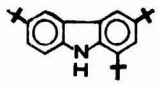
In the presence of 2,4,6-trimethylpyridine, a strong organic base, electrolysis again produces only the substituted 9,9′-bicarbazyls in near quantitative yields. They are easily isolated, since they are in some cases insoluble and can be filtered off following electrolysis; alternatively, they are easily separated from the solvent and supporting electrolyte by column chromatography (see Experimental section). Such electrolyses in basic medium exactly parallel similar chemical work involving permanganate oxidations in acetone of the bromo (9) and *t*-butyl (49) derivatives, and it appears that near quantitative yields of the 9,9′-bicarbazyls

Table III. Electrochemical characteristics of 3,6-disubstituted carbazoles

No.	R	$E_{p/2}$	$it^{1/2}/C$	*n* value	Product(s) (% yield)
XXVI	R = OMe	0.78	48-53	1.76[d]	Stable cation radical, decomposition pathway unknown
XXVII	*t*-Bu	1.07	106-115	2.91, 1.87[a]	Corresponding 9,9′-bicarbazyl[a] (90-100)
XXVIII	Cl	1.38	120-146	3.60	3,3′- and 9,9′-bicarbazyls[c]
XXIX	Br	1.37	120-143[b]	2.87, 1.93[a]	9,9′-bicarbazyl[a] (90-100)
XXX	I	1.34	104	1.88	3,3′- and 9,9′-bicarbazyls[c]
XXXI	COMe	1.50	170-217[e]	3.10	Unknown
XXXII	CN	1.71	120-136[b]	3.04	Unknown
XXXIII	NO_2	1.84	134-170	2.68	Unknown

[a] Electrolyses in MeCN/TEAP with added excess 2,4,6-trimethylpyridine.
[b] Data are distorted by strong adsorption of parent material or electrolysis product.
[c] Observed on cyclic voltammograms in MeCN/TEAP, no 2,4,6-trimethylpyridine added. The 3,3′-bicarbazyls are formed by substituent elimination and subsequent coupling.
[d] Current decays rapidly to about *n* = 1 where a low steady-state current ensues, the latter slowly dropping further to near zero.
[e] Primary oxidation wave overlaps substantially with a second wave which is also included in the potential step.

Table IV. Radical stabilities of *t*-butylated carbazoles

No.	Compound	$E_{p/2}$	Radical half-life	Decomposition product
XXVII		1.07	~1 sec	1,1'-bicarbazyl ?
XXXIV		1.17	<<1 sec	3,3'-bicarbazyl
XXXV		1.15	<<1 sec	3,3'-bicarbazyl[a]
XXXVI		1.08	~1 min	1,1'-bicarbazyl ?
XXXVII		1.09	~30 min	?

[a] Verified with an authentic 3,3'-bicarbazyl sample.

from any of the 3,6-disubstituted derivatives can be readily obtained by either chemical or electrochemical means.

In the case of 3,6-di-*t*-butylcarbazole, authentic samples of the corresponding 1,9'- and 9,9'-bicarbazyls were available to aid in product identification. Cyclic voltammetric and optical spectra indicate that these are not the major product(s) in MeCN/TEAP electrolyses, however, and so it appears by a process of elimination that the most likely reaction pathway is ring-ring coupling-deprotonation to form the 1,1'-bicarbazyl.

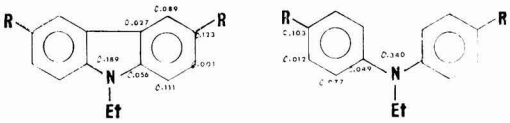
In the pathways above, it appears that there is a reaction selectivity order that is highly contingent upon the acidity of the solution near the electrode similar to the diphenylamine system previously reported by Cauquis (50). That is, in acid solution, which is the case in unbuffered MeCN after coupling is initiated and protons are released into solution, only C-C coupling occurs, while the presence of a weak base would be expected to promote mixed C-C and C-N coupling. Strong bases in solution then lead exclusively to formation of the N-N coupled products.

The series of *t*-butylated carbazoles shown in Table IV provide further valuable information on the possibilities of various coupling modes and the importance of steric factors in stabilizing the primary cation radicals. It is apparent from the radical stabilities shown that the 3 and 6 positions are far more reactive than the 1, 8, and 9 sites. Steric blocking of the 8 and 9 positions by a 1-*t*-butyl group (No. XXXVI) stabilizes the primary cation radical substantially compared to No. XXVII and introduction of another *t*-butyl substituent on the 8-carbon leads to a very stable cation radical for No. XXXVII. Stabilization through electronic effects would be minimal with *t*-butyl groups and so this is clearly an example of hindering reaction pathways by blocking reactive ring positions with inert functional groups.

The information provided by the molecules in this series is that simple blockage of the highly reactive 3 and 6 carbons does stabilize the primary cation radicals to a substantial degree, but the half-lives are still in the 0.1-1.0 sec region. An exception is the methoxy derivative which stabilizes by a delocalization mechanism similar to that operative for No. I, II and XI-XIII. When a reaction does take place, it appears to occur through the nitrogen in the presence of a strong organic base and through the 1 and 8 ring carbons in unbuffered MeCN; this last assertion is speculative at present. Introduction of blocking groups at these latter sites leads to substantially more stable primary cation radicals.

3,6-Disubstituted-N-ethylcarbazoles.—With the nitrogen alkylated (and the 1 and 8 ring positions thus somewhat sterically hindered) and both the 3 and 6 ring carbons substituted, one might anticipate that the primary cation radicals of such molecules would be quite stable. To some degree this was found to be true and as a result the electrochemistry of this series of molecules is centered about detectably stable cation radicals with $t_{1/2}$ values ranging from about 1 sec up to several days; the electroanalytical data are given in Table V.

Even at that, the lifetimes of these radicals are less than what might have been expected, since previous studies have shown that structurally similar 4,4'-disubstituted-N-alkyldiphenylamines possess very stable primary cation radical species (51, 52). In general, the carbazole radicals are at least two orders of magnitude less stable than the correspondingly substituted diphenylamines; this phenomenon appears to be largely due to the fact that the carbazoles have a very planar pi system whereas the diphenylamine rings are skewed. This leads to marked differences in electron distributions, as shown below for the alkyl derivatives (these calculations do not include the alkyl substituents, all of which are considered equivalent, but their electron densities will be proportional to the ring carbons to which they are attached)

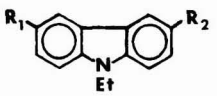


The major change is that electron density in the carbazole system is, relative to the diphenylamine skeleton, distributed more into the aromatic rings and less on the central nitrogen; this assertion has been quantitatively substantiated by EPR data (49). It is normally the case that increased delocalization leads to enhanced cation radical stability, but it appears at first glance that here the opposite is the case, *i.e.*, the more highly delocalized carbazoles are the less stable radicals. The alternate viewpoint however, is that at the same time decreased localization takes place in the carbazoles relative to the diphenylamines at the unreactive central nitrogen with an attendant increase in electron density in the more reactive aromatic rings. Interestingly, the same result can be qualitatively achieved in the HMO calculations by increasing the pi overlap between the central nitrogen and the aromatic rings in the diphenylamine systems by increasing the value for the resonance integrals for the central nitrogen and the adjacent ring carbons. The net effect is to generate a more planar diphenylamine. As expected, electron density is drained away from the central nitrogen into the aromatic rings more and more as the k_{CN} value is increased.

The same effect is seen in a comparison of the calculated orbital energies with the experimentally obtained oxidation potentials. The calculations indicate that the carbazole HOMO's are lower (more positive) in energy than the correspondingly substituted diphenylamines and in accordance with this the oxidation potentials of the carbazoles are consistently more anodic by 0.2-0.3V. This is reasonable if one considers that the carbazoles are more "hydrocarbon-like" than "amine-like" relative to the diphenylamines (because of enhanced delocalization into the aromatic rings) and thus would be more difficult to oxidize.

The net result of all this is that the ring positions in the carbazoles are more reactive, particularly the 3 and 6 carbons, and so even though the rings are heavily substituted and sterically protected radical stability is

Table V. Electrochemical characteristics of 3,6-disubstituted-N-ethylcarbazoles



No.	R_1 = R_2 =	$E_{p/2}$	$it^{1/2}/C$	n value	Product(s) (% yield), comments
XXXVIII	NH_2	0.32	47	1.09	Unstable cation radical, structure of coupled product is unknown
XXXIX	NMe_2	0.22	45	1.03	Highly stable cation radical, stable dication formed at $E_{p/2}$ = 0.60V, unstable trication radical generated at $E_{p/2}$ = 1.41V
XL	OMe	0.80	48	1.01[a]	Stable cation radical, unstable dication; mode of decomposition appears to be hydrolysis
XLI	Me	1.04	59-103[b]	2.2[a]	Moderately stable cation radical, decomposition appears to be via coupling through methyl groups
XLII	Et	1.06	119-184[b]	3.1[a]	Unstable cation radical, decomposition appears to be via coupling through ethyl groups
XLIII	*t*-Bu	1.04	43	1.07[a]	Stable cation radical, slowly decomposes probably via 1,1'-coupling
XLIV	Cl	1.48	53-67[b]	1.3[a]	Moderately stable cation radical, decomposition pathway unknown
XLV	Br	1.40	43-48[b]	1.2[a]	Moderately stable cation radical, decomposition pathway unknown
XLVI	I	1.34	78-88[b]	2.0[a]	Unstable cation radical, eliminates iodine, forms corresponding 3,3'-bicarbazyl (60-70)[c]
XLVII	COMe	1.50	79-136[b]	3.2[a]	Unstable cation radical, some deacetylation occurs to form the corresponding 3,3'-bicarbazyl
XLVIII	COEt	1.50	86-144[b]	3.4[a]	Unstable cation radical, eliminates propionyl group, forms corresponding 3,3'-bicarbazyl
XLIX	COPh	1.49	76-105[b]	2.9[a]	Unstable cation radical, eliminates benzoyl group, forms corresponding 3,3'-bicarbazyl
L	COOMe	1.56	—[c]	—[c]	Unstable cation radical, products unknown
LI	CN	1.74	81-133[b,d]	3.4[a]	Moderately stable cation radical, products unknown
LII	NO_2	1.81	116-211[b,d]	3.8[a,d]	Moderately stable cation radical, products unknown
LIII	R_1 = Me, R_2 = COMe	1.26	124-165	2.7	Unstable cation radical, alkyl coupling predominates, small amount of deacetylation
LIV	R_1 = Et, R_2 = COMe	1.25	166-188	2.9	Unstable cation radical, alkyl coupling predominates, small amount of deacetylation

[a] n value at the onset of low steady-state current.
[b] Taken from t = 1-8 sec; value increases with increasing time.
[c] Primary wave is very obscure, merges with more anodic waves; meaningful data could not be obtained.
[d] Data are affected by proximity to background; residual currents are quite high.

diminished relative to systems such as the diphenylamines. Of course, the cation radicals in this series are enormously more stable than those previously discussed herein, but even so very few could be called truly stable (half-life of 30-60 min). Interestingly, it was generally found that protecting the area around the carbazole nitrogen (with N-alkyl or N-phenyl substitution) shielded the moderately reactive 1- and 8-carbons and led to greatly enhanced activity at the nominally blocked 3 and 6 ring sites; the decay reactions of the less stable radicals in this series were thus found to take place at these latter positions.

In all cases in this series, the initial process involves removal of one electron to generate the cation radical. Of those which are reasonably stable, the dimethylamino derivative, No. XXXIX, is by far the longest lived. Not only is the primary radical stable for days, but the dication quinonediimine also appears to have a negligible decomposition rate. In fact, a third redox process can be observed which is reversible even at moderately low voltage scan rates, as shown in Fig. 5. One readily sees that switching past the first two waves (dotted lines) yields substantial reverse current and a lesser amount is observed on the third anodic wave; however, oscilloscope traces show that this latter process is completely reversible above sweep rates of about 2 V/sec. Chronoamperometric data yield constant $it^{1/2}/C$ quotients for the first two anodic processes (45 and 91, respectively) and coulometric measurements indicate n values of 1.03 past the first wave and 2.05 past the second. This third anodic wave, then, is apparently due to further oxidation of the stable dication and so the reversibility seen at high sweep rates indicates that this molecule has a moderately stable trication radical with $t_{1/2} \simeq 1$ sec. This is an extremely rare species, of which few examples are available (53); it offers the very exciting possibility of matching of spectral data for the cation and and trication radicals of a single species.

The amino derivative exhibits behavior similar to the previously discussed 3-aminocarbazoles except that the electrolysis product is much more in evidence on cyclic voltammograms. Since this same general electrochemical behavior was noted for 3-amino- and 3-amino-N-ethylcarbazole this would imply that the carbazole nitrogen is not implicated and the common reaction pathway, if it is indeed common, is N-N or N-ring coupling involving the amino groups and the 1, 4, 5, or 8 ring carbons. Again, the primary cation radical is short-lived ($t_{1/2} \simeq 1$ sec), but its existence was verified by rapid-sweep cyclic voltammetry.

Of the other derivatives in this series, both the methoxy and *t*-butyl compounds were found to have stable primary radicals with half-lives of 1 hr or more. The 3,6-dimethoxy-N-ethylcarbazole cation radical is exceptionally stable, probably due to the low charge density at the 1 and 8 ring sites and the blocking action

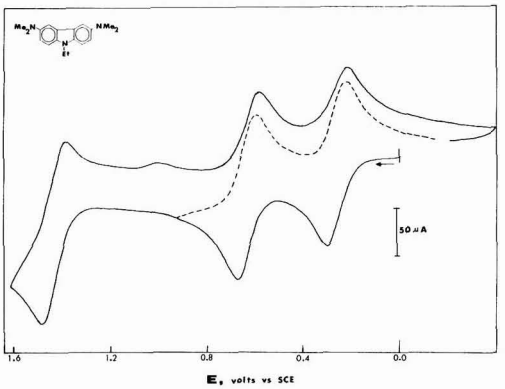
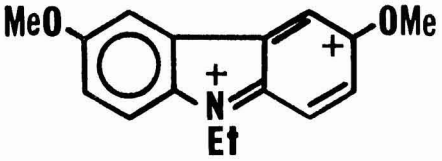


Fig. 5. Cyclic voltammogram of 1.0 × $10^{-3}F$ 3,6-bis(dimethylamino)-N-ethylcarbazole in MeCN/TEAP, sweep rate = 667 mV/sec.

of the N-ethyl group. The cation radical is oxidized to the dication in a second anodic process at $E_{p/2} = 1.36$V; no reverse current was observed even at a swep rate of 10 V/sec. The dication of this molecule would have

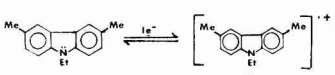


several resonance forms but the one shown above would be very susceptible to nucleophilic attack by trace amounts of water in the MeCN to generate the corresponding hydroxy derivative, 3-hydroxy-6-methoxy-N-ethylcarbazole. This is suggested by the cyclic voltammetric curves for this compound which are very similar in shape to other aromatic amine systems where a similar hydrolysis mechanism has been shown to occur (54, 55). The primary cation radical probably reacts via this same route, but at a markedly slower rate.

The 3,6-di-*t*-butyl-N-ethylcarbazole cation radical was also found to be quite stable, but slow decomposition was evident. Reaction probably occurs via 1-1 ring coupling, as was speculated for the *t*-butylated carbazoles No. XXVII and XXXIV-XXXVII. Nevertheless, a half-life of 30-40 min (stability for this compound, as for many of the others, is dependent upon concentration and solvent purity) ensures that this radical can be easily studied.

The methyl and ethyl derivatives, No. XLI and XLII, have cation radicals that are considerably more reactive than the *t*-butyl analog and beyond this the ethyl is much less stable than the methyl. This assertion is graphically illustrated in Fig. 6, where cyclic voltammograms for the three alkyl derivatives are shown. The *t*-butyl curve is seen to be perfectly reversible with no sign of decomposition products (however, holding the potential at the anodic limit for about 1 min and then sweeping back to more cathodic potentials yields a ratio of cathodic to anodic peak currents of about 0.92, indicating that the primary radical is in fact reacting very slowly). The methyl compound also shows considerable reverse current, but a small cathodic wave near −0.2V corresponding to reduction of protons indicates that the cation radical is not exceptionally stable ($t_{1/2}$ = 1-2 min); the ethyl curve shows extensive reaction and reversal just past the primary wave (dotted line) shows very limited stability for the cation radical ($t_{1/2} \simeq 0.8$ sec).

These data are consistent with a mechanism whereby the electrogenerated cation radical diffuses away from the electrode surface and a proton is lost from the alkyl carbon alpha to the carbazole skeleton, thus generating a benzylic-type free radical. Coupling of the resulting free radicals out in solution would ensue to generate a bridged bicarbazyl in a fashion similar to that proposed for No. XIV and previously published systems (46, 56). The relative stabilities of the methyl, ethyl and *t*-butyl compounds are thus explained by ring alkyl proton loss from the cation radical; a proton will eliminate more readily from a secondary carbon (ethyl) than from a primary (methyl) and when no alpha hydrogens are present (*t*-butyl) elimination cannot occur and enhanced stability is to be anticipated, as well as slow reaction via a different pathway. These relative stabilities are also nicely mirrored in the chronoamperometric data in Table V, which show the *t*-butyl derivative having a fairly constant one-electron value, and the others having much higher, and rapidly increasing, $it^{1/2}/C$ quotients. The *n* value data also point up the same disparity. The general mechanism is shown below for No. XLI but would also apply to No. XLII



I [10]

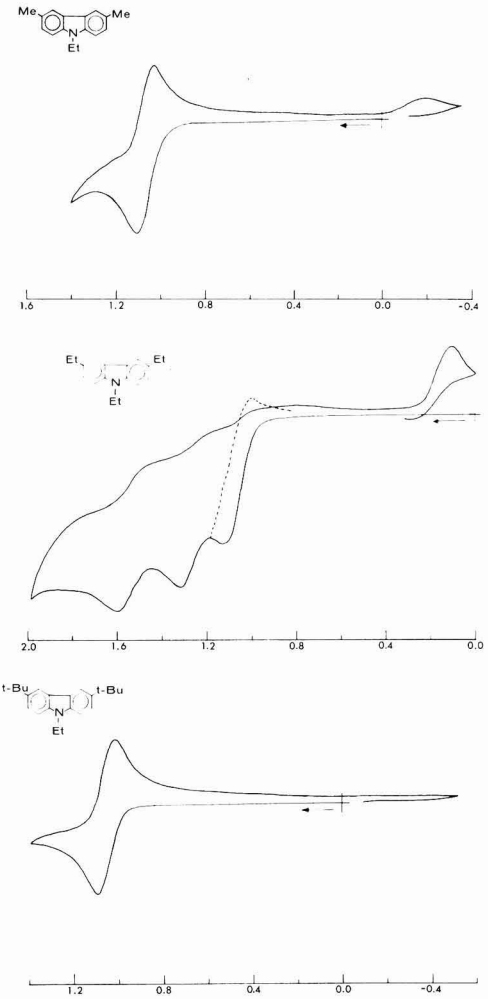
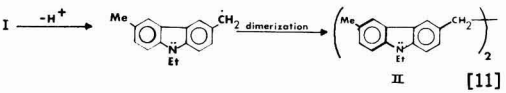


Fig. 6. Cyclic voltammograms of 3,6-dialkyl-N-ethylcarbazoles in MeCN/TEAP. Abscissa is in volts *vs.* SCE and for all curves the solutions were 1.0×10^{-3}F and the sweep rate was 150 mV/sec.



[11]

II —oxid'n→ UNKNOWN PRODUCTS [12]

The halogen derivatives, No. XLIV-XLVI, offer an interesting contrast in that the iodo compound eliminates iodine from the primary cation radical quite rapidly ($t_{1/2} \simeq 0.5$ sec) with subsequent coupling to form 6,6′-diiodo-N,N′-diethyl-3,3′-bicarbazyl, the same compound that is generated by oxidation of 3-iodo-N-ethylcarbazole. The products from electrolysis of the mono- and diiodo-N-ethylcarbazoles were found to be identical by matching of cyclic voltammetric curves and visible absorption spectra run on exhaustively electrolyzed solutions; in both cases the match-up is perfect.

The bromo and chloro analogs (No. XLIV and XLV), however, have reasonably stable primary cation radicals with half-lives of several minutes. In addition, it does not appear in our as yet cursory studies of these

latter two compounds that the radicals decompose by halogen elimination and subsequent coupling; the primary reaction route may instead be some form of ring-ring coupling. This observation is also in marked contrast to the data on the 3,6-dihalocarbazoles, No. XXVIII and XXIX, for which appreciable halogen elimination and subsequent 3,3'-coupling was noted, even though the cation radicals were much less stable than for the N-ethyl analogs and the 1, 8, and 9 positions are less protected.

As a group, No. XLVII-XLIX are characterized by unstable cation radicals which appear to react via elimination and subsequent 3,3'-coupling as the dominant, but not exclusive, pathway. Acetyl and benzoyl group eliminations are indicated by the fact that as with the 3-iodo- and 3,6-diiodo-N-ethylcarbazoles above identical cyclic voltammetric curves and visible absorption spectra were obtained from exhaustively electrolyzed solutions of the mono- and diacetyl-N-ethylcarbazoles (No. XX and XLVII) and the mono- and dibenzoyl-N-ethylcarbazoles. Of the cation radicals here, the acetyl derivative is least stable ($t_{1/2} \simeq 0.6$ sec), followed by the propionyl ($t_{1/2} \simeq 0.9$ sec) and the benzoyl ($t_{1/2} \simeq 1.5$ sec) compounds. The enhanced stability of the latter compound may be due in small part to increased delocalization afforded by the phenyl rings of the benzoyl groups by a mechanism other than direct conjugation, since this cannot be invoked here. This mode of cation radical reaction is quite unique and so we are at present pursuing kinetic and mechanistic studies of this novel pathway.

Little has been determined for No. L, the methyl ester, beyond the facts that the primary cation radical is unstable ($t_{1/2} \simeq 0.5$ sec) but detectable and it appears to react by direct ring coupling rather than by elimination and subsequent 3,3'-coupling; cyclic voltammograms of electrolyzed solutions show no 3,3'-bicarbazyl present.

The carboxylic acid derivative, N-ethylcarbazole-3,6-dicarboxylic acid, was prepared but its electrochemistry could not be investigated due to its complete lack of solubility in MeCN/TEAP.

The nitro and cyano derivatives, No. LII and LI, respectively, were also only lightly studied, but it appears here that ring coupling is the mode of cation radical reaction. In addition, the primary radicals have surprisingly long half-lives; $t_{1/2}$ for the cyano compound is 5-7 sec and that for the nitro derivative is 2-3 sec.

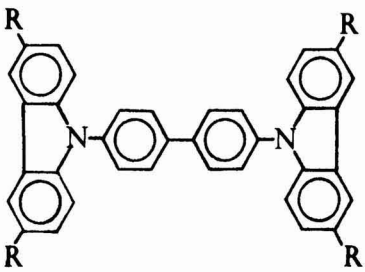
Compounds LIII and LIV offer a fascinating comparison between alkyl coupling and acetyl group elimination as competitive pathways. Cyclic voltammetric data indicate that alkyl coupling is the dominant pathway, with a small amount of acetyl elimination observed. Thus, the radical for No. LIII is considerably more stable ($t_{1/2} \simeq 1$ sec) than for No. LIV ($t_{1/2} \simeq 0.1$ sec) but both are much shorter lived than their dialkyl analogs due to the destabilizing influence of the acetyl group. This is indicative of a fairly drastic change in electron distribution which makes the alkyl groups much more acidic in No. LIII and LIV than in No. XLI and XLII.

Whereas in the previous section we saw that blockage of the highly reactive 3 and 6 ring carbons largely forced the radical reactions to the area around the carbazole nitrogen, the data presented in this section indicate that N-alkyl substitution in many cases shifts the center of reactivity back to the 3 and 6 sites. The primary radicals are much more stable than if either of these positions is open and so in all cases they can be readily detected. These data clearly show that relatively few substituents can be considered "inert" as possible agents for blocking reactive sites in cation radicals. For intrinsic inertness to reactivity and for having the additional property of affecting as little as possible the electron distribution in the molecular skeleton, the *t*-butyl group seems to be most satisfactory, a view previously forwarded by Neugebauer in his EPR spectral work on carbazole derivatives (49).

Substituted N-phenylcarbazoles.—Substitution of a phenyl group on the carbazole nitrogen would be expected to have at least two beneficial effects with regard to radical stability. The phenyl ring extends the pi system of the carbazole skeleton and thus contributes to radical stabilization through enhanced delocalization. In addition, the bulky phenyl group acts as an efficient blocking agent for the 1 and 8 ring sites, more so than an N-alkyl group. On the other hand, the phenyl ring introduces the possibility of another coupling site, namely the phenyl carbon *para* to the carbazole nitrogen. Since these molecules are structurally quite similar to triphenylamines such a reaction is not unlikely, but it was not detected in the previous study on the anodic oxidation of N-phenylcarbazole (7).

With the above stabilizing factors in mind, we might expect that 3,6-disubstituted N-phenylcarbazoles such as No. LXXI-LXXIV should have primary radicals more stable than their N-ethyl analogs, No. XLIII-XLVI. In fact, this was found to be the case, although it is not apparent in the chronoamperometric or n value data. The iodo derivatives are probably the easiest to compare, since for these there is rapid reaction via iodine elimination, a reaction contingent upon the electron density at the 3 and 6 ring positions. Whereas the 3,6-diiodo-N-ethylcarbazole cation radical was observed to have a half-life of roughly 0.5 sec, the phenyl analog has $t_{1/2} \simeq 1$ sec. This twofold gain in stability appears to be due to the extended delocalizing influence of the N-phenyl ring.

The other three compounds in this series (No. LXXI-LXXIII) appear to have a common mode of radical reaction that is different from the N-ethyl analogs. All exhibit a quasi-reversible (anodic to cathodic peak separation of about 250 mV) redox couple about 0.2-0.4V less anodic than the primary oxidation waves. It is not altogether unlikely that these radicals may slowly undergo a triphenylamine-type coupling to generate something akin to a tetraphenylbenzidine, as shown below.



This species would be more easily oxidized than the parent carbazole and the twisted nature of the N-ring-ring-N portion would lead to irreversible redox behavior (57, 58). Further support for this view is afforded by the observation that no such follow-up couple is seen in the current-voltage curves for No. LXXV and LXXVI, compounds in which the *para* position of the N-phenyl group is substituted. In addition, the cation radical for No. LXXV was qualitatively observed to be more stable than that for No. LXXII by about a factor of three.

The major factor mitigating against this mode of reaction is the rather low electron density that would be predicted for the potential coupling site assuming a moderate amount of twisting of the N-phenyl ring due to steric interaction with the 1 and 8 ring protons. HMO calculations show that as the twist angle is increased from a nominal value of about 45° (that assumed for a freely rotating triphenylamine-type system) the electron density at the *para* site on the N-phenyl ring drops dramatically. Unfortunately, we have no data on the twist angles in cation radicals of

this type, but molecular models show that such twisting would be expected to be substantial. Obviously, the question can best be answered by isolation and characterization of the electrolysis product; we are at present attempting to carry this out.

Stabilization through enhanced delocalization is also indicated by the somewhat greater stability of No. LXXVI as compared to No. XLI, N-substituted-3,6-dimethylcarbazoles. Though both radicals appear to react by alkyl coupling through the 3 or 6 methyl groups, the radical half-life of the N-phenyl derivative is 4-5 min, as compared to 1-2 min for the N-ethyl analog. The disparity is seen even more clearly in the chronoamperometry and n value data in Tables V and VI.

Other effects of the N-phenyl group upon the carbazole skeleton were detected in the electrochemcial behavior of No. LV-LXX. These are all N-(*p*-substituted) phenylcarbazoles with both the 3 and 6 carbabole ring positions open for coupling. Not surprisingly, then, it was found that the 3,3'-coupling mode dominates this series, as can be seen in Table VI; the bicarbazyls are generated in high yields and can be readily isolated following controlled-potential preparative-scale electrolyses (see Experimental section).

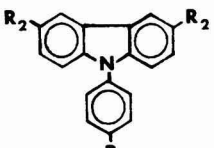
Two exceptions to this are the amino and dimethylamino derivatives, No. LV and LVI, whose anodic oxidation pathways are more characteristic of *para*-substituted anilines and N,N-dimethylanilines, respectively. In both cases, the carbazole skeleton functions as a rather inert substituent and HMO calculations show most of the electron density residing in the aminophenyl rings; thus, it is not surprising that 3,3'-coupling is not observed. The electrochemical behavior for these compounds appears to be similar to that discussed previously for carbazole derivatives with an amino or dimethylamino group *para* to the carbazole nitrogen, *i.e.*, the N-(*p*-dimethylaminophenyl) carbazole shows two reversible one-electron redox processes; the first leads to a stable cation radical and the second to a moderately stable quinonediimine form that slowly decomposes to a product other than a 3,3'-bicarbazyl. The amino derivative has an irreversible one-electron wave (the cation radical was, however, detected by rapid-sweep cyclic voltammetry), and it appears that again some sort of N-ring or N-N (amino nitrogen) coupled product is generated in a fashion similar to the other amino-substituted carbazoles.

Interestingly, if the amino group is deactivated by acetylation (No. LVIII) the redistribution of electron density is such that the radical reacts predominately via the 3,3'-coupling-deprotonation route.

Another exception to the 3,3'-coupling mode is the methylthio derivative, No. LVIX. This compound has a very unstable cation radical that decomposes to an unknown product, probably involving oxidation of the methylthio substituent. As can be seen in Table VI, the over-all process involves a one-electron transfer, but no radical species could be detected using EPR spectroscopy with *intra muros* electrochemical generation.

All of the other compounds in this series undergo an initial one-electron oxidation to generate a very reactive cation radical ($t_{1/2} << 1$ msec); two of these then couple at the 3 positions to yield a N,N'-bis(*p*-substituted phenyl)-3,3'-bicarbazyl. This species is then oxidized more easily than the corresponding carbazole to a stable dication, so over-all one has a classic two-electron ECE mechanism identical to that previously characterized for *para*-substituted triphenylamines (45). The reaction is quantitative and these systems are extremely "clean," as is seen in Fig. 7 for the *t*-butyl derivative. On the time scale of chronoamperometry or rotating disk experiments this reaction appears to be quantitative for all the derivatives studied with the exceptions mentioned above. This group thus constitutes an unusual series of organic molecules in that one has a single, quantitative homogeneous chemical reaction following the initial electron transfer process in a classic ECE pathway for a wide variety of substituents.

Table VI. Electrochemical characteristics of substituted N-phenylcarbazoles



No.		$E_{p/2}$	$it^{1/2}/C$	n value	Product(s) (% yield), comments
LV	R_2 = H, R_1 = NH_2	0.84	46	1.01	Unstable cation radical, product unknown
LVI	NMe_2	0.71	49-50[a]	1.03[b]	Stable cation radical, second reversible wave at $E_{p/2}$ = 1.18V, forms moderately stable quinonediimine
LVII	OMe	1.19	84	1.98	Bicarbazyl (100)[c,e]
LVIII	NHCOMe	1.19	68[d]	1.93	Bicarbazyl,[e] insoluble, forms black perchlorate salt
LVIX	SMe	1.13	50	1.05	No bicarbazyl formed, product unknown
LX	Ph	1.24	85	2.11	Bicarbazyl (80-90)[c,e]
LXI	Me	1.24	89	1.98	Bicarbazyl (100)[c,e]
LXII	*t*-Bu	1.22	92	2.04	Bicarbazyl (100)[c,e]
LXIII	F	1.26	90-93[a]	2.08	Bicarbazyl (90-100)[c,e]
LXIV	Cl	1.28	91-93[a]	2.14	Bicarbazyl (80-90)[c,e]
LXV	Br	1.30	90-95[a]	2.12	Bicarbazyl (80-90)[c,e]
LXVI	I	1.31	89	2.04	Bicarbazyl (90-100)[c,e]
LXVII	COOMe	1.31	84-66[d]	1.96	Bicarbazyl,[e] insoluble, forms black perchlorate salt
LXVIII	CN	1.33	88-92[a]	2.05	Bicarbazyl (90-100)[c,e]
LXIX	NO_2	1.36	86-94[a]	2.36	Bicarbazyl (60-70)[c,e]
LXX	H	1.24	88	2.03	Bicarbazyl (100)[c,e]
LXXI	R_1 = H, R_2 = *t*-Bu	1.12	47-49[a]	1.10[f]	Stable cation radical, slowly decomposes to an unknown product
LXXII	Cl	1.38	47-53[a]	1.07[f]	Stable cation radical, slowly decomposes to an unknown product
LXXIII	Br	1.38	52-58[a]	1.10[f]	Stable cation radical, slowly decomposes to an unknown product
LXXIV	I	1.40	76-111[a]	1.94	Unstable cation radical, eliminates iodine to form 6,6'-diiodo-N,N'-diphenyl-3,3'-bicarbazyl
LXXV	R_1 = R_2 = Cl	1.42	48-50[a]	1.06[f]	Stable cation radical, slowly decomposes to an unknown product
LXXVI	Me	1.08	56-61[a]	1.09[f]	Stable cation radical, slowly decomposes to an unknown product

[a] Taken from t = 1-8 sec; value increases with increasing time.
[b] Low steady-state current at the end of the electrolysis.
[c] Estimated from peak currents of cyclic voltammograms run on exhaustively electrolyzed solutions.
[d] Data are distorted by strong filming of the electrode surface.
[e] Cation radicals are very unstable ($t_{1/2}$ < 1 msec); 6,6'-disubstituted-N,N'-diphenyl-3,3'-bicarbazyls are formed in all cases.
[f] Drifts slowly to n = 2.

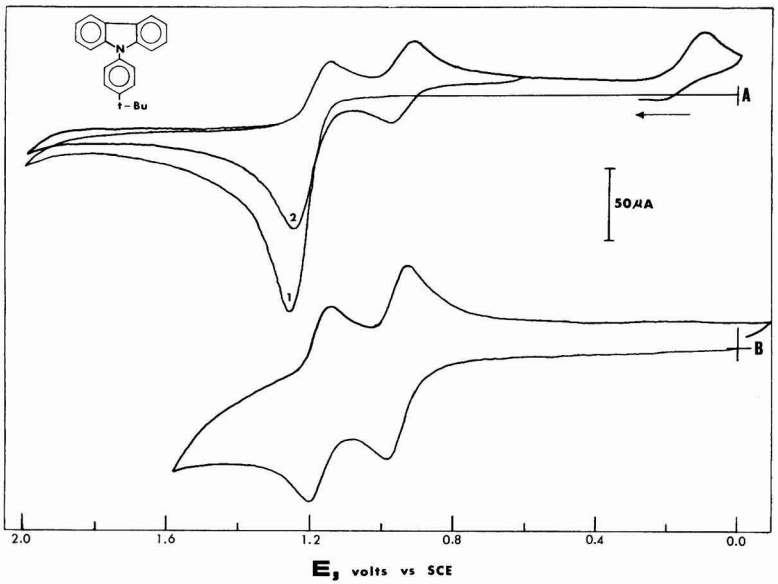
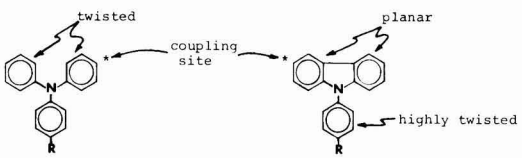


Fig. 7. Curve A: Cyclic voltammogram of 8.0 × $10^{-4}F$ N-(*p*-*t*-butylphenyl)carbazole in MeCN/TEAP, sweep rate = 100 mV/sec. Curve B: Cyclic voltammogram of the same solution following exhaustive electrolysis at 1.4V, sweep rate = 67 mV/sec.

Unfortunately, the rate constants for the coupling reactions are extremely rapid and as such are difficult to measure. However, some preliminary data have been obtained from rotating disk experiments at very low (10^{-4} to $10^{-5}F$) parent concentrations and these numbers are presented in Table VII, along with similar data for a series of correspondingly substituted triphenylamines; these data provide some interesting comparisons concerning the reactivities of organic cation radicals as a function of geometry.

The basic difference between these compounds is that the carbazoles are planar across two rings while the triphenylamines have all three rings at angles to one another. Also, as mentioned, the substituted ring in the carbazole is highly twisted because of steric interaction with the 1 and 8 ring hydrogens



Thus, two effects are to be anticipated, namely that due to the planarity of the carbazole system and the attendant high electron density at the reactive sites (cf. the comparison of diphenylamine and carbazole HMO calculations) the coupling rates will be much faster than for the triphenylamines. Also, there will be a diminished substituent effect on the coupling rate constants for the carbazoles due to the lesser interaction of the substituted rings with the rest of the system. The much enhanced carbazole coupling rate constants can readily be seen even in the rough data in Table VII; greater reactivity for the carbazole systems relative to the corresponding triphenylamines is also predicted by HMO calculations.

Table VII. Comparative electrochemical and kinetic data for triphenylamine and carbazole derivatives

				
	$E_{p/2}$, V	k^a	$E_{p/2}$, V	k^a
R = OMe	0.76	$6 \pm 2 \times 10^{-1}$	1.19	$7 \pm 4 \times 10^{8}$
Me	0.87	$9.0 \pm 1.0 \times 10^{1}$	1.24	$8 \pm 4 \times 10^{8}$
C_6H_5	0.89	$6.0 \pm 0.6 \times 10^{1}$	1.24	
H	0.97	$1.2 \pm 0.4 \times 10^{3}$	1.24	$9 \pm 6 \times 10^{7}$
Cl	1.02	$6.5 \pm 1.3 \times 10^{2}$	1.28	
Br	1.02	$1.4 \pm 0.3 \times 10^{3}$	1.30	
NO_2	1.22	$1.4 \pm 0.4 \times 10^{4}$	1.36	

[a] Bimolecular coupling rate constant in mol^{-1} sec^{-1}.

Conclusions.—The foregoing data allow us to formulate a series of "selection rules" for the various radical reaction pathways. It appears that in many organic systems there is a series of possible reaction pathways for the electrogenerated cation radicals, one being most favorable with the others then occurring in a given sequence as the molecular structure is changed by introduction of various substituents at different sites. The following selection rules apply to carbazole derivatives:

1. The cation radical of the parent molecule, carbazole, reacts by both 3,3′- and 9,9′-couplings, the former taking place in acidic unbuffered MeCN and the latter dominating in basic solution; the same applies for 3-substituted carbazoles with the exception of the amino and dimethylamino derivatives.

2. Blockage of the 9-nitrogen with alkyl or phenyl groups results in exclusive formation of 3,3′-bicarbazyls; the same holds true if the 3 position is substituted but the 6 carbon left open, as in the 3-substituted-N-ethylcarbazoles, again with the exception of the amino and dimethylamino compounds.

3. Substitution of the 3 and 6 sites with the 9 nitrogen left open results in unstable, but detectable, cation radicals which decompose by substituent elimination (I, Br, Cl) or (presumably) ring-ring coupling (OMe, *t*-Bu, OAc, CN, NO_2); the systems are poorly behaved. Electrolysis in basic MeCN leads smoothly in all cases to the 9,9′-bicarbazyls. Further substitution of the 1 and 8 ring positions protects the 9 nitrogen and leads to considerably more stable cation radicals.

4. Blockage of the 3, 6, and 9 sites, as in the 3,6-disubstituted-N-ethylcarbazoles, predictably yields quite stable cation radicals (relative to the other series of substituted carbazoles) since all the active coupling positions are substituted. Many of the derivatives react relatively slowly by as yet undetermined ring-ring coupling modes. A number of compounds in this series show unusual reactions through the 3 and 6 substituents such as alkyl coupling (Me, Et) and group elimination (I, COMe, COEt, COPh). Analogous N-phenyl derivatives appear to have more stable cation radicals because of enhanced delocalization and more efficient blockage of the 1 and 8 ring sites; an additional complication, however, is the possibility of coupling through the N-phenyl rings.

5. Compounds with NH_2 or NMe_2 groups (and presumably OR-type substituents) *para* to the carbazole nitrogen behave very much like *p*-phenylenediamine derivatives. The electron distributions in these compounds are changed so much that they no longer are characteristic of carbazole systems; thus, the cation radicals are quite stable relative to others in the same series and in the cases of the dimethylamino-substituted molecules reasonably stable dication diimines are generated by a second one-electron process. In all cases, the reaction pathways appear to be more representative of aniline-type molecules than of carbazoles.

Spectroscopic Studies

The spectroscopic studies were undertaken in order to obtain information concerning electron distributions in carbazole cation radicals and correlate these data with the chemical reactivities monitored electrochemically. In addition, it was deemed desirable to provide some basic spectral data on these types of radicals since little is available in the literature. It was hoped that optical spectra would provide an idea of the degree of delocalization of the unpaired electron in the cation radicals and the EPR spectra would give a concrete picture of electron distributions from coupling constant data. The data collected thus far, along with those from other sources, are generally consistent with the electrochemical studies in the previous sections.

Optical spectra.—Ledwith first reported optical data on the carbazole and N-methylcarbazole cation radicals (59), which were proposed to arise through charge-transfer interaction with tropylium tetrafluoborate and exhibited absorption maxima at 506 and 520 nm, respectively. N-isopropylcarbazole was also shown to form charge-transfer complexes with a number of acceptors (60), and it was subsequently claimed that the optical spectrum of the N-isopropylcarbazole cation radical had been obtained by electrolytic oxidation in MeCN (61). However, for the latter two studies the data reported correspond quite closely to optical and EPR spectra previously published for similar carbazole systems where assignments were made to oxidized forms of the corresponding 3,3′-bicarbazyls (7, 62), the optical spectra having two broad maxima positioned at roughly 400 and 800 nm. More recently, cation radical optical spectra for carbazole (63) and N-vinylcarbazole (64) have been reported, the former having an absorption maximum of 610 nm, the latter a series of bands ranging from 508-780 nm.

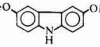
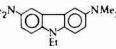
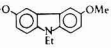
From this array of conflicting data and the electrochemical data in the previous sections of this paper, it is obvious that optical spectra of carbazole and its N-alkyl derivatives must be considered with caution. Although we have not as yet measured rate constants for the decomposition reactions of these radicals, it is clear from the electrochemical studies that their half-lives are, at best, in the microsecond region. As we have seen, though, by proper substitution these radicals can be stabilized and more reliable spectral data should then be obtainable. Thus, Neugebauer has reported λ_{max} values for 1,3,6,8-tetra-*t*-butylcarbazole cation radical with the primary absorption band being at 925 nm and lesser peaks at 583 and 547 nm (49). We have also obtained spectral data for a numbr of carbazole derivatives and these data, as shown in Table VIII, verify the fact that carbazole cation radicals have primary absorption bands in the 750-850 nm region, with the exception of the dimethylamino derivatives, which have absorption spectra more characteristic of *p*-substituted-N,N-dimethylanilines (65). It is noteworthy that these primary electronic transitions are at quite long wavelengths compared to other known cation radicals. Such facile transitions are suggestive of a very "loose" pi system in which there is extensive delocalization of the unpaired electron, assuming that these primary bands correspond to a transition of the unpaired electron from the highest filled to the lowest unfilled molecular orbitals.

In addition, these data cast considerable doubt on many of the previously reported λ_{max} values for the carbazole and N-alkylcarbazole cation radicals. From the absorption maxima shown in Table VIII for the series of 3,6-disubstituted-N-ethylcarbazoles, we feel that we can safely predict that the carbazole and N-alkylcarbazole cation radicals will have absorption maxima for the longest wavelength primary electronic transitions in the 750-790 nm region (58). This assertion will be expanded upon and reported in full in the near future.

EPR studies.—The degree of delocalization can be more quantitatively ascertained from EPR coupling constants, since these latter parameters are generally analogous to unpaired electron densities at the various atoms in a cation radical.

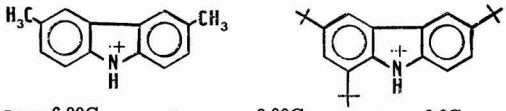
We have obtained moderately well-resolved EPR spectra for all of the radicals shown in Table VIII, but interpretations at this time have not been realized. Neugebauer has, however, obtained interpreted EPR spectra for the substituted carbazole radicals shown below (49, 66), and these can be used as indicators of the degree and direction of delocalization in the carbazole nucleus. These molecules are particularly well suited, since the alkyl substituents will not perturb the

Table VIII. Wavelengths of principal absorption bands of carbazole cation radicals

Compound	λ_{max}, nm	Compound	λ_{max}, nm
	611		800 (780)[a]
	625		794 (722)[a]
	758 (684)[a]		823 (775)[a]
	715, 664		811 (738)[a]
	758 (682)[a]		787[a]
	787 (707)[a]		
	798 (716)[a]		860[a]
	809 (728)[a]		

[a] Principal band is at left; a broad shoulder to the blue is present, with a secondary peak in parentheses in some cases.

electron distribution greatly relative to the parent carbazole nucleus



$a_N = 6.89G$	$a_{H(NH)} = 8.09G$	$a_N = 6.6G$
$a_{H_1} = 3.84G$	$a_{H_2} = 0.80G$	$a_{H(NH)} = 7.8G$
$a_{H_4} = 0.80G$	$a_{H(CH_3)} = 6.57G$	$a_{H_1} = 3.4G$

These coupling constants correlate nicely with the qualitative reactivity data determined electrochemically in showing that large spin densities exist at the central nitrogen and the ring positions *ortho* and *para* to it (the 1,3,6,8 sites). Thus, these are shown quantitatively to be the centers of reactivity in these molecules and so the relatively short radical lifetimes encountered are not unexpected with so many active sites.

The rather large coupling constant for the methyl groups in 3,6-dimethylcarbazole is also consistent with the proposal of alkyl coupling through the substituent groups in No. XIV, XLI, and XLII, since the alkyl group deprotonation is contingent upon a high unpaired electron spin density at the benzylic position.

The spectra of the 3-dimethylamino derivatives (No. II and XII) have not been fully interpreted, but it is apparent that the coupling constant pattern is much more like that of *p*-substituted-N,N-dimethylanilines than substituted carbazoles in showing large spin densities on the dimethylamino group and the ring positions *ortho* and *para* to it and virtually none in the unsubstituted ring. Again, this is compatible with the electrochemical data.

Acknowledgments

We are indebted to the Petroleum Research Fund (Grant No. 1039-G3) and the National Science Foundation (Grant No. GP-20606) for financial support of this work. A substantial portion of this study was done at Sacramento State College, and we are grateful for the use of facilities there. Samples of various carbazoles were kindly donated by Southern Dyestuffs Company, Charlotte, North Carolina, Dr. N. P. Buu-Hoi of the Institute for the Chemistry of Natural Substances in Gifsur-Yvette, France, and Dr. Franz Neugebauer of the Max-Planck Institute in Heidelberg, Germany. Technical assistance by Larry Line, Sam Creason, and Kurtz Carpenter proved to be invaluable. Special thanks are also due to Drs. R. N. Adams and D. E. Smith for their support and encouragement.

This work was extracted in part from the M.S. thesis of one of the authors (J.F.A.) at Sacramento State College (1968).

Manuscript submitted Aug. 22, 1974; revised manuscript received March 17, 1975. This was Paper 145, presented at the New York, New York, Meeting of the Society, May 4-9, 1969.

Any discussion of this paper will appear in a Discussion Section to be published in the June 1976 JOURNAL. All discussions for the June 1976 Discussion Section should be submitted by Feb. 1, 1976.

Publication costs of this article were partially assisted by the Petroleum Research Fund.

REFERENCES

1. N. P. Buu-Hoi and Do-Phuoc Hien, *Biochem. Pharmacol*, **17**, 1227 (1968).
2. J. I. Fernandez-Alonso, L. Carbonell-Vila, and R. Domingo, *J. Am. Chem. Soc.*, **79**, 5839 (1957).
3. N. P. Buu-Hoi, *Cancer Res.*, **24**, 1511 (1964).
4. H. Hoellinger, N. P. Buu-Hoi, and Ph. Mabille, *J. Chem. Soc.* (C), **1968**, 2209.
5. D. Hoffman, G. Rathkamp, and S. Nesnow, *Anal. Chem.*, **41**, 1256 (1969).
6. D. Hoffman, G. Rathkamp, and H. Wozowodzki, *Beitr. Tabakforsch.*, **4**, 253 (1968); *Chem. Abstr.*, **71**, 19643z (1969).
7. J. F. Ambrose and R. F. Nelson, *This Journal*, **115**, 1159 (1968).
8. S. H. Tucker, *J. Chem. Soc.*, **1926**, 3033.
9. J. McLintock and S. H. Tucker, *ibid.*, **1927**, 1214.
10. M. Kuroki, *Y. Gosei Kagaku Kyokai Shi*, **23**, 447 (1965); *Chem. Abstr.*, **63**, 4238d (1965).
11. P. Maitland and S. H. Tucker, *J. Chem. Soc.*, **1927**, 1368.
12. W. H. Perkin, Jr. and S. H. Tucker, *ibid.*, **1921**, 216.
13. G. K. Branch and W. H. Hall, *J. Am. Chem. Soc.*, **46**, 438 (1924).
14. S. C. Creason and R. F. Nelson, *J. Electroanal. Chem.*, **27**, 189 (1970).
15. L. S. Marcoux, R. N. Adams, and S. W. Feldberg, *J. Phys. Chem.*, **73**, 2611 (1969).
16. A. J. Bard and E. Solon, *Anal. Chem.*, **34**, 1181 (1962).
17. T. C. Whitner, Jr., *J. Am. Chem. Soc.*, **46**, 2326 (1924).
18. J. A. Miller and E. C. Miller, *J. Exptl. Med.*, **87**, 139 (1948).
19. F. L. Allen and H. Suschitzky, *J. Chem. Soc.*, **1953**, 3845.
20. P. A. Smith, J. M. Clegg, and J. H. Hall, *J. Org. Chem.*, **23**, 524 (1958).
21. P. A. S. Smith and B. B. Brown, *J. Am. Chem. Soc.*, **73**, 2435 (1951).
22. R. Preston, S. H. Tucker, and J. Cameron, *J. Chem. Soc.*, **1942**, 500.
23. S. H. Tucker, *ibid.*, **1926**, 546.
24. V. Shishkina, S. Omel'chenko, and W. Soshin, *Tr. Ural'sk Politekh. Inst.*, 19 (1960); *Chem. Abstr.*, **55**, 24715c (1961).
25. N. P. Buu-Hoi and N. Hoan, *J. Org. Chem.*, **16**, 1327 (1951).
26. D. P. Chakraborty, K. C. Das, and S. P. Basak, *J. Indian Chem. Soc.*, **45**, 84 (1968).
27. S. G. Plant and M. L. Tomlinson, *J. Chem. Soc.*, **1932**, 2188.
28. H. Lindemann, *Ber.*, **57B**, 555 (1924).
29. N. P. Buu-Hoi and R. Royer, *J. Org. Chem.*, **15**, 123 (1950).
30. P. Bruck, A. Ledwith, and A. White, *J. Chem. Soc. (B)*, **1969**, 205.
31. N. P. Buu-Hoi and R. Royer, *Rec. Trav. Chim.*, **66**, 533 (1947).
32. H. Gilman and S. Spatz, *J. Am. Chem. Soc.*, **63**, 1553 (1941).
33. H. M. Grotta, C. J. Riggle, and A. E. Bearse, *J. Org. Chem.*, **29**, 2474 (1964).
34. D. Mitchell and S. G. Plant, *J. Chem. Soc.*, **1936**, 1295.
35. R. F. Nystrom and C. R. A. Berger, *J. Am. Chem. Soc.*, **80**, 2896 (1958).
36. H. Gilman and R. Kirby, *J. Org. Chem.*, **1**, 146 (1936).
37. G. deMontmollin and M. deMontmollin, *Helv. Chim. Acta*, **6**, 94 (1923).
38. M. Nelmes and S. H. Tucker, *J. Chem. Soc.*, **1933**, 1523.
39. O. Neuenhoeffer and P. Heitmann, *Chem. Ber.*, **94**, 2511 (1961).
40. M. Kuroki, *Nippon Kagaku Zasshi*, **88**, 463 (1967); *Chem. Abstr.*, **68**, 95187g (1968).
41. H. Gilman and J. Honeycutt, *J. Org. Chem.*, **22**, 226 (1957).
42. H. G. Dunlop and S. H. Tucker, *J. Chem. Soc.*, **1939**, 1945.
43. C. Buchanan and S. H. Tucker, *ibid.*, **1958**, 2750.
44. R. Hand and R. F. Nelson, *This Journal*, **117**, 1353 (1970).
45. S. C. Creason, J. Wheeler, and R. F. Nelson, *J. Org. Chem.*, **37**, 4440 (1972).
46. M. Melicharek and R. F. Nelson, *J. Electroanal. Chem.*, **26**, 201 (1970).
47. E. T. Seo, R. F. Nelson, J. M. Fritsch, L. S. Marcoux, D. W. Leedy, and R. N. Adams, *J. Am. Chem. Soc.*, **88**, 3498 (1966).
48. R. F. Nelson and R. N. Adams, *ibid.*, **90**, 3925 (1968).
49. F. A. Neugebauer, H. Fischer, S. Bamberger, and H. O. Smith, *Chem. Ber.*, **105**, 2694 (1972).
50. G. Cauquis, H. Delhomme, and D. Serve, *Tetrahedron Letters*, 4645 (1971).
51. P. Berkenkotter and R. F. Nelson, Unpublished data.
52. R. F. Nelson, Ph.D. Thesis, University of Kansas (1966).
53. K. Bechgaard and V. D. Parker, *J. Am. Chem. Soc.*, **94**, 4749 (1972).

54. R. Hand, M. Melicharek, D. I. Scoggin, R. Stotz, A. K. Carpenter, and R. F. Nelson, *Collection Czech. Chem. Commun.*, **36**, 842 (1971).
55. L. Line, R. Reynolds, and R. F. Nelson, *J. Am. Chem. Soc.*, **96**, 1087 (1974).
56. V. D. Parker, *Chem. Commun.*, 848 (1969).
57. F. T. Eggertsen and F. T. Weiss, *Anal. Chem.*, **28**, 1008 (1956).
58. R. F. Nelson, Unpublished data.
59. A. Ledwith and M. Sambhi, *Chem. Commun.*, 64 (1965).
60. J. H. Sharp, *J. Phys. Chem.*, **70**, 584 (1966).
61. W. Klopfer, *Z. Naturforsch.*, **24a**, 1923 (1969).
62. D. H. Iles and A. Ledwith, *Chem. Commun.*, 498 (1968).
63. V. E. Sahini, M. Dobrescu, and C. Bendic, *Rev. Roum. Chim.*, **16**, 1131 (1971).
64. Y. Shirota, K. Kawai, N. Yamamoto, K. Tada, H. Mikawa, and H. Tsubomura, *Chem. Letters*, 145 (1972).
65. J. Wheeler and R. F. Nelson, Submitted for publication.
66. F. A. Neugebauer, Private communication.

Electrohydrodimerization Reactions

V. Liquid Ammonia as a Solvent for Reductive Coupling of Diethyl Fumarate, Cinnamonitrile, and Acrylonitrile

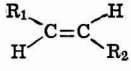
Iuliana Vartires,[1] Wayne H. Smith, and Allen J. Bard*

Department of Chemistry, The University of Texas at Austin, Austin, Texas 78712

ABSTRACT

Cyclic voltammetric (CV) and controlled potential coulometric investigations of the reduction of several activated olefins in anhydrous liquid ammonia containing either 0.1*M* methyl-tri-n-butylammonium iodide or 0.1*M* potassium iodide as supporting electrolytes are reported. For diethyl fumarate and cinnamonitrile the studies provide evidence for formation of a radical anion, which undergoes dimerization and polymerization reactions, and of dianion formation at more negative potentials. The effect of adding isopropanol and glacial acetic acid was also investigated.

The reduction of activated olefins in aprotic media has been the subject of numerous investigations [see (1, 2) and references therein]. Diactivated olefins (R) react via formation of the radical anion and produce, depending upon the acidity of the medium, hydrodimer (R_2H_2), reduced monomer (RH_2), and polymer. At more negative potentials, where dianion is produced, extensive polymerization apparently occurs, so that the second reduction waves observed in voltammetry are frequently much smaller than the first waves. We have previously shown that anhydrous liquid ammonia is a useful medium for studies of the electroreduction of organic compounds (3, 4) and that stable dianions of benzophenone and nitrobenzene could be prepared in this solvent. This stability of radical anions and dianions in ammonia can be attributed to the low acidity of the solvent, the possibility of preparing highly pure solutions through the use of vacuum line techniques and solvent treatment with sodium, and the fact that these studies are carried out at low temperatures, decreasing the rate of homogeneous chemical reactions following the electron transfer steps. Previous studies of amalgam reductions leading to hydrodimerization in liquid ammonia have also been described (5). In this paper we describe preliminary cyclic voltammetric and coulometric experiments on the reduction of several activated olefins in liquid ammonia; the structures of the substances studied are shown below



Diethyl fumarate (DEF) $R_1 = R_2 = -C(=O)-O-CH_2CH_3$

Cinnamonitrile (CN) $R_1 = -C_6H_5$ $R_2 = -CN$

Acrylonitrile $R_1 = H$ $R_2 = -CN$

* Electrochemical Society Active Member.
[1] Permanent address: Research Center for Physical Chemistry, Bucharest, Roumania.
Key words: cyclic voltammetry, coulometry, electrochemical dimerizations, organic electrochemistry.

Experimental

General experimental techniques were the same as those reported previously (2-4); a detailed description is available (6). The four-compartment cell, containing separate chambers for the working, reference, and auxiliary electrodes, and an intermediate chamber between the working and auxiliary compartments was employed. A gold working microelectrode, polished with AB ALPHA polishing alumina (Buehler Limited, Evanston, Illinois) before each experiment, was employed in cyclic voltammetric experiments and a 3 cm by 8 cm platinum electrode was used in coulometry. A silver wire (Ag. R.E.) isolated in a separate compartment closed with a sintered-glass disk was used as reference electrode. All experiments were carried out with a Princeton Applied Research Corporation Model 170 electrochemistry system using positive feedback resistance compensation. All experiments were conducted on a high vacuum line (10^{-5} Torr) at −43°C.

Results and Discussion

Diethyl fumarate.—The cyclic voltammetric (CV) reduction of DEF in DMF solution shows a fairly reversible first reduction wave at fast scan rates and has been characterized by reversible reduction to the radical anion followed by a coupling reaction (2). The second reduction wave is very small or even characterized by a current decrease in polarography or RDE voltammetry, which has been ascribed to production of the dianion which initiates a rapid polymerization reaction removing parent from the vicinity of the electrode. In liquid ammonia, the CV reduction occurs in two reversible waves at fast scan rates (Fig. 1a) with the reversal wave heights decreasing at slower scan rates (Fig. 1b) indicating decomposition reactions of the electrogenerated species. Typical data for CV experiments for DEF are shown in Table I. The theory of CV for electrode reactions with following dimerization reactions has been presented (7, 8); application of this theory in estimating the rate constant for the dimerization step from the variation of i_{pa}/i_{pc} for the first reduction wave yields a value of about 0.1 M^{-1} sec^{-1}.

Table I. Cyclic voltammetric data for reduction of diethyl fumarate in liquid ammonia[a]

Concentration, C (mM)	Scan rate, v (mV/sec)	First wave i_{pc} (μA)	First wave i_{pa}/i_{pc}	First wave $-E_{pc}$[b] (V)	Second wave i_{pc} (μA)	Second wave i_{pa}/i_{pc}	Second wave $-E_{pc}$[b] (V)
		A. 0.1*M* Methyl-tri-butylammonium iodide					
1.5	50	28	0.41	0.87	10	0.42	1.40
	100	36	0.48	0.88	16	0.87	1.41
	200	49	0.64	0.89	24	0.86	1.42
	500	71	0.87	0.91	52	0.96	1.45
	20,000	620	1.0	0.94	450	1.0	1.50
	$i_{pc}(1)/v^{1/2}C = 1.95$						
3	50	49	0.64	0.87	13	0.66	1.40
	100	63	0.54	0.88	24	0.33	1.41
	200	84	0.60	0.90	41	0.68	1.44
	500	123	0.78	0.92	82	0.9	1.48
	$i_{pc}(1)/v^{1/2}C = 2.0$						
4.6	50	65	0.50	0.85	15	0.46	1.42
	100	90	0.53	0.86	29	0.43	1.39
	200	128	0.53	0.87	56	0.70	1.40
	500	200	0.67	0.88	120	0.80	1.42
	$i_{pc}(1)/v^{1/2}C = 2.4$						
		B. 0.1*M* KI[c]					
2.3	50	12.5		0.74			1.33
	100	22.5		0.75			1.34
	200	29		0.76			1.35
	500	38		0.77			1.37
	$i_{pc}(1)/v^{1/2}C = 0.98$						

[a] Solution contained indicated supporting electrolyte in anhydrous liquid ammonia.
[b] *vs.* Ag-wire reference electrode.
[c] Second reduction wave and reversal waves were to ill-defined for precise current measurements.

The addition of alkali metal ions has been shown to increase the rate of the coupling reaction in DMF, probably by formation of ion pairs with the radical anions (2). The CV reduction of DEF is similarly affected by the addition of KI in liquid ammonia (Fig. 1c), although the kinetics of the reactions were not studied in this case. The addition of a threefold excess of a proton donor, either the weak acid, isopropanol (i-PrOH), or the strong acid, acetic acid (HOAc) to the DEF/MTBAI/NH_3 system has essentially no effect on the first reduction wave, but decreases the reversal current of the second wave and shifts the second wave to more positive potentials. The extent of the shift increases linearly with the log of the proton donor concentration; for acetic acid $\Delta E_p/\Delta\log[\text{HOAc}] = 39$ mV; and for i-PrOH, $\Delta E_p/\Delta\log[\text{i-PrOH}] = 57$ mV. These results suggest that protonation of the radical anion species does not occur, even with the strong acid HOAc, while the dianion reacts with acid. This scheme is reminiscent of that found with benzophenone (3), and the CV reaction order treatment of Savéant and Vianello (8) probably applies here as well. From the limiting slopes of the peak shift with log proton donor concentration we find a reaction order of dianion (m) and proton donor (m_Z) of 0.5 and 1.9, respectively, for i-PrOH and 0.4 and 1.2 for HOAc. This half-order dependence on dianion is the same as that observed for benzophenone dianion and probably indicates kinetic complications in the electron transfer reaction or interferences due to the dianion polymerization reaction.

Controlled potential coulometry of DEF in the presence of either MTBAI or KI as supporting electrolyte (Table II) at potentials beyond the first reduction peak show n_{app} values less than one, even in the presence of proton donor. This result suggests, as do the similarly low values of n_{app} in DMF, that a slow polymerization reaction of the radical anion occurs on the coulometric time scale. CV experiments after coulo-

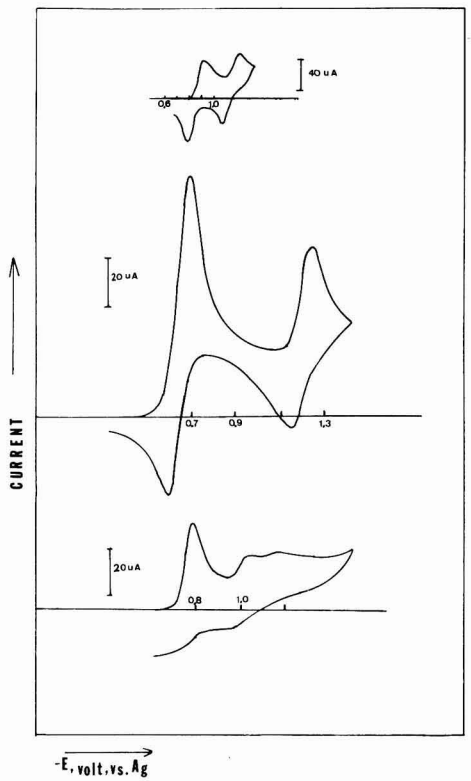


Fig. 1. Cyclic voltammograms of diethyl fumarate in liquid ammonia: (a) 1.75 mM DEF, 0.1M MTBAI, $v = 20$ V/sec; (b) 3 mM DEF, 0.1M MTBAI, $v = 0.2$ V/sec; (c) 3.5 mM DEF, 0.1M KI, $v = 0.2$ V/sec.

Table II. Controlled potential coulometry results

Compound	Concentration (mM)	Conditions	n_{app}
DEF	4.3	0.1M MTBAI	0.6
	10	0.1M MTBAI	0.5
	20	0.1M MTBAI + 40 mM i-PrOH	0.5
DEF	7	0.1M KI	0.4
DEF	3	0.1M KI + 14 mM HOAc	0.5
CN	10.4	0.1M MTBAI	0.16
	13.6	0.1M MTBAI	0.04
CN	20	0.1M MTBAI + 40 mM i-PrOH	0.27
AN	3	0.1M MTBAI	0.05
	14	0.1M MTBAI	0.17
AN	10	0.1M KI + 10 mM i-PrOH	0.96
AN	20	0.1M KI + 20 mM i-PrOH	0.88
AN	20	0.1M KI + 10 mM HOAc	2

metric reduction showed no reduction or oxidation peaks.

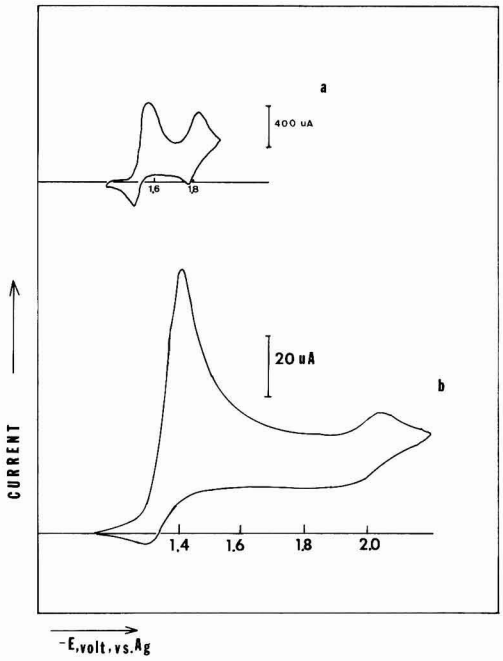


Fig. 2. Cyclic voltammograms of 3.2 mM cinnamonitrile in liquid ammonia containing 0.1M MTBAI with a v of (a) 20 and (b) 0.2 V/sec.

Cinnamonitrile.—The CV reduction of CN at high scan rates (Fig. 2) also shows two reduction waves with appreciable anodic currents on reversal. Typical CV data for CN are shown in Table III. At slower scan rates the second reduction peak decreases in size and the reversal currents decrease. For CN, as opposed to DEF, the value of $i_p/v^{1/2}C$ decreases significantly with increasing concentration of CN, suggesting that the polymerization reaction of the radical anion is important, even on the CV time scale. Treatment of the i_{pa}/i_{pc} data for the first reduction wave, assuming a following coupling reaction of the radical anion, yields a dimerization rate constant of about 5.7 M^{-1} sec^{-1}. The CV behavior in the presence of proton donor resembles that of DEF: the first wave is unaffected by additions of i-PrOH or HOAc, while the second wave is shifted to more positive potentials. The limiting E_p *vs.* log proton donor concentration plots for the second wave yield reaction orders m and m_Z of 0.4 and 2, respectively, for i-PrOH and 0.7 and 1 for HOAc. Controlled potential coulometry of CN (Table II) in the absence of proton donor or with i-PrOH showed very low n_{app} values suggesting abundant polymerization.

Table III. Cyclic voltammetric data for reduction of cinnamonitrile in liquid ammonia[a]

Concentration, C (mM)	Scan rate, v (mV/sec)	i_{pc} (μa)	$-E_{pc}$[b] (V)	$-E_{pc}$[c] (2) (V)
1.6	50	38	1.27	1.90
	100	55	1.28	1.88
	200	73	1.28	1.88
	500	105	1.33	1.90
	$i_{pc}/v^{1/2}C = 3.3$			
3.2	50	52	1.26	1.90
	100	88	1.27	1.90
	200	120	1.28	1.90
	500	140	1.36	1.88
	$i_{pc}/v^{1/2}C = 3.1$			
7.2	50	82	1.27	
	100	133	1.27	
	200	195	1.28	
	500	260	1.33	
	$i_{pc}/v^{1/2}C = 2.2$			
10	50	127	1.25	
	100	175	1.27	
	200	240	1.28	
	500	300	1.34	
	$i_{pc}/v^{1/2}C = 1.6$			
20	50	170	1.24	
	100	212	1.25	
	200	280	1.27	
	500	395	1.35	
	$i_{pc}/v^{1/2}C = 0.8$			

[a] Solution contained 0.1*M* MTBAI.
[b] First wave, *V vs.* Ag-wire reference electrode.
[c] Second wave. Peak too ill-defined at higher concentrations for precise measurement.

Acrylonitrile.—The CV reduction of AN at all scan rates up to 20 V/sec in both MTBAI and KI electrolytes occurs in a single irreversible wave (Fig. 3); typical CV data are shown in Table IV. The very low $i_p/v^{1/2}C$ values observed with MTBAI as electrolyte are evidence of a very rapid polymerization of AN, as is also observed in aprotic solvents in the absence of proton donor. In the KI electrolyte however the $i_p/v^{1/2}C$ values are larger and closer to those of DEF and CN. Controlled potential coulometric reduction of AN (Table II) also shows evidence of polymerization in MTBAI. In a KI + i-PrOH medium, however, n_{app} values close to one are obtained, suggesting significant formation of the hydrodimer product. Product analysis

Table IV. Cyclic voltammetric data for reduction of acrylonitrile in liquid ammonia

Concentration, C (mM)	Scan rate, v (mV/sec)	i_{pc} (μA)	$-E_{pc}$ (V *vs.* Ag R.E.)
	A. 0.1*M* Methyl-tributyl ammonium iodide		
4.3	50	12	1.86
	100	20	1.86
	200	24	1.91
	500	27	1.96
	$i_{pc}/v^{1/2}C = 0.55$		
5.8	50	5	1.78
	100	9	1.83
	200	15	1.86
	500	23	1.98
	$i_{pc}/v^{1/2}C = 0.25$		
8.6	50	10	1.84
	100	12	1.86
	200	16	1.86
	500	19	1.96
	$i_{pc}/v^{1/2}C = 0.07$		
11.5	50	6	1.86
	100	10	1.86
	200	15	1.90
	500	29	2.05
	$i_{pc}/v^{1/2}C = 0.13$		
14.6	50	18	1.91
	100	20	1.90
	200	24	1.91
	500	37	1.96
	$i_{pc}/v^{1/2}C = 0.06$		
23.2	50	16	1.93
	100	21	1.99
	200	28	2.00
	500	49	2.06
	$i_{pc}/v^{1/2}C = 0.11$		
	B. 0.1*M* Potassium iodide		
5.8	50	85	1.61
	100	120	1.62
	200	205	1.64
	500	285	1.67
	$i_{pc}/v^{1/2}C = 1.7$		
10.3	50	70	1.62
	100	130	1.64
	200	220	1.68
	500	340	1.70
	$i_{pc}/v^{1/2}C = 1.8$		
11.5	50	55	1.62
	100	93	1.64
	200	225	1.68
	500	430	1.70
	$i_{pc}/v^{1/2}C = 2.1$		
20.12	50	95	1.62
	100	135	1.63
	200	195	1.64
	500	335	1.67
	$i_{pc}/v^{1/2}C = 1$		

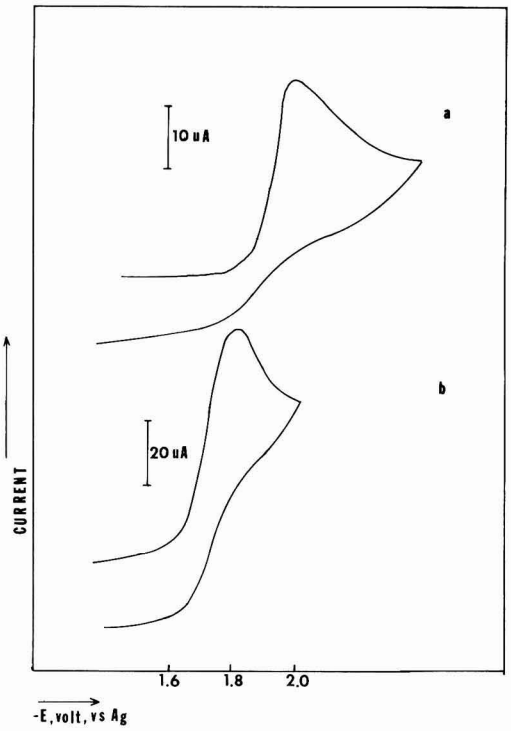


Fig. 3. Cyclic voltammograms of acrylonitrile in liquid ammonia; (a) 5.75 mM acrylonitrile, 0.1M MTBAI, $v = 0.2$ V/sec; (b) 5.16 mM acrylonitrile, 0.1M KI, $v = 0.2$ V/sec Curves are of same form at higher scan rates.

of these solutions by gas chromatography was attempted, but unambiguous analyses were not obtained. The addition of HOAc yields n_{app} values near 2, probably signalling the production of some of the two-electron protonated product, propionitrile, in the presence of strong acid.

The preliminary results show the formation of radical anions and dianions of the diactivated olefins DEF and CN and suggest that with the addition of suitable amounts of proton donor, hydrodimerization reactions can be carried out in liquid ammonia. After this paper was submitted, a communication by Chiba *et al.* (9) appeared, in which the electrolytic reduction of acrylonitrile in liquid ammonia containing ammonium perchlorate as supporting electrolyte at a mercury cathode was described. These authors found a high yield of adiponitrile with some formation of propionitrile under these conditions with constant current electrolysis.

Acknowledgment

The support of the National Science Foundation (GP 31414X) and fellowship support to Iuliana Vartires by the International Research and Exchanges Board is gratefully acknowledged.

Manuscript submitted Jan. 20, 1975; revised manuscript received March 20, 1975.

Any discussion of this paper will appear in a Discussion Section to be published in the June 1976 JOURNAL. All discussions for the June 1976 Discussion Section should be submitted by Feb. 1, 1976.

Publication costs of this article were partially assisted by The University of Texas at Austin.

REFERENCES

1. M. M. Baizer in "Organic Electrochemistry," M. M. Baizer, Editor, Chap. XIX, Marcel Dekker, Inc., New York (1973).
2. M. J. Hazelrigg, Jr. and A. J. Bard, *This Journal*, **122**, 211 (1975).
3. A. Demortier and A. J. Bard, *J. Am. Chem. Soc.*, **95**, 3495 (1973).
4. W. H. Smith and A. J. Bard, *ibid.*, In press.
5. Y. Arad, M. Levy, H. Rosen, and D. Vofsi, *J. Polymer Sci., Pt. B*, **7**, 197 (1969).
6. W. H. Smith, Ph.D. Dissertation, The University of Texas at Austin (1974).
7. M. L. Olmstead, R. G. Hamilton, and R. S. Nicholson, *Anal. Chem.*, **41**, 260 (1969).
8. J. M. Savéant and E. Vianello, *Electrochim. Acta*, **12**, 629 (1967).
9. T. Chiba, Y. Takata, and A. Suzuki, *Chem. Letters*, **1974**, 1241

Electrochemical Oxidation of Iminobibenzyl and Related Compounds

S. N. Frank* and Allen J. Bard*
Department of Chemistry, University of Texas at Austin, Austin, Texas 78712

and Anthony Ledwith
Donnan Laboratories, University of Liverpool, Liverpool L693BX, England

ABSTRACT

Electrochemical oxidation of iminobibenzyl and several related compounds has been investigated in acetonitrile. The mechanism of the oxidation is best described by an ECE process with coupling of the product of an initial one-electron oxidation in a subsequent but very fast reaction to form a dimeric compound that is further oxidized by an over-all two-electron process at potentials more negative than those required for oxidation of the parent compounds. The electrochemistry of these compounds is complicated by the release of protons during the oxidation which protonate the starting materials and the neutral dimerized products rendering them electrochemically inactive. Differences in the electrochemistries of the various coupled products are discussed in terms of structural variations.

In recent years considerable effort has been expended in elucidating the mechanisms of electrolytic oxidation of heterocyclic nitrogen and amine compounds as well as other nitrogen containing species. [See Ref. (1) and (2) for reviews of the work in this area.] One of the prominent characteristics of aromatic amines is oxidative coupling to form a variety of dimerized derivatives of the original parent compounds. Certain heterocyclic nitrogen compounds such as carbazole which may be considered as being derived from diphenylamine also undergo a similar coupling process on oxidation (3).

The present investigation was initially undertaken to compare the electrochemistry of imipramine hydrochloride, a widely prescribed antidepressant drug, with the electrochemical behavior of the structurally similar but physiologically less active iminobibenzyl and 5-methyliminobibenzyl. We also felt it worthwhile to compare the electrochemistry of these compounds with that of the related carbazoles (I) whose primary structural difference with the above compounds is the nature of the biphenyl linkage.

The homogeneous oxidation of most of the present compounds along with a number of carbazoles with chemical oxidants (*e.g.*, 2,3-dichloro-5,6-dicyano-p-benzoquinone) has shown recently (4) that all of the compounds undergo oxidative coupling with ultimate formation of the cation radical salt of the coupled product. The electrochemical coupling of the carbazoles has been previously investigated by Ambrose and Nelson (3) who showed that the neutral coupled products can be oxidized to corresponding cation radicals and dications at potentials negative of those for the oxidation of the parent compounds. The electrochemical behavior of the carbazoles was consistent with an ECE mechanism with oxidative peak heights of the potential sweep voltammograms being twice those expected for a 1-electron process (3). Controlled potential electrolysis also gave an n value of 2. Ambrose and Nelson (3) proposed the following mechanism for the oxidative coupling of the carbazoles (3).

$$RH - e \leftrightarrows RH^{\cdot +} \qquad [1]$$

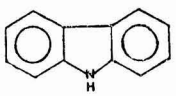
$$2RH^{\cdot +} \xrightarrow{k_1} R_2 + 2H^+ \qquad [2]$$

$$R_2 - e \leftrightarrows R_2^{\cdot +} \qquad [3]$$

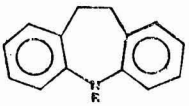
$$R_2^{\cdot +} - e \leftrightarrows R_2^{2+} \qquad [4]$$

The chemical reaction in Eq. [2] is undoubtedly very rapid, since under no circumstances was it possible to observe the reduction of the radical cation of the oxidized parent ($RH^{\cdot +}$). In neither study (3, 4) were the investigators able to determine if the protons are lost before or after coupling.

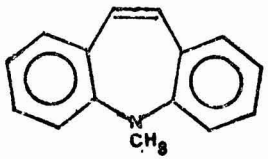
We report here the electrochemical oxidation of iminobibenzyl (**II**), 5-methyliminobibenzyl (**III**), imipramine·$HClO_4$ (**IV**) and 5-methyliminostilbene (**V**), and the electrochemical behavior of the products of the oxidation



I Carbazole



II R = H, iminobibenzyl
III R = CH_3, 5-methyliminobibenzyl
IV R = $(CH_2)_3\overset{H}{\underset{|}{N}}(CH_3)_2{}^+ClO_4^-$
imipramine·$HClO_4$



V 5-methyliminostilbene

Experimental

The preparation of the compounds used in this study has been described (4). Tetrabutylammonium perchlorate (TBAP), the supporting electrolyte in all experiments, was of polarographic grade and purchased from Southwestern Analytical Chemicals. The TBAP which is contaminated with water was dried under vacuum at about 100°C for 24 hr. All other chemicals were of reagent grade quality and used without further purification.

Acetonitrile used as the solvent in these experiments was prepared from spectrograde acetonitrile by vacuum distillation from P_2O_5 at room temperature. The distillation was repeated at least three times with periodic freeze-pump-thawing to remove air.

* Electrochemical Society Active Member.
Key words: cyclic voltammetry, coulometry, oxidative coupling, imipramine, 5-methyliminostilbene.

Table I. $i_p/Cv^{1/2}$ ratios and oxidation and reduction peak potentials for parent and product of the oxidation of parent

Compound	$i_p/Cv^{1/2}$ [a] Parent	E_p ox[b] Parent	E_p ox[b] Product	E_p red[b] Product
Carbazole[a]		+0.86	0.86, 0.56	0.8, 0.5
Iminobibenzyl	17.9	+0.48	0.42, 0.24	0.36, 0.18
5-Methyliminobibenzyl	18.3	+0.61	0.48	0.40
Imipramine $HClO_4$[c]	17.7	+0.75	0.61	0.55
5-Methyliminostilbene	17.9	+0.58	−0.27	−0.30
10-Methylphenothiazene[d]	16.1			

[a] i_p in μA, C in mM, v in V/sec. Within experimental error the $i_p/Cv^{1/2}$ values were independent of sweep rate between 0.2 and 10 V/sec.
[b] Sweep rate = 0.2 V/sec. E_p *vs.* Ag/0.1M $AgNO_3$.
[c] Imipramine hydrochloride was converted to the perchlorate by passing an aqueous solution through an anion exchange column in the perchlorate form and freeze drying the eluent.
[d] A standard one-electron oxidant of similar geometric size to the compounds under investigation. Due to the similarity in size the diffusion coefficients should be nearly the same for all compounds.

The cell used in this study for coulometric and electrochemical characterizations was of conventional design (5). The working electrode for coulometry was a platinum gauze. The working electrode for cyclic voltammetry was a small platinum disk electrode sealed in glass (~0.013 cm^2) and was polished before each use with 0.5μ alumina polishing powder. The auxiliary electrode was a platinum wire and the reference electrode a silver wire which for certain experiments was in contact with a solution of 0.1M $AgNO_3$ in acetonitrile; the potential of this electrode was +0.333V *vs.* an aqueous SCE. All potentials are reported *vs.* this Ag/Ag^+ electrode.

All electrochemical experiments were carried out under an inert helium atmosphere in a Vacuum/Atmospheres Corporation (Hawthorne, California) dry box. A PAR Model 170 electrochemical system (Princeton Applied Research Corporation, Princeton, New Jersey) was used for the electrochemical experiments.

Infrared measurements were made with a Beckman Model IR5A spectrophotometer (KBr pellets). Mass spectra were obtained on a Bell & Howell Model 21-491 low resolution mass spectrometer.

Results

Iminobibenzyl.—At a voltammetric sweep rate of 0.2 V/sec iminobibenzyl shows an oxidation wave with E_{pa} at +0.48V *vs.* the Ag/0.1M Ag^+ electrode. The height of this peak corresponded to that for a one-electron process by calibration against the peak height for the known one-electron oxidation of 10-methylphenothiazene (Table I). This result contrasts with the two-electron peak height previously observed for the carbazoles (3). On sweep reversal two reduction peaks were observed with E_{pc}'s at +0.36 and +0.18V (Fig. 1). Upon repeated cycling two new oxidation peaks were evident at +0.42 and +0.24V. The peak potentials for iminobibenzyl and the other compounds in this study are summarized in Table I.

Table II. Coulometric n_{app} values for parent compounds and the products of a controlled potential oxidation of the parent compounds

Compound[a]	n_{app} ox Parent	n_{app} red Product	n_{app} ox of red product	n_{app} red of H^+
Iminobibenzyl	2.02	0.96	0.94	0.95
5-Methyliminobibenzyl[b]	1.0	0.5	0.5	0.5
	2.2	0.93	0.9	0.98
Imipramine $HClO_4$	0.92	0.45	0.44	1.5
5-Methyliminostilbene	0.95	0.45	0.43	0.47

[a] The concentration of compound ~1 mM in all coulometric experiments.
[b] The two values listed correspond to the two breaks observed in the Q-t curve.

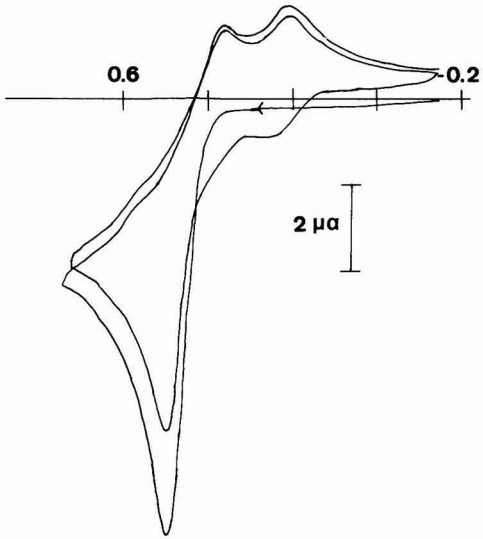


Fig. 1. Cyclic voltammogram of 1.25 mM iminobibenzyl. Conditions: sweep rate = 0.2 V/sec; 0.1M TBAP supporting electrolyte; X-axis is E, V, *vs.* Ag/0.1M Ag^+ reference electrode.

Controlled potential electrolysis at +0.85V gave an n_{app} value of 2 (where n_{app} represents the coulombs of electricity per mole of electroactive compound) (Table II) which is twice the value indicated by the voltammetry results. The oxidized solution had an intense blue color. Cyclic voltammetry of the solution following oxidation showed a redox couple centered at about +0.5V (Fig. 2) and a hydrogen ion reduction wave commencing at about −0.5V. Controlled potential coulometry of this solution indicated that the product of the initial oxidation could be reduced (at E = +0.2V) and then reoxidized again (at E = +0.85V) with an n_{app} = 1. Controlled potential reduction at −1.3V (following the oxidation at +0.85V) showed the release of one H^+ per parent molecule oxidized (*i.e.*, n_{app} = 1.0) during the initial oxidation at +0.85V. After the reduction of the protons only the two redox couples observed after repeated cycling of a solution of unoxidized parent were present (Fig. 3). There was no evidence of any

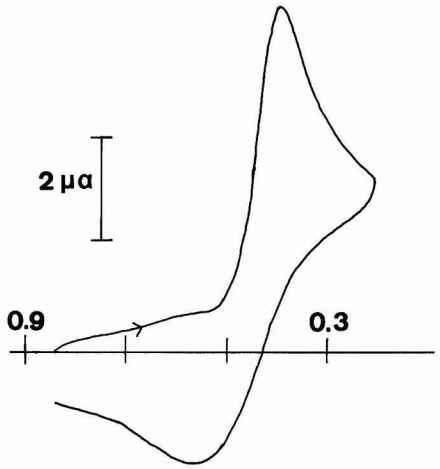


Fig. 2. Cyclic voltammogram of 1.25 mM iminobibenzyl after oxidative electrolysis at +0.85V. Conditions: Same as Fig. 1.

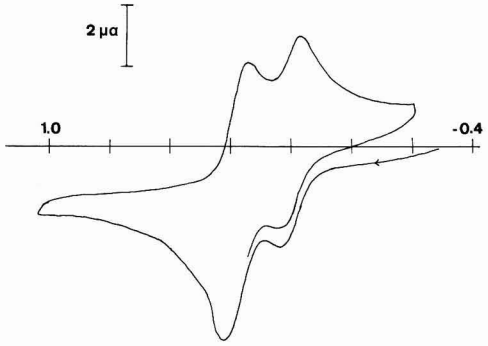
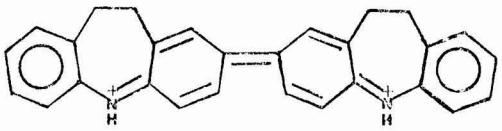


Fig. 3. Cyclic voltammogram of 1.25 mM iminobibenzyl following electrolysis at +0.85 and at −1.3V. Conditions: Same as Fig. 1.

remaining parent or the couple observed at +0.5V following the initial oxidation at +0.85V. The separation between E_{pa} and E_{pc} for each couple was 60 mV and indicates that each couple corresponds to a one-electron process. Coulometry demonstrated that a total of one electron was necessary to oxidize and then reduce both couples. In the absence of protons the product of the oxidation of parent at +0.85V behaved electrochemically in an entirely analogous manner to the carbazole products where two one-electron couples were also seen. In fact, except for the anomalous voltammetric peak height observed for the parent and the electrochemical behavior of the product of the oxidation of iminobibenzyl in the presence of protons, the electrochemistry is similar to that for the carbazoles. It seems likely therefore that a similar mechanism is operative in the case of iminobibenzyl with ultimate formation of a product (**VI**) which, by analogy with homogenous studies (4), probably arises by coupling at the 2-position



VI

The rate of the coupling reaction is fast because no evidence was obtained for reduction of the parent radical cation during the voltammetry experiments.

In order to confirm that **VI** is indeed the major product of the oxidation at +0.85V, an attempt was made to isolate the neutral analog of **VI** prepared by a controlled potential reduction of a solution of **VI**. At the relatively high solution concentrations necessary to isolate a reasonable quantity of material (≧ 20 mM), the electrochemistry of iminobibenzyl was not as clean as observed at lower concentrations (~ 1 mM). This is probably because of precipitation of the electrolysis products onto the working electrode. At these concentrations it was not possible to carry the oxidations or reductions to theoretical completion before the electrolysis currents decayed to very small values. The solutions that resulted upon reduction of an oxidized solution of iminobibenzyl contained significant quantities of unreduced material as indicated by an intense bluish-green color. Removing the acetonitrile solvent after reduction on a vacuum line followed by dissolution of the solid in benzene to separate the neutral from most of the charged products and extraction of the benzene solution with water to remove most of the remaining charged species resulted on freeze-drying in a brown solid with a slight violet tinge. Infrared spectra of this material showed a strong absorption at 805 cm^{-1}. This is the same absorption expected for the iminobibenzyl dimer with coupling at the 2-position (4). The parent peak of a mass spectrum of this compound occurred at a molecular weight of 388 the same as the bibenzyl dimer. The mass spectrum also indicated the presence of minor amounts of higher molecular weight materials.

Possible complications due to the presence of H^+ that may explain the anomalous behavior of the coupled product and one electron peak height of the parent will be discussed later.

5-Methyliminobibenzyl.—Investigations of the homogeneous oxidation of 5-methyliminobibenzyl have demonstrated a similar coupling process as was found for iminobibenzyl with coupling also taking place at the 2-position (4). In view of this and the strong supporting evidence presented above demonstrating that the homogeneous and electrochemical oxidations of iminobibenzyl result in the same reaction product, it is assumed that the product of the electrolytic oxidation of 5-methyliminobibenzyl is structurally similar to **VI**.

5-Methyliminobibenzyl also had a voltammetric peak height on oxidation the same as that expected for a 1-electron process (See Table I). On sweep reversal, a reduction peak approximately one-half the height of the oxidation peak was observed (Fig. 4). The ratio of the two peak heights was independent of sweep rate up to 10 V/sec. At a sweep rate of 0.2 V/sec E_{pa} and E_{pc} were 0.61 and 0.40V, respectively. If cycling was continued, a new oxidation peak develops at about +0.48V.

A number of controlled potential electrolysis experiments were performed with 5-methyliminobibenzyl. Q-t curves for electrolysis at +0.8V showed a sharp break at an n_{app} value of 1. The oxidized solutions were an intense blue color. The slope of the Q-t curves after this break was small but definitely larger than the slope usually found after complete electrolysis. On continuing the electrolysis, another break in the Q-t curves was observed at an n_{app} value of 2-2.2. If the electrolysis was stopped after the first break ($n = 1$) and a cyclic voltammogram obtained, a redox couple was seen centered at +0.44V (Fig. 5). There was no evidence for the original peak at +0.61V. When the scan was continued to negative enough potentials, a number of irreversible and distorted peaks corresponding to proton reduction was seen between −0.3 and −1.2V. When the electrolysis was continued until $n_{app} = 2$, cyclic voltammetry (with the initial potential at the potential of the electrolysis) showed only the reduction peak at +0.4V. There were no oxidation peaks at +0.48 or 0.61V. Stopping the electrolysis at +0.8V at any stage and electrolyzing at

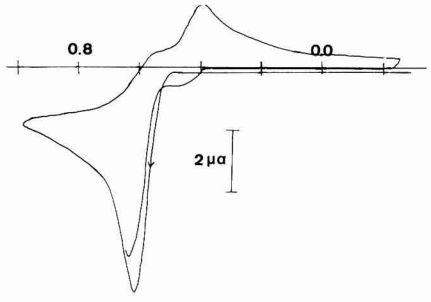


Fig. 4. Cyclic voltammogram of 0.85 mM 5-methyliminobibenzyl. Conditions: Same as in Fig. 1.

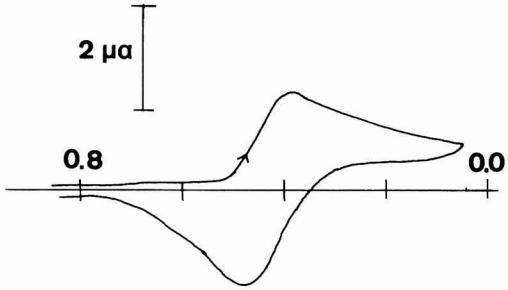


Fig. 5. Cyclic voltammogram of 0.85 mM 5-methyliminobibenzyl after one electron of electrolysis at +0.8V. After two electrons of electrolysis the oxidation peak is not observed. Conditions: Same as in Fig. 1.

+0.2V always resulted in half of the number of coulombs for reduction as had been passed during oxidation at +0.8V. The number of electrons obtained in reduction at −1.3V after electrolysis at +0.2V was the same as the number that had been obtained at +0.2V. Cyclic voltammetry following this reduction at −1.3V showed oxidation waves at +0.48 and +0.61V (Fig. 6), unless a complete electrolysis had been carried out at +0.8V (n_{app} = 2) at which time the +0.61V peak was absent.

A mechanism consistent with the above results is

$$RH - e \rightleftarrows RH^{+\cdot} \quad [5]$$

$$2RH^{+\cdot} + 2RH \rightarrow R_2 + 2RH_2^{+} \quad [6]$$

$$R_2 - e \rightleftarrows R_2^{+\cdot} - e \leftrightarrows R_2^{+2} \quad [7]$$

$$RH_2^{+} \overset{K_1}{\rightleftarrows} RH + H^{+} \quad [8]$$

$$R_2 + H^{+} \overset{K_2}{\rightleftarrows} R_2H^{+} \quad [9]$$

and/or

$$R_2 + 2H^{+} \overset{K_2'}{\rightleftarrows} R_2H_2^{+2} \quad [10]$$

Equation [6] above implies no mechanistic interpretation since it cannot be ascertained whether coupling occurs before or after loss of a proton from the cation radical. The proposed mechanism is the same as that for carbazole except for the protonations of the neutral parent and coupled product. The chemical reactions in Eq. [6] are undoubtedly very rapid as demonstrated by the absence of a reverse reduction peak accompanying the oxidation peak at +0.61V. The reduction peak at +0.40V and the oxidation peak at +0.48V correspond to the redox processes of Eq. [7]. Both redox processes occur at similar potentials since only one peak is observed. The apparent total one-electron oxidation of the 5-methyl parent plus coupled product; whereas two would be expected by analogy to carbazole, comes about because of the protonation of the parent molecule in Eq. [6] which renders the parent molecule electrochemically inactive. By the time half the parent has become oxidized the remaining parent is protonated. The small residual slope of the Q-t curves after one electron of oxidation is due to the oxidation of the small amount of parent that can remain in equilibrium with protons and protonated parent, Eq. [8]. If the resulting dication is now reduced, the neutral dimer itself can be protonated and rendered inactive to oxidation, Eq. [9]. This mechanism is consistent with the fact that 5-methyliminobibenzyl is a stronger base than the related carbazoles (*vide infra*) where protonation of parent introduced no complications.

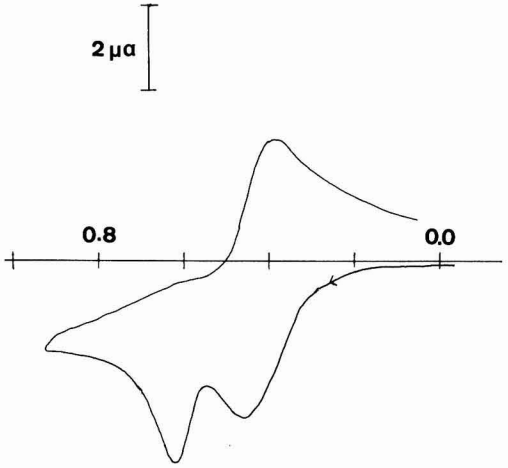


Fig. 6. Cyclic voltammogram of 0.85 mM 5-methyliminobibenzyl after one electron of electrolysis at +0.8V followed by electrolysis at −1.3V. After two electrons of electrolysis, the oxidation peak at 0.61V is not observed. Conditions: Same as in Fig. 1.

In an attempt to verify the role of protons, several experiments were carried out in the presence of the nucleophile pyridine in the hope of scavenging protons. When a large excess of pyridine was present (>10:1), cyclic voltammograms indicated that two electrons were transferred. Controlled potential electrolysis, however, showed that eventually in excess of four electrons were transferred. Pyridine apparently attacks the dication dimer forming a species that is oxidized further. The rate of the attack cannot be too rapid or else the voltammetry and electrolysis would have indicated the same number of electrons. Cyclic voltammetry showed no evidence of the couple at +0.44 following an oxidation with a large excess of pyridine. Also, the solution did not attain the intense blue color found after electrolysis performed without pyridine. If the electrolysis was carried out until the first break in the Q-t curves with a somewhat less than stoichiometric amount of pyridine followed by a reductive electrolysis at +0.2, the yield of the neutral dimerized product was 30% greater than was found in the absence of pyridine (n_{app} = 0.65 *vs.* 0.5, the time of the oxidative electrolysis was about the same). Some proton scavenging is apparently taking place. Interestingly, pyridine acted only as a proton scavenger in the electrolysis of carbazoles (3).

Experiments were also performed with added acid. According to the proposed mechanism, the acid should protonate the parent and no oxidation should be observed. Addition of equivalent amounts of acetic acid resulted in no change in the electrochemical behavior. However, when acetic acid was in large excess (100:1), the peak height of the +0.61V oxidation was somewhat diminished. At these concentrations of acetic acid a new smaller peak approximately 100 mV positive of the main oxidation appeared. With equivalent amounts of H_2SO_4, the +0.61V peak was absent and the new peak at ~ +0.7V attained its maximum development, about one-third the peak height of the original oxidation. Further addition of H_2SO_4 resulted in the disappearance of this peak also. The results suggest that acetic acid is too weak an acid to protonate the 5-methyliminobibenzyl parent. Blank experiments where only supporting electrolyte and acid were present showed oxidative currents in the region of the peak observed above at +0.7V. These currents are probably due to added impurities such as water which undergoes a pH dependent oxidation in this region.

Imipramine · $HClO_4$.—A number of electrochemical experiments were also performed on the $HClO_4$ salt of

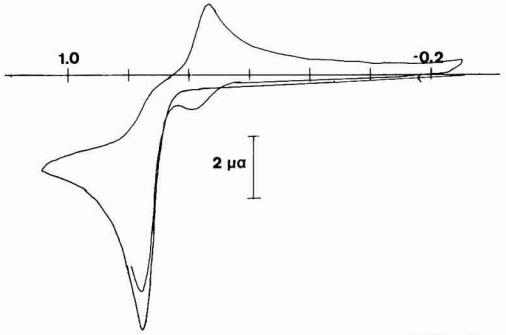


Fig. 7. Cyclic voltammogram of 1.0 mM imipramine $HClO_4$. Conditions: Same as in Fig. 1.

imipramine. After reduction of the proton of the tertiary amine group, the tertiary amine probably serves as a base for scavenging protons. The electrochemistry of the protonated imipramine was in all ways similar to 5-methyliminobibenzyl. An apparent one-electron oxidation was observed at +0.75V and an apparent one-half electron reduction at +0.55V (Fig. 7). These ratios and numbers were confirmed with controlled potential oxidations and reductions. Reduction of the amine proton (−1.2V) apparently activated the amine group which was oxidized before 0.75V. Controlled potential electrolysis at +0.9V indicated that considerably more than two electrons were necessary for complete oxidation. The mechanism, however, appeared to be complicated and was not pursued further.

5-Methyliminostilbene.—Homogeneous oxidations of 5-methyliminostilbene (4) have shown that the coupling process may be more complicated than with the related bibenzyl compounds. A possibility of coupling at both the 2 and 10 positions was postulated (4). Electrochemical oxidation might then be expected to result in a more complex product distribution than was observed with the above compounds.

Cyclic voltammograms of 5-methyliminostilbene were characterized by two oxidation peaks at +0.58 and +1.0V at 0.2 V/sec (Fig. 8). The height of the 0.58V peak corresponded to 1 electron (Table I). The peak at +1.0V was more rounded and corresponded to about 0.2 electrons. On sweep reversal a new redox couple was observed at −0.28V (peak separation = 30 mV). There was no evidence for reduction of the oxidized parent (radical cation). Coulometry at +0.7V resulted in an initial $n_{app} = 1$. The oxidized solution (with a yellow color) had a reduction peak at −0.30 and an accompanying oxidation peak at −0.27 (Fig. 9). No evidence was seen of the original oxidation peaks at +0.58 and +1.0V suggesting that the +1.0V peak may be oxidation of the parent or a species formed at +0.58V. Close inspection of the region around −0.28V showed evidence of another redox couple at somewhat more positive potentials suggesting that at least two products may result from the oxidation at +0.7V. Controlled potential reductions and oxidations of the couples in the −0.28V region showed that one-half the number of electrons are required as are initially consumed at +0.7V. Reduction of protons at −1.3 suggest that one proton is liberated per parent molecule oxidized. Reduction of protons results in the reappearance of the +0.58 and +1.0V peaks (Fig. 10) which are about one-half of their original height. The mechanism of oxidative coupling of 5-methyliminostilbene at +0.7V appears similar to 5-methyliminobibenzyl except more coupling positions are available.

An apparent change in mechanism occurs when the oxidation is performed at a potential positive of the +1.0V peak. Performing such an electrolysis resulted in an n_{app} of about 1.85 and the product distribution appears to be much more complicated. The resulting products are reduced with one-half of the number of electrons required for the oxidation. Electrolysis at −1.3V requires the same number of electrons as required for reduction of the products of the oxidation.

Discussion

The general oxidative behavior of all of the above compounds is probably similar. The likely initial step in the oxidation is the formation of a cation radical of the parent compound. In a very fast follow-up reaction the cation radicals couple at the 2-position (except possibly for iminostilbene where more coupling modes are possible) with the loss of one proton per parent. The proposed mechanism now deviates from the carbazole mechanism in that the parent and neutral coupled product may be protonated by the protons released during coupling and become electrochemically inactivated. A similar inactivation by released protons has been proposed for the anodic oxidation of N-alkylanilines (6).

Differences in electrochemical behavior between the compounds may in part be explained by differences in basicity of the parents. A relatively minor decrease in basicity of iminobibenzyl as compared to 5-methyliminobibenzyl would probably not increase the concentration of unprotonated parent that can remain in equilibrium with protons enough to have an easily measurable effect on the height of the oxidation wave. Because of the difference in time scale between potential sweep and coulometric experiments, this relatively small increase in unprotonated parent could have a significant effect on the shape of the Q-t curve. What might be expected would be a more drawn out Q-t curve with a less well-defined break. This is in fact the case with iminobibenzyl and supports the contention that iminobibenzyl is less basic than the 5-methyl analogue. Protonation of the neutral iminobibenzyl dimer might well be responsible for the merging and shifting of the two product couples observed in cyclic

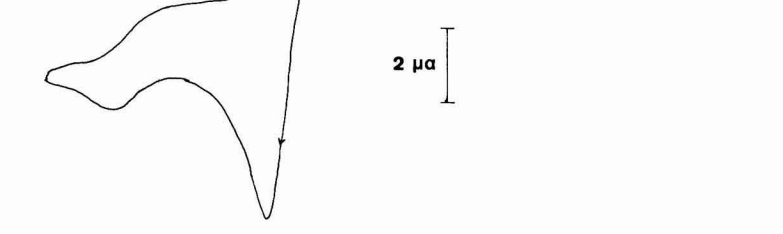


Fig. 8. Cyclic voltammogram of 1.0 mM 5-methyliminostilbene. 1, 1st sweep; 2, 2nd sweep. Conditions: Same as in Fig. 1.

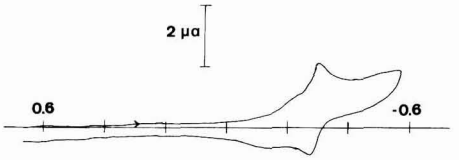


Fig. 9. Cyclic voltammogram of 1.0 mM 5-methyliminostilbene after electrolysis at +0.7V. Conditions: Same as in Fig. 1.

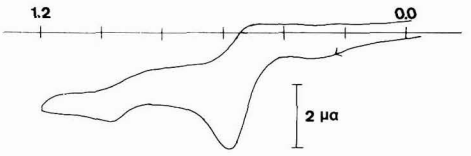


Fig. 10. Cyclic voltammogram of 1.0 mM 5-methyliminostilbene after electrolysis at +0.7V followed by electrolysis at −1.3V.

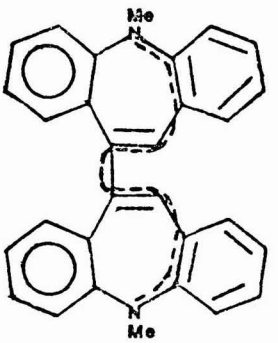
voltammetry of the parent compound as indicated by the reappearance of these couples upon reduction of protons.

The difference in basicities between the present compounds and the carbazoles can be explained in terms of structural considerations. The planar structure of the carbazoles permits the interaction of the lone pair of electrons on the nitrogen with the pi-electrons of the benzene rings making the lone pair less nucleophilic and very much less basic. X-ray structures of iminobibenzyl-type compounds of interest in this study have not been obtained. However, x-ray studies of related compounds (7) and other considerations (8) indicate that the ethylene bridge of iminobibenzyl, 5-methyliminobibenzyl, and imipramine prevents easy attainment of a planar structure thus making the nitrogen lone pair more available. Although some increase in planarity is expected for 5-methyliminostilbene due to the unsaturated nature of the ethylene linkage, consideration of molecular models indicates that this bridge is highly strained and some rotation out of the plane is expected with a subsequent increase in basicity as compared to carbazole.

The subtle variation in basicities among the studied compounds is not as easily explained. The greater basicities of the N-substituted iminobibenzyls may partly result from the electron-donating properties of the aliphatic substituents on the nitrogens. Comparisons of the changes in basicity that result from substituting an aliphatic chain for hydrogen in a variety of amine compounds [*e.g.*, pK_a's for anilinium and N,N-dimethylanilinium are 4.63 and 5.15, respectively (9)] indicate that the effect may not be large.[1] However, it may be that only small effects are necessary to explain the observed differences. An attractive aspect of this explanation is that it may explain why 5-methyliminostilbene is apparently a stronger base than iminobibenzyl even though it should be more planar. Arguments are presented below that suggest that iminobibenzyl is more planar, and therefore less basic, than 5-methyliminobibenzyl, perhaps because of some nonbonding interaction between the nitrogen methyl group and the benzene rings (9). Steric hindrance around the nitrogen atom of iminobibenzyl is well established from N-alkylation studies (10). Several attempts were made at determining the pK_a's for these compounds by titration of the base-forms in acetonitrile with perchloric acid (made anhydrous by addition of an excess of acetic anhydride). However, the basicity of these compounds (less than that of acetate ion) was too small to show glass electrode responses larger than the drifts we observed for this electrode in changing from one calibration solution to another (up to 100 mV). Moreover, to account quantitatively for the differences in these compounds, differences in the acidity of the very unstable radical cations would also have to be considered.

Differences in planarity should also have some effect on the redox potentials of these compounds. Unfortunately, the irreversible nature of the following chemical reaction prevents using peak potentials as a reliable guide as to the ease of oxidation of the parent compounds although where known the differences in potentials correlate with the differences in ionization potentials (11). For the most part the redox processes of the coupled products are reversible or nearly so. Inspection of Table I shows that no real trend exists for the redox potentials of the coupled products, and it is likely that a number of effects such as the relative stabilization of reduced and oxidized forms by delocalization and conformational effects may play important roles. Related substituent effects are apparent in the anodic oxidation of N-akyl anilines (6).

Deserving special note, though, is the unusual ease with which the 5-methyliminostilbene dimer may be oxidized. A reasonable explanation is that the major product of the 5-methyliminostilbene oxidation is a dimer coupled at the 10-position rather than the 2-position as is the case for the other compounds. A structure **VII** reminiscent of a



VII

diamiminobutadiene results (dotted line outlines the butadiene backbone). Compounds such as this are known to be exceedingly easy to oxidize (12). One might also consider **VII** to be related to the dihydro forms of bipyridylium dications which are very easily oxidized (13). **VII** cannot be isolated in the presence of atmospheric oxygen because of its low oxidation potential. Attempts at isolating the dication salt of **VII** after bulk electrolysis were unsuccessful.

If the parent molecules are sufficiently nonplanar, the two parent moieties of the dimers are effectively electronically decoupled. Removing an electron results in most of the positive charge residing on one of the parent moieties. Removing the second electron should then not be much more difficult than the first. The oxidation peaks for the two processes would then appear close together. This appears to be the case for 5-methyliminobibenzyl and imipramine. The two oxidation peaks observed for iminobibenzyl suggests on the basis of the above argument that iminobibenzyl is more planar than the 5-methyl analogue.

Since the coupled 5-methyliminostilbene also has only one oxidation peak, one might be tempted to suggest that a reaction scheme analogous to that of 5-methyliminobibenzyl was occurring. However, the peak separation between the oxidation is 30 mV and it is, therefore, not possible to ascertain whether these peaks correspond to two 1-electron processes occurring at the same potential or one 2-electron process.

[1] Most pK_a's determined are for aqueous solutions where as pK_a's for nonaqueous solvents would be more appropriate. For certain nonaqueous solvents such as acetonitrile pK_a's and the differences between pK_a's may well be much larger than found in aqueous systems.

A nuance of the 300 mV separation between the two oxidations of bicarbazoles is that any neutral bicarbazole formed as a transient in the oxidation of carbazole can react with dication to yield the radical cation. A measurable ESR signal might be expected during electrolysis. Such an ESR signal was observed for carbazole (3). The closeness of the two oxidations for the dimeric 5-methyliminobibenzyl make the driving force for such a reaction sequence much smaller. Accordingly, the probability of producing a sufficient number of free radicals to observe during an electrolysis in an ESR cavity is much less. In line with this reasoning, an *in situ* electrolysis of 5-methyliminobibenzyl in an ESR (14) cavity resulted in no ESR signal.

Acknowledgment

The support of this research by the National Science Foundation (GP-31414X) and the Robert A. Welch Foundation is gratefully acknowledged. The cooperative Texas-Liverpool effort was made possible by a grant from NATO (Research Grant No. 668).

Manuscript submitted Oct. 21, 1974; revised manuscript received Feb. 17, 1975.

Any discussion of this paper will appear in a Discussion Section to be published in the December 1976 JOURNAL. All discussions for the June, 1976 Discussion Section should be submitted by Feb. 1, 1976.

Publication costs of this article were partially assisted by the University of Texas at Austin.

REFERENCES

1. "Organic Electrochemistry: An Introduction and Guide," M. M. Baizer, Editor, Marcel Dekker, Inc., New York (1973).
2. C. K. Mann and K. K. Barnes, "Electrochemical Reactions in Nonaqueous Systems," Marcel Dekker, Inc., New York (1970).
3. J. F. Ambrose and R. F. Nelson, *This Journal*, **115**, 1159 (1968).
4. P. Beresford, D. H. Iles, L. J. Kricka, and A. Ledwith, *J. Chem. Soc. Perkin I*, 276 (1974).
5. W. V. Childs, J. T. Maloy, C. P. Keszthelyi, and A. J. Bard, *This Journal*, **118**, 874 (1971).
6. R. L. Hand and R. F. Nelson, *J. Am. Chem. Soc.*, **96**, 850 (1974).
7. L. J. Kricka and A. Ledwith, *Chem. Rev.*, **1**, 101 (1974).
8. J. R. Huber and J. E. Adams, *Ber. Bunsenges. Phys. Chem.*, **78**, 217 (1974); R. J. Abraham, L. J. Kricka, and A. Ledwith, *J. Chem. Soc. Perkin II*, In press.
9. Handbook of Chemistry and Physics, 51st ed., The Chemical Rubber Co., P D120, (1970); "Determination of Organic Structures by Physical Methods," E. H. Braude and F. C. Nachod, Editors, p. 567, Academic Press, New York (1955).
10. L. J. Kricka and A. Ledwith, *J. Chem. Soc. Perkin I*, 2292 (1972).
11. H. J. Haink, J. E. Adams, and J. R. Huber, *Ber. Bunsenges. Phys. Chem.*, **78**, 436 (1974).
12. J. M. Fritsch, H. Weingarten, and J. D. Wilson, *J. Am. Chem. Soc.*, **92**, 4038 (1970).
13. E. Steckhan and T. Kuwana, *Ber. Bunsenges. Phys. Chem.*, **78**, 253 (1974).
14. I. B. Goldberg and A. J. Bard, *J. Phys. Chem.*, **75**, 3281 (1971).

Emf's across CdI_2-Cd_2I_2 Electrolytes Using Electrodes of Bare W, Molten Cd, and Molten Au-Cd: Bare Electrode Effects, Use of $n \neq 2$, Premonitory Phenomena and Liquid Structure in Au-Cd, and the Cd-CdX_2 Phase Diagrams

David Nin-Kou Wang[1]

Department of Mining, Metallurgical, and Fuels Engineering, University of Utah, Salt Lake City, Utah 84112

Guy R. B. Elliott*[,2]

University of California, Los Alamos Scientific Laboratory, Los Alamos, New Mexico 87544

and Charles H. Pitt

Department of Mining, Metallurgical, and Fuels Engineering, University of Utah, Salt Lake City, Utah 84112

ABSTRACT

Emf measurements have been made on cells with CdI_2-Cd_2I_2 mixed-valence electrolytes (*a*) to establish structural and thermodynamic properties for molten Au-Cd alloys and (*b*) to study the source and behavior of some unexpected voltages associated with bare W electrodes dipping into these electrolytes. Changes with temperature and composition of the partial molal entropies, enthalpies, and free energies of the Cd component in the Au-Cd melts point out the existence of premonitory changes a few degrees above the liquidus as well as of liquid structural changes far from the liquidus; these changes correlate with earlier studies by vapor pressure and by electrical conductivity in the Au-Cd system at higher temperatures. $n = 1.87 + 0.001(773T)$ is used to evaluate the effective valence for these electrolytes when saturated with Cd; this n appears in calculation of $\Delta\overline{F} = -n\mathbf{F}\epsilon$. Apparently the mixed-valence electrolyte, plus probable oxide impurities, reacts with the bare electrode (in this case W) surfaces by direct chemical action to form surface films which protect the metal below against direct chemical attack. These films are in equilibrium with the electrolytes. When, however, electrochemical attack is permitted, as when an emf measurement is made, then the underlying metal becomes subject to attack and another reactant enters the reaction. This effect leads to anomalous voltages in electrodes which are normally considered to be inert in molten salts, *e.g.*, W, Mo, and graphite. If these sources of voltage are recognized, then proper determinations of activities and phase boundaries can be made; some earlier measurements of this type which neglected these voltages, however, must be re-evaluated. Application of these proper techniques to the Cd-CdI_2 system is made.

In aqueous systems the usual "inert" electrodes are platinum, gold, silver, etc. These electrodes are unsatisfactory in many molten salt systems, however, because of their tendency to form alloys with many metals. Attack can occur either by direct contact with these metals or by secondary reaction with the products formed by dissolution of the metals in their molten salts. Thus platinum dipping into pure molten CdI_2 is stable, but if the CdI_2 is in contact with a molten Cd phase below, then the platinum is attacked by the CdI_2-Cd_2I_2 mixture formed by the dissolution of Cd in CdI_2, and a Pt-Cd alloy is formed.

In order to avoid alloying attack in molten salt systems it is customary to turn to "inert" electrodes, *i.e.*, tungsten, molybdenum, graphite, etc. It is the thesis of this paper that such electrodes are often not inert and that a number of apparent thermodynamic conflicts in the literature can be resolved if this fact is recognized. As corollary we offer a thermodynamically acceptable interpretation of these anomalies and of the electrode behavior.

To study this problem we have used cells of the types

$$\text{W, Cd/CdI}_{2(\text{Cd satd})}\text{/W} \quad [1]$$

$$\text{W, Cd-Au/CdI}_{2(\text{Cd-Au satd})}\text{/W} \quad [2]$$

$$\text{W, Cd/CdI}_{2(\text{Cd satd})}\text{//CdI}_{2(\text{Cd unsatd})}\text{/W} \quad [3]$$

$$\text{W, Cd-Au/CdI}_{2(\text{Cd-Au satd})}\text{//CdI}_{2(\text{Cd-Au unsatd})}\text{/W} \quad [4]$$

Here all phases are molten except W, and one must recognize that the shiny, cleaned W will be coated with traces of oxides. These cells have been studied as functions of composition, temperature, and time.

In addition usual [*e.g.*, Ref. (1-3)] stirred H-cell measurements were made between molten Cd and molten Cd-Au alloy. There the cell is represented exactly as

$$\text{W, Cd-Au/CdI}_{2(\text{Cd-Au satd})}\text{//CdI}_{2(\text{Cd satd})}\text{/Cd, W} \quad [5a]$$

but it can be represented to a close approximation by

$$\text{W, Cd-Au/CdI}_{2(\text{Cd satd})}\text{/Cd, W} \quad [5b]$$

as long as the Cd activity in Cd-Au is close to unity, thus making the CdI_2/Cd_2I_2 ratio essentially identical at both electrodes, as set by the equilibrium constant

$$K = (a_{Cd_2I_2})/(a_{CdI_2})(a_{Cd}) \quad [6]$$

* Electrochemical Society Active Member.

[1] Present address: IMRD, Lawrence Berkeley Laboratory, Berkeley, California 94720.

[2] Present address: CNC-2, LASL, Los Alamos, New Mexico 87544.

Key words: mixed valence electrolytes, alloy activities, surface reactions.

Experimental Chemicals, Apparatus, and Operations

Emf cells.—Two modifications of the usual stirred H-cells mentioned above were used. These cells allow for composition changes *in situ* by additions of preweighed solids in the sidearms, for stirring and long equilibrations to assure that phases are homogeneous and at equilibrium, and for initial cleanup operations such as the vacuum melting of CdI_2 before it is melted and poured or vaporized into the H-cell portion of the system. Temperatures are very uniform (to $< 0.01°K$) because of the heat distribution and heat ballast from nesting copper cylinders.

Type I.—This version differs from the usual stirred H-cell only in that a second W lead in each cell leg is mounted on the stirrer so as to be exposed bare to the electrolyte. As is customary the exposed portion of the other lead was completely immersed in molten cadmium or alloy. (See Fig. 1.)

This cell type was used for almost all the data presented here.

Type II.—In this modification the bottoms of the H-cell legs were joined so that a single alloy touched the electrolyte in both legs. The electrolyte in each leg was essentially independent of that in the other, and stirring one side did not agitate the other. (See Fig. 2.)

Two types of electrodes dipped into the electrolyte, namely (*a*) large current collectors made by wrapping ~100 cm of 10 mil W wire around each stirrer but not touching the alloy, and (*b*) small potential sensors exposing ~3 cm of 10 mil rod to the CdI_2, there being two of these in each cell leg.

Chemicals and their purification.—Commercial cadmium of purity reported as 99.999% was melted in vacuum and washed with boiling, molten CdI_2. Reagent grade CdI_2 was sometimes (cell type II) melted under vacuum and washed with molten Cd. Later this material or new reagent grade CdI_2 (cell type I) was loaded into the sidearm of the cell and remelted repeatedly under vacuum, the final melting being used to introduce the salt into the cell legs. Commercial argon was condensed at liquid nitrogen temperatures, flash frozen by evacuation to flush out the more volatile impurities, then gently warmed and distilled into the cells at ~0.5 atm.

For cells of type I the electrodes were cleaned by a-c electrolysis in NaOH solution, then were water washed and dried by touching tissue. With cells of type II the working electrodes on the stirrers were made from commercially cleaned and still shiny 10 mil W wire. Additional potential sensors were made from a different commercial tungsten; these electrodes were oxidized to a dark color during a Pyrex anneal and were not cleaned further. The electrodes represent two commercial sources and two levels of preliminary oxidation of the W surface.

Gases adsorbed on the Pyrex or chemicals were removed by evacuation at 10^{-5}-10^{-6} Torr while the system was in the furnace, and then the purified argon was added.

Electrical equipment.—Usual measurements with potentiometers having no connection to house current were employed (Wenner, K-2, etc.). Pt/Pt-10% Rh thermocouples were used.

For further discussion of these various techniques, see our earlier papers, *e.g.*, Ref. (1-3).

Cell operation.—Consistent with earlier observations (1), cadmium solutions required much stirring before equilibrium was reached, as compared with Sn-$SnCl_2$ solutions [*e.g.*, (2)]. When a cell could be stirred with almost negligible effect on the voltage, and when it also returned in a few minutes to the original voltage, the system was accepted as being at equilibrium. (As must always be faced, a system can often be in equilibrium with regard to one type of reaction while it is

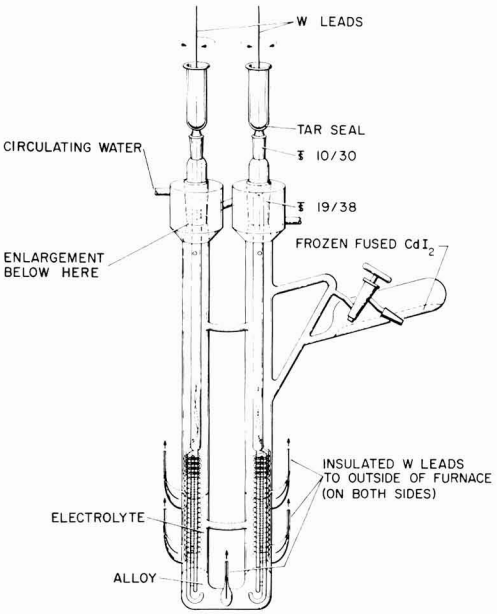


Fig. 2. Multiple electrode cell for checking reproducibility of bare electrode emf's (reaction [2]) with time, with stirring, with composition, and with different sources of tungsten having different levels of initial oxidation on their surfaces.

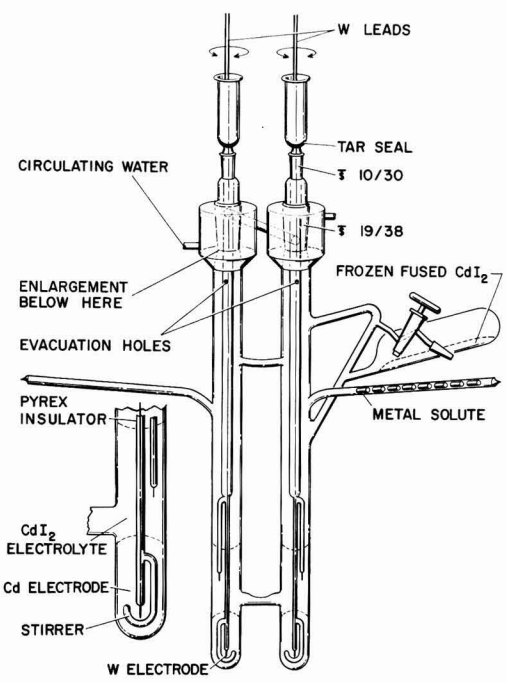


Fig. 1. Stirred H-cell for studying various usual reactions (*e.g.*, reaction [5a]) as well as the bare electrode reactions (*e.g.*, reactions [1]-[4]). Sometimes the metal solute sidearm included a standard taper joint which could be turned to make sequential solute additions more easily as they were needed. Only the lower sections of the legs are involved in the emf measurements; the upper portions are outside the furnace and are used during loading. This is the type I cell design.

far off of equilibrium with regard to other reactions.) The equilibrium condition was achieved in about 2 hr after adding Cd to the CdI_2 electrolyte, if stirring had been frequent. For gold additions, equilibrium was achieved in 4 hr or more, and further stirring or long standing did not alter the emf except at the highest temperatures studied, where a small amount of Cd evaporated. For temperature changes at a single composition, some measurements were taken about one-half hour apart, but most were taken more quickly.

Solubility measurements.—The cell that had been used for the study of Au-Cd alloys was held in the furnace at 773°K with sufficient stirring to ensure that equilibrium had been achieved. The cell was then taken out of the furnace at 773°K and cooled rapidly, consistent with a technique that had been used earlier (1). The cadmium that had dissolved into the electrolyte over the reference electrode was determined by breaking open the cell, washing away the electrolyte, and establishing the weight loss of the cadmium electrode.

Results, Methods of Calculation, and Conclusions

The significant figures carried reflect the differences between compositions which can be identified. The absolute compositions vary slightly because of the dissolution of some Cd into CdI_2 to form the equilibrium concentration of Cd_2I_2 which is unstable as the pure condensed phase but can be present in solution in the salt melt.

The effect of this solubility on n in $\Delta\bar{F} = -n\mathbf{F}\epsilon$ must be considered in the evaluation of thermodynamic properties from the emf data. (Contrary to popular assumption, the value of n is seldom whole-numbered for molten salt systems, and the effect of solubility equilibria such as for Eq. [6] must be considered even if an inert carrier solvent such as LiCl-KCl is being used.) For CdI_2 at 773°K the value of n has been recently determined by three independent experimental checks. First, and most directly, Houseman and Elliott (1) have shown that the value of the apparent n is markedly dependent on the charging rate, and Houseman (4) has carried out very slow conduction experiments which can be extrapolated to zero current. His value of effective n, reflecting both the concentrations and mobilities of the Cd_2^{++} and Cd^{++} species, is 1.87. Second, $n = 1.87$ is what agrees with the vapor pressure measurements for several systems as reported by Conant and Elliott (5). Third, $n = 1.87$ is what brings a number of dilute solutions into asymptotic approach to Raoult's law when activities are calculated from emf's, as shown by Conant (6), by Houseman and Conant (7), and by Conant and Elliott (5).

Because Houseman (4) has shown that the mobilities of Cd^{++} and Cd_2^{++} are nearly the same and that the solubility measurements by Topol and Landis (8) and by us here can be used for predicting n at 773°K, we will use the temperature dependence of solubility from Topol and Landis and will assume that equal mobilities continue to other temperatures in order to make our calculations of thermodynamic properties. These solubility values from Topol and Landis also agree with our solubility measurements at 713°K, as is discussed later.

By using the assumption and solubilities just discussed, we get the calculation of n by the equation

$$n = 1.87 + 0.001(773T) \qquad [7]$$

(Although solubilities often follow a logarithmic dependence on T, Topol and Landis's values do not appear to require this form.)

To understand the calculations using Eq. [7], recognize that Topol and Landis's solubility of Cd at 773°K is 0.065 mole fraction, leading to 0.065 of the Cd having zero valence and 0.935 having a valence of 2. Our value for this solubility is 0.063 in this present paper. Doubling the 0.935 (or 0.937) leads to a value of $n =$ 1.87. This calculation is independent of what species form as long as mobilities of the species and their charges are equal.

Results with Cell Type I

Measurements using cells as in Fig. 1 were made on two types of emf's: (*a*) between the cadmium reference electrode and the alloy whose composition could be varied, and (*b*) between cadmium or alloy and bare electrodes made of tungsten which dipped into molten CdI_2, the CdI_2 being partially or completely saturated with Cd. As will be developed, the former were of "thermodynamically" expected form, but the latter did not conform to usual expectations.

Metal vs. alloy studies.—The experimental emf values at 4 mole fractions of the solvent taken over a temperature range of 50°K are represented in Fig. 3-6.

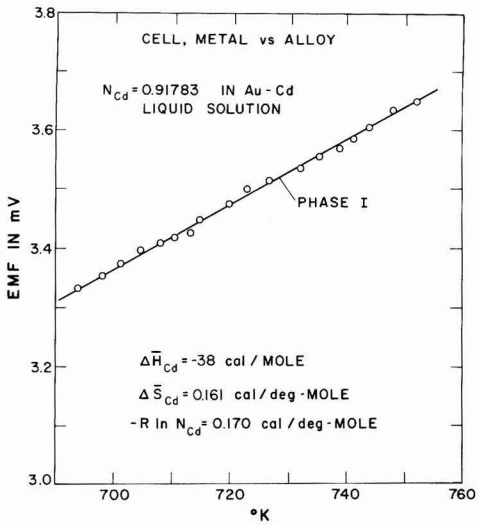


Fig. 3. Reaction [5a] for Cd vs. Au-Cd at $N_{Cd} = 0.91783$. No phase boundary for liquid Au-Cd solution is detected over the temperature range studied.

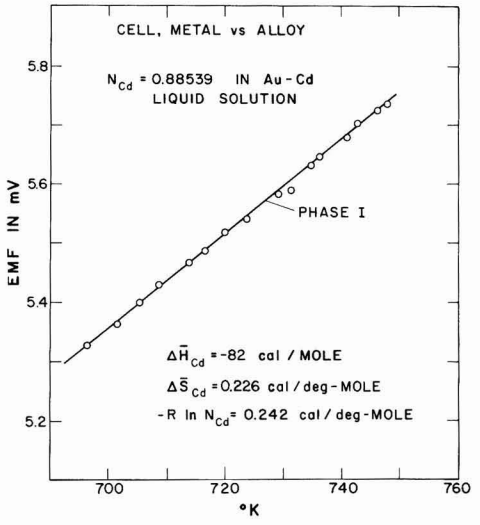


Fig. 4. Reaction [5a] for Cd vs. Au-Cd at $N_{Cd} = 0.88539$. No phase boundary for liquid Au-Cd solution is detected over the temperature range studied.

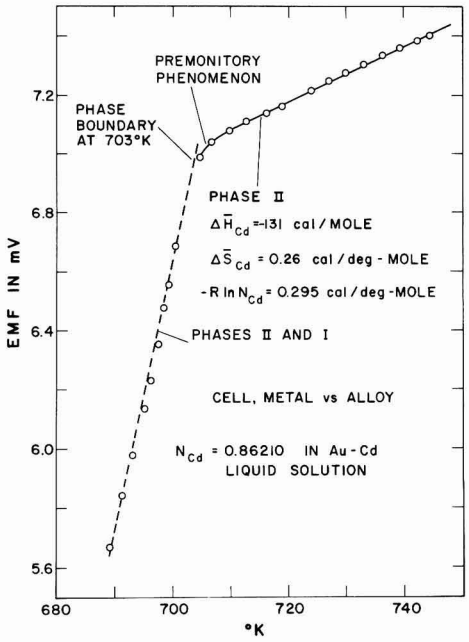


Fig. 5. Reaction [5a] for Cd *vs.* Au-Cd at $N_{Cd} = 0.86210$. The liquidus is detected at 703°K, and premonitory phenomen are detected about 4°K before the liquidus temperature is reached.

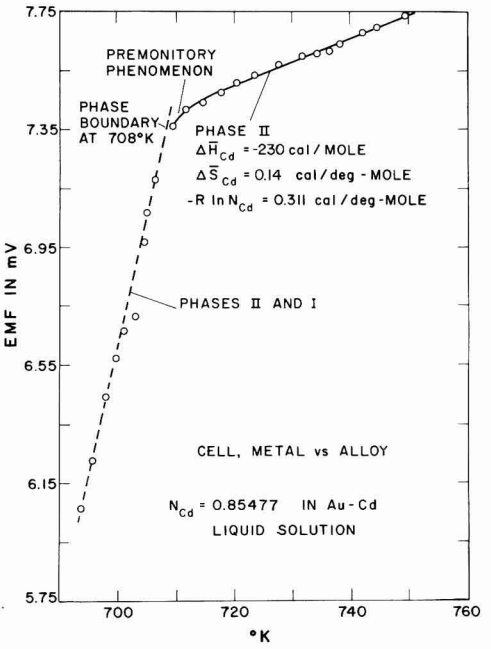


Fig. 6. Reaction [5a] for Cd *vs.* Au-Cd at $N_{Cd} = 0.85477$. The liquidus is detected at 708°K, and premonitory phenomena are detected for perhaps 4°K before the liquidus temperature is reached.

Pure single-phase region is observed at $N_{Cd} = 0.91783$ and 0.88539 (Fig. 3 and 4), but for $N_{Cd} = 0.86210$ and 0.85477 (Fig. 5 and 6) there are phase changes as indicated by the slope shift in the emf-temperature data. In the transition region between pure single-phase region linearity and the two-phase region linearity there is in each case a transition region labeled "premonitory phenomena."

The thermodynamic quantities listed have been calculated using Eq. [7], but we have neglected the small changes of alloy composition as the solubility of Cd in CdI_2 changes with temperature.

Note that with correction of n off the usually accepted 2, the partial molal entropy of the Cd falls close to the ideal random solution value for the three higher concentrations. If n were accepted as 2, the apparent partial molal entropies would be about 50% larger than the ideal values.

Figure 7 and Table I give the variation of emf and activity with composition for a single temperature using $n = 1.93$ corresponding to the equation above. Table I indicates both the added alloy composition and the corrected composition due to Cd_2I_2 formation in the iodide.

Conclusions from the Cd vs. Au-Cd emf studies.—The liquidus is detected at two compositions (Fig. 5 and 6) and occurs at temperatures consistent with the accepted phase diagram (9).

Premonitory phenomena (depressions of the cell voltage) are observed slightly above the liquidus at these same compositions. In further support of this view, premonitory phenomena near phase boundaries (including the liquidus) have already been detected in this same system by vapor pressure-composition studies at constant, but higher, temperature (939°K) using an isopiestic balance (10).

Note that these premonitory phenomena show smaller voltages than extrapolation would predict. Of course, the total activity must drop for any such reaction to occur, so we conclude that the necessary component activity decrease and phase stabilization must occur for the nonvolatile component. This kind of activity behavior is not uncommon: For example, the

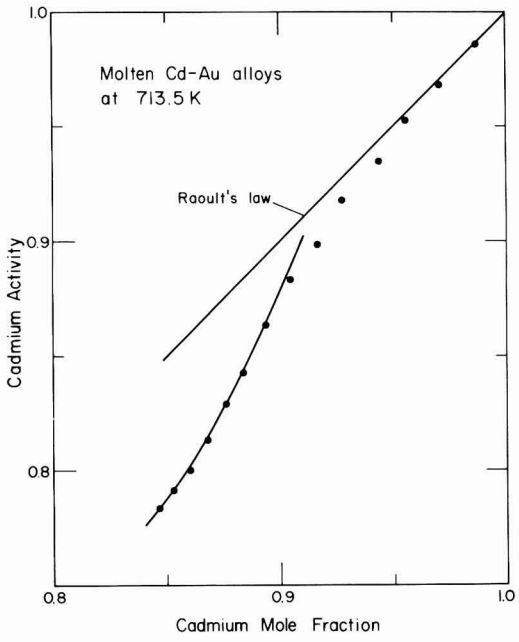


Fig. 7. Cadmium activity-mole fraction relations from emf's (reaction [5a]) for various molten Au-Cd alloys at 713.5°K. At least one liquid alloy structural change is probable at ~0.9 mole fraction of Cd, consistent with a change detected earlier at this composition by vapor pressure at 939°K.

Table I. Composition-emf data for the cell of: W, Cd, Au (liquid solution)/CdI_2 (l)/Cd(l), W at temperature 713.5°K

Gold added, total g	Cadmium mole fraction Added[a]	Corrected[b]	Temperature (°K)	Emf[c] (mV)	a_{Cd}[d]
0	0	0	713.5	(0.0240)	
0.70255	0.98647	0.98624	713.2	0.4584[c]	0.98570
1.55000	0.97055	0.97013	713.2	1.0400	0.96785
2.35210	0.95609	0.95536	713.6	1.5571	0.95228
3.02770	0.94418	0.94327	713.5	2.1572	0.93449
3.93975	0.92857	0.92742	713.3	2.7480	0.91729
4.58530	0.91783	0.91652	713.6	3.4178	0.89823
5.27025	0.90670	0.90477	713.5	3.9637	0.88295
5.97820	0.89547	0.89385	713.7	4.6829	0.86329
6.62940	0.88539	0.88364	713.6	5.4602	0.84246
7.13005	0.87780	0.87594	713.9	5.9759	0.82899
7.67010	0.86975	0.86779	713.7	6.5903	0.81312
8.19260	0.86210	0.86004	713.6	7.1122	0.79988
8.70165	0.85477	0.85263	714.0	7.4418	0.79175
9.14515	0.84849	0.84627	713.7	7.7597	0.78362

[a] The amount of Cd added was 29.2264g.
[b] Assumed solubility of Cd in CdI_2 from present investigation (same as Topol's and Landis's data): 713°K, N_{Cd} = 0.0348.
[c] Corrections have been added to the observed emf to give the listed readings. This correction, 0.0240 mV, was measured when no solute had been added to either cell leg. Those emf readings were taken after sufficient stirring and did not change after further stirring or long standing.
[d] Calculated for 1.93 electrons involved per cadmium atom transferred.

solid $CeCd_{\sim 4.5}$ microphases showed metastable extensions which include many examples of both too high and too low Cd component activity before the transformation took place (11).

The change of activity-composition behavior at $N_{Cd} \approx 0.9$ shown in Fig. 7 was noted also at higher temperatures in the earlier vapor pressure studies (10). Likewise, comparing Fig. 3-5 *vs.* 6, there is a sharp decrease of the $\Delta\bar{S}_{Cd}$ from that for ideal solutions as we pass from 0.86210 to 0.85477 mole fraction of Cd. It seems likely that this change of entropy behavior corresponds with the liquid-liquid transformation at 0.8620-0.8625 shown at 939°K in the isopiestic balance studies just mentioned.

Metal or alloy vs. bare electrode studies using cell type I and CdI_2-Cd_2I_2 electrolytes.—In the development of the stirred H-cell design (1, 2) it became clear that, if the W or Mo current leads to metal and alloys were not insulated as they passed through the electrolyte, then the cell behavior would be erratic in the μV range. It was important sometime to learn the causes and implications of this behavior.

Preliminary studies (to be presented in part later under the heading cell type II) had indicated that W, Mo, and graphite all showed persistent voltages in the millivolt range when bare electrodes dipping in CdI_2 were compared against Cd or Au-Cd in contact with the bottom of the electrolyte. Furthermore, use of cell type I with Mo or W electrodes in $SnCl_2$-based electrolytes *vs.* Au-Sn molten alloy shows similar behavior. [This latter work was carried out along with the Au-Sn alloy liquid structure work (3) but was not included in the publication of that already complex paper.]

For the present studies measurements were made on both saturated and unsaturated solutions of Cd in CdI_2 (*i.e.*, CdI_2-Cd_2I_2 solutions).

Unsaturated solutions.—Cells as in Fig. 1 were operated with initially no liquid Cd phase on the right side and with small solid Cd pieces in the sidearm. The emf-temperature relationships for reaction [4], *i.e.*

$$W, Cd/CdI_2\text{-}Cd_{(satd)}//CdI_2\text{-}Cd_{(unsatd)}/W$$

at unsaturated solution compositions are plotted in Fig. 8-11. The compositions, N_{Cd} = 0.0143 and 0.0348, do achieve saturation at the lower temperatures, however.

For the first few days the solutions in one leg of the H-cell were not allowed to become saturated. First, limited Cd was added to the CdI_2 to partially saturate it, and the solution was stirred periodically for a day while composition and temperature equilibrium was being achieved.

The next day more Cd was added and the solution was stirred periodically for 4 hr. Then the stirring was stopped, and the system was cooled slowly. The emf changes were systematic (Fig. 8) with the two electrodes agreeing to about 1 mV. The system was then reheated and again slowly cooled, this time over a two day period with cooling by increments rather than steadily (Fig. 9). By this time the two electrodes agreed within ~0.2 mV. A further heating and cooling cycle is shown on Fig. 10.

Because we do not know how to handle the mixed n values (the CdI_2/Cd_2I_2 ratios are different in the two cell legs), we have calculated apparent values of $\Delta\bar{H}_{Cd}$ and $\Delta\bar{S}_{Cd}$ as shown on Fig. 9 by using $n = 2$.

Although the solutions followed a single relationship during a heating or a cooling half-cycle, there were slower over-all changes in the apparent values of both the magnitude of the emf and of the slope of the emf-temperature relationships. The magnitudes of the emf values did not appear to be approaching zero, however. Considering the emf at 740°K, the emf dropped from 82.5 mV on the second day, to 64 on the third day, to 56 on the fifth day, to 55 on the sixth day. Likewise, the corresponding apparent $\Delta\bar{S}_{Cd}$ fell from 25 to 18 eu to 15 eu and remained 15 eu. After the initial changes, the major changes of emf and slope seemed to be associated with hysteresis following electrolyte phase changes such as freezing. (Does the electrode surface crack and strain?) For example, in Fig. 9 the freezing of CdI_2 is detected in the initial cooling, but the emf's are lowered for the higher temperatures as well (Fig. 10 *vs.* Fig. 9).

Comparing Fig. 10 and 11 will show the influence of electrolyte composition upon the emf. Likewise, these data pick off the Cd-CdI_2 phase boundary both on cooling and on heating. Finally, they show that shorting the two "inert" electrodes together allows an

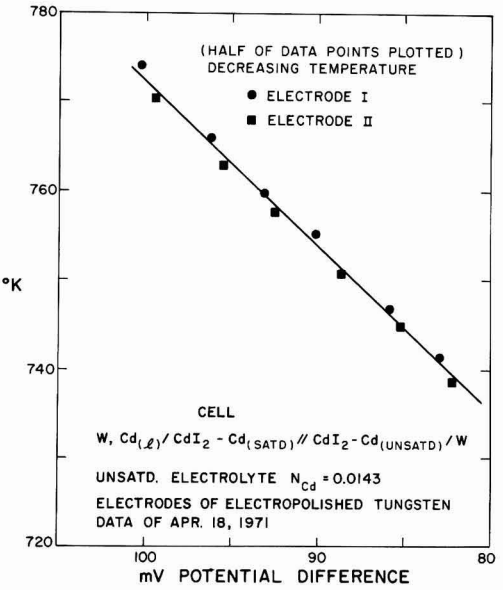


Fig. 8. Studies of the emf between a cadmium electrode in one leg of an H-cell and tungsten electrodes in an unsaturated Cd-CdI_2 solution in the other leg. (Electrode I was high in the solution and electrode II was low.)

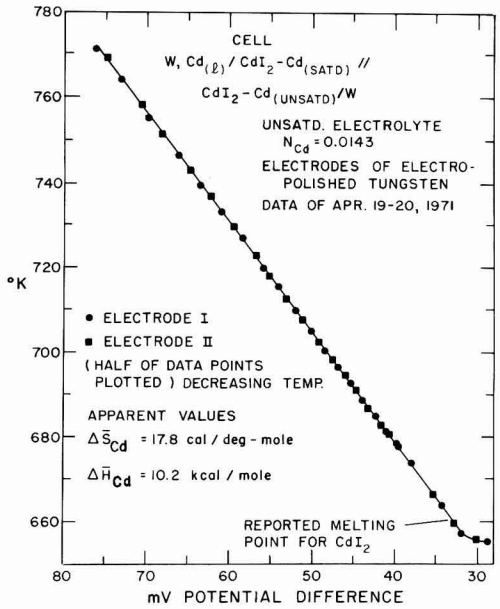


Fig. 9. Two-day cooling of the cell in Fig. 8. Cooling was not continuous. $\Delta\bar{H}_{Cd}$ and $\Delta\bar{S}_{Cd}$ calculated with $n = 2$, *i.e.*, no correction for Cd_2^{++} was made here. See text.

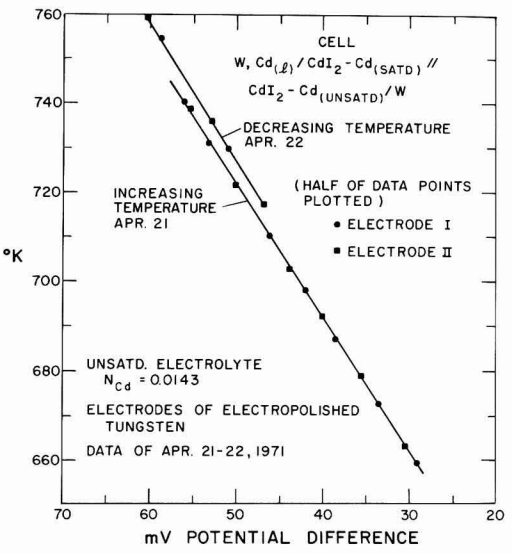


Fig. 10. Cell behavior for the cell in Fig. 8 and 9 as shown 3 and 4 days after freezing then remelting the electrolyte.

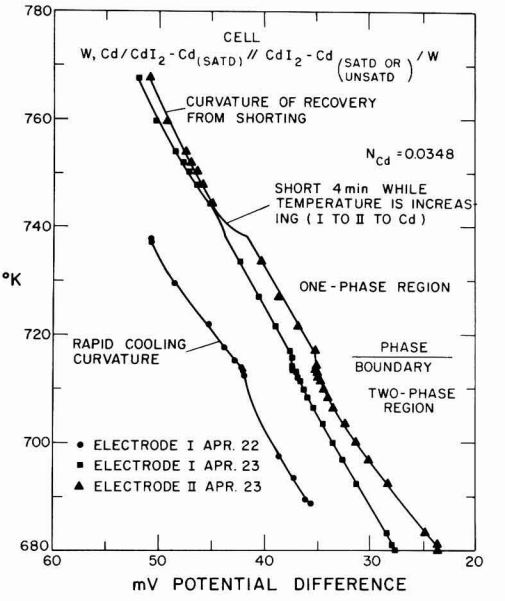


Fig. 11. Saturated and unsaturated electrolyte and effects of electrochemical drain at $N_{Cd \text{ in } CdI_2} = 0.0348$ on the emf of bare tungsten electrodes.

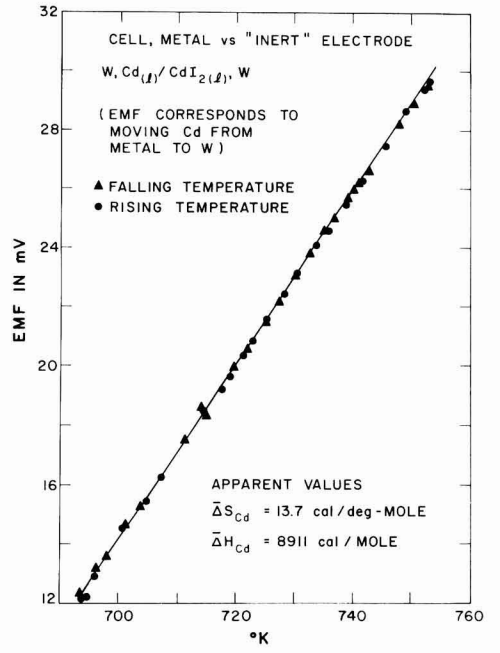


Fig. 12. The effect of temperature on the bare tungsten electrode emf in CdI_2 solutions saturated with Cd. The CdI_2 and Cd phases in contact were stirred intermittently during heating and cooling stages. Heating and cooling stages were separated by 3 days.

electrochemical drain which does change the electrode behavior temporarily.

Saturated solutions.—These measurements refer to the potentials observed in comparing a molten Cd reference electrode with a bare tungsten electrode dipping into molten CdI_2-Cd_2I_2 solution. The Cd_2I_2 concentration is set by equilibration with either molten Cd or molten Au-Cd.

Figure 12 shows tests of reaction [1]. Physically, referring to Fig. 1, the reference Cd was in the left leg and the bare electrodes were over a second Cd melt in the right side. Later, gold would be added to the right-side melt to give the data in Fig. 13, again with reference to the same Cd in the left side.

With regard to Fig. 12 note that the heating and cooling half-cycles gave the same results even though the half-cycles were separated by three days. Similar

temperature coefficients of emf are shown by the W *vs.* Cd couples where Au-Cd alloys supplied the Cd_2I_2 to the electrolyte in the W region (Fig. 13).

These voltages were stable, reproducible, and (according to usual expectation) very large. The changes of voltage with alloy composition (~3 mV on Fig. 13) were smaller than would have been expected from the changes of alloy activity (~7.5 mV on Fig. 6) and the temperature coefficients were different. Part of the difference in temperature coefficient is a consequence of carrying out the measurements for Fig. 13 without stirring; the metal-electrolyte and the alloy-electrolyte interfaces adapt quickly to the changing n but the electrolyte CdI_2-Cd_2I_2 mixture in the bulk of that phase readily supersaturates relative to metallic Cd. There are further differences, however, because the line for $N_{Cd} = 0.85477$ as the saturating solution does not follow the other trends of voltage. (Remember that the $\Delta\bar{S}_{Cd}$ at $N_{Cd} = 0.85477$ was also anomalous, Fig. 6.)

Apparently traces of impurity (probably CdO) do influence the voltage significantly, since the long-term stability was not achieved until after the cell had been at temperature with much stirring for a month. A few milligrams of material had then vaporized to form a brown condensate ring. (This could, for example, have been volatile tungsten oxyiodides whose vaporization removed $O^=$ from the electrolyte solution.)

In this case the effect of stirring was not large. The data for Fig. 12 were taken with stirring during heating and cooling while the alloy solutions were stirred extensively at the highest temperature before cooling but not during the cooling.

Conclusions from the unsaturated and saturated solution studies using type I cells.—These emf's are real, large, and roughly reproducible. They satisfy many usual tests of equilibrium. They vary with composition. They react to phase changes. They vary reproducibly with temperature during tests over several hours. They react to and recover from drains and imposed voltages.

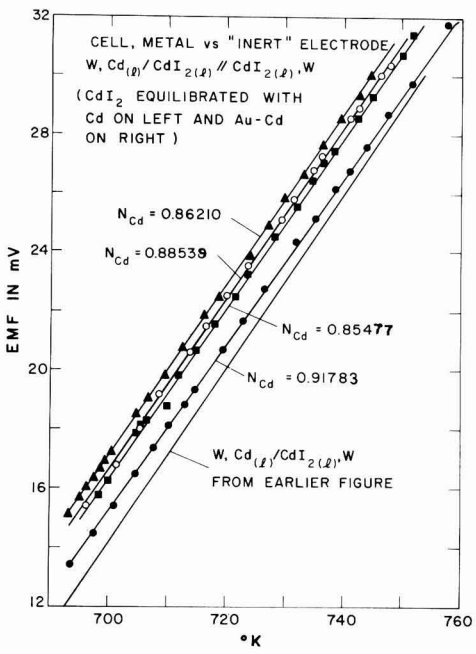


Fig. 13. The effects of temperature and composition on the emf of cells in which bare tungsten electrodes dip into CdI_2 equilibrated with Cd-Au alloys of various compositions.

Considering that (for Henry's law solutions) 30 mV would correspond to about one-fourth of the saturation concentration at these temperatures, it would be most difficult to write the voltages off as due to reproducible partial saturation of the CdI_2 by Cd. Furthermore, the electrolyte phase is at least nearly homogeneous as shown by comparison between different electrodes in different parts of the electrolyte. This homogeneity is much more strongly emphasized by results from the type II cells to be discussed later. Finally, including information from our unpublished work, different electrode materials do show different voltages in the same electrolyte solutions. Another aspect of this difference in behavior is discussed later during analysis of published phase diagrams and solution activity studies.

Likewise, these voltages cannot be written off as the "stray voltages which always occur when one dips metal into electrolyte." Here there is several per cent of Cd_2I_2 so that the activity of Cd as set by metal or alloy is well buffered even though metallic Cd is, of course, not an electrolyte species. This is not a case where a tiny concentration of a species varies tremendously during any attempt to measure it.

It is our interpretation that W (and at least most other potentially useful solid electrodes for these molten salt systems) will form a protective film (probably oxide) over the metal surface. The surface comes into equilibrium fairly rapidly with the electrolyte, and it reacts to changes in the electrolyte activity. Thus the chemical equilibria available involve electrolyte and surface.

But the electrochemical equilibrium permits attack on the base W because the surface passes ions and the metal passes electrons. Thus it can reflect very different reactions from those which have come into equilibrium during the long purely chemical equilibration.

Because unit activities of the base W and the surface film are not involved, we see no way to predict the magnitudes of the emf effects superimposed on the usually expected voltages.

Solubility of Cd in CdI_2.—The cell which had been used for the unsaturated electrolyte studies was broken open after cooling rapidly from 773°K. The remaining metallic Cd was found to contain 2.07055g less than initially had been added, the loss being due to saturating 100g of CdI_2. The corresponding solubility of Cd in CdI_2 at 773°K is 0.063 mole fraction.

The solubility from the temperature coefficient of emf (Fig. 11) is 0.0348 at 713°K.

Both of these solubilities are completely in agreement with Topol's and Landis's results (8).

Results with Cell Type II

This cell design is shown in Fig. 2. The cell was (*a*) loaded with 78.361g Cd, 18.573g Au, 183.5g CdI_2, and ~0.5 atm Ar, (*b*) heated at 773°K for nearly 3 months, (*c*) stirred occasionally, (*d*) electrically drained periodically, and (*e*) monitored for open circuit at six tungsten *vs.* alloy couples.

The results of the emf measurements are indicated on Fig. 14. The following observations should be made.

1. The plots are offset on the ordinate to avoid overlap.
2. On any particular day all six W *vs.* Au-Cd couples showed nearly the same voltage.
3. The stirrer voltages (electrodes made from W wire) were consistently slightly larger, by 1-2 mV, than those of the potential sensors (made from W rod).
4. All voltages increased together with time. Apparently this change was associated with the change of alloy composition resulting from slow evaporation of Cd to cooler portions of the cell. Melting the evaporated Cd (~10% of the Cd) back into the alloy decreased the voltage.
5. Electrically shorting the large stirrer leads together and to the alloy caused the voltage to drop.

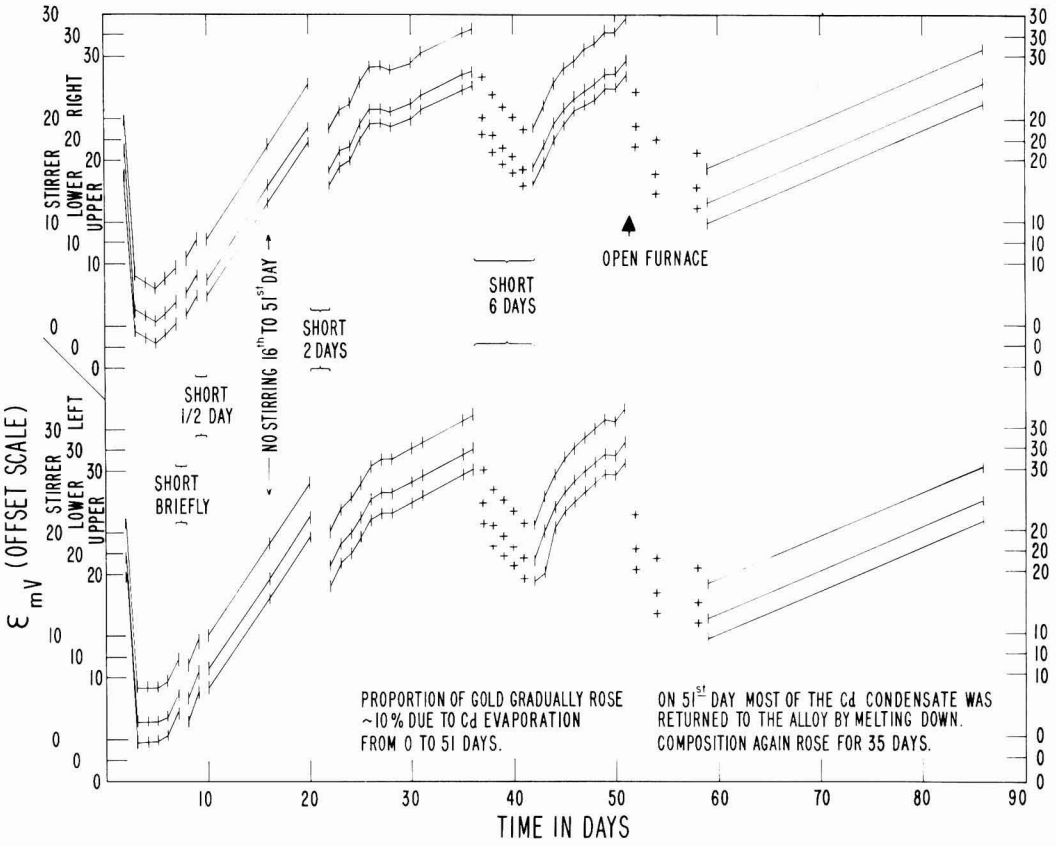


Fig. 14. Offset-scale plots for the open-circuit voltages of W vs. Cd-Au couples (reaction [2]) in a type II cell. Six electrodes vs. Cd-Au are represented as identified beside the ordinate: three in left leg, three in right; upper and lower are potential sensors; indicated shorting is via outside connections between the stirrer electrodes and the alloy. See text.

The potential sensors followed the drained electrodes.

6. Reaction of the alloy with the electrolyte appeared to create nearly identical conditions in the two electrolyte regions.

7. Reaction of the electrolyte with the oxidized potential sensors and with the unoxidized current collectors on the stirrers yielded nearly equivalent behavior in both (except for the 1-2 mV difference which we associate with compositional and strain differences between W wire and rod).

Conclusions from the type II cell measurements.— With adequate stirring and equilibration time, the metal or alloy sets the Cd_2I_2 concentration in the electrolyte following K in reaction [6]. The chemical reaction of the electrolyte with the electrode surfaces sets the surface activities. The electrochemical reaction can involve the base metal, not just its surface coat, and can be very different from the feasible purely chemical reactions. This difference can lead to anomalous voltages in what have been treated as inert electrodes in molten salts.

See also the conclusions regarding type I cells given earlier and the applications to published data to follow.

Applications of These Conclusions to Published Data

We have long believed that a major source of irreproducibility and scatter in the published data for molten salt emf cells lies with improper equilibration with the electrolyte and with failure to insulate the "inert" leads which pass through the electrolyte. These present measurements strongly support that belief.

A number of papers have been published in which the activities of dissolved species have supposedly been determined by measuring the voltages of bare W, Mo, or graphite "inert" electrodes dipping into unsaturated solutions as compared with saturated solutions. In principle these are cells with provision to carry out reactions like reaction [3], but many systems can be used. In physical design the cells can look much like cell type I.

As noted in this present paper, one can determine solubilities and activities as long as he corrects for the residual "inert" electrode voltage some way, *e.g.*, note the correct determination of the solubility of Cd in CdI_2 at 713°K by the change of emf-temperature pattern in Fig. 11. However, one would be incorrect to assume that zero voltage difference between bare electrode and reference metal gave the saturation composition.

Figures 15 and 16 show data where people have neglected the bare electrode voltage. In Fig. 15 Mashovets and Poddymov (12) and Crawford and Tomlinson (13) have attempted to establish the activity of Cd in $CdCl_2$ solutions by calculation from the emf's of bare Mo, W, or graphite *vs.* molten Cd, assuming the electrodes are inert. These voltages differ by as much as 5 mV, corresponding to a 15% difference in apparent activity. In Fig. 16 we see the Cd-$CdCl_2$ liquidus as established by standard techniques and as "established" by extrapolating to zero voltage by Mashovets and Poddymov.

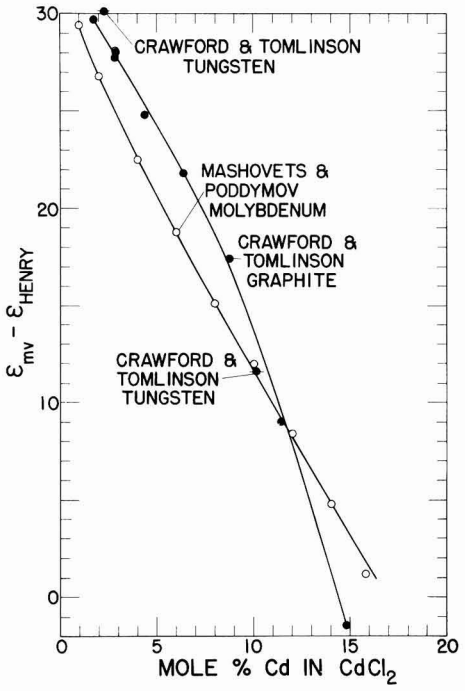


Fig. 15. Cd-$CdCl_2$ activity studies by emf using "inert" graphite, molybdenum, and tungsten electrodes at 873°K.

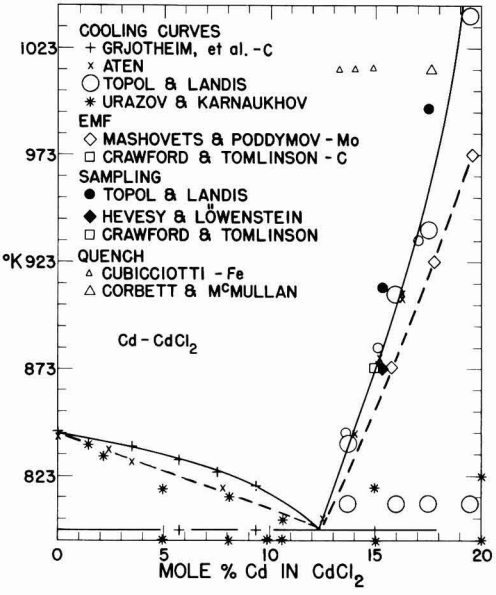


Fig. 16. Cd-$CdCl_2$ phase diagram measurements by different techniques with use of electrical conductors indicated. Hedger and Terry data are indicated by small circles.

Melting, Freezing, and Premonitory Phenomena

Both here in emf and earlier in vapor pressures (10), there has been evidence of unexpected variations of activity with composition near phase boundaries for molten Au-Cd alloys. Similar phenomena have often been reported in sensitive properties such as changes of viscosity with temperature; thus the phenomena are detectable whether the phase boundary is approached with changing composition or with changing temperature.

Changes in property near a phase boundary are often called "premonitory phenomena," and we accept the term even though our measurements indicate that these deviations in the trends of properties reflect the true, equilibrium condition rather than some phenomenon akin to prescience. For molten alloys in this case, but also apparently for other kinds of solutions, *e.g.*, molten salts, when a composition is close to the phase boundary there can sometimes exist significant quantities of atoms in atomic groupings which are similar to the atomic groupings which will be met when the adjacent phase becomes stable. These structures exist primarily because a large entropy of mixing overcomes an unfavorable enthalpy, thus they are often inherently dilute, but the fact of their existence indicates the solution free energy is decreased by their formation. In the case of metallic bonds in alloys, the shift of expected activities is particularly sharp; this sharpness reflects the fact that impurities weaken the metallic bond, and the new structures look like impurities to the resonance in the existing "metallic lattice."

Melting and freezing.—Premonitory phenomena and clustering similar to those we observe have been examined for pertinence to the relationship of solids to liquids, *e.g.*, (14) and (15). This relationship has been subject to controversy. For example, Borelius (16) argues with experimental support that a continuous (but physically unattainable) curve joins the properties of a liquid metal to those of its solid, Danilov and Neimark [see Neimark in Ref. (17)] show x-ray correlations between solid and liquid mercury, and Saxton and Sherby (18) demonstrate good correlation between solid and liquid properties. Turnbull (19) presents the thermodynamic argument that melting occurs because of the crossing of the free energy-temperature curves, which for the solid and liquid, are "quite independent" of each other. He concludes that, "Therefore there should be no unusual changes in the properties of either the liquid or the crystal when they pass from their stable to their metastable condition." Also supercooling is sometimes used to conclude that the melting-freezing phenomena involve changes only in the solid, since the liquid may be unchanged at the melting point while the solid always does change. Assigning all the pretransformation effects to the solid leads to a further theoretical concern about the sharpness of the melting point and the absence of rapid changes in the solid properties close to the melting point as calculated by melting models related to that of Lennard-Jones and Devonshire.

In our view prenuclei similar to those discussed in the previous section would be important to certain solid-liquid equilibria. Where the solid and liquid structures were very different, there would be two possible liquid structures at the melting point: (*i*) One form would be a simple continuation of the usual liquid properties to lower temperatures; this structure would be metastable (though otherwise showing equilibrium behavior), supercoolable, and unable to exist in equilibrium with the solid. (*ii*) The second and stable liquid form would contain the solid precursors (prenuclei) at an equilibrium concentration. It is this latter form that might pass along a continuous but hypothetical curve relating solid and liquid properties as Borelius proposes. Stabilizing the liquid by the presence of prenuclei would remove part of the temperature region in which the solid was stable and would reduce the opportunity to observe premelting phenomena in such a system.

Once a prenucleus happened to form it would presumably act as a template for the formation of the equilibrium concentration of prenuclei. This is indicated in our systems by the absence of vapor pressure results intermediate between those for the presence or

absence of prenuclei, even in the prenuclei region the results are reproducible. Likewise, our second phases apparently form without difficulty once their equilibrium concentration has exceeded their solubility in the liquid, as indicated by the absence of metastable extensions (supersaturation) into two-phase regions by solutions containing prenuclei.

The pertinence of this work to the freezing of pure substances seems to be as follows: If the usual solid and liquid structures are rather different as emphasized by Turnbull, then the solid and liquid cannot be in equilibrium until the liquid becomes saturated with prenuclei. The freezing point is that point where the cooling liquid becomes saturated with prenuclei, *i.e.*, where the equilibrium concentration or size of prenuclei becomes greater than the liquid can hold in solution. In this view the deviation in properties between the supercoolable and nonsupercoolable liquids occurs not at the freezing point but rather at some higher temperature.

If the solid and liquid metal structures are very simply related as emphasized by Borelius, then any supercooling would seem to result largely from the metallic resonance energy which would have to be overcome in the region where the solid first formed in the liquid phase. In this case there would be no particular reason to expect that a significant concentration of prenuclei would exist in the liquid at equilibrium with the solid.

Acknowledgment

The work reported in this paper was sponsored in part by the United States Atomic Energy Commission.

Manuscript submitted July 26, 1973; revised manuscript received Oct. 7, 1974. This work was presented in part as Paper 145 presented at the Houston, Texas, Meeting of the Society, May 7-11, 1972.

Any discussion of this paper will appear in a Discussion Section to be published in the June 1976 JOURNAL. All discussions for the June 1976 Discussion Section should be submitted by Feb. 1, 1976.

Publication costs of this article were partially assisted by Los Alamos Scientific Laboratory.

SYMBOLS

$\Delta\bar{F}_{Cd}$, $\Delta\bar{H}_{Cd}$, and $\Delta\bar{S}_{Cd}$ partial molal free energy, enthalpy, and entropy of the Cd component of solution

K equilibrium constant

n effective valence for the Cd_2^{++}-Cd^{++} mixture for use in calculation of activity and free energy from emf; the calculations involve both concentrations and mobilities of species where mixed valences are involved

$\mathbf{F}$ Faraday constant (23,061 cal/V equiv)

e cell potential

N_{Cd} Cd mole fraction

a activity

T degrees Kelvin

X Cl, Br, or I

REFERENCES

1. B. L. Houseman and G. R. B. Elliott, *This Journal,* **116,** 1363 (1969).
2. G. R. B. Elliott and J. F. Lemons, *ibid.,* **114,** 935 (1967).
3. P. L. Robinson and G. R. B. Elliott, *High Temp. Sci.,* **4,** 1 (1972).
4. B. L. Houseman, Submitted for publication.
5. D. R. Conant and G. R. B. Elliott, Submitted for publication.
6. D. R. Conant, *J. Chem. Eng. Data,* **16,** 430 (1971).
7. B. L. Houseman and D. R. Conant, Submitted for publication.
8. L. E. Topol and A. L. Landis, *J. Am. Chem. Soc.,* **82,** 6291 (1960).
9. R. Hultgren, P. D. Desai, D. T. Hawkins, M. Gleiser, and K. K. Kelley, "Selected Values of the Thermodynamic Properties of Binary Alloys," p. 247, American Society for Metals, Metals Park, Ohio (1973).
10. G. R. B. Elliott, C. C. Herrick, J. F. Lemons, and P. C. Nordine, *High Temp. Sci.,* **1,** 58 (1969).
11. G. R. B. Elliott and J. F. Lemons, in "Nonstoichiometric Compounds," R. Ward, Editor, p. 153, American Chemical Society, Washington, D. C. (1963).
12. V. P. Mashovets and V. P. Poddymov, *Zh. Prikl. Khim.* (English), **37,** 815 (1964).
13. G. A. Crawford and J. W. Tomlinson, *Trans. Faraday Soc.,* **62,** 3046 (1966).
14. A. R. Ubbelohde, *Angew. Chem. Intern. Ed. Engl.,* **4,** 587 (1965).
15. K. Furukawa, B. R. Orton, J. Hamor, and G. I. Williams, *Phil. Mag,* (**8**), 141 (1963).
16. G. Borelius, *Arkiv Fysik,* **11,** 217 (1956).
17. A. M. Samarin, Editor, "Structure and Properties of Liquid Metals," Academy of Sciences USSR, Moscow (1960). Translated as AEC-tr-4879, May 1962.
18. H. J. Saxton and O. D. Sherby, *Am. Soc. Metals, Trans. Quart.,* **55,** 826 (1962).
19. D. Turnbull, *Trans. AIME,* **221,** 422 (1961).

Sodium Phosphate Solubility and Phase Relations Basis for Invariant Point Chemistry Control

A. J. Panson, G. Economy, Chia-tsun Liu, T. S. Bulischeck, and W. T. Lindsay, Jr.*

Westinghouse Research Laboratories, Pittsburgh, Pennsylvania 15235

ABSTRACT

A study of sodium phosphate solubility and phase relations was made in the temperature region of 300°C. A sharp retrograde temperature dependence of solubility was observed for disodium phosphate solutions. Solubility at constant temperature is strongly dependent on the composition of the solution. A low-Na/PO_4-ratio solid precipitates incongruently from solutions that have Na/PO_4 ratios from 2.13 to 1.6. A high-ratio solid phase precipitates incongruently from solutions with Na/PO_4 above 2.13, which corresponds to an invariant or "drying-up" point in the system. Both solid phases have a range of variable composition, indicating that they are solid solutions. The effects of concentration and dry-up in localized zones are discussed in terms of this new information. The work shows that chemistry variations can be controlled by maintaining solution composition above the invariant point in the phase diagram.

Sodium phosphate has been used in boiler applications to serve as a pH buffer for corrosion control and for prevention of scale by precipitation of hardness ions. Phosphate concentrations in the bulk solution usually are maintained at low levels, for example in the range of 10^{-4} M or about 10 ppm or less. However, boiling in regions of restricted flow can lead to concentration and precipitation of sodium phosphate salts. Thus, it is important to know the composition and concentration of the saturated solutions that can be produced and the effects of salt precipitation on the composition of saturated solutions as dry-up progresses.

The work of Ravich and Shcherbakova (1) has provided key information on solubility and phase relations of sodium phosphate salts in the 300°C region. These workers determined that, at 300°C, trisodium phosphate solutions show retrograde solubility, and solutions of Na/PO_4 mole ratio 2.85 precipitate a congruent solid solution phase, while solutions of greater than 2.85 mole ratio precipitate a solid solution phase of lower mole ratio. Thus, an increase in solution mole ratio results when precipitation occurs. Significantly, solutions of mole ratio greater than 3 can be produced in this manner so that a "free caustic" condition which may be detrimental to boiler materials can be produced. The work of Ravich and Shcherbakova thus provided a basis for controlling chemistry variations on precipitation to prevent formation of "free caustic." By maintaining boiler water solutions at a mole ratio less than the congruent ratio of 2.85, formation of high mole ratio solutions can be prevented. Precipitation from solutions of mole ratio less than the congruent ratio, 2.85, leads to a decrease in solution mole ratio since a solid solution of higher mole ratio precipitates. This operating strategy for sodium phosphate solutions is known as congruent control (2).

The work described in this paper was undertaken to provide more complete information on solubility and phase relations of sodium phosphate solutions.

This work has investigated solubility and phase relations in the system Na_2O-P_2O_5-H_2O at Na/PO_4 molar ratios primarily from 1.6 to 2.4 at 300°C (572°F). Some additional data have been obtained at 275°C and 324°C, and also at some compositions of higher molar ratios.

* Electrochemical Society Active Member.

Key words: sodium phosphate, solubility, phase, precipitates, invariant point.

Experimental

The experiments were carried out in two-liter autoclaves of stainless steel (A.I.S.I. Type 316) and Inconel Alloy 600 fitted with internal sampling tubes and filters. Three different experimental procedures were followed in obtaining the solubility results: nonisothermal procedures with slow, steady heating and continuous sampling of the autoclave contents; isothermal experiments with saturation approached from below by increasing the temperature, followed by equilibration for periods ranging from hours to many days; and experiments in which saturation was approached by evaporation at approximately isothermal conditions. Samples of solution were periodically removed from the autoclaves and analyzed by potentiometric acid-base titrations. The results from all three methods were essentially in agreement within experimental error.

The compositions of solids precipitated from the saturated solutions were calculated from differences between successive solution samples. In some instances it was possible to recover solids from the vessels for direct determination of sodium-to-phosphate ratios and comparison with calculated compositions. The agreement was satisfactory.

Results

Disodium phosphate solubility.—The solubility of Na_2HPO_4 hydrates has been shown to increase with temperature (3, 4). Above the 95°C temperature for transition from the dihydrate to anhydrous Na_2HPO_4, the solubility appears to be nearly independent of temperature up to about 240°C. The results of our work show that the solubility becomes sharply retrograde above 240°C. Figure 1 shows this information in the form of a binary melting point phase diagram. The diagram suggests that a new solid is the stable saturating phase above 220°C at pressures close to the vapor pressure of the saturated solution.

We have found that the solids which precipitate from disodium phosphate solutions are incongruent as evidenced by our observation of a decrease in solution Na/PO_4 mole ratio on precipitation. Thus, the solids precipitating from solution have Na/PO_4 mole ratios greater than 2. At 300°C, the precipitating solid phase has a mole ratio of 2.1.

The solubility of disodium phosphate solutions shown in Fig. 1 was obtained by slowly heating under-

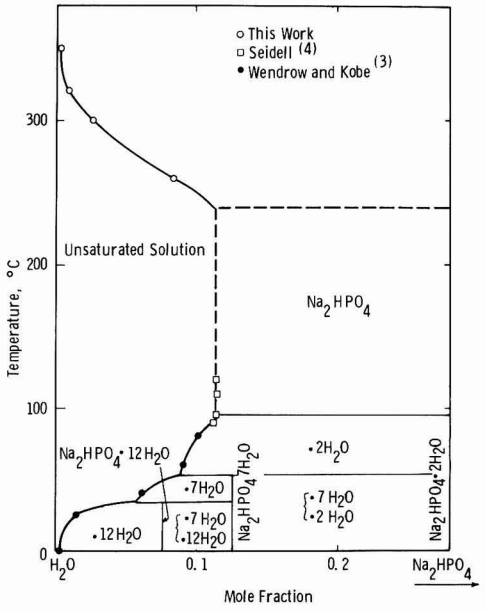


Fig. 1. Solubility of Na_2HPO_4 vs. temperature

saturated solutions in a Type 316 stainless steel autoclave and determining the temperature at which precipitation first occurred. Solution samples were withdrawn at temperatures by means of an internal sampling tube. The samples were conveniently checked for onset of precipitation by measuring their room temperature conductivity. Figure 2 presents these data. The solution compositions were determined by a potentiometric acid base titration. Tables I and II present the data of two experiments which show how the solution composition of disodium phosphate solutions proceed to lower mole ratio as precipitation proceeds on heating to higher temperatures. Mole ratios as low as 1.6 were obtained.

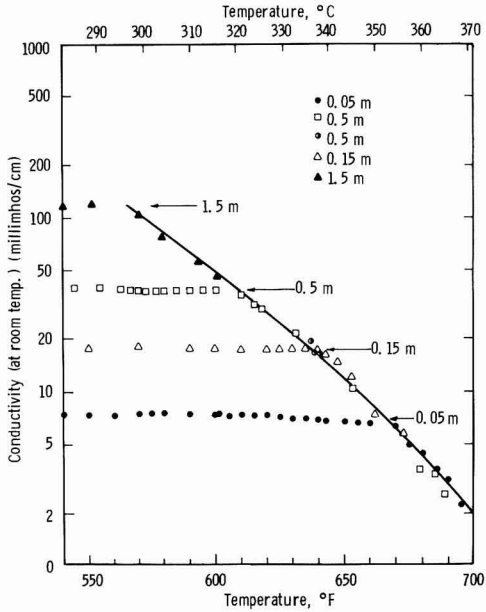


Fig. 2. Conductivity variations of disodium phosphate solutions on heating.

Table I. Precipitation from 0.5 molal solution initially $Na/PO_4 = 2$

Temp. on sampling (°F)	pH of sample diluted fivefold	m moles PO_4 in 5 ml	Na/PO_4 in soln (by titration)
100	9.08	2.41	2.00
205	9.02	2.43	2.00
310	9.00	2.43	2.00
400	8.88	2.45	1.98
495	8.46	2.42	1.97
555	8.23	2.38	1.95
600	7.98	1.29	1.86
640	7.80	0.76	1.83
645	7.73	0.54	1.87
660	7.51	0.20	1.75

Table II. Precipitation from 0.5 molal solution initially $Na/PO_4 = 2$

Temp. on sampling (°F)	pH of sample	m moles PO_4 in 5 ml	Na/PO_4 in soln (by titration)
Room temp.	9.06	2.41	2.01
510	8.55	2.41	2.01
617	8.25	1.61	1.93
648	7.83	0.57	1.86
677	7.3	0.16	1.69
679	7.3	0.16	1.63

Retrograde solubility and formation of low ratio solutions on precipitation from disodium phosphate solutions were not anticipated and were considered to be undesirable in the steam generator since corrosive reactions could result from the changed composition of the solutions.

Invariant point determination.—Application of the phase rule provided a means to avoid solution composition changes on precipitation. We anticipated that if the disodium phosphate solubility curve intersection with the trisodium phosphate solubility curve could be found then, at the point of intersection, two solid phases would be present, and the three component system, Na_2O, P_2O_5, H_2O, would be invariant. On evaporation, precipitation then would proceed with no solution composition changes as long as the two equilibrium solid phases were present.

A conceptual idea of the ternary phase diagram is provided in Fig. 3, which shows a solution invariant composition at the intersection of two solubility curves and a congruent composition. On this diagram, a solution of composition to the left of the congruent composition but to the right of the invariant composition will precipitate higher ratio solids and proceed in composition toward the invariant ratio at which point a second solid will precipitate and the system will be invariant.

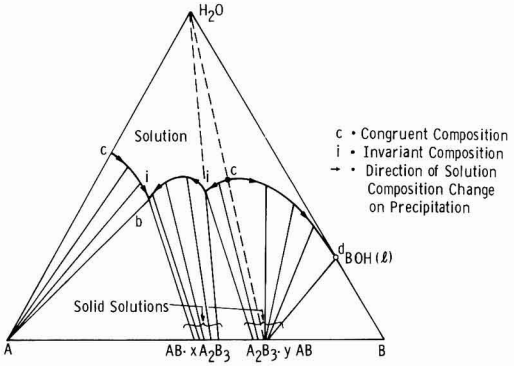


Fig. 3. Isothermal solubility diagram illustrating series of solid solutions between two compounds.

The solution composition is fixed and the over-all composition of the precipitating solid solutions will lie in the range covered in the gap between the two solids or in compositions between the solid solution composition limits. The final over-all composition depends on the initial solution composition.

A series of isothermal solubility determinations were made and the results are presented in Table III. The composition of the precipitating solids was determined by a mass balance and also, in some cases, by direct analysis of the solids as a check. Good agreement was found as shown in Table IV.

Figure 4 shows a plot of solution compositions in equilibrium with the various solid compositions formed at 300°C. The horizontal center section of the curve indicates that two solid phases coexist along with a solution of invariant composition at Na/PO_4 approximately 2.13. The other segments of the curve show variable composition for both solid and solution, indicating that the solids are solid solution phases. An upper congruent composition of 2.85 Na/PO_4 is indicated by the intersection with the dashed line. A lower congruent composition appears to occur at 1.6 Na/PO_4.

Table III. Results of isothermal solubility measurements and phase relationship studies

Run No.	Na/PO_4 ratio in solution	Na/PO_4 ratio in precipitated solid	Solubility, PO_4 molality
	275°C (527°F)		
56	2.0	—	>8.0
58	2.10	—	>2.5
82	2.15	2.13	3.79
85	2.15	2.23	3.26
30	2.24	2.87	1.29
31	2.25	2.86	0.64
44	2.32	2.73	0.74
57	2.57	2.84	0.42
75	2.69	2.76	0.41
72	3.24	2.83	0.26
	300°C (572°F)		
25	1.58	1.62	5.73
39	1.60	1.60	5.68
42	1.65	1.65	6.95
23	1.75	1.84	2.94
76	1.81	1.91	0.94
56	1.92	1.99	1.06
18	1.97	2.04	0.85
52	2.00	2.22	0.51
90	2.10	2.37	0.64
19	2.11	2.23	0.68
91	2.13	2.56	0.33
88	2.13	2.63	0.44
26	2.14	2.28	0.47
28	2.14	2.44	0.55
21	2.14	2.35	0.66
30	2.16	2.33	0.67
44	2.18	2.55	0.38
31	2.19	2.58	0.43
57	2.46	2.82	0.25
70	2.89	2.75	0.14
	324° (615°F)		
42	1.48	1.71	2.08
22	1.55	1.79	0.70
39	1.56	1.66	3.63
46	1.63	1.70	3.86
76	1.71	1.90	0.38
83	1.89	2.03	0.28
41	1.93	2.16	0.33
35	1.97	2.01	0.34
52	1.97	2.14	0.19
90	1.98	2.27	0.26
28	2.08	2.29	0.24
30	2.13	2.37	0.26
97	2.14	2.54	0.17
31	2.15	2.44	0.20
44	2.17	2.48	0.19
91	2.32	2.42	0.07
57	2.54	2.76	0.11
78	3.04	2.74	0.08
70	3.28	2.72	0.06

Table IV. Comparison between solid phase composition determinations

Run No.	Final temperature °C (°F)	Precipitate compositions: Direct analysis of recovered solids	Precipitate compositions: Result of mass balance calculation
18	316 (600)	2.00	2.01
19	300 (572)	2.22	2.15
21	300 (572)	2.33	2.35
22	321 (610)	1.80	1.79
26	301 (574)	2.24	2.28
27	321 (610)	1.77	1.72
30	324 (615)	2.37	2.37

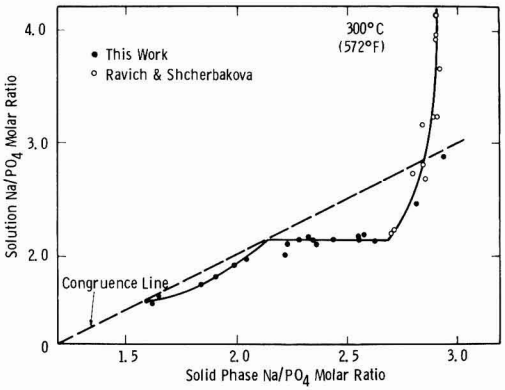


Fig. 4. Phase relationship in sodium phosphate precipitation equilibrium at 300°C.

Solubility is plotted as a function of solution mole ratio and temperature in Fig. 5. The curves were drawn as an intersection of two solubility curves as indicated by the plateau or two-phase region in the phase relation plot. The intersection is the invariant point at which two solid phases precipitate. On both Fig. 4 and 5, the data of Ravich and Shcherbakova are seen to be consistent with this extension of their work to lower Na/PO_4 ratios.

A test of the invariant point could now be made by heating undersaturated solutions of composition greater than the invariant ratio to cause them to precipitate and proceed to the invariant composition. Table V shows the results of experiments in which solutions of initial ratio greater than the invariant ratio were heated to cause precipitation. No further compositional decrease was observed after an initial decrease to the invariant ratio. The result is in strong contrast to the behavior of disodium phosphate solutions in the experiments described earlier in which a significant ratio decrease below 2 was observed. These solutions were initially at a composition lower than the invariant ratio so that they proceeded to decrease in ratio on precipitation moving towards some lower invariant ratio.

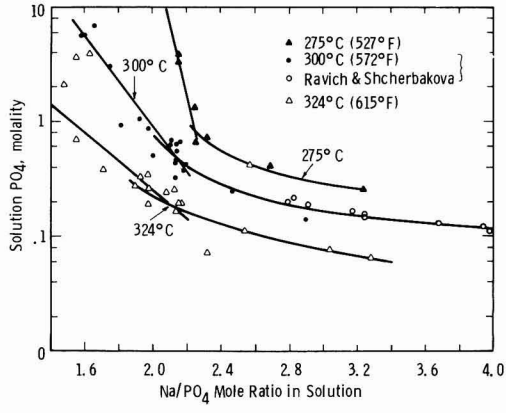


Fig. 5. Solubility of sodium phosphate solutions as a function of Na/PO_4 solution mole ratio.

Table V. Solution composition variation on precipitation of solids from solution initially close to and above invariant point

	Temperature range (°F)	Percent depletion of dissolved salt by precipitation	Solution Na/PO_4 ratio
A.	<541	0	2.31
	570-582	18	2.22
	591-605	45	2.15
	608-625	63	2.20
	633-653	76	2.18
	657-664	85	2.21
B.	<532	0	2.21
	570-590	14	2.17
	595-607	29	2.16
	612-627	56	2.15
	630-640	75	2.14
	649-667	89	2.14
C.	<467	0	2.19
	478-518	1	2.18
	575-587	16	2.15
	593-594	36	2.13
	610-614	49	2.14
	628-636	65	2.13
	636-659	82	2.11

Thus, solution mole ratio decrease below 2 in an acid direction on precipitation can be prevented by using solutions of mole ratio above the invariant ratio.

Discussion

In this work, we have found that disodium phosphate solutions have a sharply retrograde solubility above 240°C. Incongruent solids of higher mole ratio than 2 precipitate so that precipitation causes the solution mole ratio to proceed to lower or more acid values. An invariant composition of 2.13 at 300°C was found. The solubility increases sharply with decreasing mole ratio from the invariant point of 2.13 to 1.6.

These results provide a rational basis for controlling the composition of sodium phosphate solutions in boilers. As previously recognized by Marcy and Halstead (2), the Na/PO_4 ratio should be maintained below the upper congruent composition to avoid excessive alkalinity caused by incongruent precipitation during evaporative concentration. This work indicates that the Na/PO_4 ratio should also be maintained above the invariant composition to avoid composition shifts toward the lower ratio compositions of very high solubility as evaporative concentration and dry-up proceed.

Manuscript submitted Oct. 17, 1974; revised manuscript received March 12, 1975. This was Paper 81 presented at the New York, New York, Meeting of the Society, Oct. 13-17, 1974.

Any discussion of this paper will appear in a Discussion Section to be published in the June 1976 JOURNAL. All discussions for the June 1976 Discussion Section should be submitted by Feb. 1, 1976.

Publication costs of this article were partially assisted by Westinghouse Electric Corporation.

REFERENCES

1. M. I. Ravich and L. G. Shcherbakova, *Izvest. Sektora Fiz-Khim Analiza, Inst. Obshch. Neorgan. Khim., Akad. Nauk SSSR*, **26**, 248 (1955).
2. V. M. Marcy and S. L. Halstead, *Combustion*, **35**, 45 (1964).
3. B. Wendrow and K. A. Kobe, *Ind. Eng, Chem.*, **44**, 1439 (1952).
4. A. Seidell and W. F. Linke, "Solubilities of Inorganic and Metal Organic Compounds," 4th ed., Vol. II, American Chemical Society, Washington, D.C. (1965).

Chemisorption on Powdery Indium Amalgams: Catalysis of the Oxygen Reduction

R. Barrue* and J. F. Rialland

Laboratoire de Génie Electrique (LGEP-LCIE), 92260 Fontenay-Aux-Roses, France

ABSTRACT

A number of works have described the catalytic properties of powdery indium amalgams in the electrochemical reduction of oxygen in basic media. X-ray diffraction studies of these powders exhibit that their surface mainly consists of the three following compounds: $In(OH)_3$, InOOH, and In_2O_3. The chemisorption isotherms, determined in the pressure range 0-1.5 atm, show that only In_2O_3 can take a predominant part in the catalytic properties of the powdery amalgams. Electrochemical measurements of oxygen cathodic reduction in aqueous basic solutions corroborate the previous result.

Indium amalgams are liquid at room temperature for indium concentrations lower than 69 atomic per cent (a/o). These liquid alloys may yield a powdery material through strong mechanical shaking under atmosphere. This phenomenon seems to be attributed to a superficial enrichment in indium and an adsorption of gases. X-ray diffraction studies have led us to suggest a grain model which consists in a liquid core surrounded with a quasi solid superficial layer (1).

A number of works (1-3) have described the catalytic properties of those powdery amalgams in the electrochemical reduction of oxygen in basic media. X-ray analyses have established that the superficial layer of grains mainly consists of the three following compounds: indium oxide (In_2O_3), indium oxyhydrate (InOOH), and indium hydroxide ($In(OH)_3$).

In this paper, our purpose is to specify if the catalytic properties of the powdery indium amalgams may be specifically attributed to one of those three compounds.

Oxygen Chemisorption Isotherms

In heterogeneous catalysis, the adsorption of the reactive compounds is the first step of the catalytic process. This fact led us to determine the oxygen chemisorption isotherms on the powdery amalgams and on the three above-mentioned compounds. The isotherms have been plotted for usual pressures in heterogeneous catalysis and at room temperature.

* Electrochemical Society Active Member.

Key words: chemisorption, catalysis, indium amalgams, indium oxide.

Experimental

The powdery amalgam samples were obtained from a liquid alloy of 16 a/o In through mechanical shaking under atmosphere (1). Indium oxide and indium hydroxide were made and then analyzed by means of x-ray diffraction, in our laboratory. For InOOH, an ultrapure product (Ventron U.S.A.) was used. The powdery samples consisted of particles of about 50 μm diameter. Oxygen and nitrogen were high purity gases ($O_2 \geqq 99.995\%$; $N_2 \geqq 99.998\%$).

The diagram of the apparatus is shown in Fig. 1. The volume of the cell is about 500 cm^3. In a first step, a 10g sample was put in the cell. After a 48 hr long desorption in a high vacuum (10^{-6} Torr), a mixture of oxygen and nitrogen (an unchemisorbed gas) was introduced into the cell. The number of moles for each of the two gases contained in the cell was determined by means of the gas-chromatography analysis of a 1 cm^3 gaseous sample. The change of the partial pressures of the two gases as a function of time was obtained in the same way.

As an example, Fig. 2 shows the superposition of two chromatograms obtained at the start (s) and the end (e) of adsorption on a powdery amalgam sample. The first peak is the one of oxygen, and the second peak is the one of nitrogen. The numbers of moles for each gas are in ratio to the corresponding peak areas. The examination of the chromatograms shows that the N_2 peak is unchanged, while the O_2 peak area is strongly reduced, exhibiting a large adsorption of this gas.

Results

No adsorption on $In(OH)_3$ and InOOH could be detected, while oxygen adsorption on In_2O_3 and on the powdered amalgam was measurable by the experimental method.

The specific surface areas were determined from the BET transforms (4) of the nitrogen physical adsorption isotherms at 77°K. The values deduced from these measures are: 115 m^2/g for the powdery amalgam and 74 m^2/g for In_2O_3.

The times for establishing the adsorption-desorption equilibrium were relatively long. The time constants were related mainly to diffusion phenomena through the powdery material. Thus in order to quicken the rate of reaction, the powdery samples were shaken by using a magnetic device. With this agitation, the equilibrium was reached after about 7 days for the powdery indium amalgam and after about 15 days for In_2O_3. In Fig. 3 the amounts of adsorbed oxygen are plotted *vs.* time for the two adsorbents.

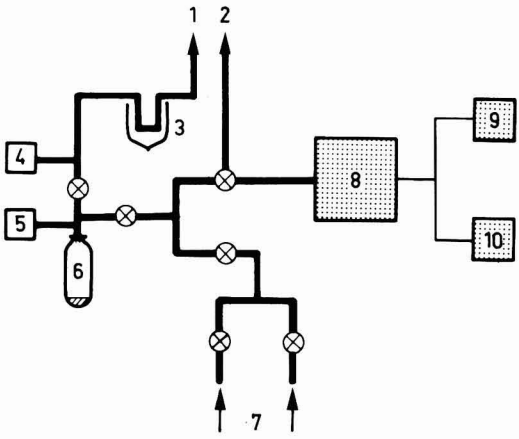


Fig. 1. Apparatus for chemisorption isotherms measurements. 1, To high vacuum; 2, to vacuum; 3, trap; 4, vacuum gauge; 5, pressure gauge; 6, adsorption cell; 7, gas supplies; 8, chromatograph; 9, recorder; 10, digital integrator.

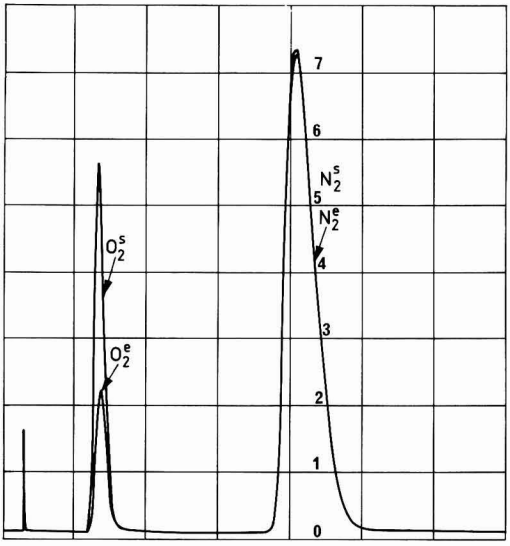


Fig. 2. Superposition of chromatograms. Adsorbent: powdery indium amalgams. Lasting of adsorption: 5 days; $T = 25°C$. $P_{O_2}{}^s = 0.2$ atm; s = start; e = end.

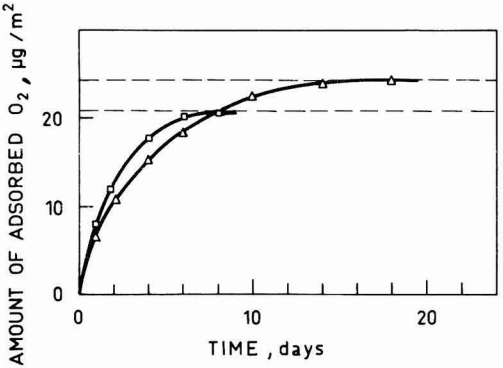


Fig. 3. Kinetics of oxygen adsorption referred to unit surface area. Temperature: $T = 25°C$. Initial pressure: $P_{O_2}{}^s = 0.5$ atm. Square, on powdery amalgams; triangle, on indium oxide

The isotherms are plotted in Fig. 4. For the two curves, a saturation quickly occurs in terms of pressure. For oxygen partial pressures over 1 atm, the powdery amalgam isotherm increases again; in addition, the adsorbed oxygen could not be desorbed fully by the usual ways. This behavior may be attributed to the existence of a secondary chemical reaction, as in the oxidation of a metallic phase (mercury or indium).

Oxygen Reduction on an Indium Oxide Electrode

The catalytic effect of indium oxide in the electrochemical reduction of oxygen in basic media has been specified by electrochemical measurements.

Experimental

Gas porous electrodes were made with indium oxide. Two grams of indium oxide and 2g of powdered metallic indium were mixed and compressed in a cylindrical matrix. The binding material was sintered at 150°C for 24 hr. The powdered indium was included to ensure good cohesion and good electrical conductivity in the sintered material. The area of the electrode was about 1.5 cm^2. Electrolyte was an aqueous solution of sodium hydroxide (1M NaOH); the temperature was 25°C. The

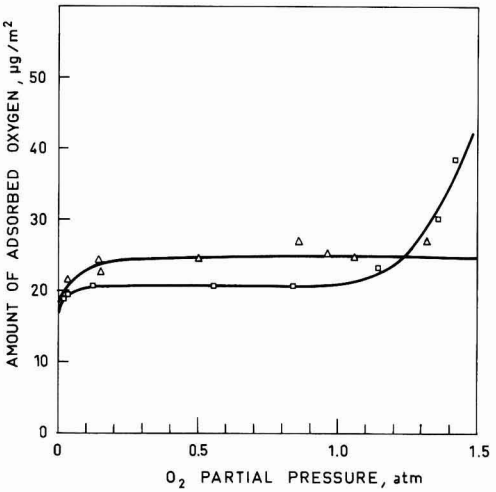


Fig. 4. Oxygen chemisorption isotherms referred to unit surface area. Temperature: $T = 25°C$. Square, on powdery amalgams; triangle, on indium oxide.

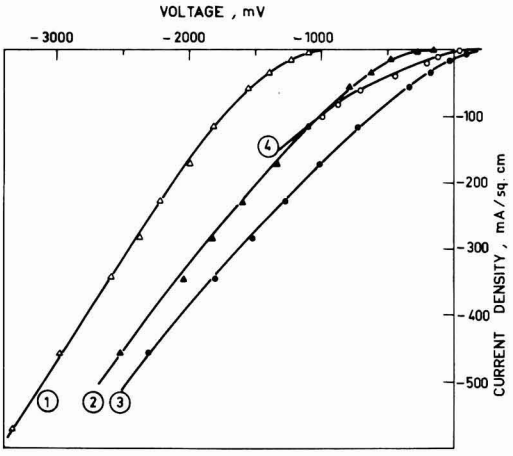


Fig. 5. Effect of O_2 pressure on polarization curves. 1, In_2O_3-O_2 pressure = 0; 2, In_2O_3-O_2 pressure = 1 atm; 3, In_2O_3-O_2 pressure = 2 atm; 4, powdery indium amalgams-O_2 pressure = 2 atm. Temperature: $T = 25°C$. Electrolyte: 1M NaOH. Reference: Hg/HgO · 1M NaOH.

cathodic potentials were recorded *vs.* the Hg/HgO potential.

Results

Three reactions were possible

$$2\,H_2O + O_2 + 4e \rightarrow 4\,OH^- \quad [1]$$

$$3\,H_2O + In_2O_3 + 6e \rightarrow 2\,In + 6\,OH^- \quad [2]$$

$$2\,H_2O + 2e \rightarrow 2\,OH^- + H_2 \quad [3]$$

Only reaction [1] was associated with the catalytic process. This reaction occurred with the reduction of oxide to metal (reaction [2]). In the studied current density range, reaction [3] was so slow that the current corresponding with the H_2-release was negligible.

The current density potential curves are plotted for different pressures of oxygen in Fig. 5. The curves are typical of electrodes for which the oxide capacity is 4160 coulombs (2g of In_2O_3). Curve 1 is associated with the reduction of oxide. The differences between this curve and curves 2 and 3 show the effect of oxygen. Curve 4 was obtained with a powdered amalgam electrode studied under the same conditions (1).

Because of its slowness, the chemisorption of oxygen is probably the limiting step of reaction [1]. In Fig. 3, the maximum rate of adsorption is given by the slope at origin; this rate is too slow to explain the effect of oxygen in the electrochemical measurements. In fact, the time constants determined in chemisorption were mainly due to diffusion through the pores of the powdery bulk. In the electrochemical measurements there is forced convection of oxygen and thus an increase in adsorption rate. Thus the rate of adsorption cannot be determined from the curves of Fig. 3.

Conclusion

Oxygen chemisorption on $In(OH)_3$ and InOOH cannot be detected by our experimental method. With regard to In_2O_3 and to the powdery indium amalgams, the amounts of adsorbed oxygen are about the same order of magnitude.

The electrochemical experiments exhibit the catalytic effect of In_2O_3 in oxygen reduction in basic media. The measured cathodic potentials are comparable with those obtained for a powdery indium amalgam electrode.

These results lead us to attribute the catalytic properties of the powdery amalgams to the presence of In_2O_3 in the surface layer of the individual grains.

At the present time, investigations on the powdery indium amalgams are being made to differentiate the kinetics of In_2O_3 reduction from that of catalytic oxygen reduction.

Manuscript submitted July 3, 1974; revised manuscript received Feb. 12, 1975. This was Paper 329 presented at the San Francisco, California, Meeting of the Society, May 12-17, 1974.

Any discussion of this paper will appear in a Discussion Section to be published in the June 1976 JOURNAL. All discussions for the June 1976 Discussion Section should be submitted by Feb. 1, 1976.

Publication costs of this article were partially assisted by the Laboratoire de Génie Electrique.

REFERENCES

1. J. F. Rialland and J. Robert, *J. Chim. Phys.*, **66, 354** (1969).
2. J. F. Rialland, Thesis, University of Paris, 1968.
3. J. Deprez, J. Rabit, J. F. Rialland, and J. Robert, *J. Physique*, **32,** 805 (1971).
4. S. Brunauer, P. H. Emett, and E. Teller, *J. Am. Chem. Soc.*, **60,** 309 (1938).

Undervoltage Deposition of Alkali Metal at Carbon Electrodes in the LiCl-KCl Eutectic Melt

S. D. James*

Electrochemistry Division, Naval Surface Weapons Center, White Oak, Maryland 20910

ABSTRACT

Voltammograms and charge-discharge curves are presented for carbon electrodes of varying graphitic crystallinity in LiCl-KCl eutectic melt at 703°K (430°C). For rods of glassy carbon, graphite, and pyrolytic graphite there is a very marked cathodic depolarization below about −2.5V *vs.* a chlorine electrode. Chemical analysis of the cathodized carbons shows that this depolarization is caused by undervoltage deposition of alkali metal. The deposited metal normally consists entirely of Li but in two cases, during potentiostatic cathodizing, significant amounts of K were codeposited. Cathodized graphite rods disintegrate before reaching the Li potential but glassy carbon rods do not and can survive about 25 charge-discharge cycles before breaking up. The uninflected charging curves obtained for glassy carbon and graphite give no indication of distinct transitions between Li intercalation compounds of different stages. However, the relatively low Li contents of cathodized carbons, their x-ray diffraction patterns and the absence of acetylene in their reaction with water all favor the presence of intercalation compounds rather than a carbide. Lithium contents of glassy carbon rods cathodized toward the Li potential range up to about 7 weight per cent compared with 8.9% for C_6Li, the richest intercalation compound and 37% for Li_2C_2. Even quite brief exposures of carbon electrodes in this melt to potentials below −2.5V have lasting effects on electrode behavior; carbon loses its melt-repellency and the electrode suffers a 1-2V lowering of its open-circuit voltage.

Unexpectedly high cathodic currents were noticed when carbon electrodes were driven below −2.5V *vs.* the chlorine electrode in LiCl-KCl melt at 703°K (430°C). This surprised us since it occurred more than a volt above the equilibrium potential of lithium in this melt, *viz.*, −3.65V *vs.* the chlorine electrode (1). Since a literature search failed to unearth any explanation of this anomaly we made tests to elucidate its cause. The present paper describes these tests and the conclusions arrived at.

Experimental

Equipment.—The LiCl-KCl eutectic melt volume was 376 cm³, occupying a 115 mm depth in a 210 mm tall, 70 mm diameter Pyrex test tube. This inner test tube rested inside a 360 mm tall, 76 mm diameter, flange-topped Pyrex pot (flange assemblies were of 3 in. Conical Pipe System from the Corning Glass Company). A flanged Pyrex lid with Teflon O-ring gasket was bolted onto the pot. This lid has six short vertical glass tubes acting as ports through which a thermocouple, a 4 mm Pyrex gas-bubbling tube and various electrodes can be fed down into the melt. Sliding seals at these ports were made using modified Teflon Tube Fittings (Beckman Instrument Incorporated). A cylindrical electric furnace was used; its temperature was controlled to ±1°K (1°C) by Versatherm Model 2157 (Cole Palmer Instrument Incorporated). A Chromel-Alumel thermocouple inside a 6 mm Pyrex tube thermowell dipped into the melt. At 703°K the 110 mm deep, normally unstirred melt was 1°K hotter at the top than at the bottom.

The Tacussel fast-rise potentiostat PIT20-2X (plus GSTP2 function generator) was used in the potentiostatic or galvanostatic mode giving rise to linear scan voltammograms and constant current charge-discharge curves, respectively. The voltammograms were displayed on a Tektronix X-Y oscilloscope model 561A with two, 2A63 differential amplifier plug-ins. The two inputs of the Y-plate plug-in were connected across a standard resistor (normally one ohm) in the counter-electrode lead, thus registering cell current. The other plug-in received the controlled voltage sweep (test electrode *vs.* reference) from a jack on the potentiostat. The voltammograms were photographed. In the constant current mode, the voltage-time curves were recorded on a strip chart recorder (Varian G-11A with B1 input chassis).

Materials.—Lithium chloride and potassium chloride powders were ACS certified reagents from Fisher Scientific Company. Chlorine gas (used both in the reference electrodes and for dehydrating the melt) was Electronic Grade, 99.98% pure, from Precision Gas Products, Rahway, New Jersey. The usual cell atmosphere was high purity argon (water pumped, 99.996%), passed through a drying train of Drierite (anhydrous calcium sulfate). Three types of carbon rods were used as electrode materials. Glassy carbon rods, 1.5 or 3 mm in diameter (grade V25-99.99% carbon) were obtained from the Carbone Company, of Boonton, New Jersey. Synthetic graphite rods of spectroscopic purity (99.999% carbon) came from Ultra Carbon Corporation, Bay City, Michigan. Both ⅛ in. (3.0 mm) and ¼ in. (6.1 mm) diameter rods were used. In one experiment, graphite rods, 254 × 6.3 mm, covered with a 0.1 mm thick coating of pyrolytic graphite were used. The graphite orientation is said to be such that the a-b planes are parallel to the coated surface at all points. These rods, designated EC-2, were bought from the General Electric Company, Detroit, Michigan.

Electrodes.—Working electrodes of glassy carbon used in getting the cyclic voltammetry data of Fig. 2 are illustrated in Fig. 1A. These were made as follows. Firstly a 25 mm length of 1.5 mm diameter glassy carbon rod was carbon-cemented 6 mm deep into the end of a 3 × 600 mm spectroscopic graphite rod. The composite rod was then sealed into a Pyrex tube and sawn off at 45°. This angular cut allows any chlorine bubbles, anodically formed during use, to escape from the electrode. A final polish was given to the Pyrex-carbon sawn surface on a 180 grit diamond-coated wheel. The geometric area of the exposed glassy carbon ellipse was 2.43 mm². The Carbone Company's

* Electrochemical Society Active Member.

Key words: molten salts, carbon electrodes, intercalation compounds, cathode depolarization, high temperature electrochemistry.

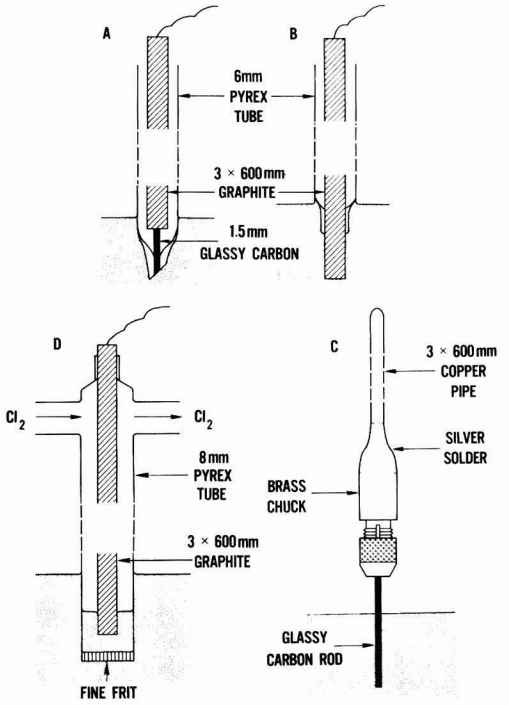


Fig. 1. Types of carbon electrode used: (A) working electrode of glassy carbon sealed in Pyrex, (B) working or counterelectrode of graphite sealed through Pyrex, (C) working electrode of glassy carbon held in chuck, (D) chlorine reference electrode.

glassy carbon has a thermal expansion coefficient of 3.2 μm/m.K at 373°K. This is almost as big as that of the Pyrex glass (3.3 for Corning 7740) and thus the carbon-Pyrex seal of Fig. 1A has little or no tendency to leak. In the early experiments it was noticed that the Pyrex tips of working electrodes like those of Fig. 1A and B cracked and admitted melt after prolonged cathodic polarization (even at potentials well positive of the Li/Li^+ equilibrium). It became apparent later that this was caused by swelling of the carbon tip due to its absorption of alkali metal deposited at undervoltage. In subsequent work designed to examine this undervoltage deposition, the Pyrex envelopes were dispensed with and the bare carbon was dipped directly into the melt. A graphite working electrode used in the initial cyclic voltammetry is shown in Fig. 1B. The end of a 3 mm diameter graphite rod (Ultra's U7, a high density grade, 1.90 g/cm^3) protruded 20 mm from the sealed Pyrex tube. The geometric area of exposed graphite was 2.0 cm^2. Electrode (C) of Fig. 1 was used when we wished to weigh the carbon before and after cathodic treatment. The carbon rod was gripped in a brass chuck (taken from an electrical test prod). The only carbon material studied in this way was glassy carbon. Rods 1.5 mm in diameter slipped easily into the chuck whereas 3 mm rods had to be tapered by filing.

The counterelectrode was a 6 × 600 mm graphite rod (Ultra, U7) dipping about 75 mm undermelt. When acting as a cathode in pure LiCl-KCl melt, graphite absorbs alkali metal plated onto it. In the anodic mode it reoxidizes this absorbed metal and/or gasses chlorine. None of these reactions significantly contaminates the melt. A graphite rod of these wetted dimensions can absorb at least 1500 coulombs of cathodic charge before there is any danger of its disintegrating under the stress of the absorbed alkali metal (see below)

The chlorine electrode was used as reference. It is illustrated in Fig. 1D. Ultra Carbon's U120 grade of spectroscopic graphite rod was normally used as the electrode substrate although other grades of pure graphite worked just as well. The chlorine flows by the carbon and over the melt rather than through the carbon and into the melt as is more customary (2). This flow-by electrode has the advantage of relative ease of construction and safety from the danger of the melt sucking back and freezing. It takes about 10-15 hr of chlorine flow to equilibrate the electrodes to within 1 mV of the reversible chlorine potential. We always used a pair of reference electrodes, regularly monitoring their interelectrode or bias potential. After the initial equilibration period the bias potential never exceeded 1 mV during weeks of continuous use. All quoted potentials are *vs.* this chlorine electrode.

Melt purification.—A charge of LiCl-KCl salt powders (mixed in the eutectic proportion) was outgassed at 2.66-6.65 N·m^{-2} (20-50μ Hg) while being heated up to about 703°K (430°C). On melting, a brisk evolution of water vapor commenced and continued for 30-45 min. Residual water was then removed by bubbling chlorine through the melt for 60 min (3). It was then freed from platable impurities by preelectrolysis at an auxiliary aluminum cathode (*vs.* a graphite anode). The cathode was 80 cm^2 in area and held at −2.95V to the chlorine electrode. Preelectrolysis was continued for 24 hr although the residual current density (at the cathode) fell to a steady value of 10 μA/cm^2 after 4 hr. The Al cathode which had become dark gray was withdrawn from the melt at the end of the preelectrolysis.

X-ray examination of cathodized carbons.—After cathodizing in the melt at constant current down to the lithium potential (−3.65V *vs.* the chlorine electrode), several different types of 3 mm carbon rod were x-rayed to see if any structural change had occurred. After filing free from adherent solidified melt the rods were laid in a Lucite x-ray sample holder and filed half round so as to expose a 10 mm × 22 mm expanse of flat carbon surface. This was all done in an argon-filled glove bag. Then each holder was securely enveloped with one layer of cellulose acetate transparent adhesive tape (Magic Tape 3M Company) and placed in its own, argon filled, screw-cap bottle. The x-ray diffraction pattern was recorded in air without removing the tape, immediately after taking the holder from its bottle. The Standard Phillips x-ray powder diffractometer was used employing CuK_α radiation.

Chemical analysis of cathodized carbons.—Cathodized carbon rods were ground up and extracted with water which was then analyzed for Li^+, K^+, Cl^-, and OH^-. The rods were first freed from solidified melt by a quick rinse with a jet of distilled water then dried, crushed in a press and ground in a mortar. The powders were then weighed; weights varied between 0.2 and 0.8g. After 4 hr of refluxing with distilled water, the extracts were filtered and analyzed for Li^+ and K^+ by atomic absorption spectroscopy and for Cl^- and OH^- by conventional titrimetry. In some cases, second extractions were done on the powder. The second extracts contained the sought ions at no more than background levels. In spite of this apparently complete removal of alkali metal, flame tests showed that most of the extracted carbons still contained appreciable amounts of Li. Hence the extracted powders were ashed to constant weight in silica crucibles at 1023°K (750°C) then digested in water which was analyzed to determine the residual alkali metal.

Results and Discussion

Voltammograms.—Figure 2 shows current-voltage curves obtained at a glassy carbon electrode of Fig. 1A

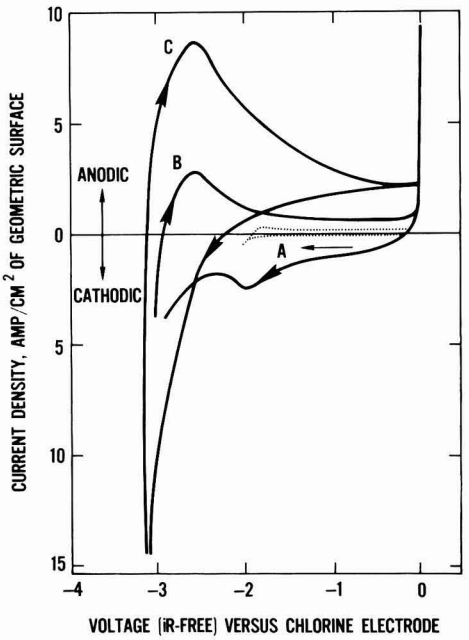


Fig. 2. Voltammograms at glassy carbon in LiCl-KCl at 430°C as a function of the range of applied voltage. Sweep cycle time was 0.2 sec.

type construction. The geometric area of the carbon ellipse was 0.0243 cm^2, and the electrode was dipping in a purified melt at 703°K (430°C). Basically similar curves were obtained using a 2.0 cm^2 graphite electrode (Fig. 1B type). The curves of Fig. 2 are the reproducible ones obtained after a train of five or more voltage triangles had been applied to the working electrode. The nominal voltage range of these triangles were: Curve A, −2.0 to 0.0V; B, −3.5 to +0.5V; C, −4.0 to 0.0V *vs.* the chlorine electrode. However, after correction for substantial iR drops the actual limits of voltage excursion were −3.2 and 0.0V. In the low amplitude sweeps of curve A the trace differs little from expected, except perhaps at −2V where cathodic current is starting followed by a small anodic peak after sweep reversal. These effects are much more marked in B which also has a pronounced cathodic peak at −2.1V. This latter peak is presumably due to reduction of chlorine generated at positive voltages since it vanishes if the positive excursion of applied voltage is restricted to 0.0V. In curve C the cathodic depolarization below −2.5V is very striking. Extremely large cathodic current densities are found and a big anodic peak appears after voltage sweep reversal as species produced in the cathodic sweep are reoxidized.

These results were unexpected; we did not look for significant cathodic current till below about −3.65V, the lithium potential in this melt (1). Such big cathodic currents (10 A/cm^2, at 0.7V above the Li potential) cannot arise from impurities at the level normally found in reagent grade salts. This is confirmed by the independence of the effect on the degree of melt purification employed. So it seems that carbon electrodes are far from inert in this metal. The rest of this paper shows that carbon rods of diverse types will, between −2.5 and −3.6V, absorb at undervoltage, large quantities of alkali metal (mainly Li). Due to a compound formation between carbon and deposited metal (probably a laminar or intercalation compound) deposition is energetically assisted, *i.e.*, occurs at undervoltage.

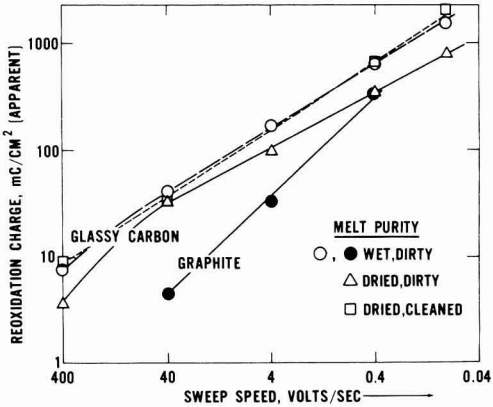


Fig. 3. Coulombic charge of anodic peaks in voltammograms at carbon electrodes. Applied voltage range: −3.5 to +0.5V, *vs.* chlorine electrode. LiCl-KCl at 430°C.

Figure 3 shows the electrical charge used to reoxidize the material plated out at undervoltage. The coulombic content of the anodic peaks in curves such as those of Fig. 2 is plotted against the voltage sweep rate. The glassy carbon was a Fig. 1A type and the graphite electrode a 1B type. There is no correlation of reoxidation charges with melt purity which, together with the very high values of the cathodic currents in Fig. 2 shows that these currents do not correspond to reduction of impurities in the melt. Thus these currents must arise from the cathodic reduction of the lithium or potassium cations. The deposited metal is obviously quitting the interface as fast as it is formed there, otherwise the cathode voltage would fall immediately to the potential range of Li or K deposition (<-3.6V). Thus the alkali metal is either soaking rapidly into the carbon rods or dissolving rapidly in the melt. Since an iron rod under the same conditions cannot sustain even 8 mA/cm^2 cathodic current without plunging at once to the Li potential (see Fig. 4) it seems the carbon must be soaking up the alkali metal in some way. Undervoltage deposition of a metallic monolayer on various substrates is well known in aqueous solution (4) and even recently in fused salts (5). However, the charges of Fig. 3 at slow sweeps correspond to many thousands of monolayers. Thus undervoltage deposition of a single superficial monolayer cannot explain our data. The alkali metal must be continuously soaking into the carbon. The slower the voltage sweep speed, the more time is available in the anodic sweep to reoxidize this metal as it diffuses back to the melt interface; hence the larger is the reoxidation charge.

Charge-discharge curves.—Figure 4 shows first-cycle charge-discharge curves at a 1.5 mm diameter rod of glassy carbon. The 76 mm long rod was carbon-cemented into the end of a 600 mm long, ¼ in. diameter graphite rod, serving as support and electrical lead. The glassy carbon protruded 70 mm from the graphite and dipped 25 mm undermelt such that its wetted area was 1.2 cm^2. On switching on cathodic current at A, carbon voltage falls sharply to about −2.7V then more gradually, leveling off when the wetted carbon whitens with a coating of tiny white Li droplets. On current reversal at B, the discharge curve after a small step due to iR drop, more or less mirrors the charging curve except that (*i*) the discharge time to chlorine evolution, τ_a, is only about 0.9 of the charging time, τ_c, (*ii*) on switching off the anodic current at C, carbon voltage falls almost to −3V, two volts lower than the original value of about −1V, the usual voltage of untreated carbon in these melts. The

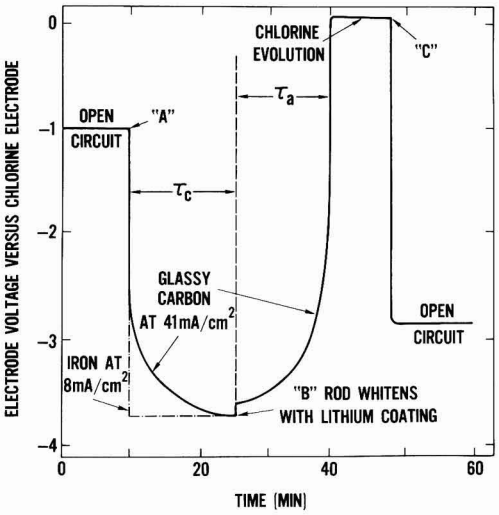


Fig. 4. Charge-discharge curves for 1.5 mm glassy carbon rod in LiCl-KCl at 430°C. Current switched on cathodically at A, reversed at B, and switched off at C.

dot-dash-dot curve depicts the behavior of a pure iron rod cathodized at 8 mA/cm^2; it was driven to the Li potential in less than 3 sec. This shows that the depolarization exhibited by carbon arises on the carbon side rather than the melt side of the interface.

The data of Fig. 4 parallel those of Fig. 2 but they go further, showing the effects to be large ones rather than merely a transitory depolarization. Large amounts of charge are passing at undervoltage. Chemical analysis of various cathodized rods showed this charge to be wholly in the form of deposited Li absorbed in the carbon, to the extent of about 5 weight per cent (w/o) Li. The rod whose first charge-discharge cycle is illustrated in Fig. 4 was subjected to 24 additional similar cycles at four successively higher current densities (43, 83, 143, and 286 mA/cm^2). It was found that the coulombic charges Q_c and Q_a corresponding to times τ_c and τ_a had no significant dependence on current density. Neither did the ratio Q_c/Q_a which remained at an average value of 0.90 ± 0.015. The first observation shows that Li permeates the glassy carbon structure quite easily. If this were not so, high current densities would soon effect, in the skin of the carbon rod, such Li enrichment on charge and Li depletion on discharge as to polarize the electrode quickly to the Li and Cl_2 potentials, respectively. The Q's would then depend sharply on current density which was not observed. The fact that $Q_a/Q_c = 0.90$ suggests either a low current efficiency for Li deposition or that some of the absorbed Li is bound too tightly to be reoxidized anodically. The lack of variation of Q_a/Q_c with current density favors the latter explanation.

Graphite rods gave very similar charging curves to that of Fig. 4. However, with graphite rods the charging curves could not be completed to the Li potential as the rods broke prior to this point. Sometimes they snapped cleanly at the melt meniscus but more often, towards the end of the charge, fine carbon powder began to fall from the meniscus area of the rod which soon necked down till the wetted part of the rod fell off. Presumably this is caused by high stresses arising at the demarcation between wetted carbon swollen with absorbed Li and relatively unaffected material above the meniscus. A few experiments with graphite rods coated with a 0.1 mm thick layer of pyrolytic graphite also gave charging curves similarly shaped to that of Fig. 4. According to the manufacturer, the graphitic planes in the pyrolytic graphite coating were parallel to the coated substrate at all points. Thus either the Li atoms can permeate freely through the carbon hexagons of the pyrolytic coating or this coating is highly imperfect. We suspect the latter since Li, atomic radius 0.153 nm (1.53Å) would be grossly deformed in passing through a carbon hexagon (inner radius 0.071 nm). On the other hand, in intercalation compounds, the alkali metal atoms are believed to be substantially ionized (6). In this case the Li^+ ionic radius of 0.068 nm, would permit it to pass through the sheets.

A series of well-defined Li graphite intercalation compounds has been made in other laboratories by reacting Li directly with crystals of natural graphite (6). These are: C_xLi where $x = 72$, 36, 18, 12, 8, or 6. None of our charge-discharge curves ever showed any arrests in voltage corresponding to the formation of compounds successively richer in Li. Arrests would have been seen in the charging curve of Fig. 4 after about 2.5, 5, and 10 min corresponding to compounds with $x = 72$, 36, and 18. On the contrary, the smooth curves of Fig. 4 suggest a continuous spectrum of interaction energies of Li with the carbon structure. Perhaps this difference is related to the relatively amorphous structure of glassy carbon and synthetic graphite used in this work as opposed to natural graphite which is much more highly crystalline.

Figure 5 shows data for five separate glassy carbon rods cathodized at different constant current densities between 9 and 144 mA/cm^2. The rods were 76 × 1.5 mm, held in a chuck as in Fig. 1C and dipped 60 mm undermelt. The original charging curves were replotted as voltage *vs.* amount of charge passed, to aid their comparison. The results show there is a small but significant concentration polarization effect. At the same stage of charge there is a 0.1V spread in voltage according to the charging rate. Thus at the higher current density there is a perceptible backup of the permeating Li. The curves merge close to the Li potential as all the rods approach saturation with Li.

Composition of cathodized carbon rods.—Glassy carbon.—Figure 6 shows the Li uptake of glassy carbon rods (determined by chemical analysis) as a function of potential. Seven, 3 mm rods, supported in chucks as in Fig. 1C were held for 60 min at various constant potentials. They were then removed from the melt and analyzed chemically for Li and K. Their Li contents rise smoothly with falling voltage with a sharp rise close to the reversible Li potential (though ostensibly from the same batch, the rod with the anomalously high Li content at −3.0V was also anomalously hard; it was very difficult filing its end tapered to enter the chuck). No study was made of Li uptake *vs.* time at constant potential so it is not certain that the data points of Fig. 6 represent true equilibrium values. However, in getting the constant current

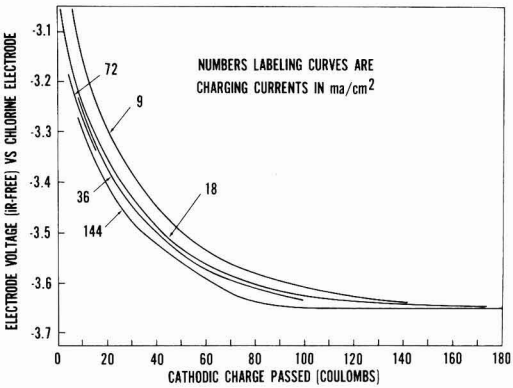


Fig. 5. Voltage *vs.* amount of charge passed for glassy carbon rods cathodized at various rates in LiCl-KCl at 430°C.

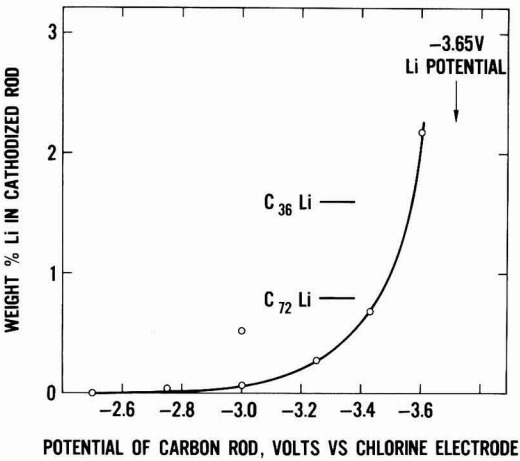


Fig. 6. Lithium uptake of glassy carbon rods as a function of potential in LiCl-KCl at 430°C. A separate rod was held at each potential for 60 min then removed from melt for Li determination by chemical analysis.

charging data of Fig. 7 we found that 1.5 mm diameter rods could be charged up to 3.6 w/o Li in only 8 min. Thus it is unlikely that the curve of Fig. 6 would be significantly altered by longer potentiostating. The smooth curve of Fig. 6 agrees with the smooth charging curves of Fig. 4 and 5. They both indicate continuous rise in Li content with falling voltage; there are no arrests in voltage as might occur during the transformation of one layer-compound to another richer in Li, *e.g.*, $C_{12}Li$ to C_8Li. This contrasts with the preparation of layer compounds from single-crystal graphite. Here at 673°-773°K (400°-500°C), steps were obtained in curves of composition *vs.* alkali metal vapor pressure for both K and Cs (6, 7). The uninflected voltage-composition curves of the present work are probably associated with the relatively amorphous nature of the glassy carbon used. This agrees with the work of Herold *et al.* (8, 9). Using the same source and grade of glassy carbon as the present work (V25 from Carbone Company) they got uninflected isotherms for the absorption of K vapor at 873°K (600°C). Their richest material was 25.8 w/o K (C_8K contains 29.0 w/o K). They considered this material to be, at least partially, an intercalation compound. This work of Herold and a brief note by Halpin (10) seem to be the only published data on the action of alkali metals on glassy carbon and is restricted to potassium. Recently (11) steps were obtained in constant-current charging curves using cathodes of synthetic graphite foil. In these room-temperature experiments, Li, K, and NMe_4 were cathodically impregnated into the graphite from salt solutions in dimethyl sulfoxide. It would seem thus that high crystallinity of the carbon and low temperature of impregnation favor the observation of steps in charging curves.

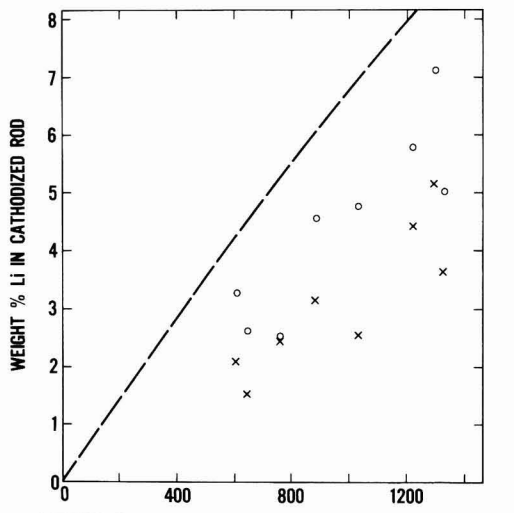


Fig. 7. Lithium uptake of glassy carbon rods cathodized at constant current toward the Li potential (LiCl-KCl, 430°C). Broken line: Assumes carbon absorbs Li, equivalent to the total charge passed. Circles: Observed per cent gain in weight. Crosses: Li contents from chemical analysis.

In the intermediate potential range of Fig. 6, significant amounts of K were found in the glassy carbon. For the rod at −3.0V, anomalously rich in Li, K/(K + Li) was 0.39 mole fraction and at −3.25V the fraction was 0.16. No chloride was found in these rods so all their K came by electrodeposition rather than by uptake of melt. These two rods were the only cases in this work where K was found to be codeposited at undervoltage with Li. It is not clear why K deposition was restricted to this intermediate range of potential. At inert iron cathodes in LiCl-KCl eutectic, highly pure Li with less than 0.1%, K is deposited (12).

Figure 7 shows the Li uptake of eight glassy carbon rods cathodized at constant current toward the Li potential. The experimental setup was the same as in the constant potential work. The rods were 76 mm long, 1.5 mm diameter and dipped 60 mm undermelt. No K^+ or Cl^- were found in the extracts of these rods and within experimental error the extracts contained Li^+ and OH^- in equivalent amounts. Thus Li deposition was solely responsible for the observed depolarization in the charging curves, and no melt is absorbed by glassy carbon rods. In spite of the scatter of the data it can be seen that the rods absorb Li proportional to the cathodic charge passed. In Fig. 7 the Li contents determined by chemical analysis (X) are almost all higher than the −3.6V value of Fig. 7. This is consistent with the open-circuit voltages of the rods at the end of charging; these varied from −3.630 to −3.654V. The Li contents of Fig. 7 range up to about 7 w/o. These relatively low values plus the absence of acetylene on reacting cathodized carbons with water show no carbide is present (lithium carbide has 37 w/o Li). The observed Li contents tally much better with those of intercalation compounds, the richest of which, C_6Li, has 8.9% Li.

In Fig. 7 it is clear that Li contents obtained by chemically analyzing the carbon rods are systematically less than those derived from weight gains, which in turn are consistently below those calculated from the total cathodic charge passing. The analytical figures average 0.69 ± 0.09 of those from weight gain which themselves average 0.67 ± 0.10 of the calculated values. During the electrolyses, the melt was pale yellow from dissolved chlorine formed at the graphite counterelectrode. However, calculation based on chlorine's solubility and diffusivity in the melt (13) shows that, even in chlorine-saturated melt, the limiting current for chlorine reduction should be below 1 mA/cm². Parallel reduction of chlorine can thus not account for the discrepancies of Fig. 7 as these data were secured at 9-144 mA/cm². Furthermore, there was no correlation at all between current density and the magnitude of deviation of measured values below the broken line. Thus at this time we have no explanation for these deviations. More work is also needed to elucidate the systematically lower measured Li contents from chemical analysis as opposed to weight gain.

Graphite.—Much less work was done with graphite rods because charging curves could not be completed to the Li potential before the rods disintegrated at the melt meniscus level. Also, at these highly negative potentials, graphite rods wicked up significant amounts of the melt. This effect precluded determining weight gains and confused the results of chemical analysis by introducing into the graphite an unknown proportion of Li^+ and K^+ from the melt. Two grades of synthetic graphite were used, U7 and UF4S from Ultra Carbon Company, having densities of 1.90 and 1.76 g/cm^3, respectively. The glassy carbon used, at 1.50 g/cm^3 was more porous than both graphites. Nevertheless glassy carbon approaches Pyrex glass in its resistance to gas flow while graphite is typically 5-10 orders of magnitude more permeable. Apparently glassy carbon's pore system is largely blind and inaccessible to the melt whereas graphite's is open and interconnected (13). Thus it is understandable that no chloride was found in any cathodized glassy carbon while significant amounts were found in each cathodized graphite rod. The wicking up of this melt into porous carbon at negative potentials was previously observed and utilized by Adams (15) with activated carbon.

Six 3 mm diameter graphite rods were cathodized to breakage in LiCl-KCl at 703°K (430°C). They averaged 590 ± 290 coulombs/g of carbon at the breaking point (glassy carbon rods were routinely charged without breaking to 1200 coulombs/g of carbon where Li droplets covered the carbon surface). Aqueous extracts of the cathodized graphite rods contained mainly Li^+ and OH^- with lesser amounts of K^+ and Cl^-. Extracts with higher K^+ contents had proportionately more Cl^-. This indicates that potassium was entering the rods via absorbed melt rather than by electrodeposition. So it seems that, with graphite also, the observed depolarizations are basically due to undervoltage deposition of Li. From the OH^- content of the most highly charged rod we derive a Li content of 4.1 w/o. This is in line with the Li contents of Fig. 7 for glassy carbon. Thus the limited amount of data secured using graphite indicates its behavior to be basically similar to that of glassy carbon with the added complication of uptake of melt into the more permeable graphite.

X-ray analysis of cathodized carbons.—Figures 8 and 9 compare the x-ray diagrams of carbon rods before and after cathodizing toward the Li potential in the melt at 700°K (427°C). Figure 8 refers to a 3 mm diameter glassy carbon rod whose Li content by chemical analysis was 4.4 w/o. Figure 9 refers to the 3 mm graphite rod which was analyzed as

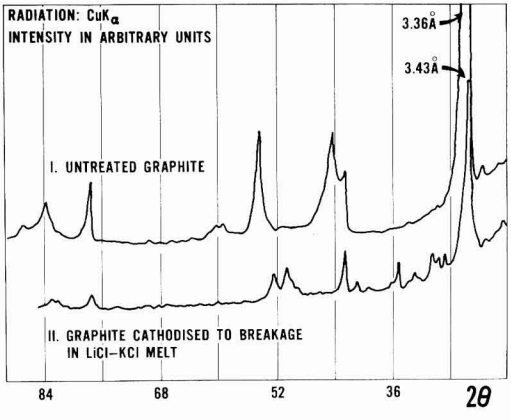


Fig. 8. X-ray diffractograms for glassy carbon rods before and after undervoltage deposition of Li in LiCl-KCl at 430°C.

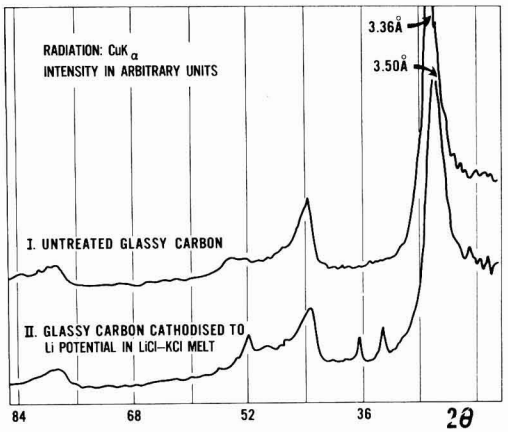


Fig. 9. X-ray diffractograms for synthetic graphite rods before and after undervoltage deposition of Li in LiCl-KCl at 430°C. (Graphite: Grade U7 from Ultra Carbon Company.)

4.1 w/o Li. The x-ray lines of glassy carbon are fewer and broader than those of graphite. This reflects the more disordered, amorphous structure of glassy carbon (14). For both types of carbon, electrolysis effected marked changes in the x-ray patterns; new lines appeared and old ones vanished or weakened. Although the data are not accurate enough to determine a- and c-spacings it is clear that the structure of the cathodized carbons is still basically graphitic. The intense reflection corresponding to the graphite hexagonal sheets is still present though the interplane distance has slightly expanded from the original 0.336 nm (3.36Å) to 0.343 nm for graphite and 0.350 nm for glassy carbon. No lines corresponding to potassium graphite or to lithium or potassium carbides are present. Thus the x-ray data are consistent with the formation of Li intercalation compounds.

Some implications of undervoltage deposition of alkali metal for the use of carbon electrodes.—Considering the very marked depolarizing effect that undervoltage deposition causes (Fig. 2 and 4) and the common use of carbon electrodes in alkali halide melts it is surprising that the phenomenon has not previously been studied. The most that is apparent in the literature is some fleeting references to the effect *e.g.,* by Laitinen (1) at synthetic graphite in LiCl-KCl at 723°K (450°C), by Mamantov (16) for pyrolytic graphite in LiF-NaF-KF at 773°K (500°C), and by Thonstad (17) for Na deposition in pyrolytic graphite from cryolite-alumina melts at 1283°K (1010°C). It is virtually certain that undervoltage deposition of alkali metal vitiated the early measurements by Neumann of decomposition voltages of metal halides between graphite electrodes (18). For fused chlorides of Li, Na, K, and Ca at 1073°K (800°C), his values were 0.77, 0.59, 0.44, and 0.51V, respectively, less than those derived from modern thermochemical data (19). This was certainly due to some form of compound formation (alkali metal carbide or intercalation compound) at the graphite cathode.

In the present work it was found that carbon electrodes exposed to undervoltage Li deposition suffered a lasting negative bias to their open-circuit voltages which could be very misleading in their subsequent use as indicator electrodes. In one case, glassy carbon and graphite rods, after cycling for an hour between −3.1 and 0.0V, *vs.* chlorine electrode, were left overnight in Ar-saturated melt. When the melt was then saturated with chlorine for an hour, the carbon voltages varied erratically between −1.1 and −2.6V and showed no sign of approaching the chlorine potential. Unelectrolyzed carbons are normally within 10 mV of the chlorine potential by this time. Thus a

worker unaware of the easy entry of Li into carbon below about −2.5V could seriously contaminate his carbon electrode without realizing it during even a brief excursion to negative potentials (such as when obtaining a background voltammogram of his melt). The electrode would then be unable for some time to function as an inert, indicator electrode.

Carbon is not normally wetted by purified chloride melts (20). However, lithiation of the carbon causes it to effectively contact the melt. This was shown in the present work where no chloride was found in graphite rods soaked in the melt for hours at open circuit whereas significant amounts had penetrated the rods after relatively brief contact at potentials close to the reversible Li value. This wetting effect was used by Adams (15) to flood activated carbon with fused LiCl-KCl and create a high-area carbon electrode. He did it by cycling the carbon between 0 and −3V *vs.* chlorine electrode. The resultant wetting was stable even during prolonged exposure of the carbon to voltages well above −2V. This emphasizes again the important and lasting effects on the carbon-melt interface of quite brief exposure to negative potentials. While vital to the operation of a high-area electrode, the stable wetting induced by lithiation would be of course fatal to the performance of a porous carbon gas-cathode. Flooding of the porous carbon by melt causes severe cathode polarization.

The lasting effects of lithiation at potentials where Li is thermodynamically quite unstable may be due to the presence of a Li residue compound. Graphite intercalation compounds on extraction or evacuation are known to retain tenaciously a minor proportion of their adduct molecules forming the so-called residue compounds (21). There is evidence that this residual adduct is tightly bound at lattice imperfections as distinct from normal adduct which can move freely between the graphite sheets.

In recent years, undervoltage deposition of Li has been reported from organic solvents into a variety of metals at room temperature, *e.g.*, Sn, Pb, Al, Au, Zn, Cd (22), and Pt (22, 23). Intermetallic Li compounds were formed. No such undervoltage deposition of the other alkali metals or of alkyl ammonium was obtained. In the paper mentioned earlier (11), Li, K, and tetramethylammonium were impregnated at undervoltage into graphite foil cathodes from dimethyl sulfoxide solutions at room temperature. Intercalation compounds resulted. However, cathodizing glassy carbon resulted in immediate deposition of free alkali metal at this relatively impermeable material. In these room temperature studies undervoltage deposition currents were limited to about 1 mA/cm^2 by the relative slowness of solid-state diffusion at this temperature. At the higher temperature of the present molten salt study much higher (hundreds of milliamperes per square centimeter) undervoltage currents were possible.

Acknowledgment

This research was supported by the Independent Research Program of the Naval Surface Weapons Center, White Oak, Maryland.

Manuscript submitted Jan. 3, 1975; revised manuscript received Feb. 25, 1975.

Any discussion of this paper will appear in a Discussion Section to be published in the June 1976 JOURNAL. All discussion for the June 1976 Discussion Section should be submitted by Feb. 1, 1976.

Publication costs of this article were partially assisted by the Naval Surface Weapons Center.

REFERENCES

1. H. A. Laitinen and C. H. Liu, *J. Am. Chem. Soc.*, **80,** 1015 (1958).
2. S. Senderoff and G. W. Mellors, *Rev. Sci. Instr.*, **29,** 151 (1958).
3. D. L. Maricle and D. N. Hume, *This Journal,* **107,** 354 (1960).
4. D. P. Sandoz, R. M. Peekema, H. Freund, and C. F. Morrison, *J. Electroanal. Chem.*, **24,** 165 (1970).
5. W. K. Behl, *This Journal,* **120,** 1692 (1973).
6. Yu N. Novikov and M. E. Vol'pin, *Russ. Chem. Rev.*, **40,** 733 (1971).
7. J. G. Hooley, in "Chemistry and Physics of Carbon," P. L. Walker, Editor, Volume 5, Marcel Dekker, New York (1969).
8. A. Herold and B. Carton, *Compt. Rend.*, **269C,** 792 (1969).
9. A. Herold and B. Carton, *Bull. Soc. Chem.*, 4264 (1970).
10. M. K. Halpin and G. M. Jenkins, *Nature,* **218,** 950 (1968).
11. J. O. Bensenhard and H. P. Fritz, *J. Electroanal. Chem.*, **53,** 329 (1974).
12. G. T. Motock, *Electrochem. Technol.*, **1,** 122 (1963).
13. J. D. VanNorman and R. J. Tivers, in "Molten Salts. Characterization and Analysis," G. Mamantov, Editor, Marcel Dekker, New York (1969).
14. V. D. Chekanova and A. S. Fialkov, *Russ. Chem. Rev.*, **40,** 413 (1971).
15. H. A. Adams, U.S. Pat. 3,428,493 (1969).
16. G. Mamantov, in "Molten Salts. Characterization and Analysis," G. Mamantov, Editor, p. 535, Marcel Dekker, New York (1969).
17. J. Thonstad, *J. Appl. Electrochem.*, **2,** 315 (1973).
18. B. Neumann and H. Richter, *Z. Elektrochem.*, **31,** 287, 296, 481 (1925).
19. W. J. Hamer, M. S. Malmberg, and B. Rubin, *This Journal,* **103,** 8 (1956).
20. H. V. Wartenberg, *Angew. Chem.*, **69,** 258 (1957).
21. R. C. Croft, *Quart. Rev. Chem. Soc.*, **14,** 1 (1960).
22. A. N. Dey, *This Journal,* **118,** 1547 (1971).
23. I. Fried and H. Barak, *J. Electroanal. Chem.*, **30,** 279 (1971).

Mass Transfer to an Eccentric Rotating Disk Electrode

Charles M. Mohr, Jr.* and John Newman**

Inorganic Materials Research Division, Lawrence Berkeley Laboratory, and Department of Chemical Engineering, University of California, Berkeley, California 94720

ABSTRACT

The mass transfer rate to a rotating disk electrode rotated about an off-center axis is calculated for eccentricities of from zero to 5 electrode radii. An asymptotic form for the transfer rate valid for large eccentricities is also derived and compared to two previous analyses. It is found that mass transfer is not affected until a critical eccentricity is reached and that the asymptotic expression provides a good approximation to the rate of mass transfer even at moderately small eccentricities. The analysis is supported by experimental data on the deposition of copper on several electrodes of eccentricities between 0.66 and 3.94.

When the active portion of a rotating disk electrode is offset from the axis of rotation, the Levich formula (1) for the mass transfer rate may no longer be applicable. Riddiford (2) implies that exact centering of the active portion is an important design consideration for such electrodes but does not estimate the change in mass transfer rate due to an eccentricity. More recently Chin and Litt (3) have treated the effect of large eccentricities, where the small active portion is located at least several diameters from the center of rotation. Also, Bardin and Dikusar (4) have attempted an analysis for moderate eccentricities (offsets slightly greater than the electrode radius).

Both of these works are limited in their applicability. Chin's paper is nearly correct for large eccentricities but is inappropriate for only slightly off-center electrodes. Bardin and Dikusar erred seriously in their simplifying assumptions, and their conclusions are incorrect for all eccentricities.

We hope to provide here a more rigorous formulation of the problem and, particularly, to describe the behavior at small eccentricities where the easily developed asymptotic form (for large eccentricities) is not applicable. The small eccentricity behavior should be found useful in assessing error limits due to machining tolerances in the manufacture of rotating disk electrodes. Attention is given to large eccentricities for the purpose of completeness only. It seems unlikely that disk electrodes would be operated in this fashion since the imbalance could be dangerous at high rotation rates.

A little contemplation suggests that the mass transfer rate is strictly constant until an eccentricity is reached where a fluid trajectory can spiral off the disk electrode and then back onto it. We have sought the value of the eccentricity at this limit as well as the behavior of the mass transfer rate for somewhat larger eccentricities.

Theory

The laminar flow pattern near a rotating disk has been described by Von Kármán with later improvement (in numerical constants) by Cochran (5). Basically, a fluid particle drawn toward the disk near its center spirals outward while approaching the disk and eventually leaves the region of interest. For Schmidt numbers typical of electrolytic solutions, the diffusion layer is very near the disk, and the radial and tangential velocities of the fluid relative to the disk may be adequately expressed as linear functions of the distance from the disk. Cochran found that these velocities are

$$v_r = 0.510 r (\omega^3/\nu)^{1/2} z$$
$$v_\theta - r\omega = -0.616 r (\omega^3/\nu)^{1/2} z \qquad [1]$$

where ν is the kinematic viscosity of the solution and ω is the rotation speed (sec^{-1}).

A fluid particle near the disk will be tracing a path $r(\theta)$, relative to the disk, described by

$$\frac{1}{r}\frac{dr}{d\theta} = \frac{v_r}{v_\theta - r\omega} = -0.828 \qquad [2]$$

Note that this is independent of either r or z within the range of validity of the linear approximations in Eq. [1]. Thus the path followed by any fluid particle near the disk is such that its direction of travel is at an angle α to a ray drawn from the center of rotation (see Fig. 1) and

$$\alpha = \cot^{-1}(0.828) = 50.38° \qquad [3]$$

Equation [2] can be integrated to yield the equation for the trajectory passing through the point (r_1, θ_1)

$$r = r_1 \exp[(\theta_1 - \theta)\cot\alpha] \qquad [4]$$

On the other hand, a point on the edge of the electrode is given by

$$r = r_0\sqrt{\epsilon^2 + 1 - 2\epsilon\cos\theta'} \qquad [5]$$

The condition of uniform accessibility, that is, uniform rate of mass transfer, will be maintained for nonzero eccentricities as long as fluid particles spiraling off the electrode never return to or pass over the electrode again. Fluid begins to return to the electrode for an eccentricity at which a trajectory first becomes tangent to the edge of the electrode. Tangency is given by $\alpha = \beta$, where β is the angle

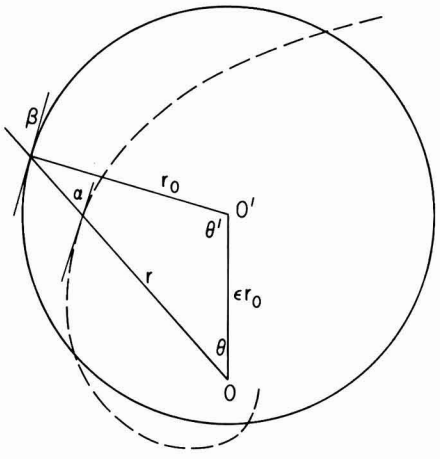


Fig. 1. Nomenclature for offset disk electrode

* Electrochemical Society Student Member.
** Electrochemical Society Active Member.
Key words: convective diffusion, diffusion coefficient measurement.

between the edge of the disk and the ray drawn from the center of rotation.

Geometrical considerations then lead to the relation

$$\alpha = \beta = \theta + \theta' - \frac{\pi}{2} \qquad [6]$$

for a tangent point on the edge. Since the relationship between θ and θ' is

$$\theta = \tan^{-1}\left(\frac{\sin\theta'}{\epsilon - \cos\theta'}\right) \qquad [7]$$

the condition for a tangent point reduces to

$$\theta' = \alpha + \cos^{-1}\left(\frac{\cos\alpha}{\epsilon}\right) \qquad [8]$$

after rearrangement using trignometric identities. This equation shows that no point of tangency exists for $\epsilon < \cos\alpha$. Thus, the critical eccentricity we seek is

$$\epsilon_c = \cos\alpha = 0.6377 \qquad [9]$$

For $\epsilon > \cos\alpha$, Eq. [8] gives two tangent points

$$\theta'_{t1} = \alpha - \cos^{-1}\left(\frac{\cos\alpha}{\epsilon}\right)$$

and

$$\theta'_{t2} = \alpha + \cos^{-1}\left(\frac{\cos\alpha}{\epsilon}\right) \qquad [10]$$

where the principal branch of $\cos^{-1}$ is now to be used.

As $\epsilon \to 1.0$, it eventually becomes possible for the same trajectory to spiral off the disk, return, spiral off again, and then return once more. Since in this analysis we will not attempt to treat this case, we must determine at what eccentricity this effect begins. At the onset of this behavior, the critical trajectory is one that is tangent to the disk at two points, (r_1, θ'_{t1}) and (r_2, θ'_{t2}), as shown in Fig. 2. To determine the eccentricity at which this occurs, we begin with 5 equations in 5 unknowns $(r_1, r_2, \theta'_{t1}, \theta'_{t2}, \epsilon)$. Equation [10] gives two relations for the angles at the tangent points. Equation [5] gives two relations for points on the edge of the electrode. Since the two points must be on the same spiral, Eq. [4] can be written

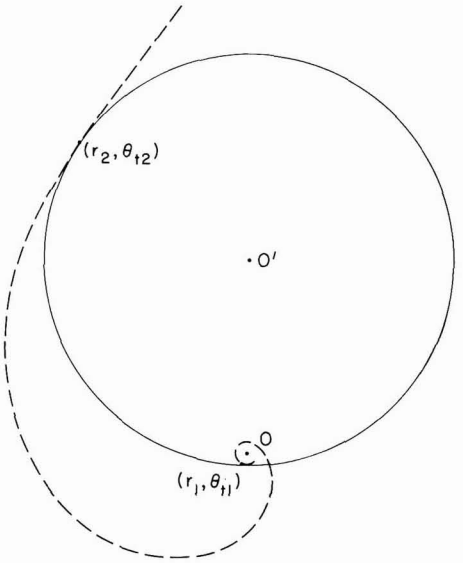


Fig. 2. Trajectory for eccentricity at which analysis fails

$$r_2 = r_1 \exp\left\{\left[\tan^{-1}\left(\frac{\sin\theta'_{t1}}{\epsilon - \cos\theta'_{t1}}\right) - \tan^{-1}\left(\frac{\sin\theta'_{t2}}{\epsilon - \cos\theta'_{t2}}\right) + 2\pi\right]\cot\alpha\right\} \qquad [11]$$

where 2π appears since the trajectory completes a full spiral before the second tangent point is reached. These 5 equations can be reduced to one equation in ϵ

$$\epsilon^2 + 1 - 2\epsilon\cos\left[\alpha + \cos^{-1}\left(\frac{\cos\alpha}{\epsilon}\right)\right] = \left\{\epsilon^2 + 1 - 2\epsilon\cos\left[\alpha - \cos^{-1}\left(\frac{\cos\alpha}{\epsilon}\right)\right]\right\} \exp\left\{\left[\pi + \cos^{-1}\left(\frac{\cos\alpha}{\epsilon}\right)\right] 4\cot\alpha\right\} \qquad [12]$$

which has two solutions

$$\epsilon_1 = 0.998476$$
$$\epsilon_2 = 1.001523 \qquad [13]$$

The second solution is significant for calculations with $\epsilon > 1$, since it gives the eccentricity at which fluid begins to pass over the disk only once. Eccentricities between these two critical values will not be treated in this analysis.

The mass transfer rate to the electrode may now be determined. It should be noted that for eccentricities $0.9985 > \epsilon > 0.6377$, some of the fluid experiences a situation similar to what would occur in a ring-disk system. That is, it spirals off the electrode, passes over an insulating surface, and then spirals over an active surface once more, after which it leaves the region of interest. It seems then that we may calculate the mass transfer rate for fluid following such a trajectory by determining the radii (r_1, r_2, r_3) at which this fluid (*i*) leaves the electrode initially, (*ii*) returns to the electrode, and (*iii*) leaves the electrode for the last time, and then use the appropriate formula (6, 7) for mass transfer to a ring-disk electrode which is operated at the limiting current for the same reaction on both the ring and disk. Similarly, for $\epsilon > 1.0015$ one could determine the radii at which a trajectory enters and leaves the electrode surface and use Levich's formula (1) for mass transfer to a ring electrode, with inner and outer dimensions identical to these, to determine the transfer rate along that trajectory. Since each trajectory would have a different ring-disk (or ring only, for $\epsilon > 1.0015$) analogue, it would be necessary to section the surface of the electrode into thin strips following the trajectories (shaded on Fig. 3) and determine, via the above method, the transfer rate to each. In the following discussion, details are presented only for the case $\epsilon > 1.0015$, which can be compared easily to previous treatments. The analysis for $0.6377 < \epsilon < 0.9985$ is similar except that the more complicated expression for mass transfer to a ring-disk system must be substituted for Levich's equation for transfer to a ring electrode only.

For a ring electrode with the active portion between r_1 and r_2, the Levich formula for mass transfer to a segment of width $d\theta$ is

$$dj = \frac{(r_2^3 - r_1^3)^{2/3}}{\sqrt{\nu/\omega}} \frac{\mathcal{D}c_\infty}{2\Gamma(4/3)} \left(\frac{0.510\nu}{3\mathcal{D}}\right)^{1/3} d\theta \qquad [14]$$

The total mass transfer to the disk will be given by this equation integrated between the two tangent points θ_{t1} and θ_{t2}. Upon changing the independent variable from θ to θ' and dividing by the rate of mass transfer to a centered disk electrode of equal area (j_{disk}), we find

$$j/j_{disk} = \frac{1}{2\pi}\int_{\theta'_{t1}}^{\theta'_{t2}} \left(\frac{r_2^3}{r_1^3} - 1\right)^{2/3} \left[\epsilon\frac{\cos(\theta' - \alpha)}{\cos\alpha} - 1\right] d\theta' \qquad [15]$$

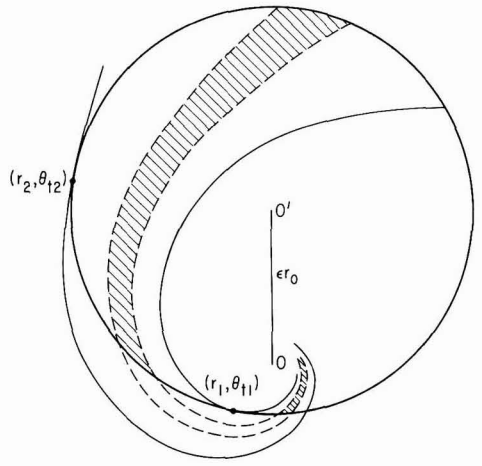


Fig. 3. Partitioning scheme for ring-disk analogy ($\epsilon < 1$)

Given θ'_1, the quantity r_2/r_1 can be determined by simultaneous solution of Eq. [4] and [5]. This must be done numerically due to the complexity of these equations. As a test of this numerical procedure, one can verify the identity

$$2\pi = \int_{\theta'_{t1}}^{\theta'_{t2}} \left(\frac{r_2^2}{r_1^2} - 1\right)\left[\epsilon\frac{\cos(\theta' - \alpha)}{\cos\alpha} - 1\right]d\theta' \quad [16]$$

which results from calculating the area of the electrode.

The asymptotic behavior as $\epsilon \to \infty$ is of some interest since it shows clearly the differences between this analysis and those of Chin and Litt and Bardin and Dikusar. As $\epsilon \to \infty$

$$\frac{r_1}{r_0} \to \epsilon - \cos\theta'$$

$$\frac{r_2}{r_0} \to \epsilon + \cos(\theta' - 2\alpha)$$

$$\theta'_{t1} \to \alpha - \frac{\pi}{2}$$

$$\theta'_{t2} \to \alpha + \frac{\pi}{2} \quad [17]$$

and with $x = \sin(\theta' - \alpha)$, Eq. [15] becomes

$$j/j_{disk} \to \frac{1}{\pi}\left(\frac{36\epsilon}{\cos\alpha}\right)^{1/3}\int_0^1 (1 - x^2)^{1/3}\,dx$$

$$= \frac{1}{\sqrt{\pi}}\left(\frac{9\epsilon}{2\cos\alpha}\right)^{1/3}\frac{\Gamma(4/3)}{\Gamma(11/6)} = 1.027\,\epsilon^{1/3} \quad [18]$$

correct to the largest order in ϵ. The method of Bardin and Dikusar leads to

$$j/j_{disk} \to \frac{1}{\sqrt{\pi}}\left(\frac{9\epsilon}{2}\right)^{1/3}\frac{\Gamma(4/3)}{\Gamma(11/6)} = 0.884\,\epsilon^{1/3} \quad [19]$$

while Chin and Litt obtained an expression equivalent to

$$j/j_{disk} \to \frac{3}{2\pi^{1/6}}\left(\frac{\epsilon}{3\cos\alpha}\right)^{1/3} = 0.998\epsilon^{1/3} \quad [20]$$

The differences arise from different schemes for segmenting the electrode before applying the ring analogy. Bardin and Dikusar took the streamlines to be radially outward from the center of rotation (Fig. 4). Chin and Litt approximate the circular electrode by a square of equal area, but with the proper angle given to the spiral streamlines. Thus we conclude that the shape approximation used by Chin and Litt introduces

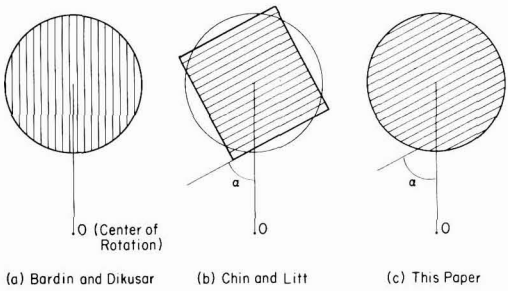


Fig. 4. Comparison of partitioning schemes ($\epsilon > 1$)

less than a 3% error in the asymptotic transfer rate, but the neglect of the fluid trajectory by Bardin and Dikusar yields a 14% error.

Experimental Technique

The mass transfer rates for centered and eccentric electrodes were determined for electrodeposition of copper onto copper electrodes. The solution used was 0.008M $CuSO_4$ in 1.5M H_2SO_4. The rotating disk electrodes were fabricated from Plexiglas, drilled and fitted with short sections of 0.25 in. copper rod. The over-all diameters of the disks were 1.5 in., except for the electrode with an eccentricity of 3.94, for which a 2.0 in. disk was used. The electrodes were polished with emery paper and then wet crocus cloth prior to use. Limiting current curves were recorded at three rotation speeds, 405, 510, and 1590 rpm, at room temperature (22°C) for electrodes of eccentricities 0.00, 0.66, 0.88, 2.13, 2.94, and 3.94. The ratios j/j_{disk} were then calculated for each electrode and rotation speed by dividing the total current to the eccentric disk by that to the centered electrode at the same rotation speed. To minimize the effect of temperature variations, the centered electrode was used for every third run, and these results used to calculate the transfer ratios for the noncentered electrodes used in the immediately preceding and following runs.

Results

The experimental results are given in Fig. 5 along with the numerical results, the large eccentricity asymptote Eq. [18]), and the analytical and experimental results of Bardin and Dikusar. The data emphasize the importance of sectioning the electrodes along streamlines in order to use the Levich equation for ring electrodes to predict the mass transfer rate. Our data disagree significantly with those of Bardin and Dikusar, due, perhaps, to their use of quite small electrodes ($\sim$ 1 mm in diameter). This small size might make accurate determination of the eccentricity difficult and would tend to emphasize edge effects. The data gathered by Chin and Litt support this analysis also, since they correlated well with their theoretical analysis, which differs from the present analysis by only 3% at the large eccentricities at which their experimental work was conducted ($\epsilon > 9$).

Although, as previously noted, this analysis fails in a limited region about $\epsilon = 1$, the curves for the results for $\epsilon < 1$ and $\epsilon > 1$ can be joined with no apparent discontinuity at $\epsilon = 1$, as shown on Fig. 5.

The close agreement between the numerical and asymptotic (analytic) results is somewhat surprising in view of the fact that curvature of the trajectories was ignored in the asymptotic analysis and becomes pronounced as ϵ becomes small. It appears that the formula

$$\frac{j}{j_{disk}} = 1.027\epsilon^{1/3} + 0.044\epsilon^{-5/3} \quad [21]$$

will be accurate to within 1.0% for $\epsilon > 0.8$. The ex-

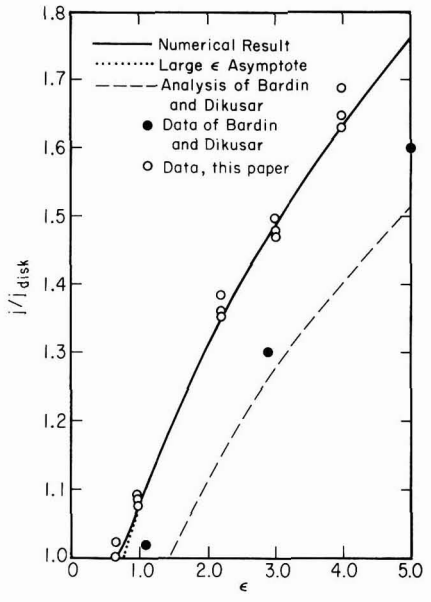


Fig. 5. Mass transfer ratio j/j_{disk} vs. eccentricity for an off-center rotating disk electrode.

ponent $-5/3$ is justified by an extension of the asymptotic analysis.

Acknowledgments

This work was supported by the United States Atomic Energy Commission.

Manuscript submitted May 17, 1974; revised manuscript received Jan. 27, 1975.

Any discussion of this paper will appear in a Discussion Section to be published in the June 1976 JOURNAL. All discussions for the June 1976 Discussion Section should be submitted by Feb. 1, 1976.

Publication costs of this article were partially assisted by the University of California.

LIST OF SYMBOLS

c_∞	bulk concentration of reactive species (g/cm³)
$\mathcal{D}$	diffusion coefficient of reactive species (cm²/sec)
j	mass transfer rate to electrode (g/sec)
j_{disk}	mass transfer rate to a centered electrode (g/sec)
O	center of rotation
O'	center of electrode
r	radial coordinate from center of rotation (cm)
r_0	radius of electrode (cm)
v_r, v_θ	velocity components relative to the disk (cm/sec)
z	coordinate normal to disk (cm)
α	angle of fluid trajectories near disk
β	angle between edge of disk and ray from O
ϵ	offset of center of rotation
ϵ_c	critical offset for nonuniform accessibility
θ	angular coodinate from center of rotation
θ'	angular coordinate from center of disk
ν	kinematic viscosity of solution (cm²/sec)
ω	rotation speed of disk (sec^{-1})

REFERENCES

1. V. Levich, "Physicochemical Hydrodynamics," Prentice-Hall, Englewood Cliffs, N. J. (1962).
2. A. Riddiford, in "Advances in Electrochemistry and Electrochemical Engineering," P. Delehay, Editor, Vol. 4, pp. 47-116, Interscience Publishers, Inc., New York (1966).
3. D. T. Chin and M. Litt, *This Journal*, **119**, 1338 (1972).
4. M. Bardin and A. Dikusar, *Elektrokhimiya*, **6**, 1147 (1970).
5. W. Cochran, *Proc. Cambridge Phil. Soc.*, **30**, 365 (1934).
6. W. Smyrl and J. Newman, *This Journal*, **119**, 212 (1972).
7. W. J. Alberry and S. Bruckenstein, *Trans. Faraday Soc.*, **62**, 1920 (1966).

An Electrochemical Study of Undercutting during Etching of Duplex Metal Films

J. J. Kelly and C. H. de Minjer

Philips Research Laboratories, Eindhoven, Netherlands

ABSTRACT

For various technological applications patterns are chemically etched in metal films partly covered with a nobler metal. As a result of the bimetallic contact, accelerated etching may occur, giving rise to considerable undercutting. From electrochemical considerations it was expected that the use of certain chemical polishing solutions would significantly reduce the degree of such undercutting. This was verified by studying the electrochemical properties of various polishing and nonpolishing etching agents. Suitable solutions were developed for the etching of Al, Mo, and Ni-P. These etching agents, when used to etch metal films partly covered by nobler metals, gave markedly less undercutting than nonpolishing etching agents.

In various technologies it is often necessary to etch fine patterns in metal films. Important factors determining the choice of a chemical etching agent are generally the etching rate, the degree of undercutting, the chemical aggressiveness of the solution to other materials present, and the definition of the etched patterns. One particular problem arises with duplex systems when patterns have to be etched in metal films partly covered by a nobler metal. Because of galvanic action arising from the bimetallic contact, accelerated etching may occur, causing considerable undercutting at the interface between the two metals. This paper describes an electrochemical study of such undercutting and suggests how the effect may be avoided by a suitable choice of etching agent.

Key words: aluminum, chemical polishing, duplex metal films, electropolishing, etching of metals.

The increase in the rate of dissolution of a metal due to contact with a nobler metal may be explained by considering the partial polarization curves for the

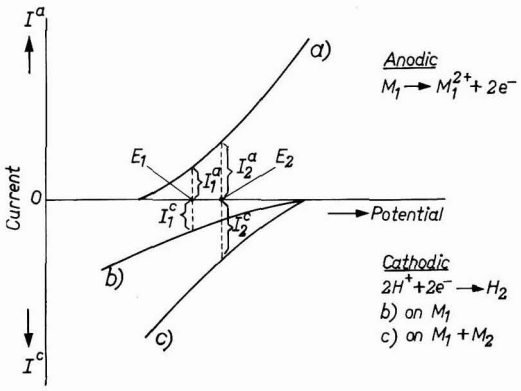


Fig. 1. Partial polarization curves for dissolution of metal M_1 in a nonpolishing solution.

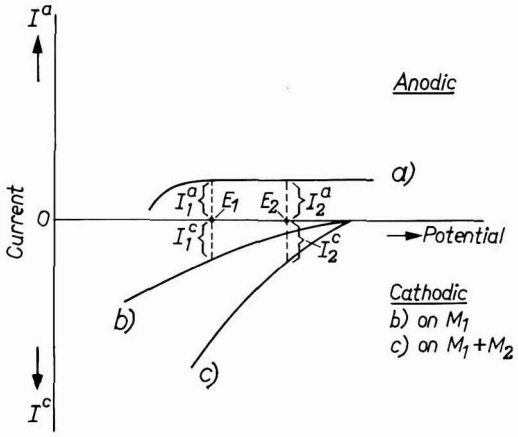


Fig. 2. Partial polarization curves for dissolution of metal M_1 in a polishing solution.

process (1). An example is shown in Fig. 1 for a metal M_1, of a given area, dissolving in acidic solution. Curves (a) and (b) are the partial anodic and cathodic polarization curves for metal dissolution and hydrogen evolution, respectively. Under open-circuit conditions (no external current) M_1 dissolves at a rest potential E_1 ($I_1^a = I_1^c$) and at a rate given by I_1^a. When M_1 is connected to a second metal M_2, which does not dissolve in the potential region shown, only hydrogen evolution will occur at M_2 and the cathodic polarization curve for $M_1 + M_2$ may be represented by curve (c). The increase in the cathodic current depends, among other factors, on the area of M_2. With this combined system, the rest potential is shifted to a more positive value E_2 ($I_2^a = I_2^c$). It is obvious that, with no external current, M_1 dissolves more rapidly when connected to M_2 ($I_2^a > I_1^a$). When the cathode area is further increased by increasing the area of M_2, then M_1 should dissolve even more rapidly.

It seemed to us that such accelerated etching might be prevented by choosing a solution for which the anodic partial current does not increase as a function of potential in a suitable potential range. Electropolishing solutions generally give such current-potential characteristics (2, 3) and a typical polarization curve for such a system is shown in Fig. 2, curve (a). At lower potentials the current increases with increasing potential and etching of the metal is observed. At higher potentials a "polishing" film, consisting of either a viscous layer or an oxide or salt film, is present on the metal. No increase in current is obtained despite an appreciable increase in potential and, as a rule, polishing is observed in this range. When an oxidizing agent with a cathodic polarization, curve (b) as shown in Fig. 2, is added to the electropolishing solution, the metal M_1 is "chemically polished" at an open-circuit potential E_1 and at a rate given by I_1^a. Enlarging the cathodic surface by combining M_1 with a noble metal M_2 leads to an increase in the cathodic current at a given potential (curve c, Fig. 2). Despite the fact that the rest potential increases to E_2 the rate of dissolution of the metal should remain the same ($I_1^a = I_2^a$). When such a solution is used as an etching agent for M_1, the etching rate should not be affected by the presence of a noble metal. The purpose of this work was to determine experimentally if this assumption was correct and in this way to develop suitable etching agents for bimetallic systems.

Our investigations were directed mainly to the study of etching agents for Al and, to a lesser extent, for Mo and Ni-P.

Experimental

Electrode materials.—Aluminum metal (99.99%) was supplied by Rebag (Grevenbroich, West Germany) in the form of 8 mm thick plate and molybdenum (99.9%) by Philips N.V. (Maarheeze, Netherlands) as cylindrical rods with a diameter of 6 mm. Nickel-phosphorus electrodes, containing approximately 10% P by weight, were made by electroless deposition of a 100 μm thick layer onto Ni strips.

The electrodes for the polarization measurements were first mechanically machined and, after cleaning, were electropolished in the same solutions as used for the electrochemical experiments (Table I). Since current-voltage curves were measured in electropolishing solutions, generally under polishing conditions, essentially no roughening of the electrode surface occurred. The metal disks for the chemical dissolution experi-

Table I. Solutions used for etching metal films

Metal	Electropolishing solution	Corresponding chemical polishing solution	Nonpolishing Solution
Al	(i) 75g Na_2CO_3 35g $Na_3PO_4 \cdot 12H_2O$ 0.5 liter H_2O	75g Na_2CO_3 35g $Na_3PO_4 \cdot 12H_2O$ 16g $K_3Fe(CN)_6$ 0.5 liter H_2O	0.25M NaOH
Al	(ii) 40 ml H_3PO_4 (85%) 40 ml CH_3COOH (100%) 20 ml H_2O	40 ml H_3PO_4 (85%) 40 ml CH_3COOH (100%) 10 ml HNO_3 (65%) 10 ml H_2O	
Mo	50 ml H_3PO_4 (85%) 50 ml H_2O	50 ml H_3PO_4 (85%) 30 ml HNO_3 (65%) 20 ml H_2O	22% (wt) $Ce(NH_4)_2(NO_3)_6$ in 1% HNO_3
Ni-P	90 ml H_3PO_4 (85%) 10 ml H_2O	(i) 90 ml H_3PO_4 (85%) 10 ml HNO_3 (65%) (ii) 30 ml H_2SO_4 (85%) 15 ml HNO_3 (65%) 4 ml HCl (37%) 1 ml H_2O	50 ml HNO_3 (65%) 50 ml H_2O

ments were either chemically or electrolytically polished, prior to use.

Metal films.—For the etching experiments metal films were prepared on glass microscope slides (18 × 18 × 0.12 mm³). Aluminum films (0.4 μm thick) were made by evaporation, Mo films (0.03 μm thick) by sputtering, and Ni-P films (10% P) (0.3 μm thick) by electroless deposition. The metal films were then partly covered either with photoresist or noble metal patterns containing details of 5 μm and greater.

The Al was provided with a noble metal pattern by first sputter-etching the metal surface to remove the oxide film and then depositing a 0.1 μm Pt film on the clean Al in the same apparatus. Through the windows of a resist pattern a 2 μm thick Au film was electrodeposited on the Pt. After removal of the resist, the thin Pt film, not protected by the thick Au film, was removed by sputter-etching.

In a similar manner a thin Au film was sputtered onto the clean Mo film and a thicker Au film was electrodeposited through the windows of a photoresist pattern. After removal of the resist the thin Au film was chemically etched to expose the underlying Mo. The Ni-P films were also provided with a Au pattern by electrodeposition.

In all cases the area of the exposed metal film was kept small compared to the area covered by resist or noble metal.

Composition of etching solutions.—Table I gives a list of the solutions used for the electrochemical and chemical etching experiments with the different metals. All chemicals used in this work were of reagent grade.

Determination of dissolved Al.—Etching rates were measured by removing 1 ml samples from the etching solution at regular intervals and determining the concentration of dissolved Al spectrophotometrically using 8-hydroxyquinoline (4).

Measurements of the polarization curves.—Polarization curves were recorded at a scanning rate of 95 mV/min using a Wenking 61 TR potentiostat and a Philips PM 8100 recorder. Because both the dissolution of metals in a potential-independent current region and the electrolytic reduction of various oxidizing agents may be diffusion controlled, we used rotating disk electrodes (RDE) for the Al study. The metal electrode (Al or Pt) in the form of a cylinder with a face area of 1 cm², was imbedded in a Teflon shaft, which was driven by a motor with an electronically regulated feedback system.

The cell consisted of a Pyrex vessel coated with a conducting tin oxide layer which acted as a heating element. The reference standard calomel electrode (SCE) was placed in a sidearm which was connected to the bottom of the main cell via an inlet fitted with a capillary extending to just below the center of the rotating disk. The counterelectrode was a Pt ring set at the bottom of the capillary inlet. For certain experiments a large area Pt strip was placed against the inner wall of the cell and connected to the rotating electrode via the mercury contact.

For experiments with Mo and Ni-P, only a stationary test electrode in the form of a flat metal strip was used with a Pt strip as counterelectrode. The SCE reference was placed in a second vessel containing the same solution and was connected to the test electrode in the working cell via a salt bridge and a Luggin capillary. The solutions were not stirred in this case.

All potentials quoted either in the text or in the figures of this paper are values with respect to SCE.

Results and Discussion

Aluminum

Numerous electropolishing agents for Al are described in the literature (2, 3). From the various solutions investigated by us, current-potential measurements indicated that two of these, an alkaline and an acidic solution, had electrochemical properties suitable for our purposes.

Alkaline polishing solution.—Anodic polarization measurements.—The current-potential characteristics of a 1 cm² Al RDE at 24°C in an electropolishing solution containing Na_2CO_3 and Na_3PO_4 (cf. Table I) are shown in Fig. 3, curve (a). For potentials greater than −0.8V the anodic current is constant. In this potential range 3 faradays are required to dissolve 1 mole of Al in agreement with Faraday's law. No cathodic reaction occurs in this region. At potentials below −0.8V hydrogen is cathodically evolved at the Al electrode. The current voltage curves were reproducible to within approximately 5% for the scan rate shown. The difference between the limiting anodic current density measured potentiostatically and during scanning at 95 mV/min was <10%.

The partial current for Al dissolution was calculated from the dissolution rate of the metal and is shown in Fig. 3, curve b. The difference between this partial current and the total current (curve a) at lower potentials is due to the cathodic reaction-hydrogen evolution.

The effect of a stationary 15 cm² Pt electrode in contact with the 1 cm² Al rotating electrode in the same solution at the same temperature and rotation rate is shown in Fig. 3, curve (c). The differences between the polarization curves (c) for Al + Pt and (a) for Al alone are due to a lower hydrogen overvoltage on Pt than on Al and to oxygen evolution at the Pt electrode as is shown in curve (d), the polarization curve for the Pt strip alone. It is obvious from Fig. 3 that a relatively wide potential region exists in which the anodic current of Al is not affected by the presence of the noble metal.

A plot of the limiting anodic current density as a function of the square root of the rotation rate gave a straight line. This indicates, that for the rotation range 100-1000 rpm, the reaction is diffusion controlled (5). The line did not pass through the origin (intercept 4 mA/cm²).

Anodic current-potential measurements performed at temperatures between 25° and 60°C and at the same rotation rate showed in each case a well-defined constant current region. The activation energy for the electropolishing process, calculated from the limiting current densities, was 9.8 ± 0.2 kcal/mole, a value which is in good agreement with that reported by Gabe (6) for a similar Brytal-type bath. This is higher than values reported for reactions in other diffusion-controlled electrochemical systems (5, 7, 8) (≤4 kcal/mole). In the case of electropolishing a highly viscous film and/or an oxide layer may be

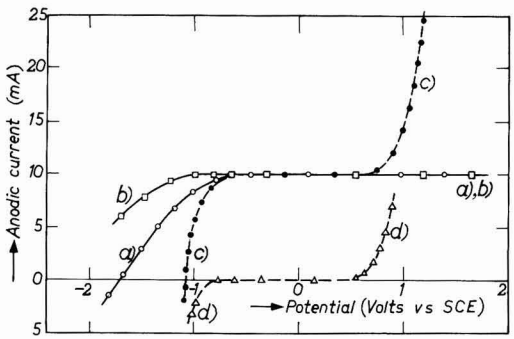


Fig. 3. Polarization curves measured in PO_4^{3-}/CO_3^{2-} solution at 24°C. Curves (a), (c), and (d) are curves recorded using: (a) 1 cm² Al RDE, 550 rpm; (c) 1 cm² Al RDE + 15 cm² stationary Pt electrode; (d) 15 cm² stationary Pt electrode. Curve (b) is the partial anodic curve for case (a) calculated from Al dissolution rates.

present on the electrode and this may be responsible for the higher activation energy.

For comparison we also measured the polarization curve for an Al RDE in a nonpolishing solution, 0.25M NaOH. In this case the anodic current density increased significantly with increasing potential.

Chemical dissolution of Al.—As an oxidizing agent for the alkaline electropolishing solution we chose $K_3Fe(CN)_6$ (0.092M). The solution shown in Table I had a pH of 12.6. The ferricyanide/ferrocyanide system in 0.01M NaOH has a standard potential of +0.22V (9) which is in the region of constant anodic current of Fig. 3.

Curve (a) of Fig. 4 shows the amount of Al chemically dissolved as a function of time at 24°C and 550 rpm for a 1 cm^2 Al RDE (circles) and for the same disk connected to a stationary Pt strip (15 cm^2) in the same solution (squares). No increase in the Al dissolution rate due to the noble metal was observed. If the rate of Al dissolution is expressed as current density, then this value agrees well with the limiting anodic current density observed in Fig. 3.

Results are also shown in Fig. 4 for chemical dissolution of Al at 36°C (curve b) and at 48°C (curve c). For Al alone (circles) the current densities calculated from these rates are lower than those expected from the corresponding limiting anodic current densities. This effect will result when the cathodic process, the reduction of ferricyanide, is rate determining at the rest potential. When the Al disk was in contact with a large area Pt strip (squares), an increase in the rate of chemical dissolution was observed at these temperatures. In this case the measured chemical dissolution rates agreed with the values calculated from the limiting anodic current densities. This must mean that the anodic process is rate determining.

Cathodic polarization measurements.—In order to check the above explanation, polarization curves for the ferricyanide reduction in the PO_4^{3-}/CO_3^{2-} solution were measured. Figure 5 shows such a curve for a Pt RDE at 24°C and 550 rpm. A well-defined diffusion-controlled cathodic current density (i_l^c) was observed. The limiting current density was directly proportional to the $Fe(CN)_6^{3-}$ concentration as can be seen in Fig. 5 and to the square root of the rotation rate (5, 8).

The cathodic limiting current was determined as a function of temperature between 20° and 60°C and an activation energy of 3.9 kcal/mole was calculated from these results. This is in the region expected for a process controlled by laminar flow (5, 7, 8).

The anodic limiting current density for Al dissolution (curve a) and the cathodic limiting current density for the reduction of ferricyanide (curve b) are

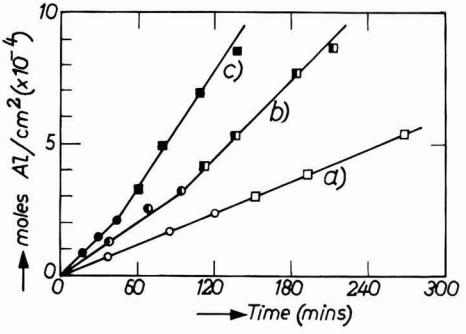


Fig. 4. Chemical dissolution of Al as a function of time for an Al RDE alone (circles) and in contact with a 15 cm^2 Pt strip (squares) in $PO_4^{3-}/CO_3^{2-}/Fe(CN)_6^{3-}$ solution, 550 rpm at (a) 24°C, (b) 36°C, and (c) 48°C.

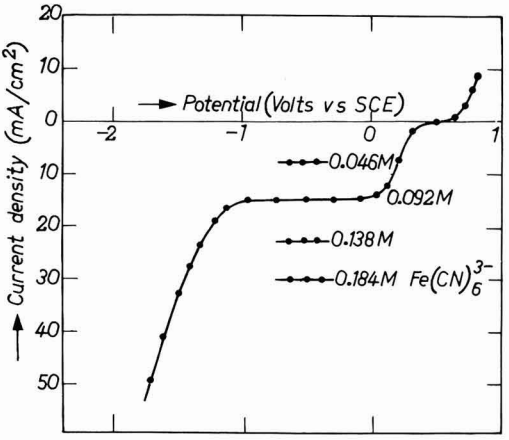


Fig. 5. Cathodic polarization curve for a 1 cm^2 Pt RDE in $PO_4^{3-}/CO_3^{2-}/Fe(CN)_6^{3-}$ (0.092M) solution, 550 rpm, 24°C. Limiting current densities are also shown for other concentrations.

plotted as a function of temperature in Fig. 6. The measured chemical dissolution rates of Al, expressed as current densities, are also plotted in Fig. 6, circles for Al alone and crosses for Al in contact with a 15 cm^2 Pt strip. It is clear that for the case of Al alone at temperatures below 32°C, the limiting anodic current density is less than the cathodic ($i_l^a < i_l^c$) and in this range the chemical dissolution rate expected from i_l^a is obtained. For temperatures above 32°C, $i_l^c < i_l^a$ and the dissolution rate for Al alone is determined by the magnitude of i_l^c. Hence the circles fall on the cathodic line (curve b). Contacting the Al with Pt leads to an increase in cathodic current, therefore $Fe(CN)_6^{3-}$ reduction is no longer rate determining and the crosses fall on the anodic curve. The chemical etching results shown in Fig. 4 can be explained in this way, using the partial polarization results.

It is obvious from the electrochemical results shown in Fig. 6 that the etching of bimetallic systems without the risk of undercutting in the $PO_4^{3-}/CO_3^{2-}/Fe(CN)_6^{3-}$ solution (Table I) is only guaranteed at or below 32°C, *i.e.*, where the etching rates of both Al alone and of Al in contact with Pt are under anodic control. For temperatures above 32°C the etch-

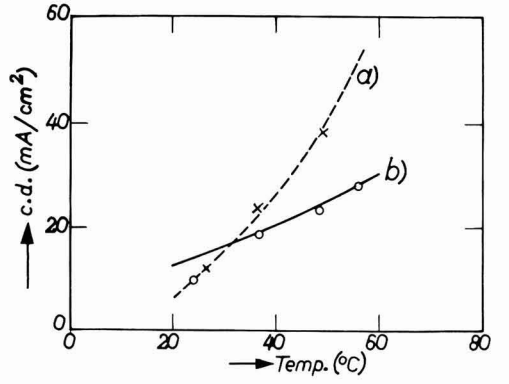


Fig. 6. Summary of electrochemical and chemical results: anodic (curve a) and cathodic (curve b) limiting current densities are plotted as a function of temperature; chemical dissolution rates of Al alone and of Al in contact with Pt are given by circles and crosses, respectively.

ant can be modified by increasing the ferricyanide concentration sufficiently (see Fig. 5) so that the etching is no longer under cathodic control.

Rest potential of Al.—The value of the rest potential of Al measured in the $PO_4^{3-}/CO_3^{2-}/Fe(CN)_6^{3-}$ solution was −1.05V. From the partial anodic Al curve measured in PO_4^{3-}/CO_3^{2-} solution (Fig. 3, curve b) and the cathodic curve measured on Pt in the $PO_4^{3-}/CO_3^{2-}/Fe(CN)_6^{3-}$ solution (Fig. 5) a much higher value of the rest potential (+0.16V) was expected, *i.e.*, 1.2V higher. The cathodic polarization curve for Al in aqueous $Fe(CN)_6^{3-}$ solution, with no PO_4^{3-}/CO_3^{2-} present, showed that ferricyanide was reduced only at potentials much more cathodic (>1V) than on Pt. This was also found to be the case for cathodic reduction of $Fe(CN)_6^{3-}$ in PO_4^{3-}/CO_3^{2-} solution. This considerable shift in the cathodic curve for Al with respect to that for Pt explains the discrepancy between measured and predicted values of rest potential. The value of the limiting cathodic current density was the same for both metals.

Petrocelli has reported similar effects for Al using $Fe(CN)_6^{3-}/Fe(CN)_6^{4-}$ in NaOH solution (10) and Ce^{4+}/Ce^{3+} in H_2SO_4 solution (1). He suggests (1, 11) that a coherent oxide film, the thickness of which increases with increasing potential, exists on Al even at cathodic potentials. He attributes the shift in the cathodic reduction curves to the fact that Al ions may diffuse or migrate through the oxide film while electrons may only pass through by quantum mechanical tunneling.

Acidic polishing solution.—The acidic polishing solution was not as extensively studied as the alkaline solution. However the same general features were also observed in this case.

The anodic current-potential curve, measured using an Al RDE (1 cm^2) at 25°C in a solution containing H_3PO_4 and CH_3COOH (Table I), was similar in form to that found for the alkaline solution. At a rotation rate of 500 rpm, a rest potential of −0.9V and a limiting anodic current density of 3 mA/cm^2 were observed. The limiting current density depended on the rotation rate. Over a broad potential range (+0.2 to +0.8V) the anodic polarization curve was essentially unaffected by contacting the Al electrode with a large area Pt strip.

Nitric acid (Table I) was a suitable oxidizing agent for this system. During chemical dissolution of Al in this solution a rest potential in the required plateau region was observed. The cathodic current was not a limiting factor for the Al dissolution rate at 25°C.

Application of polishing solutions for Al etching.—In order to test the applicability of these chemical polishing solutions as etching agents, Al films were etched through the windows of a photoresist or a noble metal pattern. Because it was more convenient to electrodeposit thick layers of gold instead of platinum, we used gold for the upper noble metal layer in these experiments. The electrochemical behavior of gold in these solutions was the same as that of platinum. During etching the solutions were stirred. The degree of undercutting was studied by observing the etched film through the glass substrate using a microscope.

Etching Al/resist films with the $PO_4^{3-}/CO_3^{2-}/Fe(CN)_6^{3-}$ and $H_3PO_4/CH_3COOH/HNO_3$ solutions gave results similar to those obtained with 0.25M NaOH, *i.e.*, a controlled etching rate, good definition, and negligible undercutting.

The etching rate of Al in 0.25M NaOH for the Al/noble metal films was much greater than for the corresponding Al/resist films. In Table II the times required to etch the two types of film are given. An increase in etching rate by a factor of 7 was observed. Figure 7a shows the results of 3 min etching of an Al film partly covered with Pt + Au. Considerable undercutting (~10 μm) has occurred at the Al/Pt + Au interface. For comparison a photograph of an Al/resist interface is also included (Fig. 7b) in which the Al film has been etched for 7 min under the same conditions. Only slight undercutting was observed.

Table II. Etching of Al films

Solution	Film	Etching time (min)
0.25M NaOH	Al/resist	7 ± 2
	Al/Pt + Au	1 ± 0.5
$PO_4^{3-}/CO_3^{2-}/Fe(CN)_6^{3-}$	Al/resist	3 ± 1
	Al/Pt + Au	3 ± 1
$H_3PO_4/CH_3COOH/HNO_3$	Al/resist	12 ± 3
	Al/Pt + Au	11 ± 2

The Al tracks, not covered by either noble metal or resist, were approximately 200 μm wide. In the NaOH solution, etching of the Al covered by noble metal was considerably accelerated both at the contact area (Fig. 7a) and in the narrow tracks (Table II). In general the effect of the noble metal in such solutions will always be greater near the bimetallic contact. Although the resistances of the metals are low and the metals have the same potential, the resistance of the solution is higher and the current density will therefore decrease with increasing distance from the contact area. Besides this, complications may also arise due to inadequate refreshing of the etching electrolyte in narrow slits, local excessive stirring, or the formation of islands in the etching metal.

The data given in Table II show that no appreciable difference in etching time was found for the Al/resist and Al/Pt + Au films using the two polishing solutions. Figure 7c shows the results of 4 min etching of the Al/Pt + Au film in the alkaline polishing solution. Very little undercutting was observed. A similar result was also found for the acidic solution.

A higher etching rate in the alkaline solution can be obtained by either increasing the temperature and/or replacing Na_2CO_3 by NaOH with equally favorable results. In both cases the $Fe(CN)_6^{3-}$ concentration must be increased to prevent the cathodic reaction from becoming rate determining.

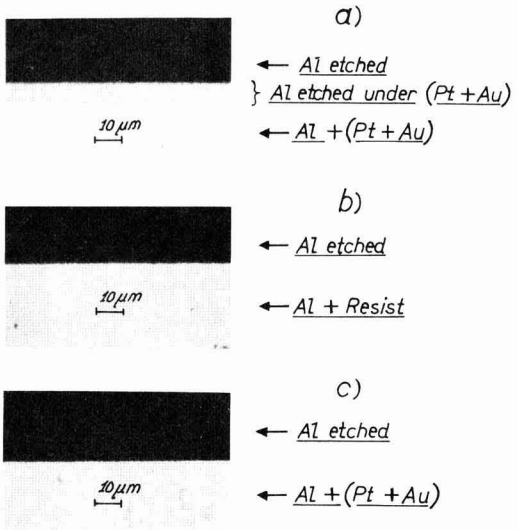


Fig. 7. Undercutting in Al films: (a) Al/(Pt + Au) film etched 3 min in 0.25M NaOH; (b) Al/resist film etched 7 min in 0.25M NaOH; (c) Al/(Pt + Au) film etched 4 min in $PO_4^{3-}/CO_3^{2-}/Fe(CN)_6^{3-}$ solution.

Molybdenum

For etching Mo a solution of $Ce(NH_4)_2(NO_3)_6$ in HNO_3 is often used (Table I). With no noble metal present, this solution etches Mo at a rate of approximately 0.1 μm/min. Thus a 0.03 μm Mo film partly covered by a photoresist film could be etched in 20-30 sec without significant undercutting. When the Mo film was etched through the windows of a gold pattern for 15 sec using the same solution, enormous undercutting (80 μm) was found (Fig. 8a). The etching rate of Mo under Au was more than three orders of magnitude greater than that of Mo under resist.

The polarization curve measured using a stationary Mo electrode in the same solution showed that the anodic current rose very steeply for very slight increases in potential. The corresponding curve for a stationary Pt electrode in this solution showed a limiting cathodic current due to reduction of Ce^{4+}, which in this case determined the etching rate. The fact that the anodic current rises so rapidly means that very large acceleration factors in etching rate are possible when the cathode area is large relative to the exposed Mo area.

Molybdenum may be electropolished in H_3PO_4 solution (2) (Table I). The polarization curve shows a wide potential region above +0.6V with an essentially constant anodic current. Nitric acid is a suitable oxidizing agent giving a rest potential of approximately +0.8V. This chemical polishing etching agent gave very little undercutting (Fig. 8b), as expected from the electrochemical results.

Nickel-Phosphorus

An etching agent often used for Ni-P films is a diluted HNO_3 solution (Table I). The anodic polarization curve of Ni-P in this solution does not show a constant current region and accordingly the etching of Ni-P under a gold pattern with this solution gives rise to undercutting.

We did not succeed in finding an electropolishing solution for Ni-P. Various solutions which are used to electropolish pure Ni (2, 3) did not give favorable results with Ni-P. Our earlier experiments had shown that the anodic behavior of Ni-P is quite different from that of pure Ni. As an example Ni tends to passivate in H_2SO_4 solutions while Ni-P does not.

Although no polishing effect was observed a concentrated H_3PO_4 solution (Table I) gave polarization curves for Ni-P in which the anodic current did not increase appreciably between 0.8 and 1.7V. Nitric acid was used as the oxidizing agent and the rest potential of Ni-P in this solution was 0.85V. Much less undercutting of Ni-P/Au films was observed with this solution than with the diluted HNO_3 solution. A solution containing HCl, HNO_3, H_2SO_4, and H_2O (Table I), which is widely used to etch Ni-P films in the presence of Cu, also gives rise to very little undercutting.

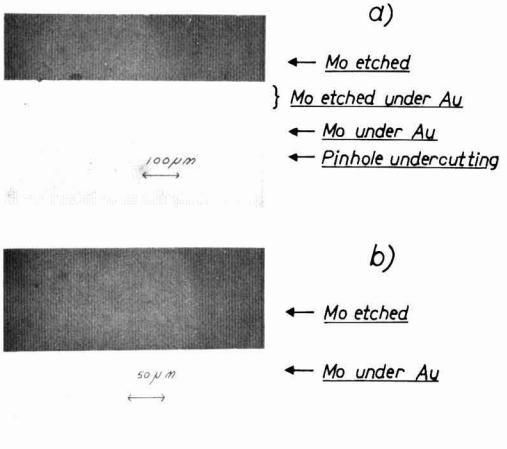


Fig. 8. Undercutting in Mo films: Mo/Au film etched using (a) $Ce(NH_4)_2(NO_3)_6/HNO_3$ solution, 15 sec, and (b) H_3PO_4/HNO_3 solution, 15 sec. In photo (a) the result of etching of the Mo at a pinhole in the Au is also shown.

Summary

The aim of this work was to investigate whether it was possible from electrochemical considerations to develop etching agents with the property that the rate of dissolution of the metal in the solution remains unaffected by contact of the metal with a nobler metal. The procedure for a given metal was to choose a solution having a suitable potential range in which the anodic current is constant and to add an oxidizing agent with a standard potential in this range. Electropolishing solutions usually fulfill the requirement of a constant current range and addition of an oxidizing agent to such a solution gives a chemical polishing solution.

As electropolishing agent for Al, a Na_3PO_4/Na_2CO_3 solution was investigated. To obtain a corresponding chemical polishing solution, $K_3Fe(CN)_6$ was added as oxidizing agent. Various aspects of the anodic and cathodic polarization curves for Al in these polishing solutions were studied, *e.g.*, dependence of the limiting current density on temperature, concentration, and rotation rate. The rates of dissolution of an Al rotating disk alone and in contact with a Pt strip were measured in the chemical polishing solution. As expected from the electrochemical results no increase in the dissolution rate of Al at 24°C due to the presence of the nobler metal was observed. This etching solution gave very little undercutting of Al films partly covered by a Pt + Au film, whereas considerable undercutting was found with a nonpolishing solution.

An acidic polishing solution for Al gave equally favorable results.

Suitable etching agents for duplex metal systems with Mo or Ni-P films, in combination with Au films, were also found.

These results confirm the hypothesis that certain chemical polishing solutions, when used to etch metals in the presence of nobler metals, give much less undercutting than nonpolishing solutions.

Manuscript submitted Oct. 15, 1974; revised manuscript received Feb. 24 ,1975.

Any discussion of this paper will appear in a Discussion Section to be published in the June 1976 JOURNAL. All discussions for the June 1976 Discussion Section should be submitted by Feb. 1, 1976.

Publication costs of this article were partially assisted by Philips Research Laboratories.

REFERENCES

1. J. V. Petrocelli, *This Journal*, **97**, 10 (1950).
2. P. V. Shchigolev, "Electrolytic and Chemical Polishing of Metals," Freund Publishing House, Holon (1970).
3. W. J. Mc. G. Tegart, "The Electrolytic and Chemical Polishing of Metals," Pergamon Press, London (1959).
4. A. Claassen, L. Bastings, and J. Visser, *Anal. Chim. Acta*, **10**, 373 (1954).
5. V. G. Levich, "Physicochemical Hydrodynamics," Prentice Hall, Englewood Cliffs, N. J. (1962).
6. D. R. Gabe, *Trans. Inst. Metal Finishing*, **51**, 32 (1973).
7. D. P. Gregory and A. C. Riddiford, *J. Chem. Soc.*, 3756 **(1956)**.
8. Yu. M. Povarov and P. D. Lukovtsev, *Electrochim. Acta*, **18**, 13 (1973).
9. Handbook of Chemistry and Physics, 51st ed., p. D-111 (1970-1971).
10. J. V. Petrocelli, *This Journal*, **99**, 513 (1952).
11. J. V. Petrocelli, *ibid.*, **106**, 566 (1959).

Technical Note

Electrochemical Determination of Porosity in Nickel Electroplates on a Uranium Alloy

L. J. Weirick*

Metallurgy and Electroplating Division 8312, Sandia Laboratories, Livermore, California 94550

Typical chemical and electrographic test procedures for the determination of porosity in electroplates are usually destructive in nature and not generally applicable to process control procedures. Electrochemical techniques are preferable because they offer good sensitivity and rapid analysis and are relatively nondestructive. A quality control technique having these characteristics was needed to determine the porosity in nickel electroplates on a uranium-3/4 weight per cent titanium alloy.

Mansfeld (1) has derived general expressions for the corrosion potential ϕ_g of galvanic couples in terms of the anodic and cathodic areas. For the case of Tafel behavior or activation control, his expression is

$$\phi_g = \frac{b_a\phi_o^C + b_c\phi_o^A}{b_a + b_c} + \frac{b_a b_c}{b_a + b_c}\log\frac{i_o^C A^C}{i_o^A A^A} \qquad [1]$$

If the influence of area variations is investigated while all other parameters are held constant and the cathodic and anodic area fractions (A_A, A_C) are introduced, Eq. [1] can be written in the form

$$\phi_g = k + \frac{b_c b_a}{b_a + b_c}\log\frac{A_C}{A_A} \qquad [2]$$

For base metal specimens coated with noble metal electroplates of moderate to low porosity, $A_C >> A_A$. In this case, A_C approaches unity, (log A_C) approaches zero, and Eq. [2] can be reduced to the form

$$\phi_g = k - \frac{b_a b_c}{b_a + b_c}\log A_A \qquad [3]$$

Starting from a general expression by Stern (2) Morrissey (3) derived an equation identical to Eq. [3], for the case of only one metal undergoing corrosion in a binary galvanic couple controlled by activation polarization.

For a second case, Mansfeld (1) assumed that the corrosion rate of metal A is controlled by the diffusion rate of the oxidizer to the surface of metal A and that metal C is acting only as an oxygen electrode. In this case, after following arguments and simplifications similar to those used for the previous case, the expression for the corrosion potential is

$$\phi_g = \phi^A - b_a \log A_A \qquad [4]$$

In summary, Eq. [3] and [4] are both linear in form, and a plot of corrosion potential *vs.* log A_A will yield a linear trace in either case. If the cathodic and anodic reactions are activation-controlled, the slope will be $(b_a b_c/b_a + b_c)$; if the cathodic reaction is diffusion-controlled, the slope will be b_a.

Luborsky, Breiter, and Drummond (4) investigated gold-copper couples in ammonium chloride solutions. They found that these couples were under activation control in 0.1M NH_4Cl, but under cathodic diffusion control in 1.0M NH_4Cl. Morrissey (3) also studied gold-copper couples in ammonium chloride solutions and found them to be activation-controlled in 0.1M NH_4Cl. He established techniques for determining calibration curves of corrosion potentials as a function of base metal area fraction of galvanically connected noble-base couples. These techniques were applied in the present study, the purpose of which was to determine the amount of porosity in nickel electroplates on a uranium alloy.

Experimental

Experiments were undertaken to determine the change in corrosion potential as a function of uranium alloy area fraction in galvanically connected nickel-uranium alloy couples. Figure 1 is a schematic of the experimental arrangement. Electroplated nickel sheet (stripped from a steel mandrel) was cut to form a 7.62 cm (3 in.) square having a geometric gross surface area of 116.13 cm^2 (18 $in.^2$). This square was used as the standard nickel specimen in all subsequent determinations and was suspended in the electrolyte by means of a platinum wire (the platinum wire caused no secondary effects in this particular arrangement).

For uranium alloy area fractions above 1%, coupons of uranium alloy were cut from a 25 mil sheet to the dimensions necessary to obtain the desired sur-

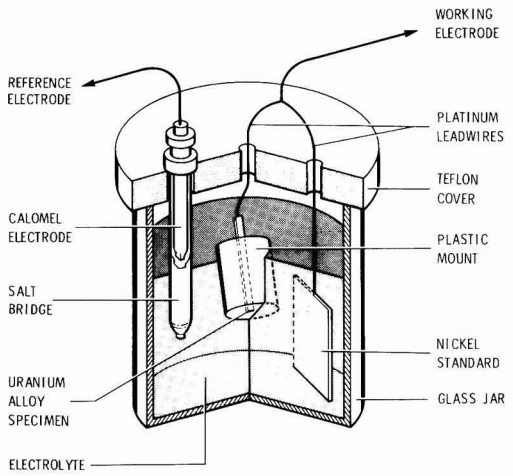


Fig. 1. Schematic of electrochemical cell

* Electrochemical Society Active Member.

Key words: galvanic couples, corrosion potentials, U-¾ Ti.

face areas. These coupons were spot-welded to platinum wires for suspension in the electrolyte. For area fractions below 1%, wires of rectangular cross section were cut from the alloy sheet and mounted in plastic with the ends of the wires exposed. After these mounts had been polished, the cross-sectional area of the alloy was determined and the area fraction ratios were calculated. The potted wires were electrically connected on the back side of the mount to leads above the electrolyte surface.

A saturated calomel electrode (SCE) was used as the reference electrode. A 0.1M KCl solution was chosen as the electrolyte for the initial calibration curve determination. Subsequent curves were generated based on other concentrations of KCl and a 0.1M solution of KBr. Electrolytes of nitric, sulfuric, acetic, and oxalic acids and sodium carbonate, oxalate, and thiocyanate were also tried.

Corrosion potentials of uranium alloy specimens electroplated with various thicknesses of nickel were measured, and the area fraction of exposed alloy was determined from the calibration curves.

Results and Discussion

Plots of measured corrosion potential (*vs.* SCE) as a function of area fraction A_A of uranium alloy for nickel-uranium alloy couples in KCl solutions are shown in Fig. 2. Deviations from linearity can be observed in Fig. 2 at large values of area fraction A_A. This is in accordance with Eq. [2], for then log A_C can no longer be considered negligible. It can also be seen that the corrosion potential for a given area fraction becomes more positive in more dilute solutions, a point further expanded in the following. In addition, the slopes of the calibration curves in Fig. 2 decreased when the solutions were more dilute. As outlined previously, the analysis by Mansfeld suggests that the couple is under activation control if the slope is equal to $b_a b_c/b_a + b_c$ and under diffusion control if the slope is equal to b_a. From Fig. 2, the slopes are approximately 90, 60, and 40 mV for 10^{-1}, 10^{-2}, and 10^{-3} KCl, respectively.

In order to compare these values for the slopes to the values calculated from the Tafel constants, thus determining whether the corrosion reaction was under activation or diffusion control, anodic and cathodic polarization curves were made for each solution, as shown in Fig. 3. However, the uranium alloy undergoes severe pitting in these KCl solutions, as indicated by the significant upturn in the anodic polarization curves. It was also observed that the pitting became more severe with increased chloride concentration. Thus the anodic polarization curves and the anodic Tafel slopes are significantly affected by, and perhaps determined by, this pitting reaction. The use of these anodic Tafel slopes to compare with the slopes of the calibration curves to determine whether the corrosion reaction is activation or diffusion controlled is thus not correct. However, indications of the type of control can be gotten from the intersections of the anodic and cathodic polarization curves in Fig. 3. These intersections occur in the diffusion-controlled region for all three electrolyte concentrations. The intersection for the most concentrated solution, however, is close to an activation-controlled region, that is, the discharge of water. Thus the resulting experimentally determined slopes are most likely a combination of both activation and diffusion control, with diffusion control the more dominate at dilute concentrations. The change in the slope of the calibration curves with concentration may be simply a reflection of a change in pitting severity with concentration.

Figure 3 also shows why the galvanic corrosion potential becomes more cathodic in more dilute solutions for a given area fraction. This is shown by the more positive values of potential at the intersection of the polarization curves (corrosion potential) for more dilute solutions.

Figure 4 is a plot of measured corrosion potential (*vs.* SCE) as a function of area fraction of uranium alloy in 0.1M KBr solution. It is observed that the corrosion potential for a given area fraction is smaller in this solution than it was in the comparable 0.1M KCl solution. Since the bromide ion Br^- is known to be less aggressive towards uranium alloys than the chloride ion Cl^-, this result is consistent with previous studies (5). The slope of the calibration curve measured in 0.1M KBr is very steep; in fact, steeper than that measured in 10^{-3}M KCl solution. Therefore, if this solution were used in process control to monitor porosity in nickel electroplates, the measurement would be less accurate than if the 0.1M KCl solution were used.

Solutions of 0.1M concentrations of nitric, sulfuric, acetic, and oxalic acids were tried as electrolytes to determine analogous calibration curves. In spite of

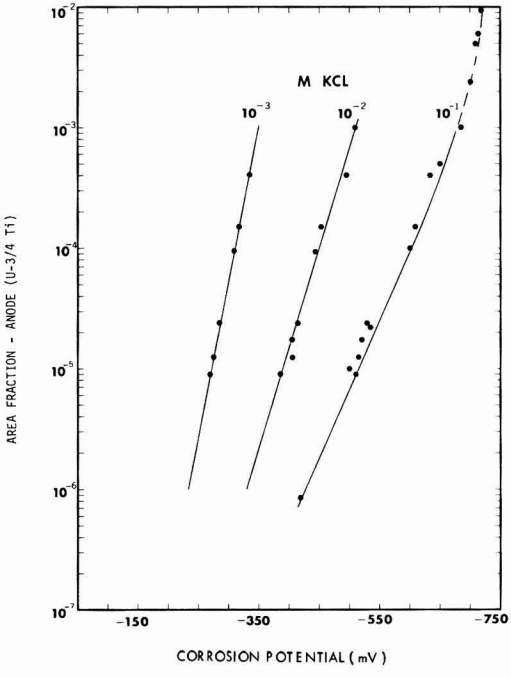


Fig. 2. Corrosion potential as a function of uranium alloy area fraction in potassium chloride.

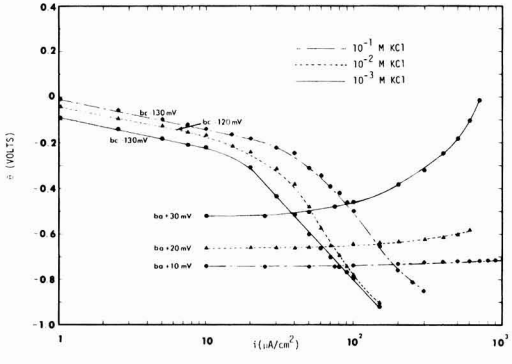


Fig. 3. Anodic (uranium alloy) and cathodic (nickel) polarization curves in potassium chloride.

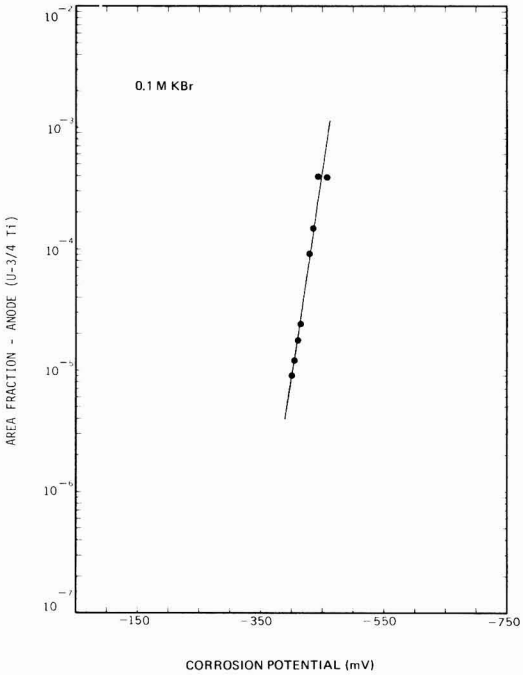


Fig. 4. Corrosion potential as a function of uranium alloy area fraction in potassium bromide.

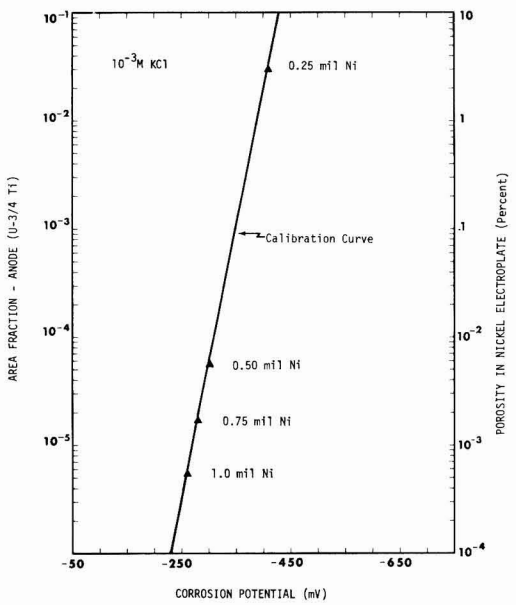


Fig. 5. Amount of porosity in nickel electroplates on a uranium alloy as a function of nickel thickness.

reported ability of these acids to dissolve uranium (6), the corrosion potential did not change with varying area fractions. The apparent reason for this was that the exchange current density of nickel was high relative to the exchange current density of uranium in these solutions. Thus, as outlined by Mansfeld (7) in his case of an active metal imperfectly coated by a noble metal, when the ratio of the exchange current densities of the substrate to the coating is small, the reaction kinetics of the coating, and not the area relationships of the couple, fix the potential of the system.

Solutions of 0.1M concentrations of sodium carbonate, oxalate, and thiocyanate were also tried as possible electrolyte candidates. However, in oxalate and carbonate solutions, insoluble compounds which suppressed the corrosion reactions were formed. Only the thiocyanate ion produced any change in corrosion potential with varying area fractions of cathode, and these changes were very small.

The utility of this electrochemical technique for determining the amount of porosity in nickel electroplates on the uranium alloy was demonstrated in further experiments. Four coupons of U-3/4 Ti of dimensions 1.9 × 2.5 × 0.32 cm (3/4 × 1 × 1/8 in.) were electroplated with nickel in a nickel sulfamate bath to thicknesses of 0.25, 0.50, 0.75, and 1.0 mil, respectively. Platinum wires were spot-welded to the specimens for electrical connection. The measured corrosion potentials of the four specimens as compared to the calibration curve generated in 10^{-3} M KCl solution are shown in Fig. 5. Progressive reductions in porosity with increasing plating thickness were observed. The total surface area of exposed uranium alloy in the specimen plated with 1 mil of nickel was extremely low, *i.e.*, porosity below 10^{-3}%.

Summary

This study has shown that for uranium alloy specimens galvanically coupled to a nickel sheet in KCl electrolytes, the corrosion potential varies linearly with the logarithm of the exposed area fraction of uranium alloy according to expressions derived by Mansfeld (1, 7). It was possible to calibrate the technique so that the exposed base metal area fractions of uranium alloy specimens plated with nickel could be estimated to a reasonable approximation. This technique is relatively nondestructive and offers the advantages of simplicity and high sensitivity, particularly at low porosities.

Acknowledgments

The author wishes to thank J. W. O'Connor of the Metallurgy and Electroplating Division at Sandia Laboratories, Livermore, for his experimental assistance during this study. The author also wishes to give special thanks to Dr. Florian Mansfeld, Science Center, Rockwell International, Thousand Oaks, California, for his assistance and instruction on the electrochemical theory of galvanic couples.

This work was supported by the United States Atomic Energy Commission, Contract Number AT (29-1)-789.

Manuscript submitted Nov. 19, 1973; revised manuscript received Feb. 20, 1975.

Any discussion of this paper will appear in a Discussion Section to be published in the June 1976 JOURNAL. All discussions for the June 1976 Discussion Section should be submitted by Feb. 1, 1976.

Publication costs of this article were partially assisted by Sandia Laboratories.

LIST OF SYMBOLS

ϕ_g	corrosion potential of galvanic couple
ϕ_o^C	reversible potential for oxidation/reduction reaction of oxidizer
ϕ_o^A	reversible potential for oxidation/reduction reaction of metal A
b_a	Tafel slope for anodic reaction on metal A
b_c	Tafel slope for cathodic reaction on metal B
i_o^C	exchange current density for oxidation/reduction reaction of oxidizer on metal C
i_o^A	exchange current density for oxidation/reduction of metal A
A^C	area of metal C

A^A area of metal A
A_C cathodic area fraction $= A^C/A^C + A^A$
A_A anodic area fraction $= A^A/A^A + A^C$

REFERENCES

1. F. Mansfeld, *Corrosion*, **27**, 436 (1971).
2. M. Stern, *ibid.*, **14**, 329 (1958).
3. R. J. Morrissey, *This Journal*, **117**, 742 (1970).
4. F. E. Luborsky, M. W. Breiter, and B. J. Drummond, *ibid.*, **119**, 92 (1972).
5. S. W. Zehr, *Corrosion*, **28**, 196 (1972).
6. R. C. Weast, "Handbook of Chemistry and Physics," 52nd ed., The Chemical Rubber Co., Cleveland, Ohio (1971).
7. F. Mansfeld, *J. Applied Electrochemistry*, **2**, 183 (1972).

JOURNAL OF THE ELECTROCHEMICAL SOCIETY

SOLID-STATE SCIENCE AND TECHNOLOGY

JULY 1975

The Effects of Lead on the Hot Corrosion of Nickel-Base Alloys

D. Chatterji,* D. W. McKee, G. Romeo,* and H. S. Spacil*

Corporate Research and Development, General Electric Company, Schenectady, New York 12301

ABSTRACT

Lead is often found as a trace impurity in fuels used in gas turbines. In addition, lead salts may form on hot superalloy parts during turbine operation in contaminated urban environments. An experimental and thermodynamic study of Na_2SO_4-induced hot corrosion of nickel-base alloys at 900°C, in the presence of small concentrations of lead salts, has shown that these contaminants can be very deleterious to alloy corrosion resistance. PbO reduces the corrosion resistance of Ni-Cr and Ni-Al alloys by complexing normally protective scale to form $PbCrO_4$ and $PbO \cdot Al_2O_3$ which are soluble in the sulfate melt. PbO is a more aggressive contaminant than $PbSO_4$, and PbO concentrations of 1 mole per cent in the salt condensate can result in catastrophic corrosion rates with Ni-Cr alloys.

Accelerated corrosion of high temperature superalloys in the presence of ingested sodium salts and residual sulfur is a problem of major concern in marine and industrial gas turbines and is the subject of an extensive literature (1). The increased use of crude oil and residual fuels in these applications has led to the recognition that severe corrosion effects can also be induced by traces of metallic impurities present in these low grade fuels. In particular, the deleterious effects of vanadium have been well documented (2). Lead impurities may arise from various sources. Industrial gas turbines may ingest particulate lead compounds during operation in contaminated urban atmospheres. Occasionally contamination of turbine fuels with lead tetraethyl from gasoline residues may occur in tankers and storage vessels. Lead compounds have been detected occasionally in crude oils in concentrations up to 2 ppm (3). However, in spite of these considerations, the effects of lead compounds on the hot corrosion behavior of superalloys have not been previously reported.

Thermodynamic calculations have shown (4) that a level of 1-2 ppm of lead in the fuel can be expected to produce a salt condensate containing up to 1 mole per cent (m/o) PbO + $PbSO_4$ in Na_2SO_4 at temperatures in the hot corrosion range of 850°C and above. Deposits on gas turbine blades formed during operation with aviation fuel containing lead have indeed been found to contain PbO (5), although the effects of lead on hot corrosion rates have not been studied. There are, however, reports that lead deposits on Ni-Cr-Fe alloy manifolds and afterburners in gasoline engines are associated with accelerated corrosion (6, 7).

This paper describes the results of an experimental investigation into the effects of low concentrations of lead salts on the Na_2SO_4-induced hot corrosion of nickel-base alloys and an attempt to interpret the observed effects from an equilibrium thermodynamic standpoint.

* Electrochemical Society Active Member.

Key words: sulfidation, high temperature alloys, molten salt corrosion.

Experimental

Binary Ni-Cr and Ni-Al alloys used in the corrosion experiments were prepared by induction melting and casting in argon. From bars of 1-in. round stock, rectangular coupons of dimensions 5/8 × 1/4 × 1/16 in. were cut and polished through 600-grit silicon carbide paper. The nominal and actual compositions of the alloy specimens are listed in Table I.

Salts used in the crucible experiments were anhydrous sodium sulfate (Mallinckrodt Analytical Reagent), lead oxide (Matheson, Coleman and Bell Reagent PbO), and lead sulfate (Fisher Certified Reagent).

Polished coupons of the alloys were placed in glazed porcelain crucibles containing 1g quantities of the powdered salt mixtures which had previously been ground in an agate mortar and blended in a Fisher Minimill. On heating the crucible and contents to 900°C, the salt melted and wetted the alloy coupon to form a thin liquid layer with the excess salt forming a pool at the bottom of the crucible. Weight changes of the crucibles and contents were measured thermogravimetrically in the Chevenard balance described previously (8). Corrosion experiments were carried out isothermally at 900°C in both air and a 0.1% SO_2-76% O_2-balance N_2 gas mixture, using a constant gas flow rate of 250 ml/min. Postexperimental examination of the corroded alloy specimens by means of conventional metallographic and electron microprobe techniques showed that the attack was generally fairly uniform throughout the length of the specimen and

Table I. Composition of alloys, weight per cent

Nominal composition	Actual composition
Ni	100 Ni
Ni-5 Cr	Ni-5.0 Cr
Ni-10 Cr	Ni-9.9 Cr
Ni-15 Cr	Ni-14.9 Cr
Ni-20 Cr	Ni-19.8 Cr
Ni-50 Cr	Ni-49.8 Cr
Ni-30 Al	Ni-29.3 Al

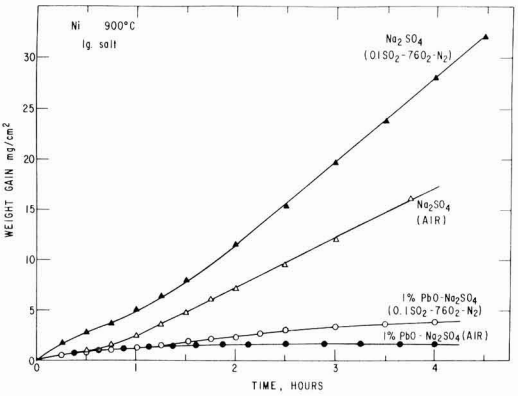


Fig. 1. Effect of 1 m/o PbO on the Na_2SO_4-induced corrosion of nickel at 900°C. Weight changes *vs.* time in air and 0.1% SO_2-76% O_2-N_2 atmospheres.

therefore the total sample geometrical area was used to compute kinetic data. A blank experiment carried out in the absence of an alloy sample showed that the crucible gained less than 0.04 mg/cm² of internal surface after exposure to a melt of 1% PbO-Na_2SO_4 for 6 hr at 900°C. Weight changes resulting from attack on the crucible were therefore considered to be negligible under the conditions of the experiments.

Results

Nickel.—Thermogravimetric data for the corrosion of pure nickel specimens by Na_2SO_4 alone and by 1 m/o PbO-Na_2SO_4 mixtures in atmospheres of air and 0.1% SO_2-76% O_2-balance N_2, are presented in Fig. 1. These experiments were all carried out at 900°C, using polished nickel coupons partially immersed in 1g of the powdered salt. In Fig. 1, weight gains of the crucibles and contents are plotted as functions of time, the extent of corrosion being computed as weight gain in milligrams per square centimeter of total alloy surface.

Corrosion of nickel by Na_2SO_4 alone took place at a rapid rate at 900°C in both gaseous atmospheres, weight gains being essentially linear with time for the duration of the experiments. The rate of attack in the 0.1% SO_2-76% O_2-N_2 environment was substantially greater than that in air, although in both cases the extent of the corrosion could be characterized as catastrophic,[1] with weight gains that exceeded 20 mg/cm² after a 5 hr exposure to the salt melt. By contrast, the experiments carried out with an initial 1% PbO-Na_2SO_4 salt mixture resulted in sharply reduced rates of corrosion, with weight gains of less than 4 mg/cm² during the 5 hr runs. Although weight increases were again larger in the SO_2-containing atmosphere than in air, in both cases corrosion of the nickel specimens was minimal in the presence of the lead salt.

Postexperimental metallographic examination of the metal coupons showed marked differences in the morphology of the corrosion layers produced in the presence and absence of the lead additive. As shown in Fig. 2(a), corrosion experiments with the PbO-Na_2SO_4 salt mixture produced a protective oxide layer on the surface of the nickel, with no evidence of subscale sulfide formation. Electron microprobe examination of this sample, shown by the traverse in Fig. 2(b), indicated that the scale was dense NiO, the concentration of Pb being too low to be detectable. Corrosion of nickel by Na_2SO_4 alone produced a thick porous scale, shown in section in Fig. 3. In this case, x-ray images of Ni and S for an area at the base of the scale (Fig. 4) indicated that finely divided sulfides were distributed in a band beneath the outer oxide layer.

Additional experiments carried out with nickel specimens immersed in salt mixtures of composition 1 m/o $PbSO_4$-Na_2SO_4 gave the same rapid weight gains and catastrophic corrosion rates as found with pure Na_2SO_4, indicating that the inhibitory effect observed with PbO is not a general effect associated with the presence of lead salts. No appreciable corrosion of nickel was observed with $PbSO_4$ alone at 900°C.

Nickel-chromium alloys.—The most significant result found with binary Ni-Cr alloys was that the presence of PbO in the salt condensate caused a considerable

[1] Hot corrosion rates are generally regarded as "catastrophic" when they amount to 1-2 orders of magnitude greater than for normal oxidation (9).

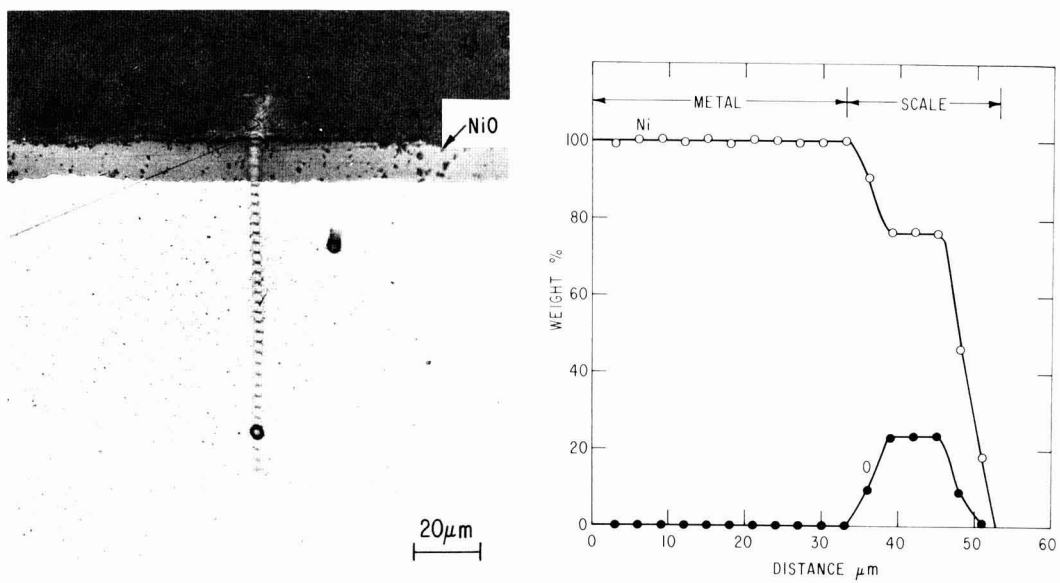


Fig. 2. Transverse section through Ni sample after 6 hr exposure to 1 m/o PbO-Na_2SO_4 at 900°C in air. (a, left) Optical micrograph showing uniform NiO scale. (b, right) Microprobe traverse along electron beam trace shown in (a).

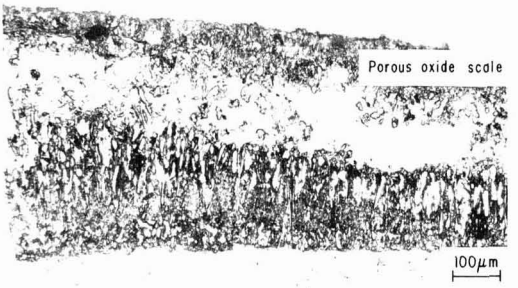


Fig. 3. Section of Ni sample after 5 hr exposure to 1g Na_2SO_4 at 900°C in 0.1% SO_2-76% O_2-N_2 atmosphere.

increase in the rate of Na_2SO_4-induced hot corrosion at 900°C. The magnitude of the effect, however, depended to a large extent on the chromium content of the alloy.

Typical thermogravimetric results for Ni-15 Cr specimens are summarized in Fig. 5, which shows weight gain data obtained in crucible experiments with Na_2SO_4 and 1 m/o PbO-Na_2SO_4 salt mixtures in both air and 0.1% SO_2-76% O_2-N_2 atmospheres. When coupons of Ni-15 Cr were immersed in pure Na_2SO_4 and heated in flowing air at 900°C, a very small weight gain was observed (<0.5 mg/cm^2) over a period of 5 hr and corrosion was very slight as the result of the formation of a protective Cr_2O_3 scale. Addition of 1 m/o PbO to the initial salt, however, resulted in a marked increase in corrosion rate and the specimen weight continued to increase during the course of the experiment. As with nickel, the corrosion rate in the PbO-Na_2SO_4 experiments was still further increased when 0.1% SO_2 was present in the ambient atmosphere, as shown in Fig. 5.

Metallographic examination of the corrosion layers produced on this alloy by the PbO-Na_2SO_4 salt melt showed (Fig. 6) a thick nonuniform Cr_2O_3 surface layer and dispersed chromium sulfide globules at depths of 40-50 μm into the bulk alloy, which are not clearly visible in the micrograph. This morphology is characteristic of sulfidation under conditions of high sulfur potential (8).

The results of an experiment on the interaction of Ni-15 Cr alloy with $PbSO_4$ alone are shown in Fig. 7. In this case the alloy specimen was partially immersed in 1g of the powdered salt and heated at 900°C in the 0.1% SO_2-76% O_2-N_2 gas mixture for a period of 5 hr. A moderate (3 mg/cm^2) weight gain was observed during this period and metallographic examination of a section of the specimen at the end of the experiment showed localized areas where sulfide particles had formed beneath the surface oxide scale. Although the extent of corrosion was greater with $PbSO_4$ than with Na_2SO_4 alone, the attack was much less intense and less uniform than with the 1% PbO-Na_2SO_4 salt mixture under the same conditions. As $PbSO_4$ is solid at 900°C, a direct comparison of corrosion rates is not possible.

A series of experiments was carried out with Ni-50 Cr alloy coupons, immersed in PbO-Na_2SO_4 mixtures of various compositions and heated at 900°C in the 0.1% SO_2-76% O_2-N_2 gas mixture. This alloy is very resistant to both oxidation and Na_2SO_4-induced hot corrosion and weight changes in pure Na_2SO_4 amounted to less than 1 mg/cm^2 in a 5 hr period at 900°C. However, as shown in Fig. 8, immersion in a 1 m/o PbO-Na_2SO_4 mixture resulted in an initial rapid weight change, which amounted to 3.6 mg/cm^2 in the first hour of the experiment. The corrosion rate then diminished as the lead concentration in the salt melt

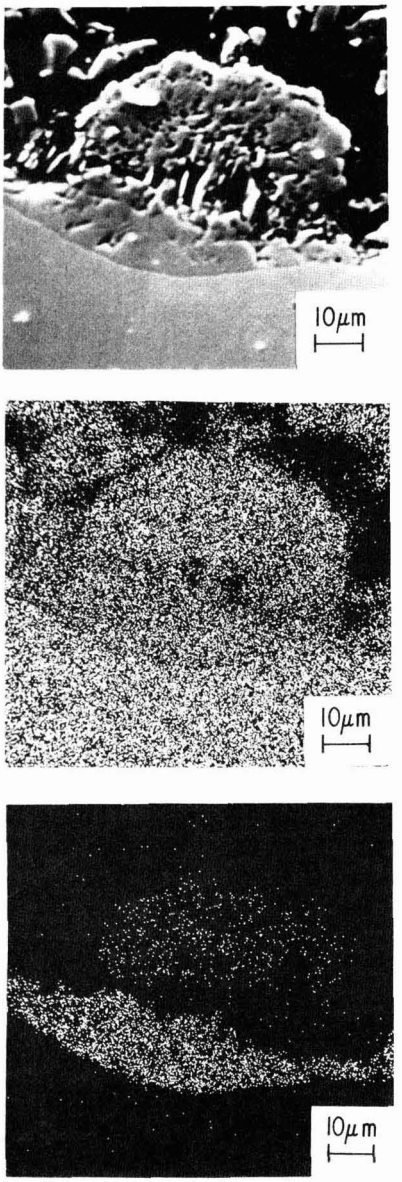


Fig. 4. X-ray images of base of corrosion layer on Ni following 5 hr exposure to 1g Na_2SO_4 at 900°C. (a) Back-scattered image, (b) $Ni_{K\alpha}$ scan, (c) $S_{K\alpha}$ scan.

became depleted. The Nomarski interference contrast micrograph of the corrosion layer on this specimen, shown in Fig. 9, revealed a thick Cr_2O_3 scale on the surface, particles of chromium sulfide in the subscale region, and a zone about 20 μm thick near the surface which has become depleted in the chromium-rich eutectic, which is visible as irregular inclusions in the bulk alloy. As shown in Fig. 8, increasing initial PbO concentrations in the salt mixture resulted in marked increases in the corrosion rate of the Ni-50 Cr alloy, initial weight gains amounting to 5 and 10 mg/cm^2-hr for initial 5 and 10% PbO-Na_2SO_4 salt compositions, respectively. (The morphology of the corrosion layer following exposure to the 5% PbO-Na_2SO_4 mixture is shown in Fig. 10. Penetration of sulfides into the bulk

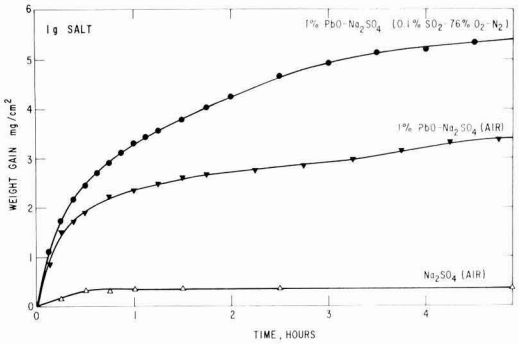


Fig. 5. Effect of 1 m/o PbO on Na_2SO_4-induced corrosion of Ni-15 Cr at 900°C. Weight changes *vs.* time in air and 0.1% SO_2-76% O_2-N_2 atmospheres.

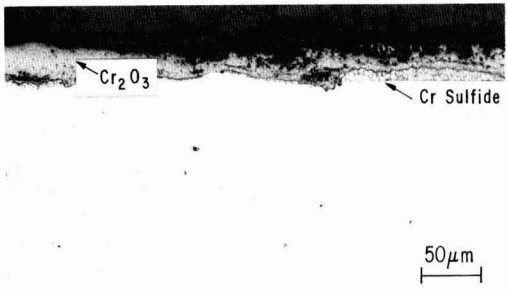


Fig. 6. Section of Ni-15 Cr sample showing corrosion morphology following exposure to 1 m/o PbO-Na_2SO_4 salt mixture for 6 hr in air at 900°C.

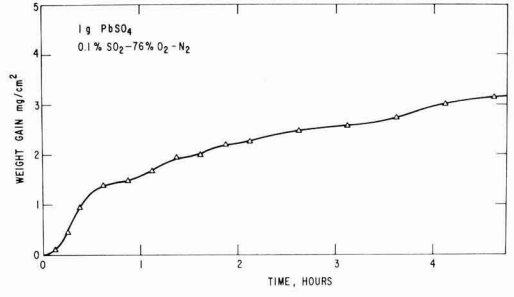


Fig. 7. Corrosion of Ni-15 Cr by $PbSO_4$ at 900°C. Weight changes *vs.* time in 0.1% SO_2-76% O_2-N_2 gas mixture.

alloy is obviously more marked than in the experiment with 1% PbO-Na_2SO_4.) In each case the salt residue at the end of the experiment was colored bright yellow, which chemical analysis showed to be due to the presence of chromate. For example, analysis of the residue from the experiment with 5 m/o PbO-Na_2SO_4 gave a $CrO_4^=$ concentration of 0.22 and 2.17 weight per cent (w/o) in the case of the run with 10 m/o PbO-Na_2SO_4 initially. With Na_2SO_4 alone in contact with the Ni-50 Cr alloy, the concentration of residual chromate after the 5 hr experiment at 900°C was 0.098 w/o. Apparently the effect of PbO in the salt was to promote the formation of chromate as a result of the reaction

$$PbO + 1/2\ Cr_2O_3 + 3/4\ O_2 \rightarrow PbCrO_4$$

A combined TGA-DTA experiment with a 2:1 molar mixture of PbO and Cr_2O_3 heated at a rate of 10°C/min

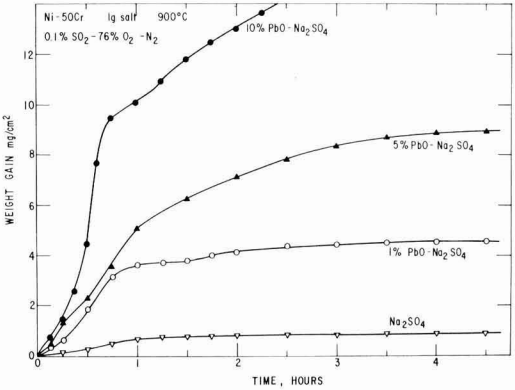


Fig. 8. Corrosion of Ni-50 Cr in PbO-Na_2SO_4 salt mixtures at 900°C. Weight changes *vs.* time for various initial PbO concentrations.

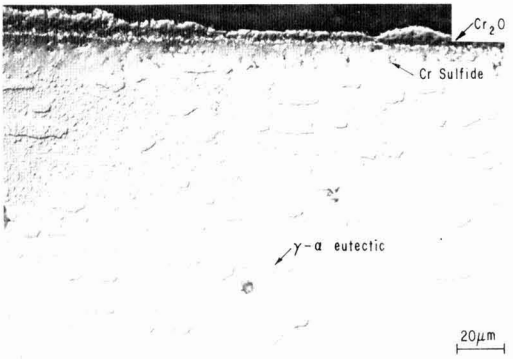


Fig. 9. Section of Ni-50 Cr sample showing corrosion morphology following exposure to 1 m/o PbO-Na_2SO_4 for 6 hr at 900°C in 0.1% SO_2-76% O_2-N_2 atmosphere.

in an atmosphere of flowing O_2 showed that this reaction began to occur at 400°C and was virtually complete at 750°C.

With the Ni-Cr binary alloys the corrosion rates were greatest during the first hour of the experiments, hence the measured weight gains for the initial 1 hr of exposure could be used as a basis for qualitative comparison of the corrosion behavior of the different alloy compositions. Figure 11 shows initial corrosion rates for the Ni-Cr alloy series computed in this manner; these are expressed in arbitrary units because the kinetics in general did not follow established rate laws. Postexperimental metallographic observations of the extent of corrosion confirmed the general trends shown in Fig. 11. The lower curve shows that the rate of corrosion by Na_2SO_4 alone decreased rapidly as chromium was added to nickel and became very low for Cr contents of 15 w/o or more, due to the formation of a protective Cr_2O_3 scale. By contrast, corrosion rates in the 1% PbO-Na_2SO_4 melt were low for pure nickel but increased rapidly as the Cr content of the alloy was increased and became very rapid for alloys containing 10-15 w/o Cr. In these cases, complexing of the surface Cr_2O_3 by the lead component of the salt melt produced a porous unprotected Cr-depleted matrix which was readily attacked by the Na_2SO_4 melt. Further increases in chromium content resulted in some decrease in the rate of corrosion because of the high residual content of Cr in the alloy matrix even after removal of the surface layer by lead complexing. However, even alloys containing 50 w/o Cr were more

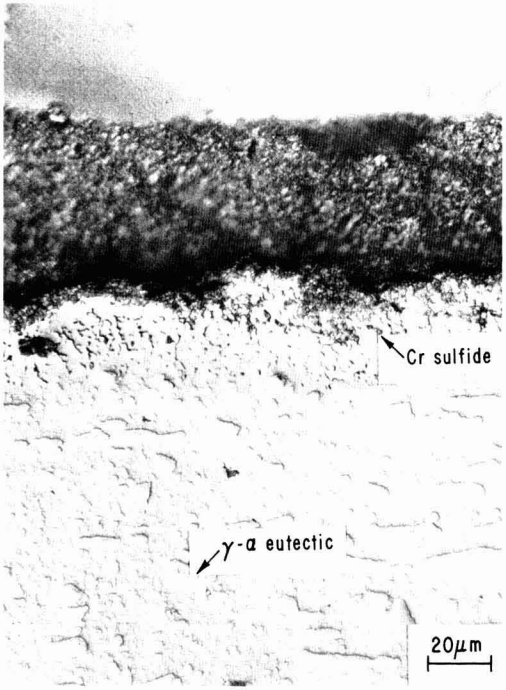


Fig. 10. Section of Ni-50 Cr sample showing corrosion morphology following exposure to 5 m/o $PbO-Na_2SO_4$ for 5 hr at 900°C in 0.1% SO_2-76% O_2-N_2 atmosphere.

readily attacked in the presence of PbO than by Na_2SO_4 alone. Typical catastrophic attack by $PbO-Na_2SO_4$ on Ni-Cr alloys in the intermediate Cr range is illustrated in Fig. 12 which shows the corrosion layer produced on a Ni-10 Cr specimen following exposure to 1% $PbO-Na_2SO_4$ for 5 hr at 900°C. The surface of the alloy is extensively degraded to form a porous oxide layer and widespread chromium sulfide globules within the alloy interior.

At higher chromium concentrations corrosion in the presence of PbO was less catastrophic. although sulfide particles were formed at considerable depths beneath the surface scale. Figure 13 shows a section of the corrosion layer formed on a Ni-20 Cr specimen after the same treatment as that described above. The extent of attack may be compared with that shown in

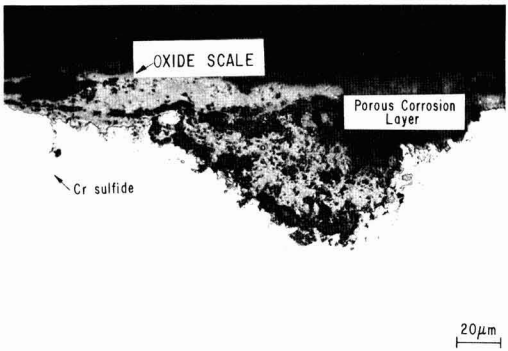


Fig. 12. Section of Ni-10 Cr sample following exposure to 1 m/o $PbO-Na_2SO_4$ for 5 hr at 900°C in 0.1% SO_2-76% O_2-N_2 atmosphere. Total salt concentration = 1g.

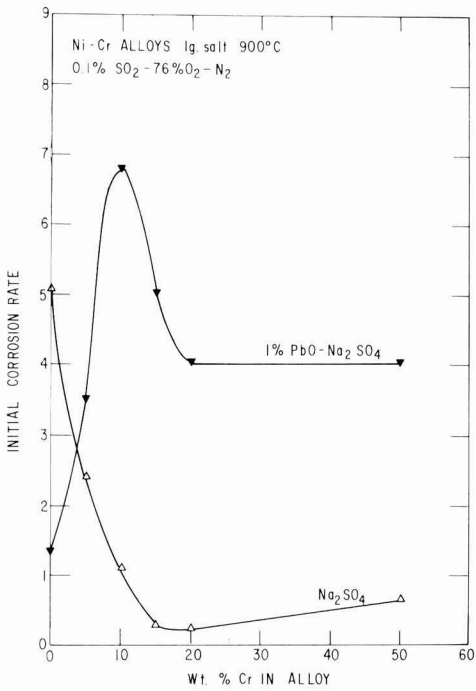


Fig. 11. Effect of PbO on initial corrosion rates of Ni-Cr alloys by Na_2SO_4. Corrosion rates after 1 hr (in arbitrary units) at 900°C in Na_2SO_4 and 1 m/o $PbO-Na_2SO_4$ as a function of Cr content.

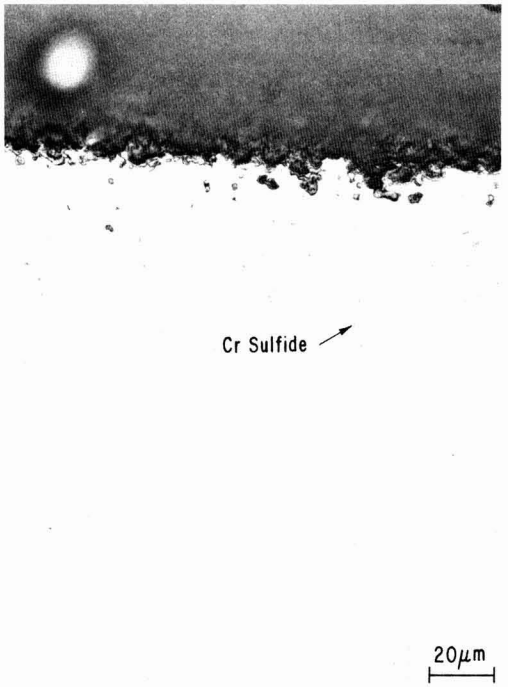


Fig. 13. Section of Ni-20 Cr sample following exposure to 1 m/o $PbO-Na_2SO_4$ for 5 hr at 900°C in 0.1% SO_2-76% O_2-N_2. Total salt concentration = 1g.

Fig. 6 for a Ni-15 Cr alloy and in Fig. 9 for a Ni-50 Cr alloy.

Nickel-aluminum alloys.—A series of crucible experiments was carried out with Ni-Al alloy specimens, of composition 5-30 w/o Al, which were partially immersed in 1g quantities of Na_2SO_4 and 1 m/o PbO-Na_2SO_4 salt mixtures and heated at 900°C in the 0.1% SO_2-76% O_2-N_2 gas mixture. Under these conditions, alloys with aluminum concentrations in the range 5-20 w/o were vigorously attacked by Na_2SO_4 alone, the corrosion becoming catastrophic at an alloy composition of Ni-13 Al (Ni_3Al). Alloy coupons of this composition were reduced to a gray porous mass after exposure to the molten salt for a period of only 2 hr (10). The presence of PbO exerted very little influence on the very high corrosion rates of these alloys. By contrast, an alloy of composition Ni-30 Al (the β-NiAl phase) was very resistant to corrosion by excess Na_2SO_4 because of the formation of a protective Al_2O_3 scale and gained only 0.5 mg/cm² during 4 hr contact with molten Na_2SO_4 at 900°C, as shown by the lower curve in Fig. 14. Addition of 1% PbO to the initial salt mixture resulted in a marked increase in the extent of corrosion of this alloy which gained weight in an almost linear manner during the course of the run, as shown by the upper curve of Fig. 14. Although the magnitude of the enhanced corrosion induced by the PbO was much less than with the Ni-Cr alloys, metallographic examination of the corroded specimen (Fig. 15) showed that a protective oxide scale was not formed in the presence of PbO, the thick corrosion layer showing a porous structure of finely dispersed particles identified by electron microprobe analysis as oxides and sulfides. Similar enhanced corrosion rates and morphology were found with a salt mixture of composition 1 m/o $PbSO_4$-Na_2SO_4. An experiment in which a coupon of Ni-30 Al was immersed in 1g of powdered $PbSO_4$ and heated in the SO_2-O_2-N_2 mixture for 5 hr at 900°C resulted in localized attack of the alloy coupon at points of contact with the salt particles. Thick porous oxides were formed in these regions, as shown in Fig. 16, in which networks of oxide particles could be identified.

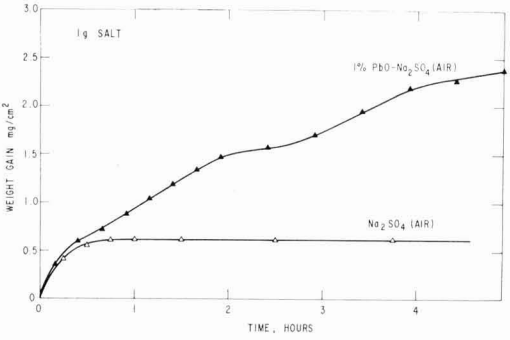


Fig. 14. Effect of 1 m/o PbO on the Na_2SO_4-induced corrosion of Ni-30 Al at 900°C. Weight changes *vs.* time in air.

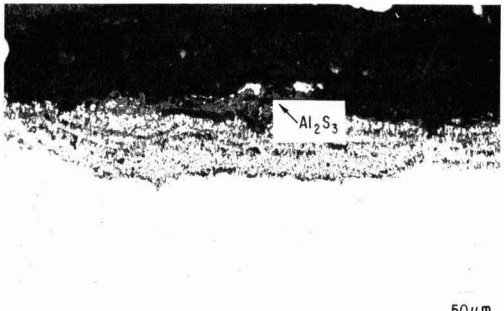


Fig. 15. Section of Ni-30 Al coupon after 6 hr exposure to 1 m/o PbO-Na_2SO_4 in air at 900°C. Total salt concentration = 1g.

Discussion

As far as oxidation behavior is concerned, the alloys selected for the present study can be broadly classified as belonging to the following groups: (*a*) NiO formers (*e.g.*, pure Ni), (*b*) Cr_2O_3 formers (*e.g.*, Ni-50 Cr), (*c*) Al_2O_3 formers (*e.g.*, Ni-30 Al), and (*d*) mixed oxide formers (*e.g.*, Ni-15 Cr, Ni-5 Al). Unlike the first three classes of alloys where only one type of oxide is observed at steady state, the mixed oxide forming alloys may exhibit a complex, multiphase external scale plus extensive internal oxidation. For example, depending on temperature and time of oxidation and grain size, Ni-15 Cr can form a duplex NiO scale with a Cr_2O_3 subscale, a scale composed entirely of Cr_2O_3 only, or a scale containing islands of Cr_2O_3 or spinel surrounded by NiO (11-14).

Since the selected alloys depend mainly on NiO, Cr_2O_3, or Al_2O_3 for protection in salt-free oxidizing environments, an understanding of the thermodynamic reactivity of these oxides to salt environments becomes essential in interpreting the salt-induced hot corrosion behavior of these alloys. Thermochemical stability diagrams (1, 15-18) are very helpful in identifying and predicting the products formed in reactions involving gases and condensed phases. Reactions likely to occur between Na_2SO_4 and oxide scales are, therefore, best discussed in terms of isothermal Na-S-O-M (M = Ni, Cr, or Al) stability diagrams (16) (Fig. 17a-d[2]). The solid lines in these diagrams outline the stability limits of individual condensed phases and represent equilibria between two coexisting compounds at unit activities and the gas phase. The shaded regions outline the stability limits of individual Na_2SO_4/metal oxide reaction products, *e.g.*, $NaNiO_2$ Na_2CrO_4, and $NaAlO_2$.

It should be emphasized that the phase boundaries shown in Fig. 17a-d were calculated assuming unit activity for all condensed phases and neglecting mutual solubility among them. In reality, however, all these compounds exist over a range of stoichiometry and show finite mutual solubilities. Thus, for example, Na_2SO_4 has a finite Na_2O activity that is determined by the experimental variables, *i.e.*, temperature, pressure, and oxygen and sulfur potentials in the gas phase.

Point A in Fig. 17 refers to the gas phase composition utilized in most of our experiments, viz., 0.1% SO_2-76% O_2-N_2. Calculations by Spacil (16) indicate that this composition closely simulates, at least as far

[2] Note that the diagrams shown in Fig. 17 are for 1200°K whereas our experiments were done at 1173°K (900°C). This temperature difference does not affect our discussions to any significant extent.

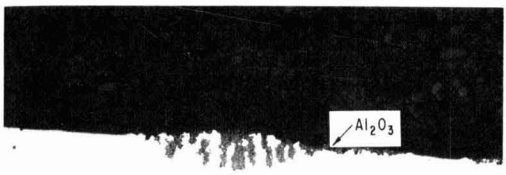


Fig. 16. Section of Ni-30 Al coupon after 5 hr immersion in 1g $PbSO_4$ at 900°C in 0.1% SO_2-76% O_2-N_2 atmosphere.

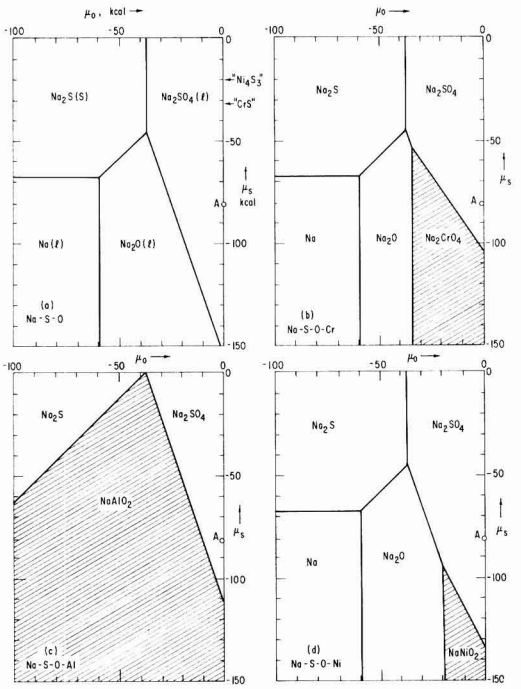


Fig. 17. Stability diagrams for (a) Na-S-O, (b) Na-S-O-Cr, (c) Na-S-O-Al, and (d) Na-S-O-Ni systems at 1200°K.

as oxygen and sulfur potentials are concerned, the nominal conditions prevailing in the first stage of a gas turbine operating at an average pressure of 5 atm with typical air/fuel ratios. The Na_2O activity in a Na_2SO_4 melt equilibriated in this environment can be calculated as follows

$$Na_2O(soln) + 1/2\,S_2(g) + 3/2\,O_2(g) = Na_2SO_4(l) \quad [1]$$

$$K_1 = \frac{a(Na_2SO_4)}{a(Na_2O)\,P_{S_2}^{1/2}\cdot P_{O_2}^{3/2}} = 1/[a(Na_2O)\cdot P_{S_2}^{1/2}P_{O_2}^{3/2}]$$

$$\Delta G^\circ_1 = -RT\ln K_1$$

$$= RT\,[\ln a(Na_2O) + \ln P_{S_2}^{1/2} + 3\ln P_{O_2}^{1/2}]$$

$$= RT\ln a(Na_2O) + \mu_s + 3\mu_o$$

$$\ln a(Na_2O) = [\Delta G^\circ_1 - \mu_s - 3\mu_o]/(RT)$$

For 1200°K and $\mu_s = -81.4$ kcal/mole, $\mu_o = -0.33$ kcal/mole (point A in Fig. 17), $\Delta G^\circ_1 = -155.5$ kcal/mole, and $a(Na_2O) = 4.8 \times 10^{-14}$. The "reactivity" of such a melt to NiO, Cr_2O_3, and Al_2O_3 scales can be estimated from considerations of the following type

$$2Na_2O(soln) + Cr_2O_3(s) + 3/2\,O_2(g) = 2Na_2CrO_4(soln) \quad [2]$$

$$K_2 = \frac{a^2(Na_2CrO_4)}{a(Cr_2O_3)\cdot a^2(Na_2O)\cdot P_{O_2}^{3/2}}$$

$$= \frac{a^2(Na_2CrO_4)}{a^2(Na_2O)\cdot P_{O_2}^{3/2}}$$

$$\ln a(Na_2CrO_4) = [2RT\ln a(Na_2O) + 3\mu_o - \Delta G^\circ_2]/(2RT)$$

$$a(Na_2CrO_4) = 9.7 \times 10^{-5}$$

Results of similar calculations for Al_2O_3 and NiO are summarized in Table II.

Table II. Expected activity of Na-M-O reaction products, i, dissolved in Na_2SO_4 equilibrated with a 0.1% SO_2-76% O_2-balance N_2 atmosphere at 1200°K ($\mu_s = -81.4$ kcal, $\mu_o = 0.33$ kcal)

Oxide	ΔG°[a]	i	a_i	% i[b]
Cr_2O_3	−103,600	Na_2CrO_4	9.7×10^{-5}	0.0097
Al_2O_3	−42,900	$NaAlO_2$	1.8×10^{-3}	0.18
NiO	−19,900	$NaNiO_2$	1.3×10^{-5}	0.0013

[a] Refers to net ΔG° for dissolution reactions similar to reaction [2].
[b] Assuming % i = 100 $N_i \simeq 100\ a_i$.

It is obvious from Table II that among the oxides considered, only Al_2O_3 may be complexed to an appreciable extent by Na_2SO_4; Cr_2O_3 and NiO are expected to dissolve in Na_2SO_4 only to limited extents. Some caution must be exercised, however, in directly extending this conclusion about the relative thermodynamic reactivities of these oxides to the actual corrosion behavior of the alloys. The above analysis does not take into account kinetic, morphological, and other nonthermodynamic features of the corrosion phenomenon, and allows calculation of upper limits of activity provided all other factors are favorable. Sometimes the kinetics are slow, as in the case of Na_2SO_4 attack of Ni-30 Al (Fig. 14), and the actual corrosion rate is less than that expected from thermodynamic reasonings alone. In some cases, the morphology of the oxide is such that a number of side processes may occur and confuse the over-all picture. Thus, the scale forming on Ni, for example, is not very dense and cannot effectively isolate the alloy from the salt. The extent of corrosion as measured by weight change is consequently quite high (Fig. 1) although NiO is relatively inert under the experimental condition employed. Considerations of oxide stability in Na_2SO_4, therefore, may play an important role in understanding the corrosion behavior of an alloy but must be supplemented by kinetic and morphological information on the system. Before proceeding to a detailed discussion of corrosion features of the various alloys, an attempt will be made to compare the corrosive capabilities of $PbSO_4$ as well as 1 m/o PbO-Na_2SO_4 following the thermodynamic framework presented earlier.

Figure 18 is a composite diagram showing the stability limits of relevant compounds in the Pb-S-O system at 1200°K as well as the products likely to be formed in presence of Cr_2O_3 and Al_2O_3. Considerable controversy exits in the literature on the thermochemistry of the Pb-S-O system (19-21). Figure 18 is based on the data that are in the authors' opinion, most acceptable. These are listed in Table III. Thermodynamic data for $PbCrO_4$ are available (22) but the same cannot be said for $PbO\cdot Al_2O_3$ (23). In view of what is known about double oxides like $PbO\cdot WO_3$, $PbO\cdot MoO_3$,

Table III. Thermochemical data used in the present investigation[a]

Compound	State	ΔG° (1200°K), cal
Na_2O	l	−58,100
Na_2S	l	−67,400
Na_2SO_4	l	−213,600
Al_2O_3	s	−308,800
Cr_2O_3	s	−197,200
NiO	s	−32,000
$NaAlO_2$	l	−204,900
Na_2CrO_4	l	−208,500
$NaNiO_2$	l	−71,000
PbO	l	−24,400
PbS	s	−15,300
$PbSO_4$	s	−109,200
$PbSO_4\cdot PbO$	s	−139,300
$PbSO_4\cdot 2PbO$	s	−165,900
$PbO\cdot Al_2O_3$	s	≃(−343,000)
$PbCrO_4$	l	−138,200
SO_2	g	−65,600

[a] Reference states: Na(g), S_2(g), O_2(g), Al(l), Cr(s), Ni(s), and Pb(l) at 1200°K.

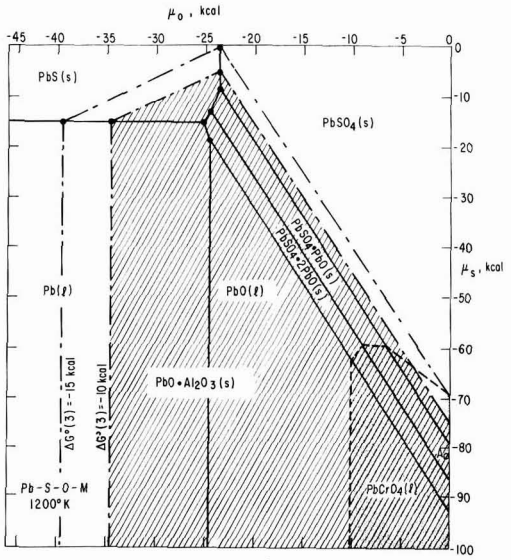


Fig. 18. Stability diagram for Pb-S-O-M system showing the regions of $PbCrO_4$ and $PbO \cdot Al_2O_3$ stability. Effect of assuming different $\Delta G°$ values for the reaction $PbO + Al_2O_3 = PbO \cdot Al_2O_3$ is indicated by dash-dot lines.

and the numerous spinels that form exclusively through condensed phase reactions, it is unlikely that $\Delta G°$ for the reaction

$$PbO(l) + Al_2O_3(s) = PbO \cdot Al_2O_3(s) \qquad [3]$$

will be more negative than −10 kcal. The boundaries of the $PbO \cdot Al_2O_3$ stability region in Fig. 18 were calculated using the reasonable value of $\Delta G°$ ($PbO \cdot Al_2O_3$) of −343 kcal. Figure 18 also shows how the stability region for $PbO \cdot Al_2O_3$ would look if a value of −15 kcal were chosen for $\Delta G°_3$, *i.e.*, −348 kcal for $\Delta G°$ ($PbO \cdot Al_2O_3$). It is clear that in going from $\Delta G°_3$ = −10 to −15 kcal, only the over-all size of the stability region has increased; no major changes have occurred in the features of the diagram.

As no Pb-Ni-O compound apparently exists, the reactivity of NiO to $PbSO_4$ or PbO cannot be discussed in terms of a complexing capability of the lead salt. The behavior of NiO formers in the presence of lead salts can nevertheless be rationalized if all the chemical and physical processes occurring in the vicinity of the alloy surface are taken into consideration. Discussion of actual corrosion processes for the individual alloys will appear later in this section.

As before, point A on the stability diagram of the Pb-S-O-M system (Fig. 18) indicates the composition of the SO_2-O_2-N_2 gas phase used in the present experiments. The Pb-S-O phase that is stable in this environment is of the type $PbSO_4 \cdot nPbO$ (most likely $PbSO_4 \cdot PbO$). In other words, irrespective of whether PbO or $PbSO_4$ is used at the beginning of an experiment, the phase likely to be found at equilibrium is Pb-oxysulfate. It is obvious from Fig. 18 that both Cr_2O_3 and Al_2O_3 are unstable in the presence of $PbSO_4 \cdot nPbO$ and will react to form $PbCrO_4$ and $PbO \cdot Al_2O_3$, respectively. That $PbCrO_4$ is the only reaction product that is liquid under these conditions should be noted at this point. Since formation of liquid phases is usually detrimental to the corrosion resistance of an alloy, Cr_2O_3 formers are more likely to be attacked by a $PbSO_4$/PbO environment than Al_2O_3 formers.

Since the presence of a pure $PbSO_4$/PbO type condensate in actual turbine practice is ruled out, the behavior of the protective oxides in a Na_2SO_4 melt containing minor amounts of Pb compounds must be considered. Spacil (4), has carried out a preliminary thermochemical analysis of the most likely reactions in a turbine burning Pb-contaminated fuels, and has concluded that the combined $PbSO_4$ plus PbO content in a typical Na_2SO_4-base condensate is not likely to exceed 1 m/o. Preliminary experiments showed that 1% PbO-Na_2SO_4 melt was more corrosive than 1% $PbSO_4$-Na_2SO_4. All subsequent work involved 1% PbO-Na_2SO_4 as the corrosive medium. It is believed that the results obtained provide an assessment of the effects of Pb contamination on hot corrosion that is somewhat overpessimistic but nevertheless realistic.

A quantitative estimation of the reactivity of Cr_2O_3 and Al_2O_3 to the PbO-Na_2SO_4 melt is a rather difficult task. The system, in either case, contains as many as five components (Na, S, O, Pb, M) and involves multiphase equilibria. Calculation of activities of individual reactive species in the melt therefore becomes a formidable problem. A simple approach may nevertheless provide qualitative information on the effect of PbO contamination on the complexing of protective scales.

Addition of 1% PbO to Na_2SO_4 is likely to produce a homogeneous melt free from second phases. The presence of PbO may or may not affect the activity of Na_2O in the melt; in view of the fact that no Na-Pb-O compound is known, it is unlikely that PbO will substantially affect the 10^{-14} value of $a(Na_2O)$ in the melt. The initial activity of PbO may be approximately equated to the concentration of PbO on the melt; *i.e.*, initial $a(PbO) \simeq N(PbO) \simeq 10^{-2}$. Although such an assumption is obviously speculative, as will be shown later, the qualitative conclusions to be derived here would remain unchanged even if $a(PbO)$ were as low as 10^{-4}, *i.e.*, even if substantial Na-Pb-O-S interactions took place. In any event, $a(PbO) >> a(Na_2O)$ and PbO is expected to be the most corrosive species in the melt. Exposure of Cr_2O_3 and Al_2O_3 to the PbO-Na_2SO_4 melt should then promote the following reactions

$$2PbO(soln) + Cr_2O_3(s) + 3/2\,O_2(g) = 2PbCrO_4(soln) \qquad [4]$$

$$PbO(soln) + Al_2O_3(s) = PbO \cdot Al_2O_3(soln) \qquad [5]$$

For these reactions, the activities of the complex compounds are related to $a(PbO)$ through the following relations (valid for 1200°K)

$$a(PbCrO_4) = (587) \cdot a(PbO)$$

$$a(PbO \cdot Al_2O_3) = (66) \cdot a(PbO)$$

These relationships over a broad activity range are graphically illustrated in Fig. 19. It is obvious from this figure that even for $a(PbO)$ in the range of 10^{-4}-10^{-5}, $a(PbCrO_4)$ and $a(PbO \cdot Al_2O_3)$ would reach values as high as 10^{-2}. In pure Na_2SO_4, on the other hand, the equilibrium activities of Na-chromate and Na-aluminate are only about 10^{-5} and 10^{-3}, respectively (Table II). The 1% PbO-Na_2SO_4 melt is, therefore, expected to complex Cr_2O_3 and Al_2O_3 to a greater extent than Na_2SO_4 alone.[3]

The above conclusion could also have been reached from an analysis of the type presented by Goebel, Pettit, and Goward (17, 18). In terms of their model, addition of PbO to Na_2SO_4 should increase oxide ion activity, $a(O^=)$, in the melt. This increase should in turn cause an increased fluxing (*i.e.*, increased aluminate and chromate ion concentrations) of the protective scales

$$Al_2O_3(s) + O^= = 2AlO_2^- \qquad [6]$$

[3] Compounds of the type $PbCrO_4$-PbO are known to be volatile (24). Rapid volatilization of reaction products may occur for Cr_2O_3-forming alloys in PbO-Na_2SO_4 melts leading to a further increase in corrosion. Although such vaporization processes might have influenced the observed weight gains in the corrosion experiments, corrections for such losses could not be applied owing to the lack of volatilization data for the complexes involved. Ir any case this effect will not invalidate the basic conclusions reached in this study.

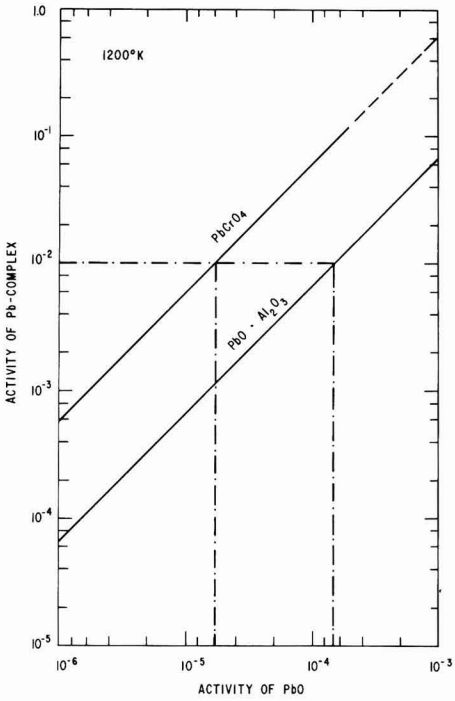


Fig. 19. Equilibrium Pb-chromate and Pb-aluminate activity in Na_2SO_4-PbO for different $a(PbO)$ values.

$$Cr_2O_3(s) + 3/2\,O_2(g) + 2\,O^= = 2CrO_4^= \quad [7]$$

The situation in the presence of PbO then roughly corresponds to that referred to by Goebel *et al.* as "accelerated corrosion due to basic fluxing."

Although the model proposed by Goebel and coworkers explains the effect of PbO on the corrosion of Cr_2O_3 and Al_2O_3, problems appear when NiO reactivity is considered. According to their fluxing model, increased $O^=$ ion activity should lead to increased NiO dissolution through nickelate ion formation

$$NiO(s) + O^= = NiO_2^= \quad [8]$$

$$NiO(s) + 1/4\,O_2(g) + 1/2\,O^= = NiO_2^- \quad [9]$$

PbO should therefore induce accelerated corrosion of Ni. The present experiments (Fig. 1) indicate, however, that PbO causes a dramatic reduction in the hot corrosion of Ni. The complexing model, on the other hand, does not predict what the effect of PbO would be on corrosion of Ni. This dilemma demonstrates clearly that processes in addition to simple fluxing or complexing may become important in particular alloy systems. The physical and chemical processes which may occur simultaneously or concurrently in the immediate vicinity of the individual alloy surfaces will now be examined in some detail.

Nickel.—In view of the work done by Goebel and Pettit (17) and the kinetic and morphological results obtained during the present work, the important stages involved in the hot corrosion of Ni in pure Na_2SO_4 can be said to have been identified. When a specimen embedded in Na_2SO_4 is heated to the experimental temperature of 900°C, the salt melts almost instantaneously and screens the specimen from direct contact with oxygen in the gas phase. Consequently, the metal oxidizes by consuming oxygen from the melt in its immediate vicinity. This locally raises the sulfur potential to such high levels that liquid Ni-S phases begin to form at (or immediately underneath) the metal surface. Occurrence of these two concurrent reactions and formation of a solid-liquid phase mixture results in the development of a porous nonprotective scale that does not prevent further Na_2SO_4 infiltration. In the presence of excess Na_2SO_4 (as in our experiments but not in Pettit's), the sequence of oxidation-sulfidation can repeat many times and accelerate the corrosion process. Figure 20(a) schematically outlines this model.

It seems likely that the presence of 1% PbO in Na_2SO_4 alters the corrosion mechanism for Ni in the following way. Following melting of the salt mixture and the formation of homogeneous solution, Ni oxidizes by reducing PbO

$$Ni(s) + PbO(soln) = NiO(s) + Pb(l) \quad [10]$$

A large thermodynamic driving force exists for this reaction

$$\Delta G = \Delta G^\circ + RT \ln a(PbO)$$
$$= -7600 + RT \ln a(PbO)$$
$$< -7600 \text{ cal}$$

Since the oxygen needed for NiO formation is obtained from PbO in the melt, the stoichiometry of Na_2SO_4 (and the sulfur potential in it) remains virtually unchanged, and no sulfides can form. In the absence of sulfide formation, dense protective NiO scale can develop over the metal. The scale formed over Ni exposed to the 1% PbO-Na_2SO_4 melt (Fig. 2) is identical in appearance to the scale observed in ordinary oxidation in a salt-free environment [Fig. 3a in Ref. (17)]. Figure 20(b) schematically summarizes the processes responsible for the development of dense sulfide-free NiO scale on Ni in the 1% PbO-Na_2SO_4 melt.

Nickel-chromium alloys.—Corrosion processes occurring in Ni-Cr alloys are more complex than in Ni because the nature of the scale on these alloys depends on alloy composition, grain size, the surface condition, and time and temperature of oxidation (11-14). All Ni-Cr alloys pass through an initial transition stage during which nuclei of NiO and Cr_2O_3 form on the surface, the amounts of each mainly depending on

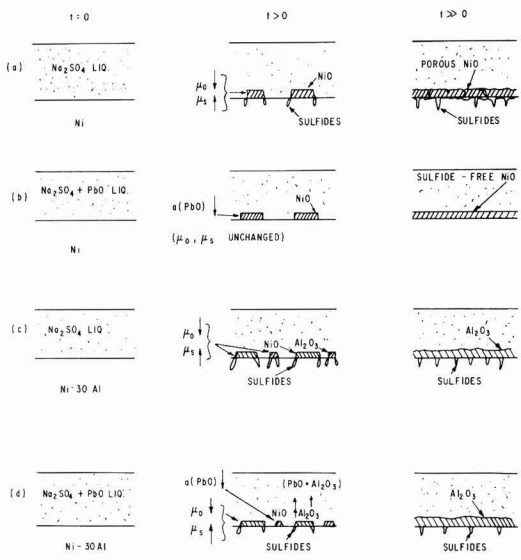


Fig. 20. Schematic summary of proposed reactions responsible for development of steady-state corrosion morphologies in (a) Ni in Na_2SO_4, (b) Ni in Na_2SO_4 + 1% PbO, (c) Ni-30 Al in Na_2SO_4, and (d) Ni-30 Al in Na_2SO_4 + 1% PbO.

the alloy composition (12). For alloys such as Ni-5 Cr, NiO rapidly covers the surface isolating and encapsulating the initially formed Cr_2O_3 particles. Some internal oxidation of Cr may also occur. Ni-Cr alloys containing 20% or more Cr, on the other hand, form Cr_2O_3 and NiO initially, the former process is more rapid however, so that the steady-state scale is essentially pure Cr_2O_3. For alloys in the 10-15% Cr range, experimental and microstructural variables determine whether a duplex NiO scale will form over a Cr_2O_3 subscale, or a Cr_2O_3 scale will cover the entire surface, or an intermediate, mixed mode of oxidation will ensue (11, 12, 14). Since earlier discussion has established that Cr_2O_3 is susceptible to complexing by PbO, the extent of corrosion in Ni-Cr alloys is expected to be a function of Cr-concentration in the alloy. Figure 11 shows that indeed such a functional relationship exists. The presence of a peak in the initial corrosion rate at about 10-15% Cr indicates that simultaneous NiO and Cr_2O_3 formation on an alloy (*i.e.*, a mixed mode of oxidation) makes it particularly vulnerable to PbO attack. It is interesting to note that attack by Na_2SO_4 alone monotonically decreases with increasing Cr-content and does not show any peak throughout the entire composition range.

Figure 21(a) schematically outlines the important stages in the morphological development of a reasonably dense NiO scale over Ni-5 Cr in pure Na_2SO_4. Corrosion processes occurring here are not very different from those occurring in pure Ni [Fig. 20(a)] except that solid Cr-sulfides form in Ni-5 Cr instead of liquid Ni-sulfides. Prevention of liquid sulfide formation helps in forming a dense scale over Ni-5 Cr and in reducing the corrosion rate in Na_2SO_4 (Fig. 11).

Figure 21(b) schematically summarizes the processes occurring on Ni-5 Cr in 1% PbO-Na_2SO_4. The processes are similar to those occurring on Ni-5 Cr in Na_2SO_4 alone except that the initially formed Cr_2O_3 is complexed away by PbO to form liquid (and possibly volatile) (24) $PbCrO_4$. Formation of liquid or volatile reaction products tends to make the NiO scale developing on Ni-5 Cr porous, at least until no more Cr_2O_3 forms. These factors together are responsible for increasing the initial PbO-Na_2SO_4 corrosion rate of Ni when 5% Cr is added to it.

Unlike Ni-5 Cr where NiO is the sole constituent of the steady-state scale, both NiO and Cr_2O_3 may persist at steady state on Ni-Cr alloys containing 10-15% Cr. NiO is generally seen to cover grains and forms the matrix, and Cr_2O_3 is found at sites where grain boundaries meet the external surface (11). Often Cr_2O_3 islands link up to form chainlike paths in the NiO matrix (11-13). Sometimes NiO and Cr_2O_3 react to form spinels within the scale, or a Cr_2O_3 subscale develops under a duplex NiO scale (13, 14). In any event, the presence of large amounts of Cr_2O_3 on Ni-(10-15%) Cr alloys makes them susceptible to PbO complexing for longer periods than with Ni-5 Cr. Removal of Cr from the alloy through Cr_2O_3 complexing as well as Cr-sulfide formation cause the Cr concentration at the scale alloy/interface to drop gradually. Ni-15 Cr and Ni-10 Cr, however, cannot sustain severe Cr depletion without becoming a virtual NiO former. After a finite time, therefore, these alloys begin to behave like Ni-5 Cr. But the scale developing at this late stage is not very protective because of all the surface irregularities already introduced by processes such as sulfidation and complexing. Figure 21(c) shows schematically how the scale may develop on Ni-15 Cr in 1% PbO-Na_2SO_4. Ni-15 Cr in pure Na_2SO_4 will show a dense thin protective layer of Cr_2O_3 plus some internal sulfide particles because Cr_2O_3 does not dissolve appreciably in Pb-free Na_2SO_4 (Table II).

Ni-50 Cr withstands Na_2SO_4 attack very well (Fig. 8) because it is a strong Cr_2O_3 former. For the same reason, however, it is expected to be susceptible to attack by the PbO-Na_2SO_4 melt. However, Cr_2O_3 is the sole constituent of the scale in this case and the protective scale develops quite rapidly. Subsequent complexing of Cr_2O_3 must then proceed solely through dissolution at the scale/melt interface. This is quite unlike the irregular dissolution behavior occurring in the NiO/Cr_2O_3 scale over Ni-15 Cr where porous scales are easy to form. Thus although Ni-50 Cr undergoes accelerated attack in 1% PbO-Na_2SO_4 in comparison to Na_2SO_4 alone (Fig. 11), the attack is not as severe as for Ni-15 Cr.

As discussed in the case of Ni-15 Cr, removal of Cr through sulfide and complex formation reduces the Cr-concentration at the scale/alloy interface in Ni-50 Cr. This appears as a band free from α-Cr particles in Fig. 9 and 10. In the case of Ni-50 Cr, however, the alloy is so rich in Cr initially that the Cr depletion cannot reduce it to a NiO former. In Na_2SO_4 alone, the processes are identical to those shown in Fig. 21(d) for Ni-50 Cr in 1% PbO-Na_2SO_4, except that no $PbCrO_4$ forms in pure Na_2SO_4 and the corrosion is lower in magnitude.

An examination of the kinetic curve for Ni-50 Cr corrosion in 1% PbO-Na_2SO_4 (Fig. 8) reveals that the alloy undergoes a relatively rapid corrosion initially, but the corrosion rate becomes negligible within a short time. This suggests that the melt becomes fully complexed and loses its potency quite quickly. This is not surprising in view of the facts that the alloy is very rich in Cr and the melt initially contains only 1% PbO. The series of experiments with 5 and 10% PbO in Na_2SO_4 (Fig. 8) showed that with larger amounts of PbO added to the melt, longer times were necessary for melt saturation and assumption of "steady-state" corrosion. In fact, for the 10% PbO melt, steady state was not reached during the course of the 4 hr experiment. That the amount of Cr depletion and over-all corrosion of the alloy also increases with increasing PbO content of the melt is clear from Fig. 9 and 10.

Nickel-aluminum alloys.—Ni-30 (β-NiAl) is the only Ni-Al alloy studied in depth in the present investigations. Alloys containing lower amounts of Al generally contained the γ-Ni_3Al phase as well and were catastrophically attacked even in pure Na_2SO_4. Experiments involving these alloys and Na_2SO_4-PbO melts were, therefore, not attempted.

Figure 14 shows that PbO in the melt increases the hot corrosion of Ni-30 Al but not as significantly as in

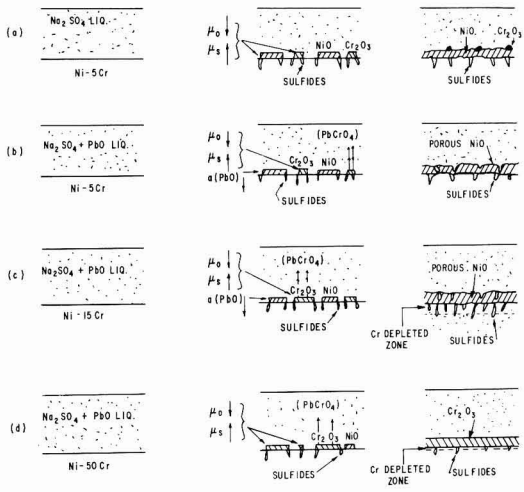


Fig. 21. Schematic summary of proposed reactions responsible for development of steady-state corrosion morphologies in (a) Ni-5 Cr in Na_2SO_4, (b) Ni-5 Cr in Na_2SO_4 + 1% PbO, (c) Ni-15 Cr in Na_2SO_4 + 1% PbO, and (d) Ni-50 Cr in Na_2SO_4 + 1% PbO.

the case of Ni-Cr alloys (Fig. 5). (Note that the vertical scale in Fig. 14 is expanded by a factor of two from that in Fig. 5.) This observation is in general agreement with the thermochemical analysis presented earlier (Fig. 19). Kinetic factors may also be responsible for the relatively small effect of PbO in increasing corrosion of Ni-30 Al. For example, unlike $PbCrO_4$ which forms a liquid at 900°C, $PbO \cdot Al_2O_3$ may first appear as a solid and then dissolve in the melt at this temperature. Processes such as these are likely to place kinetic restriction on a system.

Figure 20(c) and (d) attempt to describe schematically how the corrosion morphology may develop in Ni-30 Al exposed to Na_2SO_4 and 1% PbO-Na_2SO_4, respectively. Ni-30 Al is a strong Al_2O_3 former and the sequence of reactions occurring in Ni-30 Al in PbO-Na_2SO_4 [Fig. 20(d)] is analogous to that occurring in Ni-50 Cr [Fig. 21(d)] except for the obvious difference that Ni-50 Cr forms Cr_2O_3 on the surface. Both Ni-30 Al and Ni-50 Cr are very rich in the protective element, and the scale can continue to reform in both cases despite partial dissolution in the melt.

Before concluding the discussion, some incidental observations made during this study need to be examined briefly. One of these involves the effect of SO_2 in the environment and the other involves the relative complexing abilities of $PbSO_4$ and PbO. Corrosion experiments in SO_2-O_2-N_2 environments always produced more extensive material degradation (Fig. 1 and 5, for example) than in air. No simple explanation can be offered for this observation. If PbO complexing of oxide scales was the only reaction determining the extent of corrosion, air should have been the more aggressive environment for the equilibrium $a(PbO)$ would be higher under those conditions. Obviously the answer to this apparent contradiction must lie in the side reactions accompanying the complexing processes. One such reaction is the stabilization of PbO to Pb-oxysulfate in presence of SO_2

$$2PbO(soln) + SO_2(g) + \underline{O}(soln) = PbSO_4 \cdot PbO(s) \quad [11]$$

This reaction would consume O from the melt, increase the sulfur potential locally, and thereby enhance over-all corrosion rates. In air, on the other hand, the extent of PbO stabilization is much less, and the net effect on Na_2SO_4 stoichiometry and over-all corrosion rates, etc., should be minimal. This line of reasoning appears to explain the experimental observation but is admittedly speculative at this stage.

No apparent contradiction arises in comparing experimental observations with thermochemical arguments as far as the relative complexing capabilities of Na_2SO_4-PbO and Na_2SO_4-$PbSO_4$ melts are concerned. If the thermochemical analysis leading to Fig. 19 were repeated with $PbSO_4$ replacing PbO in the proper manner, the calculated activities of $PbCrO_4$ and $PbO \cdot Al_2O_3$ would be found to be smaller than those already derived ($<10^{-3}$-10^{-2}). This relatively low amount of corrosion observed in $PbSO_4$-Na_2SO_4 is therefore not difficult to understand. Moreover, reactions of type [11] are not expected to be important in the $PbSO_4$-Na_2SO_2 environment, and less amounts of sulfides are likely to form.

A few experiments were conducted in the course of the present work to determine the reactivity of Ni-Cr and Ni-Al alloys to $PbSO_4$ alone. Figure 7 shows the kinetics of $PbSO_4$-induced corrosion of Ni-15 Cr. A comparison with the data in Fig. 5 shows pure $PbSO_4$ to be more aggressive than pure Na_2SO_4 but less so than PbO-Na_2SO_4 (or $PbSO_4$-Na_2SO_4). Moreover, the corrosion morphology in pure $PbSO_4$ is quite irregular and is characterized by random localized attack. These features are probably due to the fact that pure $PbSO_4$ is solid at the experimental temperature whereas Na_2SO_4 and Na_2SO_4-base mixtures are liquid. As far as Al_2O_3 formers are concerned, the net corrosion in $PbSO_4$ was somewhat more than in Na_2SO_4, and the attack was again localized. Figure 16 shows the morphological features of this localized corrosion. It is interesting to note that $PbCrO_4$ is liquid at 900°C but $PbO \cdot Al_2O_3$ is solid. This fact may be partially responsible for the fact that Cr_2O_3 formers are generally more susceptible to pure $PbSO_4$ attack than Al_2O_3 formers.

Conclusions

1. Addition of 1 m/o PbO to the salt melt reduces sharply the rate of corrosion of pure nickel by Na_2SO_4 at 900°C.
2. With Ni-Cr alloys a large increase in the rate of Na_2SO_4 hot corrosion at 900°C results from addition of 1% PbO to the salt melt.
3. This effect, which is due to the formation of $PbCrO_4$ which is soluble in the molten Na_2SO_4, becomes more significant with increasing Cr content of the alloy and results in catastrophic corrosion rates with alloys containing 10-15% Cr.
4. The Na_2SO_4-induced hot corrosion of Ni-30 Al is also enhanced by the addition of PbO to the salt, probably as a result of the formation of the soluble complex $PbO \cdot Al_2O_3$, although the effect is less dramatic than with Ni-Cr alloys.
5. PbO is a more deleterious condensate than $PbSO_4$, although both are likely to form together during turbine operation with lead-contaminated fuels.
6. In general, hot corrosion rates are higher in a simulated turbine environment (0.1% SO_2-76% O_2-N_2) than in air.

Acknowledgments

The authors are indebted to R. E. Hanneman and R. L. McCarron for many useful discussions, and to A. Ritzer and B. Beach for the metallography.

Manuscript submitted Nov. 18, 1974; revised manuscript received Feb. 10, 1975.

Any discussion of this paper will appear in a Discussion Section to be published in the June 1976 JOURNAL. All discussions for the June 1976 Discussion Section should be submitted by Feb. 1, 1976.

Publication costs of this article were partially assisted by General Electric Company.

SYMBOLS

a_i	activity of species i
c	condensed phase
ΔG	free energy of a reaction
$\Delta G°$	standard free energy of a reaction
g	gas
K	equilibrium constant at a given temperature
l	liquid
μ_i	chemical potential of species i
N_i	mole fraction of species i
R	universal gas constant
s	solid
soln	solution
T	temperature

REFERENCES

1. E. L. Simons, G. V. Browning, and H. A. Liebhafsky, *Corrosion*, **11**, 505t (1955); J. Stringer, Battelle Memorial Institute, MCIC Report 72-08 (1972).
2. P. I. Fontaine and E. G. Richards, in "Hot Corrosion Problems Associated with Gas Turbines," ASTM Pub. STP 421, p. 246 (1967).
3. P. A. Bergman, in "High Temperature Metallic Corrosion of Sulfur and Its Compounds," Z. A. Foroulis, Editor, p. 224, The Electrochemical Society Softbound Symposium Series, New York (1970).
4. H. S. Spacil, General Electric Company, Unpublished results (1973).
5. P. A. Bergman, General Electric Company, Unpublished observations (1973).
6. R. W. Ross, Jr. and R. C. Scarberry, *Corrosion*, **30**, 211 (1974).
7. J. W. Sjoberg and A. I. Rozmanith, *Mater. Prot. Perf.*, **10** (9), 31 (1971).

8. D. W. McKee and G. Romeo, *Met. Trans.*, **5**, 1127 (1974).
9. J. A. Goebel, E. J. Felten, and F. S. Pettit, Symposium on "Corrosion Problems in Energy Conversion and Generation," C. S. Tedmon, Editor, p. 102, The Electrochemical Society Softbound Symposium Series, Princeton, N. J. (1974).
10. G. Romeo and D. W. McKee, *This Journal*, **122**, 188 (1975).
11. C. S. Giggins and F. S. Pettit, *Trans. TMS-AIME*, **245**, 2495 (1969); **245**, 2509 (1969).
12. C. S. Giggins and F. S. Pettit, *This Journal*, **118**, 1782 (1971).
13. G. C. Wood and T. Hodgkiess, *ibid.*, **113**, 319 (1966).
14. D. Chatterji, H. C. Graham, and H. H. Davis, Paper No. 81-B-73 presented at 75th Annual Meeting of American Ceramic Society, Cincinnati, April 1973.
15. E. A. Gulbransen and S. A. Jansson, in "High Temperature Metallic Corrosion of Sulfur and Its Compounds," Z. A. Foroulis, Editor, p. 3, The Electrochemical Society Softbound Symposium Series, New York (1970).
16. H. S. Spacil, General Electric Company, Unpublished results (1972).
17. J. A. Goebel and F. S. Pettit, *Met. Trans.*, **1**, 1943 (1970).
18. J. A. Goebel, F. S. Pettit, and G. W. Goward, *ibid.*, **4**, 261 (1973).
19. H. H. Kellogg and S. K. Basu, *Trans. TMS-AIME*, **218**, 70 (1960).
29. E. Rosen and L. Wittung, *Acta Chem. Scand.*, **26**, 2427 (1972).
21. L. Wittung, Scand. *J. Met.*, **1**, 91 (1972).
22. M. Kh. Karapet'yants and M. L. Karapat'yants, "Thermodynamic Constants of Inorganic and Organic Compounds," Ann Arbor-Humphrey Science Publishers, Ann Arbor, Michigan (1970).
23. E. M. Levin, C. R. Robbins, and H. W. McMurdie, "Phase Diagrams for Ceramists," The American Ceramic Society, Columbus, Ohio (1964).
24. R. C. DeVries and J. F. Fleischer, *J. Am. Ceram. Soc.*, **49**, 782 (1970).

Efficiency of Dy^{3+}-Activated Phosphors

J. L. Sommerdijk and A. Bril

Philips Research Laboratories, Eindhoven, Netherlands

ABSTRACT

The quantum efficiency of Dy^{3+}-activated phosphors is reasonably high in lattices where a low activator concentration ($< 1\%$) is already sufficient for effective energy transfer from the lattice to the activator ions. When more activator is needed for effective energy transfer, the quantum efficiency is limited due to concentration quenching of the Dy^{3+} emission. The results are compared with those of corresponding Eu^{3+}- and Tb^{3+}-activated phosphors.

The luminescence of Dy^{3+} is well known (1-9). Emission spectra of Dy^{3+} usually consist of narrow lines in the regions 470-500 and 570-600 nm together with some weak lines at longer wavelengths. Due to the location of the strong lines it is possible to get a near-white emission if the intensities of these lines in the two regions are of the same order. Its luminescence has therefore become of some interest in view of its possible application in low- and high-pressure mercury vapor discharge lamps (6, 7, 9). The Dy^{3+} ions cannot be excited effectively by these discharges which emit mainly at $\lambda > 250$ nm (corresponding to the wave number region $\kappa < 40.000$ cm^{-1}). The lowest charge transfer level of Dy^{3+} in oxides is situated at energies corresponding to $\kappa > 50.000$ cm^{-1} (10) and the same applies to the lowest 5d level of Dy^{3+} (11). Excitation of Dy^{3+} can therefore occur only by 4f-4f transitions. These have a relatively low oscillator strength ($\simeq 10^{-6}$) since they are in first order forbidden by the parity selection rule (12). The radiation of mercury discharges is therefore only weakly absorbed by the Dy^{3+} ions.

The problem of low absorption can be circumvented sometimes by using Dy^{3+}-activated phosphors in which the lattice strongly absorbs the mercury radiation and can transfer the absorbed energy to the Dy^{3+} ions. Some examples of such phosphors reported in the literature are: YVO_4-Dy (2, 5, 7-9), Y_2WO_6-Dy (4), and Ga_2O_3-Dy (6). To our knowledge, the efficiency of these and other Dy^{3+}-activated phosphors has not yet been systematically studied, as has been done, for example, for Eu^{3+}- and Tb^{3+}-activated phosphors (13, 14). It seemed, therefore, interesting to determine the quantum efficiencies of a number of Dy^{3+}-activated phosphors. In this paper we discuss the efficiencies of the lattice emission and that of the Dy^{3+} emission for various lattices and as a function of the Dy^{3+} concentration. We will compare our results with those reported in the literature (2, 4, 13-17) for corresponding Eu^{3+}- and Tb^{3+}-activated phosphors.

Key words: quantum efficiency, luminescence energy transfer, fluorescence energy transfer, rare earths fluorescence.

Experimental

Samples were prepared by the usual techniques as described, for example, in Ref. (2, 4, 13-17). Reaction products were checked by analysis of x-ray powder diagrams (Cu $K\alpha$ radiation). Quantum efficiencies of the Dy^{3+}-activated phosphors were measured by comparison with the standard phosphors issued by the National Bureau of Standards as described in Ref. (18, 19). As excitation source, a high-pressure mercury discharge lamp with a $Cl_2/NiSO_4/UG5$ filter combination was used, emitting mainly in the 250-270 nm region. In view of the dependence on the sample preparation (the output of the samples was not optimized) and because of the limited accuracy of the optical measurements, only approximate values are given for the quantum efficiencies. All measurements were performed at room temperature.

Results and Discussion

Table I contains the results for Dy^{3+}-activated $YNbO_4$, $LaNbO_4$, and $CeMgAl_{11}O_{19}$. In all cases the quantum efficiency of the Dy^{3+} emission is limited, both for low and high Dy^{3+} concentrations. This can be explained in the following way. For these phosphors, a large amount of Dy^{3+} is needed in order to have efficient energy transfer from the lattice to the Dy^{3+} ions. It is known that energy transfer through these lattices is not efficient (16, 20). For the niobates this is due to the poor overlap between the NbO_4^{3-} emission and absorption bands (20). For $CeMgAl_{11}O_{19}$ the overlap between the Ce^{3+} emission and absorption

Table I. Quantum efficiencies (q) of lattice emission and Dy^{3+} emission under 250-270 nm excitation of Dy^{3+}-activated $YNbO_4$, $LaNbO_4$, and $CeMgAl_{11}O_{19}$

Composition	q, % Lattice emission	q, % Dy^{3+} emission
$YNbO_4$	45	—
$YNbO_4$-0.5% Dy	35	10
1.5	30	15
5	20	12
15	10	10
$LaNbO_4$	40	—
$LaNbO_4$-0.5% Dy	30	10
1.5	25	15
5	10	15
15	<2	2
$CeMgAl_{11}O_{19}$	60	—
$CeMgAl_{11}O_{19}$-10% Dy	20	10
20	15	15
35	5	10

band is also small (16) and furthermore the shortest Ce^{3+}-Ce^{3+} distance is rather large (5.6Å). Since the energy transfer through the lattices is not effective, the transfer from excited lattice centers (NbO_4^{3-}, Ce^{3+}) to Dy^{3+} ions can occur only directly. The probability of this transfer decreases very strongly with increasing distance (21), so that this transfer in effect *is restricted to short distances. This implies that* a high Dy^{3+} concentration (> 10%) is needed for complete transfer from lattice to Dy^{3+}. The required Dy^{3+} concentration is so high that considerable quenching of the Dy^{3+} emission occurs. This concentration quenching is due to mutual Dy^{3+}-Dy^{3+} interactions (22) and starts generally at a concentration of a few atomic per cent. In conclusion, the quantum efficiency is limited at low Dy^{3+} concentrations by the ineffective energy transfer to Dy^{3+} and at high Dy^{3+} concentrations by the concentration quenching of the Dy^{3+} emission.

Table II contains the results for Dy^{3+}-activated Y_2WO_6, Lu_2WO_6, $CePO_4$, and $CaWO_4$. In these phosphors, the probability of energy transfer through the lattice is somewhat higher than for the phosphors of Table I. This is mainly due to the stronger energy overlap of the lattice absorption and emission bands. In Ref. (23) the transfer probability in Y_2WO_6 has been compared quantitatively with that in $YNbO_4$. It appeared that the average transfer distance through the lattice is twice as great for the tungstate as for the niobate. This explains why quenching of the lattice emission by Dy^{3+} occurs more effectively (*i.e.*, with less Dy^{3+}) in Y_2WO_6 than in $YNbO_4$. Similar arguments have been used in Ref. (23) to explain the difference between $YNbO_4$-Eu and Y_2WO_6-Eu. The compound Lu_2WO_6 has the same crystal structure and about the same luminescence properties as Y_2WO_6 (24). The situation of Lu_2WO_6-Dy will therefore resemble that of Y_2WO_6-Dy. Also in $CePO_4$ energy transfer through the lattice occurs. This can be derived from the concentration quenching of the Ce^{3+} emission

Table II. Values of q (*cf.* Table I) for Dy^{3+}-activated Y_2WO_6, Lu_2WO_6, $CePO_4$, and $CaWO_4$

Composition	q, % Lattice emission	q, % Dy^{3+} emission
Y_2WO_6	12	—
Y_2WO_6-1% Dy	10	15
3	5	20
10	<2	10
Lu_2WO_6	12	—
Lu_2WO_6-1% Dy	10	15
3	5	15
10	<2	10
$CePO_4$	35	—
$CePO_4$-1% Dy	15	15
3	5	10
10	<2	3
$CaWO_4$	60	—
$CaWO_4$-1% Dy[a]	10	20
3	5	25
10	<2	7

[a] Charge compensation with Na^+ according to $2\ Ca^{2+} \rightarrow Na^+ + Dy^{3+}$.

observed for $La_{1-x}Ce_xPO_4$ (17). This quenching is due to energy transfer from one Ce^{3+} ion to another until an energy sink is reached (17, 21). The efficiency of the Ce^{3+}-Ce^{3+} transfer is only moderate, however, since the maximum quantum efficiency of $CePO_4$ is still 40% (17). This explains why still some 5-10% Dy^{3+} is necessary for complete quenching of the Ce^{3+} emission of $CePO_4$. Moderate energy transfer through the $CaWO_4$ lattice has been demonstrated in Ref. (25) where the phosphor $CaWO_4$-Sm was studied. Similarly, complete quenching of the $CaWO_4$ emission occurs at a Dy^{3+} concentration of about 5-10%. Since the amount of Dy^{3+} required for complete transfer from the lattice is lower than for the phosphors of Table I, the effect of concentration quenching of the Dy^{3+} emission is less detrimental. As a result somewhat higher quantum efficiencies can be obtained.

Table III contains the results for Dy^{3+}-activated Ga_2O_3 and YVO_4. Here a small Dy^{3+} content (< 1%) *is already sufficient for effective transfer from the* lattice to Dy^{3+}. We found that only a little amount of Dy^{3+} can be dissolved into Ga_2O_3. Efforts to dissolve more than 1% Dy^{3+} into Ga_2O_3 were not successful. Instead a second phase occurred which on analysis of the x-ray diffraction diagrams was found to have the *composition* $Dy_3Ga_5O_{12}$. *This phase* had the garnet structure with cubic cell parameter $a = 12.35$Å and it was nonluminescent. In Ref. (6) it was reported that the optimum Dy^{3+} concentration for Ga_2O_3-Dy was 5-10%. In our opinion, the actual Dy^{3+} concentration in the luminescent phase is much lower (< 1%). The x-ray diffraction diagrams of our samples doped with 5-10% Dy^{3+} indicated that nearly all the Dy^{3+} went into the nonluminescent $Dy_3Ga_5O_{12}$ phase. In spite of the slight solubility of Dy^{3+} in Ga_2O_3, the energy transfer from Ga_2O_3 to Dy^{3+} is nearly complete. This implies that this transfer is very efficient. In YVO_4 effective energy transfer occurs through the lattice (23). As a result the Dy^{3+} centers can be easily reached, *cf.* Ref. (2, 7), the lattice emission being completely quenched at a Dy^{3+} concentration as low as 0.3%. The required amount of Dy^{3+} is so low that concentration quenching of the Dy^{3+} emission is not yet important. As in other Dy^{3+}-activated phosphors, concentration quenching of YVO_4-Dy sets in at about 1% Dy (Table III). By choosing the appropriate Dy^{3+} concentration (< 1%), the efficiency of this type of phosphors is therefore not limited by the effect of concentration quenching, so that reasonably high efficiencies can be obtained.

It is interesting to compare the efficiencies of the Dy^{3+}-activated phosphors with those of the corresponding Eu^{3+}- and Tb^{3+}-activated phosphors. Table IV compares the maximum quantum efficiencies under 250-270 nm excitation of some phosphors. The data for the Eu^{3+}- and Tb^{3+}-activated phosphors have been taken partly from the literature (4, 14-17). Usually, lattices giving strong rare earth emissions when activated with Eu^{3+}, do not do so when activated with Tb^{3+}. Examples of this are $YNbO_4$, Y_2WO_6, and YVO_4 (4, 14, 15). This has been ascribed to formation of Tb^{4+}-containing complexes, which is favored in these lattices and which causes radiationless relaxation to the ground state before Tb^{3+} emission can take place

Table III. Values of q (*cf.* Table I) for Dy^{3+}-activated Ga_2O_3 and YVO_4

Composition	q, % Lattice emission	q, % Dy^{+3} emission
Ga_2O_3	40	—
Ga_2O_3-<1% Dy	4	30
YVO_4	5	—
YVO_4-0.1% Dy	3	40
0.3	<1	60
0.5	<1	65
1.0	<1	65
2	<1	60
4	<1	50
5	<1	40

Table IV. Comparison between the maximum quantum efficiencies (q_m) of the rare earth emission under 250-270 nm excitation of Eu^{3+}-, Tb^{3+}-, and Dy^{3+}-activated lattices

Lattice	q_m, %		
	Eu^{3+} emission	Tb^{3+} emission	Dy^{3+} emission
$YNbO_4$	30	<5	15
$CeMgAl_{11}O_{19}$	<5	65	15
Y_2WO_6	40	<5	20
$CePO_4$	<5	40	15
Ga_2O_3	<5	<5	30
YVO_4	70	<5	65

(14, 20). Such a quenching process does not occur for the Eu^{3+}-activated phosphors since the fourth ionization potential of Eu is much higher than that of Tb. On the other hand, the compounds $CeMgAl_{11}O_{19}$-Tb and $CePO_4$-Tb show strong Tb^{3+} emission (16,17), whereas the Eu^{3+} emission of $CeMgAl_{11}O_{19}$-Eu and $CePO_4$-Eu is very weak (16, 17). The low efficiencies of Eu^{3+}-activated Ce^{3+} compounds have been ascribed to formation of Ce^{4+}-Eu^{2+} containing complexes causing radiationless losses instead of Eu^{3+} emission. This type of quenching does not occur for Tb^{3+}, since this ion has no tendency to become divalent.

Let us now consider the Dy^{3+}-activated phosphors. The tendency of Dy^{3+} to become tetravalent is much less than that of Tb^{3+}, and its tendency to become divalent is much less than that of Eu^{3+}. We can therefore expect that the formation of the type of killer complexes as formed with Tb^{4+} and Eu^{2+} is much less pronounced in the case of Dy^{3+}. In agreement with this, in none of the lattices studied was the efficiency of the Dy^{3+} emission very low. Dy^{3+} is at least the second best of the three activators due to the low efficiency of either the Eu^{3+} emission ($CeMgAl_{11}O_{19}$, $CePO_4$) or the Tb^{3+} emission ($YNbO_4$, Y_2WO_6, YVO_4) or of both (Ga_2O_3). On the other hand, the efficiency of the Dy^{3+} emission is limited in those phosphors where the required amount of Dy^{3+} is so high that considerable concentration quenching occurs (Tables I and II). For the Eu^{3+} and Tb^{3+} activated phosphors, concentration quenching usually occurs at much higher activator concentrations (26). This explains why the maximum efficiencies of $YNbO_4$-Eu, $CeMgAl_{11}O_{19}$-Tb, Y_2WO_6-Eu, and $CePO_4$-Tb are considerably higher than those of the corresponding Dy^{3+}-activated phosphors. For YVO_4-Dy and Ga_2O_3-Dy, the Dy^{3+} concentration can be held low enough to ensure that concentration quenching practically does not limit the efficiency. Correspondingly, the efficiency of YVO_4-Dy is quite comparable to that of YVO_4-Eu. The optimum Dy^{3+} concentration of YVO_4-Dy ($\simeq$ 0.5%) is considerably lower than that of Eu^{3+} in YVO_4-Eu which amounts to 3-10% (2). This suggests that the transfer from the YVO_4 lattice occurs even more effectively to Dy^{3+} than to Eu^{3+}. Finally there remains Ga_2O_3-Dy which shows Dy^{3+} emission of medium efficiency ($\simeq$ 30%). On the contrary, neither Ga_2O_3-Eu nor Ga_2O_3-Tb showed any rare earth emission. At the moment we can offer no satisfactory explanation for the exceptional behavior of Ga_2O_3-Dy. The luminescence mechanism of Ga_2O_3 itself is not known but is probably significantly different from that of the other lattices under consideration (27). It has been indicated that the properties of Ga_2O_3 are similar to those of ZnS-type phosphors (27). Probably the Dy^{3+} luminescence of Ga_2O_3-Dy resembles that of rare earth activated ZnS which has been studied by various authors (28).

Acknowledgments

The authors are indebted to Miss R. B. Engelen for the optical measurements and to Mrs. F. M. J. H. Hoex-Strik for the preparation of part of the samples.

Manuscript submitted Feb. 13, 1975; revised manuscript received March 3, 1975.

Any discussion of this paper will appear in a Discussion Section to be published in the June 1976 JOURNAL. All discussions for the June 1976 Discussion Section should be submitted by Feb. 1, 1976.

Publication costs of this article were partially assisted by Philips Research Laboratories.

REFERENCES

1. G. H. Dieke and S. Singh, *J. Opt. Soc. Am.*, **46,** 495 (1956).
2. F. C. Palilla, A. K. Levine, and M. Rinkevics, *This Journal*, **112**, 776 (1965).
3. M. J. Taylor, *Proc. Phys. Soc.*, **87,** 281 (1966).
4. G. Blasse and A. Bril, *J. Chem. Phys.*, **45,** 2350 (1966).
5. R. C. Ropp, *J. Opt. Soc. Am.*, **57,** 1240 (1967).
6. W. C. Herbert, H. B. Minnier, and J. J. Brown, *This Journal*, **115,** 104 (1968).
7. S. Faria and D. T. Palumbo, *ibid.*, **116,** 157 (1969).
8. G. W. Ludwig and J. D. Kingsley, *ibid.*, **117,** 348 (1970).
9. J. J. Opstelten, D. Radielovic, and W. L. Wanmaker, *ibid.*, **120,** 1400 (1973).
10. C. K. Jorgensen, R. Pappalardo, and E. Rittershaus, *Z. Naturforsch.*, **20a**, 54 (1965).
11. E. Loh, *Phys. Rev.*, **147,** 332 (1966).
12. B. G. Wybourne, "Spectroscopic Properties of Rare Earths," Interscience Publishers, Inc., New York (1965).
13. G. Blasse, *J. Chem. Phys.*, **45,** 2356 (1966).
14. G. Blasse and A. Bril, *Philips Res. Rept.*, **22,** 481 (1967).
15. W. L. Wanmaker, A. Bril, J. W. ter Vrugt, and J. Broos, *ibid.*, **21,** 270 (1966).
16. J. M. P. J. Verstegen, J. L. Sommerdijk, and J. G. Verriet, *J. Luminescence*, **6,** 425 (1973).
17. G. Blasse and A. Bril, *J. Chem. Phys.*, **51,** 3252 (1969).
18. A. Bril and W. Hoekstra, *Philips Res. Rept.*, **16**, 356 (1961).
19. A. Bril and W. L. Wanmaker, *This Journal*, **111,** 1363 (1964).
20. G. Blasse and A. Bril, *ibid.*, **115,** 1067 (1968).
21. D. L. Dexter, *J. Chem. Phys.*, **21,** 836 (1953).
22. L. G. van Uitert, in Proc. Int. Conf. Luminescence, Budapest, G. Szigeti, Editor, p. 1588, Akad. Kiadó, (1966).
23. G. Blasse, *Philips Res. Rept.*, **24**, 131 (1969).
24. H. J. Borchardt, *J. Chem. Phys.*, **39,** 504 (1963).
25. T. P. J. Botden, *Philips Res. Rept.*, **6,** 425 (1951).
26. L. G. van Uitert and L. F. Johnson, *J. Chem. Phys.*, **44,** 3514 (1966).
27. G. Blasse and A. Bril, *J. Phys. Chem. Solids*, **31,** 707 (1970).
28. See, for example, S. Larach, in Proc. Int. Conf. Luminescence, Budapest, G. Szigeti, Editor, p. 1549, Akad. Kiadó (1966).

Electrochemichromic Systems for Display Applications

I. F. Chang,* B. L. Gilbert, and T. I. Sun

IBM Thomas J. Watson Research Center, Yorktown Heights, New York 10598

ABSTRACT

Several electrochemical systems exhibit an intense color change when an electrochemical reaction is induced by an applied electrical field or current. The electrochemical and electro-optical properties of several such systems have been investigated. These systems are termed electrochemichromic and they can be classified into the following categories: (*i*) simple redox reaction; (*ii*) redox reaction coupled with an independent chemical reaction, resulting in variable color persistence; (*iii*) redox reaction coupled with a chemical reaction producing an insoluble colored species; (*iv*) redox reaction wherein a solid film deposited on one electrode is reduced and exhibits an intense color change. Analytical models which can describe the electrochemichromic behavior are presented for the different categories.

The spectrum of information display is very broad and fast growing. Functionally, display devices range from a simple status indicator, such as a traffic light, to a complex alphanumeric and graphic information presentation, such as a computer display with graphic and interactive capability. Physically, they vary from small electronic wrist watch displays for personal use to large screen displays for mass entertainment. Display devices are still finding new applications in the areas of automotive electronics, medical diagnosis, supermarket and department store retailing, banking terminals, etc. Not surprisingly, established display technologies cannot cope with the growth in applications, and certainly no single technology can serve all display needs and requirements. Thus new display technologies are constantly being pursued. For instance, liquid crystal displays, d-c plasma panels, and light emitting diodes have already made their entry in the low end (small number of characters) display market and there is some hint that plasma displays may very well penetrate some of the CRT strongholds in the near future (1).

Very recently, several new display devices have been introduced which are based on electrochemistry or some electrochemical effects (2-5). One such device is designated an electrophoretic (EP) display, indicating the phenomenon involved (2). The others, termed electrochromic (EC) [more properly electrochemichromic (ECC)[1]] (3), electrochemiluminescent (ECL) (4), and fluorescence quenching (FQ) displays (5) are related to electrochemical redox reactions. The electrophoretic display employs a dye suspension which changes color as a result of electrophoretic migration of dye particles. The electrochemichromic effect is the direct result of a color change induced by an electrochemical redox reaction taking place at or near an electrode. Electrochemiluminescence is produced by a recombination of two species reduced and oxidized at a cathode or an anode, respectively, in a chemical solution. Fluorescence quenching occurs when a fluorescent ion or molecule is reduced or oxidized at an electrode to a nonfluorescent species. The latter two devices are active displays, that is, light is generated by the display medium whereas the former two are passive devices which modulate the reflected or transmitted ambient light. The EP display device has a very poor threshold characteristic, which would inhibit multiplexing, and requires high operating voltages (75-100V). Comparing the other three redox systems, all have low threshold voltages (0.5-2V) and generally similar electrical behavior. However, the ECC display devices are more attractive because they have fewer chemical system constraints, simpler device operation, and better performance in terms of memory capability and high contrast under bright ambient. Therefore, it is technologically important to make a thorough investigation of various ECC systems, their electrochemical, electrical and electro-optical properties. It is also scientifically interesting to study their physical mechanisms, with the hope that such study can lead to an evaluation of the potential in display applications for ECC systems.

This paper presents a study of several ECC systems with display applications in mind. The systems which are described below in the section on electrochemichromic systems show a relatively efficient electrochemichromic effect. They are categorized into different types according to the electrochemistry involved. Their general characteristics are also presented. In the section on electrochemical and electro-optical properties of ECC systems, we describe the experimental investigation of the electrochemical, electrical, and electro-optical properties of these systems. Polarographic, voltammetric, and electrospectroscopic data are presented. In order to gain a better understanding of the ECC effect, we have devised some analytical models for describing various types of ECC systems. This is detailed in the section on the analytical model for electrochemichromic behavior. Although a different model is derived for each type of ECC system, the ECC response of all systems can be expressed in terms of a common function which represents an optimal ECC response and which, therefore, can be used to assess the ultimate potential of ECC systems for display application. The final section contains such an assessment, as well as a comparison of advantages and disadvantages, for different types of ECC systems.

Electrochemichromic Systems

Electrochromism, in the terminology of display technology, is broadly defined as the production of a color absorption band in a display medium by an applied electric field or current. A number of solid and liquid materials exhibit an EC effect, although the physical mechanisms involved may be different. For example, there are two mechanisms in solids that can lead to electrochromism, the well-known color center absorption due to trapping of an electron in an anion vacancy site in alkali halides (6) or other wide bandgap materials (7-9), and the absorption induced by charge transfer among impurity centers in insulators (10).

On the other hand, there are certain electrochemical effects (3, 11-13) occurring in liquids which also show a relatively efficient EC effect. The color change in these systems can be due to one of three different mechanisms: The first is electroplating, either of metals (12) or of nonmetallic elements (13). The sec-

* Electrochemical Society Active Member.

Key words: electrochromic, electrochemical, display, redox, electrochemichromic.

[1] Electrochromism is more broadly defined and also covers some solid-state phenomena such as color centers induced by an applied electrical field in an inorganic solid. For electrochemical electrochromic systems we propose the nomenclature electrochemichromic.

ond is based on a pH indicator effect, *i.e.*, when the pH value near an electrode is changed by an electrochemical reaction, certain chemicals in an aqueous solution may either change color or fluoresce (11). A third mechanism depends upon the fact that an ion or molecule can be reduced or oxidized at an electrode, changing to a color absorbing species. The important point is that all these effects are governed by the basic electrochemical redox reaction. Thus, we designate all these liquids ECC systems.

The experimental ECC systems investigated here are, by definition, all based on an electrochemical redox reaction; however, some of these systems couple a chemical reaction with the redox reaction, or they involve a solid film in the redox reaction. Therefore, we may classify them into different types as follows:

Type I. Simple redox reaction. Ions or molecules in solution may be either reduced at the cathode or oxidized at the anode to become color absorbing species.

Type II. Redox reaction coupled with an independent chemical reaction, resulting in variable persistence. The chemical reaction controls the rate of reversal of the colored species back to its uncolored state.

Type III. Redox reaction coupled with a chemical reaction producing an insoluble colored species. The insoluble species exhibits excellent persistence and can only be erased electrochemically.

Type IV. Redox reaction in which a solid film deposited on one electrode is reduced and exhibits an intense color change. The color formation is confined to the solid film.

The experimental systems in the present work are listed in Table I according to the above classification. Abbreviations for these systems are listed in the last column and shall be used throughout the paper. All systems are aqueous, although some can be dissolved in a nonaqueous solvent such as dimethyl formamide. Generally the nonaqueous solutions show a relatively weak ECC sensitivity limited by solubility. The electrochemical reactions for these four different types can be described by the following formulas:

Type I. $A \pm ne \rightarrow B$ (colored species)

Type II. $A \pm ne \rightarrow B$ (colored species); $B + Z \rightarrow A + Z'$, $Z' \mp me \rightarrow Z$. The example listed in Table I is $A = PTA$, $Z = H_2O_2 + 2H^+$, $B + n/2\ (H_2O_2 + 2H^+) \rightarrow A + nH_2O$, $nH_2O - ne \rightarrow n/2\ (H_2O_2 + 2H^+)$. By varying the concentration of Z, the persistence of the color absorbing species can be controlled.

Type III. $A \pm ne \rightarrow B$; $B + C \rightarrow BC \downarrow$ where BC is an insoluble compound. The example listed in Table I is $A = HV^{++}$ (diheptyl viologen ion), $B = HV^+$ (one-electron reduction), $C = Br^-$ (bromine ion). In this case, the electrochemical reaction, $HV^{++} \pm e \rightarrow HV^+$, may very well contain another reaction as suggested by Schoot *et al.* (3), $HV^{++} + 2e \rightarrow HV$, $HV^{++} + HV \rightarrow 2HV^+$. However, so long as the reactions are fast, this series of reactions may be viewed as one step.

Type IV. $mWO_3 + 2nH^+ + 2ne \rightarrow W_mO_{3m-n}$ (blue color) $+ nH_2O$ where W_mO_{3m-n} signifies that the ratio of oxygen *vs.* tungsten is reduced to allow color centers to be created. A similar equation applies to MoO_3 films.

Electrochemical and Electro-Optical Properties of ECC Systems

The general characteristics of an ECC system are outlined in Appendix I where we compare them with those of ECL, FQ, and EP systems. In this section we present electrochemical, electrical, and electro-optical properties of each type of ECC system. Polarography and cyclic voltammetry were used to investigate their threshold behavior. Electrospectroscopy was employed to obtain their ECC sensitivity and efficiency. These are the most significant performance parameters of an ECC display device.

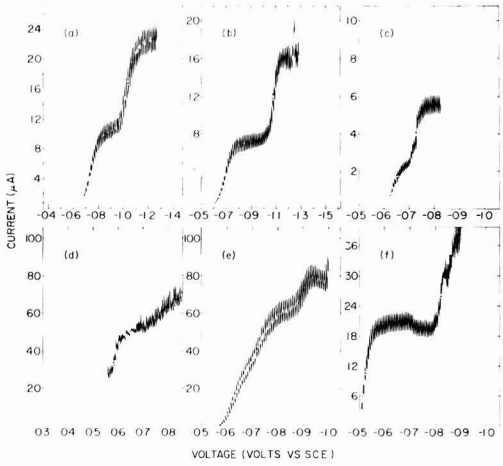


Fig. 1. Polarograph of ECC aqueous systems (a) DPDHC, 50 mg/100 cm³, pH 3.1, $E_{1/2} = -0.75, -1.05$V; (b) MVDC, 50 mg/100 cm³, pH 5.3, $E_{1/2} = -0.68, -1.07$V; (c) HVDB, 60 mg/100 cm³, pH 5.5, $E_{1/2} = -0.65, -0.725$V; (d) OTOL, 50 mg/100 cm³, pH 2.1, $E_{1/2} = +0.58$V; (e) PTA, $Na_2WO_4 \cdot 2H_2O$ 3 g/100 cm³, $ClCh_2COOH$ 2 g/100 cm³, pH 3.1, cathodic wave; (f) HVDB-KBr, 0.02M HVDB, 0.02M KBr.

Polarography.—A Sargent polarograph Model 21 was used to measure the polarographs of each ECC system. The results are shown in Fig. 1(a-f). One notes that the viologen family [Fig. 1(a-c)] all show two cathodic waves, (indicating a two-electron reduction process). The DPDHC, MVDC, and HVDB have their first half-wave potentials at −0.75, −0.68, and −0.65V and second half-wave potentials at −1.05, −1.075, and −0.725V, respectively. [All potentials are given with respect to a saturated calomel electrode (SCE).] The OTOL system with pH value of 2.1 [Fig. 1(d)] shows only one clear anodic wave (one-electron oxidation) with half-wave potential about 0.58V (*vs.* SCE). The polarograph for the PTA system [Fig. 1(e)] is rather poorly defined. There seems to be another wave at lower potential; however, this is not observed in cyclic voltammetry measurement. One does not see a clear one-electron reduction. This suggests that one may have more than one type of polytungsten anion in the solution. When H_2O_2 is added to the solution no significant change in polarographic behavior is observed. Figure 1f shows the polarograph of HVDB when KBr is added as an electrolyte. The half-wave potentials are shifted to −0.52 and −0.8V (*vs.* SCE).

Cyclic voltammetry.—Cyclic voltammetry measurements were performed using a circuit configuration de-

Table I. Electrochemichromic systems

Type	Sample	Formula	Electrolyte	Abbreviation
I	Polytungsten anion	$Na_2WO_4 + ClCH_2COOH$	—	PTA
	4,4' Dipyridinium dihydrochloride	$N_2C_{10}H_{10}Cl_2$	KCL	DPDHC
	Dimethyl viologen dichloride	$N_2C_{12}H_{14}Cl_2$	KCL	MVDC
	O'Tolidine	$[N_2C_{14}H_{18}]$	KCL	OTOL
II	PTA + H_2O_2	$Na_2WO_4 + ClCH_2COOH + H_2O_2$	—	PTA2
III	Diheptyl viologen dibromide	$N_2C_{26}H_{38}Br_2$	KBr or tetramethyl ammonium bromide	HVDB-KBr
IV	Tungsten trioxide	WO_3	H_2SO_4	WO_3
	Molybdenum Trioxide	MoO_3	H_2SO_4	MoO_3

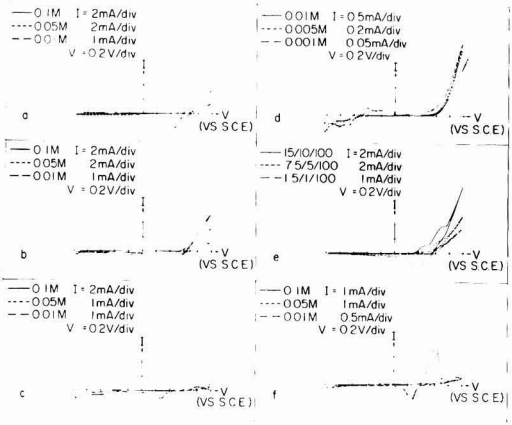


Fig. 2. Cyclic voltammetry measurements of ECC aqueous systems with gold electrode. (a) DPDHC, (b) MVDC, (c) HVDB, (d) OTOL, (e) PTA, (f) HVDB-KBr.

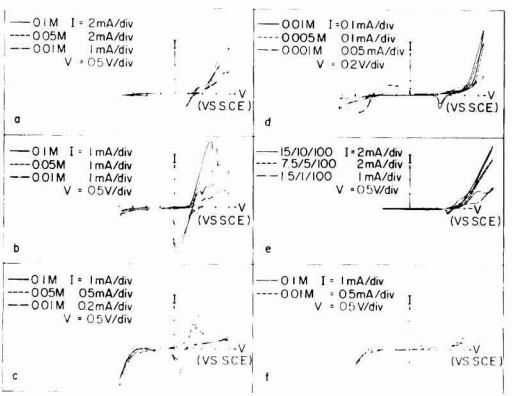


Fig. 3. Cyclic voltammetry measurements of ECC aqueous systems with tin oxide coated glass electrode. (a) DPDHC, (b) MVDC, (c) HVDB, (d) OTOL, (e) PTA, (f) HVDB-KBr.

scribed by Schwarz and Shain (14). A low frequency (0.01 Hz) triangular wave was used in all measurements. The results are shown in Fig. 2(a-f) and Fig. 3(a-f), where the working electrodes were gold and a transparent conductor (tin-oxide-coated glass[2]), respectively. In these measurements high concentrations of ECC materials and electrolyte were used. This tends to wash out the distinction between successive electron reductions. However, we were interested in the current-voltage behavior with solution impedance levels more appropriate to real device operating conditions.

One notes that in Fig. 2(a-c) (data for the viologen family) one cannot distinguish the first electron reduction and the second electron reduction; however, the two reduction steps are more noticeable in Fig. 3(a-c) for the tin oxide electrode cases. Since these scans were taken at high current level with a rate about 80 mV/sec, it might be expected that the two-electron reductions would not be as clearly distinguished in these scans as they were in the polarographs. On the other hand, for the PTA sample, the reduction with the gold electrode [Fig. 2(e)] shows more structure in the I-V scan than is the case with the tin oxide electrode [Fig. 3(e)]. In fact, Fig. 2(e) shows distinctively two reduction steps which are not apparent in the polarograph shown in Fig. 1(e). The half-wave potentials for these reductions may be approximately assigned as −0.37 and −0.6V with respect to SCE potential. Figures 2(d) and 3(d) are the voltammetry curves for OTOL. In both cases, for gold and tin oxide electrodes, the oxidation step is clearly exhibited, the half-wave potential being about +0.6V (*vs.* SCE), which is in close agreement with the value from the polarograph (+0.58V *vs.* SCE). However, one should point out that Kuwana and Strojek (15) have also observed one oxidation wave in their cyclic voltammetric trace in a *p*H 2.0 solution but observed two oxidation waves in a solution of *p*H 4.0. This is consistent with results presented in Fig. 2(e) and 3(e) where the *p*H value is about 2. One recalls that when electrolyte (KBr) is added to the HVDB solution, the polarograms obtained show significant shifts of half-wave potentials; this is not observed in the cyclic voltammetric curves [comparing Fig. 2(f) and 3(f) with Fig. 2(c) and 3(c)]. The high currents employed in the cyclic voltammetry may have masked these shifts.

Electrospectroscopy.—Color and contrast are two important parameters for a display medium. Spectroscopic data for an ECC system in the colored state and noncolored state would be very useful for performance evaluation. Unfortunately, for most of the ECC systems discussed here, there is no spectroscopic data available; therefore, it was necessary to carry out such characterizations. However, in performing absorption measurements, one problem is encountered in the Type 1 and Type 2 samples. The problem is that the colored species electrochemically induced at the electrode tends to diffuse away from it. Due to this diffusion, a nonuniform optical density distribution and a short color persistence result. The reduced (or oxidized) absorbing ion species when meeting an oxidizing (or reducing) ion in the bulk solution will be restored to the uncolored original ion species. Because of this difficulty, among all ECC systems of Type 1 and Type 2 we have measured only the electrochemically induced absorption of the PTA system. Type 3 and Type 4 ECC systems can be measured relatively more easily.

A special optical cell was constructed for the absorption measurement. The cell is O-ring sealed with two windows, either of which can be a transparent electrode serving as a cathode, or working electrode. In the case of measurements of a WO_3 film, the film is deposited on one of the windows. The central vertical port is for a reference electrode such as a SCE. A tilted port next to the central port is for the counter-electrode, which was generally a gold wire. In this cell, one can use either a potentiostatic drive (three electrodes) or a two terminal drive to induce the electrochemical reaction. One also notes that two other side ports are provided for nitrogen flushing, to minimize the oxygen content in the cell.

The three terminal drive is more advantageous than the two terminal drive since it allows a convenient erasure procedure. However, one important fact should be pointed out here: When a colored layer is induced electrochemically on one electrode, an emf is also built up at that electrode. This emf tends to supply through the circuit a reverse current which reverses the redox reaction and erases the color layer. This is especially critical in a three terminal potentiostatic drive circuit, since the back-emf is amplified by the operational amplifier. One remedy for this situation is to use a high off-impedance ($\sim 10^{10}$ ohms) FET switch in the drive circuit, so that the reverse current may be minimized.

The absorption spectrum of the reduced PTA ions is shown in Fig. 4. This is derived from many repeated measurements. One notes a broad absorption band peaked at 710 nm. Considerable asymmetry suggests that a secondary absorption in the infrared around 1000-1200 nm is perhaps superimposed on the main absorption. The resulting color for the reduced PTA ions is a deep blue.

[a] Corning Glass Works.

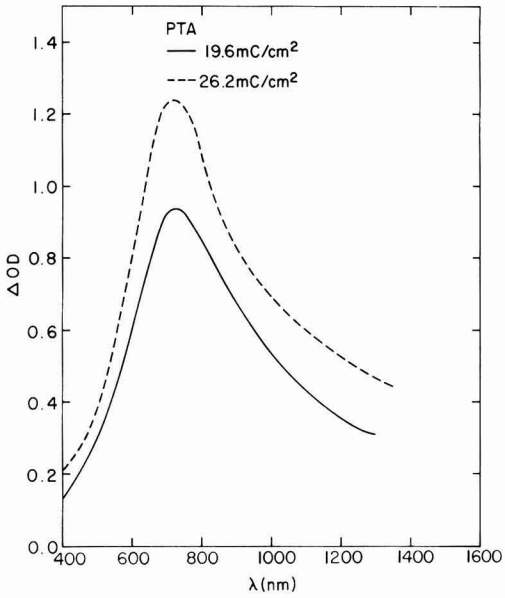


Fig. 4. Absorption spectrum for PTA

The absorption spectra for Type III and Type IV ECC systems are more reliable since there is no color drifting or diffusion in the bulk solution. Figure 5 shows the induced absorption for the HVDB-KBr system. The spectrum exhibits two absorption bands peaked around 515 and 550 nm. The reduced layer has a deep purple color. The induced absorption for a solid WO_3 film is shown in Fig. 6. A very broad absorption band centered around 980 nm is observed. The reduced WO_3 also exhibits a deep blue color. In all cases (Fig. 4-6), the induced optical density is proportional to the applied charge density.

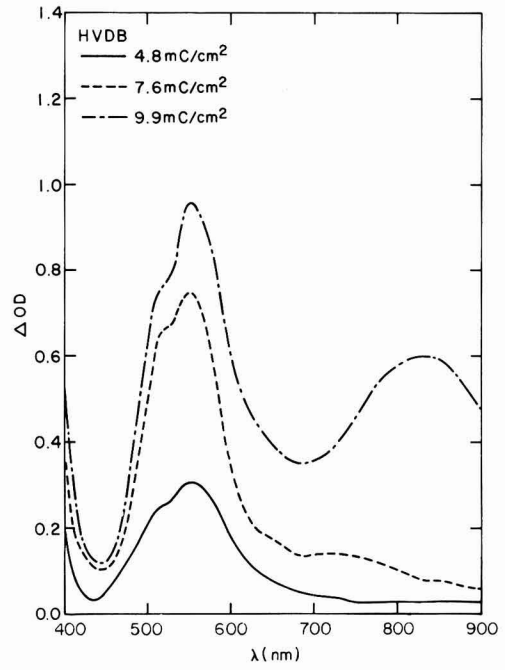


Fig. 5. Absorption spectrum for heptyl viologen bromide

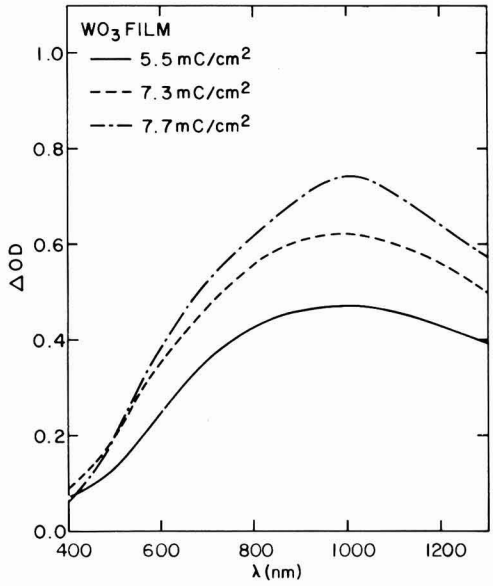


Fig. 6. Absorption spectrum for W_mO_{3m-n}

Analytical Model for Electrochemichromic Behavior

In order to assess the feasibility and ultimate potential of an ECC system for display device application, it is desirable to derive an analytical model for the ECC effect. The model should consider all first order physical mechanisms involved in the ECC effect and as a consequence should identify the physical parameters relevant to ECC behavior.

In analyzing the ECC effect, one finds that there are two major factors governing the ECC behavior, the electrochemical reaction and diffusion. Other mechanisms such as convection and ion migration can be neglected or minimized in a practical ECC solution. The first mechanism, the electrochemical redox reaction, can be characterized by two constants, the forward and backward reaction rates K_f and K_b (16). The second mechanism is the diffusion process which is characterized by the diffusion equation. The solution of the diffusion equation is governed by the boundary and initial conditions of the oxidant or reductant concentration, $C(x, y, z, t)$. The electrochemical reaction is coupled to the diffusion mechanism through the boundary conditions.

The complete solution to a three-dimensional diffusion equation is very complicated unless some simplifying approximations are made to the problem. Before we proceed to derive models for each different type of ECC system, the following assumptions are made: The first assumption is that the liquid solution is of large volume and is bounded by parallel plane electrodes having a separation much greater than a diffusion length for any species involved. The assumption is a realistic one for a typical experimental cell, although it is certainly possible to make practical cells which violate it. With this assumption one can describe the problem by a one-dimensional diffusion equation. Furthermore, one may consider that the liquid solution extends to infinity relative to the electrode under consideration, thus implying $C(x = \infty, y, z, t) =$ constant as one boundary condition. The second assumption which we make initially is that the speed of the ECC effect is not limited by the electrochemical reaction;

that is, one deals only with fast electrochemical reactions. Again, this assumption is a reasonable one, since for display application one naturally searches for an ECC with a fast reaction rate. Furthermore, in display device operation a sufficiently high voltage is always applied to the device [for instance, one may use $E = 2E_0$ or $3E_0$ in half-select or three-to-one matrix address schemes (17)] such that a fast reaction occurs. For such an operating condition, the most significant limiting mechanism governing the ECC behavior would be the diffusion process. Thus, the analytical model describing ECC systems of practical interest is just a linear diffusion model with appropriate boundary conditions. Analytical models for the four types of ECC systems are presented below.

Type I ECC systems.—Based on the initial and boundary conditions given in Appendix II, the functions C_O and C_R can be determined by the use of Laplace transforms with the result

$$C_O(x,t) = C^O[hS + \mathrm{erf}(x/2\,D_O{}^{1/2}t^{1/2})]/(1 + hS) \quad [1]$$

$$C_R(x,t) = C^O[h\,\mathrm{erfc}(x/2\,D_R{}^{1/2}t^{1/2})]/(1 + hS) \quad [2]$$

where C^O, D_O, D_R, and S are defined in Appendix II, $h = (D_O/D_R)^{1/2}$, erf and erfc are error function and complementary error function, respectively. The current flowing through the cell is given by

$$i = n\mathbf{F}AD_O \left.\frac{\partial C_O}{\partial x}\right|_{x=0} = i_a/(1 + hS) \quad [3]$$

where $\mathbf{F}$ is Faraday's constant, A is the electrode area, and n is the number of electrons involved in the reduction. i_a is the limiting current when the electrochemical reaction rate is so high that the concentration of oxidant at the electrode surface is zero, *i.e.*

$$i_a = i(S = 0) = n\mathbf{F}A\,D_O{}^{1/2}C^O\pi^{-1/2}t^{-1/2} \quad [4]$$

The optical density change induced by the electrochemical reaction is proportional to the density of the colored species produced, which in turn is proportional to the charge supplied by the electrode. Thus, we have

$$OD = \frac{a}{2.3}\int_0^\infty C_R\,dx = \frac{a}{2.3}\frac{\int_0^t i\,dt}{n\mathbf{F}A} = OD_a/(1 + hS) \quad [5]$$

where a is the absorptivity in terms of liters/M cm, and the numerical factor 1/2.3 implies that the contrast ratio for a given optical density is 10^{OD} rather than e^{OD}, and

$$OD_a = OD(S = 0) = \frac{2}{2.3}aD_O{}^{1/2}C^O\pi^{-1/2}t^{1/2} \quad [6]$$

Again the significance of $S = 0$ is that the reaction is very fast due to either K_f being very large or $E \ll E_o$. Under this condition, $C_O(0,t) = 0$, $C_R(0,t) = hC^O$, $i = i_a$, and $OD = OD_a$. This is the optimal condition for the ECC effect in Type I systems.

Type II ECC systems.—In this type of system, a catalytic chemical reaction is coupled with the electrochemical redox reaction. Therefore we have two coupled diffusion equations

$$\frac{\partial C_A}{\partial t} = D_A\frac{\partial^2 C_A}{\partial x^2} + kC_zC_B$$

$$\frac{\partial C_B}{\partial t} = D_B\frac{\partial^2 C_B}{\partial x^2} - kC_zC_B \quad [7]$$

where k is the rate of the catalytic chemical reaction and C_z is the concentration of the catalyst. The problem can be simplified considerably if we assume that C_z is constant throughout the solution cell at all times and the diffusion constants D_A and D_B are equal, say D. Applying the same boundary conditions given by Eq. [A-2]-[A-4] and setting $S = 0$ [*i.e.*, $C_A(0,t) = 0$], one obtains the following solutions

$$C_B(x,t) = \frac{1}{2}e^{-x/(D\tau)^{1/2}}\,\mathrm{erfc}[x/2(Dt)^{1/2} - (t/\tau)^{1/2}] + \frac{1}{2}e^{x/(D\tau)^{1/2}}\,\mathrm{erfc}[x/2(Dt)^{1/2} + (t/\tau)^{1/2}] \quad [8]$$

$$OD = \frac{a}{2.3}\int_0^\infty C_B\,dx = \frac{a}{2.3}C_A{}^O\sqrt{D\tau}\,\mathrm{erf}[(t/\tau)^{1/2}] = OD_a\left[1 - \frac{1}{3}(t/\tau) + \frac{1}{5\cdot 2!}(t/\tau)^2 \ldots\right] \quad [9]$$

$$i = n\mathbf{F}A\,D^{1/2}\,C_A{}^O\{(1/\tau)^{1/2}\,\mathrm{erf}[(t/\tau)^{1/2}] + (\pi t)^{-1/2}\exp(-t/\tau)\} \quad [10]$$

where $\tau = 1/kC_z$ is the oxidizing time constant. The more oxidizing agent is added, the smaller the time constant. As $kC_z \to 0$, $\tau \to \infty$ (*i.e.*, no oxidizing agent added), $i \to i_a$ and $OD \to OD_a$. Equations [9] and [10] indicate that the ECC response is reduced from the optimal response due to the catalytic action. The reduction is directly related to the chemical reaction rate and the concentration of catalyst.

Type III ECC systems.—For this type of system, modeling of its ECC response is more complicated. It is particularly so if one considers all possible intermediate reactions involving both one-electron and two-electron reductions as well as the final chemical reaction. However, based on the assumption that we are only dealing with fast reactions, *i.e.*, if both electrochemical and chemical reaction rates are high, then the ECC response of such a system may still be regarded as diffusion limited. The system would then be equivalent to the straightforward electrolytic deposition of an insoluble substance on an electrode. This is certainly a reasonable assumption for the HVDB-KBr system which exhibits very fast reactions.

The corresponding boundary conditions for this case are similar to those of the Type I ECC system, but they are complicated by the fact that the activity of the deposit, f_RC_R, is not known until the electrode is completely covered with at least one monolayer of deposit at which point it becomes equal to one. In view of the fact that the ECC system under consideration is a fast one, we neglect the initial uncertainty of the activity of the oxidant and assume that it is equal to one throughout the ECC response. The error introduced by this approximation is very small, and it applies only to the very early stage of the ECC reaction. With this approximation, the boundary condition of oxidant concentration at the electrode becomes

$$C_O(0,t) = S' = \frac{1}{f_O}\exp[n\mathbf{F}(E - E_o)/RT] \quad [11]$$

The solution for this problem is then

$$C_O(x,t) = S' + (C^O - S')\,\mathrm{erf}(x/2\,D_O{}^{1/2}t^{1/2}) \quad [12]$$

$$i = n\mathbf{F}A\,D_O\left.\frac{\partial C}{\partial x}\right|_{x=0} = i_a(1 - S'/C^O) \quad [13]$$

$$OD = OD_a\,(1 - S'/C^O) \quad [14]$$

However, in Eq. [14], OD_a should be expressed as

$$OD_a = \alpha'\frac{\int i\,dt}{A} = 2\,\alpha' n\mathbf{F}\,C^O D_O{}^{1/2}\pi^{-1/2}t^{1/2} \quad [15]$$

where $\alpha' = a/2.3n\mathbf{F}$ with units of $(\mathrm{coulomb/cm^2})^{-1}$. In this case the absorbing species is insoluble in solution; thus, its absorptivity should be defined in terms of ion charge density rather than molar concentration. One should point out that the current and the optical den-

sity functions are both related to their optimal value by a common factor $(1 - S'/C^0)$.

Type IV ECC system.—The electrochemical reaction of this system is not the same as for the above redox reactions involving soluble species. The Type 1V system is rather unique in the sense that it is the thin solid film ($\sim$ 0.2-1 μm thick) deposited on the electrode which undergoes a redox reaction. Since the film is an oxide, the reduction is facilitated by the presence of protons. This is borne out by the fact that the redox takes place easily in acidic solution. In fact, the electrochromic sensitivity is proportional to the concentration of hydrogen ions in the solution. Furthermore, we have performed cyclic voltammetry measurements on a WO_3-H_2SO_4 system. The result is shown in Fig. 7 and indicates that the reduction does occur (blue color appears) near the hydrogen redox potential. This seems to support the hypothesis that the over-all electrochemical reaction is of the form

$$mWO_3 + 2nH^+ + 2ne \rightarrow W_mO_{3m-n} \text{ (blue)} + nH_2O$$

Although the involvement of protons is certain, exactly what occurs at the electrode or inside the oxide is not clear at all. One may speculate on several possible mechanisms. One possibility is that H^+ ions are reduced at the solid film surface (since WO_3 or MoO_3 films are semi-insulating and in fact become more conducting when reduced to colored film) becoming hydrogen atoms which then diffuse into the film and reduce it. The solid film is very likely porous which would promote the diffusion of the reduction product, H_2O, out to the solution. A second possibility is that H^+ ions diffuse into the film toward the electrode, an electrochemical reduction takes place within the film, and a chemical reduction reaction follows thereafter. A third possibility is that the oxide film is reduced by receiving electrons from the electrode, and oxygen ions diffuse out of the film to combine with hydrogen ions, which diffuse toward the electrode through the solution. No matter which mechanism prevails, the over-all electrochemical reaction seems to be the one given above.

Although we do not have evidence to support any one of the above described mechanisms, it is clear that in any case the diffusion of H^+ ions in the solution is a possible speed limiting mechanism in that the supply of H^+ ions to the electrode may govern. If one assumes that the electrochemical or chemical reaction taking place in the solid film is fast, then the analytical model for this case is just a diffusion-limited electrochemical reaction of H^+. Since H^+ ions are reduced and combined with oxygen to form water which has an activity of 1, the boundary condition for this problem is the same as that for the HVDB-KBr system, as given by Eq. [A-2], [11], and [A-4]. Thus, the solutions given in Eq. [12], [13], and [14] apply here for the Type IV ECC system. In fact, electrical measurements made on the reduction of WO_3 films (18) indicate that the current is indeed a function of $t^{-1/2}$. This certainly supports the validity of this model.

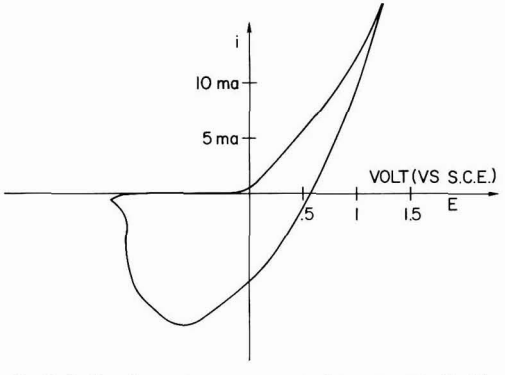


Fig. 7. Cyclic voltammetry measurement of tungsten trioxide film in sulfuric acid (0.3M).

Comparison with experimental data.—Current response, $i(t)$, and electro-optical response, $OD(t)$, of several ECC systems which belong to the four types discussed here have been performed and presented elsewhere (18). The experimental results (18) indicate that for Type I, III, and IV ECC systems, the current response is indeed a function of $t^{-1/2}$ and the optical density a function of $t^{1/2}$. This evidence certainly supports the validity of analytical models presented here. For Type II systems, the model is only confirmed for long persistence systems (*i.e.*, $\tau > 1$ sec). For systems having smaller τ (more oxidizing agent), more experimental work is required to confirm the validity of Eq. [9] and [10].

Discussion and Summary

The systems evaluated here are certainly only a small representation of all possible organic and inorganic ECC systems. The Table I ECC systems are the simplest from an electrochemical point of view. However, for display device applications, they are not practical due to the fact that the induced color species, being soluble, can diffuse or drift away from the electrode, thus causing smearing of an image. There are some possible remedies (19), such as using a gel (or semisolid) electrolyte, but such an approach appears to slow down the ECC response. The second type of ECC system eliminates the color drift problem by providing conversion back to the uncolored species. This feature is acceptable in a display device application where the information can be periodically refreshed. A refresh rate can be selected according to the type and amount of oxidizing chemical used. However, in this type of system, the ECC efficiency is reduced. This effect has been experimentally demonstrated with the PTA-H_2O_2 system (18). As one notes from Eq. [9], unless the oxidizing time constant τ is made much longer than the addressing time (or turn-on time) t, the optical density change is reduced from its optimal value. This condition (*i.e.*, $\tau >> t$) would normally prevail for a multiline matrix display, since it is desirable in that case to select τ to be approximately equal to the refresh cycle time or frame time T.

The third type of ECC system has the advantage of having "memory" capability, since the colored layer is insoluble in the solution. It can only be removed electrochemically. However, because of the presence of this layer there is a back-emf associated with it. This back-emf tends to supply a reverse current through the system if a current path is provided. This leakage current makes matrix addressing complicated (18). However, if all leakage paths are eliminated, the insoluble layer tends to persist indefinitely. This feature offers the potential of saving power in certain applications such as displays for electronic calculators or electronic watches.

The ECC system of the fourth type, namely, a solid ECC film, has similar characteristics to those of Type III. However, the solid film allows the possibility of having such a film deposited on only one electrode, thereby producing an asymmetry not present in the other cases. Figure 8 shows an experimental device arranged in such a manner. When a negative voltage is applied to an electrode coated with an electrochromic solid film, an image is produced (as shown in Fig. 8); and upon reversal of the applied potential, the colored layer is erased without creating a similar colored layer at the opposite electrode. For the other categories of ECC systems an opaque or blocking medium may be required to shield the unwanted coloration created at the opposite electrode by the erasure voltage.

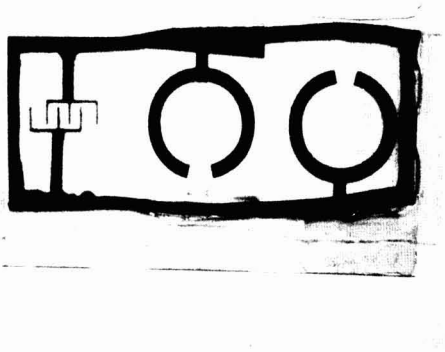


Fig. 8. A display image written on an experimental device containing WO_3-H_2SO_4 gel material.

We have argued that most ECC systems can be described by a diffusion model with appropriate boundary conditions. Solutions for each type of system are all related to an optimal ECC response function OD_a, given by Eq. [6]. One can use this optimal response function to assess the potential of ECC systems for display device applications. If one expresses OD_a as a function of addressing time (turn-on time) in a log-log plot one obtains a straight line with a slope of 1/2. Since OD_a is proportional to the concentration C^0, the absorptivity α or α' and the square root of diffusion constant D, the straight line moves up and down according to the values of these constants. Figure 9 shows a plot for a typical set of constants, $C = 0.1$ M/l, $D = 5 \times 10^{-6}$ cm^2/sec, $\alpha = 5 \times 10^4$ liters/M cm. In a transmission mode, one would require a turn-on time $\sim$ 30 msec to obtain an optical density change of 1 (10 to 1 contrast), whereas in a reflection mode (where the light passes through the absorption path twice), a turn-on time $\sim$ 9 msec would be required for $OD = 0.5$ (10 to 1 contrast). Of course, the above example illustrates the ECC response of a typical system under optimal conditions. In practice, Eq. [A-7], [14], or [5] should be used to assess a particular system. ECC device characteristics measured on various ECC systems (18) do in fact indicate that the analytical models are valid and applicable in assessing their performance.

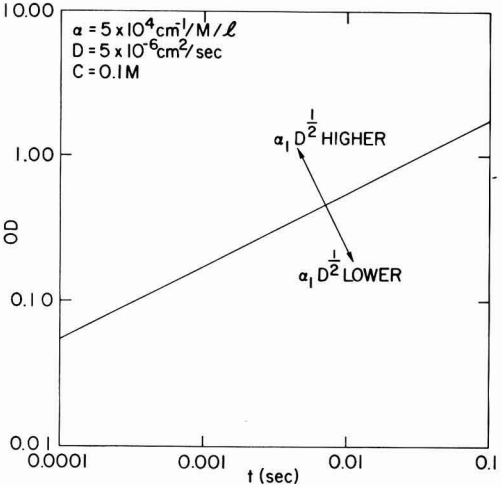


Fig. 9. Induced optical density change of a typical ECC system as a function of addressing time.

Another important question related to ECC device application is their operating life. Although, most examples discussed here were not given a life test, it is worthwhile pointing out that Schoot *et al.* (3) have demonstrated a 10^5 write-erase cycle with the HVDB-KBr system.

In summary, several ECC systems have been evaluated. They are classified into different categories according to the electrochemical reactions involved. The electrochemical, electrical, and electro-optical properties of these systems have been examined and compared. Analytical models which describe the ECC behavior have been derived for the various system types. Based on these models, a performance assessment of the ECC effect can be made. A typical efficient ECC system should have response time in the order of 10-100 msec for contrast of 10 to 1. This response, combined with characteristics such as low threshold voltage, memory capability, and wide viewing angle makes the ECC a strong candidate for direct-addressed segmented displays and small matrix-addressed displays.

Acknowledgment

We thank Drs. Jean W. Horkans, Webster E. Howard, and L. T. Romakiew for useful discussions. We also express our appreciation to Dr. B. Welber (spectroscopy laboratory) and to Dr. R. B. Laibowitz (thin film deposition laboratory) for making their equipment available to us and to W. C. Kateley for his valuable assistance in thin film preparations.

Manuscript submitted Dec. 26, 1974; revised manuscript received March 5, 1975. This was Paper 200 presented at the New York, New York, Meeting of the Society, Oct. 13-17, 1974.

Any discussion of this paper will appear in a Discussion Section to be published in the June 1976 JOURNAL. All discussions for the June 1976 Discussion Section should be submitted by Feb. 1, 1976.

Publication costs of this article were partially assisted by the IBM Corporation.

APPENDIX I

Comparison of Electrochemical Display Systems

	EP[2]	ECC	ECL[4]	FQ[5]
Mode	Passive	Passive	Active	Active
Ultimate contrast	40:1	30:1	30:1	25:1
Memory	Yes	Yes	No	No
Operating voltage	75V (d-c pulse)	1-2V (d-c pulse)	5-10V (a-c)	1-2V (d-c pulse)
Threshold	Poor	Yes	Yes	Yes
Power or energy	200 μW/cm^2	10 mJ/cm^2	40 mW/cm^2	28 mW/cm^2
Write speed	20 msec	10 msec	1 msec	10 msec
Erase speed	10 msec	10 msec	—	—
Gray scale	No	Yes	Yes	Yes

APPENDIX II

Initial and Boundary Conditions for Electrochemichromic Effect

The analytical models presented in this paper are given for a reduction process, thus, the initial conditions are

$$C_O(x, 0) = C^0$$
$$C_R(x, 0) = 0 \qquad [A\text{-}1]$$

where subscript (or superscript) O and R signify oxidant and reductant, respectively. Equation [A-1] specifies that the ECC solution initially contains only oxidant having a constant concentration C^0 throughout the cell. In the case of oxidation reactions one simply interchanges subscript (or superscript) O to R and vice versa in all derivations.

Using the semi-infinite solutions approximation, the boundary conditions are

$$C_O(\infty, t) = C^0, C_R(\infty, t) = 0 \qquad [A\text{-}2]$$

$$C_O(0, t)/C_R(0, t) = S = (f_R/f_O)\exp(n\mathbf{F}(E - E_0)/RT) \qquad [A\text{-}3]$$

and

$$D_O \frac{\partial C_O}{\partial x}\bigg|_{x=0} + D_R \frac{\partial C_R}{\partial x}\bigg|_{x=0} = 0 \qquad [A\text{-}4]$$

Equation [A-3] essentially is the Nernst equation which describes the equilibrium situation at the electrode. f_R and f_O are activity coefficients of reductant and oxidant which may be assumed to be equal for the most redox pairs. The third equation indicates that the incoming flux of oxidant to the electrode is equal to the outgoing flux of reductant. D_O and D_R are diffusion constants, for the oxidant and reductant, respectively.

The above description is based on one fundamental assumption, specifically that the electrochemical reaction rate is fast. It is therefore interesting to see what results if this assumption is removed. Most importantly, one requires a different boundary condition at the cathode

$$D_O \frac{\partial C_O}{\partial x}\bigg|_{x=0} = K_f C_O(0,t) - K_b C_R(0,t) \qquad [A\text{-}5]$$

With this boundary condition, along with that given by Eq. [A-2] and [A-4], the solutions for the current flowing through the cell and the optical density induced are

$$i = n\mathbf{F}AC^O K_f \exp(Q^2 t)\,\mathrm{erfc}(Qt^{1/2}) \qquad [A\text{-}6]$$

$$OD = \frac{1}{2.3}(\alpha C^O K_f/Q^2)\left[\exp(Q^2 t)\,\mathrm{erfc}(Qt^{1/2}) + 2Q(t/\pi)^{1/2} - 1\right] \qquad [A\text{-}7]$$

where $Q = K_f/D_O^{1/2} + K_b D_R^{1/2}$. Since one deals with a reduction when the applied potential $E << E_o$, we should have $Q = K_f/D_O^{1/2}$ substituted in Eq. [A-6] and [A-7]. These solutions apply to slow ECC systems. They approach the results for diffusion-limited current i_a and optimal optical density change OD_a if $Qt^{1/2}$ is large, for instance greater than 5.

REFERENCES

1. E. I. Gordon and L. K. Anderson, *Proc. IEEE*, **61,** 807 (1973).
2. I. Ota, J. Ohnishi, and M. Yoshiyama, *ibid.*, **61,** 832 (1973).
3. C. J. Schoot, J. J. Ponjee, H. T. Van Dam, R. A. Van Doorn, and P. T. Bolwijn, *Appl. Phys. Letters*, **23,** 64 (1973).
4. M. A. Kabayama, A. Pighin, and W. M. Coderre, SID Symposium Late News (1973).
5. D. P. Hamblen and J. R. Clarke, *IEEE Trans. Electron Devices*, **ED-20,** 1028 (1973).
6. J. H. Schulman and W. D. Compton, "Color Centers in Solids," Pergamon Press, New York (1962).
7. I. F. Chang, *This Journal*, **121,** 815 (1974).
8. I. F. Chang and A. Onton, *J. Electronic Materials*, **2,** 17 (1973).
9. S. K. Deb, *Appl. Optics*, Supplement 3, 192 (1969).
10. B. W. Faughnam, D. L. Staebler, and Z. J. Kiss, "Applied Solid State Science," Vol. 2, Academic Press, New York (1971).
11. J. R. Alburger, Electronic Industries and Tele-Tech. Feb. 1957, 50-3.
12. S. Zaromb, *This Journal*, **109,** 903 (1962).
13. C. J. Sambucetti, U.S. Pat. 3,736,043 (1973).
14. W. M. Schwarz and I. Shain, *Anal. Chem.*, **35,** 1770 (1963).
15. T. Kuwana and J. W. Strojek, *Discussions Faraday Soc.*, **45,** 134 (1968).
16. P. Delahay, "New Instrumental Methods in Electrochemistry," Interscience, New York (1954).
17. T. Kilburn, G. R. Hoffman, and R. E. Hayes, *Proc. IEEE*, **105B,** 136 (1958).
18. I. F. Chang and W. E. Howard, IEEE-SID Conf. on Display Devices and Systems, New York, Oct. 9-10, 1974; *IEEE Trans. Electron Devices*, To be published.
19. I. F. Chang, B. L. Gilbert, and K. S. Pennington, Unpublished.

On the Correction to be Applied to the Thickness of an Epitaxial Layer Measured with Infrared Multiple Interference

P. J. Severin and F. C. Eversteyn

Philips Research Laboratories, Eindhoven, Netherlands

ABSTRACT

The extreme values of k plotted against the order of the extrema yield a straight line characterized by a slope d_s and an intercept $\delta_o/2\pi$. The thickness d_m of the deposited layer can be measured with a method described by Eversteyn and van den Heuvel. It turns out that $d_s - d_m$ depends linearly on $\delta_o/2\pi$, the relations being different for N^+ and N^{++}, but further independent of substrate resistivity or thickness. After calibration for a particular growth process the thickness can be determined with d_m as a standard reference from a conventional infrared multiple interference spectrum.

The thickness of a silicon layer grown epitaxially on a conductive substrate of resistivity ρ is an important parameter for integrated circuit technology. In this note fairly conclusive experimental evidence is presented for the validity of the method of interpreting infrared multiple interference spectra described earlier and practiced in this laboratory for several years. The introduction of a new experimentally accessible standard reference allows us now to also discuss the accuracy of the method.

It is well known that the wavenumber k of an extremum depends on the order l by the relation

$$2ndk = l - \frac{1}{2} + \frac{\delta(k,\rho)}{2\pi} \qquad [1]$$

where n and d are the refractive index and the thickness of the layer, respectively. The phase shift $\delta(k,\rho)$ can be calculated from the optical parameters of the layer and the substrate. Over a limited wavenumber range, $\delta(k,\rho)$ may be approximated by a linear relationship

$$\frac{\delta}{2\pi} = \frac{\delta_o}{2\pi} - 2nk\Delta d \qquad [2]$$

which yields, with Eq. [1] and after writing $d_s = d + \Delta d$

Key words: silicon, epitaxial film thickness, infrared spectrophotometer, metallurgical film thickness.

$$2nd_sk = l - \frac{1}{2} + \frac{\delta_o}{2\pi} \qquad [3]$$

It has been shown earlier (1) that when k is plotted *vs.* l, a straight line is obtained from which the slope d_s and the intercept $\delta_o/2\pi$ can be easily determined. In a second paper (2) this formal solution, Eq. [2], has been suggested without actually specifying any experimental values of Δd and $\delta_o/2\pi$. In the absence of a well-defined and experimentally accessible reference for the thickness of an epitaxial layer, there was no point in discussing Δd and the accuracy of the infrared multiple interference method.

However, recently Eversteyn and van den Heuvel (3) outlined a method of thickness measurement particularly suited for epitaxial layers. It is based on the use of the metallurgical thickness d_m, measured with a Taylor Hobson Talystep as a standard reference. It was found that d_m is related to the thickness $d_{m(poly)}$ of polycrystalline silicon deposited simultaneously on an adjacent Si_3N_4 layer and measured in the same way, with accuracy to the second decimal, by

$$d_{m(poly)} = d_m + 0.10\ \mu m \qquad [4a]$$

and that the same layer measured with infrared interference and interpreted as described above (1, 2) yields the same thickness also within 0.01 μm

$$d_{s(poly)} = d_{m(poly)} \qquad [4b]$$

In this paper, the thickness d_s and the constant phase shift $\delta_o/2\pi$ are shown to be correlated to this metallurgical thickness d_m. The experimental data are presented in the next section and possible interpretations are also discussed in this paper. In the last section the conclusions and recommendations are summarized.

Experimental Results

A large number of epitaxial layers was grown in SiH_4 at 1050°C corrected temperature, undoped, on Sb-doped N^+ substrates and As-doped N^{++} substrates. By plotting k *vs.* l the thickness d_s and the constant phase shift $\delta_o/2\pi$ are determined as in Eq. [3]. When d_m, as measured on an adjacent polycrystalline layer, is plotted against the thickness d_s, the latter does not present the appearance of a reliable parameter. However, when the difference $d_s - d_m$ is plotted against $\delta_o/2\pi$, the parameters show correlation. In Fig. 1 the N^{++} substrate data (1.3-2 mohm-cm) turn out to be clearly separated from the N^+ substrate data (8-15 mohm-cm). The experimental data show no systematic dependence when they are labeled with the appropriate substrate resistivity or thickness values.

For N^+ substrates, $d_s - d_m$ assumes any value between 0 and 0.6 μm correlated linearly with a value of $\delta_o/2\pi$ between 0 and 0.3, satisfying

$$d_s - d_m = 2\frac{\delta_o}{2\pi}\ \mu m \qquad [5a]$$

From Fig. 1 it is also clear that the N^{++} substrate data show a greater phase shift than any N^+ substrate does roughly satisfying

$$d_s - d_m = 2\frac{\delta_o}{2\pi} - 0.45\ \mu m \qquad [5b]$$

The linear relationships are obeyed with a precision of about 0.05 μm which amounts to about 1% for 5 μm thick epitaxial layers. This error is due in the first place to the lack of precision in measuring k of the extrema for the epitaxial layer to determine d_s with Eq. [3], and for the polycrystalline layer to determine d_m with Eq. [4a] and [4b]. The error in the wavenumber depends slightly on the range but amounts to about $5\cdot10^{-3}$ with the instrument used.[1] Secondly, the refractive index n of silicon has been assumed, as usual, to be 3.42. Recently Villa (4) published measurement results, for which $2\cdot10^{-4}$ accuracy is claimed, in the range from 1.3 to 11 μm yielding 3.4371 and 3.4176 for the refractive index of two samples of silicon of nonspecified resistivity at 11 μm. Thereupon, the refractive index was measured in the range from 8 to 25 μm by multiple interference between the polished sides of an 8 ohm-cm, n-type silicon slice. It was found that the slope of the line k *vs.* l is constant with a precision of $4\cdot10^{-3}$. The thickness of the slice was measured with a precision of $2\cdot10^{-3}$ and thus the refractive index was determined to be 3.4135 ± 0.0042 which is equal to 3.42, well within the relevant accuracy and precision of $5\cdot10^{-3}$ for k.

[1] Spectrophotometer, Model Epi-G3, Hitachi Ltd., Tokyo, Japan.

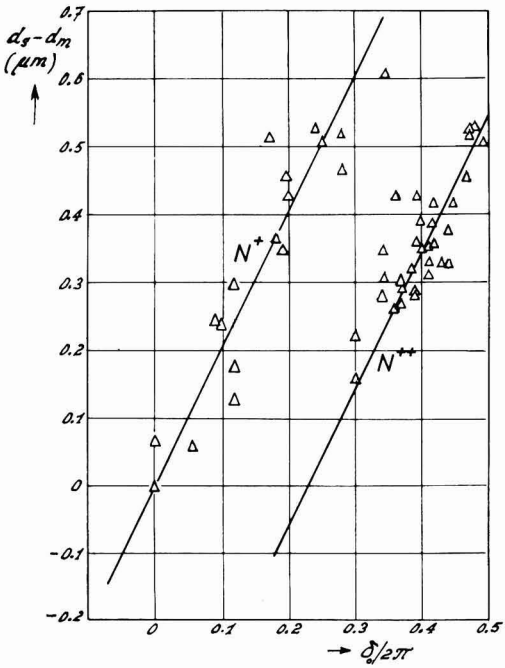


Fig. 1. The difference $d_s - d_m$ depends on the measured constant phase shift $\delta_o/2\pi$. The N^+ and N^{++} data are well separated and the lines are drawn according to Eq. [5a] and [5b].

Interpretation

A classical derivation of the dependence of the phase shift δ on the wavenumber k and the substrate resistivity ρ has been given by Schumann *et al.* (5, 6). It was based on a model with an abrupt junction for dopant atoms and charge carriers with bulk material properties on both sides of the interface. The values of Δd and $\delta_o/2\pi$ have been cursorily calculated from linear approximations to these curves, $\delta(k, \rho)$, over a limited wavenumber range (400-1200 cm^{-1}) and expediently plotted in Fig. 2. This is clearly different from Fig. 1.

For N^+ substrates, the range covered in $d_s - d_m$ and in $\delta_o/2\pi$ is larger than allowed by Fig. 2, where the classical substrate electron dispersion acts as the only cause of $\delta(k, \rho)$. Although it is difficult to speculate about this departure, it may be surmised that the particular state of this interface causes an additional and partly nonreproducible δ-dependence on k, for instance because the interface is not as strain-free as assumed.

The N^{++} substrate data are more concentrated around the values expected from Fig. 2

$$\delta_o/2\pi = 0.45 \text{ and } d_s - d_m = 0.35\ \mu m$$

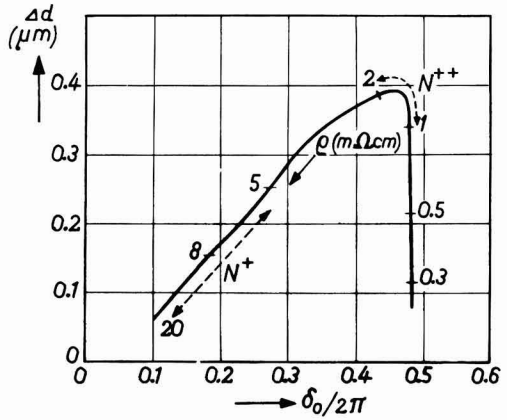


Fig. 2. The correction Δd and the constant phase shift $\delta_0/2\pi$ with the substrate resistivity ρ as a parameter, derived from Schumann's curve. The sections labeled N^+ and N^{++} cover the ranges studied.

Apparently here the phase shift is determined by the substrate resistivity more than by anything else.

It is worth stressing that there is no underlying theory to Eq. [5a] and [5b], but it is the authors' feeling that the nature of the interface conditioned by the growth parameters plays a vital role. This implies that for a range of growth conditions and substrate dopant levels relations similar to Eq. [5a] and [5b] have to be measured. Then the accuracy of the infrared multiple interference method can be established. It is important to note that, from the absence of any correlation between $\delta_0/2\pi$ and d_s or d_m, it follows that out-diffusion of substrate dopant atoms can be ruled out as a determining factor.

Summary and Conclusion

The procedure recommended (7) by the ASTM for determining the thickness of an epitaxial layer is based on the model of an abrupt interface. This definition of the thickness is used in the expression which describes the extreme values of k and in the correction formula used for $\delta(k, \rho)$. In fact, the result is defined by the procedure and cannot be verified otherwise. The precision is determined by the error with which the extreme values of k are reproduced by the instrument and can be read from the spectrum. Accuracy is not claimed.

The procedure described in this paper envisages the production of precise and accurate numerical values of the thickness of the deposited layer by properly interpreting the infrared multiple interference spectrum. In the first place, the experimental observation (1, 2) has been used that, within the attainable precision, a plot of k *vs.* l yields a straight line characterized by the slope d_s and the intercept $\delta_0/2\pi$. Because it is physically clear that the phase shift at the interface must show dispersion and decrease with increasing k, this can only be combined by employing a linear approximation to $\delta(k)$ over a small range of k. In the second place, the experimentally verified procedure has been used, outlined by Eversteyn and van den Heuvel (3), by which the thickness d_m of the deposited layer is measured. It has been shown above that d_m can be found from d_s by subtracting an amount Δd linearly related to $\delta_0/2\pi$. The parameters of this linear relation probably depend on the growth conditions of the epitaxial layer. There is no dependence on the thickness.

It has been found experimentally that the correction Δd to be applied to the measured thickness d_s is different for N^+ and N^{++} substrates, but does not show any dependence on substrate resistivity beyond that. Therefore, any correction procedure based on the substrate resistivity as a criterion for $\delta(k)$ is unsound.

Manuscript submitted Nov. 20, 1972; revised manuscript received Sept. 4, 1973.

Any discussion of this paper will appear in a Discussion Section to be published in the June 1976 JOURNAL. All discussions for the June 1976 Discussion Section should be submitted by Feb. 1, 1976.

Publication costs of this article were partially assisted by Philips Research Laboratories.

REFERENCES

1. P. J. Severin, *Appl. Opt.*, **9**, 2381 (1970); Silicon Device Processing, NBS Special Publication 337, p. 224 (1970).
2. P. J. Severin, *Appl. Opt.*, **11**, 691 (1972).
3. F. C. Eversteyn and G. van den Heuvel, *This Journal*, **120**, 699 (1973).
4. J. J. Villa, *Appl. Opt.*, **11**, 2102 (1972).
5. P. A. Schumann, R. P. Phillips, and P. J. Olshefski, *This Journal*, **113**, 368 (1966).
6. P. A. Schumann, Silicon Device Processing, NBS Special Publication 337, p. 234 (1970).
7. Annual Book of ASTM Standards, F95-73, p. 406, (1974).

Penetration of Gold and Platinum Through Phosphorus-Doped N^+ Layers in Silicon

W. Mielke

AEG-Telefunken Forschungsinstitut, Frankfurt am Main, Germany

ABSTRACT

The penetration of gold and platinum through phosphorus-doped n^+ layers in silicon was studied by diode recovery measurements and by four-point measurements together with neutron activation analysis. A sudden breakthrough of gold in a small temperature range for a given n^+ layer and diffusion time is quantitatively observed for gold, while no important inhibition for platinum could be detected. Therefore platinum is proposed as an advantageous substitute for gold in silicon semiconductor device technology. The penetration of gold may be explained by compound formation of Au_2P_3 being in chemical equilibrium with gold and phosphorus in silicon.

Gold and platinum are widely used as contact materials and recombination centers in silicon semiconductor device technology. While gold is well known to control minority carrier lifetime it was only recently realized by Bailey and Mills (1, 2) that platinum possesses similar properties. In 1962, Cicconella, Forster, and Rulison (3) took into consideration a replacement of gold by platinum for providing a controlled reduction of minority carrier lifetime. Further properties of platinum in silicon were published by Carchano and Jund (4), Conti and Panchieri (5), and Charlot and Vapaille (6), while the properties of gold in silicon were reviewed by Bullis (7) in 1966. A general review about properties of deep impurities in silicon was presented by Schibli and Milnes (8, 9).

An intricate problem with gold in silicon is its affinity to phosphorus-doped n^+ layers. This property is positively used in gettering processes (10), while its negative aspects are manifested in its uncontrolled influence on the fabrication of fast switching devices (11). Indiffused gold profiles in phosphorus-doped n^+ layers in silicon were studied by Wilcox, La Chapelle, and Forbes (12) with radiotracer experiments. They stated that these layers greatly slow down gold diffusion and as a possible explanation offered a compound formation (Au_2P_3) between gold and phosphorus. Quantitative results for an enhanced solubility of gold in uniformly heavily doped silicon were presented by Cagnina (13) who emphasized that a solubility enhancement according to the Shockley-Moll model is much too small to explain his data and therefore again cited a possible compound formation.

To give a further insight into this technologically important problem the penetration of gold through phosphorus-doped n^+ layers has been studied and compared with the behavior of platinum.

Experimental Procedure

Silicon float-zone prepared, <111>-oriented single crystals were used as a starting material. Their further data were: 20 mm diameter, 10^{15} cm^{-3} boron doping, 10^4 cm^{-2} Sirtl etch pit density, and 230 μsec photoconductive decay minority carrier lifetime. Neutron activation analysis showed a gold concentration of $0.5\text{-}3.0 \cdot 10^{10}$ cm^{-3} measured with a specimen of 250 mg Si. Platinum concentration was below the detection limit of $5 \cdot 10^{13}$ cm^{-3}.

A phosphorus indiffusion was then performed using an open tube configuration with a P_2O_5 source at 250°C and clean dry nitrogen as a carrier gas. Mirror etched slices of 500 μm thickness were treated for 2 hr at 1180°C with a subsequent cooling rate of 70°C/hr to 700°C. This diffusion step produced n^+ layers with a phosphorus glass layer thickness of 0.5 μm (2.4 g/cm^3), a sheet resistance of 1 ohm/square, and a junction depth of 10 μm. The phosphorus glass layer was removed. Net donor surface concentration was checked by successive four-point measurements to be $5 \cdot 10^{20}$ cm^{-3}. No significant change in resistivity and etch pit density of the base material was observed. Gold concentration in the base material was measured to be $0.8\text{-}9.0 \cdot 10^{10}$ cm^{-3} using 80 mg Si. Again no platinum was detectable. For a further evaluation of the phosphorus diffusion step, n^+p junctions 1.0 mm in diameter were produced by spraying 13 piceine varnish dots through a metal mask onto the n^+p slice, drying and melting the dots, and subsequently etching n^+p junctions to a depth of 20 μm and cleaning off the piceine dots. The thickness of the n^+p configuration was then 465 μm, because one n^+p side of the original 500 μm n^+pn^+ slice has been lapped away. Simple, adequate recombination contacts were applied by rubbing a gallium-wetted aluminum rod onto the silicon. Reverse currents were taken at 23°C and 1.0V and found to be from 1 to $8 \cdot 10^{-9}$A. Minority carrier lifetime was evaluated by diode recovery measurements. In this method a diode is switched from constant forward to constant reverse current and the delay time of the forward voltage to reach zero, the storage time, is measured and converted to minority carrier lifetime according to graphs for p^+n diodes with an arbitrary base width given by Grove and Sah (14). It is assumed that the p^+n graphs are aproximately the same for n^+p diodes. Diode recovery measurements were performed at low injection levels by using forward currents from 1.0 to 20 mA (reverse currents from 0.1 to 2.0 mA), paying attention to junction capacitance and neglecting surface recombination velocity. Minority carrier lifetimes ranged from 6 to 15 μsec. The diodes showed sharp reverse characteristics and breakdown voltages about 200V were observed.

On manufactured n^+pn^+ and pn^+ structures gold was evaporated or platinum sputtered to a thickness of 0.1 μm, checked by weight. This resulted in Au n^+pn^+, Au pn^+, Pt n^+pn^+, and Pt pn^+ structures. During this step the slice temperature remained below 300°C. Subsequently a number of heat-treatments, gold diffusions, and platinum diffusions were performed varying the parameter time from 10 sec to 6 hr, temperature from 800° to 1100°C, and junction depth from 4 to 10 μm. It should be noted that heat-treatments, gold diffusions, and platinum diffusions each had their own quartz tube and were all performed with an open tube configuration using dry clean nitrogen as a flow gas and a one tube diffusion furnace without ceramic protection tube. The slices were quickly put into or pulled from the constant temperature zone of the furnace, n^+pn^+ and pn^+ specimens were treated to-

Key words: diode recovery measurements, four-point measurements, neutron activation analysis.

gether. The treated slices were subjected to the same electrical measurements as before the heat-treatments, gold or platinum diffusions.

For neutron activation analysis a disk of 400 μm thickness and 10 mm diameter was symmetrically prepared out of the p zone by lapping, etching, and ultrasonically drilling. It should be emphasized that the same slice was evaluated by neutron activation analysis which has undergone the given electrical examinations.

Neutron activation analysis was performed by exposing the specimens to a thermal neutron flux of 10^{13} cm^{-2}-sec^{-1} for 10 days. The specimens were then shortly etched with the following mixture: 25% fuming nitric acid, 10% hydrofluoric acid of 40%, 45% acetic acid, 20% nitric acid of 60%. The mixture was doped with inactive gold and platinum and the specimens were then checked in a multichannel counter to examine their cleanliness. After weighing they were dissolved in inactively doped etch, the solution cooked to dryness. The remaining gold and platinum were taken up with aqua regia and measured against a standard in a multichannel counter. Gold revealed by the 411 keV γ-radiation of Au 198 with a half-life of 65 hr while platinum gave a 158 and 208 keV γ-radiation of Au 199 with a half-life of 76 hr. It should be noted that platinum was roughly a factor 1000 less detectable than gold. The reached sensitivities were: $5 \cdot 10^{10}$ cm^{-3} gold concentration and $5 \cdot 10^{13}$ cm^{-3} platinum concentration with 50 mg of silicon and a measuring time of 10 min.

Experimental Results and Discussion

Results are given by drawing minority carrier lifetime τ, specific resistivity ρ, gold concentration C_{Au}, and platinum concentration C_{Pt} of the p region from n^+pn^+ (○, ●, ⊖) or pn^+ structured specimen (□, ■, ⊟) *vs.* heat-treatment or diffusion time t, four-point conductance $1/R$ of the n^+ layer or temperature T of the heat-treatment diffusions.

For each chosen set of parameters in a diffusion experiment a heat-treatment as a control experiment was performed to check whether the observed changes in experimental data were mainly due to the intentioned gold or platinum doping. In heat-treated slices no platinum could be detected. It should be noted that the presented results are not corrected for their control values. Slices supplied with gold or platinum were weighed before and after diffusion to check constancy of these metals. A qualitative difference was observed with the "gold slices," *e.g.*, at 1000°C, 1 hr, the alloy at the p side of an Au pn^+ slice showed a "gold-like glimmering" while this could not be observed with Au n^+pn^+ slices, the gold has "disappeared" into the n^+ layer. Through phosphorus glass layers no penetration of gold during diffusion runs of 1 hr from 800° to 1000°C was observed. After diffusion the gold could be wiped off simply. No such experiments were performed with platinum.

According to Fig. 1 heat-treated n^+pn^+ structures exhibited lower gold concentrations than pn^+ structures, in accordance minority carrier lifetime was higher in n^+pn^+ structures. For gold diffusion a breakthrough of gold was observed, except for the 10 sec point for which the n^+pn^+ structure showed roughly a gold concentration three orders of magnitude lower than for the pn^+ structure. The increase of gold concentration with time is well known to be due to a "vacancy controlled" diffusion mechanism of gold in silicon (7, 15, 16). Furthermore it is well known that there is a steep increase of resistivity when the gold concentration reaches the boron concentration (10^{15} cm^{-3}) (7).

It should be noted that, because of the influence of junction capacitance of the diodes 1 mm in diameter, minority carrier lifetime could only be measured down to 0.1 μsec.

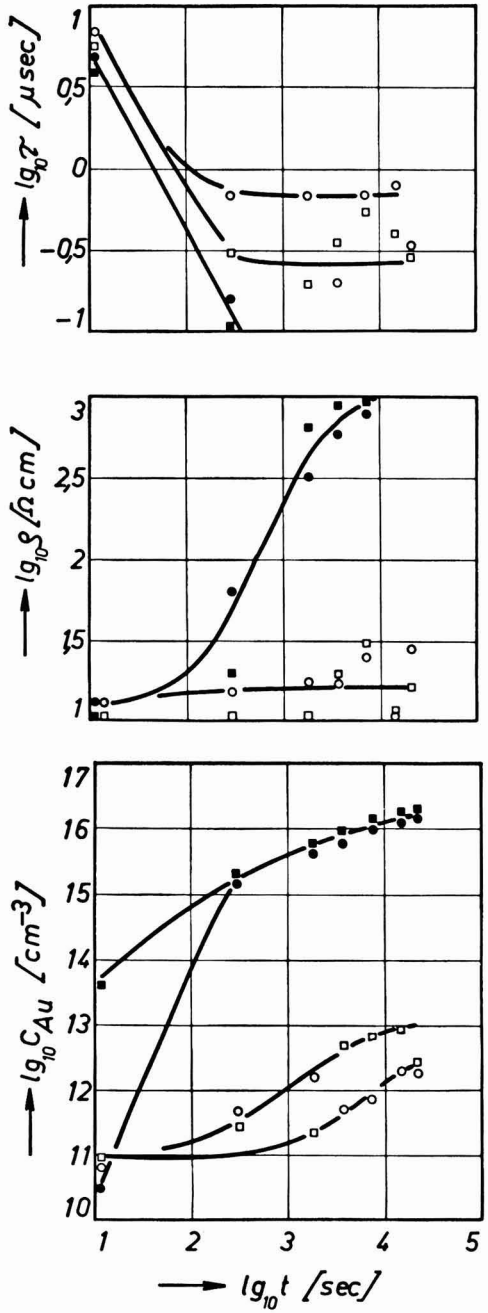


Fig. 1. Heat-treatments (○, □) and gold diffusions (●, ■) at 1100°C; junction depth, 10 μm. Circles and squares represent n^+pn^+ and pn^+ samples, respectively.

In order to check the validity of the given gold concentration values, profiles of the central disks were taken with the 30 min and 6 hr gold-diffused slices by one side etching thereby dividing the disk 400 μm thick into 7 portions: $3 \times 30 + 220 + 3 \times 30$ μm. For the 30 min pn^+ slice an increase from 3 over a central value 5-7 $\times$ 10^{15} cm^{-3} gold concentration was measured with the high value at the p side where gold

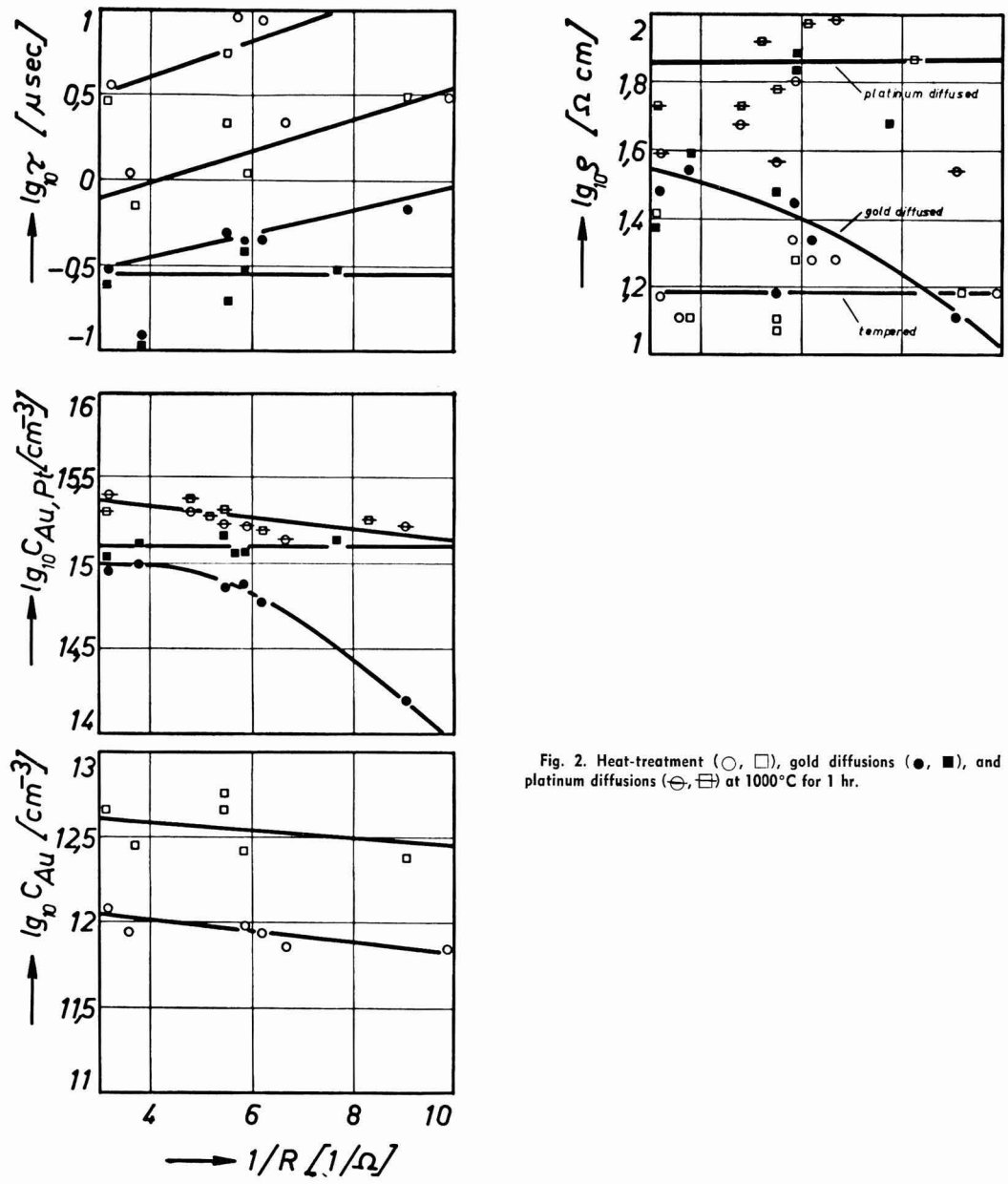


Fig. 2. Heat-treatment (○, □), gold diffusions (●, ■), and platinum diffusions (⊖, ⊟) at 1000°C for 1 hr.

had been evaporated while, for the 6 hr n^+pn^+ and pn^+ slices, concave profiles were measured with a 30% rise at the edges (17). Therefore the given gold concentration values which were averaged for the whole central disk seem to be reasonable.

According to Fig. 2 various n^+ layer thicknesses which were obtained by modifying phosphorus diffusion times are given by their four-point conductance $1/R$ because these values are roughly proportional to the number of electrically active phosphorus atoms per cm². A rough proportionality was checked for the $1/R$ values against the square root of phosphorus diffusion times. Lifetimes τ for platinum-diffused specimens were too low to be measured. It is interesting to note the decreasing gold content of gold-diffused n^+pn^+ slices with increasing $1/R$ (18). The scattering in specific resistivity ρ may be due to variations in the resistivity of the starting material. Profile checks were taken for two n^+pn^+ and one pn^+ platinum-diffused slices leading to a decrease of roughly a factor 2 from the "platinum sputtered side" to the other side of the central disk.

According to Fig. 3 the gold concentration of n^+pn^+ slices steeply increased around 965°C; this temperature being the breakthrough temperature for gold through this n^+pn^+ specimen for a 1 hr diffusion.

According to Fig. 4 no differences between n^+pn^+ and pn^+ structures diffused with platinum could be observed.

As mentioned earlier in this paper, Wilcox, La Chapelle, and Forbes (12) and Cagnina (13) in order to explain their results with the behavior of gold in

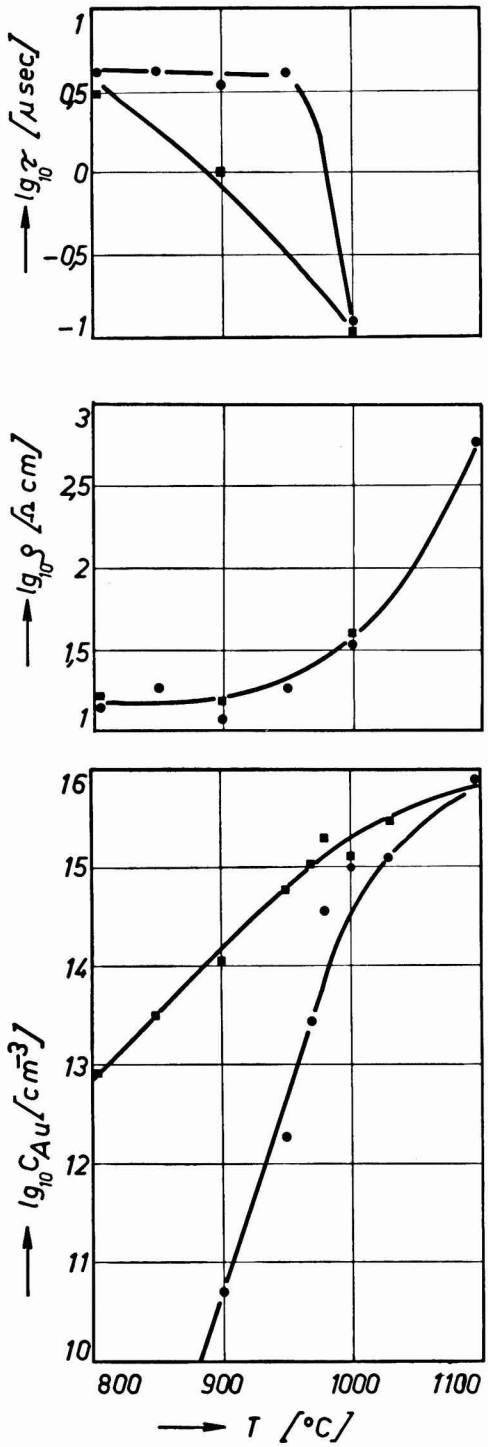


Fig. 3. Gold diffusions (●, ■) for 1 hr; junction depth, 10 μm

highly phosphorus-doped silicon assumed a compound formation of Au_2P_3, which of course is the most stable compound in the gold-phosphorus system (19), while in the gold-silicon system there is no compound formation (19). For platinum there is a stable compound PtP_2 in the platinum-phosphorus system (20), but the same is true for the platinum-silicon system with Pt_2Si and PtSi (20). Using compound formation as a hypothetical assumption the given experimental arrangement would be describable as a reactive diffusion through thin layers as treated by Sah, Sello, and Tremere (21) for explaining masking properties of silicon dioxide films against phosphorus diffusion.

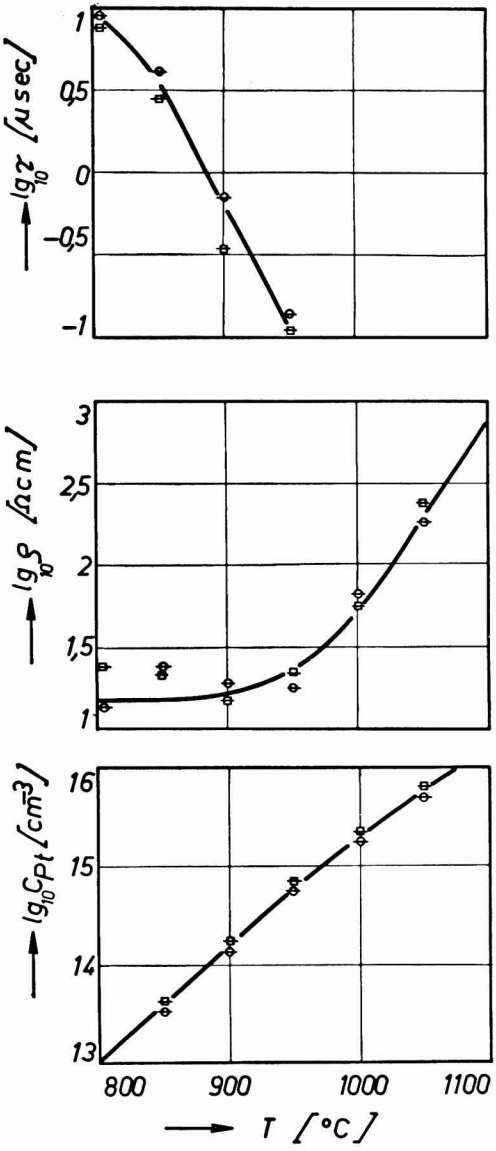


Fig. 4. Platinum diffusions (⊖, ⊟) for 1 hr; junction depth, 10 μm.

However while Au_2P_3 precipitates could be observed in gold-diffused silicon wafers (22), a similar observation of PtP_2 is not known. Together with the results of the given experiments which show no occurrence of masking or gettering of platinum by phosphorus-doped n^+ layers in silicon (Fig. 4) one may suggest that, in spite of the existence of a stable platinum-phosphorus compound PtP_2, such a compound formation does not occur in phosphorus-doped silicon.

The breakthrough according to Fig. 3 may well occur, if the amount of gold in the n^+ layer reaches the amount of phosphorus, so that no further compound formation is possible.

Considering the actual experimental procedure a 0.1 μm thick gold layer was evaporated onto the specimen which corresponds to approximately 6×10^{17} gold atoms per cm^2. Treated with temperature a gold-silicon alloy, 0.1-0.2 μm thick according to temperature, was formed. The junction depth was 10 μm with a surface concentration of 4×10^{20} cm^{-3} which roughly yields 10^{17} phosphorus atoms per cm^2, indicating that a saturation of all phosphorus atoms is indeed possible.

Conclusion

In order to avoid the affinity of gold to phosphorus n^+ layers in silicon, platinum can be used as an advantageous substitute (23).

The measured penetration of gold through these layers may be explained by assuming a compound formation of Au_2P_3, so that gold only can penetrate if all phosphorus has been saturated.

Acknowledgments

The author wishes to thank Dr. M. Reese, H. Pilz, and B. Struck, for devising and performing neutron activation analysis. Misses D. Löchel and G. Kehm prepared the samples while U. Gözinger from AEG-Telefunken, Heilbronn, provided the platinum sputtering. Drs. G. Köhl (†), H. Schlangenotto, K. Roy, and J. Hesse gave valuable comments.

Manuscript submitted Sept. 9, 1974; revised manuscript received Feb. 14, 1975.

Any discussion of this paper will appear in a Discussion Section to be published in the June 1976 JOURNAL. All discussions for the June 1976 Discussion Section should be submitted by Feb. 1, 1976.

Publication costs of this article were partially assisted by AEG-Telefunken Forschungsinstitut.

REFERENCES

1. R. F. Bailey and T. G. Mills, in "Semiconductor Silicon," R. R. Haberecht and E. L. Kern, Editors, pp. 481-489, The Electrochemical Society Softbound Symposium Series, New York (1969).
2. R. F. Bailey, U.S. Pat. 3,640,783 (1972).
3. D. F. Ciccolella, J. H. Forster, and R. L. Rulison, U.S. Pat. 3,067,485 (1962).
4. H. Carchano and C. Jund, *Solid-State Electron.*, **13,** 83 (1970).
5. M. Conti and A. Panchieri, *Alta Frequenza,* **40,** 544 (1971).
6. J.-J. Charlot and A. Vapaille, *Compt. Rend. B,* **273,** 1027 (1971).
7. W. M. Bullis, *Solid-State Electron.*, **9,** 143 (1966).
8. E. Schibli and A. G. Milnes, *Mat. Sci. Eng.*, **2,** 173, 229 (1967-1968).
9. A. G. Milnes, "Deep Impurities in Semiconductors," John Wiley & Sons, Inc., New York (1973).
10. A. Goetzberger and W. Schockley, *J. Appl. Phys.*, **31,** 1821 (1960).
11. J. M. Fairfield and G. H. Schwuttke, *ibid.*, **37** 1536 (1966).
12. W. R. Wilcox, T. J. La Chapelle, and D. H. Forbes, *This Journal,* **111,** 1377 (1964).
13. S. F. Cagnina, *ibid.*, **116,** 498 (1969).
14. A. S. Grove and C. T. Sah, *Solid-State Electron.*, **7,** 107 (1964).
15. F. A. Huntley and A. F. W. Willoughby, *ibid.*, **13,** 1231 (1970).
16. J. L. Lambert, *Phys. Status, Solidi (a)*, **4,** K33 (1971).
17. J. Martin, E. Haas, and K. Raithel, *Solid-State Electron.*, **9,** 83 (1966).
18. P. C. Parekh, *ibid.*, **13,** 1401 (1970).
19. Gmelins Handbuch der anorganischen Chemie, 8th ed., system number: 62-gold, p. 727, Verlag Chemie GmbH., Weinheim/Bergstrasse (1954).
20. Gmelins Handbuch der anorganischen Chemie, 8th ed., system number: 68-platinum, p. 128, Verlag Chemie GmbH., Weinhein/Bergstrasse (1940).
21. C. T. Sah, H. Sello, and D. A. Tremere, *J. Phys. Chem. Solids,* **11,** 288 (1959).
22. E. D. Wolley and R. Stickler, *This Journal,* **114,** 1287 (1967).
23. W. Mielke, *German Offenlegungsschrift,* **22,** (10), 200 (1973).

Developer Characteristics of Poly-(Methyl Methacrylate) Electron Resist

James S. Greeneich*

Electronics Department, General Motors Research Laboratories, Warren, Michigan 48090

ABSTRACT

We report on the solubility characteristics of poly-(methyl methacrylate) electron-resist for developer combinations of methyl isobutyl ketone (MIBK) and isopropyl alcohol (IPA). The solubility rate is determined in terms of the fragmented molecular weight which is a function of original molecular weight and the energy absorbed by the polymer in degrading to a lower molecular weight. An empirical formula for the solubility rate is $R = [R_0 + \beta/M_f^{\alpha}]e^{-E_a/kT}$, where M_f is the fragmented molecular weight, R_0, β, and α are constants characteristic of a given developer. The temperature dependence is characterized by an activation energy, E_a, for a given developer. The solubility kinetics are discussed showing a rate limited process for most developer conditions. From the solubility rate and the characteristic energy absorption in the resist, the development time and contrast are defined and calculated for a variety of exposure parameters including beam energy, resist thickness, developer, developer temperature, and original molecular weight. Compared to the standard developer, 1:3 MIBK:IPA, an improved sensitivity of 10-50 times is obtained using MIBK at the expense of increased development time. For a given contrast level the development time is greatly reduced by increasing the developer temperature. A lower original molecular weight also reduces the required development time.

Electron-beam and x-ray lithography are important new technologies for fabricating semiconductor devices and circuits with submicron dimensions. The most widely used resist medium is the positive acting poly-(methyl methacrylate), PMMA (1). In addition to a resolution requirement, the performance of the resist is measured in terms of its sensitivity to the incident radiation. Typically the sensitivity is expressed in terms of the required incident charge per unit area to produce the desired resist pattern of the desired thickness. The final resist thickness is important in terms of the suitability of the resist as an etching mask and for the metal lift-off technique (1) for positive resists.

Using the standard developer, 1:3 methyl isobutyl ketone (MIBK):isopropyl alcohol (IPA), the reported sensitivity of PMMA is in the range 5×10^{-5} to 5×10^{-4} C/cm^2. The range in reported sensitivities is primarily due to varying exposure conditions such as beam energy, resist thickness, type of substrate, and geometry of the irradiated pattern (2, 3). For this solvent the development is nearly time independent. Consequently, the sensitivity has been expressed in terms of a critical absorbed energy density (3) which is independent of the exposure parameters. This model is not adequate for time-dependent developer systems described in this paper.

What is the influence of the developer solvent and temperature on the sensitivity and development time for positive electron-beam resists? In the case of PMMA this is an important question since its sensitivity is considered low and improving its sensitivity through the development process is important. Ethyl and methyl alcohol are also used as developers for PMMA with approximately the same sensitivity as the standard developer (4). Hatzakis and Broers (5) report the use of MIBK as a time-dependent developer with increased sensitivity, but the original resist thickness was rapidly reduced. Ting (6) reported on the MIBK developer in terms of a solubility rate as a function of an "effective" charge and Greeneich (7) has shown that high contrast exposures can be made using MIBK if a very high molecular weight polymer is used.

We report a method for evaluating the sensitivity of positive electron resists in which the solubility rate is expressed in terms of the basic quantity which changes during electron radiation, namely the fragmented molecular weight. From the solubility rate the required development time and resulting contrast are defined and evaluated for many of the parameters affecting resist sensitivity.

We report on the solubility of PMMA in several developer combinations of MIBK and IPA at several temperatures. We report an empirical relationship between developer solubility rate and the fragmented molecular weight of the form $R = (R_0 + \beta/M_f^{\alpha})e^{-E_0/kT}$, where R_0, β, and α are constants and E_a is an activation energy. An improved sensitivity compared to the standard developer of from 10 to 50 times is obtained by using different developers.

The kinetics of the solubility process is found to be adequately described by a rate-limited process for most developer conditions. At high temperatures it is found that the standard developer has nonlinear solubility properties.

Relationship Between Fragmented Molecular Weight and Exposure Parameters

A positive electron resist is characterized by a reduction of molecular weight owing to chain scission of the original molecules. Since polymers with different molecular weights have different solubility characteristics in a given solvent, the resist developer is required to distinguish between the fragmented molecular weight, M_f, and the original molecular weight, M_n.

The relationship between M_f and M_n and the exposure parameters is expressed in terms of the absorbed energy density, ϵ, as (7, 8)

$$M_f = \frac{M_n}{1 + \dfrac{g\epsilon M_n}{\rho A_o}} \qquad [1]$$

where ρ is the resist density, A_o is Avogadro's number, and g is an efficiency factor proportional to the radiation chemical yield. For PMMA we take g to be 1.9×10^{-2} events/eV (9). It should be noted that [1] only applies as long as the resist degrades during electron bombardment. In the case of PMMA cross-linking events dominate at high doses of electron-beam radiation (1, 2).

* Electrochemical Society Active Member.

Key words: electron-beam lithography, electron-resist developers, contrast function, energy dissipation in resists.

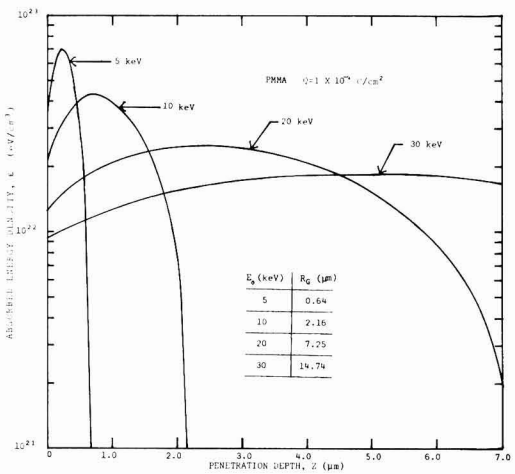


Fig. 1. Energy dissipation per unit volume for area exposures as a function of penetration depth for various incident energies. The table gives the Grun range (Eq. [4]).

The absorbed energy density is in general a complicated function of position within the resist film; the exact dependence being a function of the exposure parameters such as beam energy, resist thickness, type of substrate, and geometry of the irradiated pattern (2, 3). In the case of an area exposure on a low atomic number substrate such as silicon, ϵ is given by the depth-dose function (10) in terms of the depth, z, in the resist and the incident energy, E_o. Specifically

$$\epsilon = \frac{Q}{q}\frac{E_o}{R_G}\lambda(f) \qquad [2]$$

where

$$\lambda(f) = 0.74 + 4.7f - 8.9f^2 + 3.5f^3 \qquad [3]$$

In [2], Q is the incident charge per unit area, q is the electronic charge, $f = z/R_G$, where R_G is the Grun range given by

$$R_G = \frac{4.6 \times 10^{-6}}{\rho} E_o^{1.75} \qquad [4]$$

when E_o is in units of keV. The absorbed energy density in PMMA for an incident dose of 10^{-4} C/cm^2 is shown in Fig. 1 for several beam energies. Two important points are illustrated in Fig. 1. There is a range, R_G, (tabulated in Fig. 1) beyond which ϵ is small; consequently the resist thickness must be equal to or less than R_G. For the higher beam energies and thin resist films (<3000Å), ϵ is approximately uniform and consequently, from Eq. [1], M_f is nearly independent of depth.

Experimental Results

Various molecular weight samples of PMMA were dissolved in trichlorethylene and spin coated onto silicon wafers, resulting in a typical resist thickness of ~3000Å. The nature of the carrier solvent used in coating the resist and the pre-exposure baking play a role in the solubility characteristics of the resist. For example, Fig. 2 shows the resist thickness *vs.* time in the solvent MIBK for various prebaking conditions where MIBK and trichloroethylene were used as carrier solvents. After ~4 min in MIBK the trichlorethylene sample dissolves at about the same rate as the well-baked MIBK sample.

Similarly the solubility rate of degraded PMMA is influenced by remaining carrier solvent; we have observed ~2 times less Q is required for samples developed in the standard developer when MIBK remains. All samples used in this study were coated with trichlorethylene as the carrier solvent and baked for ≧90 min at 160°C.

Typical areas of 10^{-3} cm^2 were irradiated with 20 keV electrons using a Cambridge S4-10 scanning electron microscope (SEM) equipped with a beam blanking unit. The incident dose was varied by changing the frame scan time. Some variation in exposure was observed depending on whether or not the beam is

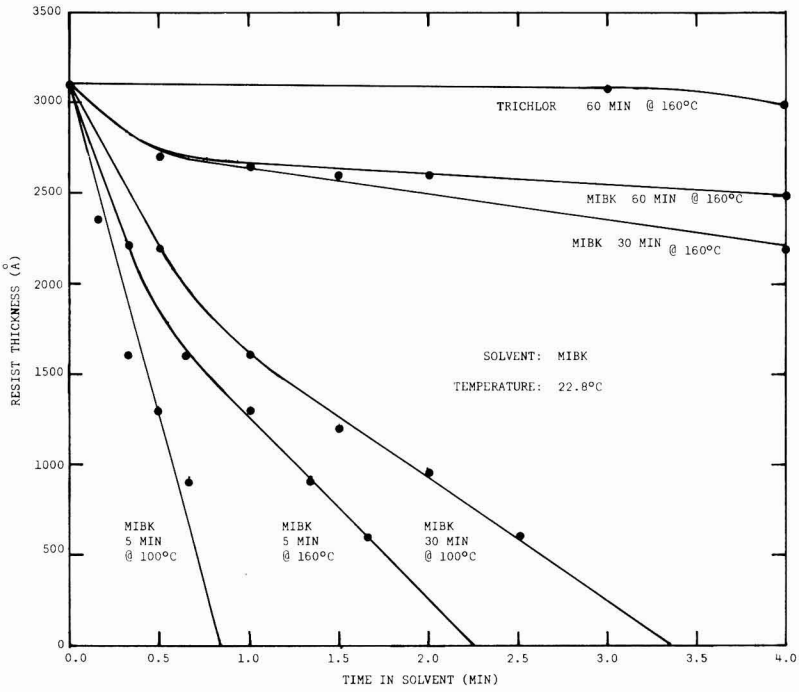


Fig. 2. The influence of the resist carrier solvent on solubility in MIBK for the indicated prebake conditions.

blanked during flyback; all results reported here are for the condition with beam blanking on.

After irradiation the samples were immersed in the developer solvent, which was not agitated. Periodically the samples were removed and the resist thickness determined by the interference color of the irradiated area. Ellipsometer measurements on nonirradiated samples established the refractive index to be 1.48 ± 0.02 and the accuracy of the interference method to be ±150Å. Only a slight increase in refractive index (≤0.04) was observed as a result of solvent migration into the film during prolonged soaking (30 min) in the developer solvents; this did not affect the measured solubility rates.

Several solvents were tested as developers; these consisted of MIBK, 1:1 MIBK:IPA and 1:3 MIBK:IPA. The temperature dependence of MIBK and 1:3 MIBK:IPA was also investigated.

Two different types of behavior were observed. Figures 3 and 4 show the results for 1:1 MIBK:IPA at

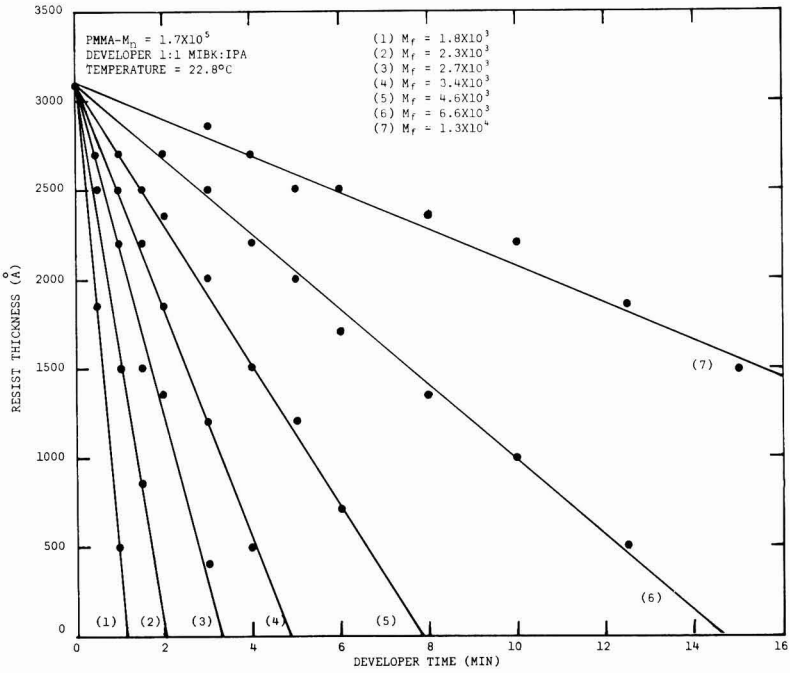


Fig. 3. A typical experimental result characteristic of a rate-limited process relating resist thickness as a function of developer time for various fragmented molecular weights.

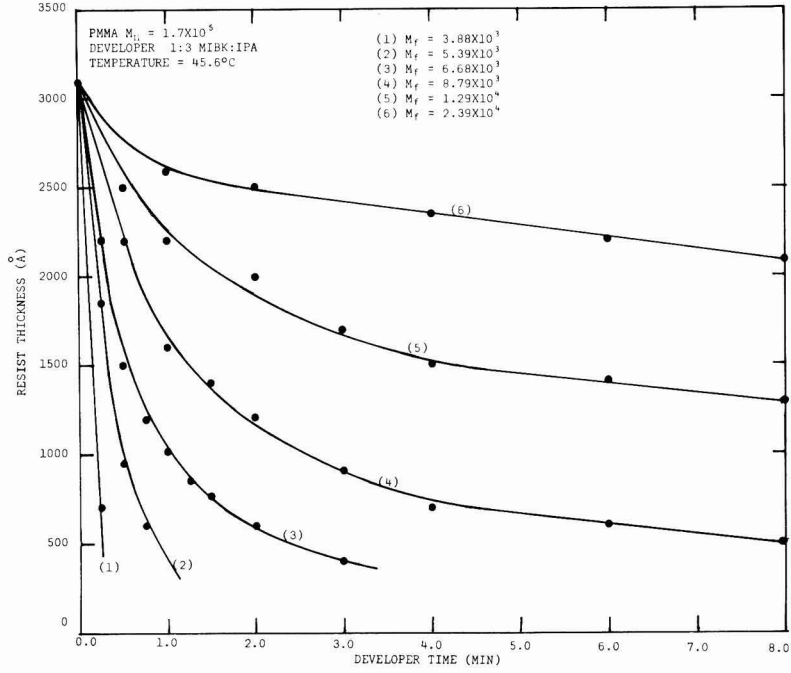


Fig. 4. Experimental results for 1:3 MIBK:IPA at 45.6°C showing the nonlinearity in the solubility rate.

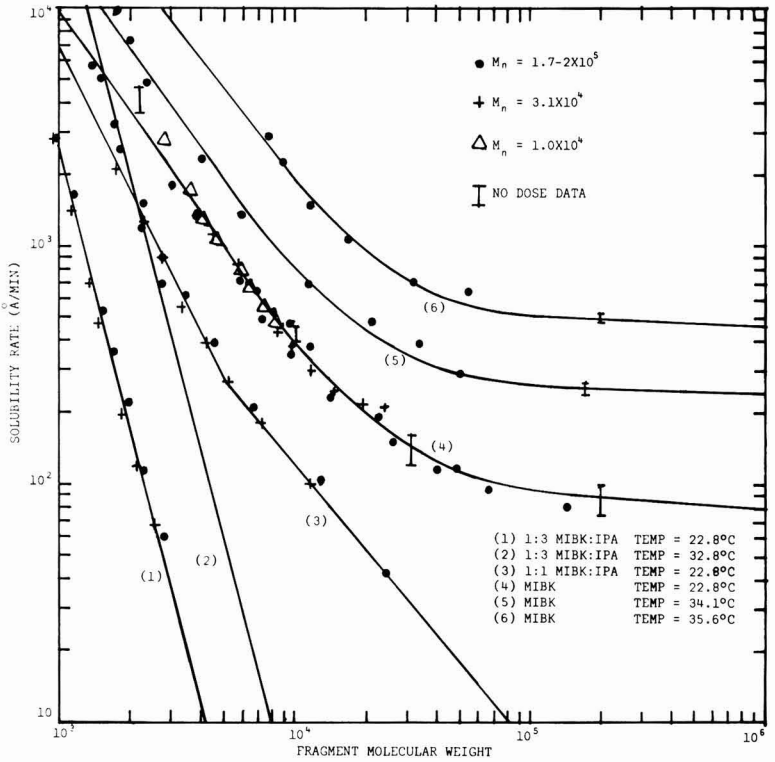


Fig. 5. The solubility rate vs. fragmented molecular weight for three different developers and for various temperatures. Data is for original molecular weights between 10^4 and 2×10^5.

22.8°C and 1:3 MIBK:IPA at 45.6°C, respectively. Figure 3 is typical of most of the developer conditions studied and is indicative of a reaction rate process while the result shown in Fig. 4 is representative of a more complicated kinetics problem. The kinetics of the solubility process is discussed in more detail in a later section.

Solubility Rate

According to [1] the results of electron radiation on positive electron resists is expressed in terms of the fragmented molecular weight. Previously (7) we showed that the solubility rate for MIBK, defined as the slope of the thickness-developer time curve, is a function of fragment molecular weight as given by [1]. This result also applies to the other developer solvents reported here. In Fig. 5 we show the solubility rate *vs.* M_f for original molecular weights between 10^4 and 2×10^5 for the indicated developer conditions. In each case the solubility characteristics are of the rate limited type.

An empirical formula of the form

$$R = R_o + \frac{\beta}{M_f{}^{\alpha}} \qquad [5]$$

was fitted to the experimental data and is shown by the solid lines in Fig. 5. In Table I the values of R_o, β, and α are given for R in angstroms per minute.

Kinetics of the Solubility Process

In this section we consider the two types of solubility characteristics illustrated in Fig. 3 and 4. We do not consider any solvent to remain in the polymer film although the increased solubility rate when solvent remains is expected on the basis of increased availability of the solvent at the plane of polymer-solvent interaction.

Ueberreiter has reviewed the solution process for polymers (11). According to the model a gel-like skin is formed between the pure solvent and the pure polymer after a short induction period.[1] For this model the solubility rate is given by

$$R = \frac{dz}{dt} = \frac{\overline{D}}{d} \qquad [6]$$

where $\overline{D}$ is a mutual diffusion coefficient of the polymer-solvent system and d is the skin thickness. Consequently, this model describes the linear decrease in resist thickness typical of most of the developer conditions reported.

According to the rate limited process the temperature dependent rate, R_T, is given in terms of an activation energy, E_a, as

[1] We have observed such an induction period for MIBK for very high molecular weight materials.

Table I. Parameters are tabulated for the solubility rate for various combinations of MIBK and IPA at several temperatures

Solvent	Temperature	R_o	β	α	Mol wt range
1:3 MIBK:IPA	22.8°C	0.0	9.332×10^{14}	3.86	—
1:3 MIBK:IPA	32.8°C	0.0	1.046×10^{16}	3.86	—
1:1 MIBK:IPA	22.8°C	0.0	6.700×10^{9}	2.00	$\leqq 5 \times 10^3$
1:1 MIBK:IPA	22.8°C	0.0	6.645×10^{6}	1.188	$>5 \times 10^3$
MIBK	22.8°C	84.0	3.140×10^{8}	1.50	—
MIBK	34.1°C	241.9	5.669×10^{8}	1.50	—
MIBK	35.6°C	464.0	1.435×10^{9}	1.50	—

$$R_T = Re^{-E_a/kT} \quad [7]$$

where the functional dependence of R on M_f is given by [5]. Figure 6 shows a plot of ln R *vs.* $1/kT$ for MIBK for the indicated molecular weights. For the highest molecular weights, 2×10^5, the straight line fit is excellent with an activation energy of 1.04 eV. For lower molecular weights the fit is somewhat worse.

The solubility rate of a polymer is determined by two factors: (*i*) the kinetic suitability of the solvent which determines $\overline{D}$, and (*ii*) the thermodynamic suitability of the polymer-solvent system is found in d which acts as a resistance to the penetrating solvent (11). In choosing a developer for positive electron resists, thermodynamic arguments are often used as commonly expressed in terms of a solubility parameter and an associated hydrogen bonding index (4, 12). For PMMA the result is a combination of a poor solvent (IPA) and a borderline solvent (MIBK). Many other solvent combinations with desirable thermodynamic properties are possible; a developer with a higher solubility rate results for solvents with high values of $\overline{D}$, and among molecules of similar chemical composition the rate depends mainly on the size of the molecule (11). This is an area for continued investigation.

As we show later it is desirable for the parameter α in [5] to be as large as possible for high contrast exposures. The temperature dependence of the developer 1:3 MIBK:IPA was investigated in hopes of increasing its solubility rate while maintaining its large value of α. Unfortunately, the solubility rate is nonlinear for temperatures $\geqq$32.8°C; a typical result is shown in Fig. 4. This nonlinear time dependence is not well understood. Initially the solubility rate behaves in a manner consistent with lower temperature data. This is evidenced by an activation energy of 2.43 eV as shown in Fig. 7 where ln R *vs.* $1/kT$ is plotted. In Fig. 7 the initial solubility rate

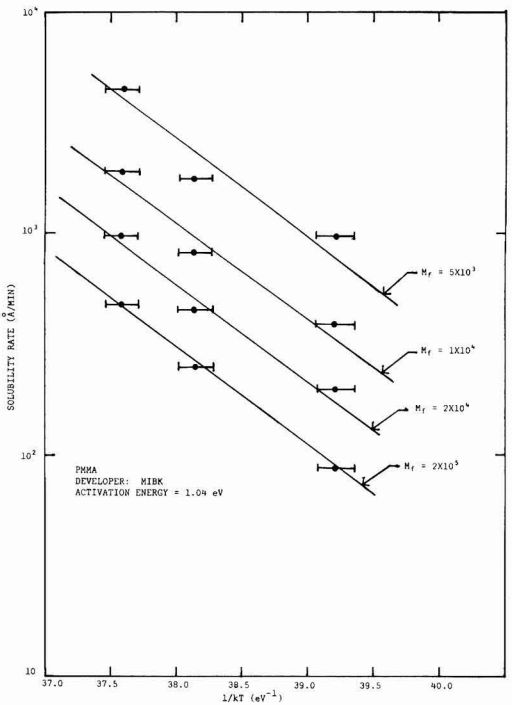


Fig. 6. Developer activation energy for MIBK

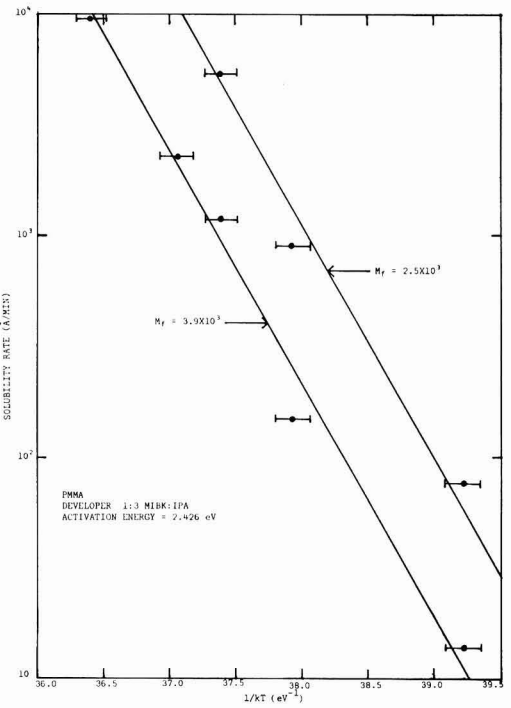


Fig. 7. Developer activation energy for 1:3 MIBK:IPA

was used for the higher temperature data. The higher activation energy of the standard developer compared to MIBK is perhaps indicative of the relatively poor thermodynamic solubility of the standard developer. From Fig. 4 it is apparent that the solubility rate saturates at a level independent of molecular weight. This behavior is found in the temperature range investigated, 37.2°-54.4°C. The temperature dependence for the saturated solubility rate is difficult to determine; however, from the limited data available it appears to be nearly independent of temperature and molecular weight. This is perhaps indicative of a diffusion mechanism in which the transport across the boundary layer is the rate-limiting step.

Development Time and Contrast

In choosing a developer solvent and the electron-beam exposure parameters, a variety of objectives may be sought. For example, one may wish to obtain the highest resolution, minimize the incident charge per unit area, or minimize the developer time. There is a trade-off between these objectives. For the purposes of this section we will be concerned with area exposures and assume that the principal objective is to minimize the incident charge. As a secondary goal, the developer time should be minimized. The influence of developers on spatial resolution will be reported elsewhere (13).

To evaluate the relative merits of various exposure conditions we compute the developer time, τ, at a given temperature as

$$\tau = \int_0^{T_0} \frac{dz}{\left(R_0 + \frac{\beta}{M_f^{\alpha}}\right)} \quad [8]$$

where T_0 is the original resist thickness and the dependence of the solubility rate on z is found from [1]-[4]. For positive resists complete development to the resist-substrate interface is required. Consequently, the contrast, Γ, is found as (7)

$$\Gamma = 1 - \left(R_o + \frac{\beta}{M_n{}^{\alpha}} \right) \frac{\tau}{T_o} \qquad [9]$$

where M_n is the original molecular weight.

In the following we examine the influence of developer solvent, developer temperature, beam energy, resist thickness, and original molecular weight on the contrast and development time. We previously established (7) that for a given contrast level a larger M_n reduces the required Q at the expense of increased developer time.

Consider 5000Å of resist, molecular weight of 2×10^5, subjected to 20 keV electrons. The required development time and contrast are shown in Fig. 8 and 9 as a function of Q for MIBK, 1:1 MIBK:IPA and 1:3 MIBK:IPA at 22.8°C and also MIBK at 35.6°C. The constrast for the 1:3 MIBK:IPA developer is taken as unity owing to the extremely small removal rate for the original molecular weight. According to [9] Γ should be independent of temperature; however, owing to the slight deviation from $\exp(-E_a/kT)$ in the experimental data, Γ varies slightly with temperature for MIBK as shown in Fig. 9.

It is apparent that a wide range of contrasts and developer times are obtained for the various developer conditions. For example, accepting a 50% contrast (2500Å of resist remains), the required charge

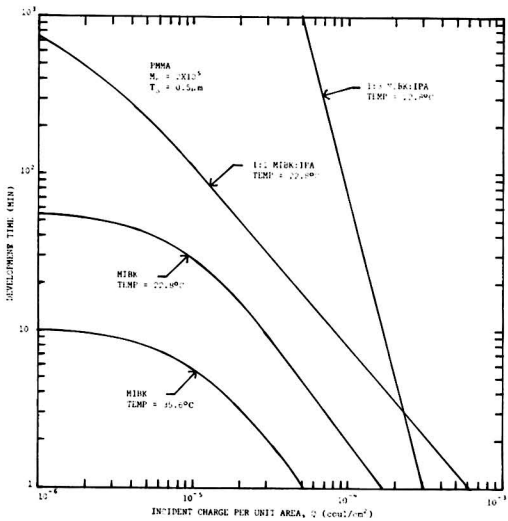


Fig. 8. The dependence of developer time on Q

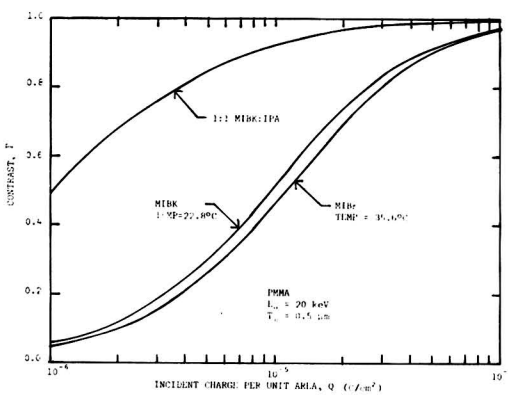


Fig. 9. The contrast as a function of Q

can be reduced by over an order of magnitude compared to the standard developer by using other developers. A penalty is paid in developer time. For example, the developer time for $\Gamma = 0.5$ for 1:1 MIBK:IPA would be 750 min, hardly a usable developer. More reasonable developer times are obtained for $\Gamma = 0.5$ for MIBK: 29 min at 22.8°C and 5.3 min at 35.6°C.

According to Fig. 1, for a given Q a lower beam energy results in a higher ϵ. This results in a smaller fragmented molecular weight and, hence, an increased solubility rate. The influence of beam energy on Γ is shown in Fig. 10 for E_o between 10 and 30 keV. The development time (upper time axis) for a given Γ is shown as the dotted line; it is the same for each of these energies except for very small Γ.

For a given resist thickness there is a lower useful limit on the incident energy; the range R_G [4] defines the thickness and hence energy beyond which the energy absorption is negligible. For positive resists, narrow linewidths are easily obtained at higher incident energies (3) and consequently reducing the beam energy to increase energy absorption may not always be compatible with the desired resolution. Another practical aspect is, for a given SEM beam diameter a decrease in beam energy decreases the beam current, I_B. This decrease is approximately first order in beam energy. Since the increase in ϵ is also first order in energy, then as the beam energy is decreased the required resist exposure time per unit area, Q/I_B, would remain constant independent of energy. Scaling the results in Fig. 10 by the ratio of beam energies confirms this conclusion.

In using a developer such as MIBK which slowly removes high molecular weight PMMA, some reduction in the required Q is achieved by using thicker resist films and taking advantage of the increased ϵ with increasing penetration depth. In this situation the remaining resist thickness, T_r, is specified. In Fig. 11 the required Q is plotted as a function of T_o for two values of T_r (solid lines) for $E_o = 10$ keV, $M_n = 2 \times 10^5$ and MIBK at 22.8°C. The right-hand axis gives the required development time and is plotted *vs.* T_o (dashed lines). Certainly a reduction in original Q is obtained as T_o increases at the expense of increased developer time. Two values of T_o might be considered as optimum. One is the thickness at which the peak in the energy dissipation occurs (0.76 μm at 10 keV) and the other is the thickness at which the energy dissipation equals that at the surface (1.6 μm at 10 keV). The former is preferred if narrow linewidths are required.

Given a desired T_r and choosing E_o and T_o, the development time is reduced by increasing the devel-

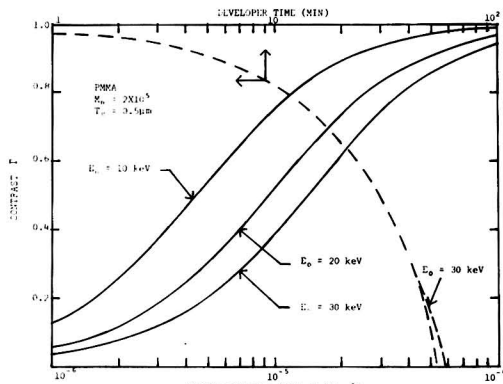


Fig. 10. Influence of beam energy on contrast. The dashed line gives the development time (upper time axis) for a given contrast level.

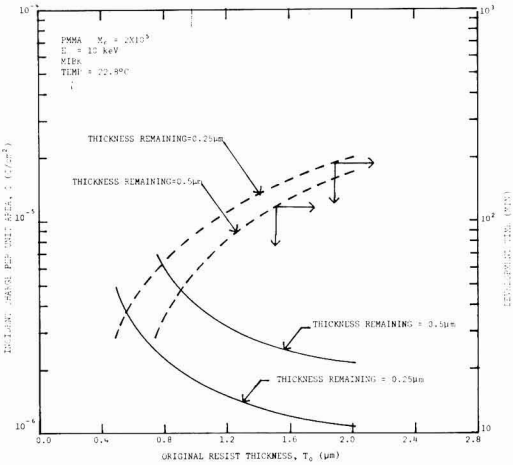


Fig. 11. The required charge per unit area as a function of the original resist thickness (solid lines) resulting in the two final resist thicknesses indicated. The corresponding development time (right axis) is shown as a function of Q by the dashed lines and indicated by the arrows.

oper temperature and/or reducing the original molecular weight. This is illustrated in Table II for $T_r = 0.25$ μm $E_o = 10$ keV, and $T_o = 0.76$ μm. The developer is MIBK at two temperatures, 22.8° and 35.6°C. Also given in Table II is the required incident charge to yield the desired resist thickness. For this situation the required incident dose is reduced by a factor of ~50 compared to the standard developer at 22.8°C.

Conclusions

The following results and conclusions are made for the combinations of MIBK and IPA used as developers for PMMA in this study.

1. A technique for predicting developer characteristics for positive electron resists has been developed in which the solubility rate is determined as a function of fragmented molecular weight.

2. An empirical formula for the solubility rate of the form $R = (R_o + \beta/M_f^{\alpha})e^{-E_a/kT}$ is found with the constants R_o, β, and α dependent upon the developer solvent. Activation energies, E_a, for MIBK and 1:3 MIBK:IPA are found to be 1.04 and 2.43 eV, respectively.

3. The contrast and development times are functions of developer, developer temperature, beam energy, resist thickness, and original molecular weight.

4. An improved sensitivity compared to the standard developer for PMMA of from 10 to 50 times is obtained by using different developers and temperatures.

5. The solubility kinetics of PMMA is characterized by a rate-limited process for most developer conditions. At high temperatures 1:3 MIBK:IPA shows a combination of a rate-limited process and a diffusion process.

Table II. The influence of original molecular weight and developer temperature on development time is tabulated. Also shown is the required minimum Q to yield the final resist thickness, 0.25 μm.

Original molecular weight	MIBK Development time (min)		Required charge per unit area (μC/cm²)	
	Temp = 22.8°C	Temp = 35.6°C	Temp = 22.8°C	Temp = 35.6°C
2.5×10^4	30.6	6.1	2.6	2.9
5.0×10^4	44.6	8.6	2.3	2.6
7.5×10^4	50.4	9.5	2.3	2.6
1.0×10^5	54.3	10.0	2.3	2.7
1.5×10^5	57.0	10.4	2.4	2.8
2.0×10^5	58.3	10.6	2.5	2.8

Acknowledgments

The author would like to thank M. C. Steele and J. W. Hile for helpful discussions of this material. Thanks are also due to L. L. Hegedus for discussions of the solubility kinetics, E. R. Cprek for use of the SEM, R. A. Ottovani for several samples of PMMA, A. M. Wims for molecular weight analysis, and B. J. Vannoy for substrate preparation.

Manuscript submitted July 17, 1974; revised manuscript received Nov. 18, 1974.

Any discussion of this paper will appear in a Discussion Section to be published in the June 1976 JOURNAL. All discussions for the June 1976 Discussion Section should be submitted by Feb. 1, 1976.

Publication costs of this article were partially assisted by General Motors Corporation.

REFERENCES

1. M. Hatzakis, *This Journal*, **116**, 1033 (1969).
2. J. S. Greeneich and T. Van Duzer, *J. Vacuum Sci. Technol.*, **10**, 1056 (1973).
3. J. S. Greeneich and T. Van Duzer, *IEEE Trans. Electron Devices*, **ED-21**, 286 (1974).
4. R. F. Herzog, J. S. Greeneich, T. E. Everhart, and T. Van Duzer, in "Record of 11th Symposium on Electron, Ion, and Laser Beam Technology," R. F. M. Thornley, Editor, San Francisco Press, San Francisco (1971). Also *IEEE Trans. Electron Devices*, **ED-19**, 635 (1972).
5. M. Hatzakis and A. N. Broers, in "Record of 10th Symposium on Electron, Ion, and Laser Beam Technology," L. Marton, Editor, pp. 107-114, San Francisco Press, San Francisco (1969).
6. C. H. Ting, in "Record of 11th Symposium on Electron, Ion, and Laser Beam Technology," R. F. M. Thornley, Editor, pp. 337-344, San Francisco Press, San Francisco (1971).
7. J. S. Greeneich, General Motors Research Publication, GMR-1547; *This Journal*, **121**, 1669 (1974).
8. J. S. Greeneich, Unpublished Ph.D. dissertation, University of California, Berkeley, California (1973). Also, Ref. (4) contains a similar expression.
9. A. Chapiro, "Radiation Chemistry of Polymeric Systems," Vol. 15, pp. 337-380, John Wiley and Sons, Inc., New York (1962).
10. T. E. Everhart and P. H. Hoff, *J. Appl. Phys.*, **42**, 5837 (1971).
11. K. Ueberreiter, in "Diffusion in Polymers," J. Crand and G. S. Park, Editors, pp. 219-257, Academic Press, London (1968).
12. M. J. Bowden and L. F. Thompson, "165th Meeting ACS-Organic Coatings and Plastics Chemistry," Dallas, Texas, April 8, 1973.
13. J. S. Greeneich, *J. Appl. Phys.*, To be published.

Cross-Slip Dislocations and Their Multiplication in (001)-Oriented Silicon Wafers

Junji Matsui

Nippon Electric Company, Limited, Central Research Laboratories, Kawasaki, 211 Japan

ABSTRACT

Dislocations consisting of a pair of half-loops are found to be characteristic of (001)-oriented silicon wafers, and they are also found to develop and multiply by a combination of cross-slipping of screw segments and their interaction with wafer surfaces. They originate from internal sources which seem to be precipitates formed during course of thermal oxidation.

Recently, silicon single crystals free from dislocations have been available for device fabrications. As is well known, however, several types of defects are often generated in dislocation-free silicon wafers during various device fabrication processes such as thermal oxidation, impurity diffusion, or application of an epitaxial layer. It has been reported that, from the device fabrication point of view, generation of these defects makes it less significant to use a dislocation-free crystal as a starting material. Among those defects, dislocations are especially harmful to the characteristics of fabricated devices, such as leakage current of diodes, whether they are complete dislocations with a Burgers vector of $a/2\langle 110\rangle$ type or partial dislocations with that of either $a/6\langle 211\rangle$ or $a/3\langle 111\rangle$ type. Therefore, it becomes important to know mechanisms in which the dislocations of any type form and multiply in silicon crystals. Several mechanisms of the dislocation formation and multiplication in (111)-oriented silicon wafers have been proposed by many investigators (1-12). Sources of the dislocations have been associated with precipitates (1, 3-4), ruptures at wafer edges (2, 5-6), scratches (7-10), surface irregularities (1-2, 11), and some other defects (12).

It has also been reported that dislocation-free silicon wafers subjected to heat-treatments often reveal a number of circular stacking faults (13-14) and prismatic dislocation loops (14-16) either in the (111)- or (001)-oriented wafers. Particularly when float-zoned, dislocation-free silicon wafers containing grown-in defects along swirls were thermally oxidized, a number of circular stacking faults were also preferentially generated along swirls. On reheating to the subsequent oxidation, hexagonal half-loops of complete dislocation were found to be formed in addition to the stacking faults (17). The nature and structure of the circular stacking faults have been investigated previously (13) but not in detail for the hexagonal half-loops. Structure and dislocation velocities of similar half-loops in the case of (111)-oriented wafers have been determined by Patel and Freeland (8) and George *et al.* (10, 18) from the experimental results of intentional load application to the materials.

This paper describes detail features of the hexagonal half-loops and discusses the multiplication mechanism which may be characteristic of (001)-oriented wafers, from the observation of the dislocations by means of x-ray diffraction topography.

Experimental

Specimens used were (001)-oriented, n-type silicon wafers with a resistivity of about 10 ohm-cm, cut from a float-zoned, dislocation-free crystal rod with a diameter of about 30 mm. Some swirl patterns could be made visible by suitable etching on surfaces of the specimen wafers. They were thinned to about 200 μm by mechanical and chemical methods. Two sequential thermal oxidations were employed. First thermal oxidation for the generation of circular stacking faults along swirls was carried out at 1200°C for 22 hr in a dry oxygen atmosphere. A rapid cooling from the first oxidation was made by extracting the specimens from the center of a furnace to the edge of a quartz tube in less than 20 sec. Second thermal oxidation was carried out in such a manner that the specimens were inserted into the furnace from room temperature to around 600°C very rapidly and then moved to the center of the high temperature zone in about 20 sec and kept there at 1200°C for 3 hr in a wet oxygen atmosphere, which gave rise to the generation of prismatic dislocation loops or hexagonal half-loops. Formation of both the stacking faults and hexagonal half-loops described in this report did not appear to be essentially dependent on whether the oxygen is dry or wet.

In order to observe configurations of both the defects and to determine their Burgers vectors, x-ray diffraction topographs were taken after each oxidation using MoKα_1 radiation. All the topographs were recorded on Fuji nuclear plates, ET-7B type, 50 or 100 μm thick emulsion.

Results

Figure 1 shows a topograph of a part of a wafer taken after the second thermal oxidation. Some contrasted ellipses designated as S have been found to correspond to circular stacking faults, each of them surrounded by a partial dislocation loop with a Burgers vector of $a/3\langle 111\rangle$ Frank sessile type (13-14). These faulted loops were found to be formed in one of {111} planes during the course of the first thermal oxidation.

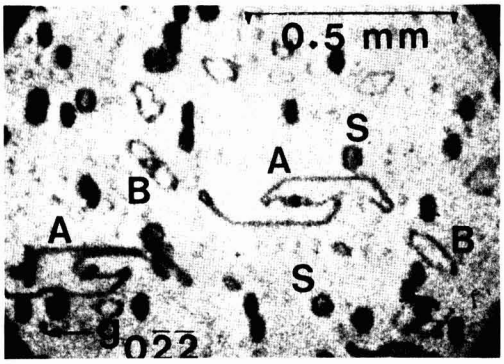


Fig. 1. Topograph of a specimen taken after double thermal oxidation. Besides a number of circular stacking faults, designated as S, which are generated after, a first thermal oxidation, several dislocations consisting of a pair of half-loops are observed. The Burgers vectors of the dislocations A and B are parallel and inclined to the wafer surface, respectively.

Key words: dislocation multiplication, cross-slip, x-ray topography.

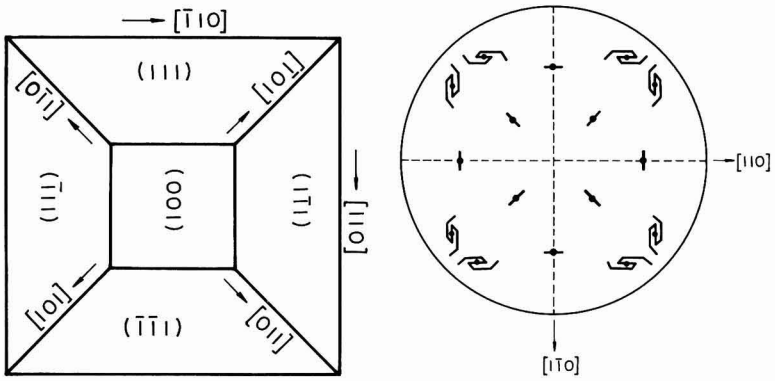


Fig. 2. a (left), Orientations of dislocation lines and glide planes. b (right), Illustration showing a rough distribution and configuration difference of dislocations in a single wafer.

At the conclusion of the second thermal oxidation, other kinds of dislocations in addition to the above circular stacking faults are seen, designated as A and B in Fig. 1. From observation of stereotopographs and topographs reflected from various planes, it is found that the dislocations A in Fig. 1 are lying in two sets of {111} planes inclined at the same angle of 54°44′ to the (001) surface plane, and that they have Burgers vectors of $a/2\langle 110\rangle$ type parallel to the surface and consist of 60° and screw segments with <110> orientation.

Figure 2 presents a schematical rough distribution and configuration difference of dislocations in a single wafer. Pairs of half-loops are mostly symmetrical in shape with respect to two equivalent {1$\bar{1}$0} planes normal to the (001) surface. These dislocations appear to be located in the vicinity of the surfaces, and dislocations close to the upper and lower surfaces give a similar feature on a projected topograph, which may be due to the effect of external stresses during heat-treatments, as will be discussed later in detail.

A typical configuration of the dislocation on a certain stage of development as seen in Fig. 1 is schematically shown in Fig. 3 judged from stereotopographic observation. Since the Burgers vector of this dislocation is parallel to the [110] direction, segment a (Fig. 3) emerging at the surface is a 60° dislocation with the [$\bar{1}$01] orientation, segment b a screw dislocation parallel to the surface, segment c a 60° dislocation with the [011] orientation, and segment d again a screw dislocation. [Hereafter, these will be abbreviated, respectively, as segments a(M, [$\bar{1}$01]), b(S, [110]), c(M, [011]), and d(S, [110]).] Thus, segments a, b, c, and d are lying in the inclined (1$\bar{1}$1) plane, while segments l(S, [110]), m(M, [0$\bar{1}$1]), n(S, [110]), and o(M, [101]) are in the ($\bar{1}$11) plane. Segments e(M, [0$\bar{1}$1]), f(S, [110]), and g(M, [101]) are parallel to segments m, n, and o, respectively, and segments i(M, [$\bar{1}$01]), j(S, [110]), and k(M, [011]) are parallel to segments a, b, and c, respectively. As this feature has not been observed in (111)-oriented wafers (8, 10), the dislocation configuration mentioned above seems to be characteristic of (001)-oriented wafers due to crystallographic orientation of the {111} glide planes, *i.e.*, a pair of inclined {111} planes, as (1$\bar{1}$1) and ($\bar{1}$11) planes in this case, which always lie symmetrically and intersect at a line parallel to the (001) surface.

Besides the fact that the dislocations, as well as the stacking faults, appear preferentially along swirls in oxidized dislocation-free crystals, it is observed that the dislocations consisting of half-loops show dark contrast of a nucleation source lying mostly along a screw segment (as segment h in Fig. 3) which connects two half-loops lying in the different {111} planes. These facts may suggest that the dislocations originate from some clustered defects such as precipitates of oxygen atoms (1, 3, 19), which seem to nucleate during the course of the first thermal oxidation at the grown-in defects usually located along swirls in float-zoned, dislocation-free silicon crystals (20-21). Although the precipitate particles can be expected to nucleate not only near the wafer surfaces but also in the bulk, growth of the dislocation loops around the precipitates may be more intensive near the oxidizing surfaces than in the interior, as will be discussed later.

Discussion

Formation mechanism of dislocations.—It has been reported that oxidized, Czochralski-pulled, dislocation-free silicon crystals reveal both stacking faults surrounded by a Frank partial dislocation and prismatic

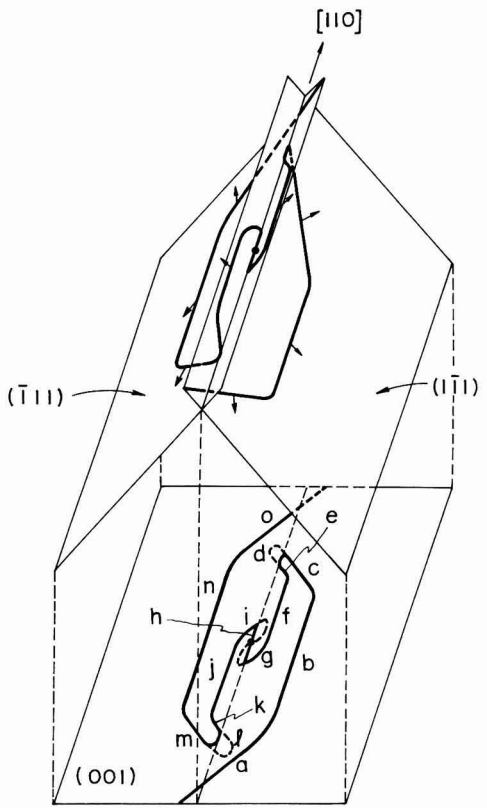


Fig. 3. Spatial illustration of a dislocation lying in two different {111} planes with its projection onto (001) plane.

dislocation loops consisting of $a/2<110>$ type complete dislocations (14-15). In case of float-zoned, dislocation-free crystals containing such grown-in defects along swirls as in the present experiment, however, extrinsic stacking faults surrounded by a Frank partial dislocation loop, *i.e.*, faulted loops, rather than prismatic dislocation loops, are believed to be preferably generated after the first thermal oxidation. But, the fact that the density of the circular stacking faults in a singly oxidized wafer is always lower than that of the grown-in defects which can be seen by etching before oxidation seems to indicate that not all of the grown-in defects turn out to be nuclei of the extrinsic stacking faults. It can be expected, therefore, that the rest of the grown-in defects may provide requisite sites for the aggregates of oxygen atoms which are pre-existent in the specimen or also induced from the surfaces.

On rapid cooling after a first high temperature oxidation, considerably large thermal strains will arise around the precipitate particles since the precipitate particles, probably SiO_2, form with larger specific volume than the silicon. It is speculated, therefore, that small prismatic loops of complete dislocation start to develop at the precipitate surfaces at the beginning of a second thermal oxidation so that the strains may be accommodated. Once the dislocation loops are formed, they will become more active emission sources of vacancies than are the stacking faults during a second thermal oxidation. These ideas seem to be supported by a previous report (22) describing the fact that circular stacking faults failed to be formed in dislocated crystals or in the vicinity of complete dislocations in low-dislocation-density crystals, and also by the fact that additional stacking faults were not observed at all after a second thermal oxidation while a number of prismatic dislocation loops and hexagonal half-loops were.

From the above consideration, the prismatic dislocation loops would be expected to be of interstitial type rather than of vacancy type and thus, as are the extrinsic stacking faults, the dislocation loops would be bulged by dislocation climb resulting from vacancy emission from the dislocation lines to the surfaces where the vacancies are consumed under oxidation conditions (23). Expansion of the loops should take place more markedly in the region close to the oxidizing surfaces for the above mechanism to be important, in order to be consistent with the present experimental result that the nucleation sources lying along the connecting screw segments are located at depths of less than 40 μm below the surfaces, which are known from the observation of the topographs.

Figures 4(a-f) reveal various configurations of the dislocations and indicate that they are on different stages of development and of multiplication probably due to the difference of magnitude of thermal stresses exerted on them during a second thermal oxidation. From the observation of those dislocations, development processes can be derived as schematically illustrated in Fig. 5 which presents successive views of dis-

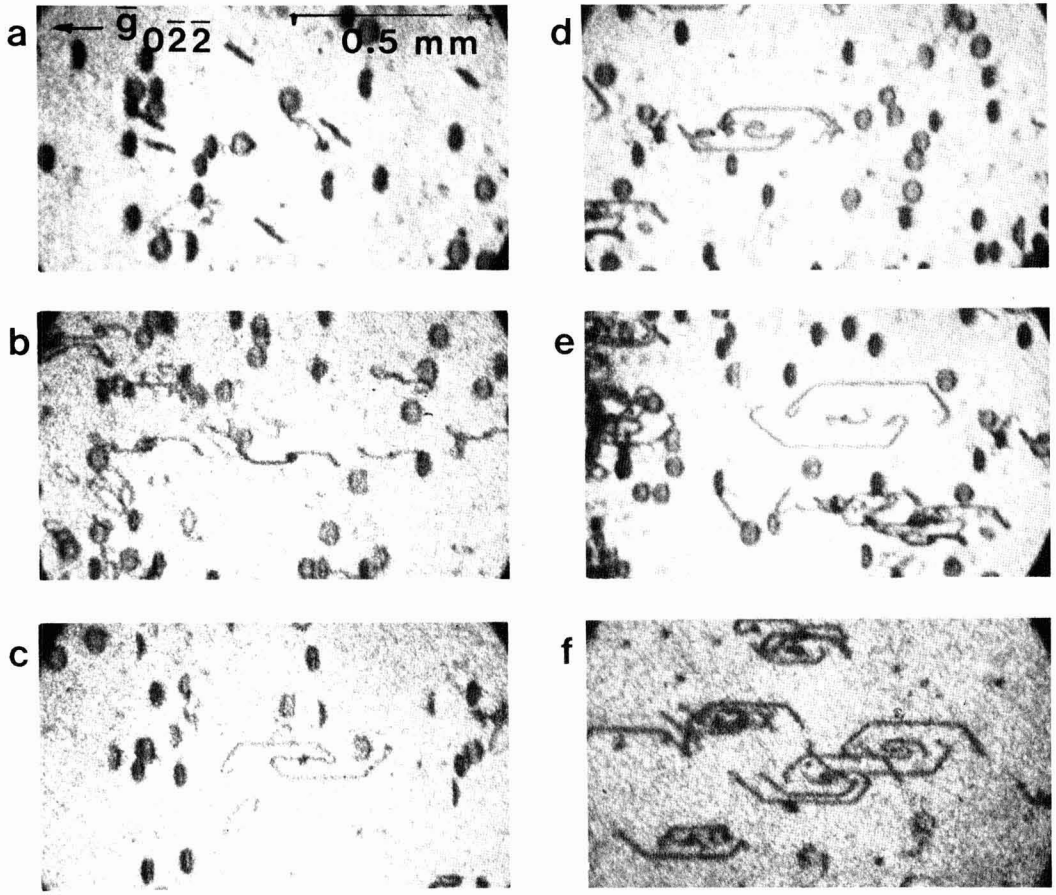


Fig. 4. Topographs showing various configurations of the dislocation half-loops. They seem to correspond to different stages of development.

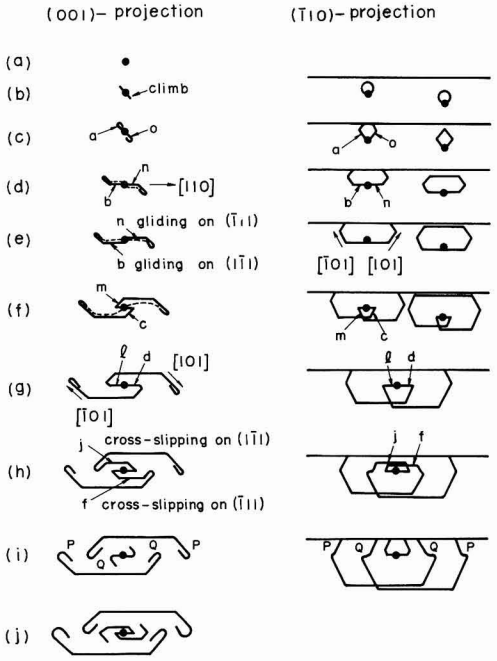


Fig. 5. Schematical illustrations showing successive views of development and multiplication processes as projections onto the (001) and (1̄10) planes. Designations to the dislocation segments correspond respectively to those in Fig. 3.

location shapes projected onto the (001) and (1̄10) planes. The dislocation half-loops shown in Fig. 4(a-f) would thus be expected to form by a combination of expansion of prismatic loops and their subjection to thermal stresses, as follows.

At the first stage, small prismatic loops of interstitial type attached to the precipitates may be emitted in order to lower strain energy increased around the precipitates. Both ends of a single dislocation line would be connected to the surface of a single precipitate. Vacancy emission may be more accelerated at the side close to the surface than the side further from the surface, as shown in Fig. 5b. Incipient alignment of the dislocation line of the climbing dislocation may not be in a particular direction because of high density of jogs on the line. However, <110> alignments would be preserved after considerable expansion of the dislocation loops since hexagonal prismatic loops consisting of straight, <110>-oriented segments have been observed so far in heat-treated silicon crystals (11, 14-15, 18). Therefore, it can be expected that, as shown in the left side of the (1̄10)-projections in Fig. 5(b and c), once a part of the dislocation loop line gets to a wafer surface, it is cut there and resolved into two dislocation lines which connect the precipitate surface and the wafer surface, and which will make a projection onto the (001) plane as is shown in Fig. 5(b and c) consistent with the actual feature of dislocations seen in Fig. 4a. Under the influence of thermal stresses which the specimen undergoes during a second thermal oxidation, each <110>-aligned segment of the prismatic dislocation loops lying in one of the inclined {111} planes would glide in the direction parallel to the Burgers vector. Since the Burgers vectors are $a/2$ <110> type parallel to the surface as already mentioned, the two <110> segments, *e.g.*, segment a(M, [1̄01]) in the (1̄11) plane and segment o(M, [101]) in the (1̄11) plane, as shown in Fig. 5d, glide inevitably in opposite directions from each other with respect to the precipitate, the phenomenon being related to the sense of resolved shear stress in each of the {111} planes. When the specimen is subjected to the thermal stress τ_1 in the [110] direction as shown in the upper part of Fig. 6, resolved shear stresses in the (1̄11) and (1̄11) planes are of such senses as seen in the right-hand part of Fig. 6, where ⊙ and ⊗ mean directions in which the stresses drive the material normally above and below the sheet, respectively. It is apparent that another shear stress τ_2 does not play a role for the movement of the present dislocations because of a null Schmid factor for either the [110]/(1̄11) or [110]/

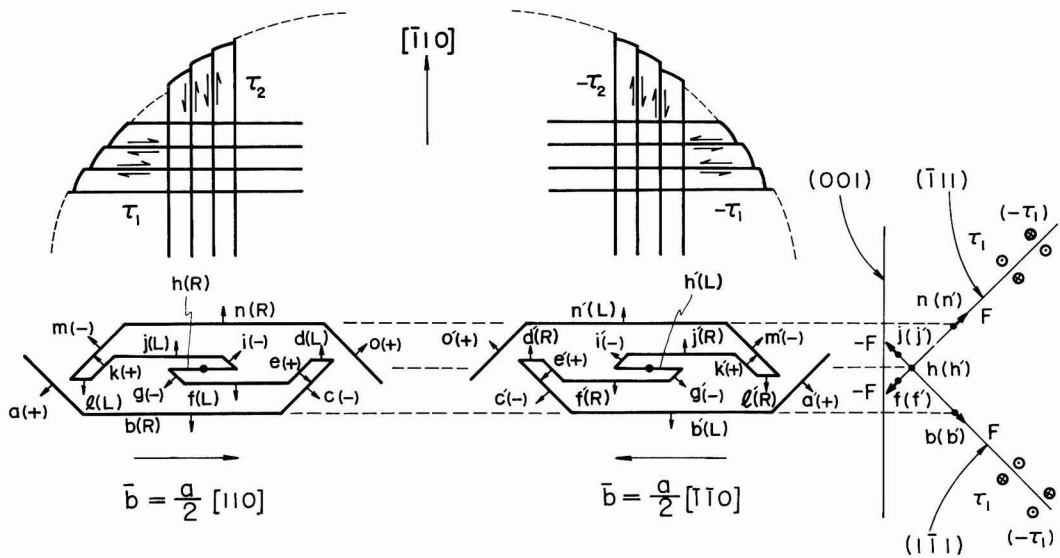


Fig. 6. Movement of each segment of half-loops under the influence of resolved shear stresses exerted parallel to the [110] directions. A 60° segment with the sign (+) has an extra half-plane above the glide plane whereas that with the sign (—) below the glide plane. A screw segment as noted by R in parentheses is of a right-hand screw character whereas that indicated by L is of a left-hand one.

$(1\bar{1}\bar{1})$ slip system. Supposing that extra half-planes which terminate at the lines of segments a and o exist above $(\bar{1}\bar{1}1)$ and $(\bar{1}11)$ planes, respectively [hereafter, segment r of 60° dislocation having an extra half-plane above the glide plane (on the side of the (001) surface) will be written as segment r(+, M, <110>) while that below the glide plane (on the side of the $(00\bar{1})$ surface as segment r(−, M, <110>)], the a(+, M, $[\bar{1}01]$) segment on the $(\bar{1}\bar{1}1)$ plane should glide in the $[\bar{1}\bar{1}0]$ direction (to the left) and the o(+, M, [101]) segment on the $(\bar{1}11)$ plane should glide in the [110] direction (to the right), under the resolved shear stresses mentioned above. This process must leave a screw segment which connects segments a and o. This screw segment is regarded as made of two parts, *i.e.*, segments b and n on both sides of the precipitate, as shown by the solid lines in Fig. 5d. From the above consideration, the screw segments should be right-hand screw dislocations [hereafter, segment r of this type will be written as segment r(R, S, <110>), while that of left-hand screw type as segment r(L, S, <110>)]. Apparently, both the b(R, S, [110]) segment in the $(\bar{1}\bar{1}1)$ plane and the n(R, S, [110]) segment in the $(\bar{1}11)$ plane exert motive forces, F, normal to the segment lines in each of the {111} planes also due to the resolved shear stresses and, as a result, each of the screw segments glides independently deeper into the wafer thickness in one of these planes. Dislocation configuration as seen in Fig. 5e and actually as shown in Fig. 4b can be thus obtained, and furthermore, formation of the other two 60° dislocations as in segments c(−, M, [011]) and m(−, M, $[0\bar{1}1]$) shown in Fig. 5f and of two screw dislocations as in segments d(L, S, [110]) and l(L, S, [110]) in Fig. 5g takes place. These segments move in such a way that each half-loop expands continuously in each glide plane, and the resulting feature is such a one as seen in Fig. 4c.

Another formation process of the dislocation shown in Fig. 5g may be possible in which the glide motions mentioned above precede arrival of a part of the dislocation line at the surface. The dislocations having not yet reached the surface are shown by the dashed lines in Fig. 5(c-f) in addition to the solid lines and are also shown in the right side of the $(\bar{1}10)$-projections. Dislocation features as seen in Fig. 7(a and b) appear to correspond to this case. By either development process, the dislocation configuration as shown in Fig. 5g can be explained. At this time, the most part of segments d and l in Fig. 5g exert motive forces, $-F$, whose sense is opposite to those on segments n and b as shown in Fig. 6. Therefore, they cross-slip on the $(\bar{1}11)$ and $(1\bar{1}1)$ planes, respectively, turning themselves into f(L, S, [110]) and j(L, S, [110]) segments connected to a pair of the other 60° dislocations, *i.e.*, e(+, M, $[0\bar{1}1]$) and g(−, M, [101]) segments for segment f and k(+, M, [011]) and i(−, M, $[\bar{1}01]$) segments for segment j as shown in Fig. 5h and also actually seen in Fig. 1 and 4d. When segments f and j reach an oxidizing surface again, then these segments disappear and only 60° segments are left, being emergent at the surface as shown in Fig. 4e and 5i. Thus, the dislocation becomes the one that consists of two half-loops and also of one inside dislocation which is of mostly screw character and suspended at the surface. The latter is ready to give off another pair of half-loops by going through the same process all over again, since it is also a right-hand screw segment as are segments b and n. Accordingly, whenever left-hand screw segments cross-slip and emerge from the surface and hence annihilate there, dislocation multiplication takes place and in turn, formation of pairs of multifold half-loops occurs as shown in Fig. 4f and 5j.

It should be noted that part of the 60° segments on both of the ends of each half-loop seem to, at their

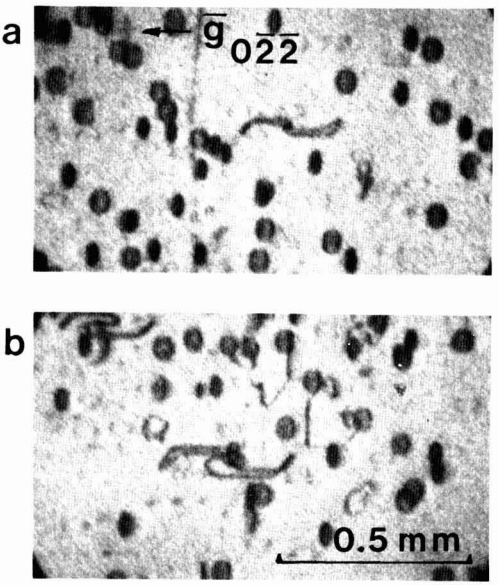


Fig. 7. Dislocations expanding by glide in the direction parallel to the surface before a part of each dislocation line arrives and annihilates at the surface. (a), Early and (b), later stages of development.

emerging points, depart from the initial glide planes since they are not in rectilinear alignments but are revealed in the shape of a hook on the projected topographs, as shown in Fig. 1 and 4e. In fact, stereotopographs give a nonplanar configuration of the dislocations at both the emerging points of each half-loop. George *et al.* (10) have reported that similar bends of the emergent segments observed in (111)-oriented wafers are caused by the cross-slip of screw segments. In the present case of the (001)-oriented wafers, however, this mechanism does not seem to hold since the emergent segments themselves are not screw but 60° dislocations. Apparently one of the bends in a single half-loop, connected to segment a or o as at P in Fig. 5i, is generated in an early stage of development, as already mentioned. The other bend, Q, is made of a 60° segment such as segment e or k, as a result of the disappearance of the cross-slipped screw segment such as f or j segment. After all, it is evident that formation of the two bends takes place due to interaction of the dislocations of screw character with the specimen surface.

The symmetry of the dislocation configuration illustrated in Fig. 2b seems quite reasonable since, as shown in Fig. 6, thermal shear stresses, felt by the dislocations in the opposite sides of the wafer with respect to the (110) plane normal to the stress direction, are in the opposite directions from each other and thus, screw segments of both the dislocations, *e.g.*, segments b(R, S, [110]) and b′(L, S, [110]), are also of opposite senses, whereas the same development mechanism may preside over both the dislocations.

Another type of dislocation.—Another type of dislocation is observed to coexist with the dislocations described above, as marked by B in Fig. 1 and also as shown in Fig. 8, the former having the shape of a full hexagon, whether regular or partly perturbed, and the latter lacking some segments. Each hexagon on the topograph projected onto the (001) plane usually consists of four <110> segments and two <100> segments. Stereotopographs show that they are also lying in two sets of adjacent {111} planes, as schematically shown

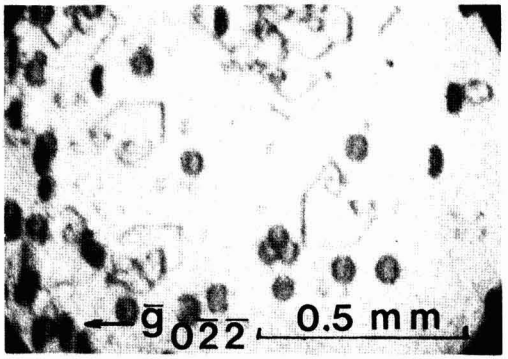


Fig. 8. Another type of dislocation of which Burgers vector is inclined to the wafer surface.

in Fig. 9. They are found to have a Burgers vector of $a/2\langle 110\rangle$ inclined to the surface, and are also found to be prismatic dislocations which contain a pair of screw segments of opposite senses, *e.g.*, as shown in Fig. 9, segments u(M, [110]) and v(S, [011]) are in the $(1\bar{1}\bar{1})$ plane, and segments x(M, $[\bar{1}10]$) and y(S, [011]) are in the $(\bar{1}\bar{1}1)$ plane, while segments w(M, $[\bar{1}10]$) and z(M, [110]) are in the $(\bar{1}\bar{1}1)$ and $(1\bar{1}1)$ planes, respectively, parallel to the x and u segments.

This type of dislocation is thought to develop through such processes as are schematically shown in Fig. 10. First, as well as the previous dislocations, sources of the dislocations are probably precipitates, although they are located at larger distances from the surface than those in the previous case. Then, round dislocation loops would be emitted from the precipitates by climb, since these loops seem to lie in planes

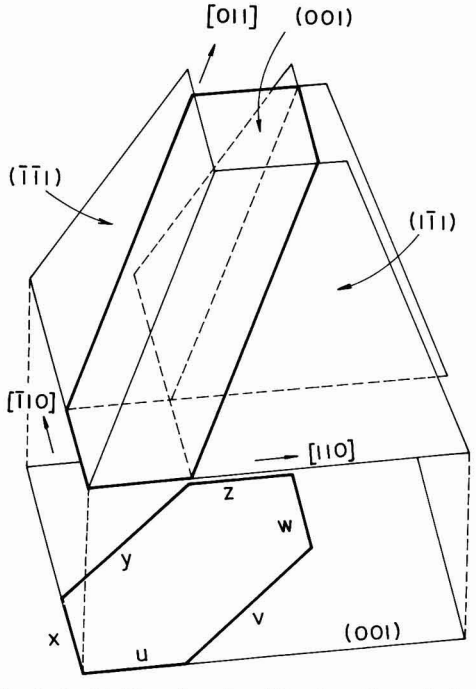


Fig. 9. Spatial illustration of a dislocation with an inclined Burgers vector as B in Fig. 1 and in Fig. 8, with its projection onto (001) plane.

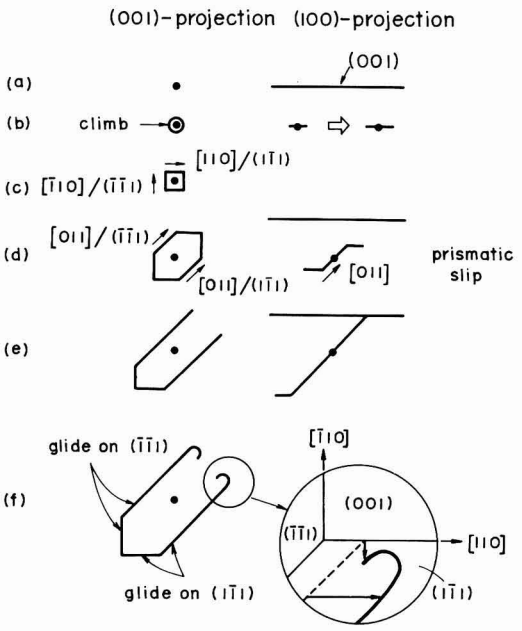


Fig. 10. Development processes of the dislocation with an inclined Burgers vector.

parallel to the (001) surface and no preference of the vacancy emission along the loop line is expected. The loops would turn to the ones with several $\langle 110\rangle$-aligned segments, as shown in Fig. 10c. When the crystal region containing the loops is affected by a resolved shear stress, two halves of each loop with the Burgers vector parallel to the stress might glide in opposite directions, and hence the dislocations would have shapes as shown in Fig. 9 and 10d. The dislocation feature is similar to the previous dislocation shown in the right side of the $(\bar{1}10)$-projection in Fig. 5d except for orientation of the screw segments. Once one of the halves arrives and annihilates at a surface, only four segments are left. This four-segmented dislocation could also be obtained by a mechanism in which two segments with $\langle 110\rangle$ orientation parallel to the surface originate at the surface due to surface irregularities and glide into the material leaving a pair of screw segments behind them. The fact that, by Sirtl-etching, the dislocations made of full hexagon or of four segments sometimes reveal an unidentified dot nearly at their center and sometimes not, seems to suggest the difference of nucleation sources, *i.e.*, the precipitates or surface irregularities.

Additionally, two emergent screw segments of opposite senses often bend toward the inside on a topograph as seen in Fig. 8. The phenomenon is thought, in contrast with the previous dislocations, to be due to cross-slips of the emergent screw segments themselves, similar to the case observed by George *et al.* (10) in addition to the pinning effect of the surface; *e.g.*, as shown in Fig. 10f, a part of the screw segment v would move in the [110] direction on the $(1\bar{1}1)$ plane, slower near the surface than at the inner part, and also could cross-slip in the $[1\bar{1}0]$ direction on the adjacent $(\bar{1}\bar{1}1)$ plane. As has been reported (10), this cross-slipping part can be a new source of another mobile dislocation. Thus, dislocation multiplication may occur also in the case of the present dislocations.

Conclusion

(001)-oriented silicon wafers subjected to two sequential thermal oxidations are found to reveal char-

acteristic dislocation configurations. These dislocations originate from the precipitates nucleated at some grown-in defects in dislocation-free silicon crystals on rapid cooling from a first thermal oxidation. Via small prismatic dislocation loops generated through climb, and under the influence of thermal stresses exerted during the course of a second thermal oxidation, the dislocations can develop and multiply giving off successively pairs of half-loops lying in two sets of symmetrically inclined {111} planes. Another type of dislocation lying in the adjacent {111} planes is also observed.

Acknowledgment

The author would like to thank Drs. S. Asanabe, Y. Nannichi, and T. Kawamura for their encouragements and discussions.

Manuscript submitted June 17, 1974; revised manuscript received March 30, 1975. This was Paper 106 presented at the Chicago, Illinois, Meeting of the Society, May 13-18, 1973.

Any discussion of this paper will appear in a Discussion Section to be published in the June 1976 JOURNAL. All discussions for the June 1976 Discussion Section should be submitted by Feb. 1, 1976.

Publication costs of this article were partially assisted by Nippon Electric Company, Limited.

REFERENCES

1. J. E. A. Miltat and D. K. Bowen, *Phys. Status Solidi (a)*, **3**, 431 (1970).
2. T. Abe, T. Ohtaki, and J. Chikawa, *Denki Kagaku*, **40**, 525 (1972).
3. J. R. Patel and B. W. Batterman, *J. Appl. Phys.*, **34**, 2716 (1963); J. R. Patel, *Discussions Faraday Soc.*, **38**, 201 (1964).
4. T. Suzuki and H. Kojima, *Acta Met.*, **14**, 913 (1966).
5. M. C. Collet, *This Journal*, **117**, 259 (1970).
6. G. Granberg, *J. Appl. Phys.*, **43**, 4801 (1972).
7. A. R. Chaudhuri, J. R. Patel, and L. G. Rubin, *ibid.*, **33**, 2736 (1962).
8. J. R. Patel and P. E. Freeland, *Phys. Rev. Letters*, **18**, 833 (1967); *J. Appl. Phys.*, **41**, 2814 (1970).
9. E. Gerward, *Phys. Status Solidi (a)*, **2**, 797 (1970).
10. A. George, C. Escaravage, W. Schröter, and G. Champier, *Crystal Lattice Defects*, **4**, 29 (1973).
11. J. R. Patel, *J. Appl. Phys.*, **34**, 2788 (1963).
12. K. V. Ravi, *Met. Trans.*, **4**, 681 (1973); *J. Appl. Phys.*, **43**, 1785 (1972).
13. J. Matsui and T. Kawamura, *Japan. J. Appl. Phys.*, **11**, 197 (1972).
14. J. R. Patel and A. Authier, Paper S-171 presented at the Ninth International Congress of Crystallography, Kyoto, Japan, 1972; *J. Appl. Phys.*, **46**, 118 (1975).
15. S. Prussin, *ibid.*, **43**, 733 (1972); *ibid.*, **43**, 2850 (1972).
16. L. I. Bernewitz, B. O. Kolbesen, K. R. Mayer, and G. E. Schuh, *Appl. Phys. Letters*, **25**, 277 (1974).
17. J. Matsui and T. Kawamura, in "Semiconductor Silicon 1973," H. R. Huff and R. R. Burgess, Editors, p. 126, The Electrochemical Society Softbound Symposium Series, Princeton, N. J. (1973).
18. A. George, C. Escaravage, G. Champier, and W. Schröter, *Phys. Status Solidi (b)*, **53**, 483 (1972).
19. J. R. Patel, *J. Appl. Phys.*, **44**, 3903 (1973).
20. T. Abe, T. Samizo, and S. Maruyama, *Japan. J. Appl. Phys.*, **5**, 458 (1966).
21. A. J. R. DeKock, *Appl. Phys. Letters*, **16**, 100 (1972).
22. T. Iizuka, *Japan. J. Appl. Phys.*, **5**, 1018 (1966).
23. I. R. Sanders and P. S. Dobson, *Phil. Mag.*, **20**, 881 (1969).

Diffusion of Cobalt out of Cobalt-Hardened Gold Measured with Auger Electron Spectroscopy

Harland G. Tompkins

Bell Laboratories, Incorporated, Columbus, Ohio 43213

ABSTRACT

The diffusion of cobalt out of a gold layer is considered. The theory is discussed to relate measured quantities to diffusion coefficients. Measurements were taken and appropriate calculations made to obtain values for the coefficients at 100° and 150°C. Arrhenius plot extrapolations are then made to obtain approximate values at ambient temperatures.

Electroplated gold is a material often used in electrical contacts because of its excellent noncorrosive properties. Because pure gold is reasonably soft it is often modified by adding a small amount of cobalt as a hardening agent to reduce its sticking tendency. Cobalt does not have the noncorrosive properties of gold, however, and if a significant amount of the cobalt were to diffuse to the surface and become oxidized, the electrical contact properties would be significantly impaired. The purpose of this work is to study the diffusion of cobalt out of a gold matrix. The theory is developed for a simple model. Measurements of surface cobalt are described and diffusion coefficients (at slightly elevated temperatures) calculated. An Arrhenius plot is made which shows extrapolated diffusion coefficients down to ambient temperatures.

Key words: cobalt, gold, diffusion, Auger electron spectroscopy.

Theory

In setting up the appropriate boundary value problem, we make the following simplifying assumptions: (*i*) Except for the cobalt content, the gold layer is homogeneous throughout. (*ii*) The diffusion coefficient for cobalt in gold is independent of the concentration of cobalt within the ranges studied. (*iii*) The cobalt does not diffuse into the underlying material (*i.e.*, into Cu or Ni). (*iv*) Cobalt which arrives at the outside surface of the gold is immediately oxidized. Formally, we say that a sink exists at the surface for the cobalt.

A few comments are in order about the appropriateness of the initial assumptions to real world conditions. This study concentrates on temperatures near ambient, gold thicknesses large enough to avoid porosity, and times of the order of 40 years or less. For these conditions we shall find that significant transfer of cobalt

occurs only near the surface of the gold and the system could have been treated as if the gold were a semi-infinite slab. We shall, however, consider a finite gold thickness, both for convenience and also to show when the diffusion process is affected by the finiteness of the gold. This information is particularly needed in the area of (possibly incorrect) accelerated aging of corrosion processes. With the semi-infinite idea in mind, the real world boundary condition at the back side of the gold is irrelevant and is chosen for mathematical convenience. The assumption of a sink at the outer surface involves assuming that the chemical and transport processes of oxidation in the film occur much faster than the transport phenomena in the gold. For an oxide with thickness of 60Å or less and gold with cobalt concentrations of tenths of a per cent, this seems reasonable.

We shall use the standard textbook approach (1, 2) in setting up and solving the boundary value problem. Let us make the following definitions. Time (in seconds) will be denoted as t. Distance (in centimeters) normal to the surface will be denoted as x (we will discuss later where the origin is to be chosen). The atomic concentration of cobalt will be denoted as c, and in fact $c = c(x)$, with the uniform concentration at time zero as c_i. The thickness of the gold layer will be taken as $h/2$ (the reason for the half will become obvious later).

The differential equation which is obeyed by the cobalt in the gold layer is

$$\frac{dc}{dt} = D\frac{d^2c}{dx^2} \qquad [1]$$

where D is the diffusion coefficient (assumed to be independent of concentration).

The actual boundary conditions which seem reasonable are that the concentration is uniform at time zero, that the concentration of free cobalt at the outside surface of the gold is zero (*i.e.*, the sink effect), and that the slope of the concentration at the inside gold surface is zero. The boundary value problem is simpler to solve, but equally applicable, if we consider the actual situation plus its mirror image. This is shown in Fig. 1 along with the appropriate mathematical boundary conditions necessary to represent the real world boundary conditions.

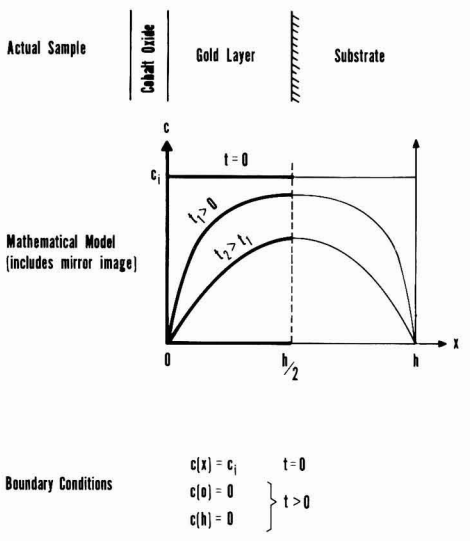


Fig. 1. Boundary value problem and boundary conditions, actual and mathematical.

The solution, expressed as an infinite sum is

$$c = \frac{4c_i}{\pi}\sum_{n=0}^{\infty}\frac{1}{2n+1}\sin\frac{(2n+1)\pi x}{h} \exp\left[-(2n+1)^2\pi^2\frac{Dt}{h^2}\right] \qquad [2]$$

which has the form shown on Fig. 1.

The integral

$$\int_0^{h/2} c(x)\,dx = \frac{1}{2}\int_0^h c(x)\,dx \qquad [3]$$

gives the total content of cobalt in the gold layer at any time, t. The quotient

$$\text{quotient} = \frac{\frac{1}{2}\int_0^h c(x)\,dx}{\frac{1}{2}\int_0^h c_i\,dx} = \frac{1}{c_i h}\int_0^h c(x)\,dx \qquad [4]$$

gives the fraction of the original amount of cobalt remaining in the gold layer. It is clear that this fraction is the same whether we consider x from 0 to $h/2$ or from 0 to h. Let us denote the fraction of the cobalt which has been removed as F. Therefore

$$F = 1.0 - \frac{1}{c_i h}\int_0^h c(x)\,dx \qquad [5]$$

performing this integration we get

$$F = 1.0 - \frac{8}{\pi^2}\sum_{n=0}^{\infty}\frac{1}{(2n+1)^2} \exp\left[-(2n+1)^2\pi^2\frac{Dt}{h^2}\right] \qquad [6]$$

The reason for concerning ourselves with the cobalt which has been removed is that this is the cobalt which appears at the surface as an oxide and can be easily measured. The reason for considering the fraction, F, is that the fraction of material removed from one-half of the hypothetical system is the same as the fraction removed from the entire hypothetical system, hence the real world problem can be considered with the mathematical boundary value problem which we have set up (and shown in Fig. 1).

The infinite sum, in Eq. [6], is a function of the variables D, t, and h, and in fact these always appear as Dt/h^2.

The infinite sum itself is not very illustrative of how these variables affect F. We can, however, with a simple Fortran program, solve for F, for various values of Dt/h^2, and plot the result. This is shown in Fig. 2.

Crank (2) indicates that for small times an error function-type expression is applicable and if, in fact, the quantity Dt/h^2 is quite small the approximation

$$F = \frac{4}{\sqrt{\pi}}\sqrt{\frac{Dt}{h^2}} = 2.26\sqrt{\frac{Dt}{h^2}} \qquad [7]$$

is valid. This expression is also plotted in Fig. 2. Above $F = 0.6$ or $Dt/h^2 = 0.07$, the curve deviates significantly from the approximation.

The above expression provides some interesting insight in the following way. It is not clear at first thought, whether using a thicker gold layer (with the same cobalt concentration) will give a thicker cobalt oxide film or not. More total cobalt is available, but it has further to travel to arrive at the surface. Equation [7] shows that, in fact, the film growth will be the same, regardless of the thickness of the gold layer in the early stages. This can be seen by rearranging Eq. [7] as follows

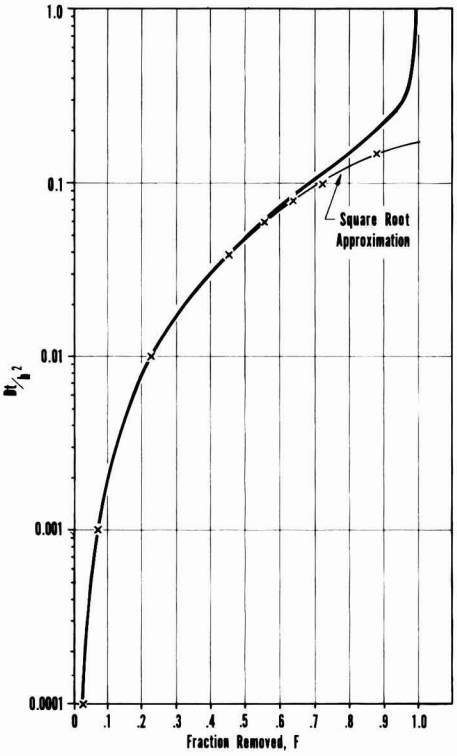


Fig. 2. Fraction of cobalt which has been removed from the gold film plotted *vs.* Dt/h^2.

$$Fh = 2.26\sqrt{Dt}$$

The amount of cobalt in the oxide film is simply the fraction removed times the original amount or

$$\text{amount} = F \cdot h \cdot (\text{area}) \cdot c_i$$

$$= 2.26\sqrt{Dt} \cdot (\text{area}) \cdot c_i$$

and hence is independent of thickness.

This is to say that until the fraction removed approaches 0.6, the thickness of the cobalt oxide film is independent of the gold layer thickness. It is very dependent, however, on the original concentration of cobalt in the gold. The dependence is one-to-one in that twice as much cobalt gives a film twice as thick.

Applying the theory, then, consists of measuring F, t, and h and calculating D, and then, by using values of D obtained, predicting values of F for other values of t and h (and as shown below, for different temperatures).

The diffusion coefficient is generally accepted to be a function of temperature and is usually represented with the Arrhenius equation

$$D = D_0 e^{-Q/RT}$$

where T is in degrees Kelvin, R is the gas constant, Q is the activation energy for diffusion, and D_0 is the preexponential factor. Data are then taken at elevated temperatures, and, using an Arrhenius plot, the values of D for lower temperatures are obtained by extrapolation using the obtained values. Calculations can then be made for F at the lower temperatures as a function of t and h. These extrapolations are based on one rather limiting assumption, *i.e.*, that the mechanism of diffusion is the same for the measured values and the extrapolated values. Serious problems can arise when the diffusion mechanism changes (3). Accordingly, the extrapolation is more likely to be acceptable if the measured values are obtained at temperatures reasonably near the temperature for the extrapolated values.

Experimental Methods

The samples used were electroplated gold films which contained 0.26% (by weight) cobalt as a hardening agent. Some of the films were plated directly on the OFHC copper substrate, and some of the samples had a nickel underplate between the gold and the copper. Results were independent of which material was immediately under the gold. The gold thickness was determined by photomicrography. All except two of the samples had 3.3 μm of gold. Two samples had 50.8 μm of gold. The cobalt content was measured by atomic absorption. The samples were coupons approximately 4 cm^2 $\times$ 0.3 cm. These were heated in air at 150° and at 100°C for extended periods of time in ovens. Temperatures were controlled to within $\pm$ 1°C. At appropriate times, the coupons were removed from the ovens and small sections were cut out of the larger coupons. These smaller (1 $\times$ 0.5 cm) pieces were then analyzed for cobalt.

The cobalt analysis was made using Auger electron spectroscopy (4, 5) along with argon ion bombardment to obtain a depth profile of the cobalt along with other elements. A commercial instrument purchased from Physical Electronics Industries was used. Sputtering and Auger analysis are done simultaneously and a plot of peak-to-peak height *vs.* sputtering time can be obtained for up to six elements. Sputtering rate was obtained by prior calibration of the sputtering parameters for gold. Sputtering rate for cobalt oxide is assumed to be that of cobalt which in turn is taken to be one-half that of gold (6).

The thickness is measured as described above and combined with the calculated value of oxide thickness if all the cobalt were oxidized to give the fraction of the cobalt removed, or F. The stoichiometry of the oxide was not measured, but it was assumed to be CoO. When density and molecular weight are taken into account, the results are within 10% for either CoO

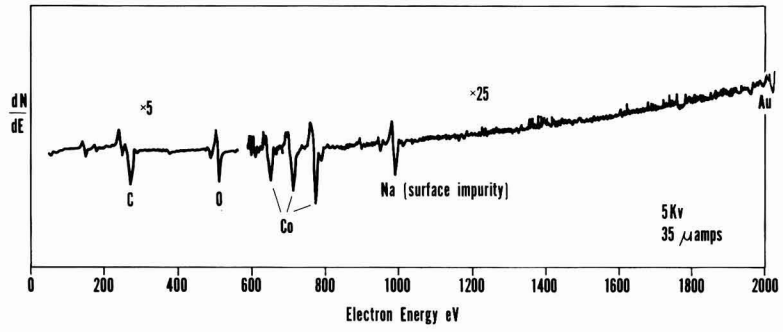


Fig. 3. Typical Auger spectrum taken before sputtering. Sample had been heated at 100°C for 6060 hr.

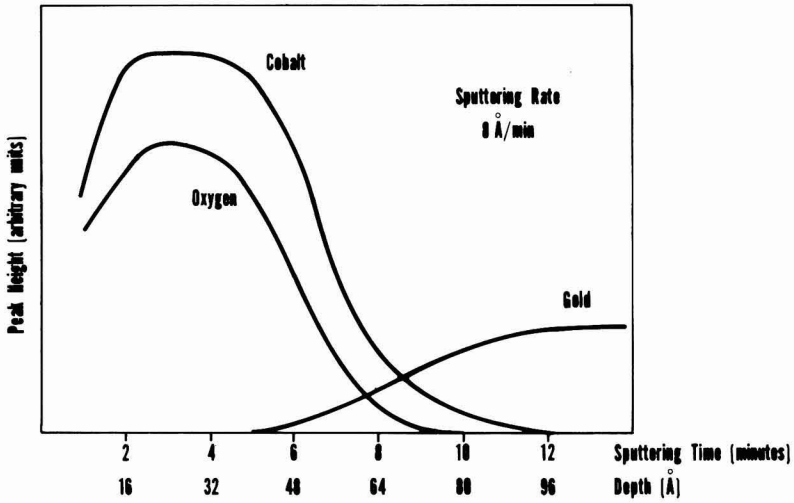


Fig. 4. Typical profile of the top few hundred angstroms. Sample had been heated at 150°C for 2927 hr.

or Co_3O_4 which are the two possibilities (7). For simplicity, then we assume CoO.

Results

Profiles were obtained for samples heated at 150°C for 2927 hr and samples heated at 100°C for 6060 hr. A typical Auger spectrum is shown in Fig. 3 and a typical profile is shown in Fig. 4.

The reason for the initial rise in the cobalt and oxygen signal is that a small layer of carbon (which typically exists on any sample which has been exposed to the atmosphere for any significant length of time) is being removed, thus, uncovering the underlying material.

The oxygen signal follows the cobalt rather closely which tends to indicate that this cobalt is in the oxide form. The gold signal goes from zero in the oxide to its bulk value after the oxide has been sputtered away. The model is, then, that the cobalt at the surface becomes oxidized leaving a lower free cobalt concentration, the cobalt in the bulk diffuses out and in turn is oxidized. The resulting structure is a cobalt oxide film on top of the gold.

Let us take the thickness where the peak height crosses the center point, half-way between maximum and zero, as the thickness of the cobalt oxide. Table I gives the values of time, temperature, thickness, and the corresponding value of diffusion coefficient obtained using methods discussed in the section on Theory.

One immediate observation is that the samples with 50.8 μm of gold give cobalt oxide films which are not significantly different in thickness from the films formed on the 3.3 μm samples. This tends to substantiate the theoretical conclusion that the amount of film formed should be independent of gold thickness.

Table I. Thickness of cobalt oxide and diffusion coefficients for various times and temperatures

Temperature, °C	Time, hr	Thickness, Å	D, cm²/sec
150	2927	53	2.0×10^{-16}
150	2927	58	2.28×10^{-16}
150*	2927	64	2.95×10^{-16}
100	6060	7.0	1.85×10^{-18}
100	6060	11.0	4.2×10^{-18}
100	6060	9.6	3.2×10^{-18}
100*	7156	11.4	3.82×10^{-18}

* Gold thickness is 50.8 μm for these samples. Others are all 3.3 μm.

The main thrusts of this work are the description of how Auger spectroscopy can be used for diffusion measurements (along with the necessary diffusion theory) and the reporting of diffusion coefficients at reasonably low temperatures (100° and 150°C). A secondary benefit obtained is that these values of the diffusion coefficient can be plotted on an Arrhenius plot to obtain an activation energy for diffusion and to make rough estimates of diffusion coefficients at even lower temperatures.

Extrapolation beyond measured data is risky, at best, and the choice of the method used for the extrapolation is up to the extrapolator. The author has used a least squares fit along with the 95% confidence limits

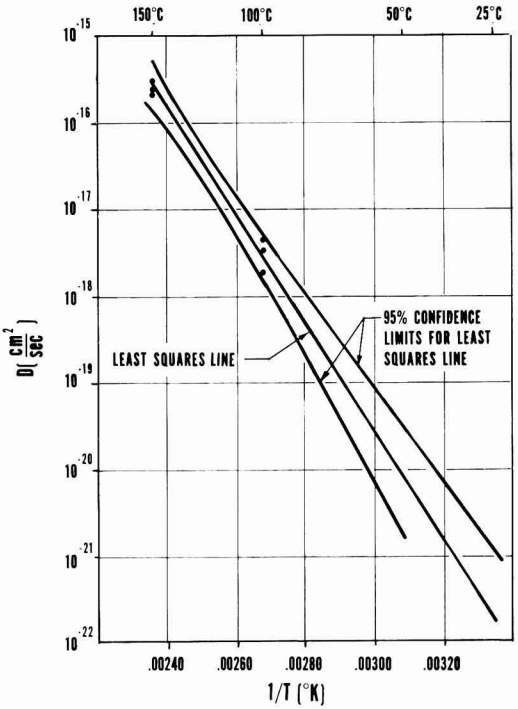


Fig. 5. Arrhenius plot of diffusion coefficient, D vs. $1/T$

of the least squares line. This is shown in Fig. 5. The activation energy for diffusion, Q, obtained from the least squares line is

$$Q = 28 \pm 6 \text{ kcal/mole}$$

Another point of interest is that the square root relation

$$F = 2.26 \sqrt{\frac{Dt}{h^2}}$$

holds for most systems of interest for this model. For gold thicknesses of 3.3 μm and temperature of 50°C (along with the corresponding diffusion coefficient $D = 10^{-19}$) the time corresponding to $F = 0.6$ is of the order of 10^4 years. If we use smaller thicknesses where the fraction might be appreciable, other transport mechanisms, *e.g.*, porosity, would prevail and the model proposed here would not be applicable.

Summary

We have considered the diffusion of cobalt out of a gold layer. The theory is discussed first to relate measured quantities to diffusion coefficients. Measurements were taken and the appropriate calculations made to obtain values for the diffusion coefficients at different temperatures. Arrhenius plot extrapolations were then made to obtain rough values for the coefficients at lower temperatures.

Acknowledgments

The author would like to acknowledge Dr. Morton Antler for preparation and aging of the samples, Dr. M. R. Pinnel for useful discussion, and J. A. Smiley for assistance in taking the Auger spectra.

Manuscript submitted Oct. 9, 1974; revised manuscript received Feb. 4, 1975.

Any discussion of this paper will appear in a Discussion Section to be published in the June 1976 JOURNAL. All discussions for the June 1976 Discussion Section should be submitted by Feb. 1, 1976.

Publication costs of this article were partially assisted by Bell Laboratories.

REFERENCES

1. W. Jost, "Diffusion in Solids, Liquids, Gases," p. 35 ff, Academic Press, New York (1960).
2. J. Crank, "The Mathematics of Diffusion," p. 45 ff, Oxford University Press, London (1956).
3. M. R. Pinnel and J. E. Bennett, *Met. Trans.*, **3**, 1989 (1972).
4. C. C. Chang, *Surface Sci.*, **25**, 53 (1971).
5. P. W. Palmberg, *J. Vacuum Sci. Technol.*, **9**, 160 (1972).
6. G. Carter and J. S. Colligon, "Ion Bombardment of Solids," American Elsevier Publishing Co., New York (1968).
7. E. A. Gulbransen and K. F. Andrew, *This Journal*, **98**, 241 (1951).

Multilayer Metallization with Planar Interconnect Structure Utilizing CVD Al_2O_3 Film

H. Mutoh,* Y. Mizokami,* H. Matsui, S. Hagiwara, and M. Ino

OKI Electric Industry Company, Limited, Hachioji, Tokyo, Japan

ABSTRACT

A new, multilayer metallization system has been developed for the purpose of fabricating a planar interconnect structure. This system comprises two levels of metal interconnection, and the first-level metal layer is buried in a low temperature CVD Al_2O_3 film pyrolytically deposited by $Al(i\text{-}C_3H_7O)_3$ at 420°C. The metal chosen for both layers is aluminum, and the insulator is phosphosilicate glass. In the metal processing, a self-aligned photolithographic technique is applied in which positive photoresist AZ-1350 plays an important role in forming the first-level Al layer and the Al_2O_3 film.

The recent development of large scale integration (LSI) of microcircuits has required the use of more than one level of metallization in order to achieve high packing density. In conventional multilevel structures, each metal layer is separated from the next by an insulating oxide, and there are many steps at metal edges which result in limiting the reliability and yield. In the fabrication of multilevel structures, it is highly desirable to provide a planar interconnect structure.

Recently, so-called "no step" metallizations appear to be possible by the use of anodically formed Al_2O_3 or polyimid (1, 2).

This paper describes a new multilayer metallization system in which a first-level metal layer is buried in chemically vapor deposited Al_2O_3 for the purpose of fabricating the planar interconnect structure.

Structure and Manufacturing Process

The schematic cross section of a two-level structure fabricated by this new method is shown in Fig. 1(a), in comparison with a conventional structure using a phosphosilicate glass (PSG) film as the insulating layer in Fig. 1(b). It was found that planarity of surface in the new structure is achieved with the first-level metal layer buried in Al_2O_3.

The metal process steps used in the fabrication of this new planar interconnect structure are shown in Fig. 2. After the diffusion processes are finished, an Al_2O_3 film is deposited on the wafer by pyrolysis of aluminum triisopropoxide $Al(i\text{-}C_3H_7O)_3$ (3-5) as shown in step (A). This CVD Al_2O_3 film can be deposited at a relatively low temperature of about 400°C so that the characteristics of the devices do not deteriorate. The required film patterns are prepared by photomasking with positive photoresist (AZ-1350) and etching in hot phosphoric acid as shown in steps (B) and (C). The Al_2O_3 film can be very quickly etched by phosphoric acid, which makes it possible to perform the etching process with negligible etching of the other oxide film underneath the etched Al_2O_3 film to form selectively desired patterns.

Next, without removing the photoresist, we evaporate aluminum onto the wafer up to the equivalent thickness of the Al_2O_3 film as shown in step (D).

* Electrochemical Society Active Member.

Key words: aluminum oxide film, planar interconnection, lift off, positive photoresist.

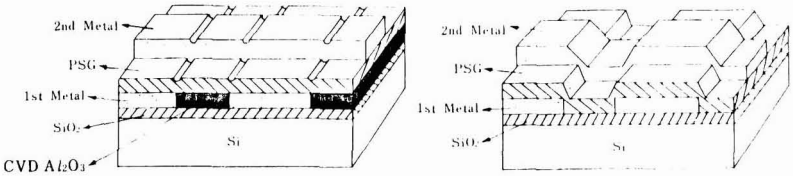


Fig. 1. Schematic cross section of two-level structure. (a, left) Structure made by new method, (b, right) structure made by conventional method.

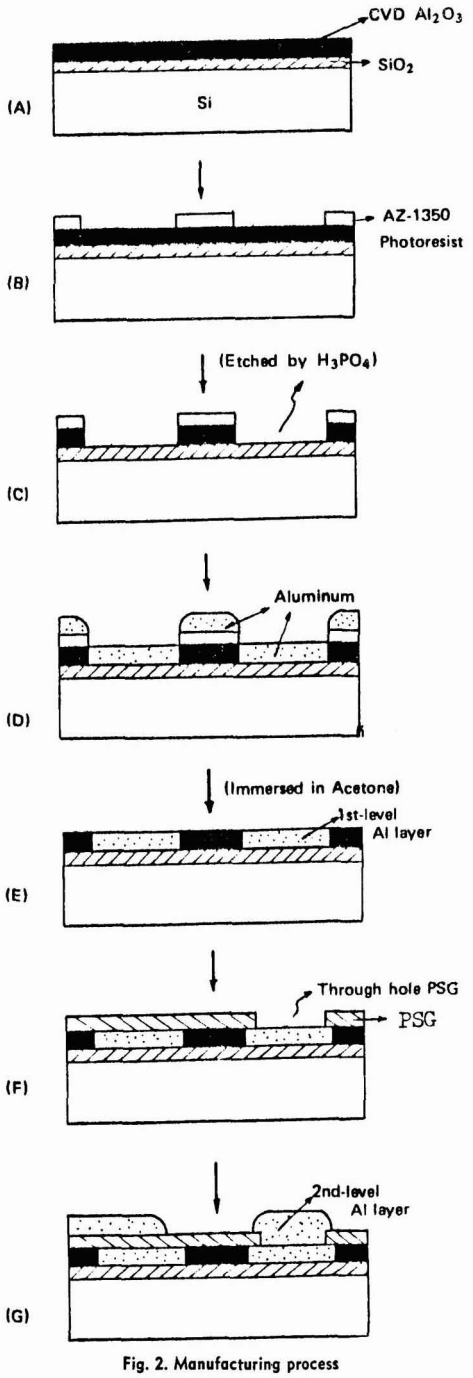


Fig. 2. Manufacturing process

When the wafer is immersed into a solution such as acetone or concentrated sulfuric acid, the AZ-1350 photoresist is dissolved in the solution and the aluminum on the resist is removed. As a result of this operation, the remaining aluminum in spaces between Al_2O_3 areas forms the first-level Al layer as shown in step (E). As mentioned, a self-aligned photolithographic technique is used in this new metallization process; *i.e.*, AZ-1350 photoresist which has been used for formation of the Al_2O_3 areas is also utilized in forming the first-level Al layer.

Additional insulator and second-level Al layer processes are the same as for conventional metal interconnection as shown in steps (F) and (G).

The insulator used in this structure is phosphosilicate glass deposited by a chemical vapor deposition technique, the insulator "through-holes" are patterned by a photoengraving technique, and the second-level Al layer is finally formed. When etching through-holes, a "plasma etching technique" is employed in our process in order to protect the first-level Al layer from corrosion by electrochemical reaction in buffered HF liquid. The specific contact resistance between the first and second-level Al layers through the through-holes was observed to be 4-5 $\times$ 10^{-8} ohm-cm^2.

Properties of CVD Al_2O_3 Film and Effects on Devices

Properties.—Formation of Al_2O_3 films.—The deposition apparatus consists essentially of a bell jar covering a rotating hot plate. A schematic of the apparatus for the deposition of Al_2O_3 film is shown in Fig. 3. Dry nitrogen gas passes through the aluminum triisopropoxide [$Al(i\text{-}C_3H_7O)_3$] vaporizer at a constant temperature of 170°C (vapor pressure = 50 mm Hg), and the organic compound vapor is mixed with more nitrogen gas and transported to the hot plate in the bell jar, where the mixture pyrolizes to form Al_2O_3. We usually deposit at 420°C in our process, when the growth rate is typically 200 Å/min. If deposition is performed in the presence of additional oxygen, the growth rate will increase.

Dielectric breakdown strength measurements.—Some dielectric breakdown strength measurements of this CVD Al_2O_3 film were made using an Al-Al_2O_3-Si structure. The results are shown in Fig. 4. The dielectric breakdown strength of films deposited at 420°C was approximately 4 $\times$ 10^6 V/cm, which is about half the breakdown strength of a thermal SiO_2 film.

Cracking.—In our experiments, we observed cracks developing if thick Al_2O_3 was deposited, or if the film was deposited in the presence of additional oxygen.

In our deposition process, however, we form the film under oxygen-free conditions, so no cracks occur for film thicknesses up to 15,000Å.

Film etch rate.—This CVD Al_2O_3 film is highly soluble in phosphoric acid, especially at high temperature.

The etch rate of Al_2O_3 film in phosphoric acid is shown in Fig. 5, in comparison with that of a thermal SiO_2 film containing P_2O_5. The etch rate for the Al_2O_3 film is approximately 4000 times that of the SiO_2 film.

As an example, the etch rate for the Al_2O_3 films prepared at 420°C was typically 4000 Å/min in 85% H_3PO_4 at 70°C, whereas that of the thermal SiO_2 film containing P_2O_5 was as low as 50 Å/hr. This considerable difference between the etch rates for Al_2O_3 and SiO_2 films makes it possible to delineate selectively buried Al_2O_3 films.

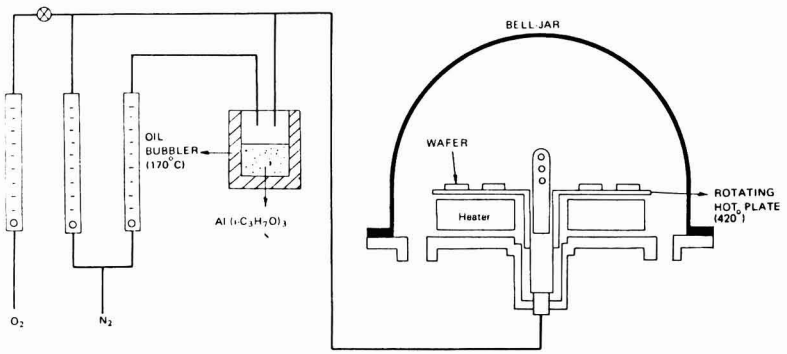


Fig. 3. Schematic of vapor deposition system for preparing Al_2O_3 film.

Effects of Al_2O_3 film on devices.—Since the CVD Al_2O_3 film is formed at a relatively low temperature of 400°-500°C, it may show several electrical properties different from high temperature formed Al_2O_3 films, especially exhibiting bad interface properties with silicon. For example, it is known from the C-V behavior that Al-Al_2O_3-Si (MAS) structures show unstable characteristics because of the presence of mobile electrons in the Al_2O_3 film and charge transfer at the gate electrodes (3, 4). In the new metallization system, however, the presence of the SiO_2 film between the Si and Al_2O_3 eliminates such effects associated with charge transfer at the Si-SiO_2 interface. The flatband surface-state charge density (N_{FB}) characteristics of Al-Al_2O_3-SiO_2-Si structures are shown in Fig. 6, where N_{FB} is plotted as a function of the Al_2O_3 and SiO_2 film thicknesses. It is noted that the thicker the SiO_2 film becomes, the less pronounced the tendency of the Al_2O_3 film to make the surface of the Si more positive.

When this structure is applied to such devices as bipolar IC's, inversion of the collector conductivity may occur. The resistivity of the collector region, however, is usually as high as about 1 ohm-cm, and the thickness of the SiO_2 film is as high as about 7000Å, so we consider it to be free from the influence of Al_2O_3. In this metal process, the Al_2O_3 film is deposited after a contact photolithographic step. Therefore, an insulating layer may be formed on the exposed silicon in the bell jar, which would make it difficult to establish good ohmic contact or to form a Schottky barrier diode. This problem can be overcome by dipping the wafer in a buffered HF liquid just before the Al evaporation step.

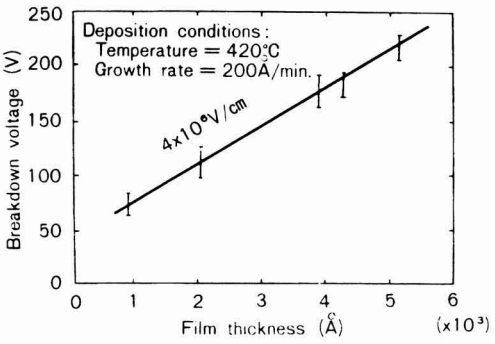


Fig. 4. Dielectric breakdown strength of CVD Al_2O_3 film

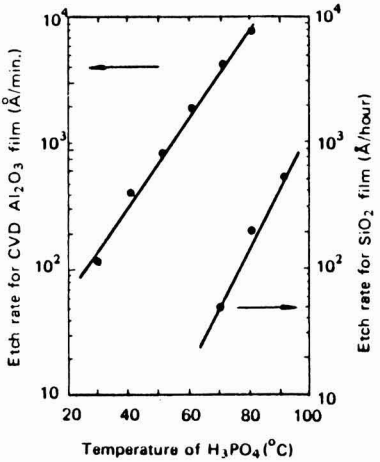


Fig. 5. Comparison of etch rates for CVD Al_2O_3 film and SiO_2 film.

Reliability

Continuity of second-level Al layer.—Observation by SEM and angle-lapping.—Scanning electron microscopy and angle-lapping were used to examine the features of crossovers of leads in new and conventional structures as shown in Fig. 7. Photograph (A) and (C) show the cross section of a chip made by the new method. The thickness of the first-level Al layer is 6500Å, the same as that of the Al_2O_3 film, the interlayer phosphosilicate glass 8000Å, and the second-level Al layer 12,000Å. On the other hand, photograph (B) and (D) show the cross section of another chip made by a conventional method under the same conditions. These photographs indicate that the new structure is very beneficial in realizing surface planarity, whereas

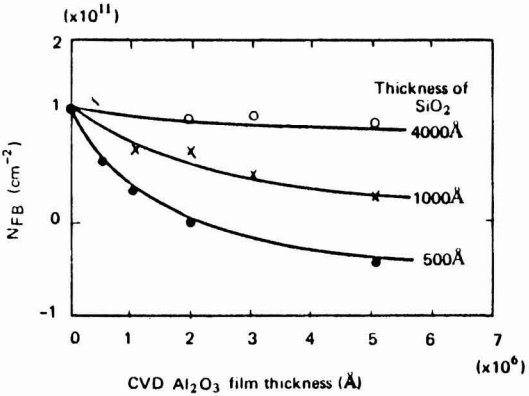


Fig. 6. Characteristics of N_{FB} in Al-Al_2O_3-SiO_2-Si structures

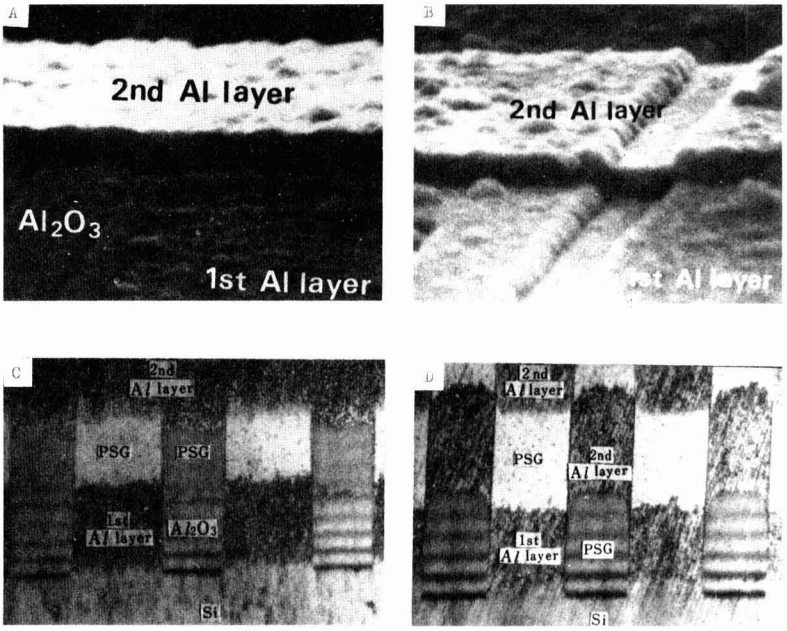


Fig. 7. Scanning electron micrographs (A and B) of crossover and optical photographs (C and D) of angle-lapped surface. A and C, structure made by new method; B and D, structure made by conventional method.

the second-level Al layer of the conventional structure is apt to be cut at the step.

Opens in second Al layer.—The continuity of the second Al layer for several different thicknesses of the first Al layer was checked.

Test patterns were fabricated in which the first Al layers of 20 μm width were 3000, 4500, 7000, and 10,000Å thick, and the second Al layers of 20 μm width were maintained 12,000Å thick. There were the same number of chips for each structure and each chip had 800 crossover points.

The contrast between the number of opens in the second Al layers for the new and conventional structures is presented in Table I. These data show that as long as the thickness of the first Al layer is less than 4500Å, there are no opens for both the new and conventional structures. But when the first Al layer is up to 10,000Å in thickness, the new structure eliminates failures resulting from opens of the second Al layer.

Mean time to failure of the first and second Al layers.—*First Al layer.*—It has been observed that electromigration in aluminum is produced by high current

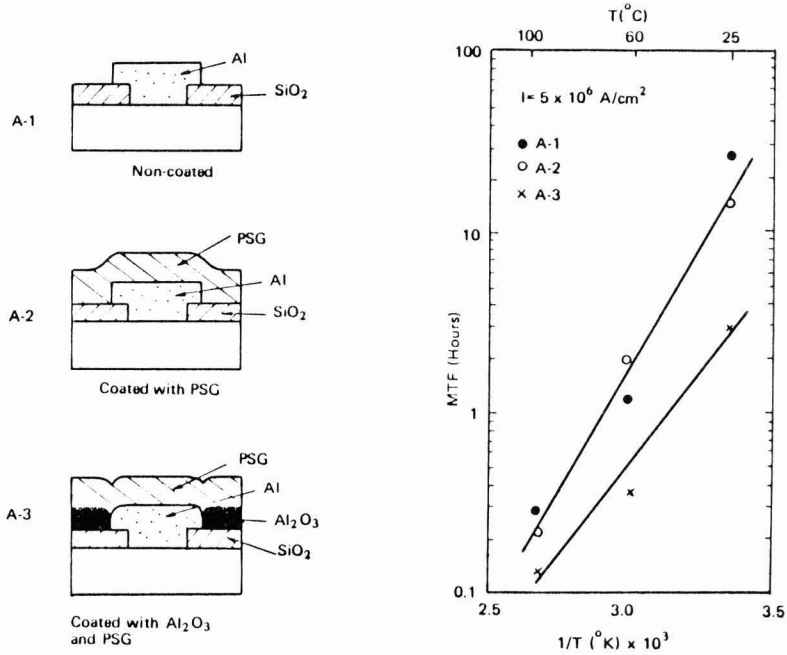
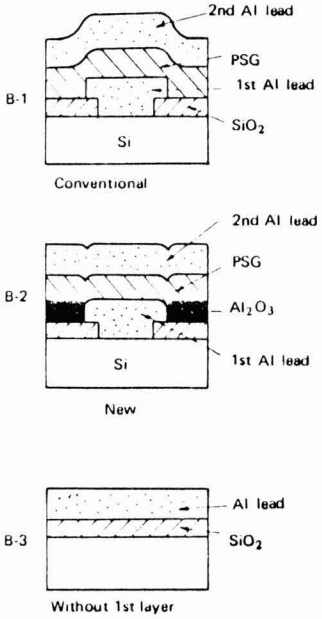
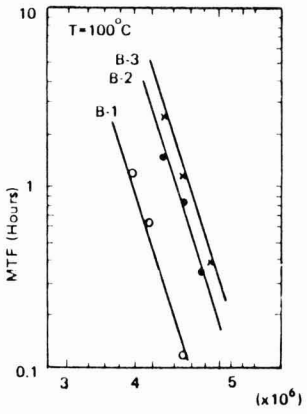


Fig. 8. Mean time to failure vs. temperature of first Al layer for three types of test structure. (a, left) Test structures, (b, right) MTF vs. temperature.



(a) Test structures



(b) MTF vs. current density

Fig. 9. Mean time to failure vs. current density of second Al layer for three types of test structures.

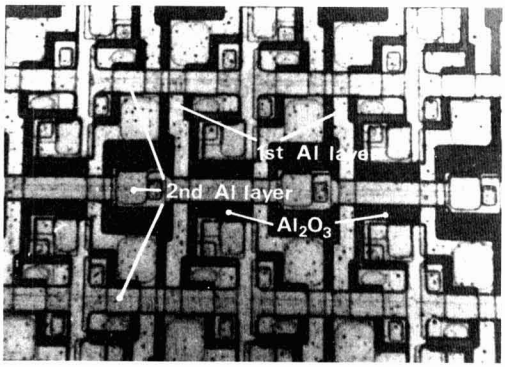


Fig. 10. Two-level LSI pattern using CVD Al_2O_3

densities, which decrease the mean time to failure (MTF) (6). The MTF can be increased by coating the aluminum layer. In the new metal structure, as the first Al layer is coated with Al_2O_3 and PSG films, the MTF is expected to be greater than that of a noncoated Al layer.

Experiments were carried out to evaluate the effects on the MTF of coated first Al layers. In order to compare the MTF of the new structure with others, three types of test structures A-1, A-2, and A-3 were fabricated as shown in Fig. 8(a) where the first Al layer of A-1 is noncoated, that of A-2 is completely coated with PSG, and that of A-3 is coated with Al_2O_3 and PSG. Test strips 20 μm in width and 3000Å in thickness were subjected to a current density of 5×10^6 A/cm^2 at 25°, 60°, and 100°C. Aluminum was evaporated at a rate of 40 Å/sec using electron beam evaporation.

Table I. Number of opens in second Al layer

Thickness of first Al layer, A	New structure	Conventional structure
3,000	0/50	0/50
4,500	0/50	0/50
7,000	0/50	23/50
10,000	0/50	50/50

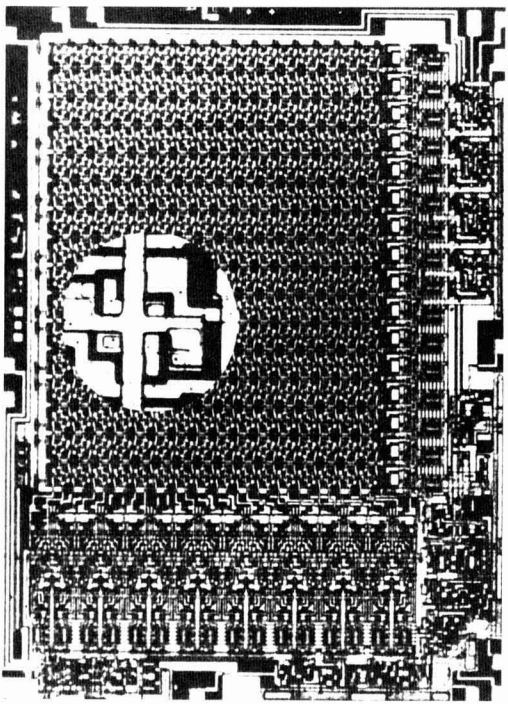


Fig. 11. 256 bit bipolar RAM chip with planar interconnect structure utilizing CVD Al_2O_3.

Data for each structure of MTF *vs.* temperature is presented in Fig. 8(b). We can see that both the new and conventional structures have almost equal MTF, which is greater than that of the noncoated structure.

Second Al layer.—Similarly, experiments were carried out to evaluate the MTF of the second Al layers. Test strips 15 μm in width and 12,000Å in thickness were subjected to a temperature of 100°C at various current densities. In order to compare the MTF of the new structure with others, three types of test structures B-1, B-2, and B-3 were fabricated as shown in Fig. 9(a), where B-1 is a conventional structure, B-2 is the new structure, and B-3 is a test structure without a first Al layer.

Data for each structure of the MTF *vs.* current density is presented in Fig. 9(b). The thickness of the first Al layer is 3000Å, and that of the PSG film is 8000Å. It is noticed that the MTF for the new structure is about five times greater than that of the conventional structure.

Applications

This new planar interconnection technique can be applied to fabricate various LSI chips.

Figure 10 shows an example of a two-level LSI pattern utilizing this technique, and a photograph of a 256 bit bipolar RAM chip fabricated using this new structure is shown in Fig. 11.

Conclusions

A new planar metallization technique has been described for fabricating a two-level structure utilizing CVD Al_2O_3.

It has been shown that a planar interconnect structure can be fabricated using low temperature CVD Al_2O_3 as an insulator between areas of the first-level Al layer, a self-aligned photolithographic technique can be applied in which positive photoresist AZ plays an important role in forming the first-level Al layer and the Al_2O_3 film, and the process for forming the CVD Al_2O_3 film is simple and economical.

This new structure should provide a useful method for establishing a new approach to LSI multilayer structures.

Acknowledgments

The authors would like to thank Dr. S. Nakaya and Dr. T. Imai for their support of this work, and Mr. T. Higashi and Mr. K. Suzuki for their advice and helpful discussions.

Manuscript submitted Aug. 27, 1974; revised manuscript received March 5, 1975. This was Paper 76 presented at the San Francisco, California, Meeting of the Society, May 12-17, 1974.

Any discussion of this paper will appear in a Discussion Section to be published in the June 1976 JOURNAL. All discussions for the June 1976 Discussion Section should be submitted by Feb. 1, 1976.

Publication costs of this article were partially assisted by OKI Electric Industry Company, Limited.

REFERENCES

1. H. Tsunemitsu and H. Shiba, "A Planar Multi-Layer Interconnection," IEDM Technical Program Abstract, Paper 18.4, October 1969.
2. K. Sato *et al., IEEE Trans. Parts, Hybrids, Packag.*, **PHP-9,** No. 3 (September 1973).
3. J. A. Aboaf, *This Journal*, **114,** 948 (1967).
4. M. T. Duffy and A. G. Revesz, *ibid.*, **117,** 372 (1970).
5. C. J. Santro and D. L. Tolliver, *Proc. IEEE*, **59,** No. 10 (1971).
6. T. Satake, K. Sawaguchi, and S. Fujimoto, Paper 67, p. 165, Electrochemical Society Extended Abstracts, Spring Meeting, Washington, D. C., May 9-13, 1971.

Determination of Excess Zn in ZnO

The Phase Boundary Zn-$Zn_{1+x}O$

K. I. Hagemark and P. E. Toren

3M Central Research Laboratories, St. Paul, Minnesota 55101

ABSTRACT

The excess Zn of Zn-doped ZnO has been determined using two different methods. An electrochemical method was used as a direct method. Hall effect measurements at 77°-300°K were used as an indirect method. The agreement between the results from the two methods is good. The Zn-$Zn_{1+x}O$ phase boundary is given in the range 700°-1100°C as log x_{Zn} (ppma) $= -4700/T + 5.6$.

Excess Zn accounts for the n-type character of ZnO. Small changes in the stoichiometric composition have a drastic effect on the physical and chemical properties. However, the Zn concentration level is less than 100 ppm and thus difficult to determine by conventional analytical techniques. Some chemical analytical methods have been reported previously (1-4).

In this paper we discuss the use of two methods, an electrochemical method as a direct chemical method and Hall effect measurements as an indirect method. ZnO single crystals have been equilibrated at 700°-1100°C in Zn vapors from Zn metal kept at the same temperature as ZnO and rapidly quenched to room temperature. As a result Zn-saturated ZnO crystals were obtained. After the Hall effect measurements at 77°-300°K, the crystals were analyzed by an electrochemical technique similar to the one developed by Engell (3). The agreement between the methods is good.

Key words: zinc oxide, coulometry, Hall effect.

Experimental

Crystals.—3M vapor phase grown ZnO crystals were used. Emission spectrometric and mass spectrographic analyses showed no major impurities above 1 ppma (atomic) (4.2×10^{16} atoms-cm^{-3}) except for Si (10-20 ppma). The crystals were cut into bars of typical size $2 \times 2 \times 15$ mm. Excess Zn was introduced into the ZnO crystals by heating the crystals in sealed silica ampuls in saturated vapor of Zn. Doping runs were performed at 700°, 800°, 900°, 1000°, and 1100°C for a length of 2 weeks at the lower temperatures to 2 days at the higher temperatures. After the heat-treatments the crystals were rapidly cooled to room

temperature. A hot concentrated H_3PO_4 etch was used to remove about 50μ from the surface.

Electrical measurements.—A conventional Hall method was used. Details of the method and apparatus are given elsewhere (5).

Electrochemical techniques.—Electrochemical measurements were carried out in a 3-compartment cell with fritted glass disks separating the compartments. The working electrode compartment contained a mercury pool which formed the electrical contact between the external circuit and the ZnO crystal which was floated on it. A platinum counterelectrode and a saturated calomel reference electrode (SCE) were placed in the other two cell compartments.

A Wenking potentiostat was used to maintain the ZnO crystal at a constant potential *vs.* the reference electrode.

Electrolysis current was integrated by a simple analog integrator, built in-house using "μA 741" integrated circuit operational amplifiers and a high quality 10 μF integrating capacitor.

Experimental measurements were carried out by filling the cell compartments with 1.8M H_2SO_4 electrolyte solution, connecting the electrodes (with the mercury pool as the working electrode), and applying the desired working electrode potential while bubbling nitrogen through the stirred solution to remove dissolved oxygen. When the background current at the preset potential (usually −0.2V *vs.* SCE) had decreased to its minimum level (less than 0.01 mA) a weighed crystal of ZnO was dropped into the cell and floated on the mercury pool. The current resulting from the oxidation of Zn° as the ZnO dissolved in the acid electrolyte was integrated and the result used to calculate the equivalents of oxidizable material present in the ZnO crystal. Most of the measurements were made at 40°-50°C to increase the dissolution rate of the ZnO and thus minimize the background current correction.

Results and Discussion

Electrical transport properties.—The electrical resistivity ρ, the carrier concentration n, and Hall mobility μ_H have been measured in the range 77°-300°K. Only the results at 300° and 100°K are given in Table I.

The concentration of excess Zn can be calculated from (*i*) the relationship of the carrier concentration *vs.* the temperature and (*ii*) the Hall mobility at lower temperatures where defect scattering is important.

Carrier concentration analysis.—From semiconduction statistics (6) the concentration of donors N_D and acceptors N_A can be calculated. A more detailed discussion of Zn-doped ZnO is given in Ref. (5) and (7). We have assumed that excess zinc is incorporated into ZnO lattice as hydrogen-type shallow donors. The results of the calculations are given in Table I. We are assuming the excess Zn, x_{Zn}, is simply given by

$$x_{Zn} = N_D - N_A \qquad [1]$$

The ZnO crystal contains 4.21×10^{22} Zn atoms-cm^{-3}. Thus 1 ppma corresponds to 4.21×10^{16} atoms-cm^{-3}.

Hall mobility analysis.—The total mobility μ can be assumed to be expressed as

$$\frac{1}{\mu} = \frac{1}{\mu_L} + \frac{1}{\mu_I} + \frac{1}{\mu_N} \qquad [2]$$

where the lattice mobility $\mu_L = 2.0 \times 10^3$ cm^2-V^{-1}-sec^{-1} at 100°K (9); μ_I is the ionized defect scattering mobility and μ_N is the neutral defect scattering mobility. The expressions for μ_I and μ_N are given in previous papers (5, 8).

The concentration of excess Zn can be estimated by calculating the concentration of ionized centers N_I and of neutral centers N_N. We will only consider the data at 100°K. Since we are dealing with strongly n-type ZnO we are assuming a low concentration of acceptors. Thus

$$N_I \approx n(100°K)$$

where n is the carrier concentration at 100°K. By knowing N_I and n, μ_I can be calculated [from Ref. (5)]. The value for μ_N can then be found from Eq. [2]. The concentration of neutral centers is then (5)

$$N_N = \frac{5.39 \times 10^{20}}{\mu_N} \text{ (cm}^{-3}\text{)}$$

and the concentration of excess Zn is

$$x_{Zn} \approx n(100°K) + N_N$$

The results of the calculations, given in Table I, compare favorably with the results from the carrier concentration analysis.

Electrochemical measurements.—The electrochemical method reported here is similar to Engell's in that both methods involve the measurement of electrochemical oxidation of zinc occurring simultaneously with the chemical dissolution of zinc oxide. Engell calculated the oxidation rate corresponding to a measured steady-state oxidation current, and compared it to the total dissolution rate of the oxide electrode. Our procedure, based on integration of the electrochemical current, is not limited to steady-state currents or electrodes of constant surface area.

Both procedures are based on two assumptions concerning the behavior of the ZnO crystal in the cell: (*i*) that the electrochemical oxidation of Zn° is much more rapid than the chemical solution of metallic zinc in dilute sulfuric acid, and (*ii*) that Zn° is the only oxidizable material present in the ZnO crystal. The first assumption was checked by adding small particles of metallic zinc to the cell in place of ZnO crystals. The integrated current corresponded to greater than 95% of that predicted by Faraday's law. The second assumption rested on the spectroscopic evidence that no metal other than zinc was present in the crystals.

The factors limiting measurement accuracy were the background current and possible integrator drift during the course of the measurement. The effect of both of these factors was minimized by carrying out the measurements at 40°-50°C instead of at room temperature. The higher temperature decreased the time required to dissolve a ZnO crystal from several hours to about 40 min.

Atomic ppm Zn was calculated from

$$\text{ppma} = \frac{\text{(coulombs) (81.38) (10}^6\text{)}}{\text{(mg ZnO) (96.5) (2)}}$$

Table I. Results

Doping temperature, °C	Electrical resistivity ρ and carrier concentration n: 300°K ρ (ohm-cm)	300°K n (cm^{-3})	100°K n (cm^{-3})	100°K μ_H (cm^2-V^{-1}-sec^{-1})	Analyses: Carrier conc x_{Zn} (cm^{-3})	Carrier conc x_{Zn} (ppma)	Mobility x_{Zn} (cm^{-3})	Mobility x_{Zn} (ppma)	El. Chem x_{Zn} (ppma)
700	0.36	1.1×10^{17}	2.0×10^{16}	930	1.6×10^{17}	4	2.2×10^{17}	5	—
800	0.14	3.1×10^{17}	6.6×10^{16}	560	5.6×10^{17}	13	4.8×10^{17}	11	23
900	0.060	7.3×10^{17}	2.0×10^{17}	350	1.0×10^{18}	24	9.5×10^{17}	23	30
1000	0.046	9.5×10^{17}	4.5×10^{17}	210	1.9×10^{18}	45	2.0×10^{18}	47	75
1100	0.017	3.6×10^{18}	3.4×10^{18}	100	$\sim 7 \times 10^{18}$	165	7.7×10^{18}	183	190

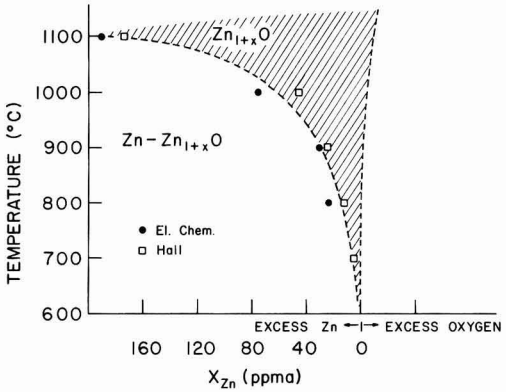


Fig. 1. A portion of the phase diagram Zn-$Zn_{1+x}O$ is shown. The excess Zn boundary has been determined. ● represents the electrochemical data and □ represents results from the Hall effect analysis. The excess oxygen boundary is suggested only.

Results of these measurements are summarized in the last column of Table I.

The phase boundary Zn-$Zn_{1+x}O$.—The values for x_{Zn} in Table I represent the phase boundary Zn-$Zn_{1+x}O$ (the maximum solubility of Zn in $Zn_{1+x}O$). A portion of the phase diagram Zn-$Zn_{1+x}O$ is shown in Fig. 1. The excess oxygen limit of $Zn_{1+x}O$ is probably very close to stoichiometric ZnO (p-type ZnO has not yet been observed).

The phase boundary is also shown in Fig. 2 as log x_{Zn} *vs.* $1/T$ and may be represented as

$$\log x_{Zn} = -\frac{4700}{T} + 5.6$$

This corresponds to average values of the heat of solution $\Delta H = 22$ kcal/mole and entropy of solution $\Delta S = 26$ eu in the temperature range 700°-1100°C of Zn saturated ZnO.

Manuscript submitted Dec. 2, 1974; revised manuscript received Feb. 27, 1975.

Any discussion of this paper will appear in a Discussion Section to be published in the June 1976 JOURNAL.

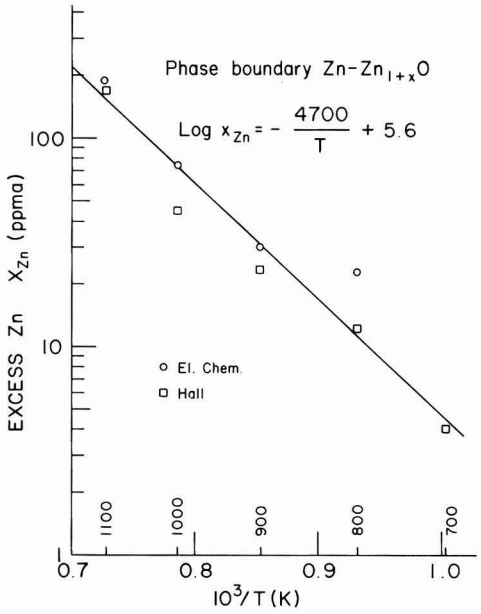


Fig. 2. The excess Zn boundary of $Zn_{1+x}O$ as shown as log x_{Zn} (ppma) *vs.* $10^3/T$(°K).

All discussions for the June 1976 Discussion Section should be submitted by Feb. 1, 1976.

Publication costs of this article were partially assisted by the 3M Company.

REFERENCES

1. H. J. Allsopp, *Analyst*, **82**, 474 (1957).
2. V. J. Normann, *ibid.*, **89**, 261 (1964).
3. H. J. Engell, *Z. Elektrochem.*, **60**, 905 (1956).
4. J. M. Kruse, *Anal. Chem.*, **43**, 771 (1971).
5. K. I. Hagemark and L. C. Chacka, To be published in *J. Solid State Chem.*
6. J. S. Blakemore, "Semiconductor Statistics," p. 133, Pergamon Press, New York (1962).
7. D. G. Thomas, *J. Phys. Chem. Solids*, **3**, 229 (1957).
8. P. Wagner and R. Helbig, *ibid.*, **35**, 327 (1974).
9. A. R. Hutson, *Phys. Rev.*, **108**, 222 (1957).

The Preparation and Properties of Aluminum Nitride Films

T. L. Chu* and R. W. Kelm, Jr.*

Institute of Technology, Southern Methodist University, Dallas, Texas 75275

ABSTRACT

Aluminum nitride films have been deposited on silicon substrates at 800°-1200°C by the pyrolysis of an aluminum trichloride-ammonia complex, $AlCl_3 \cdot 3NH_3$, in a gas flow system. The deposit was transparent, tightly adherent to the substrate, and was confirmed to be aluminum nitride by x-ray and electron diffraction techniques. The deposited aluminum nitride films were found to be polycrystalline with the crystallite size increasing with increasing temperature of deposition. Other properties of aluminum nitride films relevant to device applications, including density, refractive index, dissolution rate, dielectric constant, and masking ability, have been determined. These properties indicate that aluminum nitride films have potential as a dielectric in electronic devices.

Aluminum nitride is a refractory, large energy gap material [sublimation temperature 2400°C (1), energy gap 5.9-6.2 eV (2, 3)] and has chemical, physical, and electrical properties suitable for several applications in electronic devices. For example, its large energy gap, good thermal stability [equilibrium vapor pressure of nitrogen at 1500°C: 0.05 Torr (4)], and chemical inertness [stable in air at temperatures up to 700°C (5)] suggest that aluminum nitride is a good dielectric for active and passive components in semiconductor devices. Aluminum nitride, being a piezoelectric material with a high acoustic velocity, is also well suited for the fabrication of surface wave acoustic devices.

Aluminum nitride has been prepared by several techniques, such as the direct combination of the elements and chemical reactions of gaseous aluminum and nitrogen-containing compounds on substrate surfaces. The direct combination technique requires temperatures in excess of 1500°C (2, 5, 6) and is not suitable for device applications. On the other hand, aluminum nitride films have been deposited on the surfaces of refractory metals, insulators, and semiconductors at considerably lower temperatures by the reaction of aluminum trichloride with ammonia (1, 3, 7-12) and the reaction of trimethylaluminum with ammonia (13). Aluminum nitride films up to 5 μm in thickness have also been deposited on metallic substrates by diode reactive sputtering, and the dielectric properties of sputtered aluminum nitride films were found to be superior to those of bulk polycrystalline material (14). The chemical deposition technique appears to be more compatible with the current device technology; however, the utilization of aluminum nitride in semiconductor devices has not been explored.

In this work, aluminum nitride films have been deposited on single crystal silicon substrates by the pyrolysis of an aluminum trichloride-ammonia complex in a gas flow system. The properties of the deposited films, such as structure, composition, density, refractive index, dissolution rate, dielectric constant, masking ability, etc., have been determined. The experimental methods and results are discussed in this paper.

Preparation of Aluminum Nitride Films

The ammonolysis of aluminum trichloride is commonly used for the deposition of aluminum nitride films. Because of the hygroscopic nature of aluminum trichloride, an aluminum trichloride-ammonia complex was used as the starting material. The complex was prepared by saturating reagent grade anhydrous aluminum trichloride in a fused silica reaction tube with anhydrous ammonia at room temperature. The resulting mass was heated at 350°C in an ammonia flow, and the complex sublimed yielding a white crystalline powder. The composition of the complex, determined by dissolving a weighed amount of the specimen in a known volume of 0.1*N* hydrochloric acid and titrating the excess acid with 0.1*N* sodium hydroxide, was $AlCl_3 \cdot 3NH_3$. This complex is considerably more stable in the laboratory ambient than aluminum trichloride. Its vapor pressure was determined from the extent of vaporization in a sealed silica tube after heating at a predetermined temperature for 24 hr. The vapor pressure data in the temperature range 500°-800°K are shown in Fig. 1; the complex has sufficient vapor pressure at temperatures below 300°C for utilization in the deposition of aluminum nitride. The heat of vaporization of the complex calculated from the slope of this plot was 11.8 ± 0.2 kcal/mole.

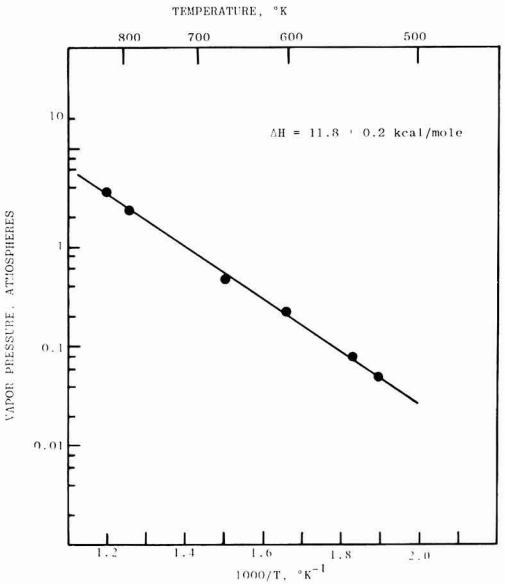


Fig. 1. Vapor pressure of aluminum trichloride-ammonia complex $AlCl_3 \cdot 3NH_3$.

* Electrochemical Society Active Member.

Key words: aluminum nitride, chemical deposition, electronic devices, silicon.

The deposition of aluminum nitride by the pyrolysis of the aluminum trichloride-ammonia complex in a gas flow system was carried out using an apparatus shown schematically in Fig. 2. The diluent gases used in the deposition process were commercial hydrogen purified by diffusion through a palladium-silver alloy and Matheson anhydrous ammonia of better than 99.99% purity. The reaction tube was made of clear fused silica, 55 mm ID and 3 ft long. A fused silica boat containing the aluminum trichloride-ammonia complex was maintained at 250°C by using an external resistance heater, and hydrogen or a 6:1 hydrogen-ammonia mixture at a flow rate of 30 liters/min was used to carry the complex to the substrate surface. The silicon substrates with main faces of {111} orientation were n-type, 5-20 ohm-cm resistivity, and were mechanically polished and chemically etched in the usual manner. They were supported on a silicon carbide-coated graphite susceptor, and the susceptor was heated externally by an rf generator. Prior to the deposition of aluminum nitride, the substrates were heated at 1150°C in hydrogen for ½ hr to remove the oxide on the surface. In some experiments, the substrate surfaces were etched *in situ* at 1170°C with a hydrogen-hydrogen chloride mixture containing 2% hydrogen chloride. The deposition of aluminum nitride was carried out at substrate temperatures in the range of 800°-1200°C, and the deposition time was usually 15-45 min. The thickness of aluminum nitride films on silicon substrates was determined by removing part of the film and measuring the height of the step generated with a Sloan Dektak and Graphic Chart Recorder.

Under the conditions described above, the deposited films are transparent and tightly adherent to the substrate. The average deposition rates in the temperature range 800°-1200°C are shown in Fig. 3. The deposition rate decreased with increasing temperature from 160 Å/min at 800°C to 120 Å/min at 900°C and 90 Å/min at 1000°C. This decrease of deposition rate is due presumably to the increased contribution of gas phase nucleation at high temperatures. The gas phase nucleation becomes more pronounced at higher concentrations of the aluminum trichloride-ammonia complex in the reactant mixture. For example, films deposited at a rate of 750 Å/min at 900°C had a cloudy appearance as a result of the enhanced gas phase nucleation.

The films deposited in the temperature range 800°-1100°C were analyzed by the x-ray diffraction technique. Silicon substrates were removed from the specimens by etching with a nitric acid-hydrofluoric acid mixture, and the resulting material was pulverized and examined by the Debye-Scherrer technique using nickel-filtered CuKα radiation. The diffraction patterns were identical with those reported for aluminum nitride (15), thus confirming that the deposited films were aluminum nitride.

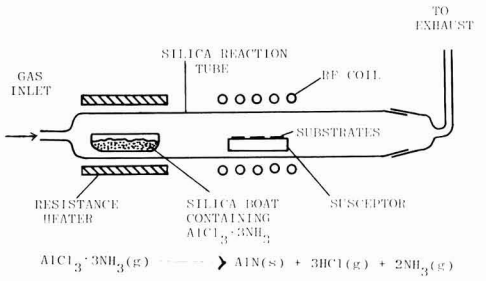


Fig. 2. Schematic of the apparatus used for the deposition of aluminum nitride films.

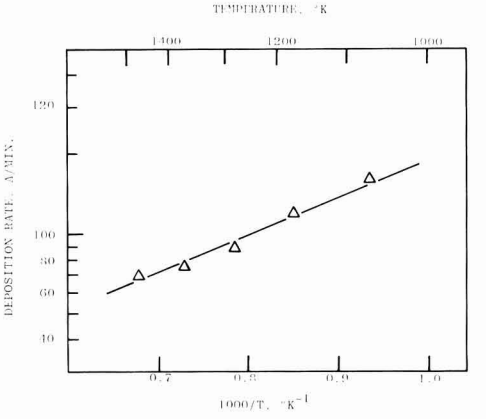


Fig. 3. Average deposition rate of aluminum nitride films as a function of temperature.

Properties of Aluminum Nitride Films

Structure.—Aluminum nitride films deposited on silicon substrates under proper conditions were uniform, transparent, and highly adherent to the substrate. They showed no structural features when examined with an optical microscope. Several films were investigated by transmission electron microscopy using a Hitachi Model 11BU electron microscope after removing the substrates with a nitric acid-hydrofluoric acid mixture. Figure 4 shows the micrographs of aluminum nitride films deposited in the temperature range 800°-1100°C. All films were polycrystalline, and the average linear dimensions of the crystallites increased with increasing deposition temperature. Typical dimensions of crystallites were 100, 200, 600, 1100, and 2200Å in films deposited at 800°, 900°, 1000°, 1100°, and 1200°C, respectively. This increase in crystallite size with temperature is to be expected. The diffraction patterns of aluminum nitride films deposited at various temperatures are shown in Fig. 5. The d-spacings measured from these patterns further confirm that all films are aluminum nitride. Figure 5

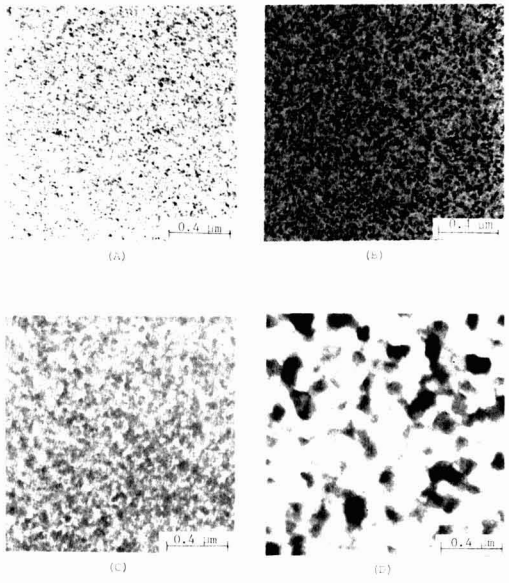


Fig. 4. Transmission electron micrographs of aluminum nitride films deposited at (A) 800°C, (B) 900°C, (C) 1000°C, and (D) 1100°C.

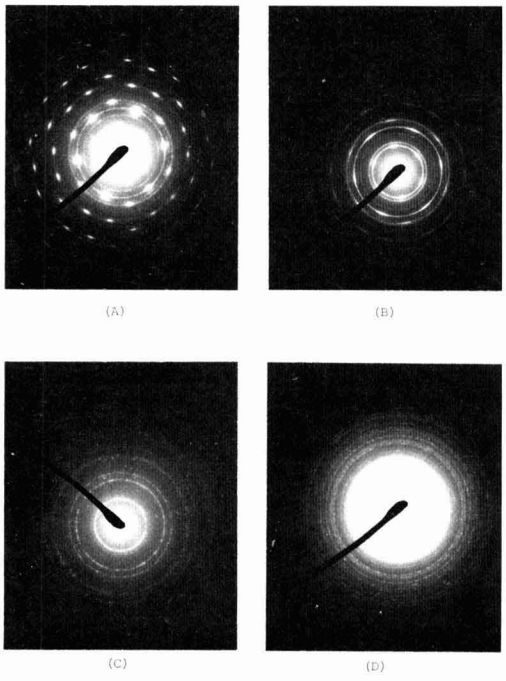


Fig. 5. Electron diffraction patterns of aluminum nitride films deposited at (A) 800°C, (B) 900°C, (C) 1100°C. and (D) 1200°C.

indicates that aluminum nitride films deposited at temperatures above 1000°K are polycrystalline and that preferred orientations are increasingly apparent with decreasing temperature of deposition. The single crystallinity of the substrates appears to have little or no effect on the structural properties of aluminum nitride since aluminum nitride films deposited on the surface of silicon dioxide were essentially the same as those on silicon substrates.

Density, refractive index, and optical absorption.—The density of aluminum nitride films deposited at various temperatures was determined by the floating equilibrium technique using a mixture of 1-bromo 2-iodo benzene and methylene iodide. The temperature of deposition was found to affect only slightly the density of aluminum nitride. Aluminum nitride films deposited at 800°, 900°, 1000°, and 1100°C have densities of 3.15, 3.18, 3.18, and 3.20 ± 0.01 g/cm^3, respectively, as compared with a reported value of 3.13 g/cm^3 (12) and the theoretical density of 3.26 g/cm^3.

The refractive index of aluminum nitride films deposited in the temperature range 800°-1200°C was determined by the Becke line method to be 1.991 ± 0.003, irrespective of the deposition temperature. A few samples were also measured by the ellipsometric technique; the results, though not as reproducible, were usually in good agreement with those by the Becke line method. However, refractive indices as high as 2.17 ± 0.05 have been reported for single crystalline aluminum nitride prepared by the direct reaction of aluminum with nitrogen (16).

The optical absorption spectra of aluminum nitride films deposited under various conditions were taken on a Beckman Model DK-2 spectrophotometer at room temperature. Typical results are shown in Fig. 6, where the thickness of the aluminum nitride film was 18 μm for curve A and 13 μm for curve B. The fundamental absorption edge for all specimens measured was found to be 5.9 ± 0.2 eV, in agreement with that observed by others (2). However, the films deposited at very high rates, 700 Å/min or higher irrespective of deposition temperature, exhibited an additional absorption band in the 3.0 to 3.2 μm region (curve A) while those deposited at low rates, 300 Å/min or lower, showed no absorption in this region (curve B). The absorption in the 3.0-3.2 μm region is presumably due to the N-H or Al-Cl bonds in aluminum nitride films deposited at high rates. As stated previously, the gas phase nucleation becomes pronounced at high deposition rates. The decomposition of the aluminum trichloride-ammonia complex in the gas phase may not proceed to completion, and the deposited material contained N-H or Al-Cl bonds. Thus, the use of low deposition rates is essential for obtaining good quality aluminum nitride films.

Dissolution behavior.—The deposited aluminum nitride films are soluble in phosphoric acid and sodium hydroxide solutions. To determine the dissolute rate of aluminum nitride films, a portion of the specimen was covered with Apiezon Q wax or photoresist, and the specimen was immersed in the etchant with constant agitation for various lengths of time. The dissolution rate was then determined by removing the protective coating and measuring the difference in the step heights using the Dektak system.

The dissolution rate of aluminum nitride films, deposited in the temperature range 800°-1200°C, in a 10% sodium hydroxide solution was determined in the

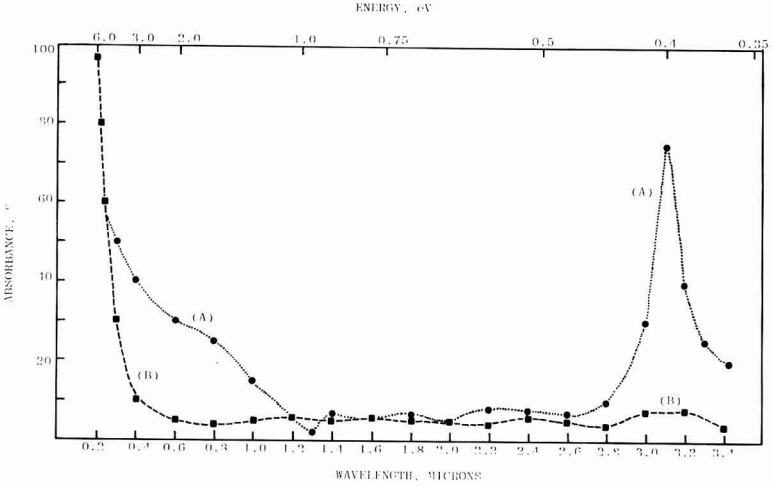


Fig. 6. Optical absorption spectra of aluminum nitride films deposited at a rate of about 700 Å/min (A) and at a rate of about 300 Å/min (B).

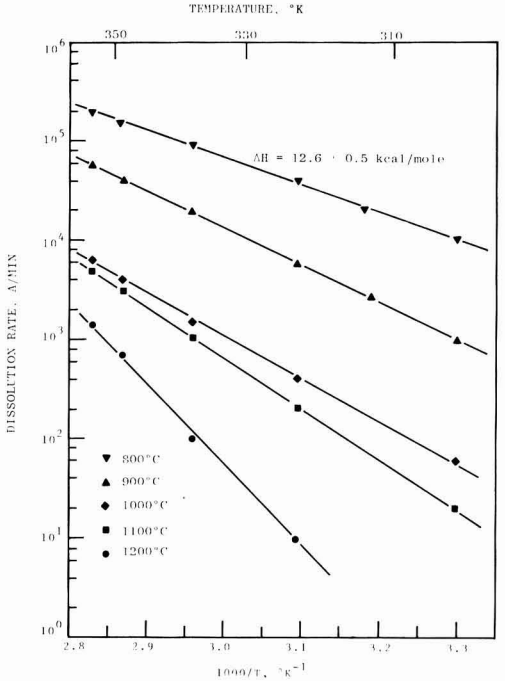


Fig. 7. Dissolution rate of aluminum nitride films, deposited in the temperature range 800°-1200°C, in 10% sodium hydroxide solution.

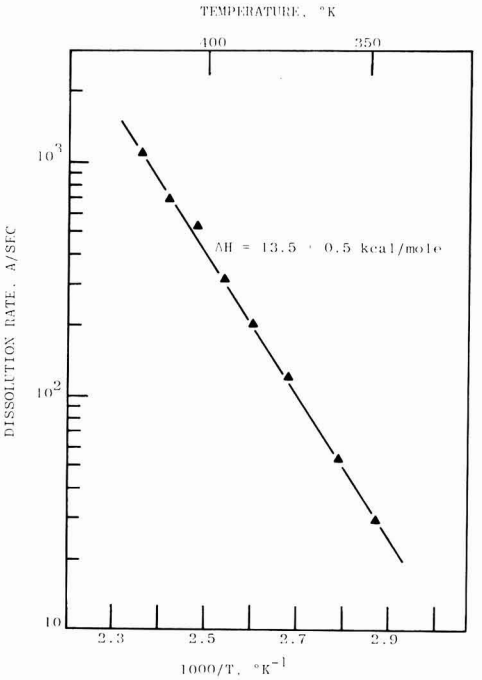


Fig. 8. Dissolution rate of aluminum nitride films deposited at 900°C in 85% phosphoric acid.

temperature range 30°-80°C. The results are shown in Fig. 7. At a given temperature, the dissolution rate of aluminum nitride films decreased with increasing deposition temperature, due presumably to the larger crystallites of aluminum nitride deposited at higher temperatures. Also, the dissolution rate of aluminum nitride films deposited at low temperatures was found to remain the same after annealing at higher temperatures, indicating negligible grain growth. The activation energy of dissolution for aluminum nitride films deposited at 800°C was found to be 12.6 ± 0.5 kcal/mole. The activation energy also increased with increasing deposition temperature. The relatively large activation energy indicates that the dissolution of aluminum nitride films is a surface-reaction controlled process.

The dissolution rate of aluminum nitride films deposited at 900°C was also determined using an 85% phosphoric acid solution. At temperatures up to 50°C, the dissolution rate of aluminum nitride was negligible. Figure 8 shows the dissolution rate in the temperature range 75°-150°C, and the activation energy of this dissolution was found to be 13.5 ± 0.5 kcal/mole, similar to the use of sodium hydroxide solution as an etchant.

Both sodium hydroxide and phosphoric acid solutions used in this work were found to produce clean and structureless surfaces, similar in appearance to the as-grown aluminum nitride films, when examined with an optical microscope.

Masking ability.—To explore the usefulness of aluminum nitride in silicon devices, its capabilities and limitations as masks against the diffusion of boron, phosphorus, aluminum, and gallium into silicon were investigated. Aluminum nitride films of 1000-1700Å thickness, deposited on silicon substrates at 900°C were used in the diffusion experiments. The substrates were n-type, 5-10 ohm-cm resistivity for the diffusion of boron, aluminum, and gallium, and were p-type, 10-20 ohm-cm for the diffusion of phosphorus. The aluminum nitride film was removed completely from circular areas (usually 500 μm diameter) of the specimen by photolithographic techniques using sodium hydroxide or phosphoric acid as an etchant. Sharp, well-defined edges were obtained with virtually no undercutting.

The boron diffusion was carried out by depositing boron oxide glass on the specimen surface at 970°C for 40 min from a boron nitride source followed by redistribution at 1300°C for 1 hr. In the phosphorus diffusion process, phosphorus oxide glass was deposited on the specimen surface at 1000°C for 30 min using phosphorus oxytrichloride as the source, and the redistribution was carried out at 1150°C for 1.5 hr. After the diffusion process, an unmasked region of the specimen was angle-lapped, and the aluminum nitride mask was removed by etching. The resistivity profile on the masked and unmasked regions of the main face and on the beveled surface was measured by the spreading resistance technique (17). The results for the boron diffusion into n-type silicon and the phosphorus diffusion into p-type silicon are shown in Fig. 9. The silicon under the aluminum nitride film was found to have the same conductivity type with essentially no change in resistivity, while p-n junctions were formed in unmasked regions. Thus, aluminum nitride films are successful for masking the diffusion of boron and phosphorus under the conditions used here.

Subsequent to the boron and phosphorus diffusion process, the dissolution rate of the aluminum nitride masks in a 10% sodium hydroxide solution was measured. Aluminum nitride films with boron oxide or phosphorous oxide coatings showed no measurable change in dissolution rate or appearance after heating at 1150°C for 1.5 hr, indicating the inertness of aluminum nitride toward the dopant oxide. However, when the heat-treatment was carried out at 1250°-1300°C after the deposition of boron oxide, the dissolution rate of the nitride films decreased appreciably, indi-

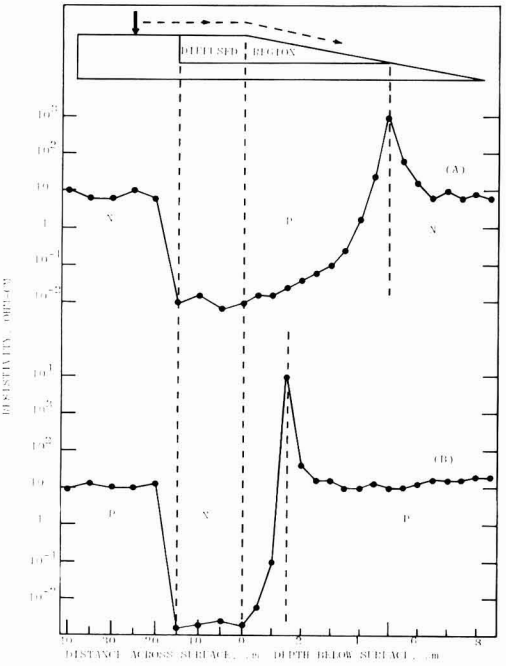


Fig. 9. Resistivity profiles in n-type (A) and p-type (B) silicon specimens after diffusion using aluminum nitride as a diffusion mask.

cating a reaction between aluminum nitride and boron oxide.

The aluminum and gallium diffusions were carried out at 1150°C for 1.5 hr in sealed fused silica tubes using the element as the source material. Aluminum nitride films failed to mask the diffusion of dopant in both cases. This is due presumably to the penetration of aluminum and gallium vapor through the grain boundaries in finely polycrystalline aluminum nitride films at high temperatures.

Dielectric properties.—The dielectric properties of aluminum nitride films were measured at room temperature using aluminum-aluminum nitride-silicon structures. Aluminum contacts of 2.5×10^{-2} cm diameter were deposited on aluminum nitride, and ohmic contacts were applied to the back surface of silicon substrates by electroless plating (18).

The dielectric strength of aluminum nitride films deposited in temperature range 800°-1000°C on low resistivity silicon substrates was measured at room temperature using d.c. and 400 kHz. The average dielectric strength of aluminum nitride was found to be 1.5×10^7 V/cm for films of 300-400Å thickness, independent of deposition temperature; it decreased to the apparent bulk value of approximately 10^7 V/cm for film thicknesses greater than about 1000Å. Aluminum nitride films deposited at 1100°C or above were found to have lower dielectric strength than those deposited at 800°-1000°C, due presumably to the inclusions in the films of the products of volume reaction where the decomposition of the aluminum trichloride-ammonia complex was not complete. The d-c dielectric strength of aluminum nitride films of 2000Å thickness prepared at 800°-1000°C was also measured at higher temperatures and was found to be approximately 10^7 V/cm at 30°C, 5×10^6 V/cm at 100°C, 2.5×10^6 V/cm at 200°C, 1.5×10^6 V/cm at 250°C, and 10^6 V/cm at 300°C.

Capacitance measurements were made on aluminum-aluminum nitride-silicon structures using a Boonton 75C Direct Capacitance Bridge operated at frequencies up to 0.5 MHz. The insulator capacitance was used to obtain the dielectric constant value. The dielectric constant of aluminum nitride films prepared at 800°, 900°, and 1000°C was found to be 11.5 ± 0.2, and that prepared at 1100°C was considerably lower, usually 8.1 ±0.3, as compared with 9.14 reported for the low-frequency dielectric constant of single crystalline aluminum nitride (19). Also, the dielectric constant of an aluminum nitride film prepared at 800°C was found to remain unchanged after heating at 1100°C in hydrogen for 1 hr, again indicating the structural stability of aluminum nitride. The dielectric constant of all aluminum nitride films prepared in the temperature range 800°-1100°C was found to be independent of frequency and temperature in the ranges 5-500 kHz and 100°-500°K, respectively.

It should be mentioned that the properties of aluminum nitride films discussed above are independent of the nature of the carrier gas, hydrogen or 6:1 hydrogen-ammonia mixture, used in the deposition process.

Summary and Conclusions

Aluminum nitride films have been deposited on silicon substrates at 800°-1200°C in a gas flow system by the thermal decomposition of an aluminum trichloride-ammonia complex, $AlCl_3 \cdot 3NH_3$. This complex was prepared by saturating aluminum trichloride with ammonia and purified by sublimation. The deposit was transparent, tightly adherent to the substrate and was verified by x-ray and electron diffraction techniques to be aluminum nitride. Transmission electron microscopy indicated that all aluminum nitride films were polycrystalline; the crystallite size increased with increasing temperature of deposition, and the preferred orientations became more apparent at lower deposition temperatures.

At deposition temperatures in the range of 800°-1000°C, the average density, refractive index, dielectric strength, and dielectric constant of aluminum nitride were found to be 3.18 g/cm^3, 1.99, 10^7 V/cm, and 11.5, respectively. Aluminum nitride films are soluble in sodium hydroxide and phosphoric acid solutions, and the standard photolithographic technique can be readily applied. Aluminum nitride films were found to be capable of masking against the diffusion of boron and phosphorus into silicon from the oxide sources. These properties indicate that aluminum nitride films have great potential as a dielectric in solid-state devices.

Acknowledgment

This research was supported by the Langley Research Center of the National Aeronautics and Space Administration under Grant NGL 44-007-042.

Manuscript submitted Feb. 6, 1974; revised manuscript received March 12, 1975.

Any discussion of this paper will appear in a Discussion Section to be published in the June 1976 JOURNAL. All discussions for the June 1976 Discussion Section should be submitted by Feb. 1, 1976.

REFERENCES

1. Th. Renner, *Z. Anorg. Allg. Chem.*, **298**, 22 (1959).
2. G. A. Cox, D. O. Cummins, K. Kawabe, and R. H. Tredgold, *J. Phys. Chem. Solids*, **28**, 543 (1967).
3. W. M. Yim, E. J. Stofko, P. J. Zanzucchi, J. I. Pankove, M. Ettenberg, and S. L. Gilbert, *J. Appl. Phys.*, **44**, 292 (1973).
4. D. L. Hildenbrand and W. F. Hall, *J. Phys. Chem.*, **67**, 888 (1963).
5. K. M. Taylor and C. Lenie, *This Journal*, **107**, 308 (1960).
6. G. A. Wolf, I. Adams, and J. W. Mellichamp, *Phys. Rev.*, **114**, 1262 (1959).
7. T. L. Chu, D. W. Ing, and A. J. Noreika, *Solid-State Electron.*, **10**, 1023 (1967).
8. A. M. Lejus, J. Thery, J. C. Giller, and R. Collongues, *Compt. Rend.*, **257**, 157 (1963).

9. A. J. Noreika and D. W. Ing, *J. Appl. Phys.*, **39,** 5578 (1968).
10. A. A. Pletyushkin and N. G. Slavina, *Neorg. Mater.*, **4,** 893 (1968).
11. M. D. Lyutaya, I. G. Chernysh, and Z. A. Yaremenko, *iibid.*, **5,** 1929 (1969).
12. D. W. Lewis, *This Journal*, **117,** 978 (1970).
13. H. M. Manasevit, F. M. Erdmann, and W. I. Simpson, *ibid.*, **118,** 1864 (1971).
14. A. J. Noreika, M. H. Francomb, and S. A. Zeitman, *J. Vacuum Sci. Technol.*, **6,** 194 (1969).
15. M. Stackelberg and K. F. Spiess, *Z. Phys. Chem.*, **A175,** 140 (1935).
16. J. Pastrnak and L. Roskovcova, *Phys. Status Solidi*, **14,** K5 (1966).
17. R. G. Mazur and D. H. Dickey, *This Journal*, **113,** 255 (1966).
18. M. V. Sullivan and J. H. Eigler, *ibid.*, **104,** 226 (1957).
19. A. T. Collins, E. C. Lightowlers, and P. J. Dean, *Phys. Rev.*, **158,** 833 (1967).

Technical Notes

Vapor Deposition of Sulfur-Doped GaAs Layers

K. H. Bachem*,[1] and H. Bruch

Institut for Semiconductor Electronics/Sonderforschungsbereich 56 "Festkörperelektronik," Technical University Aachen, Germany

Sulfur is a commonly used dopant in the vapor growth of n-type GaAs epitaxial layers (1-7). The most straightforward approach is to use H_2S as a vapor dopant. This gas can be purchased diluted with hydrogen and bled into the deposition system using a variable leak. However, it appears to be difficult to obtain well-defined and reproducible dopant concentrations due to irreversible changes of the leak rates. Experiments have shown that the variable leaks (Varian, Leybold) commonly used in vacuum systems are calibratable only to within an order of magnitude. Another alternative, the stepwise dilution of the doping gas by using fine metering valves and ball flowmeters requires an extensive apparatus and time-consuming calibration also. These problems are most likely responsible for the large discrepancies in the literature data regarding the relationship between the H_2S concentration in the gas phase and the donor concentration in the epitaxial film (5, 6).

Other workers have used solid sulfur as a primary source (2, 7). The element can be vaporized into the reactor either directly or via an H_2S generator. A drawback of this method results from the difficulties in evaporating sulfur powder or grains with a well-defined vapor pressure. Both the evaporating surface area and the crystalline form and hence the vapor pressure of the sulfur may change during heat-treatment.

In the present investigation we have attempted to find improved sulfur doping methods and to clarify the discrepancies referred to above. This was accomplished by using a capillary for the controlled injection of H_2S or by adding a liquid sulfur compound to the $AsCl_3$ bubbler in the deposition system.

The H_2S doping experiments were carried out in a standard apparatus (8) for the $Ga/AsCl_3/H_2$ process (9). Well-defined concentrations of H_2S were added to the gas stream by controlling, via a reducing valve, the input pressure to a capillary tube of ≈ 150 μm diameter and 6 cm length used for injecting the doping gas into the hydrogen carrier. The system was calibrated by determining the time required to pass a defined amount of gas through the capillary at a given input pressure. The doping gas was a mixture of H_2S (985 ppm) in H_2, bottled in a steel cylinder.

For the second approach S_2Cl_2 was selected as a liquid sulfur dopant source. This compound appears to fulfill the main requirements for use in this application: (*i*) It can be obtained in a relatively pure form. (*ii*) It will decompose at the deposition temperature. (*iii*) In the working temperature range of the $AsCl_3$ source (15°-25°C) its vapor pressure is such that expitaxial layers in the 10^{16}-10^{17} cm^{-3} doping range can be obtained.

The data in Fig. 1 show that the partial pressures of $AsCl_3$ (10) and S_2Cl_2 (11) are equal within approximately 10% around room temperature. Making the likely assumption that the two liquids form an ideal mixture, the ratio of their partial pressures in the vapor phase will be nearly the same as the ratio of their concentrations in the $AsCl_3$-bubbler.

For the S_2Cl_2 doping experiments a reactor was used with two Ga source tubes side by side, each connected to a bubbler, one for $AsCl_3$, the other for the $AsCl_3$-S_2Cl_2 mixture (Fig. 2). In the deposition zone the dopant concentration can be varied either by varying the proportion of the gas streams through the two bubblers or by changing the amount of S_2Cl_2 in the $AsCl_3$ bubbler. The results indicate that after saturation of the Ga source with As along with formation of a GaAs crust (12) a constant sulfur pressure is obtained in the system, and steady-state conditions can be expected during expitaxial growth.

The following starting materials were used: chromium-doped GaAs substrates ($\rho = 10^7$-10^8 ohm-cm, Monsanto) orientated 2° off {100} towards {110}, gallium (99.9999% Johnson Matthey), $AsCl_3$ (Suprapur, Merck), S_2Cl_2 (99%, Riedel-de Hean) redistilled, H_2S (985 ppm in H_2, Matheson). The hydrogen was purified in a Pd-diffuser.

The experimental results in Table I demonstrate the behavior of the deposition system using S_2Cl_2. The epitaxial layers were grown in the listed succession, at a deposition temperature of 740°C, a flow rate of 200 ml/min (tube diameters: source tube 25 mm, substrate tube 55 mm), and an $AsCl_3$-partial pressure of $9.9 \cdot 10^{-3}$ atm. The deposition time was 1 hr. An amount of 5 μl of S_2Cl_2 was added to 100 ml of $AsCl_3$, giving a doping level of $3.4 \cdot 10^{16}$ cm^{-3} determined by Hall effect measurements. By transferring the Ga source into the second source tube connected to the bubbler containing only $AsCl_3$ a doping level of $2.3 \cdot 10^{15}$ cm^{-3} was reached under the same growth con-

* Electrochemical Society Active Member.
[1] Presently on leave of absence at the IBM Research Center, Yorktown Heights, New York 10598.
Key words: GaAs, epitaxy, sulfur doping, gas phase deposition.

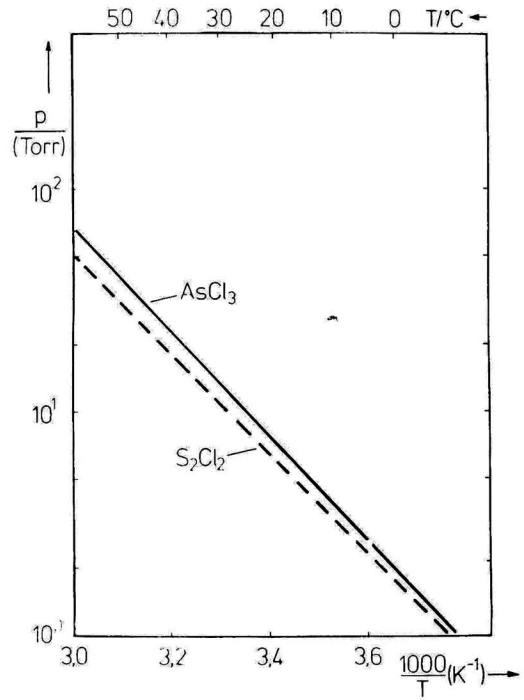


Fig. 1. Partial pressure of $AsCl_3$ and S_2Cl_2 vs. reciprocal temperature [after (9) and (10)].

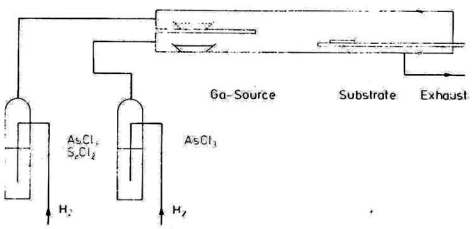


Fig. 2. Schematic diagram of the epitaxial deposition system

ditions. This value is in good agreement with the results obtained for undoped epitaxial layers grown earlier in the same reactor with identical starting material, where as an example a carrier concentration of $1.9 \cdot 10^{15}$ was obtained with an $AsCl_3$ pressure of $11.1 \cdot 10^{-3}$ atm. For the next runs the Ga source was returned to the source tube with the dopant gas stream. Carrier concentrations of $3.1 \cdot 10^{16}$ cm^{-3} and $3.05 \cdot 10^{16}$ were obtained in successive runs. Knight *et al.* (4) found that the apparatus does not exhibit a memory effect when H_2S is injected into the reactor after the Ga source. Our results show that a memory effect is even absent when the entire system

Table I. Experimental results using S_2Cl_2

Sample	Mole fraction S_2Cl_2 in $AsCl_3$ bubbler	Bubbler used	Carrier conc (cm^{-3})
15	5×10^{-5}	with S_2Cl_2	3.4×10^{16}
16	0	without S_2Cl_2	2.3×10^{15}
17	5×10^{-5}	with S_2Cl_2	3.1×10^{16}
18	5×10^{-5}	with S_2Cl_2	3.05×10^{16}
19	1.5×10^{-4}	with S_2Cl_2	1.2×10^{17}
20	1.5×10^{-4}	both	7.8×10^{16}

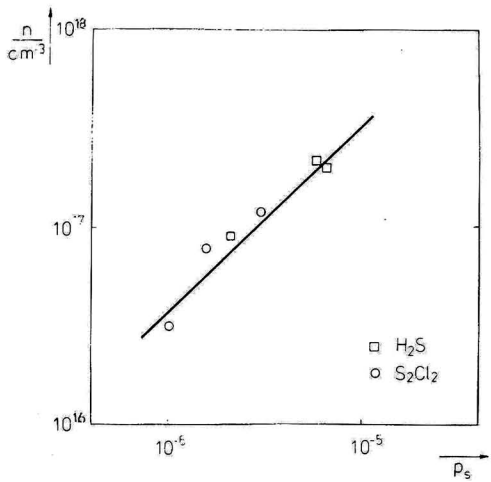


Fig. 3. Carrier concentration vs. partial pressure of sulfur in the gas phase for the H_2S and S_2Cl_2 systems.

including the Ga source has been exposed to sulfur vapor in a previous experiment. Tripling the amount of S_2Cl_2 in the bubbler leads to a roughly comparable increase in the carrier concentration. An intermediate value of $7.8 \cdot 10^{16}$ cm^{-3} was reached by mixing both gas streams with each having a flow rate of 100 ml/min.

Figure 3 compares the carrier concentration obtained for various sulfur pressures in the gas phase both for the H_2S and the S_2Cl_2 systems. Notice first the good agreement between the data for both systems. Of course, such agreement should be expected since at the deposition temperature the composition of the gas phase will be identical in both cases. These results show the proportionality between sulfur pressure and electron density. In calculating the gas phase pressure it was assumed that the system $AsCl_3$-S_2Cl_2 behaves as an ideal solution. Under the assumption that all sulfur incorporated into the films is electrically active it also appears that a relationship analogous to Henry's law exists between sulfur pressure and sulfur concentration in the GaAs. Such behavior was also reported by Rai-Choudhury (13). Of course, it should be realized that the "Henry's law constant" (Table II) derived in this case is not obtained under equilibrium conditions with respect to the GaAs deposition.

Acknowledgment

The authors are indebted to Mr. Schiffers, Institute of Inorganic Chemistry of the Technical University Aachen, for redistilling our S_2Cl_2 dopant material. They would also like to thank Prof. P. Balk for his interest in this project.

Manuscript submitted Nov. 11, 1974; revised manuscript received April 2, 1975.

Any discussion of this paper will appear in a Discussion Section to be published in the June 1976 JOURNAL.

Table II. Relationship between sulfur concentration in epitaxial layer and sulfur concentration in vapor phase

Carrier conc (cm^{-3})	Atom fraction S in epitaxial layer	Atom fraction S in vapor phase	Henry's law constant	Dopant
3.4×10^{16}	7.7×10^{-7}	9.9×10^{-7}	1.28	S_2Cl_2
3.1×10^{16}	7.0×10^{-7}	9.9×10^{-7}	1.41	S_2Cl_2
7.8×10^{16}	1.8×10^{-6}	1.5×10^{-6}	0.83	S_2Cl_2
1.2×10^{17}	2.7×10^{-6}	3.0×10^{-6}	1.11	S_2Cl_2
2.2×10^{17}	5×10^{-6}	5.8×10^{-6}	1.16	H_2S
9.4×10^{16}	2.1×10^{-6}	2.3×10^{-6}	1.09	H_2S

All discussions for the June 1976 Discussion Section should be submitted by Feb. 1, 1976.

Publication costs of this article were partially assisted by the Technical University Aachen.

REFERENCES

1. E. W. Mehal and G. R. Cronin, *Electrochem. Technol.*, **4**, 540 (1966).
2. D. V. Eddolls, J. R. Knight, and B. L. H. Wilson, "GaAs, 1966 Symposium Proceedings," the Institute of Physics and the Physical Society, p. 3 (1967).
3. D. W. Shaw, R. W. Conrad, W. W. Mehal, and D. W. Wilson, *ibid.*, p. 10.
4. S. Knight, L. R. Dawson, J. V. DiLorenzo, and W. A. Johnson," GaAs, 1970 Symposium Proceedings," the Institute of Physics and the Physical Society, p. 108 (1971).
5. J. V. DiLorenzo and G. E. Moore, Jr., *This Journal*, **118**, 1823 (1971).
6. F.-H. Dörbeck, Diss. Institute of Semiconductor Electronics, Technical University Aachen (1971).
7. S. Gisdakis, H. Kniekamp, and D. Schweizer, Verhandl. DPG (VI) **8**, 821 (1973).
8. K.-H Bachem, G. Erlaki, and W. Markert, "Chemical Vapor Deposition, Fourth International Conference," G. F. Wakefield and J. M. Blocher, Jr., Editors, p. 296, The Electrochemical Society Softbound Symposium Series, Princeton, N. J. (1973).
9. J. R. Knight, D. Effer, and P. R. Evans, *Solid-State Electron.*, **8**, 178 (1965).
10. A. Boucher and L. Hollan, *This Journal*, **117**, 932 (1970).
11. A. Landolt-Börnstein, "Zahlenwerk und Funktionen aus Physik, Chemie, Astrophysik, Geophysik und Technik," 6. Aufl., Bd. II, T2a, p. 34, Springer Verlag, Berlin, Göttingen, Heidelberg (1960).
12. D. W. Shaw, *J. Crystal Growth*, **8**, 117 (1971).
13. P. Rai-Choudhury, *ibid.*, **11**, 113 (1971).

Postirradiation Alkali Migration

William Primak

Argonne National Laboratory, Argonne, Illinois 60439

During the course of his ion bombardment studies, Hines noted that the ion charge required to alter the refractive index of glass was greater than that required to alter the refractive index of quartz. He suspected the composition of the glass was altered by selective sputtering (1). Evidence for the migration of alkali ions during electron and ion bombardment appears in the temporal changes occurring during electron and ion probe microanalysis (2). The writer noted that areas of a lithium niobate surface which had been subjected to ion bombardment became decorated with droplets, and from these droplets (over a period of weeks) small crystals formed. They were identified as $LiOH \cdot H_2O$. The decoration could be washed off and would appear again over a period of weeks, repeatedly, evidence of a continuing migration of lithium to the surface (3). Now a number of commercial optical glasses have been subjected to ion bombardment, and the decoration phenomenon has been observed for some of them.

The glasses which were studied were a variety of commercial optical glasses, crown (C-1), borosilicate crown (BSC-2), telescope flint (TF), light barium crown (LBC-1), barium crown (BAK-5), light flint (LF-2), and dense flint (DF). Small areas of polished plates were subjected to ion bombardment with 140 keV D^+ ions for the following accumulated incident charge: 0.018, 0.036, 0.072, 0.108, 0.144, and 0.18 coulombs/cm^2, respectively. Decoration with droplets following ion bombardment during the summer (relative humidity in the laboratory varied between 40 and 60%, temperature controlled to within a degree of 24°C) was most severe on C-1, TF, LF-2, and DF. It was less severe on the barium crowns and was not seen on BSC-2. Decoration reappeared following washing, the time required to obtain droplets easily observed at 50-100X magnification being several days or weeks. Several months later, when the relative humidity had dropped to 20-40% with occasional days at 60%, the specimens were reexamined, and little mounds of solid were seen on the C-1 and TF glasses. Liquid droplets and some solid material were seen on the most highly bombarded areas of the LF-2 and DF glasses. The solid material can form exotic patterns. Probably these are caused by the crystallization rather than being related to structures formed by the ion bombardment. Examples of the decoration are shown in Fig. 1.

Key words: ion bombardment, glass, decoration, electrical leakage.

Water permitted to flow over the specimens will wet the bombarded areas more readily than the surrounding glass surface; and the water will cling to the bombarded areas, but not to the unbombarded areas. Such water adhesion has been interpreted as an indication of cleanliness of the glass surface. It is now seen to have quite a different cause: the bombarded areas have become hygroscopic because of the alkali migration.

The liquid droplets are probably alkali hydroxide solutions, and the deposits which develop are probably largely alkali carbonate. In the ion microprobe work (2), electric charge appeared to facilitate the migration of alkali ions in the solid, for the effects were reduced significantly by flooding the surface with electrons during bombardment or by using neutral atoms instead of ions. Although long-term storage of charge does occur in some materials, it probably did not (in the conventional sense) occur in these glasses which were covered with a solution film and which were washed with water. The freeing of the alkali ions is therefore attributed to a chemical change (such as the change in the valency of another ion or the substitution of some kind of center for the ion) or a structural change. It may be noted that the severity of the decoration effect for these glasses accords with their usually accepted chemical durability (3). Thus the factors which are involved in the chemical attack of glass by water and aqueous solutions (4) are involved in the transport of the alkali ions to the surface, which thus becomes a secondary process following the initial alteration of the glass by the ion bombardment.

When decoration of ion-bombarded lithium niobate was observed, it was the first example of the phenomenon seen in this laboratory. The appearance of liquid droplets could not be accounted for on the basis of the vapor pressure depression caused by lithium hydroxide, because the relative humidity in the laboratory was too low, and the possibility of an electrical effect associated with the charge of a strained piezoelectric material was considered. Now it has been found that irradiation can destroy the piezoelectric effect in lithium niobate. This may serve both to explain the reason why some highly bombarded surfaces showed a lesser decoration effect and to lend support to the hypothesis of an electrical effect. Such an effect is not necessary in the case of these glasses because they contain sodium, and sodium hydroxide is sufficiently more soluble than lithium hydroxide that liquid droplets could form at relative humidities occurring in

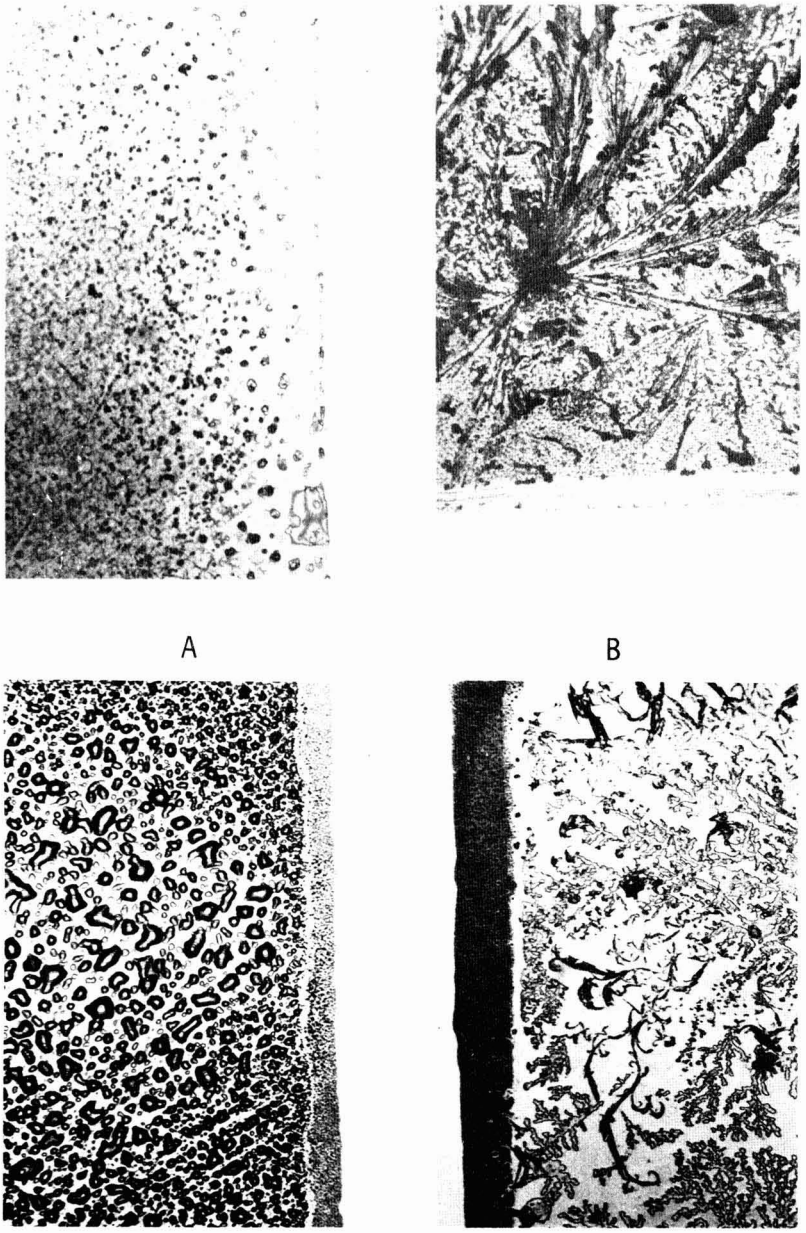


Fig. 1. Decoration of ion bombarded glass caused by water vapor condensation. The specimen areas shown are 0.75 × 1.08 mm. The "penumbral zones" are caused by lack of registry of masking arrangements. All of the decoration begins as liquid droplets. The crystallization depends on the relative humidity, length of storage, the particular glass, and the dose. All of these examples were seen following 140 keV deuteron bombardment (and may have been washed with water) for the following doses: A, C-1 glass, 0.018 coulombs/cm^2; B, C-1 glass, 0.108 coulombs/cm^2; C, TF glass, 0.036 coulombs/cm^2; D, TF glass, 0.108 coulombs/cm^2.

our laboratory. However, the new observations raise the question whether surface impurities may be involved in some of the phenomena observed in the decoration of the lithium niobate. To this end it may be profitable to explore the system LiOH-NaCl-H_2O, and this is planned.

It had been customary to subject glass surfaces intended for coating to ion bombardment. The effect of alkali migration on the film should be considered.

Electrical leakage in ceramic electrical insulation used in radiation environments is a notorious problem. The problems arising from the formation of nitrates in such environments was pointed out many years ago (6). Now effects caused by the alkali migration in these environments should be considered.

The alkali migration may contribute to the difficulties of evacuating glass vacuum systems and to the deterioration of glass structures subjected to bombardment or located in radiation fields.

Acknowledgment

This paper is based on work performed under the auspices of the U.S. Atomic Energy Commission.

Manuscript submitted Jan. 13, 1975; revised manuscript received March 17, 1975.

Any discussion of this paper will appear in a Discussion Section to be published in the June 1976 JOURNAL. All discussions for the June 1976 Discussion Section should be submitted by Feb. 1, 1976.

Publication costs of this article were partially assisted by Argonne National Laboratory.

REFERENCES

1. R. L. Hines, *J. Appl. Phys.*, **28**, 587 (1957); private communication.
2. D. V. McCaughan and R. A. Kushner, in "Characterization of Solid Surfaces," P. F. Kane and G. B. Larabee, Editors, chap. 22, pp. 627-640, Plenum Press, New York (1974).
3. G. W. Morey, "The Properties of Glass," Van Nostrand Reinhold Co., New York (1938).
4. R. H. Doremus, "Glass Science," pp. 242-250, Wiley-Interscience, New York (1973).
5. W. Primak, in "Electrets, Charge Storage and Transport in Dielectrics," M. M. Perlman, Editor, p. 546, The Electrochemical Society Softbound Symposium Series, Princeton, N. J. (1973).
6. W. Primak and L. F. Fuchs, *Nucleonics*, **13**, 3, 38 (1955); *Phys. Today*, **7**, 9, 15 (1954).

JOURNAL OF THE ELECTROCHEMICAL SOCIETY

REVIEWS AND NEWS

JULY 1975

Alkaline Primary Cells[1]

S. Ruben*

Ruben Laboratories, New Rochelle, New York 10801

I would like to relate some history and development of sealed zinc/mercuric oxide alkaline cells. Thirty-two years have passed since the work on sealed zinc/mercuric oxide alkaline cells was initiated, and its history may be of interest.

At the start of World War II there was a need for transreceiver batteries having the ability to withstand tropical conditions with high capacity per unit volume, and maintain a low voltage drop during their effective discharge life.

In 1942 the work initiated at my laboratory utilized the experience obtained in the mid thirties in developing the hermetically sealed C-bias cell and the dry electrolytic capacitor. The bias cell had as its anode a cadmium container separated by a grommet and crimped to the cathode composed of a sintered disk of vanadium pentoxide, sealing in an enclosed gel electrolyte of ammonium glyco-borate. The first sealed alkaline cell structure utilized the type of capacitor structure shown in Fig. 1, with a wide area rolled anode and close spacing to its cathode for low internal resistance (Fig. 2). The cathode in the rolled structure was a 2 mil sandblasted steel strip coated with a layer of cupric oxide and graphite, bonded with a 5% polystyrene solution. This coated strip was rolled at high pressure, producing a low resistance flexible cathode layer. The spacers were a combination of an ionically conductive cellophane layer as a barrier in contact with the oxide to prevent migration of cathode particles, and an absorbent nylon gauze element in contact with the zinc. A dusting of mercuric oxide was applied to the anode before winding, so as to cause amalgamation of its surface when in contact with the alkaline electrolyte. In order to reduce solubility of the cupric oxide in the potassium hydroxide electrolyte, a solidified high concentration electrolyte was used and impregnated into the rolled unit at the electrolyte melting point. After impregnation and electrolyte solidification, the unit was fastened to a composite insulating top. The cupric oxide coulombic capacity and its voltage of 1.06 was not adequate, and other oxide coatings such as mercuric oxide, manganese dioxide, cadmium oxide, and silver oxide were comparatively tested. The mercuric oxide (1.34V) produced the best over-all results. Since the main object was to provide a sealed alkaline cell with maximum capacity per unit volume, the design was changed to one using a steel can cathode in the bottom of which a densely pressed mixture of mercuric oxide and micronized graphite was consolidated. The anode was composed of a spirally wound corrugated zinc strip with an intervening absorbent cotton paper spacer. The winding was in an offset manner, so that the corrugated zinc extended at one end, and paper at the other. Corrugation of the anode was found essential, since it provided space for the zinc oxide produced at the anode when the cell was discharged. After impregnation of the wound unit and its porous spacers, the anode was amalgamated by applying a measured quantity of mercury to the exposed turns of the corrugated zinc, providing an amalgamated junction with zinc top contact without local galvanic action. The barrier was a microporous dialysis paper disk, and other barriers such as sintered magnesium oxide were also used. The potassium hydroxide electrolyte was zincated by dissolving zinc oxide at a temperature of about 100°C.

In order to obtain maximum anode area, another type of rolled anode was used in which zinc was sprayed onto one side of cellophane strip with a "Schori" gun, producing a powdered porous layer of zinc. This was corrugated, wound, and amalgamated in the same manner as the solid zinc strip, but did not make suitable cells because of impurities derived from the spraying equipment. In later cells, the use of pressed

* Electrochemical Society Emeritus Member.

[1] Introductory address at the Alkaline Primary Cells Symposium at the New York, New York, Meeting of the Society, Oct. 13-17, 1974.

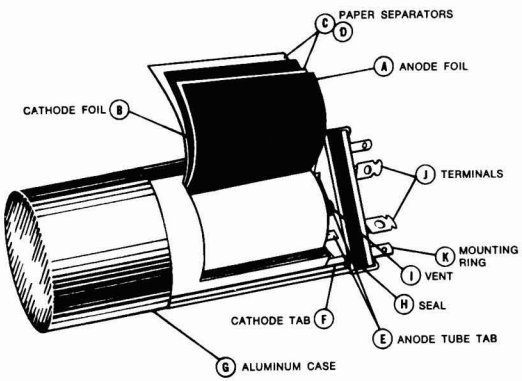


Fig. 1. Dry electrolytic capacitor structure

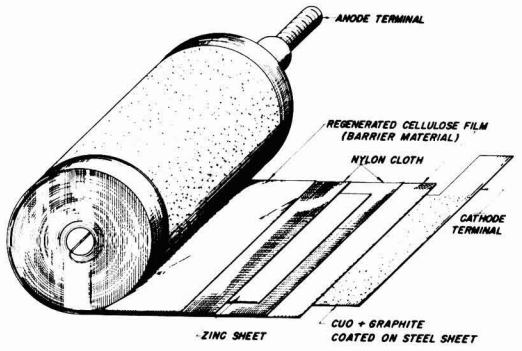
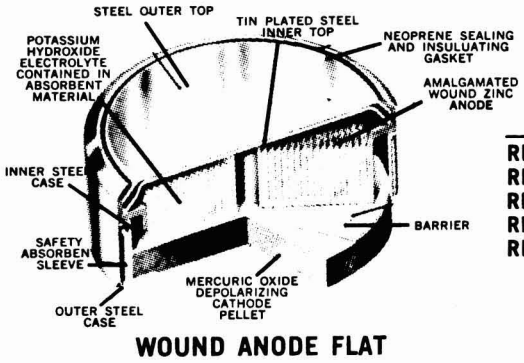


Fig. 2. Wound anode/cathode assembly on first alkaline sealed cells tested.

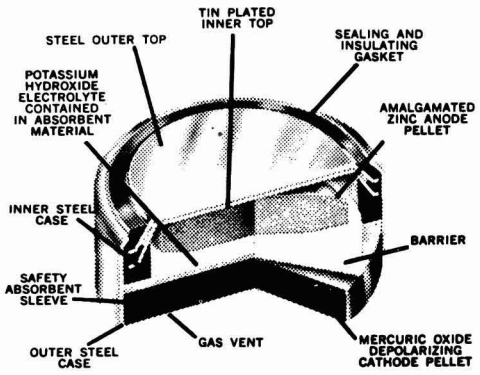


Wound Anode Cells

Type #	Max. Diam. (cm)	Height (cm)	Weight (g)	Rated Capacity (mah)
RM 640	1.587	0.965	9.68	360
RM 3	2.498	1.37	22.56	1500
RM 1438	3.71	1.003	36.22	2700
RM 1450	3.71	1.36	51.80	4500
RM 2550	6.58	1.394	165.20	13,000

Table 1

Fig. 3. Relation of geometry to capacity of wound anode RM cells

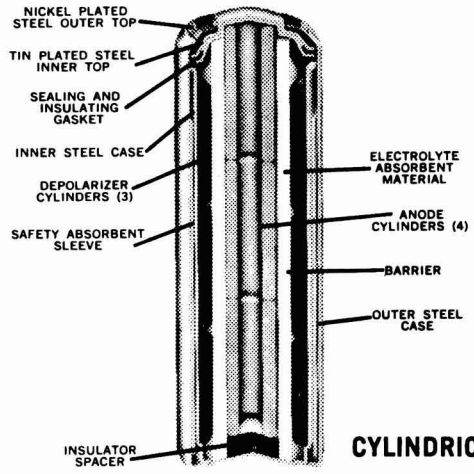


Flat Pressed Powder Cells

Type #	Max. Diam. (cm)	Height (cm)	Weight (g)	Rated Capacity (mah)
RM 312	0.87	0.34	0.56	36
RM 575	1.143	0.33	1.4	100
RM 675	1.143	0.54	2.24	160
RM 630	1.549	0.58	4.76	350
RM 640	1.574	1.104	7.84	500
RM 4R	3.02	1.66	40.88	3,400

Table 2

Fig. 4. Pressed powder flat and button RM cells



Cylindrical Pressed Powder Cells

Type #	Max. Diam. (cm)	Height (cm)	Weight (g)	Rated Capacity (mah)
RM 24	1.0	4.396	14.0	900
RM 601	1.59	2.857	34.16	1800
RM 3R	2.489	1.651	28.56	2200
RM 502	1.358	4.90	30.44	2400
RM 401	1.133	2.844	11.20	800
RM 1R	1.579	1.638	12.04	1000
RM 12R	1.519	4.959	30.88	3600
RM 42R	2.922	6.032	148.33	14,000

Table 3

Fig. 5. Pressed powder cylindrical cathode/anode RM cells

powdered zinc amalgam served the same purpose without the impurity factor.

The most important development for producing sealed alkaline cells was the development of the coulombmetrically balanced cell having equivalent anode and cathode capacities. Since the hydrogen deposition potential is 0.989V and the container overvoltage is 0.15V, the sum of both is less than the zinc half-cell potential of 1.332V in the electrolyte, so that any residual unoxidized zinc would cause hydrogen generation at cathode on continued application of load after the oxygen content of the depolarizer was exhausted. It also basically required that the anode top contact be composed of a nonconsumable but amal-

gamatable material such as copper or tinned steel. In order to compensate for errors in the required measured weights of the anode and cathode materials, an excess amount of cathode was used, in most cases the addition of a small per cent of electrolytic manganese dioxide sufficing. On larger cells an added safety factor against possible gas producing impurities in the cathode materials is applied by using a pressure-vented structure with an outer steel container separated by a cardboard tube which absorbs any electrolyte that may be vented.

Natural manganese ore, on account of its ferrous content, was found to produce dendritic growth on the zinc that caused internal discharge. The available large scale supply of pure manganese dioxide has made possible sealed manganese alkaline cells which, while not having the small voltage change of mercuric oxide during discharge and being of lower capacity per unit volume, have lower cost and are produced on a high volume scale.

Figures 3, 4, and 5 show the relation of capacity to the geometry of the present three types of sealed zinc mercury cells; corrugated wound anode, pressed powder anodes in flat or button form, and pressed powder cylindrical anode cells.

Committees of The Electrochemical Society, Inc., 1975-1976

Executive Committee of the Board of Directors

Theodore R. Beck, Chairman	Spring 1976
Douglas N. Bennion	Spring 1976
Paul C. Milner	Spring 1976
Michael J. Pryor	Spring 1976
Frederick J. Strieter	Spring 1976
Dennis R. Turner	Spring 1976

Admissions Committee

Gunnar D. Stendahl, Chairman	Spring 1976
John L. Everhart	Spring 1977
Martin F. Quaely	Spring 1978

Contributing Membership Committee

Henry F. Ivey, Chairman	Spring 1976
Duane N. Goens	Spring 1976
Howard R. Huff	Spring 1976

Education Committee

Roger Staehle, Chairman	Spring 1976
Ragnar P. Tischer	Spring 1976
Howard Pickering	Spring 1977
Maurice M. Wright	Spring 1977
George R. Gillooly	Term as Chairman, Council of Local Sections
Douglas N. Bennion	Term as Chairman, Technical Affairs Committee
Patricia L. Castro	Term as Chairman, Individual Membership Committee

Finance Committee

Frederick J. Strieter, Chairman	Elected Term as Treasurer
Paul C. Milner	Elected Term as Secretary
Michael J. Pryor	Spring 1976
J. Paul Pemsler	Spring 1976
Donald M. Smyth	Spring 1976

Financial Policy Advisory Committee

Ivor E. Campbell, Chairman	Spring 1976
Frederick J. Strieter	Elected Term as Treasurer
R. Homer Cherry	Spring 1977
Theodore D. McKinley	Spring 1977
N. Corey Cahoon	Spring 1979

Honors and Awards Committee

Erik M. Pell, Chairman	Spring 1979
Theodore R. Beck	Elected Term as President
Morton E. Jones	Spring 1976
J. Bruce Wagner, Jr.	Spring 1976
Sigmund Schuldiner	Spring 1977
Robert E. Visco	Spring 1977
John M. Blocher, Jr.	Spring 1978
David K. Roe	Spring 1978
Glenn C. Cullen	Spring 1979

Individual Membership Committee

Patricia L. Castro, Chairman	Spring 1978
John Broadhead	Spring 1976
Robert S. Karpiuk	Spring 1977

Nominating Committee

David A. Vermilyea, Chairman	Spring 1976
Douglas N. Bennion	Spring 1976
Elton J. Cairns	Spring 1976
Charles K. Mann	Spring 1976
Jerry M. Woodall	Spring 1976

Perkin Medal Award Committee

Theodore R. Beck	Elected Term as President
Michael J. Pryor, Alternate	Spring 1976

Publication Committee

Newton Schwartz, Chairman	Spring 1979
Paul C. Milner	Elected Term as Secretary
Norman Hackerman	Term as Editor
Jerome S. Prener	Spring 1976
Jack H. Westbrook	Spring 1976
Jerome Kruger	Spring 1976
Bruce E. Deal	Spring 1977
Robert T. Foley	Spring 1977

Society Meeting Committee

Paul C. Milner, Chairman	Elected Term as Secretary
Frederick J. Strieter	Elected Term as Treasurer
Ernest G. Enck	Term as Executive Secretary (ex officio) non voting
Donald Tuomi	Spring 1976
Marcus C. B. Hotz	Spring 1977
Walter O. Freitag	Spring 1978

Technical Affairs Committee

Douglas N. Bennion, Chairman	Spring 1976
Dennis R. Turner	Spring 1976
Erik M. Pell	Spring 1976
Thomas B. Reddy	Spring 1977
Ralph J. Brodd	Spring 1978
Forrest A. Trumbore	Spring 1978

Tellers of Election

George L. Schnable, Chairman	Spring 1976
John Broadhead	Spring 1976
Robert P. Frankenthal	Spring 1976
George Bodamer, Alternate	Spring 1976
Glenn C. Cullen, Alternate	Spring 1976
George F. Nordblom, Alternate	Spring 1976

Ways and Means Committee

Michael J. Pryor, Chairman	Elected Term as Vice-President
Douglas N. Bennion	Elected Term as Vice-President
Dennis R. Turner	Elected Term as Vice-President
Richard C. Alkire	Spring 1976
Arnold Reisman	Spring 1976
Joan B. Berkowitz	Spring 1977
Walter W. Smeltzer	Spring 1977

Board Representative for Administration of the Corrosion Handbook Fund

Dennis R. Turner	Spring 1976

Diamond Jubilee Committee (Ad Hoc)

Ralph J. Brodd, Chairman	Spring 1976
Theodore D. McKinley	Spring 1976
Charles W. Tobias	Spring 1976

REPRESENTATIVES TO OTHER SOCIETIES

American Association for Advancement of Science

Alvin J. Salkind	Spring 1976

American National Standards Institute

Subcommittee C-18, Jack Davis	Spring 1976

National Research Council—Assembly of Mathematical and Physical Sciences

Paul C. Milner	Elected Term as Secretary

American Society for Testing and Materials

Committee G-1, Robert T. Foley	Spring 1976

American Electroplaters Society Representative of Electrodeposition Division

John L. Griffin	Spring 1976

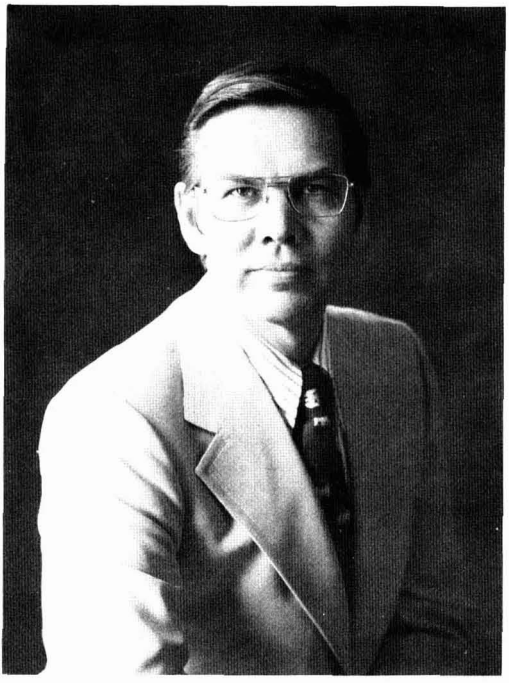
Intersociety Energy Conversion Engineering Conference

Ralph J. Brodd	Spring 1976

Ernest G. Enck To Retire as Society Executive Secretary— To be Succeeded by V. H. Branneky



Ernest G. Enck



V. H. Branneky

Society President David A. Vermilyea announced at the Annual Society Luncheon in Toronto, Canada, a forthcoming change in Society Headquarters personnel. Ernest G. Enck is to become Executive Secretary Emeritus effective September 1, 1975, retiring in February 1976. V. H. Branneky, the present Assistant Executive Secretary, will assume Mr. Enck's responsibilities as Executive Secretary on September 1.

Quoting from President Vermilyea's remarks: "In accordance with long standing plans, Ernie Enck, our Executive Secretary, will retire after twelve years of service on February 1, 1976. On September 1, 1975, he will become Executive Secretary Emeritus in order that we can continue to have his help and advice during the time when the new Executive Secretary will be starting his new duties. All past presidents, officers, and anyone associated closely with this Society knows the contributions which Ernie has made over the years. His knowledge and expertise about the Society are fabulous. He has an extraordinary ability to keep presidents on the track and steer them clear of pitfalls they do not see. His sage counsel and adroit assistance will be badly missed."

A banquet in Mr. Enck's honor will be held during the Dallas, Texas, Meeting of the Society in October of this year when tribute will be paid to the many years of devoted service that Mr. Enck has contributed to the Society's benefit.

Born in Lititz, Pennsylvania, in 1907, Mr. Enck attended Drexel University in Philadelphia, specializing in chemical engineering. His entire professional career from 1926 until 1957 was spent with the Foote Mineral Company, Philadelphia. He joined the company as chemist and became its chemical director in 1934. Elected to its Board of Directors and Secretary of the company in 1936, Mr. Enck became director of procurement for Foote in 1947, in which capacity he traveled extensively, especially in Africa.

Always active in community affairs, Mr. Enck served as Chairman of the Planning Commission of Lower Gwynedd, Pennsylvania, and as President of the Wissahickon Valley Watershed Association, Pennsylvania, for 10 years. He has been a Trustee of the Cape Cod Museum of Natural History, Cape Cod, Massachusetts, and a member of the Advisory Committee of the Chatham Conservation Foundation, Chatham, Massachusetts.

Joining The Electrochemical Society in 1938, Mr. Enck was soon active in Society affairs, especially at first in those of the Philadelphia Section, which he served as Treasurer, as Vice-Chairman, and later as Chairman. He was a member of its Executive Committee and at one time represented his Section at the Council of Local Sections. General Convention Chairman for the Society Meetings held in Philadelphia in 1949 and again in 1959, Mr. Enck was also Finance Chairman for the 1952 Society Meeting. He has also served the Society on the Acheson Award Committee, on the Investment Advisory Committee, and on the Convention Advisory Committee.

Mr. Enck ran successfully for Society office in 1960 to become Society Treasurer 1961-1964. He was re-elected to serve a second three-year term (1964-1967) as Treasurer in the fall of 1963, but his keen interest in the Society was also to be appreciated in another capacity, when, on the unexpected death of the then Executive Secretary, Robert K. Shannon, in January 1964, Mr. Enck was able and willing to assume the added responsibilities of Acting Executive Secretary. At this

continued over

time he was, of course, already heavily involved in Society affairs as Treasurer, Chairman of the Finance Committee, and member of the Board of Directors and Executive Committee. At the May 1964 Society Meeting in Toronto, it was announced that Mr. Enck would resign from his office of Treasurer in order to become the Society's Executive Secretary. Mr. Enck has been keeping things running smoothly ever since, and under his guidance major reorganizations of financial and publication procedures took place, Extended Abstract and Symposium Volumes came under Society sponsorship, membership records were computerized, and a new approach to planning Society Meetings was developed. It was also under his supervision that the removal of Society Headquarters from New York City to its present location in Princeton, New Jersey, took place.

V. H. (Bud) Branneky, who for 6 years has been Assistant Executive Secretary of the Society, was born in St. Charles, Missouri, in 1927. After enlisting in the Army Specialized Training Program upon graduation from high school, he was sent to the Universities of Kansas and Wyoming, graduating in June 1949 cum laude from Elmhurst College, Elmhurst, Illinois, on his return from the Pacific theater. Mr. Branneky proceeded to work toward his master's degree, and in the summer of the next year he received his M.B.A. in financial and marketing management from Washington University, St. Louis, Missouri.

Mr. Branneky's early professional career was spent in the St. Louis area where he worked in the financial and cost analysis field for 10 years. Before moving to Boston in October 1960, he was senior financial planner for McDonnell Aircraft. Since 1960 Mr. Branneky has been involved almost entirely with non-profit organizations: he was Assistant Executive Secretary of the Metallurgical Society of A.I.M.E. and Secretary-Treasurer of the Radio Free Europe Fund.

So it was with this strong professional background that Mr. Branneky joined The Electrochemical Society Headquarters staff in April 1969. It is of interest to note that he was by that time no stranger to Mr. Enck, as they had cooperated in 1966 when the Metallurgical Society of A.I.M.E. and The Electrochemical Society cosponsored the Second International Conference on Electron and Ion Beam Science and Technology in New York City in that year. Mr. Enck was to remember Mr. Branneky's organizational and planning abilities when, in 1968, an Assistant Executive Secretary for the Society was being sought, and at that time he suggested to Mr. Branneky that he "come aboard."

Since joining Society Headquarters staff, Mr. Branneky has been deeply involved in the planning of Society Meetings. The Board of Directors decided in 1972 that Society Meetings would become the responsibility of The Electrochemical Society Headquarters, thus allowing the Local Sections involved to be free to perform their duties as Host Committees, and Mr. Branneky has borne the responsibility for these operations. Mr. Branneky is also Secretary to the Individual Membership Committee, the Society Meetings Committee, and to the Symposium Subcommittee of the Technical Affairs Committee. He was in charge of the mechanics of the Headquarters office move to Princeton, New Jersey, in 1971, and has most recently been responsible for the preparation and execution of the Publication Survey of Society members, subscribers, and contributors.

A long-time interested and willing participant in community activities, on his relocation to New Jersey in 1973 Mr. Branneky was elected a trustee of the First Presbyterian Church of Pennington, New Jersey. He is also a member of the Missouri Club of New York and of the Elmhurst Alumni Association, for which he has organized reunion meetings.

ECS SUMMER FELLOWSHIP AWARD WINNERS FOR 1975



Mary R. Suchanski



James B. Flanagan



Thomas P. DeAngelis

The Summer Fellowship Awards Committee of the Honors and Awards Committee has selected the recipients of three Summer Fellowship Awards for the summer of 1975. Each award is in the amount of $1000, to cover the period June-September 1975, one designated as the Edward Weston Fellowship, one as the Colin Garfield Fink Fellowship, and one as the Joseph W. Richards Fellowship. The funds for these awards are derived from the Edward Weston Fund, the Colin Garfield Fink Fund, and the Consolidated Fellowship Fund.

The Summer Fellowship Awards are made "without regard to sex, citizenship, race, or financial need. They shall be made to graduate students pursuing work between the degrees of B.S. and Ph.D., on a subject in a field of interest to The Electrochemical Society, in a college or university in the United States or Canada, and who will continue their studies after the summer period."

The following are the recipients of the Fellowship Awards for 1975:

Miss Mary R. Suchanski, a graduate student at Northwestern University, Evanston, Illinois, was designated as the winner of the Edward Weston Fellowship.

Mr. James B. Flanagan, a graduate student at California Institute of Technology, Pasadena, California, was awarded the Colin Garfield Fink Fellowship.

Mr. Thomas P. DeAngelis, a graduate student at the University of Cincinnati, Cincinnati, Ohio, was selected as the recipient of the Joseph W. Richards Fellowship.

Miss Suchanski's area of research is resonance Raman spectroelectrochemistry (RRSE) in which advantage is taken of the greater sensitivity of resonance Raman spectroscopy (RRS) vs. normal Raman spectroscopy (NRS) to monitor visible absorbing radical ions generated electrochemically. The radical cations and anions can be generated in bulk solution by controlled potential coulometry or in the diffusion layer at a microelectrode by cyclic potential step methods. Monitoring transients generated via the cyclic potential step method affords the observation of species which are stable on the order of 1 sec but which decay over longer periods of time. In addition to permitting identification and monitoring of electrogenerated species, this technique provides fundamental spectroscopic information, such as the frequencies of the totally symmetric normal modes of ground-state radical ions.

These techniques will be used by Miss Suchanski this summer to investigate a series of phenyl substituted alkenes in the hopes of observing both the monopositive and mononegative species of the same molecule. Miss Suchanski will study isotopically substituted aromatic amines by these methods to aid in the interpretation of the resonance Raman spectra of their radical cations and dications. Miss Suchanski also plans to obtain the resonance Raman spectra of tetracyanoquinodimethane (TCNQ) salts covalently attached or chemisorbed on an electrode surface by cyclic potential step RRSE. She anticipates that cyclic potential step RRSE will allow positive identification of surface electrode species and open the way for further surface work at electrodes.

Mr. Flanagan has been investigating the relatively new electrochemical technique called coulostatics and its implementation using a laboratory digital computer for experiment control and data acquisition and analysis during the last year. In the coulostatic technique an electronic charge is injected into the double layer capacitance of an electrode, and the potential decay as a result of a Faradaic process is observed at open circuit. Advantages of this approach include no IR drops in solution and very rapid injection times, allowing the study of very fast electrode reactions. A significant disadvantage is that there is no general mathematical solution for the potential-time transient. Mr. Flanagan has developed a method of "simulating" the transient which converges to high accuracy in only a few seconds of computer time. Combining the simulation with a nonlinear regression routine allows the on-line analysis of data to determine the characteristic constants (e.g., standard rate constant, transfer coefficient, standard potential, etc.) of the reaction. In addition to data analysis, Mr. Flanagan has also been concerned with hardware design and interfacing with the minicomputer in his laboratory. The full integration of hardware and software should be completed within the next few months, allowing a fully automated data acquisition and analysis scheme for the study of very rapid electrode reactions via coulostatics.

Mr. DeAngelis's general area of research involves the development and characterization of thin-film mercury electrodes which are optically transparent. Optically transparent electrodes allow one to monitor optical changes in the system under study with simultaneous electrochemical measurements. Mercury film electrodes take advantage of greater hydrogen overvoltage, extending the negative potential range beyond that of solid electrodes such as platinum. Mercury film electrodes can also be used in the thin layer configuration, allowing spectroelectrochemical study of small volumes of solution. They have also proven useful in the analysis of trace metal ions by differential pulse polarography on small volumes (50 μl) of solution.

To date Mr. DeAngelis has developed and characterized a mercury film nickel minigrid (333 lpi; 57% T) optically transparent thin layer electrode. Among its main advantages are: (i) greater cathodic potential range than the mercury-platinum optically transparent electrode, (ii) no decrease in transparency of the electrode on addition of mercury as opposed to mercury-platinum optically transparent electrodes, and (iii) qualitative and quantitative analysis on small volumes (50 μl) of solution. The electrode has been shown to be particularly useful in studies involving mediators such as methyl viologen and in a spectroelectrochemical, mechanistic study of vitamin B_{12}. Differential pulse anodic stripping voltammetry has been applied to this thin layer cell permitting analysis of Pb^{2+} at the low ppb level on 50 μl of solution. In many cases the small volume cell makes dilution of the sample unnecessary thus lowering the detection limit and increasing sensitivity.

Due to slow amalgamation of nickel with mercury, the nickel grid has a limited lifetime as does a mercury-platinum optically transparent electrode. The lifetime is limited by physical deterioration of the minigrid and is dependent on the amount of mercury deposited. Mr. DeAngelis's work this summer will involve investigation of other metal substrates which are less soluble in mercury, and hence might be expected to contribute less surface catalytic effect toward the formation of H_2. Certain metals available in thin foil form and also a new grade of carbon show very limited if not complete absence of amalgamation with mercury. This should extend the lifetime of the electrode and minimize the effects of the substrate metal on the electrode's properties. If the foils prove useful as electrode substrates, the above metals could be vapor deposited onto glass forming an optically transparent electrode.

Characterization of the thin-film electrodes with the above metals as substrates would involve the following: (i) electrodeposition of mercury on the substrate and subsequent measurement of the shift in hydrogen overvoltage, (ii) cyclic voltammetry, charge-potential, and current-potential measurements on known systems, (iii) study of the mercury film deposit by surface analysis with scanning electron microscopy and ESCA, (iv) study of the durability and reproducibility of the electrode, and (v) determination of potential analytical applications of the electrode. Mr. DeAngelis will further pursue the utility of differential pulse polarography in thin layer electrodes. The best substrate possible is required here to minimize amalgamation, reduce intermetallic compound formation, and limit residual current.

DIVISION NEWS

Electrodeposition Division

Symposium on Selective Plating

The Electrodeposition Division is planning a symposium on Selective Plating for the Fall 1976 Society Meeting in Las Vegas, Nevada. Selective plating is a very active field these days especially where precious metals are involved such as gold. This symposium will present a broad overview of the science and technologies involved in selective plating of all types. It will also provide a forum for presentation of new work which contributes new knowledge or new technology to the general topic of selective plating.

Papers are solicited for the symposium on such topics as: chemical and mechanical masking; fluid flow masking; anode shape effects and techniques; plating cell design theory and techniques; electroless plating; and selectively catalyzed surfaces.

Suggestions and inquiries should be sent to Symposium Co-Chairmen: Dennis R. Turner, Bell Laboratories, 600 Mountain Ave., Murray Hill, N.J. 07974 or Warren R. Doty, Udylite Corp., 21441 Hoover Rd., Detroit, Mich. 48234.

H. JERMAIN CREIGHTON, 1886-1975

Henry Jermain Maude Creighton was born in Dartmouth, Nova Scotia, on March 2, 1886. He received the degrees of Bachelor of Arts in 1906 and Master of Arts in 1907 at Dalhousie University. From 1908 to 1910 he was an 1851 Exhibition Scholar at the University of Birmingham, England, where he received the degree of Master of Science in 1909. He studied at Heidelberg University during the years 1909 and 1910 and received the degree of Doctor of Science at the Technische Hochschule in Zurich in 1911 after a year's study.

After receiving his doctorate Dr. Creighton joined the faculty of Dalhousie University as Lecturer in Physical Chemistry. In 1912 he was invited to Swarthmore College, Pennsylvania. He became head of the Department of Chemistry in 1928 and retained that position until his retirement in 1949. In 1948 he received the honorary degree of Doctor of Laws from Dalhousie University.

In 1943 he was on leave of absence to join the Manhattan Project with which he was associated until February 1946. For over a year he was liaison officer between the SAM-laboratories and the Houdaille-Hershey Company.

Dr. Creighton carried out two outstanding researches for which he received honors.

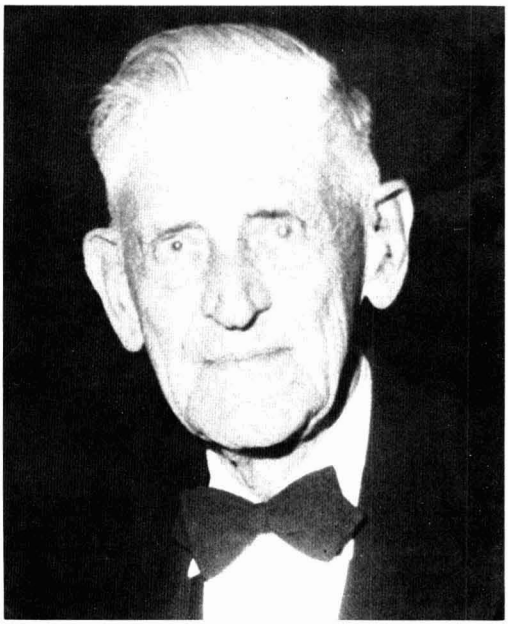
During the year 1913 he was called upon to investigate a concrete building which had collapsed. He noted that the foundation had been in contact with salt water. As a result of his observation he became interested in studying the action of salt water on concrete and on the iron reinforcements. In 1918 he received the Longstreth Medal from the Franklin Institute for a paper entitled "The Deteriorating Action of Salt and Brine on Reinforced Concrete."

At about this time Dr. Creighton was asked by the Atlas Powder Company to study the problem of producing mannitol. The price of glycerine was excessively high then, and it was thought that mannitol could be used as a substitute. It was known that the hexose sugars could be reduced to the alcohols by sodium amalgam, but this was not industrially feasible. Dr. Creighton saw that the problem might be solved if the reduction were carried out electrolytically. This he succeeded in doing at a mercury cathode. There were certain disadvantages in the use of mercury, however, among which were a large capital investment and the cost of agitation. A cathode which could be placed in a vertical position was, therefore, necessary, past which the catholyte could be transported by a circulation pump. Dr. Creighton found that amalgamated lead was inexpensive and extremely effective. The Atlas Powder Company put the process into operation in 1937 and used it for twenty years.

In 1939 Dr. Creighton was awarded the Potts Medal for "his distinguished work in developing a process for the electrolytic reduction of simple sugars on a large scale." In 1940 he received the Modern Pioneer Award from the National Association of Manufacturers. The citation in part was as follows: "Dr. Creighton has developed a process for the electrolytic reduction of simple sugars on a large scale. This work has been responsible for the development of a new large-scale industry and is distinguished as a pioneer development in the use of any electrochemical organic reduction process." In 1946 he received the Acheson Medal and Award from our Society. It is believed that at that time this was the only large-scale electro-organic process in operation in this country, and Dr. Creighton was the first electro-organic chemist to receive the Acheson Medal.

Dr. Creighton's chemical interests have been wide. He began to contribute to the chemical journals very early in his career. In fact, his first publication appeared when he was a student at Dalhousie University. He has published in the following fields: organic chemistry, biochemistry, photochemistry, radiochemistry, quantitative analysis, colloid chemistry, theoretical and applied electrochemistry, physical chemistry, inorganic chemistry, corrosion, dyes, sanitary chemistry, and chemical education.

Dr. Creighton was interested in many societies. He served our Society in many capacities, on committees, as a member of the Board, and in 1939, as President. He was instrumental in organizing the former Electro-Organic Division. He was Chairman of two committees of the Franklin Institute and a member of its medal committee. He was Chairman of the Philadelphia Section of the American



H. Jermain Creighton

Chemical Society, Councilor of the American Association for the Advancement of Science, Vice-President of the Maritime Chemists Association, Councilor of the Nova Scotian Institute of Science, and Editor of its Transactions. He was a Fellow of the Chemical Institute of Canada and a member of The Chemical Society, the Faraday Society, and the Deutsche Bunsen Gesellschaft. He was a member of Phi Beta Kappa, The English Speaking Union, the Royal Commonwealth Society, and the Overseas League of London.

A most important part of Dr. Creighton's life was his teaching. He wrote one of the very best books on the principles of electrochemistry, which went into a fourth edition. He taught both elementary and advanced physical chemistry for many years. In appraising his teaching ability it was said by one of his former students, himself a distinguished head of a chemistry department, that Dr. Creighton's advanced course was particularly stimulating and that his elementary lectures were so good that a textbook was unnecesssary.

Dr. Creighton was a man who enjoyed good company and good food. He attended the monthly meetings of the Board of the Society until Dr. Fink retired as Secretary. He would then have dinner and take the train back to Philadelphia with another friend, who was also a member of the Board. On occasions he would be accompanied by yet another friend. When he was liaison officer for the Manhattan Project he would have dinner with friends in Chicago. He spent his summers in a cottage in Nova Scotia, where he spent most of his summers, sailing, fishing, and cooking his own meals, which visitors described as wonderful. After retirement he established the routine of spending his summers in the north and winters in the southern hemisphere to avoid the cold weather. He would travel from the west coast, after seeing friends there, as the only passenger on a freighter around South Africa to "his" England, where he visited friends in London and bought his clothes. Upon his arrival in New York after contacting his son and daughter, when possible, he would return to Swarthmore to relax with a friend and would visit others at the University of Pennsylvania and suburban Philadelphia. He often attended the fall meetings of the Society, particularly those in or near Canada. The last meeting he attended was that in Atlantic City, where he sat alone. The Society has lost one of its most loyal members.

Sherlock Swann
Kenneth Graham

SECTION NEWS

Metropolitan New York Section

Following a long-standing tradition, speakers were judiciously chosen for the 1974-1975 season who were expert in their field, covering as many facets of electrochemistry as possible. All meetings were held in the beautiful new wing of the Stevens Institute of Technology in Hoboken, New Jersey, overlooking the Hudson River.

Donald Tuomi explained how thermoelectric cooling promised a solid-state device for transferring heat between two surfaces without moving parts other than electrons in n- and p-type semiconductors. Thus, the familiar mechanical compressor and associated lines for moving gaseous and liquid freon in refrigeration systems would be replaced by a solid-state structure much as the transistor replaced the fragile vacuum tube. Dr. Tuomi enumerated the problems which have prevented the large scale realization of solid-state thermoelectric cooling as a commercially viable technology.

Paul Stonehart dealt with the present trends in electrocatalysis as applied to fuel cells. Catalysis is the science of maximizing reaction rates for the production of preferred products, so it is as important to develop catalysts with high surface areas as it is to prepare special surface features on those catalysts. This high surface area aspect has not previously been given much emphasis in electrocatalytic studies, which is unfortunate in many ways, since the extension of catalytic properties from low surface area metals (foils, wires) to highly dispersed catalysts on supports is tenuous at best. Indeed, the development of porous electrode structures with highly dispersed electrocatalysts as an analytical tool for measuring electrode kinetics has taken place recently, yet this is only an application of the early studies of Thiele and Wheeler on reactions of porous catalysts. Electrocatalysis is considered to be a special case of heterogeneous catalysis, with the singular advantage that electrons, as reactants or products, are easy to measure at low concentrations. Conversely, concluded Dr. Stonehart, the greatest disadvantage is that the catalyst particles and supports must be electronically conductive, thereby restricting the availability of electrocatalytic materials.

Theodore R. Beck, Vice-President of the Society, was guest speaker at the Annual President's Night. Dr. Beck made the special journey from Seattle for this meeting. He elaborated most lucidly that the electrochemical and corrosion behavior of titanium is dominated by the presence of a passivating oxide film. The rate and mechanism of repassivation when the film is mechanically disrupted and conditions under which passivity breaks down, were discussed. Breach of the film occurs in pitting, crevice corrosion, and stress corrosion cracking.

Huk Yuk Cheh was guest speaker at a joint meeting with the American Electroplaters Society. His talk was based on AES research project 35, "The Application of Pulsed Plating Techniques to Metal Deposition," published in Plating Magazine, June 1974. The object of this project was to determine the mechanism of copper deposition under pulsed current conditions. Dr. Cheh pointed out that the program emphasized the measurement and correlation of physical properties of metal deposits to plating conditions.

In all cases, the scientific address was preceded by a meeting of the Executive Committee of the Section followed by a cocktail hour and dinner. The meetings were extremely well attended and included a percentage of Student Members since it has been the Section's policy to put Student Members on the mailing list without charge.

Regular membership increased by twenty-five over the previous year. The season culminated in Ladies' Night held at Stevens Institute on April 30, 1975, and attended by members, old and new, their spouses, and friends. Martin Sulkes was the chairman for this very popular evening which included a most interesting presentation on "Gold" by Dr. D. G. Foulke of Sel Rex Corp. Gifts received from The Hill Cross Co., International Nickel, American Gas and Chemical Co., Metal Finishing Magazine, Ryaby Associates, Energy Research Co., ESB Inc., Bright Star Industries, and Sel Rex Corp. permitted the ladies present to receive beautiful door prizes.

Jack Davis
Program Chairman

Southern California—Nevada Section

The 1974-1975 meetings started in October with Dr. Douglas O. Raleigh's talk about "Fun with Solid Electrolytes." Dr. Raleigh, technical staff member at Rockwell International Science Center, discussed the entertainment factor as a significant criterion in the choice of a research area. He then told us of the ease in which solid-electrolyte cell systems can be set up and their uniqueness as electrochemical systems, where the ratio of interesting results to effort justifies the use of the frivolous noun "fun." Unique results were developed from embarrassingly simple experiments. In December the Section listened to Dr. William M. Riggs, Product Manager for E. I. du Pont de Nemours and Co., discuss "The Application Research Utilizing the Unique Capabilities of ESCA." Dr. Riggs showed examples of the depth profiling capability of ESCA and described recent results from a study of ion exchange phenomena at surfaces.

1975 started with our February meeting and the speaker for the evening was Dr. M. J. Pryor, Director of Research, Olin Corporation and Vice-President of The Electrochemical Society. He talked on "Control of Corrosion Kinetics by Resistive Reaction Product Films," which was well illustrated and included the substitutional mechanisms of cation from alloying additions in various metal substrates. In April, Dr. Karl M. Kadish, Professor of Chemistry, California State University, Fullerton, gave a talk on his research interests in the chemistry and electrochemistry of species of biological interest, e.g., "Metalloporphyrins." Special emphasis was placed on those model compounds which have been shown to reversibly bind molecular oxygen.

The next local Section meeting will be held in June, which will be Ladies' Night (i.e., wives, husbands, and/or friend). Also, at this meeting the officers elected for the coming year will be announced.

Alan L. Harrington
Secretary

Committees of The Electrochemical Society, Inc., 1975-1976 ..... 202C
Ernest G. Enck to Retire as Society Executive Secretary—To be Succeeded by V. H. Branneky 203C-204C
ECS Summer Fellowship Award Winners for 1975 ..... 204C-205C
Division News 205C
H. Jermain Creighton, 1886-1975 . 206C
Section News 207C
New Members 208C
News Items 208C
People 208C
Book Reviews 209C-210C
Position Available 210C
Positions Wanted 210C
Fifth International Conference on Chemical Vapor Deposition, Information and Program 213C-216C
Call for Papers—Washington, D.C. Meeting 217C-220C

NEW MEMBERS

It is a pleasure to announce the following new members of The Electrochemical Society as recommended by the Admissions Committee and approved by the Board of Directors in June 1975.

Active Members

Baerg, W., Palo Alto, Ca.
Battles, J. E., Oak Forest, Il.
Blank, M., New York, N.Y.
Buehler, M. G., Gaithersburg, Md.
Burkhardt, P. J., Poughkeepsie, N.Y.
Cabral, U. Q., Rio de Janeiro, Brazil
Caldwell, D. L., Lake Jackson, Tx.
Chianelli, R. R., Brooklyn, N.Y.
Chu, W-K., Hopewell Junction, N.Y.
Coleman, J. P., Hazelwood, Mo.
Devine, T. M., Jr., Schenectady, N.Y.
d'Heurle, F., Yorktown Heights, N.Y.
Dirlam, P. B., Southbridge, Ma.
Eaton, D. A., Plymouth, Mn.
El-Reghy, S. M., Cairo, Egypt
Enggist, K. F., Bramalea, Ont., Canada
Fields, D. A., Phoenix, Az.
Fletcher, S., Ottawa, Ont., Canada
Forest, H., Melrose Park, Il.
Hakim, M. J., Hamilton, Ont., Canada
Hanck, K. W., Raleigh, N.C.
Harnish, D. F., Orchard Park, N.Y.
Ismail, N., Ottawa, Ont., Canada
Lerner, M., Brighton, Ma.
Lumsden, J., Avonmouth, Bristol, England
Martinez, V., Gottingen, West Germany
Mayer, P., Burlington, Ont., Canada
McIntyre, J. M., Freeport, Tx.
Medford, R. C., Newport News, Va.
Mrowec, S., Krakow, Poland
Murphy, D. W., Murray Hill, N.J.
Nagamori, M., Ste-Foy, Que., Canada
Porter, M. C., Pleasanton, Ca.
Ramde, A., Plymouth, Mn.
Rauh, R. D., Jr., Watertown, Ma.
Schaefer, R. R., Sindelfingen, Germany
Schulte, A. J., Setauket, N.Y.
Shepela, A., Worcester, Ma.
Silversmith, D. J., Slatersville, R.I.
Steele, B. C. H., London, England
Stephens, D. E., Grand Island, N.Y.
Stock, A. J., Port Huron, Mi.
Stuart, A. K., Toronto, Ont., Canada
Taskier, H. T., Summit, N.J.
Tokuda, K., Buffalo, N.Y.
Ullman, D. L., II, Milwaukee, Wi.
Wilson, E. J., Midland, Mi.
Witzke, H., Princeton, N.J.
Young, P. L., Corning, N.Y.
Zelman, A., Nashville, Tn.

Student

Apte, P., Hamilton, Ont., Canada
Barnett, B., Ottawa, Ont., Canada
Bezilla, B. M., Jr., Morgantown, W.V.
Bhide, V. S., Hamilton, Ont., Canada
El-Demerdash, M. F., Hamilton, Ont., Canada
El Kasabgy, T. D., Hamilton, Ont., Canada
El-Refaie, F. A. A., Hamilton, Ont., Canada
Harris, D., University Park, Pa.
Harvie, W. F., Fredericton, N.B., Canada
Jain, H., New York, N.Y.
Jolson, J. D., Buffalo, N.Y.
Kapoor, V. J., Bethlehem, Pa.
Lindemanis, A. E., Philadelphia, Pa.
McCarthy, J. C., Poway, Ca.
Nauman, J. D., Somerville, Ma.
Siu, W. M., Willowdale, Ont., Canada
Takeda, K., Toronto, Ont., Canada

Reinstatement

Angus, J. C., Cleveland, Oh.
Bittmann, C. A., Los Altos Hills, Ca.
Fromhold, A. T., Jr., Auburn, Al.
Kuwana, T., Columbus, Oh.

Transfer

Arora, M. R., Montreal, Que., Canada
Carmichael, N. R., Scarborough, Ont., Canada
Cooper, J. F., Livermore, Ca.
Fernandez, C. G., Midland, Mi.
Hebbar, R. K., Hightstown, N.J.
Landau, U., Summit, N.J.
Toth, L. F., Jr., South Plainfield, N.J.

NEWS ITEMS

I.S.E. Meeting 1976

A plenary meeting of the International Society of Electrochemistry (I.S.E., formerly C.I.T.C.E.) will be held in Zurich, Switzerland, September 6-11, 1976. The main themes will be: Electrochemical Engineering, Experimental Methods in Electrochemistry, and Anodic Films and Passivating Layers. Sessions covering all divisions of I.S.E. are planned, including those not directly related to the main themes. A colloquium on "Non-Isothermal Electrochemistry," sponsored by the Commission for Electrochemistry of the International Union of Pure and Applied Chemistry, will also be held on September 10 and 11 within the frame of the meeting.

The deadline for submission of papers is December 31, 1975, and should include an abstract of approximately 75 words. Please address any inquiries to Dr. O. Dossenbach, Technisch-chemisches Labor ETHZ, Universitätstrasse 6, CH-8006 Zurich, Switzerland.

Institute on Hybrid Microelectronics

An Institute on Hybrid Microelectronics will be held at the University of Pittsburgh on August 11, 12, and 13, 1975. The Institute will be offered by the University in collaboration with the IEEE, Parts, Hybrids and Packaging Group. A limited number of tuition scholarships will be available to faculty and students.

The Institute will give coverage of the thin and thick film technologies coupled with I.C. chips to form hybrid circuits. Practicing engineers will discuss materials, design, and fabrication techniques, emphasizing their applicability to both large and small manufacturers. A special session will be devoted to microelectronics research and teaching at universities.

Additional information and enrollment forms may be obtained by contacting: Minor C. Hawk, Assistant Dean, 231 Benedum Engineering Hall, School of Engineering, University of Pittsburgh, Pittsburgh, Pa. 15261, (412) 624-5253.

Workshop on Electrocatalysis on Non-Metallic Surfaces

The National Bureau of Standards is organizing a "Workshop on Electrocatalysis on Non-Metallic Surfaces," to be held at their Gaithersburg, Maryland, laboratories on December 9-12, 1975. Topics covered will include theory of the electronic states and of electrocatalysis on non-metals, electron transfer reactions, characterization of electrocatalytic surfaces, experimental studies of electrochemical processes, and electrochemistry at solid electrolyte interfaces. Brief abstracts should be sent to Dr. A. D. Franklin, A355 Materials, National Bureau of Standards, Washington, D.C. 20234, U.S.A., by July 1, 1975.

PEOPLE

W. William Harvey has joined EIC, Inc. (Environmental Impact Center, Inc.) in Newton, Massachusetts, as vice president and director of process development. This independently owned and operated company carries out research and development in electrochemical and other energy conversion systems and in pollution abatement. In his new affiliation, Dr. Harvey will continue the technical consulting in hydrometallurgy in which he has engaged since leaving the Ledgemont Laboratory of the Kennecott Copper Corporation in Lexington, Massachusetts. EIC, Inc. is enlarging its activities in geothermal energy utilization and extractive metallurgy, and it is with these technical areas that Dr. Harvey will be mainly concerned. Dr. Harvey is an Active Member of the Electrochemical Society.

Certificates, Pins, and Keys Now Available

The Society announces the availability of the following items:

Membership Certificates	$ 5.00
Gold Membership Pin	$ 7.50
Gold Membership Key	$15.00

Those interested should send their order accompanied by check to The Electrochemical Society, Inc., P.O. Box 2071, Princeton, N. J. 08540

BOOK REVIEWS

"Electrolytic Manufacture of Chemicals from Salt," by D. W. F. Hardie, revised by W. Watson Smith. Published by the Chlorine Institute, Inc., New York (1975). 92 pages; $4.00.

"Electrolytic Manufacture of Chemicals from Salt," commissioned by Imperial Chemical Industries Ltd. and published by The Chlorine Institute, Inc., was initially written in 1959 by D. W. F. Hardie, B.Sc., Ph.D., and has been updated in this 1975 edition by W. Watson Smith, B.Sc., Ph.D.

This book deals with the electrolysis of salt for the manufacture of chlorine, caustic soda, sodium, chlorates, and hypochlorites. The history and technology of mercury, diaphragm, chlorate, and fused salt cells is described. Information on the properties, storage, transport, and uses of the chemicals is provided.

The original text was one of a series written to bridge the gap between the chemistry learned in school and the same chemistry as applied in industrial practice. Changes in the 1975 edition include the economic and commercial aspects of the processes such as a fourfold increase in world production of chlorine and important new developments in the same basic processes.

The chapters have the following titles: I. Fundamental Aspects of Brine and Salt Electrolysis; II. Raw Materials and Energy; III. The Manufacturing Processes; IV. Packing, Storage and Transport of the Products; V. Production Statistics and Trends; VI. Physical and Chemical Properties of the Products; VII. Principal Uses of the Products; and VIII. Outline of Historical Development. Two appendices contain a chronology of early developments and a glossary of technical terms. A bibliography refers to 13 texts, trade publications, and cell manufacturers' brochures. There are 19 illustrations and seven tables.

Recent trends that are discussed include: the use of metal anodes, increased current density and capacity of diaphragm cells, diaphragms modified by addition of polymeric fibers to the asbestos fibers, use of porous inert material of the polyfluoroethylene type, use of nonporous ion-exchange membranes, an improved chlorate cell process, the general and political effects of mercury contamination on use of mercury cells, and the chlorine-caustic soda balance. It is predicted that pulp bleaching will be affected by chlorine dioxide during the '70's, and that oxygen bleaching will not have an important effect until the '80's.

Modern diaphragm cells are described with references to the new Hooker, Diamond Shamrock, and PPG-DeNora bipolar electrolyzer cells. Advances by Solvay and several Japanese companies are not mentioned. The "bluish-purple color" in diaphragm cell caustic is blamed on traces of complex iron compounds rather than on the chlorinated aromatic compound isolated by Heller (Trans. Electrochem. Soc.).

Liquefaction of chlorine is described using the pressure unit "bars," which is missing from the glossary in Appendix II.

Several industrial uses of sodium amalgam are not mentioned.

The chronology in Appendix I stops with the Downs sodium cell patent in 1924. This could be updated with such inventions as mercury arc, mechanical and silicon rectifiers, the deposited asbestos diaphragm, and metal anode.

The gap between schoolbook and industrial chemistry has been well bridged. This book is highly recommended as a text for teachers of industrial electrochemistry and for industrialists in the chlor-alkali industry, whether in management, production, sales, or research.

William C. Gardiner
Stratford, Connecticut

Book Reviewers Needed

The Electrochemical Society needs competent individuals to review books for the Journal.

Any Society member who wishes to volunteer his services should send his name, address, and field of competence to the attention of the Book Review Editor, Dr. Julius Klerer, c/o The Electrochemical Society, P.O. Box 2071, Princeton, N.J. 08540

"Annual Review of Materials Science," Vol. 4, edited by R. A. Huggins, R. H. Bube, and R. W. Roberts. Published by Annual Reviews, Inc., Palo Alto, Calif. (1974) 461 pages; $15.00.

As in preceding volumes in this series, the editors aim at reviews of current research and trends, emphasizing aspects of structure, properties, and phenomena which cut across traditional disciplinary lines or materials classes. They now categorize the individual reviews in the series under the headings: experimental and theoretical methods; structure; preparation, processing, and structural changes; properties and phenomena; and special material. Review articles in general may also be classified as to their functional approach, e.g., tutorial, descriptive (almost an annotated index to the literature), and creative (where a new synthesis is essayed of the topic). In this sense, the articles in this volume are mostly tutorial with but two or three each in the descriptive and creative classes. The articles are authoritatively written by a widely diversified group of authors, U.S. and foreign, and by those with university, government, and industrial affiliations.

Articles of particular interest to readers of **This Journal** discuss fast ion conductors, semiconductors, ion implantation, nonlinear optics, dielectric properties of order/disorder crystals, and extended defect solids. The latter two are examples of that most valuable and difficult class of review, the new synthesis. It is also noteworthy that these two articles are by international groupings of authors, an Australian-Swedish-American quadrumvirate in the case of the extended defect solids and a Brazilian-American pair in the other. In a review of Vol. 1 of this series [This Journal, 119, 307C (1972)], note was made of the omission of coverage in polymers, biomaterials, and glasses. This imbalance has since been rectified, not only in Vol. 2 and 3, but also in the present case which includes articles on fire-resistant polymers, biomedical materials, and noncrystalline solids and liquid crystals. Other articles, not yet cited, treat NDT and NMR techniques, tribology, 1-D and 2-D magnetic systems, and strong, high temperature ceramics.

In sum, the diversity of topics and the quality of the individual articles maintain the high standard of excellence originally set for this series. The present volume includes both author and subject indices to its own contents as well as cumulative indices to the contributing authors and to the chapter titles of all four volumes thus far published in the series. As with other members of the Annual Reviews family, reprints from all volumes in the series are available from inventory at the very nominal price of $1.00.

J. H. Westbrook
General Electric Company
Schenectady, New York

ADVERTISERS' INDEX

Princeton Applied Research 193C

Texas Nuclear Corporation 195C

Book Reviews continued

"Proceedings of the Twelfth Seminar on Electrochemistry." Published by Central Electrochemical Research Institute (CECRI), Karaikudi, India (1972). 495 pages; $12 (Air Mail) or $8 (Sea Mail).

"Proceedings of the Thirteenth Seminar on Electrochemistry." Published by CECRI, Karaikudi, India (1972). 430 pages.

"Proceedings of the Fourteenth Seminar on Electrochemistry." Published by CECRI, Karaikudi, India (1973). 593 pages.

For the past two decades or so, Central Electrochemical Research Institute (CECRI) in Karaikudi, India, has been a prominent center of research in electrochemistry and has had associated with it a number of notable electrochemists. Under the able and aggressive direction of K. S. G. Doss (co-discoverer of faradaic rectification) and, more recently, H. V. K. Udupa (who is distinguished for his work on batteries, electrodeposition, and various other aspects of electrochemical technology), CECRI has continued to be quite productive, both in electrochemical science and industrial electrochemistry. These introductory comments have been prompted by the fact that electrochemists in North America, with some exceptions, have generally not paid enough attention to the work coming out of CECRI, although British and European electrochemists have benefited from their interaction with CECRI for quite some time.

Now, to the contents of the above volumes. These Proceedings are reviewed together mainly because they constitute very similar themes. They contain papers presented at the three indicated seminars, attended primarily by Indian electrochemists, although some significant contributions from Japan, USSR, and a number of western countries are also included. Some subjects covered in each of these volumes are: electrodeposition and metal finishing; electrosyntheses; electrothermics and electrometallurgy; electrode kinetics and electroanalysis; corrosion; solid-state electrochemistry; and batteries. The volumes thus cover a very broad spectrum of electrochemistry and are bound to be of interest to many electrochemists.

Most of the papers presented are neither very fundamental nor of a lasting academic value. They do contain, however, a wealth of useful technological information and appear to be of great immediate interest to industrial electrochemists. Since CECRI, and hence many of the authors in the above volumes, is quite heavily involved with industry and production problems (a most commendable attitude in the opinion of the reviewer), it is natural that the flavor of these volumes be highly technological. Of course, CECRI scientists also publish excellent fundamental work (which complements the information contained in the above volumes) in the standard research journals.

In summary, these volumes contain a great deal of technological electrochemistry and are a good starting point to introduce the North American reader to the activities in applied electrochemistry being carried out at CECRI and other laboratories in India.

Ashok K. Vijh
Hydro-Quebec Institute of Research
Varennes, P.Q., Canada

POSITION AVAILABLE

Postdoctoral Fellow—There is an immediate opening for a postdoctoral fellow with experience in electrochemistry to work under the direction of Dr. D. G. Lee and Dr. K. E. Johnson on the electrochemistry of a variety of ruthenium compounds including the synthesis and characterization of Ru(V) and the properties of Ru(II)-N_2 moieties. Equipment available includes the PAR 170 system. The starting salary is $800 per month. Apply to: Dr. K. E. Johnson, Department of Chemistry, University of Regina, Regina, Saskatchewan S4S OA2, Canada, giving curriculum vitae and the names and addresses of two references.

Positions Wanted

Society members of any class may, at no cost and for the purposes of professional employment, place not more than three identical insertions per calendar year, not to exceed 8 lines each. Count 43 characters per line, including box number, which the Society will assign.

POSITIONS WANTED

Please address replies to the box number shown, c/o The Electrochemical Society, Inc., P. O. Box 2071, Princeton, N. J. 08540.

Chemical Metallurgist—Expert in all aspects of tantalum capacitor technology can identify faults in your business and correct them. Do you have right product mix? Adequate yields? Lowest costs? Right equipment? Satisfactory quality? Is your market target realistic and profitable? Will accept consulting. Reply Box C-153.

Materials Scientist/Solid-State Physicist—Ph.D. expected July 1975. Extensive experience in thin films, sputtering, radiation damage, electron microscopy, electrical properties, and vacuum technology. Six years industrial research experience in thin films and microelectronics. Seeks challenging R&D position. Reply Box C-154.

Executive Research Director (V.P.)—Presently directing large energy research group in major company. Well known, numerous publications in catalysis, materials science, chemical engineering, and electrochemistry. Advanced technology in energy research; technology transfer and acquisitions. Electrochemical power generation, catalysis in energy related systems. Reply Box C-155.

Physical Chemist/Electrochemical Engineer—Ph.D. with over 15 years supervisory R&D work on batteries, corrosion control, electroplating, semiconductors, photochemistry, electro-optical devices. Strong theoretical, experimental, linguistic, and business management background. Over 50 patents/publications. Reply Box C-156.

Physicist/Electrochemist—25 years experience in electrodeposition of metals, alloys, semiconductors; mechanical and physical properties of films and deposits (e.g., magnetic films); adsorption; electrochemical kinetics. 180 publications, 2 scientific books, Ph.D.s in solid-state physics and electrochemistry, professorship for many years. Seeking R&D position. Reply Box C-157.

Metallurgist—Ph.D. (1975), presently working on corrosion projects with stainless steels and other materials. Dissertation dealt with mechanical behavior of high temperature materials, unique specialties in electron microscopy (theory and experiments), and scientific and engineering computer applications. Seeking industrial positions. Salary and location open. Please contact: Dr. Wen-Shian Tzeng, 9 Cheney Dr., Storrs, Conn. 06268.

ATTENTION, MEMBERS AND SUBSCRIBERS

Whenever you write to The Electrochemical Society about your membership or subscription, please include your Magazine address label to ensure prompt service.

Mail to the Circulation Department, The Electrochemical Society, Inc., P. O. Box 2071, Princeton, N.J. 08540.

ATTACH LABEL HERE

Change of Address

To change your address, place magazine address label here. Print your NEW address below. If you have any question about your subscription or membership, place your magazine label here and clip this form to your letter.

name

address

city state zip code

APPLICATION FOR ADMISSION

TO

The Electrochemical Society, Inc.

Return completed application to:

Secretary
The Electrochemical Society, Inc.
Post Office Box 2071, Princeton, New Jersey 08540

Do not write in this space

No.	Checked:
Info. Req. Rec'd	Approved:
Notice of Ackn. Accep.	Elected:
$ recap	Adv. Date

To the Board of Directors of The Electrochemical Society, Inc:

Full Name .....
(please print)

residing at .....
(please print)

and at present associated with .....

as .....

hereby makes application for admission to The Electrochemical Society, Inc., as a ..... member, and encloses check in amount of $ ..... covering first year's dues. (See reverse side for proper class of membership and dues applying thereto.)

1. Date, and Place of Birth: ..... 2. Citizen or Subject of: .....

3. Education: Institution	Dates Attended	Major Subject	Degree Earned

4. Employment Record: Name of Employer	Dates	Position

5. Please indicate your primary DIVISIONAL interest by writing the number 1 in front of that Division name. If you have other divisional interests, indicate by placing succeeding numbers in front of Division names.

____ Battery	____ Electrodeposition	____ Electrothermics and Metallurgy
____ Corrosion	____ Electronics	____ Industrial Electrolytic
____ Dielectrics and Insulation	☐ Semiconductors	____ Organic and Biological Electrochemistry
	☐ Luminescence	____ Physical Electrochemistry

6. Please check LOCAL SECTION with which you wish to affiliate:

____ Boston	____ Detroit	____ Niagara Falls	____ Pittsburgh	____ North Texas
____ Chicago	____ Indianapolis	____ Ontario-Quebec	____ Rocky Mountain	____ South Texas
____ Cleveland	____ Midland (Mich.)	____ Pacific Northwest	____ San Francisco	____ Natl. Capital Area
____ Columbus	____ Metropolitan N.Y.	____ Philadelphia	____ So. Calif.-Nevada	____ None

7. Our Constitution provides that two Active Members of the Society (who can substantiate the above record) must recommend you for admission to membership. It would facilitate the handling of your application if you are able to have your references sign this application form; if not convenient, please list their names and addresses.

Name (please print)	Signature	Address
Name (please print)	Signature	Address

The undersigned certifies that the above statements are correct and agrees, if elected to the Society, that he will be governed by its Constitution and Bylaws. He furthermore agrees to promote the objects of the Society as far as shall be in his power.

SIGNATURE AND ADDRESS TO WHICH PUBLICATIONS AND COMMUNICATIONS SHOULD BE SENT.

..... (Signature)

..... (Street Address)

..... (City, State, Zip Code)

Date ..... 19 .....

(over)

3/78

EXTRACTS FROM THE CONSTITUTION AND BYLAWS

CONSTITUTION—Article II

Membership

Section 1. The individual membership shall consist of Active, Honorary and Emeritus Members. The Board of Directors may from time to time authorize other classifications of membership as defined in the Bylaws of the Society.

(Active Member—Annual Dues $30.00)

Section 2. An Active Member shall be interested in electrochemistry or allied subjects and possess a Bachelor's degree, or its equivalent, in engineering or natural science. In lieu of a Bachelor's degree, or its equivalent, any combination of years of undergraduate study and years of relevant work experience in electrochemistry or allied subjects adding to at least seven years shall be required. Election to Active Membership shall require the recommendation of two Active Members in good standing.

BYLAWS—Article II

Non-Voting Membership
(Student Member—Annual Dues $3.00)

Section 1. Student Member. A Student Member shall be a full-time undergraduate or graduate student registered for a degree in natural science or engineering. The applicant for Student Membership shall be recommended by a member of the faculty of the school. Upon graduation with a Bachelor's degree or equivalent in natural science or engineering, the Student Member may apply for Active Membership. The application shall be approved by two Active Members of the Society in good standing. If the Student Member enters graduate school as a full-time student, the person may choose to apply for Active Membership or remain a Student Member.

BYLAWS—Article XXI

Dues and Fees

Section 1. The annual dues for Active Members shall be thirty dollars. The annual dues for Student Members shall be three dollars. Each member shall receive the JOURNAL OF THE ELECTROCHEMICAL SOCIETY.

Section 2. When individuals are elected to membership, they must elect to initiate their membership as of January 1 or July 1 of the year of election; or, if elected during the last quarter, January 1 of the year following election. In the case of a July 1 election for starting membership, dues will be prorated.

Section 3. Any Active Member who shall pay in one lump sum the amount equivalent to two-thirds of the remaining dues to age sixty-five at the time of payment, but not less than an amount of 5 years of full dues, shall be exempt from payment of any further dues and shall be considered an Active Member during the remainder of his or her life.

Section 5. Emeritus Members shall be exempt from the payment of annual dues and shall have all the rights and privileges of an Active Member.

CONSTITUTION—Article III

Admission and Dismissal of Members

Section 1. Application for individual membership shall be in writing on a form adopted by the Board of Directors.

Section 2. The Admissions Committee shall be a rotating committee consisting of three members. One member shall be appointed each year by the President with the approval of the Board of Directors for a term of three years to replace the outgoing member. This Committee shall receive from the Secretary all properly executed and properly recommended applications for admission which he has received from persons desirous of becoming members of the Society. It shall be the duty of this Committee, after examining the credentials of applicants, to make appropriate recommendation to the Board as to approval or rejection of the applications. Unanimous approval of an applicant by this Committee shall be required before the candidate's name may be submitted to the Board of Directors for election. The election to membership shall be by a mail vote of the Board of Directors. The candidate shall be considered elected two weeks after the date the proposed membership list is mailed to the Board if no negative votes have been received by the Secretary. If a candidate receives one negative vote, his application shall then be considered and voted upon at the next meeting of the Board of Directors. Two negative votes cast at this meeting shall exclude a candidate. The Board of Directors may refuse to elect a candidate who, in its opinion, is not qualified for membership. The names of those elected shall be announced to the Society. Duly elected candidates shall have all the rights and privileges of membership as soon as their entrance fee, if any, and dues for the current year have been paid.

Section 3. A member desiring to resign shall send a written resignation to the Office of the Society.

Section 4. Upon the written request of ten or more Active Members that, for cause stated therein, a member be dismissed, the Board of Directors shall consider the matter and, if there appears to be sufficient reason, shall advise the accused of the charges against him. He shall then have the right to present a written defense, and to appear in person before a meeting of the Board of Directors, of which meeting he shall receive notice at least twenty days in advance. Not less than two months after such meeting the Board of Directors shall finally consider the case and, if in the opinion of the majority of the Board of Directors a satisfactory defense has not been made and the accused member has not in the meantime tendered his resignation he shall be dismissed from the Society.

Section 7. The entrance fee, if any, annual dues and any other payments to be made by the members of the Society shall be paid in accordance with regulations set forth in the Bylaws.

Section 8. Any member delinquent in dues after April 1 shall not receive the Society's publications and will not be allowed to vote in any Society election until such dues are paid. All members in arrears for one year after April 1 shall lose their membership status and can be reinstated only by action of the Board of Directors.

FIFTH INTERNATIONAL CONFERENCE ON CHEMICAL VAPOR DEPOSITION

September 21-25, 1975

Conference Centre, Fulmer Grange
Stoke Poges, Buckinghamshire, England

General Information

The Fifth International Conference on Chemical Vapor Deposition, sponsored by the Electrothermics and Metallurgy Division of The Electrochemical Society, Inc. and hosted by the Fulmer Research Institute, Ltd., is designed to bring together those having a common interest in the fundamentals and applications of techniques for depositing materials by chemical reaction from the gas phase. A full four day program is planned, with single sessions on Monday, Tuesday, and Thursday, and parallel sessions on Wednesday. Social functions will include an informal Mixer on Monday evening and an informal Reception and Buffet at historic Guild Hall, Windsor, on Wednesday evening. Visits to nearby Fulmer Research Institute can be made on any day during the week of the Conference. Visits on Friday, September 26, to facilities such as The National Physical Laboratories at Harwell and Warren Springs and to other research laboratories can be arranged for those interested. Provisions will be made for interesting activities and tours on Monday through Thursday for wives of male registrants.

Registrants should plan to arrive Sunday afternoon or evening and depart Thursday evening or Friday. Special arrangements can be made for a limited number of "commuters" from nearby, or for those who cannot attend the full four day program.

All technical sessions of the Conference will be held at the Conference Centre where the facilities limit the total participation to 200. The housing facilities available at the Centre for most of the registrants will provide for a maximum of informal personal contact among registrants and the exchange of information and ideas. Copies of the Conference Proceedings, containing the full papers in English, will be provided to the registrants to enable them to follow oral presentations that may be given in other languages. Translation facilities will not be available on a formal basis.

Registration

Registration will be in advance by filling out the attached forms and enclosing the registration fee of £35 and accommodations fee deposit of £13, totalling £48 (see exception for commuters). To ensure inclusion within the 200 registrant limit, those interested are urged to register as soon as possible before the August 25, 1975, deadline. Badges, to be issued on arrival at the Centre, will admit registrants to technical sessions, the Monday Mixer, and the Wednesday evening Reception and Buffet.

Housing

The first 160 four day registrants will be housed at the Conference Centre Sunday afternoon through Thursday at 6 P.M. in single rooms with bath. Arrangements for an additional night's housing with Thursday dinner and Friday breakfast can be made on arrival (£12.75 additional). An additional 40 registrants can be housed in a nearby hotel at a somewhat higher cost per night (these reservations to be handled by the Conference Centre). Wives of male registrants can be accommodated at the Centre by placing an additional bed in the limited space available in a room, or, if permitted by a registration of less than 160, by use of an adjacent room at an appropriate additional fee. (Please indicate the need for such arrangements on the accompanying form.)

Meals

Meals will be provided at the Centre for the 160 four day registrants as part of the accommodations cost. Additional dining room capacity up to 200 is available for others at the following rates: Breakfast, £1.50; Lunch, £2.25; and Dinner, £2.75; arrangements to be made at the Conference. Special diet problems should be noted with the registration form. Owing to variations of arrival time, the Sunday evening meal at the Centre will be in the form of a buffet, open until 8:45 P.M. A cash bar will also be available each evening until 10:30 P.M. throughout the Conference.

Transportation

Transportation on Sunday, September 21, 1975, from 2 P.M. through 10 P.M. from the London airport will be provided on the following schedule: Terminal No. 1 passengers, rear of taxi ramp, departing on the hour; Terminal No. 2 passengers, Queens Building forecourt, five minutes past the hour; and Terminal No. 3 passengers, Group Travel Charter Coach Station, 10 minutes past the hour. The bus to the CVD-V Conference will be accompanied by a Fulmer Research Institute representative, and will be clearly marked. The equivalent service will be provided on Thursday evening. The cost of this transportation is included in the registration fee.

Local transportation by taxi is available, and trains run frequently to London from the nearby station at Slough.

Mixer

The informal Mixer on Monday night is open to registrants and guests to promote their becoming better acquainted. Beer, tea, coffee, and light refreshments will be provided. The cash bar will also be open.

Reception and Buffet

The Reception and Buffet at Guild Hall will be informal, with an elegant cold buffet, including wines. Additional tickets to this function will be available at the Conference at a cost of £4.50 each. The program will include an entertaining and informative talk on "The Royal Borough of Windsor" by Mr. G. Waldram, the Town Clerk. Transportation to Guild Hall from the Centre and return will be provided at no additional cost.

Plant Tours

A list of accessible facilities of technical interest will be posted at the Conference. Those wishing to visit these locations on Friday, September 26, 1975, should make arrangements as indicated at the Conference. Transportation costs will vary with the nature of the visit.

Ladies' Program

From 10 A.M. to 5 P.M. on the days of the conference, tours will be available for the ladies to points of local interest such as Oxford, Blenheim Palace, Windsor Castle, Eton, and St. Albans. A shopping trip to London is also planned. The cost of these excursions (except the shopping trip) will be £5 to £6 each, including lunch, coffee, and tea; arrangements to be made at the Conference.

Communications

The address of the Conference Centre is: Conference Registrar, Conference Centre, Fulmer Grange, Stoke Poges, Slough SL2 4QS, Bucks., England. Telephone: Fulmer 2727. Telex: 84352 Advicret Slough.

PROGRAM *(subject to change)*

Monday, A.M., September 22, 1975

FUNDAMENTALS

Fundamentals of Chemical Transport and Novel Vapor Species Suitable for Chemical Transport and Chemical Vapor Deposition, Harald Schafer, Westfalische Wilhelms-Universitat, Munster, Germany

SiO_2 Deposition Using Mixtures of SiH_4, O_2, and Ar, J. Middelhoek and A. J. Klinkhamer, Twente University of Technology, Enschede, The Netherlands

Oxynitride Deposition Kinetics in a SiH_4-CO_2-NH_3-H_2 System, A. K. Gaind, G. K. Ackermann, V. J. Lucarini, and R. L. Bratter, IBM Corp., Hopewell Junction, New York, U.S.A.

Experimental Investigation of the Gas Phase in a Chemical Vapor Deposition Reaction. Application to the Silane-Ammonia Reaction Leading to Silicon Nitride Deposits, G. Cochet, H. Mellottee, and R. Delbourgo, Centre de Recherches sur la Chimie de la Combustion et des Hautes Temperatures, Orleans–Cedex, France

Calculation of Activity Coefficient of B, P, As, and Sb in Solid Silicon Based on Experimental Data on Growth of Doped Silicon Layers in CVD Processes, G. A. Kokovin, G. Kosza, N. A. Testova, and F. A. Kuznetsov, Institute of Inorganic Chemistry of the USSR Academy of Sciences, Novosibirsk, USSR

Monday, P.M.

Thermodynamic Domains of the Various Solid Deposits in the B-C-H-Cl Vapor System, M. Ducarroir and C. Bernard, Laboratoire des Ultra-Refractaires, C.N.R.S., Font-Romeu, France

Kinetics of Boron Deposition by the Hydrogen Reduction of Boron Trichloride, R. M. Mehalso and R. J. Diefendorf, Rensselaer Polytechnic Institute, Troy, New York, U.S.A.

The Influence of Co on the Nucleation and Preliminary Growth of TiC, H. Gass, H. Mantle, and H. E. Hintermann, Laboratoire Suisse de Recherches Horlogeres, Neuchatel, Switzerland

Chemical Vapor Deposition in the Ternary System Ti-Si-C: Quantitative Analysis and Application for Adapted Corrosion Resistant Coatings for Ni-Base Superalloys, K. K. Schweitzer and J. J. Nickl, Universitat Munchen, Germany

Thermodynamic and Experimental Results in Chemical Vapor Deposition of Titanium Carbide, M. Ducarroir and M. Nadal, Laboratoire des Ultra-Refractaires, C.N.R.S., Font-Romeu, France

Mechanism of Pyrocarbon Formation from Propylene, R. Gower and J. Hill, Atomic Weapons Research Establishment, Adlermaston, Reading, England

Comparison Between Physical and Chemical Vapor Deposition (Application and Cost Evaluation), A. M. Shroff, Thomson-CSF, Paris, France

Tuesday, A.M., September 23, 1975

UNUSUAL CVD PROCESSES

Kinetics and Mechanism of Growing Diamond from a Gaseous Phase, B. V. Derjaguin, D. V. Fedoseev, S. P. Vnukov, and K. S. Uspenskaja, Institute of Physical Chemistry of the USSR Academy of Sciences, Moscow, USSR

The Application of the Low-Temperature CVD Process, H. Lukas *et al.* Battelle-Institut e.V., Frankfurt, Germany

Low Temperature Deposition of Metal Nitrides by Thermal Decomposition of Organometallic Compounds, K. Sugiyama, S. Pac, Y. Takahashi, and S. Motojima, Gifu University, Kagamigahara, Japan

Preparation of a Tantalum-Based Alloy by a Unique CVD Process, W. A. Bryant and G. H. Meier, University of Pittsburgh, Pittsburgh, Pennsylvania, U.S.A.

Thermal Decomposition of Gaseous Metallic Fluorides on Metals, G. Dejachy, P. Rigny, and J. Oudar, Ecole Nationale Superieure de Chimie de Paris, Paris, France

Indium Oxide Deposition on Glass by Aerosol Pyrolysis (Pyrosol® Process), G. Blandenet, Y. Lagarde, and J. Spitz, Centre d'Etudes Nucleaires de Grenoble, Grenoble–Cedex, France

Comparative Study of Tantalum Deposition by Chemical Vapor Deposition and Vacuum Evaporation, J. Spitz and J. Chevallier, Centre d'Etudes Nucleaire Grenoble, Grenoble—Cedex, France

Tuesday, P.M.

HYBRID PROCESSES

Some Properties of Rare Earth Metal Films Obtained by Reactive Vapor Deposition, G. V. Samsonov, A. F. Andreeva, and I. Ya. Gil'man, Academy of Sciences, Kiev, USSR

Kinetics of the Reactive Sputter Deposition of TiO_x Phases, K. G. Gerraghty and L. F. Donaghey, University of California at Berkeley, Berkeley, California, U.S.A.

Preparation of Silicon-Aluminum, Nitrogen Compounds by Reactive Ion Plating, J. Chin and N. B. Elsner, General Atomic Company, San Diego, California, U.S.A.

Preparation of Niobium Nitride and Niobium Carbonitride Thin Films by Reactive Sputtering, J. Spitz and A. Aubert, Centre d'Etudes Nucleaires de Grenoble, Grenoble–Cedex, France

Deposition of SiO_2 with Low Impurity Content by Oxidation of $SiCl_4$ in a Nonisothermal Plasma, J. Konings, D. Kuppers, H. Lydtin, and H. Wilson, Philips Forschungslaboratorium Aachen GmbH, Aachen, Germany

Silicon Nitride Deposition by Plasma Activation of Silane and Nitrogen at Low Pressure, B. Bourdon and G. Sifre, ALSTHOM–DRE, Massy, France

Formation, Reactions, and Spectra of Gaseous Transient Species in the Plasma Zone, K. K. Yee, Sulzer Brothers Limited, Winterthur, Switzerland

Combination of PVD and CVD Techniques to Improve Protective Coatings of Superalloys, R. Pichoir, Office National d'Etudes et de Recherche Aerospatiels (ONERA), Chatillon, France

Wednesday, A.M., September 24, 1975

SINGLE CRYSTAL GROWTH (Session A)

Growth Mechanism of Epitaxial GaAs Under Gas-Transport Technique, Yu. G. Sidorov, V. M. Zaletin, E. A. Krivorotov, L. N. Aleksandrov, S. A. Dvoretsky, and V. L. Maksimov, Institute of Semiconductor Physics, Siberian Branch of the USSR Academy of Sciences, Novosibirsk, USSR

Chemical Transport of ErTe and DyTe, A. Kahn and L. Manzi, Universidad de Oriente, Cumana, Sucre, Venezuela

Growth of LuTe, TmTe and $(Lu_xTm_{1-x})Te$ Crystals from the Vapor Phase, A. Kahn and C. Vallenina, Universidad de Oriente, Cumana, Sucre, Venezuela

Open Tube Vapor Phase Crystallization of Stoichiometric FeS, J. Mercier, G. Dalberto, P. Lacour, and J. J. Since, Centre National de la Recherche Scientifique, Grenoble–Cedex, France

[110] Preferentially Oriented CVD Tungsten, A. M. Shroff, G. Delval, and J. Lebreton, Thomson-CSF, Paris, France

ELECTRONIC APPLICATIONS (Session A)

Behavior of Impurities during Chemical Vapor Deposition of GaAs, Yu. G. Sidorov, L. F. Vasil'eva, I. V. Sabinina, and S. A. Dvoretsky, Institute of Semiconductor Physics, Siberian Branch of the USSR Academy of Sciences, Novosibirsk, USSR, and A. V. Sidorova, Electrotechnical Institute, Novosibirsk, USSR

continued over

Wednesday, P.M.

Preparation and Properties of Phosphorus-Doped Polycrystalline Silicon Films, M. Kuisl and W. Langheinrich, AEG-TELEFUNKEN, Forschungsinstitut, Ulm, Germany

Vapor Deposition of Tungsten by Hydrogen Reduction of Tungsten Hexafluoride, Power Semiconductor Applications, R. Barandon and G. Sifre, ALSTHOM-DRE, Massy, France

Chemical Vapor Deposition of SiO_2 and Boro- and Phosphosilicate Glasses by the Reaction of SiH_4, B_2H_6, or PH_3 with Oxygen, G. Wahl, Brown, Boveri & Cie, AG, Mannheim Central Research Laboratory, Heidelberg, Germany

Formation of PSG Film Using Organic Compounds and Its Application to Silicon Device Fabrication, K. Sugawara, T. Yoshimi, and H. Sakai, Hitachi, Ltd., Kodaira, Tokyo, Japan

Quantitative Analysis of Phosphorus in Phosphosilicate Glass Using X-Ray Fluorescence, P. DuRant, NCR Microelectronics Division, Colorado Springs, Colorado, U.S.A.

Preparation of CVD Molybdenum, Tantalum, and Tantalum-Oxide Layers, K. Hieber and M. Stolz, Siemens AG, Munchen, Germany

MISCELLANEOUS COATINGS (Session A)

Chemical Vapor Deposition of Amorphous Boron on a Massive Substrate, L. Vankenbulcke and G. Vuillard, Centre National de la Recherche Scientifique, Orleans, France

Pyrolytic Boron Nitride (Concerning Its Operating Limits at High Temperature in Vacuum), G. Clerc and P. Gerlach, Thomson-CSF, Paris, France

Wednesday, A.M., September 24, 1975

HARD COATINGS (Session B)

Nucleation of Al_2O_3 Layers on Cemented Carbide Tools, J. Lindstrom and R. T. Johannesson, Sandvik AB, Stockholm, Sweden

Coating of Cemented Carbide Cutting Tools with Alumina by Chemical Vapor Deposition, R. Funk, H. Schachner, C. Triquet, M. Kornmann, and B. Lux, Battelle, Geneva Research Centre, Geneva, Switzerland

Observations Concerning the Adherence of Amorphous CVD Alumina Coatings on Copper and Copper Alloys, H. Schachner, R. Funk, and H. Tannenberger, Battelle, Geneva Research Centre, Geneva, Switzerland

Boronizing and the Deposition of Layers Containing Boron by the CVD Process, R. Bonetti, D. Comte, and H. E. Hintermann, Laboratoire Suisse de Recherches Horlogeres, Neuchatel, Switzerland

Dispersions of Boron Carbide in a Tungsten Carbide-Cobalt Matrix, G. Arthur and M. P. Johnson, International Research and Development Company, Ltd., Fossway, Newcastle upon Tyne, England

Structure and Strength Effects in CVD Titanium Carbide and Titanium Nitride Coatings, W. Schintlmeister, O. Pacher, and K. Pfaffinger, Metallwerk Plansee, Reutte-Tirol, Austria, and T. Raine, Cutanit Ltd., Grappenhall, Warrington, England

Chemical Vapor Deposition of Tungsten Carbide (WC), H. Mantle, H. Gass, and H. E. Hintermann, Laboratoire Suisse de Recherches Horlogeres, Neuchatel, Switzerland

Wednesday, P.M.

Tungsten Carbide Coatings on Steel, N. J. Archer, Fulmer Research Institute, Stoke Poges, Slough, England

FIBERS AND COMPOSITES (Session B)

CVD Strengthening of Carbon-Fiber Glassy-Carbon Composites, L. Boyne, J. Hill, and K. Turner, Atomic Weapons Research Establishment (AWRE), Aldermaston, Reading, England

Deposition of Silicon Carbide on Carbon Monofilaments, E. Fitzer, D. Kehr, D. Morin, and M. Sahebkar, Universitat Karlsruhe, Karlsruhe, Germany

TiC-Coatings on Graphite by CVD, L. Aggour, E. Fitzer, and J. Schlichting, Universitat Karlsruhe, Karlsruhe, Germany

Protective TiC and TiN Coatings on Carbon Fibers in a Nickel Matrix, R. Warren and M. Carlsson, Chalmers University of Technology, Gothenberg, Sweden

TiN- and TiC-Coated Carbon Fibers, R. Warren and M. Carlsson, Chalmers University of Technology, Gothenberg, Sweden

Chemical Vapor Deposition of Hafnium Nitride and Hafnium Carbide on Tungsten Wires, M. J. Hakim, Westinghouse Canada Ltd., Hamilton, Ontario, Canada

Thursday, A.M., September 25, 1975

ENERGY CONVERSION APPLICATIONS

Chemical Vapor Deposition of Silicon on Pyrolytic Carbon, T. L. Chu, H. C. Mollenkopf, H. I. Yoo, and S. S. Chu, Southern Methodist University, and G. F. Wakefield, Texas Instruments Inc., Dallas, Texas, U.S.A.

Progress in Chemical Vapor Deposition of Thin Silicon Films for Solar Energy Conversion, H. S. Gurev and B. O. Seraphin, University of Arizona, Tucson, Arizona, U.S.A.

SnO_2 Film on Silicon Synthesized by CVD Method, O. Tabata, Government Industrial Research Institute, Osaka, Japan

Chemical Vapor Deposition of NbB_2 and TaB_2 Through Heating by Concentration of Solar Radiation, B. Armas, C. Combescure, and F. Trombe, Laboratoire de l'Energie Solaire, Odeillo, Font-Romeu, France

The Preparation of High T_c Nb_3Ge Superconductors by Chemical Vapor Deposition, L. R. Newkirk, F. A. Valencia, and T. C. Wallace, Los Alamos Scientific Laboratory, Los Alamos, New Mexico, U.S.A.

Superconducting V_3Si Coatings, C. Hayman, Fulmer Research Institute, Stoke Poges, Slough, England

Microspherical Laser Targets by CVD, W. J. McCreary, Los Alamos Scientific Laboratory, Los Alamos, New Mexico, U.S.A.

Thursday, P.M.

The Liquid State Hypothesis of Pyrocarbon Deposition from the Gas Phase, K. Koizlik, H. Luhleich, and H. Nickel, Institut fur Reaktorwerkstoffe, Julich, Germany

Factors Affecting the Microstructure of Pyrolytic Carbon Coatings on Nuclear Fuel Particles, J. Guilleray, R. L. R. Lefevre, M. S. T. Price, and J. P. Thomas, Dragon Project Office, A.E.E., Winfrith, Dorchester, Dorset, England

CVD SiC Heating Elements: Alteration of Electrical Resistance by Doping, H. Beutler, S. Oesterle, and K. K. Yee, Sulzer Brothers Limited, Winterthur, Switzerland

MISCELLANEOUS COATINGS

Chemical Vapor Deposition of Silicon Nitride, J. J. Gebhardt, R. A. Tanzilli, and T. A. Harris, General Electric Company, Valley Forge Space Center, Valley Forge, Pennsylvania, U.S.A.

Erosion Resistant Tungsten Coatings for Rocket Nozzle Applications, P. J. Sherwood, Ministry of Defense, Rocket Propulsion Establishment, Westcott, England, C. Hayman and A. Bowry, Fulmer Research Institute, Stoke Poges, Slough, England

The Influence of $MoCl_5$ on the Chemical Vapor Deposition of Tungsten From WF_6, W. Seymour and J. G. Byrne, University of Utah, Salt Lake City, Utah, U.S.A.

Erosion and Heat Transfer Characteristics of Tungsten Coated Steel, R. W. Haskell, Benet Weapons Laboratory, Watervliet Arsenal, Watervliet, New York, U.S.A.

FIFTH INTERNATIONAL CONFERENCE ON CHEMICAL VAPOR DEPOSITION

Stoke Poges, England—September 21-25, 1975

Sponsored by the Electrothermics and Metallurgy Division of
The Electrochemical Society, Inc.

REGISTRATION

Full Name _____

Mailing Address _____

_____

Affiliation and Address _____

_____

Registration fee (includes technical sessions, Mixer, Reception-Buffet, and Conference Proceedings) £35

ACCOMMODATIONS

Name _____

Address _____

_____

Accommodations fee (includes single room and bath for four nights and meals through Thursday lunch) £63

Total Cost (Registration and Accommodations) £98

Please check if appropriate

☐ I will be accompanied by (Name)_____for whom additional accommodations and ladies' program costs will be paid at the Conference.

☐ I will be commuting to the Conference daily and will not require housing. Payment for meals will be arranged at the Conference.

☐ I will be attending Conference only on_____and_____, and ask that appropriate hotel reservations be made, the accommodations fee deposit to be appropriately credited.

Please mail the registration and accommodations forms with a bank draft for £48 (registration fee, ≈ 20 per cent of accommodations fee except for commuters) to: **Conference Registrar, Conference Centre, Fulmer Grange, Stoke Poges, Slough SL2 4QS, Bucks., England,** to arrive by **August 25, 1975.** The balance of the accommodation fee is to be paid upon arrival. It is understood that if a registrant is unable to attend the Conference, the accommodations deposit and registration fee are fully refundable prior to August 25, 1975. After August 25, **no** refund of the accommodations deposit will be made; however, the registration fee is refundable less 20 per cent handling charge plus the cost of the Proceedings if the registrant desires to have the volume mailed to him.

Call for Papers

149th Meeting, Washington, D.C.

May 2-7, 1976

Divisions which have scheduled sessions are listed on the overleaf, along with symposium topics.

1. Symposium Papers.

Authors desiring to contribute papers to a symposium listed on the overleaf should check first with the symposium chairman to ascertain appropriateness of the topic.

2. General Session Papers.

Each of the several Society Divisions which will meet in Washington, D.C., can plan a general session. If your paper does not fit readily into a planned symposium, you should specify "General Session."

3. To Submit a Meeting Paper.

Each author who submits a paper for presentation at a Society Meeting must do three things:

A—Submit one original 75-word abstract of paper to be delivered. Use the form printed on the overleaf or a facsimile. **Deadline for receipt of 75-word abstract is December 1, 1975.**

B—Submit original and one copy of an Extended Abstract of the paper. **Deadline for receipt of Extended Abstract is January 1, 1976.** See (5) below for details.

C—Determine whether the meeting paper is to be submitted to the Society Journal for publication. See (6) below for details.

Send all material to The Electrochemical Society, Inc., P.O. Box 2071, Princeton, N.J. 08540.

Unless the 75-word and required Extended Abstracts are received at Society Headquarters by stated deadlines, the papers will not be considered for inclusion in the program

4. Meeting Paper Acceptance.

Notification of acceptance for meeting presentation, along with scheduled time, will be mailed to authors with general instructions no earlier than two months before the meeting. Those authors who require more prompt notification are requested to submit with their abstracts a self-addressed postal card with full author-title listing on the reverse.

5. Extended Abstract Volume Publication.

All scheduled papers will be published in the EXTENDED ABSTRACTS volume of the meeting. The volume is published by photo-offset directly from typewritten copy submitted by the author. Therefore, special care should be given to the following instructions to insure legibility.

A—Abstracts are to be from 500 to 1000 words in length and should not exceed two pages, single spaced. The abstract should contain to whatever extent practical all significant experimental data to be presented during oral delivery.

B—Abstracts should be typed single spaced on the typing guide forms which are sent to each author after the submission of a short abstract. If it is necessary to use white bond paper, it should be 8½ x 11 inches with 1¼ inch margins on all sides. Submit all copy in black ink. Do not use handwritten corrections.

C—Title of paper should be in capital letters. Author(s) name and affiliation and address should be typed immediately below in capital and lower case letters. Please include zip code in address. It is not necessary to designate paper as "Extended Abstract" or to quote the divisional symposium involved.

D—If figures, tables, or drawings are used, they should follow the body of the text and should not exceed one page. Submit only the important illustrations and avoid use of halftones. Lettering and symbols should be no smaller than ⅛ inch in size. Figure captions should be typed beneath the figure and be no wider than the figure. Table titles should be typed above, and the same width as, the table.

E—Mail original and one copy of the abstract to: The Electrochemical Society, Inc., P.O. Box 2071, Princeton, N.J. 08540, unfolded.

Abstracts exceeding the stipulated length will be returned to author for condensation and retyping.

6. Manuscript Publication in Society Journal.

All meeting papers upon presentation become the property of The Electrochemical Society, Inc. However, presentation incurs no obligation to publish. If publication in Journal is desired, papers should be submitted as promptly as possible in full manuscript form in order to be considered. If publication elsewhere after presentation is desired, written permission from Society Headquarters is required.

Washington, D.C., Meeting Symposia Plans—Spring 1976
May 2-7, 1976

a.) For receipt no later than December 1, 1975, submit a 75-word abstract of the paper to be delivered, on the form overleaf.
b.) For receipt no later than January 1, 1976, submit two copies of an extended abstract, 500-1000 words.
c.) Send all abstracts to The Electrochemical Society, Inc., P.O. Box 2071, Princeton, N.J. 08540. See details on preceding page.

BATTERY AND ELECTRONICS DIVISIONS

Materials for Batteries and Fuel Cells

This symposium is intended, in part, to be a continuation of the "Materials Problems in Batteries and Fuel Cells" symposium conducted at the Toronto Meeting (May 1975). Again, emphasis will be placed on the materials aspects of electrochemical power source components; papers dealing with these general subject areas are solicited. In particular, papers are solicited in the context of the following topics:

1. Battery systems with high energy per unit volume.
2. New button cell materials and technology.
3. Self-discharge processes induced by cell operation.
4. Sealants and sealing technology for portable power sources.
5. High rate charging of portable, ambient temperature batteries.
6. Materials of construction for high temperature power sources.
7. Low weight, portable fuel cells.
8. The low cost fuel cell system.
9. High capacity, electrochemical stand-by power systems.

Several invited papers will be presented, and contributed papers are solicited. Suggestions and inquiries should be directed to the Symposium Co-Chairmen: Raymond J. Jasinski, Texas Instruments Inc., P.O. Box 5936, M/S 147, Dallas, Texas 75222; or John M. Parry, Arthur D. Little, Inc., Acorn Park, Cambridge, Mass. 02140.

CORROSION DIVISION

General Session

The Corrosion Division will schedule a General Session. All aspects of low temperature and high temperature corrosion will be considered. Techniques for the study of corrosion phenomena are of interest. Suggestions and inquiries should be directed to: Roger W. Staehle, Dept. of Metallurgical Engineering, Ohio State University, 116 West 19th Ave., Columbus, Ohio 43210.

CORROSION AND INDUSTRIAL ELECTROLYTIC DIVISIONS

Electrochemistry and Corrosion Processes in Caustic Solutions

Papers are solicited for a symposium session, sponsored by the Corrosion and Industrial Electrolytic Divisions, on Electrochemistry and Corrrosion Processes in Caustic Solutions. Included are topics dealing with:

1. Low temperature and high temperature corrosion studies with or without electrochemical monitoring.
2. Other electrochemical studies, such as reaction rates on various substrates, gas evolution, or other electrolytic breakdown.
3. Caustic solutions, pure fused caustics, or fused caustic mixtures.
4. Batteries.

The purpose of having a symposium covering all aspects of caustic studies is to make all researchers in this general area aware of ongoing research that may not be directly related to their particular realm of endeavor. Therefore, review papers and scientific theoretical papers are welcome as well as papers dealing with engineering studies. A symposium volume of the papers is planned.

Please direct suggestions and inquiries to the Symposium Co-Chairmen: Arun Agrawal, Dept. of Metallurgical Engineering, Ohio State University, 116 West 19th Ave., Columbus, Ohio 43210; or George J. Theus, Babcock & Wilcox Co., Alliance Research Center, 1562 Beeson Rd., Alliance, Ohio 44601; or Anthony Misercola, Hooker Chemical Co., P.O. Box 344, Niagara Falls, N.Y. 14302.

DIELECTRICS AND INSULATION DIVISION

General Session

A General Session is planned at this meeting. Suggestions and inquiries for papers pertaining to dielectrics and insulators should be directed to: B. H. Vromen, IBM Corp., Dept. 265, Bldg. 300-100, Hopewell Junction, N.Y. 12533.

DIELECTRICS AND INSULATION AND ELECTRONICS DIVISIONS

Etching

This symposium is directed toward current advances in electronic materials etching and an exchange of ideas on the theory and practice of etching for pattern definition. Insulators, semiconductors, and metals are included, and gaseous as well as aqueous etching. Contributed papers are solicited on such topics as:

1. Etch rates, kinetics, and reactions mechanisms; autocatalysis, induction periods, and inhibition.
2. Gas-phase etching and etch phenomena, including reactive plasma, ion milling, reactive sputtering, and equipment therefor; etch stops.
3. Aqueous etching including the chemistry and scientific basis of etch formulations, electrochemistry, electrolytic etching, circuit pattern potentials and sensitivity in conductor etching and equipment.
4. Novel etches, alternative etches to meet problems in environmental effects, safety, and chemical shortages.
5. Factors influencing contours and topography of etched patterns, etch step profiles, etch mask adherence, and the associated photoresist technology.
6. Resistant spots, etch residues, and alloy or compound etching.
7. The influence of film deposition techniques on etching characteristics, including orientation dependence.

Each presentation including discussion will be scheduled for 25 min. Longer times can be arranged if requested at the time the short abstract is submitted. A symposium volume may be published if sufficient interest develops. Suggestions and inquiries should be directed to the Symposium Co-Chairmen: Myron J. Rand, Bell Laboratories, 555 Union Blvd., Allentown, Pa. 18103; or Henry G. Hughes, Motorola, SPD, M/S B136, 5005 East McDowell Rd., Phoenix, Ariz. 85008.

DIELECTRICS AND INSULATION, ELECTRONICS, AND ELECTROTHERMICS AND METALLURGY DIVISIONS

Control and Utilization of Defects in Nonmetallic Solids

This jointly sponsored symposium will focus attention on the control and use of defects (point, line, and/or surface defects) in nonmetallic solids. Papers are solicited which involve ceramics and semiconductors used in all types of applications, such as in solid-state electrolytes, dielectric layers, light emitting diodes, photovoltaic devices, sensors, insulators, electrodes, etc. The emphasis will be on the definition of the number and type of defects and their relation to the end use of the material. Papers on the subject of gettering in semiconductor device technology are also solicited. This will include gettering on or in insulators as well as the semiconductor itself.

Suggestions and inquiries should be directed to the Symposium Co-Chairmen: J. Bruce Wagner, Jr., Northwestern University, Materials Research Center, Evanston, Ill. 60201; Donald M. Smyth, Lehigh University, Materials Research Center, Bethlehem, Pa. 18015; or Edward Nicollian, Bell Laboratories, 600 Mountain Ave., Murray Hill, N. J. 07974.

ELECTRONICS DIVISION

Semiconductors

General Session

A broad range of topics in semiconductor device fabrication and materials characterization will be treated in the Semiconductors General Session. Invited tutorial and review papers will be presented in several of the sessions. Original papers are requested on the following topics:

1. Characterization of processed semiconductor material; profiling and surface characterization techniques, process monitors and nondestructive testing, correlation with device characteristics, and cross-correlation between various techniques.
2. Doping of semiconductors; diffusion, ion implantation, segregation phenomena, crystalline defects, and radiation enhanced diffusion.
3. Device isolation and gettering techniques; yield, reliability, and density implications, leakage defects, and gettering models.
4. Compound and amorphous semiconductors; preparation, characterization, and device modeling.
5. Thin-film device technology; characterization, reliability, dual dielectrics, and processing effects on thin-film integrity.
6. Semiconductor processing technology; homo- and hetero-epitaxy, photolithography, metallization, interconnections, passivation, encapsulation, and large scale integration.

Suggestions and inquiries concerning the general sessions will be welcomed by: W. A. Keenan, IBM Corp., Dept. G34, Bldg. 966-1, P.O. Box A, Essex Junction, Vt. 05452.

Luminescence

Surface Properties of Phosphors and Photoconductors

Invited and contributed papers will address the problem of understanding the surface properties of powder, thin-film and single crystal luminescent and photoconductive materials by both physical and chemical methods.

Of particular interest will be which factors in the processing of these materials effect their surface properties and, consequently, their behavior in the systems in which they are used. These factors may include:

1. Methods of synthesis.
2. Treatments.
3. Coatings.

Papers concerning instrumental methods of characterizing surfaces of powders, thin films, and single crystals are also encouraged. These may include LEED, ESCA, ISS, Auger, SEM, and SIMS.

Suggestions and inquiries should be directed to the Symposium Chairman: Peter M. Plaksin, United States Radium Corp., P.O. Box 409, Hackettstown, N.J. 07840.

General Sessions

General sessions will be held around all topics of luminescence in inorganic solids, of which the following are only illustrative examples: phosphor efficiency, cathodo-luminescence mechanisms, energy transfer, thin-film electroluminescence, low voltage phosphors, luminescence in insulators and semiconductors, radioluminescence, radiation damage in phosphors, and performance of phosphors in CRT's display panels and other devices.

Twenty-five minutes will be allotted for each paper including discussions. Review or survey papers of a didactic nature requiring a longer time will also be considered. Suggestions and inquiries for papers should be directed to: Herbert N. Hersh, Zenith Radio Corp., Research Dept., Chicago, Ill. 60639.

General Materials and Processes

General Session

This session covers the general area of materials and processes which are not sufficiently electronic in nature to be included in the semiconductor general session or symposia. Follow-up papers in areas covered in recent symposia of the Electronics Division are encouraged as well as papers in new emerging areas of materials science and technology. Papers are solicited in areas such as magnetic bubbles, integrated optics, energy generation and storage, material preparation, device processing, and other areas of interest.

Suggestions and inquiries should be directed to: T. S. Plaskett, IBM Corp., Thomas J. Watson Research Center, P.O. Box 218, Yorktown Heights, N.Y. 10598.

ELECTRONICS AND ELECTROTHERMICS AND METALLURGY DIVISIONS

International Symposium on Solar Energy

Contributed papers for this symposium are solicited covering materials aspects of solar energy conversion. Topics pertinent to this symposium include: preparation and properties of monolithic and thin-film solar energy cells based on silicon, CdS-Cu S, GaAs, and other III-V and II-IV semiconductors; photogalvanic cells; selective absorbers for solar thermal applications; long term stability of solar hardware; storage for solar energy conversion systems; materials and energy utilization in solar system fabrication; and corrosion in liquid-cooled collectors and ocean thermal gradient systems.

It is planned that the symposium proceedings will be published and available for distribution at the time of the meeting. Final manuscripts will be required from the author by December 15, 1975.

Suggestions and inquiries should be directed to the Symposium Co-Chairmen: Joan B. Berkowitz, Arthur D. Little, Inc., Acorn Park, Cambridge, Mass. 02140; or I. Arnold Lesk, Motorola Inc., Central Research Laboratories, 6143 East Exeter Blvd., Scottsdale, Ariz. 85251.

Seventh International Conference on Electron and Ion Beam Science and Technology

The Seventh International Conference on Electron and Ion Beam in Science and Technology seeks papers which will permit the scheduling of the following sessions:

1. Physics of electron and ion beams and physics of beam material interactions.
2. New developments in the application of electron and ion beams considering both the field of instrumentation and production equipment.
3. Electron beam welding. It is our intention this year to include a special session on numerical control electron beam welding operations and possibly a round table discussion on the subject.
4. Electron and ion beams in microelectronics. Here we are seeking contributions in the following areas: Electron beams in devices and IC manufacture, electron beams in devices and IC production monitoring and control, sputtering processes, and ion implantation considering both systems and applications.
5. The success of our session on x-ray photolithography and the continuation of activities here make it desirable to again schedule a session on the subject.
6. Electron beams in material processing including production, equipment, and properties of electron beam processes materials.
7. Electron beams in recording, information storage, and retrieval.
8. Electron and ion beams in surface analysis.

Suggestions and inquiries should be directed to the Symposium Chairman: Robert Bakish, Bakish Materials Corp., 171 Sherwood Place, Englewood, N.J. 07631.

INDUSTRIAL ELECTROLYTIC DIVISION

Engineering Analysis and Scale-Up of Electrochemical Systems

The purpose of the symposium is to contribute to the understanding of industrial problems which involve current and potential distribution phenomena within electrochemical cells. Of special interest are those topics which emphasize industrial aspects of high-rate processes such as:

1. Scale-up, optimization, and over-all analysis of electrochemical systems.
2. New concepts in electrosynthesis.
3. Methods for early evaluation of electrochemical synthesis and related process routes.
4. Examples of laboratory to pilot plant to full scale case histories.
5. Current and potential distribution phenomena, especially modeling of electrochemical systems.
6. New developments in theoretical methods of analysis.
7. New design concepts for high-rate cells, including flow-through porous electrodes.
8. Effect of electric fields on liquid-liquid extraction processes.

Suggestions and inquiries should be directed to the Symposium Co-Chairmen: Richard Alkire, Dept. of Chemical Engineering, University of Illinois, Urbana, Ill. 61801; or Robert E. Visco, Western Electric Corp., 4500 South Laburnum Ave., Richmond, Va. 23231.

INDUSTRIAL ELECTROLYTIC AND ORGANIC AND BIOLOGICAL ELECTROCHEMISTRY DIVISIONS

Industrial Electro-Organic Processes

This joint symposium (under the guidance of D. N. Goens of the Industrial Electrolytic Division and M. M. Baizer of the Organic and Biological Electrochemistry Division) aims to bring together the electro-organic chemists and the electrochemical engineers to focus on the unique factors involved in development of organic electrochemical reactions. Examples of topics which may be included are:

1. Novel electrode and cell design.
2. Economic considerations.
3. Pilot plant operations (scale-up studies).
4. Potential industrial reactions.

A number of invited papers will be presented and contributed papers are solicited. Suggestions and inquiries should be directed to the Symposium Chairman: John H. Wagenknecht, Monsanto Co., Corporate Research Dept., 800 North Lindbergh Blvd., St. Louis, Mo. 63141.

ORGANIC AND BIOLOGICAL ELECTROCHEMISTRY DIVISION

Electrochemical Oxidations

This symposium reflects the rapidly growing quantity of research on anodic reactions in recent years. Papers relating to all aspects of electro-organic oxidations may be included, e.g.:

1. New reactions.
2. Effects of electrolytes.
3. Effects of solvents.
4. Effects of electrode material.
5. Stereochemistry.
6. Substituent effects.
7. Mechanistic studies by electroanalytical techniques.

A number of invited papers will be presented and contributed papers are solicited. Suggestions and inquiries should be directed to the Symposium Chairman: John H. Wagenknecht, Monsanto Co., Corporate Research Dept., 800 North Lindbergh Blvd., St. Louis, Mo. 63141.

General Session

In addition to the joint symposium with the Industrial Electrolytic Division on Industrial Electro-Organic Processes and the symposium on Electrochemical Oxidations, the Division's program will include a General Session.

Suggestions and inquiries should be directed to: M. Manuel Baizer, Monsanto Co., 800 North Lindbergh Blvd., St. Louis, Mo. 63141.

PHYSICAL ELECTROCHEMISTRY DIVISION

Spectroscopic Methods in Electrochemical Studies

This international symposium is intended to provide a comparison between the various spectroscopic methods which have recently become available to electrochemists as an aid to characterizing electrode surfaces and the electrode-solution interface. Sessions are planned covering the use of rapid scanning spectrometry, laser scattering from electrodes, photoemission techniques, electrode surface reflection spectroscopy, and the various high energy spectroscopies (ESCA, LEED/Auger, mass spectrometry, Mössbauer) in electrochemical studies. Emphasis will also be placed on the application of these methods to heterogeneous kinetic processes as well as homogeneous follow-up chemical events.

Many invited papers will be presented and contributed papers are solicited. Suggestions and inquiries should be sent to the Symposium Chairman: Nicholas Winograd, Dept. of Chemistry, Purdue University, West Lafayette, Ind. 47907.

General Session

In addition to the symposium on Spectroscopic Methods in Electrochemical Studies, the Division's program will include a General Session. Suggestions and inquiries should be directed to: James D. E. McIntyre, Bell Laboratories, 600 Mountain Ave., Murray Hill, N. J. 07974.

NEW TECHNOLOGY SUBCOMMITTEE, CORROSION, ELECTROTHERMICS AND METALLURGY, AND INDUSTRIAL ELECTROLYTIC DIVISIONS

International Symposium on Molten Salts

This symposium seeks to convene the leading active participants in molten salt research and technology from throughout the world to assess the current status of the field and to provide an outlook for the future. Sessions will contain keynote addresses, invited, and contributed papers.

Molten Salt Community-at-Large.—Thermodynamic and transport properties, physical property measurements, structure of highly concentrated ionic liquids, inorganic and organic reactions in molten salts, electroanalytical chemistry, catalysis, hydrous melts, information sources.

Corrosion Division.—Corrosion of metals, alloys, and nonmetallic solids; determination of corrosion product.

Electrothermics and Metallurgy Division.—Applications of mathematical modeling of metal extraction and purification processes in laboratory and plant scale studies; thermodynamics of alloys from galvanic cells.

Industrial Electrolytic Division.—Electrolytic processes for recovering and purifying metals; kinetics and mass transfer phenomena at phase boundaries and electrodes; preparation handling, transfer, and recovery of molten salts; applications in fume abatement, heat transfer, and crystal growth.

Suggestions and inquiries should be directed to the Symposium Co-Chairmen: (General) J. Paul Pemsler, Kennecott Copper Corp., 128 Spring St., Lexington, Mass. 02173; or (Corrosion) K. Nobe, University of California, School of Engineering and Applied Science, Los Angeles, Calif. 90024; or (Electrothermics and Metallurgy) D. R. Morris, Dept. of Chemical Engineering, University of New Brunswick, Fredericton, N.B., Canada; or (Industrial Electrolytic) N. E. Richards, Reynolds Metal Co., P.O. Box 191, Sheffield, Ala. 35661; or (Molten Salt Community-at-Large) J. Braunstein, Oak Ridge National Laboratory, Chemistry Div., P.O. Box X, Oak Ridge, Tenn. 37830.

NEW TECHNOLOGY SUBCOMMITTEE AND DIELECTRICS AND INSULATION AND ELECTRONICS DIVISIONS

Inorganic Dielectric Materials for Display and Storage Devices

It is intended to cover under this general title a number of sessions dealing with related materials, so that parallel sessions will be avoided. The individual sessions are as follows:

1. Chromic Materials.—Papers are solicited on the preparation and characterization of photochromic, cathodochromic, electrochromic, and chromic energy conversion materials. Papers should be sent to: P. N. Yocom, RCA Laboratories, Princeton, N.J. 08540.

2. Ceramic and Glass Materials for Display Devices.—This symposium will be devoted to the study of nonmetallic inorganic materials employed in electronic display devices and their packaging. Emphasis will be placed on the dielectric properties of such materials. Of particular interest are conventionally formulated glasses and ceramics now widely used in the electronics industry as dielectric and sealing materials. Suggested topics are: electric properties of multilayer ceramic structures, mechanism of conduction in dielectric materials in display devices, dielectric properties as a function of composition of glasses, characterization of dielectric films in display devices, effect of hostile environment on dielectric materials and seals, and surface and interfacial properties of dielectric layers with substrates or metallic conductors.

Keynote papers from invited speakers will be presented and contributed papers are solicited. Suggestions and inquiries should be directed to the appropriate chairman. Those papers primarily concerned with the chemical aspects of dielectric materials should go to: R. G. Frieser, IBM Corp., East Fishkill Facility, Dept. 365, Bldg. 330-J15, Hopewell Junction, N.Y. 12533. Papers which have as their main interest the physical aspects of dielectrics should be sent to: L. D. Locker, Airpax Electronics, Corporate Offices, P.O. Box 8488, Fort Lauderdale, Fla. 33310.

3. Dielectrics for Image and Hologram Storage and Display.—Papers are solicited on hologram storage in lithium niobate, SBN, and similar materials; image storage and display using PLZT, Pockel's effect readout devices, and on related effects and devices. It is intended to include papers on the basic physical processes and on materials' properties, as well as papers on specific devices or potential device applications. Inquiries and suggestions should be directed to: Lawrence Young, Dept. of Electrical Engineering, University of British Columbia, Vancouver B.C., Canada. Papers on PLZT materials, their characterization and performance, should be submitted to: C. E. Land, Sandia Laboratories, Div. 5133, Albuquerque, N.M. 87115.

75-Word Abstract Form

(Deadline for receipt—December 1, 1975)

WASHINGTON, D.C., MEETING—MAY 2-7, 1976

Submit to: **The Electrochemical Society, Inc.**
P.O. Box 2071, Princeton, N.J. 08540

Schedule for ..... of .....
Symposium **ECS Division**

Abstract No. .....
(do not write in this space)

(Title of paper) .....

.....

(Authors) (Underline name of author presenting paper) .....

.....

(Business Affiliation and Address) .....

.....

.....
(ZIP Code) (Tel. No.)

(Type abstract in this area—double spaced.)

Do you require any audiovisual equipment?
☐ 35 mm (2 x 2 in.) slide projector
☐ vugraph
☐ other (specify)
Is a full length paper on this work to be submitted for Society Journal publication?
☐ Yes ☐ No

Papers presented before a Society technical meeting become the property of the Society and may not be published elsewhere without written permission of the Society. Papers presented at Society technical meetings must be authored by a member or sponsored by an active member.

.....
Insert name of Society member author or sponsor

THE ELECTROCHEMICAL SOCIETY PATRON MEMBERS

Bell Telephone Laboratories, Inc.
Murray Hill, N.J.

Dow Chemical Co.
Inorganic Chemicals Dept., Midland, Mich.

General Electric Co.
Battery Business Section, Gainesville, Fla.
Chemical Laboratory, Knolls Atomic Power Laboratory, Schenectady, N.Y.
Electronic Capacitor & Battery Dept., Irmo, S.C.
Lamp Div., Cleveland, Ohio
Materials & Process Laboratory, Large Steam Turbine-Generator Dept., Schenectady, N.Y.
Research and Development Center, Physical Chemistry Laboratory, Solid State Physics Laboratory, Schenectady, N.Y.
Semiconductor Products Dept., Syracuse, N.Y.

The International Nickel Co., Inc.
New York, N.Y.

Olin Corporation
Chemicals Div., Research Dept., New Haven, Conn.

Philips Research Laboratories
Eindhoven, Holland

Union Carbide Corp.
Battery Products Div., Corporate Research Dept., New York, N.Y.

Westinghouse Electric Corp.
Electronic Tube Div., Elmira, N.Y.
Lamp Div., Bloomfield, N.J.
Semiconductor Div., Youngwood, Pa.
Research Laboratories, Pittsburgh, Pa.
K. W. Battery Co., Westinghouse Subsidiary, Skokie, Ill.

THE ELECTROCHEMICAL SOCIETY SUSTAINING MEMBERS

Airco Speer Carbon-Graphite
St. Marys, Pa.

Allied Chemical Corp.
Industrial Chemicals Division
Solvay, N.Y.

Aluminum Co. of America
New Kensington, Pa.

Aluminum Co. of Canada, Ltd.
Montreal, P.Q., Canada

American Gas & Chemicals, Inc.
New York, N.Y.

American Metal Climax, Inc.
New York, N.Y.

American Smelting and Refining Co.
South Plainfield, N.J.

AMP Incorporated
Harrisburg, Pa.

Analog Devices, Inc.
Norwood, Mass.

Applied Materials, Inc.
Santa Clara, Calif.

BASF Wyandotte Corporation
Wyandotte, Mich.

Beckman Instruments, Inc.
Fullerton, Calif.

Bell-Northern Research
Ottawa, Ont., Canada

Bethlehem Steel Corp.
Bethlehem, Pa.

Boeing Co.
Seattle, Wash.

The Borg-Warner Corp.
Roy C. Ingersoll Research Center
Des Plaines, Ill.

Brown, Boveri & Co., Ltd.
Research Center
Baden, Switzerland

Canadian Industries Ltd.
Montreal, P.Q., Canada

Carborundum Co.
Niagara Falls, N.Y.

Cominco Ltd.
Trail, B.C., Canada

Corning Glass Works
Corning, N.Y.

Crawford & Russell Inc.
Stamford, Conn.

Diamond Shamrock Corp.
Painesville, Ohio

E. I. du Pont de Nemours and Co.
Central Research Department
Wilmington, Del.

Eastman Kodak Co.
Rochester, N. Y.

Electrode Corporation
Chardon, Ohio

Eltra Corp.
Prestolite Div., Toledo, Ohio
C&D Batteries, Conshohocken, Pa.

Engelhard Minerals & Chemicals Corp.
Murray Hill, N.J.

ESB Inc.
Philadelphia, Pa. (2 memberships)

Esso Research and Engineering Co.
Engineering Technology Div.
Florham Park, N.J.

SUSTAINING MEMBERS (CONTINUED)

Ever Ready Co. (Holdings) Ltd.
Whetstone, London, England

Exmet Corporation
Bridgeport, Conn.

Fairchild Camera & Instrument Corp.
Research and Development Laboratory
Palo Alto, Calif.

Falconbridge Nickel Mines Ltd.
Thornhill, Ont., Canada

FMC Corp.
Inorganic Chemicals Div.
Buffalo, N.Y.

Foote Mineral Co.
Exton, Pa.

Ford Motor Co.
Dearborn, Mich.

GAF Corporation
Inorganic Chemicals Department
Glens Falls, N.Y.

General Motors Corporation
Delco Electronics Div., Kokomo, Ind.
Delco-Remy Div., Anderson, Ind.
Research Laboratories Div., Warren, Mich.

Globe-Union, Inc.
Milwaukee, Wisc.

GTE Laboratories
Waltham, Mass.

B. F. Goodrich Chemical Co.
Cleveland, Ohio

Gould Inc.
Gould Laboratories, Rolling Meadows, Ill.
Gould Laboratories—Energy Research, St. Paul, Minn.
Gould Laboratories—Materials Research, Cleveland, Ohio

Great Lakes Carbon Corp.
New York, N.Y.

Harshaw Chemical Co.
Cleveland, Ohio (2 memberships)

Hill Cross Co., Inc.
West New York, N.J.

Honeywell, Inc.
Power Sources Center
Horsham, Pa.

Hooker Chemical Corp.
Niagara Falls, N.Y. (2 memberships)

HP Associates
Palo Alto, Calif.

Hughes Research Laboratories
Div. of Hughes Aircraft Co.
Malibu, Calif.

International Business Machines Corp.
New York, N.Y.

Kaiser Aluminum & Chemical Corp.
Pleasanton, Ca.

Kawecki Berylco Industries, Inc.
Boyertown, Pa.

Kennecott Copper Corp.
New York, N.Y.

Kerr-McGee Corporation
Technical Center
Oklahoma City, Okla.

Arthur D. Little, Inc.
Cambridge, Mass.

Mallory Battery Company
Tarrytown, N.Y. (2 memberships)

Marathon Battery Co.
Cold Spring, N.Y.

The Marstolin Group
Hamilton, Bermuda

Matsushita Electric Industrial Co., Ltd.
Osaka, Japan

Metallurgical Research Center of Iran
Tehran, Iran

Microwave Associates, Inc.
Burlington, Mass.

Molybdenum Corporation of America
New York, N.Y.

Monsanto Company
St. Louis, Mo.

Motorola Inc.
Phoenix, Ariz.

M&T Chemicals Inc.
Detroit, Mich.

National Steel Corp.
Weirton, W. Va.

NL Industries, Inc.
New York, N.Y.

OKI Electric Industry Co., Ltd.
Tokyo, Japan

Olin Corporation
Metals Research Laboratories
New Haven, Conn.

Owens-Illinois Glass Co.
Toledo, Ohio

Phelps Dodge Refining Corp.
Maspeth, N.Y.

Philips Laboratories. Inc.
Briarcliff Manor, N.Y.

PPG Industries, Inc.
Chemical Div.
Pittsburgh, Pa.

Princeton Applied Research Corp.
Princeton, N.J.

RCA Corporation
Electronic Components and Devices
Lancaster, Pa.

Republic Foil
National Aluminum
A Unit of
National Steel Corp.
Danbury, Conn.

Reynolds Metals Co.
Reduction Research Div.
Sheffield, Ala.

Rockwell International
El Segundo, Calif.

SAFT America, Inc.
Metuchen, N.J.

Signetics Corp.
Sunnyvale, Ca.

Sobin Chemical Co.
Orrington, Maine

Sprague Electric Co.
North Adams, Mass.

Stackpole Carbon Co.
St. Marys, Pa.

Standard Telecommunication Laboratories Ltd.
Essex, England

Stauffer Chemical Co.
Dobbs Ferry, N.Y.

Teletype Corp.
Skokie, Ill.

Texas Instruments Inc.
Attleboro, Mass.
Dallas, Texas

Tokyo Shibaura Electric Co., Ltd.
Toshiba Research and Development Center
Kawasaki, Japan

Udylite Corp.
Detroit, Mich. (4 memberships)

United States Steel Corp.
Research Laboratory
Monroeville, Pa.

Varian Associates
Palo Alto, Calif.

Wacker Chemitronic
Burghausen, Germany

Xerox Corporation
Rochester, N.Y.

Yardney Electric Division
Pawcatuck, Conn.

Zenith Radio Corp.
Chicago, Ill.

26.11.2019